2021

The tectonic evolution of the Dras-Nindam Terrane, Ladakh Himalaya, NW India

Jessica Margaret June Walsh

UNIVERSITY
OF WOLLONGONG
AUSTRALIA

THE TECTONIC EVOLUTION OF THE DRAS-NINDAM TERRANE, LADAKH HIMALAYA, NW INDIA

Jessica Margaret June Walsh

(she/her)

Supervisors:

Dr Solomon Buckman and Prof. Allen Nutman

This thesis is presented as part of the requirement for the conferral of the degree:

Doctor of Philosophy

University of Wollongong

School of Earth, Atmospheric and Life Sciences

February 2021

Certification

I, *Jessica Margaret June Walsh*, declare that this thesis submitted in fulfilment of the requirements for the conferral of the degree *Doctor of Philosophy*, from the University of Wollongong, is wholly my own work unless otherwise referenced or acknowledged. This document has not been submitted for qualifications at any other academic institution. This research has been conducted with the support of the Australian Government Research Training Program Scholarship.

_____

Jessica Margaret June Walsh

5th February 2021

Abstract

Unravelling the tectonic processes responsible for the uplift of the Himalaya requires in-depth investigation of individual terranes caught up along the Indus Suture Zone that separates the continents of India and Eurasia. The Himalayan Orogen represent the complex amalgamation of, not only the two colliding continents with one plate subducting underneath the other, but also fragments of oceanic crust (ophiolites) and intraoceanic arcs that developed within the vast expanse of the now extinct Neotethyan Ocean. The aim of this thesis was to resolve the tectonic evolution of the Dras-Nindam terrane in the Ladakh Himalaya using standard geological mapping, geochemistry and sophisticated zircon U-Pb geochronology. The Dras-Nindam terrane is sandwiched between Indian and Eurasian continental crust along the Indus Suture Zone in the Ladakh Himalaya, NW India. This tectonostratigraphic unit includes basaltic to andesitic rocks of the Dras Volcanics and associated deep marine, volcaniclastic rocks of the Nindam Formation. Debates exist as to whether this terrane developed as a marginal forearc basin to the larger Ladakh Arc which developed along the southern margin of Eurasia above a single subduction zone or whether it represents a juvenile, intraoceanic island arc that developed above a separate subduction zone much further south within the Neotethyan Ocean. A lack of data relating to the provenance and age-range of the Dras-Nindam terrane further complicates hypotheses related to its early development. Its collision with either India or Eurasia prior to final continent-continent collision was also unresolved, leading to multiple conflicting tectonic reconstructions that required further testing. The increased accessibility to zircon U-Pb dating and easier access to key field localities has provided an opportunity to better constrain the tectonic evolution of a key unit along the Indus Suture Zone that is integral to developing more accurate reconstructions of the world's largest mountain range.

The overarching aim of this investigation is to test competing hypotheses regarding the tectonic evolution of the Dras-Nindam terrane that occurs along the Indus Suture Zone of the India-Eurasia collision in the Ladakh Himalaya, NW India. This project addresses key tectonic questions by providing robust, new observations, descriptions and geochronology of the Dras-Nindam terrane in Ladakh, using an integrated approach including field relations, petrography, whole rock geochemistry and zircon U-Pb geochronology. The objectives of this investigation are, (i) to determine the maximum age of deposition and provenance of the forearc basin Nindam Formation using detrital zircon U-Pb geochronology to ascertain whether the Dras Arc (a component of the Dras-Nindam terrane) initiated in an intraoceanic setting or was continental-related; (ii) to constrain the timing of initiation and early evolution of the Dras Arc using zircon U-Pb geochronology of extrusive (Dras Volcanics) and intrusive (Kargil Intrusives) magmatic

episodes, and; (iii) to establish the youngest magmatic phases within the Dras Arc in order to constrain the maximum age of arc-continent collision. The results of this investigation demonstrate that the Dras and Spong (a component of the Spongtang Ophiolite-Spong Arc complex) arcs developed together as an intraoceanic arc system, that initiated in the Neotethyan Ocean just outboard of the northern margin of India during the Late Jurassic. Some of these earliest low-Mg adakitic felsic volcanic rocks are derived from the partial melting of basaltic ocean crust during incipient stages of arc development. The deep-marine volcaniclastic rocks of the Nindam Formation were deposited in a forearc basin setting with little to no influence from continental rocks and more akin to deposition in an intra-oceanic, island arc setting similar to other Neotethyan ophiolites along the Indus-Yarlung-Tsangpo Suture. Early Eocene (~53 Ma) zircon U-Pb ages obtained from gabbroic blocks within the Sapi-Shergol mélange at the southern thrust contact with the Indian Zanskar Supergroup relate to the youngest phase of magmatism within the Dras Arc. Thus, the Dras Arc was a long-lived, island arc complex spanning some ~108 m.y., between initiation around ~160 Ma, peak arc magmatism between 125-84 Ma and final arc magmatism at ~53 Ma, before the onset of stage 1, or 'soft' arc-continent collision at ~50 Ma. Accretion of the Dras Arc onto the northern Indian continental margin extinguished any further arc magmatism and led to partial continental subduction and eclogite metamorphism between 50-47 Ma at Tso Morari. The Dras Arc is geochemically and geochronologically distinct from the continental Ladakh Arc that was active along the southern margin of Eurasia. The Ladakh Arc remained active until at least ~41 Ma, before it collided with the India-Dras margin resulting in terminal continental collision or stage 2 'hard' collision at about the Eocene-Oligocene boundary. This final phase of continental collision led to the uplift of the Himalaya which continues today.

Acknowledgements

I acknowledge the Traditional Custodians of the lands on which the University of Wollongong is situated. I pay my respects to Aboriginal Elders past, present and emerging, who are the knowledge holders and teachers. I acknowledge their continued spiritual and cultural connection to Country. I also pay respect to the knowledge embedded forever within the Aboriginal Custodianship of Country.

This research would not have been possible without the guidance and encouragement of many people. I would first like to thank my supervisor Dr Solomon Buckman, whose has been an advisor, mentor and champion of myself and the work of this thesis. Solomon, thank you for introducing me to the wonderous geology of the Ladakh Himalaya, as well as teaching me to always see the 'bigger picture'. I could not be more grateful for your support and encouragement throughout the publishing process and the candidature more generally. You go to extraordinary lengths to foster and promote your students, for which I am very thankful.

I also owe an enormous amount to my co-supervisor Professor Allen Nutman, whose expertise in 'SHRIMP-ology' and all things zircon was invaluable in formulating the methodology and the broader scope of this research. Allen, thank you for your insightful feedback, which pushed to sharpen my thinking and brought this research to a higher level.

A special thanks to my collaborator and coauthor Dr Renjie Zhou (The University of Queensland) for LA-ICP-MS analyses and data reduction of zircon U-Pb geochronologic data. Renjie, thank you for your patience and answering many questions.

Much of the work presented in this thesis would not have been possible without the assistance of the technical and administrative staff at the School of Earth, Atmospheric and Life Sciences (SEALS). In particular, José Abrantes is thanked for petrographic and geochemical sample preparation, and Thomas McMahon is thanked for assistance with cathodoluminescence (CL) imaging. I would also like to thank the academic staff members from SEALS for discussions, advice and general hallway banter. Of these people, I would specifically like to thank (listed alphabetically, not by the calibre of advice or jokes): Alex Mackay, Brian Jones, Chris Fergusson, Nicolas Flament and Llyod White.

Many thanks go to field-guide extraordinaire Jigmet Punchok. Jigmet, thank you for guidance and logistical support in the Ladakh Himalaya. Thank you also to all those who were involved organising fieldwork in India.

To my research group ('The Geologists Conglomerate'), thank you for your valuable guidance and stimulating discussions, as well as happy distractions. Thank you to Wanchese Saktura for always being incredibly supportive and kind. From the early beginnings of stumbling over eclogites in China, to scaling mountains in India, I couldn't be more grateful for your friendship over these past few years. Thank you to both Ryan Manton and Qing Zhang for fun fieldwork campaigns at your respective study sites, but also your wise counsel and sympathetic ears.

I was fortunate to demonstrate for many Earth Science subjects throughout my candidature. I am forever grateful for these teaching opportunities. I would especially like to thank Dominique Tanner and Amy Dougherty for providing me with many tools and resources. Dominique (Dom) and Amy, thank you both for sharing your wealth of knowledge.

Thank you to all the students from SEALS, friends, cycling crew and D&D campaigners who provided a constant reminder that there is more to life then rocks from a foreign land (although, that depends on how strictly the term *foreign* is applied, as some of these rocks have Gondwanan provenance).

An immense thank you to my family from the 'Town that Built Sydney'. I have my parents, Rhonda and Stephen 'Potter' Walsh, and brother Isaac Walsh to thank for teaching me how to work hard, telling me when it's time to sit back and smell the roses, and for keeping me grounded. Thank you for your constant encouragement and supporting every milestone.

Finally, to Katie Newton. Thank you for your immeasurable patience, proofreading and unconditional love and support. I could not be more grateful to have you by my side. Onto the next adventure.

Table of Contents

List of Figures

Chapter One: Introduction

Chapter Two: Material and Methods

Chapter Three: Literature Review

Chapter Four: Age and provenance of the Nindam Formation, Ladakh, NW Himalaya: Evolution of the intraoceanic Dras Arc before collision with India

Chapter Four: Supporting Information

Chapter Five: The significance of Upper Jurassic felsic volcanic rocks within the incipient, intraoceanic Dras Arc, Ladakh, NW Himalaya

Chapter Five: Supporting Information

Chapter Six: Youngest magmatic age (Early Eocene) from the Neotethyan intraoceanic Dras Arc, Ladakh Himalaya, NW India

Chapter Six: Supporting Information

Chapter Seven: Discussion

Chapter Eight: Conclusion

List of Tables

Chapter Two: Materials and methods

Chapter Four: Age and provenance of the Nindam Formation, Ladakh, NW Himalaya: Evolution of the intraoceanic Dras Arc before collision with India

Chapter Four: Supporting Information

Chapter Five: The significance of Upper Jurassic felsic volcanic rocks within the incipient, intraoceanic Dras Arc, Ladakh, NW Himalaya

Chapter Five: Supporting Information

Chapter Six: Youngest magmatic age (Early Eocene) from the Neotethyan intraoceanic Dras Arc, Ladakh Himalaya, NW India

Chapter Six: Supporting Information

List of Publications during Candidature

Peer-reviewed publications

Walsh, J. M., Buckman, S., & Nutman, A.P (*in preparation*). Youngest magmatic age (Early Eocene) from the Neotethyan intraoceanic Dras Arc, Ladakh Himalaya, NW India.

Walsh, J. M., Buckman, S., Nutman, A. P., & Zhou, R. (2020). The significance of Upper Jurassic felsic volcanic rocks within the incipient, intraoceanic Dras Arc, Ladakh, NW Himalaya. *Gondwana Research*, *90*, 199-219. https://doi.org/10.1016/j.gr.2020.11.007 [Google Scholar].

Walsh, J. M., Buckman, S., Nutman, A. P., & Zhou, R. (2019). Age and provenance of the Nindam Formation, Ladakh, NW Himalaya: Evolution of the intraoceanic Dras Arc before collision with India. *Tectonics*, Special Edition: "Collisional orogenic systems as recorders of collisions between arc and continents". *38*(8), 3070-3096. https://doi.org/10.1029/2019TC005494 [7 citations, as of 5th February 2021; Google Scholar].

Buckman, S., Aitchison, J. C., Nutman, A. P., Bennett, V. C., Saktura, W. M., **Walsh, J. M**., Kachovich, S., & Hidaka, H. (2018). The Spongtang Massif in Ladakh, NW Himalaya: An Early Cretaceous record of spontaneous, intraoceanic subduction initiation in the Neotethys. *Gondwana Research*, *63*, 226-249. https://doi.org/10.1016/j.gr.2018.07.003 [21 citations, as of 5th February 2021; Google Scholar].

Conference abstracts (see Appendix A for full details of conference abstracts and proceedings)

Walsh, J. M., Buckman, S., Nutman, A. P., & Zhou, R. (2021). Unravelling the Himalaya: One intraoceanic arc at a time. *Australian Earth Sciences Convention 2021*.

Walsh, J. M., Buckman, S., Nutman, A. P., & Zhou, R. (2020). Upper Jurassic adakitic felsic volcanism within the incipient, intraoceanic Dras Arc, Ladakh, NW Himalaya. *American Geophysical Union (AGU) Fall Meeting, 2020*, T029-06.

Walsh, J. M., Buckman, S., Nutman, A. P., & Zhou, R. (2019). Age and provenance of the Dras Arc, Ladakh, NW Himalaya: A detrital zircon record of the Nindam Formation. *European Geosciences Union (EGU) General Assembly, 2019*, EGU2019-413.

Walsh, J. M., Buckman, S., Nutman, A. P., & Zhou, R. (2019). Evolution of the intraoceanic Dras Arc before collision with India. *Dorothy Hill Women in Earth Sciences Symposium (DHS), 2019*, DHS19-27.

Buckman, S., Aitchison, J. C., Nutman, A. P., Bennett, V. C., **Walsh, J. M. J**., Saktura, W. M., Kachovich, S., & Langlois, L. (2017). The Age, Origin and Collision of the Spongtang Ophiolite, Ladakh Himalaya. *American Geophysical Union (AGU) Fall Meeting, 2017*, T43E-02.

Walsh, J. M., Buckman, S., & Nutman, A. P. (2017). Tectonic evolution of the Dras-Nindam terrane along the Indus Suture Zone, Ladakh Himalaya, NW India. *Dorothy Hill Women in Earth Sciences Symposium (DHS), 2017*, DHS17-12.

Chapter One: Introduction

1.1 Background

The Himalaya are the largest active collisional orogen on Earth. As such, it provides an ideal natural laboratory to study tectonic and mountain building processes (Aitchison et al., 2007a; Allègre et al., 1984; Yin and Harrison, 2000 and references therein). The Himalaya represent an ongoing collision between the Indian and Eurasian continents, and Mesozoic-Cenozoic deformed supracrustal sequences of diverse provenance now exposed along the suture zone record the closure of the vast (up to 2,500 km wide) Neotethyan Ocean (Rowley, 1996). This dramatic geological feature, along with its western continuation through Iran and Iraq into the European Alps and eastwards into southeast Asia, is the textbook example of continental collision. However, collision zones are complex geological regions because they are not necessarily restricted to the simplistic collision of two continents but may include the accretion of numerous intraoceanic terranes (e.g., ophiolites, island arcs, accretionary complexes, or seamounts) prior to final continental collision (Aitchison et al., 2003; Dewey and Bird, 1970; Hébert et al., 2012).

For this reason, important aspects of the Himalaya remain unresolved, including the timing of "final" (i.e., terminal) continent-continent collision and the nature of earlier "soft" collisions (i.e., an arc with a continental margin before final ocean closure) versus the final "hard" collision. Estimations of the timing of collision first emerged soon after the acceptance of the plate tectonic theory (Figure **1.1**). A pre- middle Eocene age (~56-40 Ma) was proposed based on the age of the youngest marine rocks in the Himalaya (Chang and Zheng, 1973; Powell and Conaghan, 1973). Paleomagnetic data obtained from the Indian Ocean led Molnar and Tapponnier (1975) to suggest a slow-down of the Indian continent at ~40 Ma, which they interpreted as the onset of continental collision. They also provided further constraints to the timing of collision by indicating that the presence of Upper Cretaceous exotic blocks in the Indus-Yarlung-Tsangpo Suture (IYTS) zone associated mélange meant that the Neotethyan Ocean was still forming at ~70 Ma, and the presence of early Eocene marine strata along the suture meant collision must be post- early Eocene. The existing "consensus" age of 55 Ma for continent-continent collision was initially proposed by Patriat and Achache (1984) on the basis of paleomagnetic drift history reconstructions, and was subsequently adopted as the most likely collision age by numerous workers (e.g., Gansser, 1991; Garzanti et al., 1987; Rowley, 1996; see also review by Hu et al., 2016a). Searle et al. (1987) pointed out that calc-alkaline I-type magmatism within the Gangdese Batholith should stop at the commencement of continental collision and favoured a younger collision timing of 50-40 Ma, based on radiometric ages obtained on the youngest Gangdese

Batholith granites, and the switch from marine to terrestrial sedimentation. Rowley (1996, 1998) suggested that collision must be diachronous, starting at ~52 Ma in the west and becoming younger to the east, based on the age of youngest marine strata. An extensive literature review by Yin and Harrison (2000) reverted to the possibility of a late Cretaceous (~70 Ma) collision which was taken up by Ding et al. (2005) who suggested that the northern extent of "Greater India" was some 1300 km broader than previously thought to account for paleomagnetic data that has northern India situated at equatorial latitudes, while southern Eurasia is at about 20°N when collision was meant to be occurring. Aitchison et al. (2007a) showed that the extent of the northern margin of India is actually well constrained by the Wallaby-Zenith Fracture Zone in Western Australia. This negates the possibility of a "Greater India", and paleomagnetic constraints of India with respect to Tibet show that collision at 55 Ma was impossible (Acton, 1999). Instead, Aitchison et al. (2007a) used provenance studies of a distinct conglomerate (Liuqu conglomerate; see Davis et al., 2002; Leary et al., 2016; Li et al., 2015) to suggest an early collision (pre-final convergence of India and Eurasia) between India and an ophiolite-island arc terrane (Dazhuqu terrane) at 55 Ma, which was followed by continent-continent collision much later at 34 Ma and marked by deposition of the post-collisional, lower Miocene Gangrinboche conglomerates (Aitchison et al., 2002).

For such a hotly debated topic there remains a paucity of data for key lithologies within and along the suture zone between India and Eurasia. Given the advances in zircon geochronology and its application to provenance studies, there exists an opportunity to provide high-quality data for poorly constrained units such as the Dras-Nindam terrane in Ladakh (Figure **1.2**), located along the Indus Suture Zone (Gehrels et al., 2011; Thomas, 2011). Collectively, the Dras-Nindam terrane consists predominantly of basaltic-andesites (Dras Volcanics) in the west, which transitions to a volcaniclastic sequence to the east (Nindam Formation). The complex is generally assumed to have developed in an island arc setting in the Neotethyan Ocean, before colliding with India or Eurasia prior to continental collision (Robertson and Degnan, 1994). Investigating this complex is important as it will contribute to knowledge on the development of the Himalaya Orogen, while also contributing to existing models on the lifecycle of intraoceanic arcs, including their collision and accretion onto continental margins. Additionally, extra work can be undertaken to test previous zircon results of key lithologies such as the Kargil Intrusives, which intrude the Dras Volcanics. This is important as the intrusive suite was dated in the early 1980's (Honegger et al., 1982; Schärer et al., 1984a) before cathodoluminescence (CL) imaging of zircons was undertaken to identify older inherited cores from younger magmatic rims that may influence age determination.

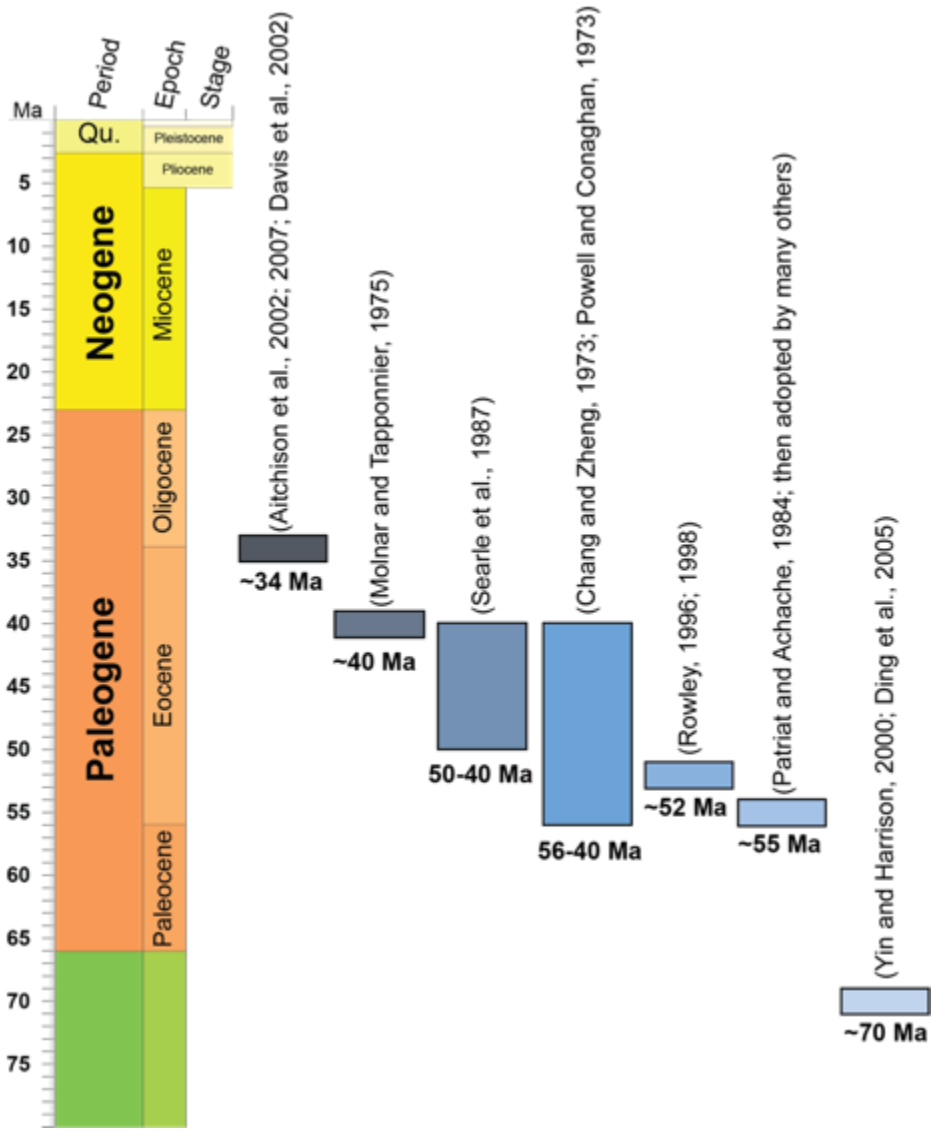

Figure 1.1: Timeline demonstrating differing estimations of the timing of continental collision between India and Eurasia (Aitchison et al., 2007a; Aitchison et al., 2002; Chang and Zheng, 1973; Davis et al., 2002; Ding et al., 2005; Molnar and Tapponnier, 1975; Patriat and Achache, 1984; Powell and Conaghan, 1973; Rowley, 1996, 1998; Searle et al., 1987; Yin and Harrison, 2000). Note, the common consensus age of 55 Ma has been adopted by many workers (e.g., Gansser, 1991; Grazanti et al., 1987; Hu et al., 2016a).

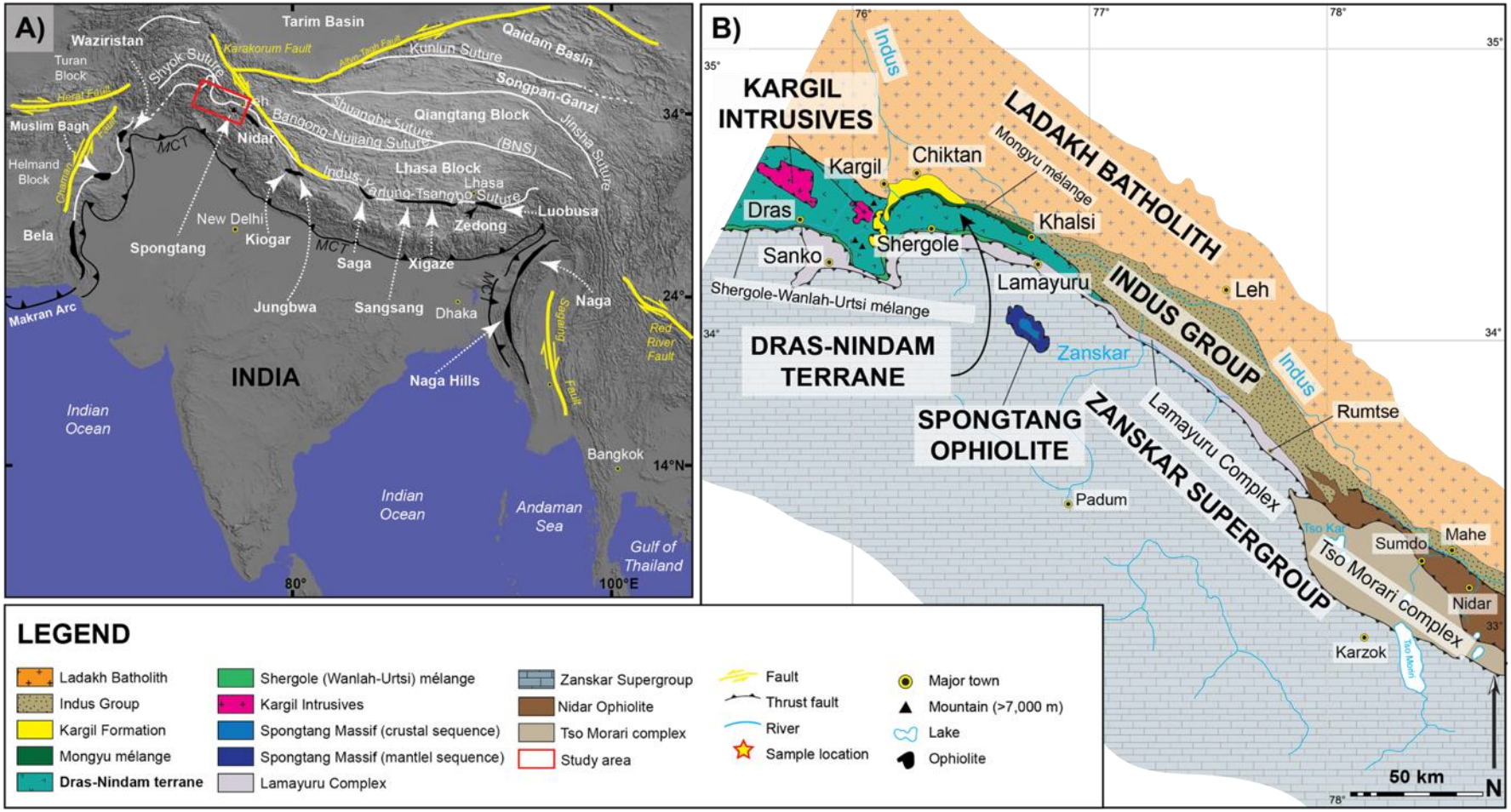

Figure 1.2: Main geological units of the Indus Suture Zone, Ladakh Himalaya, NW India. **A)** Geographic map indicating the location of the study site (red rectangle). Map modified from Buckman et al. (2018). DEM sourced from Global Mapper software (Global Mapper, 2009); **B)** Geological units of the study area (after Bhattacharya et al., 2020; Corfield et al., 2000; Reuber, 1987; Walsh et al., 2019; 2020).

1.2 Key issues

Continental collisions involve the colliding and compression of two (or more) buoyant terranes, brought together by the interplay of subduction and accretion. The suture zone occurring between these terranes often contain fragments of both sides of the collision. The terranes involved in continental collisions are not exclusively other continents and micro-continents, and can vary in origin, composition, and scale. For example, other components could include seamounts, intraoceanic arcs and ophiolites which may have accreted onto either side of the convergent boundary, before final continent-continent collision. Additionally, continental margins can already have very complex histories even before orogenesis takes place, therefore determining the timing of initiation of continent-continent collision can prove to be difficult and is often controversial (Condie, 2015; Dewey and Şengör, 1979; Montes et al., 2019; Song et al., 2015). Commonly used lines of evidence to determine the initiation of continental collision or to 'date' continent-continent collision include paleo-latitudinal overlaps between tectonic blocks across the suture (e.g., Li et al., 2017; Ma et al., 2016; Parsons et al., 2020; van Hinsbergen et al., 2019) the first arrival of detritus of one block on the other (e.g., Garzanti, 2019; Garzanti et al., 1996; Zhang et al., 2021), the onset of shortening and metamorphism of particularly the down-going plate (Guillot et al., 2003; White et al., 2001), and/or the end of marine sedimentation in the suture zone (Green et al., 2008; Searle et al., 1987). Considerable emphasis has been placed on the recognition of accreted (intraoceanic) arc complexes in orogenic belts, as these can potentially be used for the along-strike correlation of tectono-stratigraphic terranes, and form a key element of geodynamic and paleogeographic reconstructions. The work presented here aims to describe and characterise the Neotethyan intraoceanic Dras Arc and to place this tectonic feature in the broader context of the continent-continent collision between India and Eurasia.

There is general consensus that the basalts, andesites and volcaniclastic rocks of the Dras arc are of island arc affinity (Fuchs, 1982; Honegger et al., 1982) and that these volcanic rocks are overlain by deep marine volcaniclastic turbidites, cherts, siltstones and tuffs of the Nindam Formation (Clift et al., 2000; Robertson and Degnan, 1994). However, the provenance and age range of the Dras-Nindam terrane is not well constrained and thus prior to this study its initiation as a juvenile, intraoceanic island arc or a marginal forearc basin to southern Eurasia was contentious. Its collision with either Eurasia or India before final continent-continent collision was also unresolved, leading to multiple, conflicting tectonic reconstructions that prompted further testing (Brookfield and Reynolds, 1981; Buckman et al., 2018; Clift et al., 2000; Clift et al., 2002a; Clift et al., 2002b; Corfield et al., 2001; Henderson et al., 2010; Henderson et al., 2011; Klootwijk et al., 1979; Reuber, 1989; Robertson and Degnan, 1994; Searle, 1983). Consequently, the current state of thinking revolves around two classes of competing hypotheses:

Hypothesis 1:

Early interpretations by Fuchs (1982) and Honegger et al. (1982) of the Dras-Nindam complex suggested that this arc evolved throughout the Jurassic to Cretaceous in a forearc of a convergent margin on the southern margin of Eurasia (Figure **1.3**). This forearc basin developed on top of ophiolitic basement in front of the Ladakh Arc (Trans-Himalayan Batholith) as part of a single subduction complex responsible for the consumption of the entire Neotethyan Ocean, before the onset of the India-Eurasia continent-continent collision at about 55 Ma (Fuchs, 1982). Although this model is elegant in its simplicity, there are inconsistencies that do not fit the hypothesis. Most significant are the nature and age of ophiolites and island arc terranes along the suture that appear to have completely juvenile, intraoceanic characteristics rather than having signatures expected of a marginal continental basin.

Hypothesis 2:

Other researchers have noted the juvenile, intraoceanic nature of the Dras-Nindam terrane and ophiolites along the Indus Suture (Clift et al., 2000; Corfield et al., 2001), which bear no provenance links to felsic volcanism associated with the Ladakh Arc. Corfield et al. (2001) invoked multiple north-dipping subduction zones (Figure **1.4**) to explain the coeval development of the Spongtang Ophiolite, the intraoceanic Dras-Nindam terrane and the continental Trans-Himalayan Batholith (Ladakh Arc).

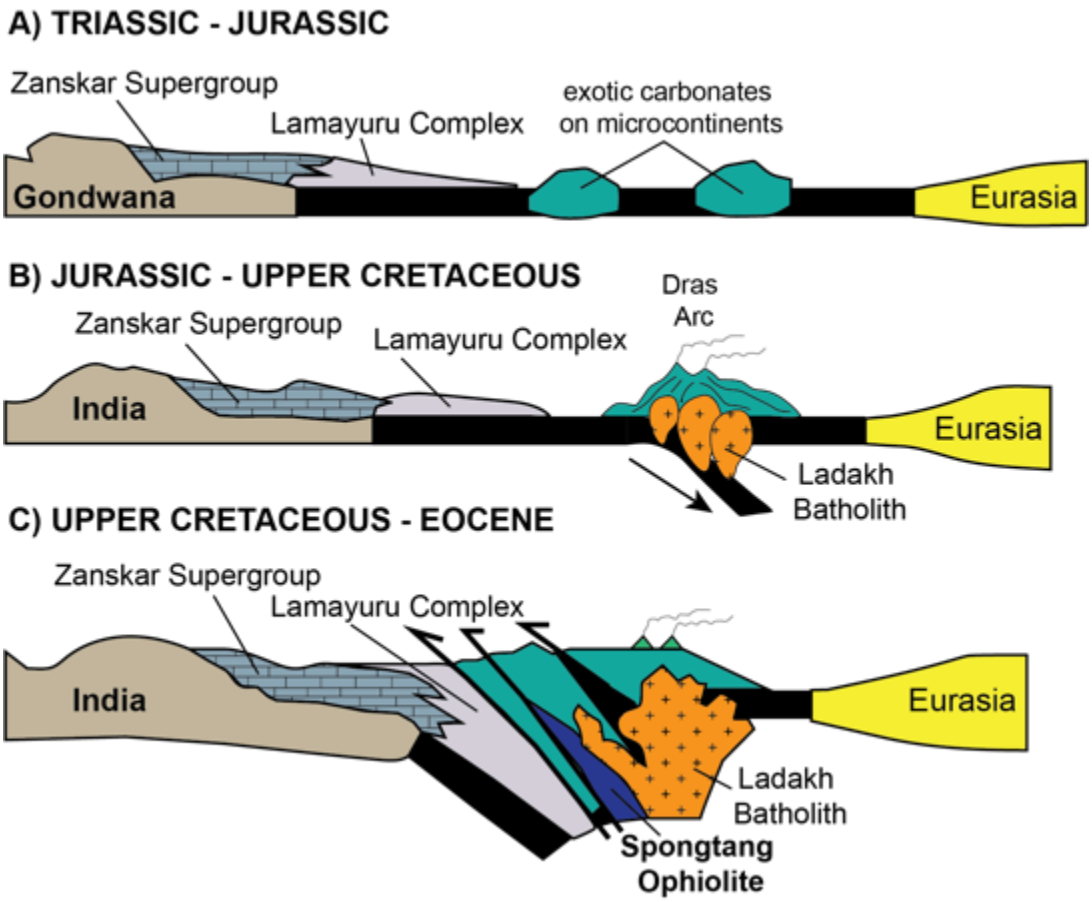

Figure 1.3: Hypothesis 1, where Fuchs (1982) has interpreted the Dras Arc as evolving in a forearc setting outboard of the southern margin of Eurasia before evolving into the more mature Ladakh Arc in the Late Cretaceous, before the onset of the India-Eurasia continental collision between the latest Cretaceous and Early Eocene. Adapted from Fuchs (1982).

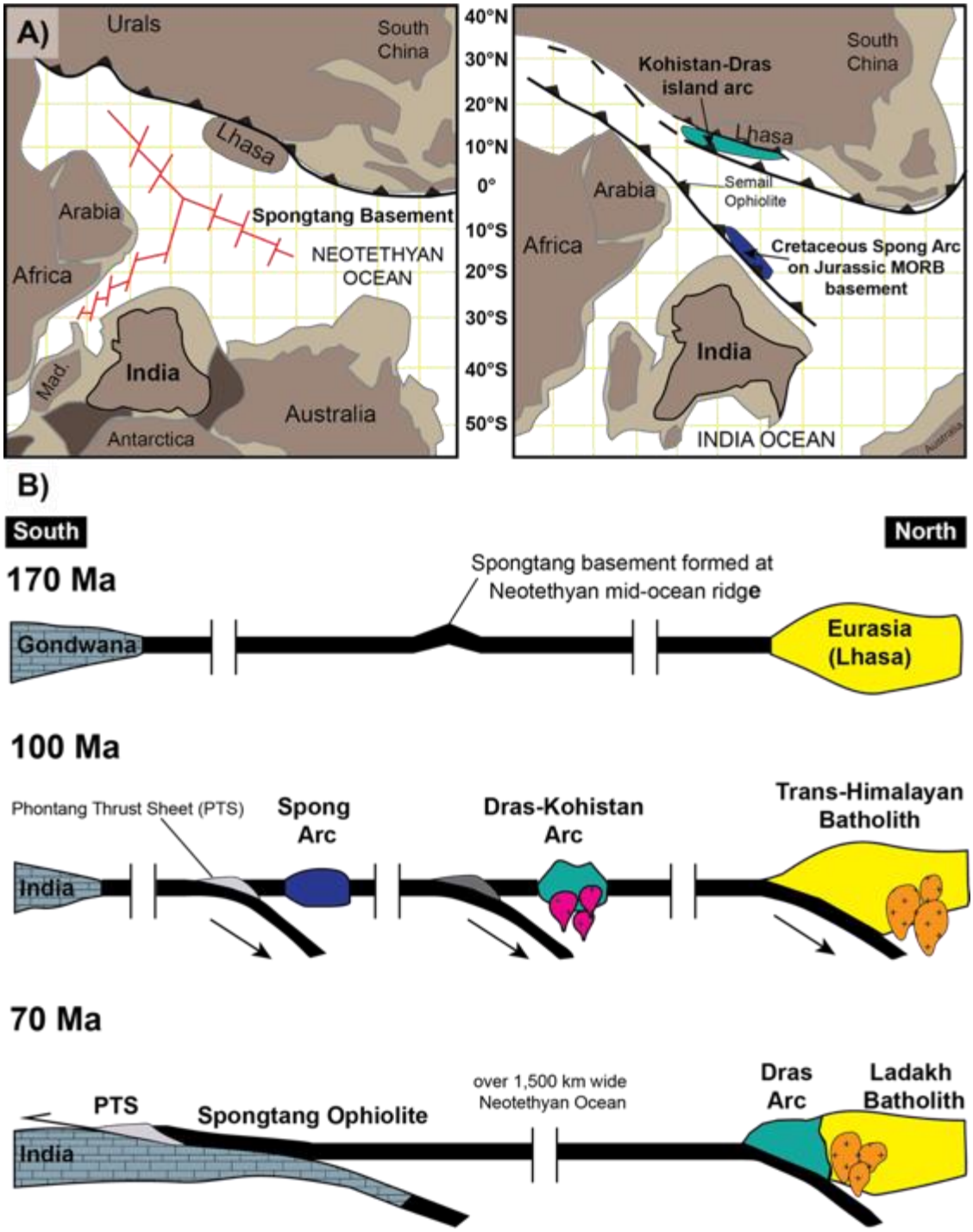

Figure 1.4: Hypothesis 2, where Corfield et al. (2001) recognises the intraoceanic nature of the Spongtang Ophiolite and the Dras-Kohistan arc, and the difference to the continental Trans-Himalayan Batholith evolving along the southern margin of Eurasia. They do not correlate the Spongtang Ophiolite with the Dras Arc because of previous interpretations that suggest the Dras Arc collided with Eurasia before continental collision (Coward et al., 1987). Adapted from Corfield et al. (2001).

Thus, the relationship between the Dras-Nindam terrane and various ophiolites along the suture, for example the Spongtang and Nidar ophiolitic complexes, has been ambiguous, as was the timing of collision with either India or Eurasia before the onset of final continent-continent collision. Similar ophiolite-island arc terranes occur along strike towards the east in Tibet (Aitchison et al., 2000; McDermid et al., 2002), which along with the age of collision-related conglomerates (Aitchison et al., 2002) led Aitchison et al. (2007a, 2011) to revise drastically the timing of the India-Eurasia collision from the generally held consensus view of 55-50 Ma to 34 Ma (Figure **1.1**). In other models based on a larger northern extent of Greater India, the age of collision is interpreted to be much earlier at ~70 Ma (Ding et al., 2005).

Therefore, it is evident that the age of juvenile ophiolitic and island arc terranes that developed within the Neotethyan Ocean and the nature and timing of their collision with either India or Eurasia is an essential aspect of developing accurate reconstructions of the India-Eurasia continent-continent collision and the rise of the Himalaya. Specifically, for the Dras-Nindam terrane, its age and provenance are restricted to only a few fossil occurrences in these generally unfossiliferous deep marine turbidites, plus some K-Ar radiometric ages of the Dras volcanic rocks (Reuber et al., 1989) and some U-Pb zircon dates of granites intruding the Dras Volcanics (Honegger et al., 1982; Schärer et al., 1984a). While there have been studies of detrital zircon populations of the pre- and post-collisional Indus molasse deposits north of the Indus Suture (Bhattacharya et al., 2020; Henderson et al., 2010; Henderson et al., 2011; Wu et al., 2007) to date there have been no detrital zircon studies of the Dras-Nindam terrane which lies south of the suture. Detrital zircon studies in this project will help establish both the provenance and maximum depositional age of the Nindam Formation, while tuffaceous units in the predominantly basaltic to andesitic Dras Arc will be targeted to provide accurate ages of the volcanic arc.

Mélange zones are integral to tectonic reconstructions because they are a mixture of all crustal elements involved in subduction and subsequent collision (Draut and Clift, 2013). These zones will often include ophiolitic fragments of gabbro, basalt and chert scraped off the subducting plate, as well as blocks of the overriding island arc and the continental crust onto which the intraoceanic terrane was emplaced. In the case of the Dras-Nindam terrane, gabbroic blocks from the southern mélange zone at the thrust contact with Indian rocks were targeted for zircon U-Pb dating, to establish the latest stages of arc development and to constrain the timing of arc-continent collision.

1.3 Significance

This research provides the first detailed detrital zircon geochronology and provenance study on the volcano-sedimentary Nindam Formation of the Dras-Nindam terrane from the Indus Suture Zone, Ladakh Himalaya. Detrital zircon age data provide constraints as to the maximum deposition age of the Nindam Formation. Provenance studies of volcaniclastic turbidites within the Nindam Formation assisted in determining whether this was truly an intraoceanic island arc system or whether it developed proximally to either India or Eurasia, before colliding with one or the other, prior to continent-continent collision. Magmatic phases related to the Dras Arc including extrusive (Dras Volcanics) and intrusive (Kargil Intrusives) episodes were also investigated using zircon U-Pb geochronology in combination with the detrital studies, to determine the age of the arc system, the duration of its existence in the Neotethyan Ocean, and its relationship to other arc terranes (e.g., Ladakh Arc of NW India, Kohistan Arc of Pakistan and/or Zedong Terrane of Tibet). The youngest age for typical subduction-related magmatic components in any ancient arc complex is a critical age constraint for the timing of arc-continent collision (Shervais, 2001). Therefore, gabbroic blocks within the southern mélange zone were also targeted for zircon U-Pb dating, to establish the latest stages of development of the Dras-Nindam terrane. More broadly, this investigation contributes to existing models on the development of intraoceanic arcs and their collision and accretion onto continents, shedding further light on the mechanisms behind the growth of continental crust and ongoing debates concerning the relevant importance of growth at continental margins versus accretion of island arcs onto continental margins (Aitchison and Buckman, 2012; Huang et al., 2018).

1.4 Aim and objectives

The overarching aim of this investigation is to test competing hypotheses regarding the tectonic evolution of the Dras-Nindam terrane that occurs along the Indus Suture Zone of the India-Eurasia collision in the Ladakh Himalaya, NW India. This project will address key tectonic questions by determining the age and characterising the nature of the Dras-Nindam terrane in Ladakh. There are three objectives of this investigation:

(i) To determine the maximum age of deposition and provenance of the Nindam Formation using detrital zircon U-Pb geochronology to ascertain whether the Dras Arc initiated in an intraoceanic setting or was continental-related.

(ii) To constrain the timing of initiation and early evolution of the Dras Arc using zircon U-Pb geochronology of extrusive (Dras Volcanics) and intrusive (Kargil Intrusives) magmatic episodes.

(iii) To establish the latest stages of development of the Dras Arc in order to constrain the timing of arc-continent collision.

1.5 Thesis style

This is a thesis by compilation whereby the overarching aim of the investigation, this being '*to test competing hypotheses regarding the tectonic evolution of the Dras-Nindam terrane that occurs along the Indus Suture Zone of the India-Eurasia collision in the Ladakh Himalaya, NW India*', is weaved throughout each chapter. However, the three objectives of this project, as previously outlined, are separated into three respective chapters (Chapters 4-6), which have been published (two) or prepared (one) for publication. All associated supporting information for each paper follows directly after the relevant chapter. However, all references are detailed at the end of this thesis, as per convention.

The use of the word "we" is used in many chapters. It is important to note that this research did not occur in isolation and rather involved the collaboration of others, particularly for those chapters which are publication materials (Chapters 4-6). That is not to say that the work of this thesis not my own. Coauthor contributions are detailed after the acknowledgements section of each chapter. The author statements follow the Contributor Roles Taxonomy (CRedIT) as outlined by Allen et al. (2019), with terms and definitions outlined in the Appendix.

Minor alterations have been made to those papers which have been published to ensure they are 'thesis appropriate', and therefore are not verbatim to those published by the respective journals. Moderate alterations have been made to Chapter 6, as this was originally submitted to a short-form journal, which required strict word-limits and formatting. Therefore, additional work to supplement this paper can be found in the respective supporting information, following the thesis chapter.

1.6 Chapter summary

Chapter 1: Introduction

This chapter provides an introduction to the thesis, including background information, key issues, significance, aim and objectives, and a description of the style of the thesis.

Chapter 2: Materials and methods

This chapter provides detailed descriptions of the materials and methods used for this

investigation. Note, that each of the paper-formatted chapters (Chapters 4-6) include descriptions of the specific methods used for each study.

Chapter 3: Literature review

This chapter provides a summary of the previous studies and aims to introduce the Dras-Nindam terrane, along with other important units of the Indus Suture Zone, Ladakh Himalaya. The following chapters (Chapter 4-6) each have their own literature review, which is detailed in the 'geological setting' sections.

Chapter 4: Paper I – Age and provenance of the Nindam Formation, Ladakh, NW Himalaya: Evolution of the intraoceanic Dras Arc before collision with India

This chapter addresses the first objective of this project, this being '*to determine the maximum age of deposition and provenance of the Nindam Formation using detrital zircon U-Pb geochronology to ascertain whether the Dras Arc was intraoceanic or continental-related*'. This chapter has been published in a Special Edition (collisional orogenic systems as recorders of collisions between arc and continents) of **Tectonics** (impact factor: 3.54). The citation is as follows: Walsh, J. M., Buckman, S., Nutman, A. P., & Zhou, R. (2019). Age and Provenance of the Nindam Formation, Ladakh, NW Himalaya: Evolution of the Intraoceanic Dras Arc before Collision with India. *Tectonics*, 38(8), 3070-3096. [7 citations, as of 5th February 2021; Google Scholar].https://doi.org/10.1029/2019TC005494

Chapter 5: Paper II – The significance of Upper Jurassic felsic volcanic rocks within the incipient, intraoceanic Dras Arc, Ladakh, NW Himalaya

This chapter addresses the second objective of this project, this being '*to constrain the timing of initiation and early evolution of the Dras Arc using zircon U-Pb geochronology of extrusive (Dras Volcanics) and intrusive (Kargil Intrusives) magmatic episodes*'. This chapter has been published in **Gondwana Research** (impact factor: 6.17). The citation is as follows: Walsh, J. M., Buckman, S., Nutman, A. P., & Zhou, R. (2020). The significance of Upper Jurassic felsic volcanic rocks within the incipient, intraoceanic Dras Arc, Ladakh, NW Himalaya. *Gondwana Research, 90*, 199-219 [Google Scholar]. https://doi.org/10.1016/j.gr.2020.11.007

Chapter 6: Paper III – Youngest magmatic age (Early Eocene) from the Neotethyan intraoceanic Dras Arc, Ladakh Himalaya, NW India

This chapter addresses the third and final objective of this project, this being '*to establish the*

latest stages of development of the Dras Arc in order to constrain the timing of arc-continent collision'. This chapter is *in preparation* for **Gondwana Research** (impact factor: 6.17). The citation is as follows: Walsh, J. M., Buckman, S., & Nutman, A. P. (*in prep*.). Youngest magmatic age (Early Eocene) from the Neotethyan intraoceanic Dras Arc, Ladakh Himalaya, NW India

Chapter 7: Discussion

This chapter includes a general discussion or 'overview', and details specific contributions from each paper-formatted chapter (Chapters 4-6). Recommendations for future research are also included in this chapter.

Chapter 8: Conclusion

This chapter includes concluding remarks for this investigation and finalises the thesis. A model is included to illustrate the tectonic evolution of the Dras-Nindam terrane that occurs along the Indus Suture Zone of the India-Eurasia collision in the Ladakh Himalaya, NW India.

Appendices

This section includes Appendix A: Conference abstracts and proceedings, and Appendix B: Coauthor contribution framework following 'Contributor Roles Taxonomy' (CRediT).

Chapter Two: Materials and methods

2.1 Overview

The following is a description of the main materials and methodological approaches used in this investigation. Samples were collected during three field campaigns to the Ladakh Himalaya, NW India (2015-2017). Descriptions of sample localities, lithologies and methods are also provided in each paper-formatted chapter (Chapters 4-6), either in the main text or the following supporting information and data.

2.1.1 Petrography

2.1.1.1 Sample preparation

Sample preparation for thin section petrography was undertaken at the University of Wollongong (UOW). Samples were first washed in water to remove any potential surficial contaminants. Samples were dried then cut to just over the dimensions of a standard glass thin section slide using a diamond-edged saw. It was particularly important to locate the regions within each sample that were the least affected by weathering processes; this commonly resulted in extracting sections from the middle of the rock samples. Care was taken to ensure the width of each prepared sample was thicker (~20 mm) than required for a standard thin section, to allow for replication if required. The representative blocks of sample were then mounted on glass slides using epoxy resin on a 50°C hot plate and left overnight. Each sample was ground down on a rotating carborundum plate to reduce the thickness to just before the standard thickness of a thin section (30 μm). The final stage of polishing was performed manually by hand on a glass plate to obtain the correct thickness. Regular thin sections were made with coverslips, for viewing under light that is transmitted through the sections. Thickness was controlled optically based on quartz and/or plagioclase birefringence.

2.1.1.2 Standard thin section petrography

The mineral assemblage and, textural and structural relationships of individual samples were examined using a Leica DM 2500P upright petrographic microscope, housed in the GeoMicroscopy Laboratory, UOW. Plane-polarised (PPL) and cross-polarised light (XPL) images were acquired and processed using the *Leica Application Suite* (LAS) software.

2.1.1.3 Provenance studies

There are a variety of different methods for determining the detrital mineral composition of sandstones. For the purposes of this investigation, the Gazzi-Dickinson point counting method was employed (Dickinson and Suczek, 1979). This method divides volcanic lithic fragments into various types, which is especially important in magmatic arc settings, whereby volcaniclastic components may constitute the sand fraction (Ingersoll et al., 1984).

The mineralogy and model composition of volcaniclastic sandstones were determined using a mechanical stage point counter, attached to the stage of a Leica DM 2500P upright petrographic microscope. As a first step investigation, the thin sections were examined qualitatively, to assist in defining grain type categories to be included in the point count analysis. Following this, a quantitative investigation was undertaken, whereby a total of at least 300 framework grains were counted at even increments in a grid pattern for each volcaniclastic sandstone sample. Grid spacings that maximised the coverage of the thin sections were used and were larger than the maximum grain size. Each 'point' or grain that fell under the microscope cross hairs was recorded. The categories of different grain types that were identified and used in point counting investigations were: monocrystalline quartz (Qm), polycrystalline quartz (Qp), total quartz (Q), plagioclase (P), K-feldspar (K) and total feldspar (F). The unstable lithic fragments consist of volcanic/metavolcanic rocks (Lv) and minor fragments of both sedimentary/metasedimentary (Ls) and metamorphic (Lm) rocks. Totalled lithic fragments include all unstable lithic fragments and chert (Lc) fragments (i.e., Lv + Ls + Lm + Lc). If chert is in high abundance, then it is considered a lithic fragment, rather than a sub-type of quartz (i.e., polycrystalline, or monocrystalline quartz).

2.1.2 Whole rock geochemistry

2.1.2.1 Sample preparation

All sample preparation for whole rock (major and trace element) geochemical analysis took place at the University of Wollongong (UOW). Samples were first washed and dried to remove any potential surficial contaminants. Outside layers were removed with a diamond-edged saw to expose fresh, unweathered rock. The remaining rock underwent a two-stage crushing regime, first using a hydraulic press, and secondly using either an agate mortar and pestle, or conventional tungsten carbide (WC) TEMA ring-mill. Samples were crushed into fine powder to allow for analysis.

2.1.2.2 Major and trace elements

Whole rock geochemical analysis (major and trace elements) was undertaken using a SPECTRO XEPOS energy dispersive polarisation X-ray fluorescence (XRF) spectrometer at the University of Wollongong (UOW), Australia. *Spectro* software was utilised for spectral investigation and subsequent element identification. The software maintains accuracy through calibrating against various natural and synthetic materials. The spectrometer was calibrated from a range of natural and artificial standards, including the international standards G-2, BIR-1, and AC-E, as well as a local standard, to ensure that the range of trace element concentrations was covered (Table **2.1**). The analytical precision from 35 analyses of the standards was mostly between ± 2-6 % of the standard values.

Homogenous fused buttons were made of standards and samples for XRF major element analysis. Depending on elemental concentrations estimated in trace element analysis, different flux blends were used. Pure metaborate was used for high silica samples, 35.3% tetraborate to 64.7% metaborate was used for mafic samples, and 57% tetraborate to 43% metaborate was used for ultramafic samples. Sample (400 mg) was added to each flux (300 mg for pure metaborate). The mixtures were then placed in platinum crucibles for the duration of one hour where they were heated from 600°C to 970°C to create glass discs or buttons from the fused material. Loss on ignition (LOI) was determined by measuring the difference between the initial and subsequent weights after the heating of 1 g of powder for each sample at 1050°C for two hours. Homogenous pressed pellets were created of standards and samples for XRF trace element analysis by mixing approximately 5 g of sample with 8-10 drops of 5% polyvinyl acetate (PVA) binder and pressed into aluminium cups using a hydraulic hand press at 2500 psi. Trace element pressed pellets were then oven dried at 60 °C for 12-24 hours.

Table 2.1: Measured concentration of trace elements in international standards.

International standards	Ni	Cr	Cu	Zn	Pb	As	Br	Rb
G-2 (mean)	3.0	5.6	10.7	90.1	31.7	0.3	0.1	169
G-2 (s.d)	0.5	3.3	1.1	0.9	0.5	0.3	0.1	0.7
BIR-1 (mean)	164.1	408.6	130	68.5	1.2	0.5	0.4	1.0
BIR-1 (s.d)	2.0	7.5	1.9	0.7	0.2	0.5	0.2	0.0
AC-E (mean)	9.5	1.2	5.3	230	38.5	1.6	0.7	151
AC-E (s.d)	3.3	1.0	0.6	1.7	0.5	0.5	0.4	0.6

Notes:
The analytical precision from 35 analyses was mostly between ± 2-6 %. s.d = standard deviation.

2.1.2.3 Rare earth elements

Rare earth element (REE) and additional trace element analyses were undertaken at Australian Laboratory Services (ALS) Minerals Division, Brisbane, Australia using Inductively Coupled Plasma-Mass Spectrometry (ICP-MS; geochemical procedure code ME-MS81). Lithium (Li) metaborate and Li tetraborate were used as fluxes with and after fusing beads in a furnace, the resultant melt was then dissolved in nitric, hydrochloric, and hydrofluoric acid mixes (acid digestion). This solution was then analysed by ICP-MS to produce analyses for a broad suite of trace elements, including REE. Standards OREAS 120 and STSD-1, as well as five sample duplicates and three blanks, were analysed to determine the error tolerance.

2.1.2.4 Data validation and processing

The effect of modern weathering was addressed at the sample selection and preparation stage, whereby homogenous samples were selected, and surficial layers were removed with only central, fresh rock was used for analysis. Whereas the degree of ancient weathering was assessed using the mafic, felsic, and weathering (MFW) indices of Ohta and Arai (2007). The 'M' and 'F' indices discriminate whether the material is mafic or felsic, respectively; while the 'W' index indicates the degree of weathering the rock sample has undergone. Sample thin sections were also examined to determine the degree of weathering, whereby emphasis was placed on identifying alteration minerals (e.g., chlorite). Loss on ignition (LOI) values for each sample were also examined and crosschecked with MFW ternary diagrams and thin section observations. Additionally, since a selection of samples were crushed using a tungsten carbide (WC) TEMA ring-mill, trace amounts of W, Cr, Co and Sc may be compromised, and thus these elements have not been used in interpretations. Also, regarding lithological classification and tectonic discrimination, immobile elements (e.g., high field strength elements; HFSE and REE) were preferentially used, as these are less susceptible to both weathering and hydrothermal alteration (MacLean, 1990). Mobile elements, including large ion lithophile elements (LILE), were used for those samples regarded as fresh rock, evidenced by MFW ternary diagrams and, field and petrographic observations. Geochemical data was processed using a combination of different software including, *IgPet* (Carr and Gazel, 2017) and *GCDkit* (Janoušek et al., 2006), for displaying data in relevant lithological classification, tectonic discrimination and REE diagrams and plots. The mineralogical composition of nominally anhydrous samples was determined by applying a CIPW normative mineralogy calculation using whole rock geochemical data. This method determines the most abundant minerals that crystallised from a low-pressure, anhydrous melt, while providing an estimate of their final normative proportions (Kelsey, 1965). Where this normalisation has been applied, it is noted in the main text or supporting information.

2.1.3 Zircon U-Pb geochronology

2.1.3.1 Zircon preparation

Samples were first washed and dried at the University of Wollongong (UOW) to remove any potential surficial contaminants. Outside layers were removed with a diamond-edged saw to expose fresh, unweathered rock. Zircon grains were separated at the Institute of Hebei Regional Geology Survey, China. The samples were chipped in a pre-contaminated jaw crusher, using a subsample first. Chips were thoroughly washed with water, then dried prior to being ground into a coarse powder using a jaw crusher. The coarse powder was separated into heavy and light fractions using heavy liquids to obtain the >3.31 zircon-bearing fraction. The heavy fraction was washed and dried prior to being passed through a Franz Isodynamic Magnetic Separator to obtain zircons (normally the non-magnetic fraction at 2A).

Select zircon-poor samples were also processed at the mineral separation laboratory of the Australian National University (ANU), Australia. The samples were chipped in a pre-contaminated jaw crusher. Chips were thoroughly washing with water, then dried, prior to coarse powdering in a tungsten carbide (WC) TEMA ring-mill. The coarse powder was then placed in a large beaker of water, with gentle overflow, to ensure any micro dust particles were removed. The samples were dried, then treated with bromoform (specific gravity = 2.84) and diiodomethane (specific gravity = 3.31) in glass funnels, in order to divide the > 3.31 zircon-bearing fraction. The heavy fraction was passed through a Franz Isodynamic Magnetic Separator to obtain zircons (normally the non-magnetic fraction at 1.25A).

Following separation, zircon grains were examined using a binocular microscope, handpicked and mounted with standard TEMORA II grains on double-sided tape on a glass plate, which were then cast with epoxy resin in a mould. The mounts were ground on 1200 grade wet and dry paper to reveal approximately half sections through the grains and then polished with 1 µm diamond paste. Transmitted and reflected light photomicrographs were taken, along with cathodoluminescence (CL) imaging.

2.1.3.2 Reflected light imaging

Reflected light images of individual samples and entire zircon mounts were obtained using a Leica DM 6000M upright microscope. The ‘stitching’ function of *Leica Application Suite* (LAS) was used, whereby a series of overlapping images were taken at the same magnification. The software automatically combines these without visual edges. These reflected light images were combined with optical microscope observations to select the most suitable grains for analysis.

2.1.3.3 Cathodoluminescence imaging

Cathodoluminescence (CL) images were obtained using a Scanning Electron Microscope (SEM) JEOL JSM-6490LA conventional tungsten filament thermionic source coupled with a Gatan MonoCL4 cathodoluminescence spectrometer used in panchromatic mode at the Electron Microscope Centre (EMC), Innovation Campus, UOW. The instrument was used in low vacuum mode to avoid coating which would diminish the CL signal observed. The beam settings included an optimised spot size (typically 80 nA) and acceleration voltage of 5 kV to bias excitations to the surface while maintaining acceptable spatial resolution. The aperture was also removed to maximise electron flux. *Digital Micrograph*, Gatan Microscopy Suite, was used to view the acquired data and images. Reconnaissance low resolution CL imaging allowed for analytical site selection, then follow-up high resolution CL imaging on analysed grains was performed to ensure proper identification of the characteristics of the analysed sites.

2.1.3.4 LA-ICP-MS

Zircon U-Pb dating using Laser Ablation-Inductively Coupled Plasma-Mass Spectrometry (LA-ICP-MS) was undertaken at the Centre for Geoanalytical Mass Spectrometry (CGMS), The University of Queensland (UQ), Australia. The zircon 91500, which has a $^{206}Pb/^{238}U$ age of 1062.4 ± 0.4 Ma and $^{206}Pb/^{207}Pb$ age of 1065.4 ± 0.3 Ma, was used as the primary reference material (Wiedenbeck et al., 1995). TEMORA II was also employed as a secondary reference material, which has a $^{206}Pb/^{238}U$ age of 416.78 ± 0.33 Ma (Black et al., 2004). Laser ablation was undertaken using an ASI RESOlution 193 ArF nm excimer laser system. Following evacuation of air, He carrier gas was introduced into the laser cell at a flow rate of 0.35 l/min. 0.05 l/min of N_2 gas was also introduced to the laser cell to enhance the measurement sensitivity. The gas mixture was then introduced into the plasma torch of a Thermo iCAP RQ quadruple ICP-MS with 0.85 l/min Ar nebuliser gas. No reaction gas was employed. The laser was run with a 30 µm diameter round spot at 10 Hz, with a measured instrument laser-fluence (laser pulse energy per unit area) of 2.9 J/cm^2. For each spot, 5 s of blank was collected, followed by 25 s of ablation and 10 s of wash out. Prior to data acquisition, ICP-MS signals were optimised during tuning. Parameters particular to the analytical sessions include, ~400 K cps of ^{238}U counts, ~1 of $^{238}U/^{232}Th$, ~0.21 of $^{206}Pb/^{238}U$ were achieved for measuring NIST612 glass using line scans of 3 µm/s, 10 Hz, 50 µm round laser pit, and 3 J/cm^2. The following isotopes were collected using a single collector: ^{88}Sr (dwell time=0.005 s), ^{91}Zr (dwell time=0.001 s), ^{200}Hg (dwell time=0.01 s), $^{204}Pb + ^{204}Hg$ (dwell time=0.01 s), ^{206}Pb (dwell time=0.045 s), ^{207}Pb (dwell time=0.055 s), ^{208}Pb (dwell time=0.01 s), ^{232}Th (dwell time=0.01 s), ^{238}U (dwell time=0.01 s). A single cycle took ~0.155 s. Therefore, during a 25 s ablation, ~160 measurements were made on each mass. No common Pb correction on zircon 91500 was undertaken. From the session, a $^{206}Pb/^{238}U$ age of

419.0 ± 1.1 Ma, uncorrected for common Pb (95% confidence, n = 93, MSWD = 7.7) for the TEMORA II secondary reference material was obtained, which has a TIMS $^{206}Pb/^{238}U$ age of 416.78 ± 0.33 Ma determined by ID TIMS (i.e., data calibrated using zircon 91500 analyses; Black et al., 2004). $^{206}Pb/^{238}U$ ages are reported for <1000 Ma grains, whereas $^{207}Pb/^{206}Pb$ ages are reported for >1000 Ma grains. Details relevant to individual analytical sessions and details on rejected grains are provided in each of the relevant chapters (Chapters 4-6).

2.1.3.5 SHRIMP

Zircon U-Pb dating using Sensitive High-Resolution Ion Microprobe Reverse Geometry (SHRIMP-RG) was undertaken at the Australian National University (ANU), Australia. The more expensive analysis using SHRIMP was reserved for difficult, small zircon grains due to the less destructive technique compared to the laser ablation method. Zircon mounts were cleaned and coated with ~10 nm of high purity Au (>99.999%) before analysis and followed the analytical procedure of Williams (1998). Sites within the zircon grains were selected according to their apparent reflectance (brightness) on the polished surface (information gained from reflected light photomicrographs), along with well-formed structure (information gained from CL images). Note was made to avoid analysing cracked or damaged zircons and dark zones within grains (indicative of high U + Th content). Uranium abundance was calibrated based on the reference zircon SL13 (U = 238 ppm) in a set-up mount.

After site selection was made the instrument was alternated between running manually and programmed to run automated at night. A total of five to six cycles were made at each of the nominal mass stations: ^{196}Zr, ^{204}Pb, background $^{204.1}Pb$, Pb (^{206}Pb, ^{207}Pb, ^{208}Pb), ^{238}U, ^{248}ThO ($^{232}Th + {}^{16}O$) and ^{254}UO ($^{238}U + {}^{16}O$). Parameters particular to the analytical sessions include a spot size of ~15-20 μm, with the primary O^{2-} ion beam of 4-6 nA, with each site rastered for 120 seconds prior to analysis. TEMORA II was analysed for U-Pb calibration after every three to four unknowns. Quoted errors on isotopic ratios also take into account non-linear fluctuations in ion count rates above that expected from counting statistics alone (Williams, 1998). This is particularly important for old, damaged high U + Th zircons, where damage is attributed to post-crystallisation heterogeneity of species on the sub-micron scale, as now documented by atom probe-analysis (Peterman et al., 2016). Reliance on counting statistics only of such targets would result in under-estimation of analytical error. Correction for common Pb was made in accordance to the measured ^{204}Pb and common Pb composition for the likely age of the sample from Cumming and Richards (1975). $^{206}Pb/^{238}U$ was calibrated using the TEMORA II standard with a concordant age of 416.78 ± 0.33 Ma (Black et al., 2004). $^{206}Pb/^{238}U$ ages are reported for <1000 Ma grains, whereas $^{207}Pb/^{206}Pb$ ages are reported for >1000 Ma grains. Details relevant to

individual analytical sessions and details on rejected grains are provided in each of the relevant chapters (Chapters 4-6).

2.1.3.6 Data validation and processing

For data acquired by SHRIMP, the standard (TEMORA II) was distributed as several groups of grains (between 5-10 grains per group) in different parts of the zircon mount to increase confidence in the accuracy of calibration of U-Pb across the entire mount (Figure **2.1**). These were visited randomly, throughout analytical sessions. If the standards are located in a single group, at a distance far enough away from the unknowns, then subtle differences between the standards and the unknowns can lead to a systematic calibration error of $^{206}Pb/^{238}U$. This can arise due to, (i) imperfections in the gold coat causing variation in its conductivity or, (ii) micro-scale topography of the mount leading to the need to slightly refocus the secondary ion optics for different parts of the mount. There were no cases during the analytical sessions where such systematic variations were detected between different clusters of TEMORA II grains. This allows for greater confidence to be placed on the U-Pb ages of the unknowns and that accurate comparisons can be made between different samples on the same zircon mount.

The reduction of raw data from LA-ICP-MS analysis was accomplished using the program *IOLITE* (Paton et al., 2011), while the raw data from SHRIMP were reduced using the program *POXI-SC* developed by ANU. *POXI-SC* combines the functionality of the previous two ANU applications *Prawn* and *Lead*, which require the redundant Mac OS9 operating system and spreadsheet software *Kaleidagraph*. The reduced and calibrated data were then assessed and plotted using *Isoplot 4.1*.

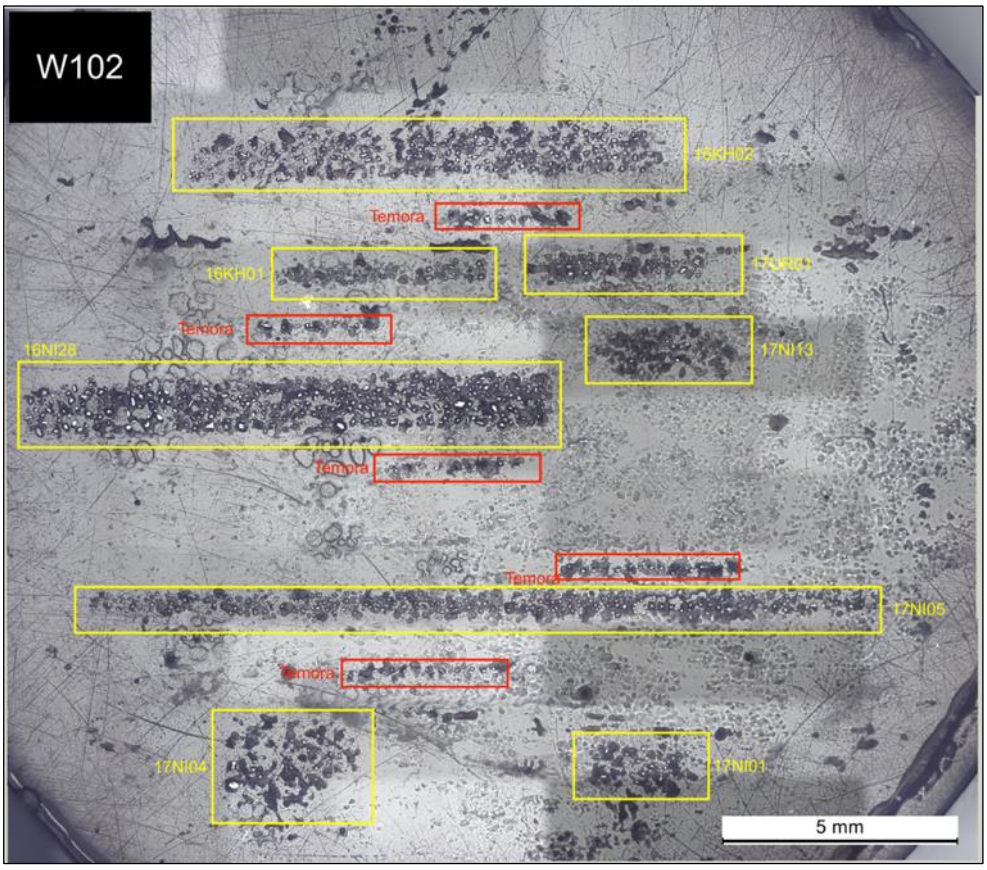

Figure 2.1: Representative zircon mount (W102) where standard (TEMORA II) is distributed as several groups of grains in different parts of the zircon mount to increase confidence in the accuracy of calibration of U-Pb across the entire mount when analysed by microbeam techniques. Where red rectangles indicate standard and yellow rectangles indicate unknowns.

Chapter Three: Literature review

3.1 Dras-Nindam terrane

3.1.1 Tectonic setting

The Dras-Nindam terrane, incorporating the Dras Volcanics and correlative volcaniclastic rocks of the Suru, Naktul and Nindam formations, stretches some 400 km along the Indus Suture, the western extent of the Indus-Yarlung-Tsangpo Suture (IYTS), in the Ladakh Himalaya (Figure **3.1**). The 15 km wide Dras-Nindam terrane is dominated by basaltic-andesites of the Dras Volcanics in the west, and in the east the unit transitions into dominantly forearc volcaniclastic rocks of the Nindam Formation (Bhat et al., 2019; Clift et al., 2000; Clift et al., 2002b; Dietrich et al., 1983; Fuchs, 1982; Honegger et al., 1982; Reuber, 1989; Robertson and Degnan, 1994; Schärer et al., 1984a; Sharma et al., 1978; Walsh et al., 2019). To the north the complex is faulted against the Ladakh Arc, associated (Eurasian) forearc basin sedimentary rocks of the Tar Group and the post collisional Indus Group (Fuchs, 1982; Henderson et al., 2010). The fault is marked by the Mongyu mélange, which is a serpentine-matrix mélange containing blocks of the adjacent Dras-Nindam terrane as well as blocks derived from the Ladakh forearc basin and post collisional complex (Tar and Indus groups) to the north (Robertson, 2000). As determined by field work for this investigation, the Mongyu mélange also contains rare gabbro blocks which may represent either the Dras island arc crust or an unidentified disrupted ophiolite sequence representing ocean crust that lay between the Dras-Nindam terrane and southern Eurasia (Ladakh Arc). To the south the Dras-Nindam terrane is thrust over the highly disrupted Lamayuru Complex and the passive Indian margin Zanskar Supergroup (Robertson and Degnan, 1993). Slivers of discontinuous ophiolitic mélange also occur along this southern contact and contain numerous basalt, chert, gabbro and blueschist blocks (Corfield and Searle, 2000; Honegger et al., 1989; Robertson, 2000; Robertson and Degnan, 1994). The Dras-Nindam terrane can be divided stratigraphically into four different units; these include the (i) Dras Volcanics, (ii) Suru Formation, (iii) Naktul Formation and (iv) Nindam Formation.

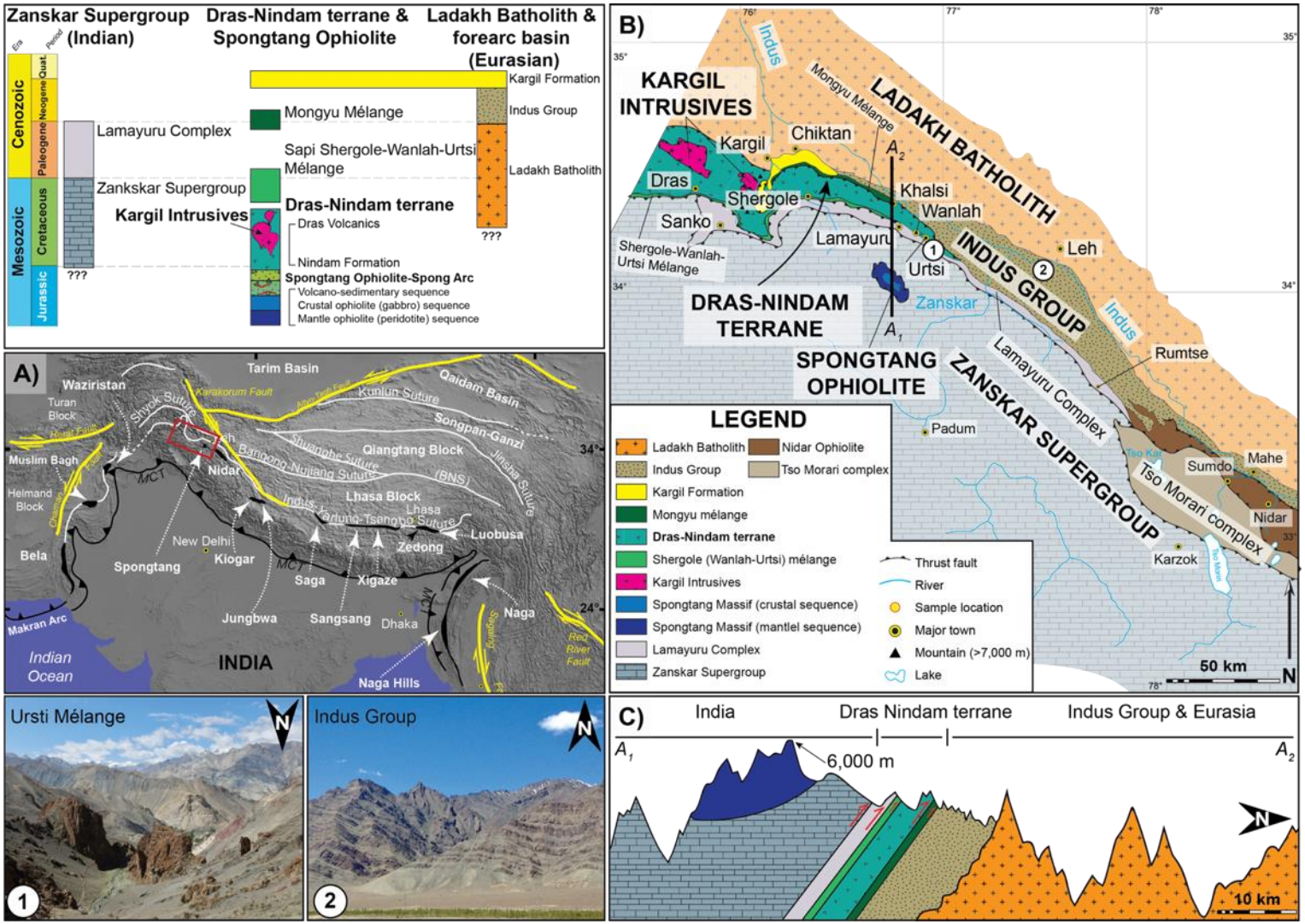

Figure 3.1: Main geological units of the Indus Suture Zone, Ladakh Himalaya, NW India. **A)** Regional map of India and the Indus Suture Zone ophiolite occurrences (after Buckman et al., 2018); **B)** Geological units of the study area (after Bhattacharya et al., 2020; Corfield et al., 2000; Reuber, 1987; Walsh et al., 2019; 2020); **C)** Schematic cross-section ($A_1 – A_2$) through the main geological units.

3.1.2 Stratigraphy

3.1.2.1 Dras Volcanics

The Dras Volcanics, also referred to as the Dras Formation have been described as irregular basaltic to basaltic-andesite flows (typical of modern day, juvenile island arc environments), intercalated with volcaniclastic rocks, pyroclastic material and radiolarite (Bhat et al., 2019; Honegger et al., 1982; Reuber, 1989), see column A on Figure **3.2**. Minor dolerite sills and dykes are common, along with rare tuff layers and andesites. Radiometric K-Ar dating of amphiboles from the Dras Volcanics produced an age cluster between 105-95 Ma, with one exception from a fine-grained fraction which produced an age of 79 ± 3 Ma (Reuber et al., 1989). Sharma et al. (1978) produced a younger K-Ar age of 78 ± 1 Ma for the Dras Volcanics, sampled from Chiktan township (~35 km ENE of Kargil; Figure **3.1**). The majority of the age constraints for the Dras Volcanics either come from cross-cutting and intrusive relationships of the gabbroic to granodioritic rocks from the Kargil Intrusives (also referred to as the Kargil Intrusive Suite) or intercalated fossiliferous sedimentary layers. Granodiorite from the Kargil Intrusives sampled near Kargil have zircon U-Pb multi-grain TIMS ages of 103 ± 3 Ma and 101 ± 2 Ma, respectively (Honegger et al., 1982; Schärer et al., 1984a). Reuber et al. (1989) dated a diorite pluton from this same intrusive suite, producing a biotite K-Ar age of 94 ± 3 Ma. However, this latter result has been interpreted as a cooling age, with the crystallisation age closer to those ages previously produced by Honegger et al. (1982) and Schärer et al. (1984a). However, Brookfield and Reynolds (1981) produced a younger age for the intrusive complex, with a syenite intruding the Dras Volcanics at Kargil producing a hornblende $^{40}Ar/^{39}Ar$ age of 82 ± 6 Ma. Honegger et al. (1982) also dated granodioritic intrusions near Mount Somau (~10 km SW of Kargil) producing K-Ar biotite and white mica ages of 75 ± 3 Ma and 70 ± 3 Ma. Interbedded calcareous layers within the Dras Volcanics yielded Albian to Cenomanian (113-94 Ma) *Orbitolina* (Reuber et al., 1989) and an ammonite (*Oxytropidoceras*) reported from Kargil was proposed to be late Albian (Thieuloy et al., 1990). Sections of the Dras Volcanics are reportedly underlain by plutonic mafic cumulates and Middle-Upper Jurassic (Callovian-Tithonian; 166-145 Ma) radiolarian cherts (Honegger et al., 1982).

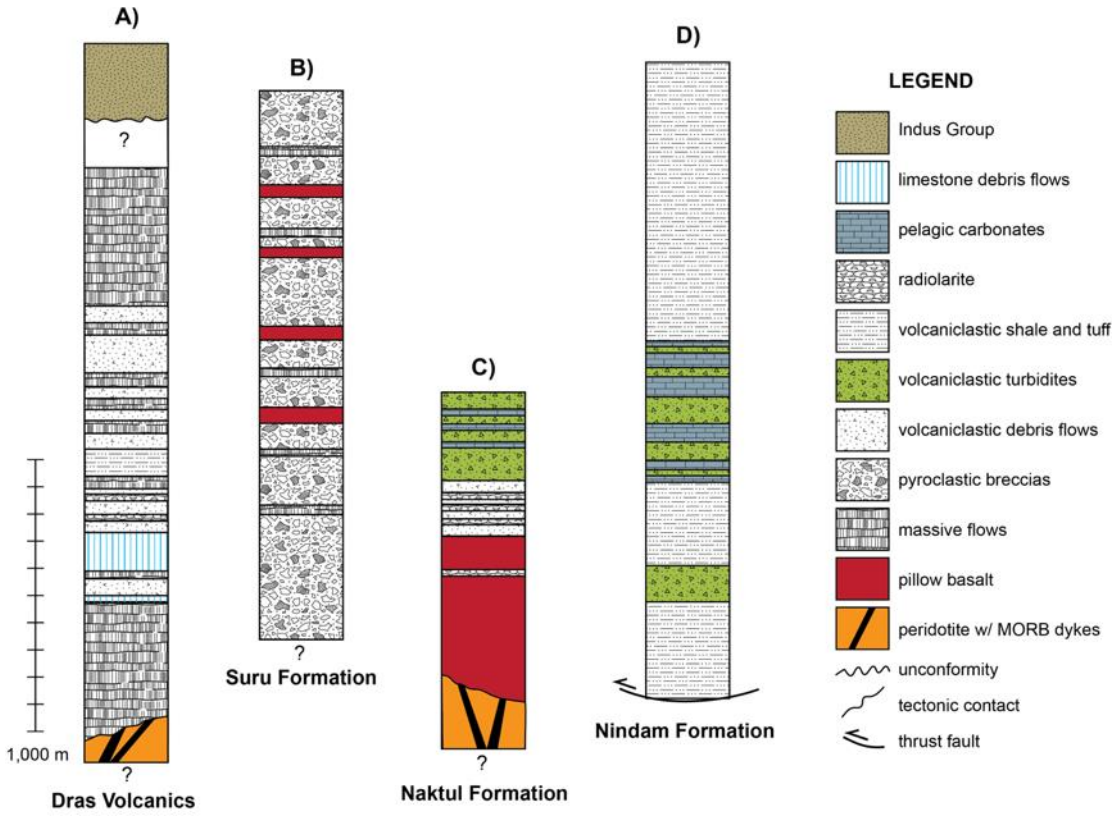

Figure 3.2: Representative stratigraphic columns of key units within the Dras-Nindam terrane. Adapted from Robertson and Degnan (1994). **A)** Representative stratigraphic column of the Dras Volcanics; **B)** Representative stratigraphic column of the Suru Formation; **C)** Representative stratigraphic column of the Naktul Formation; **D)** Representative stratigraphic column of the Nindam Formation.

3.1.2.2 Suru Formation

The Suru Formation (column B on Figure **3.2**) is the western-most part of the Dras-Nindam terrane, and incorporates island arc intrusive rocks, volcanic rocks and related volcano-sedimentary material (Robertson and Degnan, 1994). This unit is up to 5 km thick in some sections and is considered to represent the largely preserved interior of the Dras Arc. Structurally, the Suru Formation overlies oceanic crust of the Neotethyan Ocean and mantle-derived material, including pillow basalts, gabbros and ultramafic rocks (Honegger et al., 1982; Reuber, 1989). The Suru Formation can be further divided into the Dras I and Dras II sub-units (Reuber, 1989).

3.1.2.3 Naktul Formation

The Naktul Formation (column C on Figure **3.2**) is approximately 3 km thick and structurally overlies the Suru Formation. The unit is composed of coarse-grained volcaniclastic material with minor basic intrusives, limestones and chert (Reuber, 1989; Sutre, 1990). The formation has an elongated outcrop and is exposed east of the township of Kargil and is absent of arc plutonic rocks. Robertson and Degnan (1994) interpreted this succession to represent a marginal-arc

setting, with sedimentation occurring along the flanks of the Dras Arc. The Naktul and Nindam formations can be separated from each other on the basis of a thin strip of serpentinite-matrix mélange (Robertson and Degnan, 1994).

3.1.2.4 Nindam Formation

The Nindam Formation (column D on Figure **3.2**) is the eastern-most section of the Dras-Nindam Terrane and represents the distal facies of this stratigraphic sequence. Following the Suru (Dras I and Dras II) and Naktul formations, the Nindam Formation comprises up to 2.5 km of interbedded volcaniclastic turbidites and shales, with minor pelagic carbonates and a limestone clast dominated conglomerate package. The Nindam Formation is an overturned sequence demonstrating overall younging towards the north evidenced in the direction of mass sediment transportation (Clift et al., 2000; Robertson and Degnan, 1994). Upadhyay and Sinha (1998) were the first to suggest that the forearc Nindam Formation received sediment not only from the Dras Arc, but also the leading passive margin of India. Following this work, palynological studies from the Nindam Formation produced Permian, Mesozoic and Palaeocene palynomorphs from volcaniclastic sandstones (Upadhyay et al., 2004). The Permian and Mesozoic palynomorphs were found to be of Gondwanan affinity and are suggested to be derived from the Indian passive margin (Upadhyay et al., 2004). Palynomorphs of Palaeocene age (~66-56 Ma) were also reported from the Nindam Formation. This Palaeocene age is the youngest reported age for the Nindam Formation (Upadhyay et al., 2004). Prior to this thesis, zircon isotopic U-Pb dating of the Nindam Formation had not been undertaken.

3.1.3 Structure and metamorphism

With regard to the structure of the Dras-Nindam terrane, large-scale northward back-thrusting and folding is attributed to post-collisional (continent-continent) uplift of the High Himalaya, however the succession is largely intact overall, aside localised faulting and has largely only undergone low-grade greenschist facies metamorphism in some sections (Clift et al., 2000; Searle et al., 1988). With regard to the Dras Volcanics, Sharma et al. (1978) produced a younger K-Ar age of 78 ± 1 Ma for the Dras Volcanics, sampled from Chiktan township (~35 km ENE of Kargil; Figure **3.1**). This sample was associated with the northern ophiolitic mélange zone, which may be comparable to the Mongyu Mélange farther to the east (Robertson, 2000). It has been suggested that this younger age used for the Dras Volcanics could represent metamorphic overprint and is considered secondary, relating to deformation (Bhat et al., 2019; Reuber et al., 1989). With regard to the Suru Formation located in the west near Kargil, the unit has undergone greenschist facies metamorphism with higher-grade contact metamorphism located in the north associated with arc intrusive rocks. Further, the Dras I and Dras II sub-units of the Suru

Formation represent a lower metamorphosed and deformed unit, and an upper unconformably overlying unmetamorphosed and less-deformed unit, respectively (Reuber, 1989). The Dras I sub-unit demonstrates high-grade amphibolite-facies metamorphism at shear zones located in the north, which has been interpreted to relate to collision of the arc with continental crust (Reuber, 1989). The distal Nindam Formation exhibits large-scale folding and localised thrust faults. Through a series of transects, Clift et al. (2000) reported a series of north-vergent asymmetrical folds.

3.2 Neotethyan Indus ophiolites

3.2.1 Spongtang Ophiolite

The Spongtang Ophiolite, also referred to as the Spongtang Massif and Spongtang Ophiolite-Spong Arc Complex, has been reviewed by Buckman et al. (2018), with previous descriptions provided by Fuchs (1982), Gansser (1964), Reuber (1986) and Searle (1986). The complex is located in the Zanskar mountain range in Ladakh, approximately 30 km south of the Indus Suture Zone, proximal to the township of Photoskar (Figure **3.1**). It has been described as the best preserved Neotethyan oceanic crust of the Indus Suture Zone ophiolites, with the next most complete being the Nidar Ophiolite, located farther east. The Spongtang Ophiolite-Arc Complex is an important record of the long-lived Neotethyan Ocean and intraoceanic activity, including subsequent obduction, prior to continent-continent collision (Buckman et al., 2018).

There is limited radiometric dating of the Spongtang Ophiolite-Spong Arc Complex, with Pedersen et al. (2001) presenting a zircon U-Pb age of 88 ± 5 Ma from an andesite of the Spong Arc and an age of 177 ± 1 Ma from a Spongtang Ophiolite diorite. Their interpretation was that the Early Jurassic age represents the mid-ocean ridge material that the Spong Arc developed on top of, whereas the Late Cretaceous age was indicative of the minimum age of subduction initiation to form the Spong Arc. Using K-Ar dating Reuber (1989) was able to identify two amphibole age groups, with the first at approximately 170 Ma and the second ranging from 140-125 Ma. These ages loosely fit with those U-Pb ages determined from Pedersen et al. (2001) and coincides with the model that sees a Jurassic Ophiolite age and a Cretaceous period of island arc igneous activity. With regard to biostratigraphic work, Baxter et al. (2010) were able to extract and determine Early Cretaceous radiolarian faunal assemblages from red cherts associated with the Spong Arc. Buckman et al. (2018) portray a temporally better-constrained tectonic model for the Spongtang Ophiolite-Spong Arc Complex with new zircon U-Pb geochronology and isotopic Hf data. Zircons extracted from gabbro and plagiogranite collected from the Spongtang ophiolite yield zircon U-Pb (SHRIMP) ages of ~135 Ma and zircon initial εHf values of +14 to +16

indicating extremely juvenile, depleted mantle sources. Buckman et al. (2018) interpreted the Jurassic (177 ± 1 Ma) zircon age determined from a diorite by Pedersen et al. (2001) to represent the older MORB Neotethyan protolith, upon which a younger intraoceanic, supra-subduction zone island arc (Spong Arc) was able to develop as a result of subduction initiation during the Early Cretaceous (~ 135 Ma), consistent with biostratigraphic constraints provided by Early Cretaceous radiolarian (Baxter et al., 2010).

3.2.2 Nidar Ophiolite

The Nidar Ophiolite (Figure **3.1**) is preserved in eastern Ladakh located farther east of the Spongtang Ophiolite (Ahmad et al., 2008; Mahéo et al., 2004). The Zildat mélange occurs along the southern margin of the Nidar ophiolite and represents the thrust contact between it and Indian passive margin sequences (Ahmad et al., 2008; Thakur and Misra, 1984). The southward thrusted Nidar ophiolite exhibits a near complete ophiolitic stratigraphy, with (i) foliated gabbros (~100 m), (ii) massive gabbros cross-cut by well-developed dykes (~500 m), and (iii) volcanic rocks, including pillow basalt plus radiolarian cherts representing the crustal portion (~500 m; Mahéo et al., 2004). With regard to tectonic evolution of the Nidar Ophiolite, earlier workers proposed that the complex represented relics of the oceanic crust including an archetype section of ultramafic rocks at the base, followed by gabbros, volcanic rocks and associated sediment (Thakur, 1990; Thakur and Virdi, 1979). More recent investigations have suggested that the Nidar ophiolitic complex represents the remnants of an intraoceanic island arc, as opposed to the previously assumed oceanic floor sequence (Mahéo et al., 2000; Mahéo et al., 2004; Sachan, 2001). Mahéo et al. (2004) noted that emplacement of the ophiolite was poorly constrained. Stratigraphic evidence by Thakur and Virdi (1979) determined a wide age range of Cretaceous to Eocene radiolarian faunal assemblages. However, $^{39}Ar/^{40}Ar$ dating of mafic rocks (gabbro and basaltic-andesite) from the Nidar ophiolitic complex indicate that the intraoceanic arc developed during the Lower Cretaceous (130-110 Ma; Mahéo et al., 2004). The presence of ~55 Ma eclogites (Tso Morari) to the south of the Nidar Ophiolite record subduction of Indian continental rocks (Panjal Traps) associated with arc collision (de Sigoyer et al., 2000). This corresponds well with the Eocene emplacement age established at Spongtang (Buckman et al., 2018).

3.3 Collisional mélange zones

There are two distinct mélange zones either side of the Dras-Nindam terrane which, as described by Robertson (2000), is wedged between the Indian and Eurasian continents (Figure **3.1**). The first mélange zone occurs along the southern contact of the Dras-Nindam terrane with the Indian Zanskar Group and includes the Urtsi, Wanlah and Sapi-Shergol mélange zones and

in places grades into the mud-matrix mélange of the Lamayuru Complex. This mélange probably developed during the collision of a Neotethyan intraoceanic arc with India. The second mélange is located along the north of the Indus Suture and includes the Mongyu mélange and possibly represents the final continent-continent collision between India and Eurasia.

3.3.1 Southern mélange zone

The Urtsi-Wanlah-Sapi-Shergol mélange, also referred to as separate entities including the Urtsi mélange (Robertson and Degnan, 1994) in the east, the Wanlah mélange (Corfield and Searle, 2000) in the centre and the Sapi-Shergol mélange (Groppo et al., 2016; Mahéo et al., 2006) in the west, or collectively as the southern mélange zone (Robertson, 2000) was first described by Gansser (1974), Frank (1977) and Gansser (1980). The Urtsi-Wanlah-Sapi-Shergol mélange is in fault contact with the Nindam Formation to the north, and transitions into the mud-matrix mélange of the Lamayuru Complex to the south. Laterally, the southern mélange zone extends from the townships of Urtsi in the east to Shergol in the west, outcropping discontinuously over a distance of ~250 km (Figure **3.1**). This was previously mapped as the 'Ophiolitic Mélange Unit' of Honegger et al. (1989).

Collectively, the southern mélange zone ranges from 800-1000 m thick, and transitions from mud-matrix in the east to serpentinite-matrix mélange in the west. Detached blocks within the mélange range from <1 m to several tens of meters in size, and include, (i) ophiolitic, volcanogenic and associated material (pillow basalt, brecciated basalts, volcaniclastic rocks, radiolarite, gabbro and serpentinised ultramafic rocks), (ii) clastic and carbonate sedimentary rocks (siltstones, sandstones, conglomerates, limestones and limestone breccia), (iii) calc-silicates and marble and, (iv) blueschist facies rocks (Corfield and Searle, 2000; Groppo et al., 2016; Honegger et al., 1989; Mahéo et al., 2006; Robertson, 2000; Robertson and Degnan, 1994).

3.3.1.1 Urtsi mélange

The Urtsi mélange is best exposed directly north of Urtsi village. The unit can be described as a dark grey mud-matrix mélange and is approximately 1 km thick consisting of detached blocks ranging from <1 m to several tens of meters in size and include, (i) volcanogenic and associated material (pillow basalt, volcaniclastic rocks, red and green radiolarite), (ii) clastic and carbonate sedimentary rocks (siltstones, sandstones, limestone and limestone breccia), and (iii) calc-silicates and marble (metamorphosed carbonate-bearing sedimentary rocks; Robertson and Degnan, 1994). Blueschist has also been reported within the Urtsi mélange (Honegger et al., 1989).

3.3.1.2 Wanlah mélange

The same dark grey mud-matrix observed at the Urtsi mélange can also be identified at Wanlah, with the mélange best exposed north of Wanlah village and being approximately 800 m thick (Corfield and Searle, 2000). Blocks range from <1 m to several tens of meters in size, and include, (i) volcanogenic and associated material (most notably a transitional block of basalt, brecciated basalt and red-green ribbon radiolarite), (ii) clastic and carbonate rocks (siltstones, sandstones, coarse conglomerates and limestones) and (iii) serpentinite (occurring as rare matrix material and clasts within conglomerates).

3.3.1.3 Sapi-Shergole mélange

The Sapi-Shergol mélange is best exposed north of the township of Shergol and represents the western-most extension of the southern mélange zone. Contrary to the eastern section of the mélange at both Urtsi and Wanlah, the Sapi-Shergol mélange exhibits a typical serpentinite-matrix. The mélange at this locality is approximately 1 km thick. Blocks range from <1 m to several of meters in size, and include, (i) ophiolitic and volcanic related rocks (basalts, volcaniclastics, undated gabbros and serpentinite/ultramafics), (ii) clastic sedimentary rocks (siltstones, sandstones) and (iii) blueschist facies rocks (Groppo et al., 2016; Mahéo et al., 2006).

3.3.2 Northern mélange zone

The Mongyu mélange, also referred to as the northern mélange zone, has been described in detail by Robertson (2000). The unit is a serpentinite-matrix mélange and is approximately 100 m thick consisting of detached blocks ranging from <1 m to several meters in size and includes, (i) plutonic rocks (gabbros, including pegmatitic gabbros occurring as blocks and dykes), (ii) clastic and carbonate rocks (siltstones, sandstones and dirty-limestones), (iii) volcanic rocks and associated material (basalts, including basic dykes, brecciated basalt, tuffs, volcaniclastic rocks and chert), and (iv) ultramafic rocks (peridotite with varying degrees of serpentinisation). The Mongyu mélange is well exposed along strike, trending east-west for approximately 30 km between the villages of Mongyu in the east to Hungru in the west (Robertson, 2000; Figure **3.1**). The unit separates the Lower to Upper Cretaceous forearc volcaniclastic Nindam Formation (Dras-Nindam terrane) in the south from the Lower Cretaceous (Aptian to Albian; Cherchi et al., 1984; Masse and Maresca, 1997; Mathur and Vogel, 1988) Khalsi Formation in the north (Robertson, 2000).

3.4 Indian passive margin

3.4.1 Lamayuru Complex

The Lamayuru Complex (also referred to as the Lamayuru Flysch and Lamayuru mélange) was first described by Frank (1977), Bassoullet et al. (1981) and Thakur (1981). The unit consists of shales, siltstones and sandstones, with exotic blocks of limestone, volcanic rocks and other associated material enveloped within a mud-matrix (Brookfield and Andrews-Speed, 1984; Robertson and Degnan, 1993). The Lamayuru Complex occurs north of the Zanskar Supergroup and bounds the southern edge of the Nindam Formation (Figure **3.1**). The unit was initially interpreted as representing channel-filled debris flows, containing large olistoliths that had slumped off the Indian passive margin (Zanskar Supergroup) before being chaotically incorporated into deep water muds and sands (Robertson and Degnan, 1993). Petrographic studies of sandstones within this unit by Brookfield and Andrews-Speed (1984) confirmed a continental provenance and they attributed the disrupted nature of the Lamayuru Complex to multiple regimes of extension and collapse, before final compression during continental collision. Buckman et al. (2018) provided an alternative interpretation of the Lamayuru Complex as a tectonic mud-matrix mélange rather than a depositional olistostromal debris flow. This was based on the lack of any stratigraphic consistency to the Lamayuru Complex and its association with major fault contacts between the Spongtang Massif, the Zanskar Group and the Dras-Nindam terrane. The scaly mud-matrix of the Lamayuru Complex is typical of over-pressuring associated with crustal flexure and the diapiric rise of mud-matrix mélanges along suture zones between arc-continent collisions, as exemplified by the Lichi Mélange in Taiwan (Huang et al., 2000) and the Yamdrok mélange, along strike with the Lamayuru Complex, in Tibet (Jianbing and Aitchison, 2002).

3.4.2 Zanskar Supergroup

The Zanskar Supergroup generally occurs to the south of the Indus Suture (Figure **3.1**), representing the shallow marine Indian passive margin and has been described in detail by Fuchs (1982), Garzanti et al. (1987) and Gaetani and Garzanti (1991). It consists predominantly of Permian to lower Eocene carbonates, shales and sandstones. Importantly, this sequence structurally underlies obducted ophiolitic nappes, such as the Spongtang Massif and Nidar Ophiolite, emplaced on top of the Indian passive margin (Reuber, 1986). The youngest known units overlying the Zanskar Supergroup are the Eocene Chulung La and Kong Formations (Fuchs, 1982; Fuchs and Willems, 1990). The youngest detrital zircon U-Pb population of the Chulung La Formation is 53.7 ± 1.5 Ma, while the Kong Formation has produced a youngest detrital zircon population of 56.3 ± 1 Ma (Najman et al., 2017).

3.5 Eurasian margin

3.5.1 Ladakh Batholith

The Ladakh Batholith is a segment of the Trans-Himalaya Batholith (Figure **3.1**), which extends some ~3000 km over the entire length of the Himalaya Orogen and represents the convergent margin that developed as a result of north dipping subduction beneath the southern margin of the Eurasian plate prior to final continent-continent collision between India and Eurasia (Harris et al., 1988; Yin and Harrison, 2000). The Trans-Himalayan Batholith is subdivided into the Gangdese Batholith east of the Karakoram Fault in Tibet, the Ladakh Batholith west of the Karakoram Fault in NW India, and the Kohistan Arc further west in Pakistan (Ahmad et al., 1998; Debon et al., 1987; Harris et al., 1988; Honegger et al., 1982). In Tibet, the Gangdese Batholith was intruded into the Lhasa terrane, which represents a rifted Gondwanan continental fragment that docked with Eurasia along the Bangong Suture to the north (Borneman et al., 2015). The extent and width of the Lhasa terrane diminishes to the west to the point that it is not recognised on the western side of the Karakoram Fault in Ladakh. Hence, the Ladakh and Kohistan batholiths are interpreted to have developed in more of an island-arc setting and separated from southern Eurasia by the Mesotethyan Shyok Ocean. There are parallels here with that observed in western Iran, where the Sanandaj-Sirjan Zone of Gondwana provenance has docked first onto Eurasia, by closure of the Paleotethyan Ocean (Fergusson et al., 2016).

The Ladakh Batholith extends for ~600 km and is bound in the north by the Shyok Suture Zone and in the south by the Indus Suture Zone (Singh et al., 2007). The Batholith has been described in detail by Honegger et al. (1982) and Singh et al. (2007). The complex consists of calc-alkaline (I-type) intrusive rocks ranging from gabbroic to granitic in composition (Honegger et al., 1982; Singh et al., 2007; White et al., 2011) and associated extrusive rocks of the Khardung Volcanics which are andesitic to rhyolitic in composition (Dunlap and Wysoczanski, 2002). Reports have also been made of leucogranite intrusions (Reichardt et al., 2010) and andesitic dykes (Heri et al., 2015) cross-cutting the Ladakh complex. The Ladakh Batholith intrudes Jurassic rocks of the Shyok ophiolite and associated volcaniclastics (Reuber, 1990).

Honegger et al. (1982) reported that the formation of the Ladakh Batholith was formed through multiple phases spanning between 110 – 40 Ma with the most voluminous and pervasive having occurred at approximately 60 Ma. However, White et al. (2011) determined that granitoid emplacement of the Ladakh Batholith occurred episodically between 66 Ma and 46 Ma. They proposed that the bulk of the batholith was emplaced between 63 Ma and 55 Ma, with a final

phase of magmatism resulting in aplitic cross-cutting leucogranites, pegmatitic dyke swarms and sub-volcanic dykes. White et al. (2011) also found no evidence for a major magmatic phase at the previously reported 103 – 101 Ma, near the township of Kargil in western Ladakh. The apparent switch from I- to S-type magmatism has been used as evidence for the initiation of continental collision between India and Eurasia (Searle et al., 1988; Searle et al., 1987; St-Onge et al., 2010; Bouilhol et al., 2013). However, White et al. (2011) found that there was no major shift in the geochemistry that could correlate with a change in magma type.

It has been argued that the Dras-Nindam terrane could be related to the Ladakh Batholith of the Trans-Himalayan Batholith. For example, Honegger et al. (1982) and Schärer et al. (1984a) produced U-Pb ages for the Kargil gabbroic to granodioritic plutons (103 Ma and 101 Ma, respectively), which intrude the Dras Volcanics. These plutons are geochemically similar to the calc-alkaline Ladakh and Gangdese batholiths in that they are arc magmas, however this is not conclusive proof that they are indeed related and consanguineous. Rather, it simply indicates coeval arc magmatism, and additional evidence is required to demonstrate that they are portions of the same tectonically-dismembered arc, or they developed as separate terranes, with links to different subduction zones. Buckman et al. (2018) suggested that the Kargil Intrusives may represent the core of the Dras Arc, which it intrudes into, rather than representing an older phase of the separate Ladakh Arc.

3.5.2 Tar Group

The Tar Group consists of Cretaceous (Albian) to lower Eocene clastic and carbonate rocks, including interbedded siltstones, shales and sandstones, debris-flow immature turbidites, conglomerates and breccias and deep marine limestones to shallow-water platform carbonates and represents the forearc basin material of the Ladakh Batholith (Clift et al., 2002a; Garzanti and Van Haver, 1988; Henderson et al., 2010; Searle et al., 1990; Sinclair and Jaffey, 2001; Steck et al., 1993). From base to top, the Tar Group consists of the Jurutze Formation, Khalsi Limestone, Sumda Formation, Chogdo Formation and finally a distinct Nummulitic Limestone unit (Henderson et al., 2010). The Jurutze Formation and the Khalsi Limestone are the oldest sections of the Tar Group and are tectonically juxtaposed against the Nindam Formation to the south. This south dipping thrust fault is marked by the Mongyu Mélange (Robertson, 2000).

3.6 Indus Group

The Indus Group (commonly referred to as the Indus Molasse; Figure **3.1**) consists of mid Eocene to early Miocene post-collisional sedimentary deposits resulting from the initiation of

continental collision between India and Eurasia, and mass-shedding from the resultant topographic uplift (Clift et al., 2002a; Henderson et al., 2010; Searle et al., 1990; Sinclair and Jaffey, 2001; Wu et al., 2007). The conglomerates and sandstones of the post collisional Indus Group were deposited through the alternation between shallow marine, fluvio-deltaic and alluvial settings. In some areas the Indus Group also directly and conformably overlies exposed granites of the Ladakh Arc, implying that deposition would have occurred following substantial uplift and erosion of the underlying batholith in the later stages of development.

The stratigraphy of the Indus Group is still rather contentious with unit boundaries and its definition debated. Folding and thrusting has further complicated the sequence and obscured some of the original stratigraphic relations during continental collision. Different workers (Brookfield and Andrews-Speed, 1984; Clift et al., 2001; Garzanti and Van Haver, 1988; Henderson et al., 2010; Henderson et al., 2011; Searle et al., 1990; Sinclair and Jaffey, 2001; Van Haver, 1984) have divided the Indus Group into a number of formations. Importantly, recent work by Henderson et al. (2011) has revealed that the youngest detrital zircon population of 41 Ma in the Upper Nimu Formation may represent the latest stage calc-alkaline magmatism of the Ladakh Arc and as such, provides the maximum possible age for the basal deposition of the Indus Group. Although significant work has been completed on the Indus Group, it is often over-simplified as representing continuous sedimentation between India and Eurasia in a single basin, rather than distinguishing between units that may have been starting to form at the same time in several depocenters on the flanks of the approaching continents as continent-continent collision initiated. However, importantly, this group represents both, (i) complexly interfingered and interleaved stratigraphic units that developed contemporaneously on both the Indian and Eurasian margins prior to and during continental collision, and the (ii) first post-collisional units, following final continental collision, as such it demonstrates a mixture of detritus from both the Indian and Eurasian continents.

Chapter Four: Age and provenance of the Nindam Formation, Ladakh, NW Himalaya: Evolution of the intraoceanic Dras Arc before collision with India

Jessica M.J. Walsh[1], Solomon Buckman[1], Allen P. Nutman[1], and Renjie Zhou[2]

[1]GeoQuEST Research Centre, School of Earth, Atmospheric and Life Sciences, University of Wollongong, Wollongong, NSW 2522, Australia.
[2]School of Earth and Environmental Sciences, The University of Queensland, Brisbane, QLD 4072, Australia.

Research highlights:

- The Nindam Formation was deposited in an intraoceanic forearc basin as distal deposits, largely sourced from ~84-125 Ma Dras Arc rocks.
- A distinct "Gondwanan" signature comprised of Precambrian populations occurs in all samples.
- The intraoceanic Dras Arc collided and accreted onto the passive margin of India before final continental collision.

Key words:

Forearc basin, India-Eurasia collision, Ladakh Himalaya, Dras-Nindam terrane, Dras Arc, Nindam Formation

Citation:

Walsh, J. M., Buckman, S., Nutman, A. P., & Zhou, R. (2019). Age and Provenance of the Nindam Formation, Ladakh, NW Himalaya: Evolution of the Intraoceanic Dras Arc before Collision with India. Special Edition: "Collisional orogenic systems as recorders of collisions between arc and continents". *Tectonics, 38*(8), 3070-3096. [7 citations as of 5th February 2021; Google Scholar]. http://dx.doi.org/10.1029/2019TC005494

Foreword:

This chapter addresses the first objective of this project; '*to determine the maximum age of deposition and provenance of the Nindam Formation using detrital zircon U-Pb geochronology to ascertain whether the Dras Arc was intraoceanic or continental-related*'.

4.1 Abstract

The Dras Arc in NW India Himalaya is a belt of basaltic-andesites intercalated with arkose-dominated volcaniclastic rocks of the Nindam Formation situated along the Indus Suture between India and Eurasia. Debates exist as to whether these rocks developed in a forearc basin to the Eurasian margin or as part of an intraoceanic island arc system that collided with either India or Eurasia before final continental collision. Detrital zircons from the Nindam Formation yield U-Pb age spectra with dominant youngest age populations of ~84-125 Ma, corresponding with arc magmatism. Sandstone provenance analysis from the Nindam Formation indicates that the Dras Arc evolved from an undissected arc to dissected arc over a period of ~41 million years. Slightly older, smaller populations occur at ~135-185 Ma, corresponding with reported ages of Neotethyan ophiolites (e.g., Spongtang). The basal section of the Nindam Formation reveals the presence of arc-derived basaltic-andesite and tonalite clasts, plus ophiolitic components sourced from an adjacent accretionary complex. There is a distinct absence of quartz or felsic granitic clasts, suggesting that the Nindam Formation did not develop as a forearc basin to the Ladakh Batholith of southern Eurasia but rather as separate intraoceanic island arc. A distinct minor "Gondwanan" signature occurs in all samples, with zircon age peaks at ~514-988 Ma, ~1000-1588 Ma, ~1627-2444 Ma and ~2500 Ma. We suggest that the Dras and Spong arcs are part of the same intraoceanic island arc system that developed as a result of subduction initiation along NNE-SSW transform faults perpendicular to the Indian and Eurasian continents.

4.2 Introduction

The collision and accretion of juvenile intraoceanic arcs and ophiolite complexes is an important mechanism of continental growth (Charvet, 2013; Lee et al., 2007; Rioux et al., 2007). Collisional events involving island-arc complexes colliding with continental crust can result in drastic, widespread deformation, for example, the Semail ophiolite on the Arabian margin (Searle et al., 2004) or the Luzon Arc colliding with Eurasia in Taiwan (Huang et al., 2008). Examples of arc-continent collisions also occur in older orogens such as Central Asia (e.g., Xiao et al., 2004) and western North America (e.g., Coney, 1989), where they are recognised as important "quantum" additions to the growth of continental margins (Aitchison and Buckman, 2012) compared to the usual accretionary processes (Cawood and Buchan, 2007). The recognition of oceanic, island arc terranes onto continental margins is often complicated by the intense deformation and fragmentation associated with collision, uplift and subsequent erosion. Obducted island arc terranes transferred from the downgoing subducting plate to the overriding plate are often poorly preserved or completely missing due to the destructive nature of collision and subsequent erosion following uplift (Draut and Clift, 2013). This, combined with the zircon-poor nature of the predominantly mafic-intermediate (basaltic-andesitic) composition of magmatism within the early stages of most island arcs, means that unveiling their inception and early history can be hard to ascertain. On the other hand, marine forearc basins can provide a near continuous detrital record of arc evolution whilst they remain a depocenter for material shed from the active arc. Well-preserved forearc basin sequences such as the Nindam Formation in Ladakh, NW India, permit study of the evolution of the Dras Arc before it collided with either India or Eurasia. Forearc basins record the history of arc massif unroofing and evolution, as well as the influx of detritus from more distal sources (Moore et al., 2015). These basins are not only important reservoirs for detritus shedding directly off the arc, they are also able to provide insight into other allochthonous terranes which may have contributed detritus, as evidenced by detrital zircon populations and provenance studies.

The Dras Arc is located along the Indus Suture, the westerly extent of the Indus-Yarlung-Tsangpo Suture (IYTS) in NW India (Figure **4.1**). To the west near the township of Kargil, it is dominated by basaltic andesites of the Dras Formation, while further east near the township of Khalsi it is dominated by forearc arkose-dominated volcaniclastic rocks of the Nindam Formation (Clift et al., 2000; Clift et al., 2002b; Robertson and Degnan, 1994). Given the unambiguous stratigraphic relationships between the Dras Formation and sedimentary Nindam Formation compared to the clearly faulted contacts marked by extensive mélange with the Indus Molasse and Ladakh Batholith to the north and the Indian Lamayuru Complex to the south, we use the term Dras-Nindam terrane to refer collectively to this mafic, island arc complex. The

Dras-Nindam terrane is generally regarded as equivalent to the lower crustal Chilas Complex of the Kohistan Arc to the west in Pakistan (Bilqees et al., 2016; Khan et al., 1989; Schaltegger et al., 2002). However, debates exist as to whether the Dras-Nindam terrane developed as the forearc basin to the Eurasian margin (Fuchs, 1982; Honegger et al., 1982) or as a purely intraoceanic island arc that may have collided with either India or Eurasia before final continental collision (Clift et al., 2000; Corfield et al., 2001). In this paper, detailed field mapping, provenance studies, whole rock geochemistry and detrital zircon geochronology are presented to help resolve debate concerning the age and origin of the Dras-Nindam terrane and the nature of this arc-continent collision in relation to the final continent-continent collision of India and Eurasia.

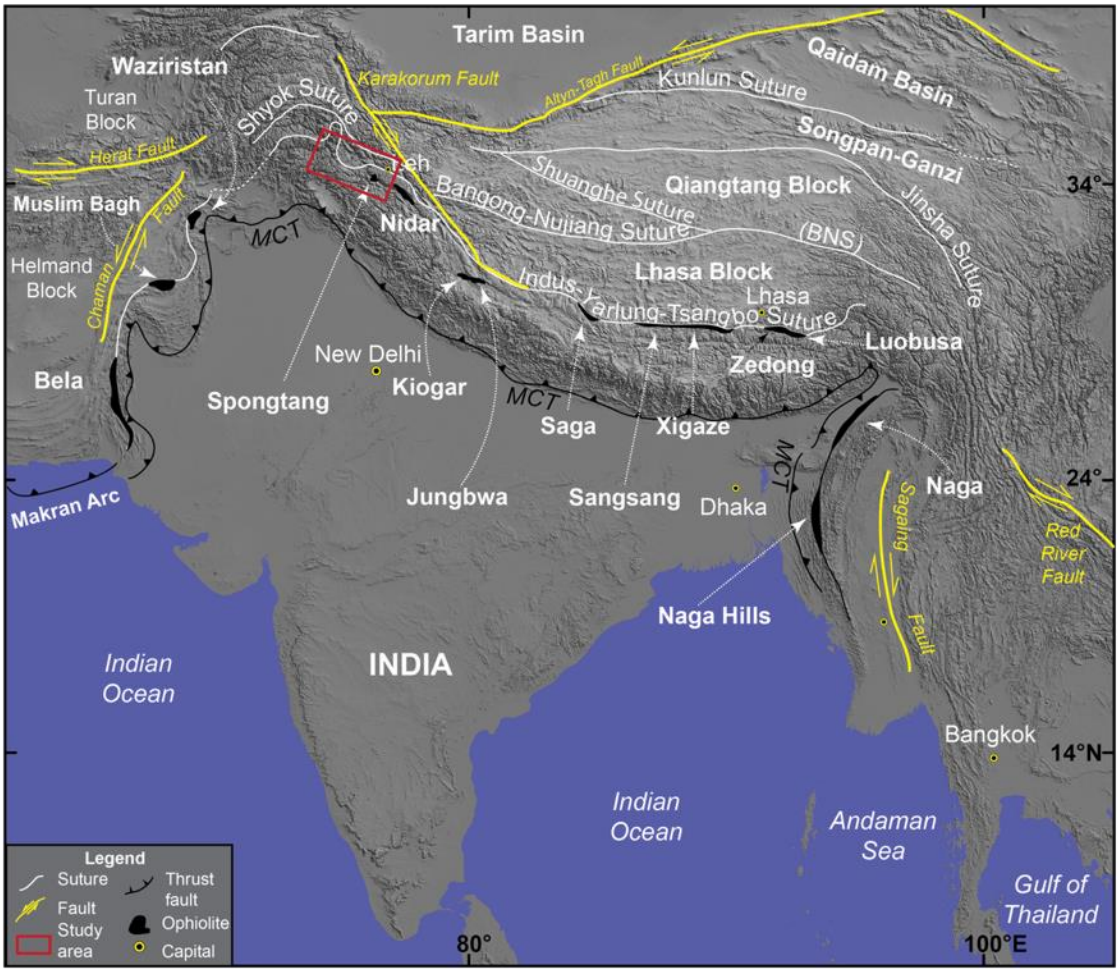

Figure 4.1: Regional tectonic setting of the Himalayan-Tibetan orogen, displaying Tethyan ophiolite remnants in black. Map modified from Buckman et al. (2018). DEM sourced from Global Mapper software (Global Mapper, 2009). The study area is shown with a red rectangle.

4.3 Geological setting

The Indus-Yarlung-Tsangpo Suture (IYTS) separates Eurasian and Gondwanan continental rocks but also includes fragments of intraoceanic ophiolitic, island arc and seamount material accreted onto either continent before final collision (Aitchison et al., 2003; Hébert et al., 2012). To understand fully and reconstruct the collision, it is imperative to distinguish between Eurasian, Gondwanan or intraoceanic units across the suture.

4.3.1 Indian passive margin

4.3.1.1 Zanskar Supergroup

The Zanskar Supergroup occurs to the south of the Indus Suture, representing the shallow marine Indian passive margin (Fuchs, 1982; Gaetani and Garzanti, 1991; Garzanti et al., 1987). It consists predominantly of Permian to lower Eocene carbonates, shales and sandstones. Importantly, this sequence structurally underlies obducted ophiolitic nappes, such as the Spongtang Massif (Reuber, 1986). The youngest known units overlying the Zanskar Supergroup are the Eocene Chulung La and Kong formations (Fuchs, 1982; Fuchs and Willems, 1990), with the youngest detrital zircon age of these units being 54 ± 2 Ma and 56 ± 1 Ma, respectively (Najman et al., 2017).

4.3.2 Neotethyan Indus ophiolites

4.3.2.1 Spongtang Ophiolite

The Spongtang Massif is located ~30 km south of the Indus Suture as an almost complete ophiolite klippe thrust over the Indian Zanskar Supergroup (Buckman et al., 2018; Fuchs, 1982; Gansser, 1964; Reuber, 1986; Reuber et al., 1992; Searle, 1986). Gabbro from the Spongtang Ophiolite was initially dated by Pedersen et al. (2001) as 177 ± 1 Ma, using the zircon U-Pb (TIMS) method. The Spong Arc developed on top of, and into, the ophiolitic complex as subduction continued after arc initiation at ~135 Ma (Buckman et al., 2018) and up until at least 88 Ma as indicated by U-Pb age of a Spong Arc andesite (Pedersen et al., 2001). Baxter et al. (2010) reported Early Cretaceous radiolarian faunal assemblages from red cherts associated with the Spong Arc. The Spongtang Massif is generally interpreted as an Early Jurassic (Pedersen et al., 2001) fragment of mid-ocean ridge material that the Spong Arc developed on top of throughout the Cretaceous from ~135 Ma to at least 88 Ma (Buckman et al., 2018; Pedersen et al., 2001). There is debate surrounding the age for emplacement of the Spongtang Ophiolite, with some proposing obduction between 75-60 Ma (Searle, 1986), while others prefer an emplacement age between 55-50 Ma (Buckman et al., 2018; Garzanti et al., 2005) based on the

fact the Spongtang Ophiolite is thrust over the youngest Eocene Chulung La and Kong formations (Najman et al., 2017) that are units of the Indian Zanskar Supergroup.

4.3.2.2 Nidar Ophiolite

The Nidar Ophiolite is preserved in eastern Ladakh, located to the east of the Spongtang Massif (Ahmad et al., 2008; Mahéo et al., 2004) and developed at about the same time (130-110 Ma) as the Spong Arc (Mahéo et al., 2004). The presence of ~55 Ma eclogites (Tso Morari) to the south of the Nidar Ophiolite record subduction of Indian continental rocks (Panjal Traps) associated with arc collision (de Sigoyer et al., 2000). This corresponds well with the Eocene emplacement age established at Spongtang (Buckman et al., 2018).

4.3.3 Dras-Nindam terrane

The Dras-Nindam terrane extends some 400 km along the Indus Suture in the Ladakh Himalaya and is 15 km wide (Clift et al., 2000; Fuchs, 1982; Reuber, 1989; Robertson & Degnan, 1994); (Figure **4.2**A). To the north, the complex is faulted against the Ladakh Batholith and associated forearc basin material of the Tar Group (Henderson et al., 2010). The fault is marked by the serpentinite-matrix Mongyu Mélange (Robertson, 2000; Figure **4.2**B). This mélange contains blocks of the adjacent Dras-Nindam terrane and Eurasian-derived Tar Group. To the south, the Dras-Nindam terrane is thrust over the highly disrupted Lamayuru Complex, which represents the mud-matrix mélange developed at the faulted contact with Indian continental rocks (Robertson and Degnan, 1993). Slivers of disrupted ophiolitic mélange also occur along this southern contact and contain numerous basalt, chert, gabbro and blueschist blocks (Corfield and Searle, 2000; Groppo et al., 2016; Honegger et al., 1989; Robertson, 2000; Robertson and Degnan, 1994). Most of the deformation within the Dras-Nindam terrane is the result of large-scale north-directed, back-thrusting and folding attributed to post-collisional (continent-continent) uplift of the High Himalaya (Searle et al., 1988). The succession is largely an intact overturned sequence, aside from localised faulting. The Dras-Nindam terrane can be divided into four structural units; (i) the Dras Arc, (ii) Suru Formation, (iii) Naktul Formation and (iv) Nindam Formation. The Chilling Formation, demonstrating arc-derived sedimentation is also described.

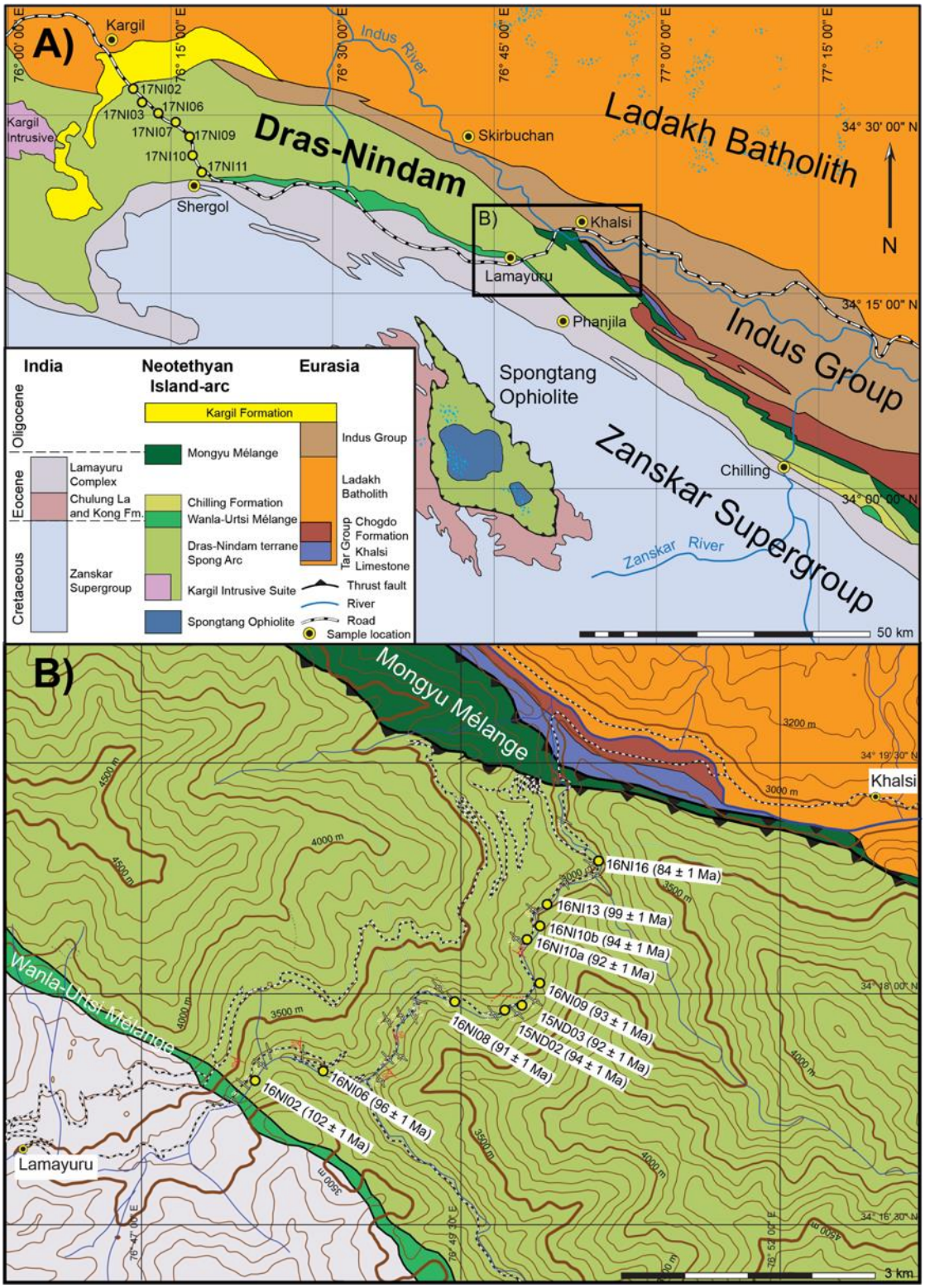

Figure 4.2: Regional tectonic setting of the Dras-Nindam terrane, Ladakh NW India. **A)** Extent of the Dras-Nindam terrane along the Indus Suture, including major tectonic units; **B)** Inset geological transect through the Nindam Formation between the townships of Khalsi (north) and Lamayuru (south). The youngest indistinguishable zircon population is given for each sample. Adapted from Robertson and Degnan (1994) and Steck (2003).

4.3.3.1 Dras Formation

The Dras Formation, informally referred to as the Dras Volcanics, consists of a belt of basaltic-andesitic volcanic rocks and associated volcaniclastic turbidites situated between the Ladakh Batholith and associated Indus Group/Molasse deposits to the north and the Indian Lamayuru Complex to the south. The mafic volcanic rocks have geochemical signatures typical of modern day, juvenile island arc environments in which there is little or no continental influence (Dietrich et al., 1983; Robertson and Degnan, 1994). The Dras Arc has been correlated with the Kohistan Arc of Pakistan (Clift et al., 2002a) and may be similar to the Zedong terrane in Tibet (Aitchison et al., 2000; McDermid et al., 2002). Correlations with the Kohistan Arc have been made on the basis of geographic proximity, radiometric ages and common lithologies (Coward et al., 1987; Khan et al., 1993; Robertson and Degnan, 1994), but it is important to note that there is no continuous exposure between the Dras and Kohistan arcs. Honegger et al. (1982) and Schärer et al. (1984a) produced zircon U-Pb ages for gabbroic to granodioritic plutons of 103 ± 3 Ma and 101 ± 2 Ma, respectively. These plutons intrude the Dras Formation, indicating it is at least 100 Ma. Reuber (1989) produced K-Ar dates of the Dras Formation ranging between 105-95 Ma and an age range between 98-92 Ma for a diorite intruded into the volcanic rocks. Diorite plutons within the Dras Arc are geochemically similar to the calc-alkaline Ladakh and Gangdese batholiths of the Trans-Himalayan intrusive suites, in that they are calc-alkaline, albeit more intermediate than the granitic Ladakh Batholith. For that reason, Coward et al. (1987) interpreted the Kohistan-Dras Arc as originally a single entity that collided with Eurasia at ~100 Ma. Similarly, other researchers propose that the Kohistan and Ladakh terranes were once a single entity, referred to as the Kohistan-Ladakh island arc (KLIA). They suggest that the Dras Arc is a component of this Aleutian-style island arc system which developed on the southern margin of Eurasia, which has the Nindam Formation developing as the equivalent forearc basin sequence (Bouilhol et al., 2013; Burg, 2011).

4.3.3.2 Suru Formation

The Suru Formation (Robertson & Degnan, 1994) is the western-most part of the Dras-Nindam terrane and incorporates island arc intrusive rocks, extrusive and related volcaniclastic/sedimentary material. Large blocks of neritic limestone were interpreted by Robertson and Degnan (1994) as collapsed oceanic atolls. This unit is up to 5 km thick and is considered to represent the interior of the Dras Arc. Structurally, the Suru Formation overlies Neotethyan oceanic crust and mantle-derived material, including pillow basalts, gabbros and ultramafic rocks (Honegger, 1983; Reuber, 1989). The Suru Formation can be divided into the Dras I and Dras II sub-units (Reuber, 1989), which represent a lower metamorphosed and deformed unit, and an upper, unconformably overlying unmetamorphosed and less-deformed

unit, respectively. Robertson and Degnan (1994) describe the Dras II sub-unit as acidic volcanic rocks and fine-grained volcaniclastic turbidites. They suggest this largely undeformed and nearly horizontal unit represents post-collisional magmatism, whereby the intraoceanic Dras Arc collides with Eurasia, and is overlain by volcanic and associated material of the Dras II sub-unit (Robertson & Degnan, 1994). The Suru Formation overlies Callovian-Tithonian radiolarian cherts (Honegger, 1983). Within the lavas of this formation, interbedded calcareous units yielded foraminifera (*Orbitulina*; Reuber, 1989), while an ammonite (*Oxytropidoceras*) reported from nearby Kargil was presumed to be mid-Cretaceous (late Albian; Thieuloy et al., 1990). The oldest K-Ar and U-Pb ages are 110-90 Ma, while the youngest are 80-60 Ma (Honegger et al., 1982; Reuber et al., 1989; Sharma, 1987; Sharma et al., 1978).

4.3.3.3 Naktul Formation

The Naktul Formation structurally overlies the Suru Formation and is composed of coarse-grained volcaniclastic material intercalated with minor basic intrusive rocks, limestones and chert (Reuber, 1989; Sutre, 1990). The formation is elongated in outcrop and exposed east of the township of Kargil. It is devoid of any arc plutonic rocks. Robertson and Degnan (1994) interpreted this formation to represent a marginal-arc setting, with sedimentation occurring along the flanks of the Dras Arc. The Naktul Formation and the Nindam Formation are separated from each other by a thin strip of serpentinite-matrix mélange. Within the Naktul Formation *Orbitulina* and other foraminifera are assigned Aptian-Cenomanian in age (125-94 Ma) by Sutre (1990), with Robertson and Degnan (1994) reporting Late Cretaceous foraminifera ages. Basaltic dykes cross-cutting ultramafic basement of the Naktul Formation have been dated at 97 ± 7 Ma using K-Ar (Reuber, 1989).

4.3.3.4 Nindam Formation

The Nindam Formation overlies the Suru and Naktul formations and is the eastern-most part of the Dras-Nindam terrane, representing the most-distal facies of this stratigraphic sequence. It comprises up to 2.5 km of interbedded volcaniclastic turbidites and shales, with minor pelagic carbonates and a conglomerate package dominated by limestone clasts. Robertson and Degnan (1994) provided detailed stratigraphic and petrographic descriptions of sections through the Nindam Formation. They interpreted the Nindam Formation to have developed in a deep marine environment, dominated by juvenile volcaniclastic lithofacies, calci-turbidites, minor chert and tuff and some mass-flow conglomerates derived from the nearby Dras intraoceanic arc complex. Between the townships of Lamayuru and Khalsi (Figure **4.2**B), the Nindam Formation is an overturned sequence demonstrating overall stratigraphic younging towards the north. In the eastern section of the Nindam Formation, *Globotruncana* and various macro-fossils have been

biostratigraphically placed as Upper Cretaceous (Sutre, 1990), while other beds exhibit redeposited shallow water microfossils assigned as Lower Cretaceous (Sutre, 1990). Isotopic dating of the Nindam Formation has not been undertaken previously.

4.3.3.5 Chilling Formation

The Eocene Chilling Formation, previously referred to as the Chilling Molasse (Fuchs, 1986) or Khalsi Molasse (Clift et al., 2002b) was first recognised and described by Sterne (1979) as a unit faulted between the Zanskar Supergroup and the Nindam Formation. The unit consists of green-purple-red siltstones, shales and mass-flow conglomerates. Clasts within the conglomerates of the Chilling Formation include ophiolitic-derived peridotite, gabbro, basalt, chert and volcaniclastic material, similar in composition to blocks within the southern mélange zone (Urtsi-Wanlah-Shergole Mélange) located along the southern contact of the Dras-Nindam terrane. Other clasts have been sourced from the Zanskar Supergroup and Lamayuru Complex and include nummulitic limestone and quartzite, respectively. Chrome spinels from the Chilling Formation are geochemically similar to *in situ* samples taken from the Spongtang Ophiolite, for which Baxter et al. (2016) used to illustrate arc-derived sedimentation in NW India during the earliest Eocene.

4.3.4 Collisional mélange zones

Two distinct mélange zones flank the Dras-Nindam terrane (Figure **4.2**). The Mongyu Mélange occurs along the northern margin near the township of Khalsi and has been described in detail by Robertson (2000). It is well exposed along strike, trending east-west for ~30 km between the villages of Mongyu in the east to Hungru in the west, where it separates the volcaniclastic sandstones and turbidites of the Nindam Formation in the south from the shallow-water platform carbonates of the Lower Cretaceous Khalsi Limestone in the north (Robertson, 2000). The southern mélange zone occurs along the contact between the Dras-Nindam terrane and the Indian Zanskar Supergroup. It includes the Urtsi, Wanlah and Shergol mélanges and grades into the mud-matrix mélange of the Lamayuru Complex (Danelian and Robertson, 1997; Robertson and Sharp, 1998). The Urtsi-Wanlah-Shergol Mélange has been interpreted as either representing the Late Jurassic oceanic basement of the Nindam Formation (Sutre, 1990) or a thrust-bound subduction-accretionary complex (Searle et al., 1987; Sinha, 1990; Thakur, 1990).

4.3.5 Eurasian margin

The southern margin of Eurasia consists of the Jurassic to Cretaceous (162-95 Ma) continental Karakoram Arc in the Ladakh region (Borneman et al., 2015; Heuberger et al., 2007; Le Fort et

al., 1983), which was active until closure of the Shyok Ocean and collision with the Jurassic Shyok ophiolite-arc complex (Robertson and Collins, 2002). Closure of the Shyok Ocean coincides with onset of the Ladakh Arc.

4.3.5.1 Ladakh Batholith

The Ladakh Batholith, extending for ~600 km, is bound in the north by the Shyok Suture Zone and to the south by the Indus Suture (Singh et al., 2007). The batholith consists of calc-alkaline (I-type) intrusive rocks ranging from gabbroic to granitic in composition (Honegger et al., 1982; Singh et al., 2007; White et al., 2011) and associated extrusive rocks of the Khardung Formation, which are andesitic to rhyolitic in composition (Dunlap and Wysoczanski, 2002). The Ladakh Batholith is generally accepted as the equivalent of the Kohistan Batholith in Pakistan but separated by the Nanga Parbat Syntaxis. Together, these two entities are commonly referred to as the Kohistan-Ladakh island arc (KLIA); (Bouilhol et al., 2013; Ewing and Müntener, 2018). The Ladakh Batholith intrudes Jurassic rocks of the Shyok ophiolite (Reuber, 1990). Honegger et al. (1982) suggested that the Ladakh Batholith was episodically active between 110-40 Ma, with the most voluminous and pervasive phase occurring at ~60 Ma. Zircon dating by White et al. (2011) indicated that the Ladakh Batholith was emplaced episodically between 66 Ma and 46 Ma. They proposed that the bulk of the batholith was emplaced between 63 Ma and 55 Ma, with a final phase of magmatism resulting in aplitic cross-cutting leucogranites, pegmatitic dyke swarms and sub-volcanic dykes at ~46 Ma, which also constrains the maximum age of final continent-continent collision. They found no evidence for an older 103-101 Ma magmatic phase similar to ages reported for the Kargil Intrusive Complex (Honegger et al., 1982; Schärer et al., 1984a), which led Buckman et al. (2018) to suggest that the Kargil Intrusives may represent the core of the Dras Arc, which it intrudes into, rather than representing an older phase, of the separate Ladakh Arc.

4.3.5.2 Tar Group (Ladakh forearc basin)

From base to top, the Tar Group consists of the Jurutze Formation, Khalsi Limestone, Sumda Formation, Chogdo Formation and finally a distinct Nummulitic Limestone unit (Henderson et al., 2010). These units were deposited in a shallow marine forearc basin to the Ladakh Batholith (Clift et al., 2002b; Garzanti & Van Haver, 1988; Sinclair & Jaffey, 2001; Steck et al., 1993). The group consists of Cretaceous (Albian) to lower Eocene clastic rocks and carbonates, including interbedded siltstones, shales and sandstones, debris-flow immature turbidites, conglomerates and breccias and deep marine limestones to shallow-water platform carbonates (Clift et al., 2002b). The Jurutze Formation and the Khalsi Limestone are the oldest sections of the Tar Group and are juxtaposed against the Nindam Formation to the south. This south dipping

thrust fault is marked by the Mongyu Mélange (Robertson, 2000; Figure **4.2**). The Lower Cretaceous (Aptian-Albian) Khalsi Limestone includes interbedded limestone with deep marine turbidites with minor siltstone and shale (Brookfield & Andrews-Speed, 1984; Clift et al., 2002b). The Jurutze Formation has a youngest detrital zircon population of 53.4 ± 1.4 Ma with almost all ages between 53-100 Ma, reflecting the age range of the Ladakh Batholith (Henderson et al., 2010). The overlying, granite-rich, conglomerates of the Sumda and Chogdo formations contain detrital zircon populations between 50-100 Ma again reflecting almost exclusively Ladakh Arc provenance. The overlying Nummulitic Limestone has a biostratigraphic age of 49.4-50.8 Ma (Green et al., 2008), which correlates closely with the youngest detrital zircon age of 52.5 ± 0.7 Ma (Henderson et al., 2010), but also shows the first sign of a change in provenance with the presence of an additional 150-160 Ma detrital zircon population.

4.3.6 Post-collisional Indus Group

The Indus Group (commonly referred to as the Indus Molasse) unconformably overlies the Tar Group and consists of mid Eocene to early Miocene post-collisional sedimentary deposits which record the timing of continental collision between India and Eurasia; but the age and stratigraphic relations of these highly deformed and disrupted units are debated (Brookfield & Andrews-Speed, 1984; Clift et al., 2001; Garzanti & Van Haver, 1988; Henderson et al., 2010; Henderson et al., 2011; Searle et al., 1990; Sinclair & Jaffey, 2001; Van Haver, 1984). The Indus Group has been divided into a number of formations; importantly, recent work by Henderson et al. (2011) has revealed that the youngest detrital zircon population of 41 Ma in the Upper Nimu Formation may represent the latest stage calc-alkaline magmatism of the Ladakh Batholith and thus constrain the onset of final continental collision.

4.4 Methods

4.4.1 Field investigations

Samples were collected along two stratigraphic traverses from the Dras Formation and the Nindam Formation (Figure **4.2**). See Supporting Information (Table S4.1) for sample localities and lithological descriptions. The traverse through the Dras Formation was between the townships of Kargil (NW) and Shergol (SE). The traverse through the Nindam Formation was between the townships of Khalsi (NE) and Lamayuru (SW) on the new road along the Yapola River tributary of the Indus River which replaced the Lamayuru Loops road along which Robertson and Degnan (1994) conducted their work.

4.4.2 QFL point counting

The modal composition of ten volcaniclastic sandstones (Table **4.1**; Supporting Information Table S4.2) of the Nindam Formation was determined by adopting the point counting method of Dickinson and Suczek (1979). The detrital grains of the Nindam Formation are categorised as monocrystalline quartz (Qm), polycrystalline quartz (Qp), total quartz (Q), plagioclase (P), K-feldspar (K) and total feldspar (F). The unstable lithic fragments consist of volcanic/metavolcanic rocks (Lv) and minor fragments of both sedimentary/metasedimentary (Ls) and metamorphic (Lm) rocks. However, total lithic fragments (L) stands for unstable lithic fragments and chert (Lc) fragments (Lv + Ls + Lm + Lc). If chert is in high abundance then it is considered a lithic fragment, rather than a sub-type of quartz (i.e., polycrystalline or monocrystalline quartz).

4.4.3 Whole rock geochemistry

Fifteen volcaniclastic six shale and seven basaltic-andesite samples (Supporting Information Table S4.3) were crushed using a tungsten carbide TEMA ring mill. Fused buttons were made for X-ray fluorescence (XRF) major element analysis. Depending on elemental concentrations estimated in trace element analysis, different types of flux were used. Pure metaborate was used for high silica samples, 35.3% tetraborate to 64.7% metaborate was used for mafic samples, and 57% tetraborate to 43% metaborate was used for ultramafic samples. Sample (400 mg) was added to each flux (300 mg for pure metaborate). Pressed pellets for trace element analysis were created by mixing ~5 g of sample with a polyvinyl acetate (PVA) binder and pressed into an aluminium cup using a hydraulic hand press. Trace element pressed pellets were then oven dried at 60 °C for 12 hours. Whole rock geochemical analysis was conducted using a SPECTRO XEPOS energy dispersive polarisation X-ray fluorescence spectrometer at the University of Wollongong (UOW), Australia. Additional trace elements and the rare earth element (REE) analyses were undertaken at Australian Laboratory Services (ALS) Minerals Division, Brisbane, Australia using ICP-MS (geochemical procedure code ME-MS81). Li metaborate and Li tetraborate were used as fluxes with and after fusing in a furnace and the resultant melt was dissolved in nitric, hydrochloric and hydrofluoric acid mixes. This solution was then analysed by ICP–MS. Standards, OREAS 120 and STSD-1, as well as five sample duplicates and three blanks, which were analysed in order to determine the error tolerance. All were within 10% of error.

4.4.4 Zircon U-Pb geochronology

4.4.4.1 Zircon preparation

Zircons were separated at the Institute of Hebei Regional Geology Survey, China. The samples were chipped in a pre-contaminated jaw crusher, using a subsample first. Chips were thoroughly washed with water, then dried prior to being ground into a coarse powder using a jaw crusher. The coarse powder was separated into heavy and light fractions using heavy liquids to obtain the >3.31 zircon-bearing fraction. The heavy fraction was washed and dried prior to being passed through a Franz Isodynamic Magnetic Separator to obtain zircons (normally the non-magnetic fraction at 2A). Zircon grains were examined using a binocular microscope, handpicked and mounted with standard TEMORA II grains on double-sided tape on a glass plate, which were then cast with epoxy resin in a mould. TEMORA II was distributed as several clusters of grains in different parts of the zircon mount to increase confidence in the accuracy of calibration of U-Pb across the entire mount when analysed. The mounts were ground on 1200 grade wet and dry paper to reveal approximately half sections through the grains and then polished with 1 μm diamond paste. Transmitted and reflected light photomicrographs were taken, along with cathodoluminescence (CL) imaging. The CL images were obtained using a Scanning Electron Microscope (SEM) JEOL JSM-6490LV with a 15-kV conventional tungsten filament thermionic source coupled with a Gatan MonoCL4 used in polychromatic mode at the Electron Microscope Centre (EMC), Innovation Campus, UOW.

4.4.4.2 LA-ICP-MS

A total of 791 zircon grains were chosen from eight samples (Supporting Information Table S4.4) for detrital zircon U-Pb dating using the LA-ICP-MS instrument at the University of Queensland (UQ), Australia. One hundred and forty-four unknowns were rejected based on not having concordant U-Pb ages or having Sr (cps) ≥ 2000. Regarding discordance, 1% was accepted. The rejected grains were excluded from age assessments. The zircon 91500, which has a $^{206}Pb/^{238}U$ age of 1062.4 ± 0.4 Ma and $^{206}Pb/^{207}Pb$ age of 1065.4 ± 0.3 Ma, was used as the primary reference material (Wiedenbeck et al., 1995). TEMORA II was also employed as a secondary reference material, which has a $^{206}Pb/^{238}U$ age of 416.78 ± 0.33 Ma (Black et al., 2004). Laser ablation was undertaken using an ASI RESOlution 193 ArF nm excimer laser system. Following evacuation of air, He carrier gas was introduced into the laser cell at a flow rate of 0.35 l/min. 0.05 l/min of N_2 gas was also introduced to the laser cell to enhance the measurement sensitivity. The gas mixture was then introduced into the plasma torch of a Thermo iCAP RQ quadruple ICP-MS with 0.85 l/min Ar nebuliser gas. No reaction gas was employed. The laser was run with a 30 μm diameter round spot at 10 Hz, with a measured instrument laser-fluence

(laser pulse energy per unit area) of 2.9 J/cm^2. For each spot, 5 s of blank was collected, followed by 25 s of ablation and 10 s of wash out. Prior to data acquisition, ICP MS signals were optimised during tuning. Parameters particular to the analytical session include, ~400 K cps of ^{238}U counts, ~1 of ^{238}U/^{232}Th, ~0.21 of ^{206}Pb/^{238}U were achieved for measuring NIST612 glass using line scans of 3 μm/s, 10 Hz, 50 μm round laser pit, and 3 J/cm^2. The following isotopes were collected using a single collector: ^{88}Sr (dwell time=0.005 s), ^{91}Zr (dwell time=0.001 s), ^{200}Hg (dwell time=0.01 s), ^{204}Pb + ^{204}Hg (dwell time=0.01 s), ^{206}Pb (dwell time=0.045 s), ^{207}Pb (dwell time=0.055 s), ^{208}Pb (dwell time=0.01 s), ^{232}Th (dwell time=0.01 s), ^{238}U (dwell time=0.01 s). A single cycle took ~0.155 s. Therefore, during a 25 s ablation, ~160 measurements were made on each mass. Reduction of raw data was accomplished using the program *IOLITE* (Paton et al., 2011). No common Pb correction on zircon 91500 was undertaken. From the session, a ^{206}Pb/^{238}U age of 419.0 ± 1.1 Ma, uncorrected for common Pb (95% confidence, n = 93, MSWD = 7.7) for the TEMORA II secondary reference material was obtained, which has a TIMS ^{206}Pb/^{238}U age of 416.78 ± 0.33 Ma determined by ID TIMS (Black et al., 2004). ^{206}Pb/^{238}U ages are reported for <1000 Ma grains, whereas ^{207}Pb/^{206}Pb ages are reported for >1000 Ma grains.

4.4.4.3 SHRIMP

A total of 50 grains from samples 15ND02 and 15ND03 (Supporting Information Table S4.5) were chosen for zircon U-Pb dating using the SHRIMP-RG instrument at the Australian National University (ANU). Zircon mounts were cleaned and coated with ~10 nm of high purity Au (>99.999%) before analysis and followed the analytical procedure of Williams (1998). Two unknowns were rejected on the basis of not having concordant U-Pb ages. The rejected grains were excluded from age assessments. Sites within the zircon grains were selected according to their apparent reflectance (brightness) on the polished surface (information gained from reflected light photomicrographs), along with well-formed structure (information gained from CL images). Particular note was made to avoid analysing cracked or damaged zircons and dark zones within grains (indicative of high U + Th content). U-Th abundance was calibrated based on the reference zircon SL13 (U = 238 ppm). After site selection was made the instrument was alternated between running manually and programmed to run automated at night. A total of five cycles were made at each of the nominal mass stations: ^{196}Zr, ^{204}Pb, background $^{204.1}$Pb, Pb (^{206}Pb, ^{207}Pb, ^{208}Pb), ^{238}U, ^{248}ThO (^{232}Th + ^{16}O) and ^{254}UO (^{238}U + ^{16}O). Parameters particular to the analytical session include a spot size of ~15-20 μm, with the primary O_2^- ion beam of 5 nA. TEMORA II was analysed for U-Pb calibration after every three to four analytical sites (17 times in total). Five analyses of TEMORA II had to be rejected based on anomalously low UO/O ratios (< 3.65 versus typically ~6). On the basis of higher Zr count rates, it is possible that the rejected grains were in fact not zircon, but another Zr-bearing mineral species (possibly baddeleyite). The

raw data were reduced using the program *POXI-SC* developed by ANU, which combines the functionality of the previous two ANU applications *Prawn* and *Lead*. Quoted errors on isotopic ratios also take into account non-linear fluctuations in ion count rates above that expected from counting statistics alone (Williams, 1998). This is particularly important for old, damaged high U + Th zircons, where damage has resulted in post-crystallisation heterogeneity of species on the sub-micron scale, as now revealed by atom probe-analysis (Peterman et al., 2016). Reliance on counting statistics only of such targets would result in under-estimation of analytical error. Correction for common Pb was made in accordance with the measured ^{204}Pb and common lead composition for the likely age of the sample from Cumming and Richards (1975). ^{206}Pb/^{238}U were corrected using the TEMORA II standard with a concordant age of 416.78 ± 0.33 Ma (Black et al., 2004). The reduced and calibrated data were then assessed and plotted using *Isoplot 4.1* (Ludwig et al., 2003). Calculated mean ages were presented at 95% confidence. ^{206}Pb/^{238}U ages are reported for <1000 Ma grains, whereas ^{207}Pb/^{206}Pb ages are reported for >1000 Ma grains.

4.5 Results

4.5.1 Field relations

The Nindam Formation section between Lamayuru and Khalsi consists of deep marine, volcaniclastic turbidites, hemipelagic shales and silty limestones and minor mass-flow conglomerates. The minimum stratigraphic thickness of the unit is ~4.1 km thick (Figure **4.2**). The dominantly fine-grained facies of the unit make up just over half of the formation and include red and green shales interbedded with planar bedded siltstones and calci-turbidites. The medium- to coarse-grained facies include planar, bedded volcaniclastic calci-turbidites with minor conglomerate lenses as described in detail by Robertson and Degnan (1994). To the north the Nindam Formation is bound by the Mongyu Mélange, which crops out along the road and occupies a thrust fault that dips at ~35° to the south (Figure **4.3**A). Kinematic S-C fabrics in the mélange indicate the Nindam Formation has been thrust northward over the Tar Group to the north which locally includes the Cretaceous Khalsi Limestone. Overlying the Tar Group on the northern side of the Indus River are the post-collisional Indus Group sedimentary rocks. The measured Nindam Formation section (Figure **4.2**B) is generally overturned and steeply dipping with younging toward the north as determined from graded beds and sedimentary flame structures (Figure **4.3**B-D). There are no observable unconformities or breaks in sedimentation suggesting the entire 4.1 km thickness accumulated continuously in a deep marine setting on the flanks of the Dras Arc, which outcrops extensively along strike farther west, near the township of Kargil. The Nindam Formation is faulted against the highly disrupted Lamayuru Complex of the Indian margin to the south. This contact is usually marked by the presence of serpentinite-

matrix mélange containing basalt, chert, limestone and volcaniclastic blocks as described by Robertson (2000) for the Urtsi Mélange (Figure **4.2**).

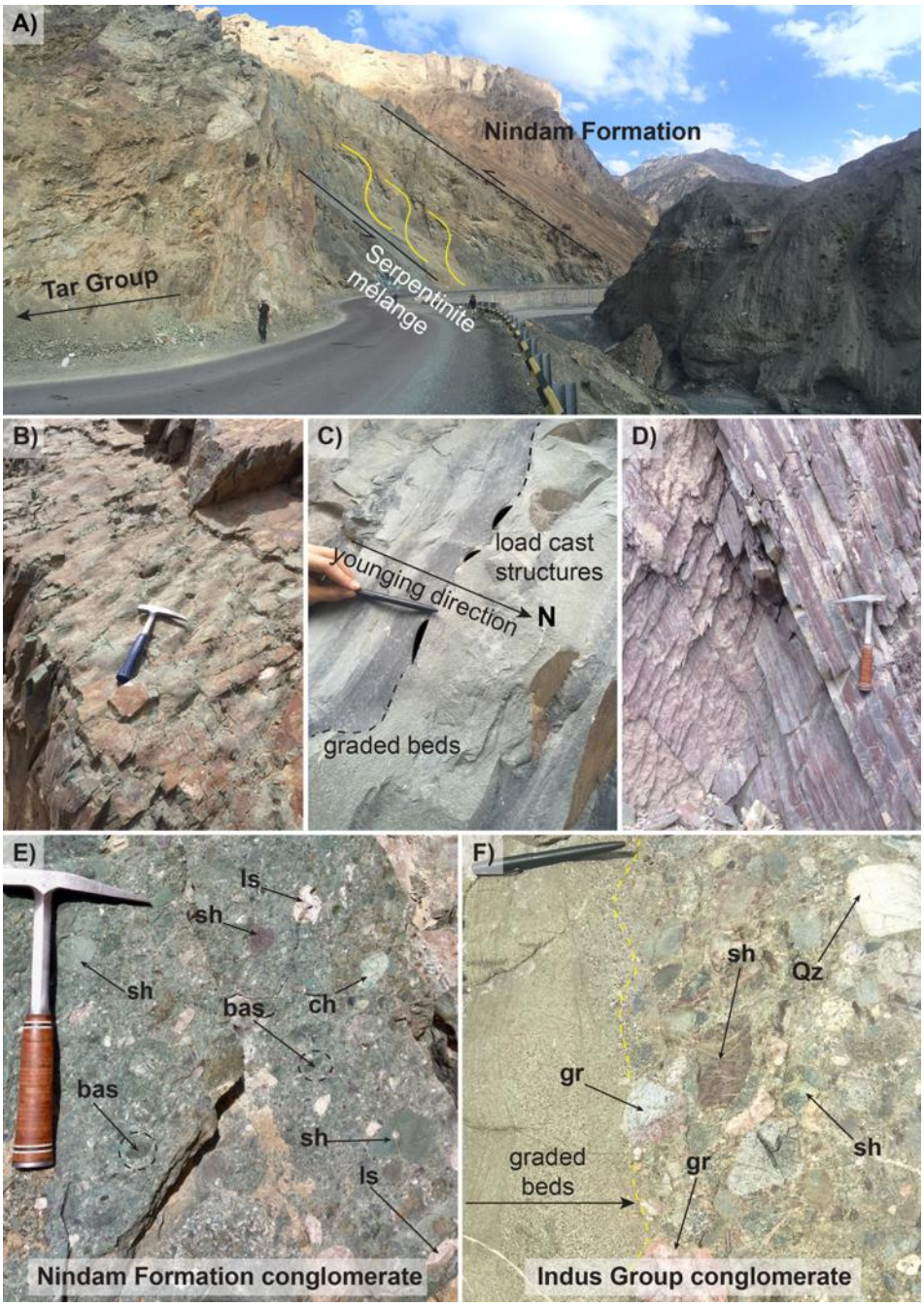

Figure 4.3: Field relations of the Nindam Formation. **A)** The Nindam Formation is bound to the north by the serpentinite-matrix Mongyu Mélange, which outcrops along the road and occupies a thrust fault that dips ~35° to the south. Kinematic S-C fabrics present in the mélange are represented in yellow. Position: 34.32083°N, 76.83833°E; **B)** Flute clast structures in the basal section of distal turbidites from the Nindam Formation. Position: 34.29361°N, 76.80028°E; **C)** Flame structures within the turbidites with younging direction indicated by a black arrow. Position: 34.29750°N, 76.83194°E; **D)** Interbedded green sandstone and red shale. Beds at this locality range from 2-10 cm. Position: 34.29383°N, 76.80006°E; **E)** Representative Nindam Formation conglomerate, with clasts including limestone (ls), shale (sh), chert (ch) and basalt (bas). Position 34.29916°N, 76.82138°E; **F)** Representative Indus Group (Hemis-Nurla Molasse) conglomerate, with clasts including granite (gr), shale (sh) and quartz (Qz). Position 34.32944°N, 76.83694°E.

4.5.2 Petrography and mineralogy

4.5.2.1 QFL diagrams

The Nindam Formation volcaniclastic sandstones are poorly to moderately sorted. Clasts vary from angular to sub-rounded and are surrounded by a fine-grained, silty matrix which is generally cemented by calcite (Figure **4.4**). Lithic fragments are the most abundant detrital component contributing on average 71% of modal composition. Lithic volcanic rocks (average 41%) are more abundant than lithic chert (average 31%), with little to no sedimentary rock lithic fragments observed (Table **4.1**; Supporting Information Table S4.2). The volcanic lithic fragments are mafic volcanic rocks ranging from basalt to basaltic andesite. They are generally characterised by the presence of plagioclase laths as phenocrysts. No felsites or microgranitic fragments were observed. The lithic chert fragments exhibit typical cryptocrystalline texture. Feldspar fragments constitute ~24% of the Nindam Formation volcaniclastic sandstones. Plagioclase fragments are generally altered, exhibiting seritisation. Quartz occurs as subordinate amounts, making up an average of only 4% of the detrital components with monocrystalline quartz (average 4%) more abundant than polycrystalline quartz (<1%). The rare grains of monocrystalline quartz exhibit undulose extinction. Other detrital components of the Nindam Formation volcaniclastic sandstones are carbonates, alteration products, pyroxenes, micas and amphiboles in order of decreasing abundance. Calcite is exhibited as both matrix and detrital grains. Alteration products, including chlorite with minor kaolinite, occur as rims around grains, matrix material and replacement alteration. There are rare grains of augite and orthopyroxene. Mica is represented by minor biotite as thin flakes. Hornblende also occurs as a rare detrital component. The modal sandstone ternary plots for the Nindam Formation volcaniclastic rocks demonstrate an almost linear trend, from undissected arc to transitional arc (Figure **4.5**). In contrast, the Indus Group (Henderson et al., 2010) demonstrate a very different spread of data which fall in the fields of transitional arc, dissected arc and basement uplift.

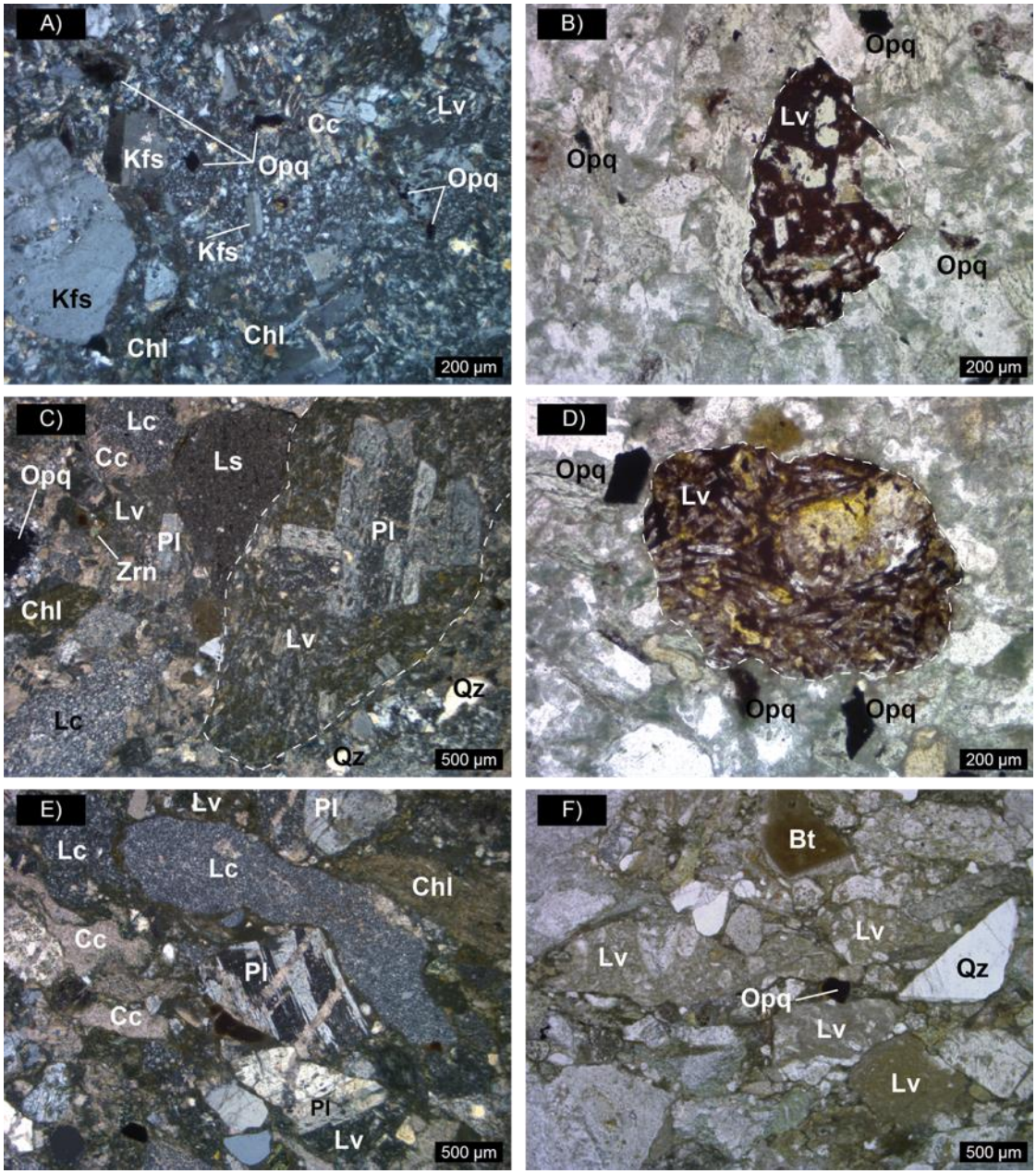

Figure 4.4: Representative photomicrographs of the Nindam Formation volcaniclastics. **A)** Poorly to moderately sorted, detrital grains varying from angular to sub-rounded (XPL, sample 16NI08); **B)** Volcanic lithics have undergone significant alteration (PPL, sample 16NI08); **C)** Lithic fragments are the most abundant detrital component, with volcanic fragments (basaltic-andesite) making up the majority followed by lithic chert fragments (XPL, sample 16NI06); **D)** Volcanic lithic fragments are mafic volcanic rocks ranging from basalts to basaltic-andesites. They are generally characterised by the presence of plagioclase laths as phenocrysts (PPL, sample 16NI08); **E)** Plagioclase fragments are generally altered, exhibiting internal grain seritisation. Less altered grains display typical multiple twinning (XPL, sample 16NI01); **F)** Quartz occurs as subordinate amounts, making up an average of only 4% of the detrital component with monocrystalline quartz (average 3%) more abundant than polycrystalline quartz (<1%) (PPL, sample 16NI01). Where, Bt = biotite; Cc = calcite cement; Chl = chlorite; Kfs = K-feldspar; Lc = lithic chert; Ls = lithic sedimentary; Lv = lithic volcanic; Opq = opaque mineral; Pl = plagioclase; Qz = quartz; Zrn = zircon.

Table 4.1: Framework modal results of the Nindam Formation volcaniclastics.

Samples	Q	F	L	Qm	Qp	P	K	Lv	Lc	Total point counting values
15ND02	3	32	65	2	0	17	15	41	24	312
15ND03	6	6	88	5	1	5	1	65	23	308
16NI01	7	25	68	5	2	13	13	25	42	365
16NI02	4	9	88	4	0	5	4	32	55	337
16NI03	5	14	81	5	0	6	8	32	49	348
16NI06	6	6	88	5	0	3	3	62	26	415
16NI08	3	47	51	3	0	19	28	19	32	316
16NI09	5	24	71	5	0	9	15	37	34	388
16NI13	4	29	67	3	1	24	6	54	13	377
16NI16	2	43	55	2	0	37	6	44	11	316
Average (%)	4	24	72	4	0	14	10	41	31	

Notes:

Where, Q = total quartz: monocrystalline quartz (Qm) + polycrystalline quartz (Qp); F = total feldspar: plagioclase (P) + alkali-feldspar (K); L = total lithics (including chert): volcanic fragments (Lv) + sedimentary fragments (Ls) + metamorphic fragments (Lm) + chert fragments (Lc).

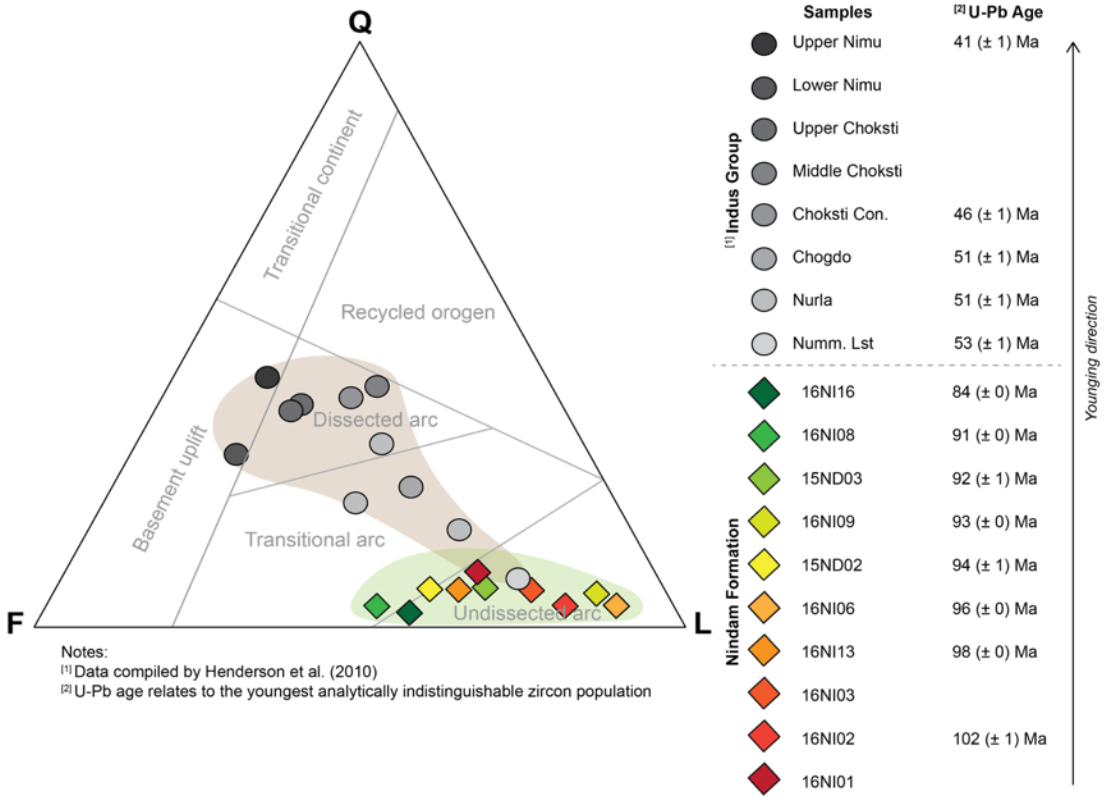

Figure 4.5: Ternary diagram of the Nindam Formation volcaniclastic samples based on the point counting method of Dickinson and Suczek (1979). Where, Q = total quartz: monocrystalline quartz (Qm) + polycrystalline quartz (Qp); F = total feldspar: plagioclase (P) + alkali-feldspar (K); L = total lithics (including chert): volcanic fragments (Lv) + sedimentary fragments (Ls) + metamorphic fragments (Lm) + chert fragments (Lc).

4.5.3 Geochemistry

Whole rock major and trace element compositions of samples from the Dras Formation, Nindam Formation and Indus Group are given in Supporting Information Table S4.3. Our geochemical analyses are combined with previous analyses of Nindam Formation by Clift et al. (2000) and Dras Volcanics by Bhat et al. (2019) and Corfield et al. (2001). Loss on ignition (LOI) values for the sedimentary rock samples are about 8 wt.% reflecting the carbonate cement and minor alteration while volcanic rock samples are only ~4 wt.% LOI. The M (mafic)-F (felsic)-W (weathering) ternary diagram (Ohta & Arai, 2007) indicates that the majority of samples fall in the field of fresh calc-alkaline/mafic igneous rocks (Figure **4.6**A) indicating minimal weathering, from source to sink.

4.5.3.1 Alteration

To account for modern weathering, homogenous samples were selected for analysis where surficial layers were removed and only central, fresh rock was used for analysis. The degree of ancient weathering related to transport and early diagenesis was assessed using the MFW indices of Ohta and Arai (2007). The MFW ternary diagram (Ohta & Arai, 2007) indicates that samples from the Dras Formation (basalts, n = 29) and Nindam Formation (volcaniclastic sandstones, n = 31) fall in the fields of fresh alkali basalt to calc-alkali andesite (Figure **4.6**A) indicating minimal weathering of the samples. Shales from the Nindam Formation (n = 7) have also been plotted on the MFW ternary diagram, with some samples showing intermediate weathering (Figure **4.6**A). Immobile elements, including the HFSE and REE, which are less susceptible to both weathering and hydrothermal alteration are used in lithological classification and tectonic discrimination (MacLean, 1990). Those elements regarded as mobile, including LILE have only been used with those samples regarded as fresh rock (see MFW ternary diagram fields), evidenced by field and petrographic observations. Additionally, because samples were crushed using a tungsten carbide TEMA ring, trace amounts of W, Cr, Co and Sc may be compromised, and thus are not used in interpretations.

4.5.3.2 Dras Formation

The Dras Formation rocks are characterised by SiO_2 contents between 45-58% and are generally classified as basaltic andesites (Figure **4.6**B). Two samples are classified as ultramafic based on <45 wt.% SiO_2 (ranging 41-43 wt.%), and one other sample is classified as intermediate (59 wt.%). The volcanic rocks have high $Fe_2O_3^*$ + MgO contents (usually 9-24 wt.%, average 17 wt.%; where $Fe_2O_3^*$ represents total iron as Fe_2O_3). Ratios of K_2O/Na_2O are 0.03-0.77, average 0.31. TiO_2 contents range from 0.4-3.9 wt.% (average 0.87 wt.%). Some high MgO (>8 wt.%),

low TiO_2 (<0.5 wt.%) samples are present possibly indicating the presence of boninitic lavas, as defined by Crawford et al. (1989; Figure **4.6**C). The Dras Formation rocks consistently plot in the volcanic arc array in immobile discriminant plots (Figure **4.6**D and 4.6E). Primitive mantle-normalised trace and REE patterns are characterised by pronounced negative Nb and Ta anomalies and variable enrichment in large ion lithophile elements (LILE, Rb, Ba, Th) typical of supra-subduction zone arc magmas (Pearce & Peate, 1995). A negative Ti anomaly is associated with boninitic samples and reflects high degrees of partial melting (Figure **4.6**F).

4.5.3.3 Nindam Formation

The Nindam Formation volcaniclastic sandstones are characterised by generally low SiO_2 contents (45-60%). This is consistent with derivation from a predominantly mafic source region as reflected by the abundance of basaltic to andesitic lithic clasts in the conglomerates and sandstones. The volcaniclastic sandstones have high $Fe_2O_3^*$ + MgO contents (usually 5-13 wt.%, average 9 wt.%) with one sample with 23 wt.%. Ratios of K_2O/Na_2O are 0.05-2.61, average 0.67. TiO_2 contents range from 0.5-0.9 wt.% (average 0.7 wt.%). The weathering plot of Ohta and Arai (2007) shows that detritus forming the Nindam Formation underwent very little weathering prior to deposition (Figure **4.6**A). This is consistent with derivation off an active island arc that was largely submerged and underwent very little sub-aerial weathering, or rapid source to sink of detritus in an active environment, and thus the sandstone whole rock geochemistry can be used as being representative of the volcanic source region of the Dras Arc. Indeed, the Nindam Formation sandstones plot congruent to the Dras Formation within island arc fields of basalt discrimination plots and show similar mafic (Figure **4.7**A), island arc signatures (Figure **4.7**B) using the sandstone geochemical discriminant plots of Roser and Korsch (1986, 1988). The Nindam Formation volcaniclastic rocks also plot congruent to the Dras Formation on the primitive mantle-normalised spider diagram (Figure **4.6**F).

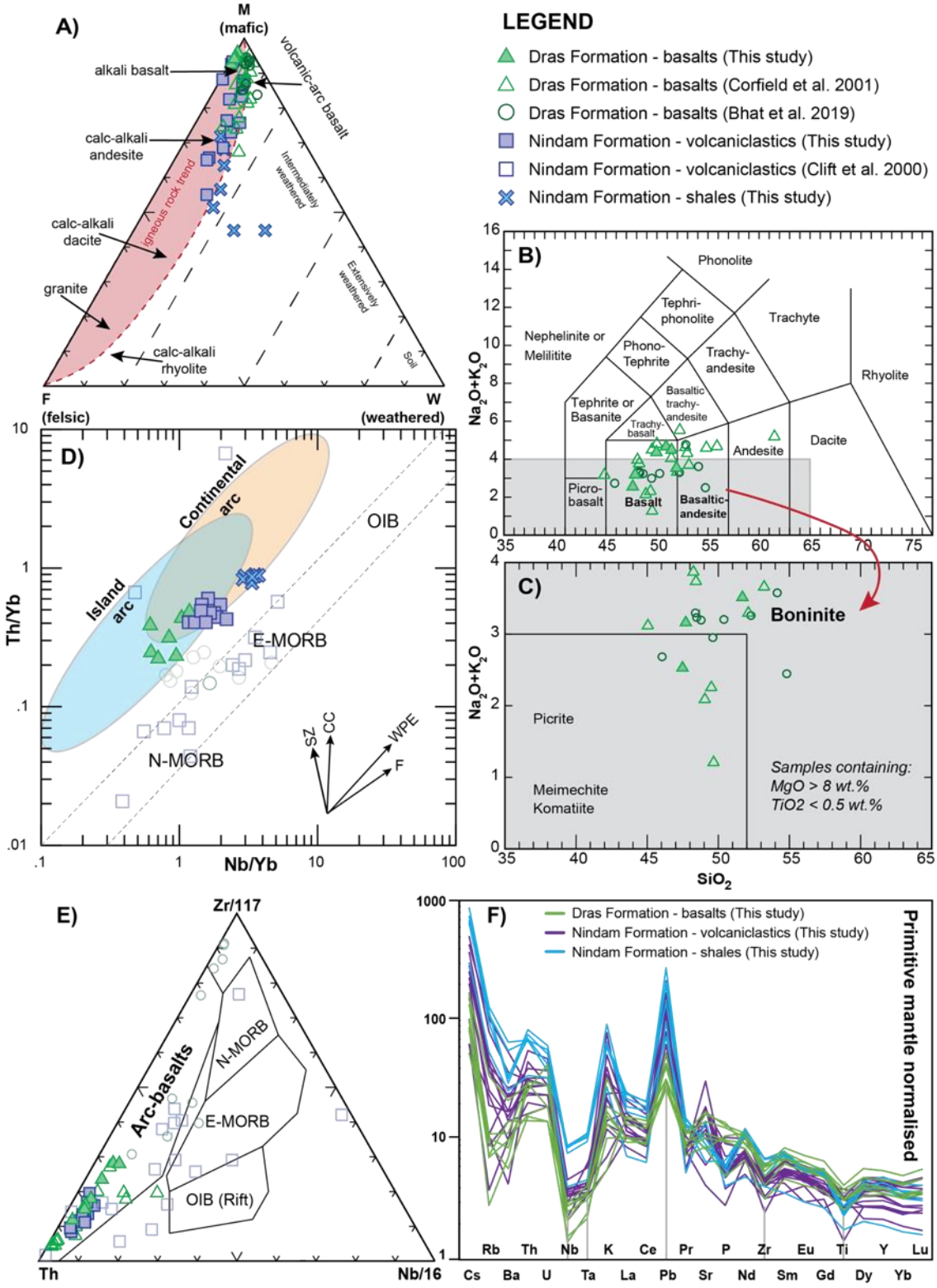

Figure 4.6: Geochemical plots. **A)** Mafic-Felsic-Weathering (MFW) ternary diagram of Ohta and Arai (2007); **B)** Total alkali vs. silica (TAS) diagram of Le Maitre et al. (1986); **C)** TAS diagram for high-Mg rocks (Le Bas, 2000); **D)** Immobile and trace element tectonic discrimination diagrams of Meschede (1986); **E)** Volcanic rock tectonic discrimination ternary diagram of Wood (1980); **F)** REE spider plot, normalised against Primitive Mantle (McDonough & Sun, 1995).

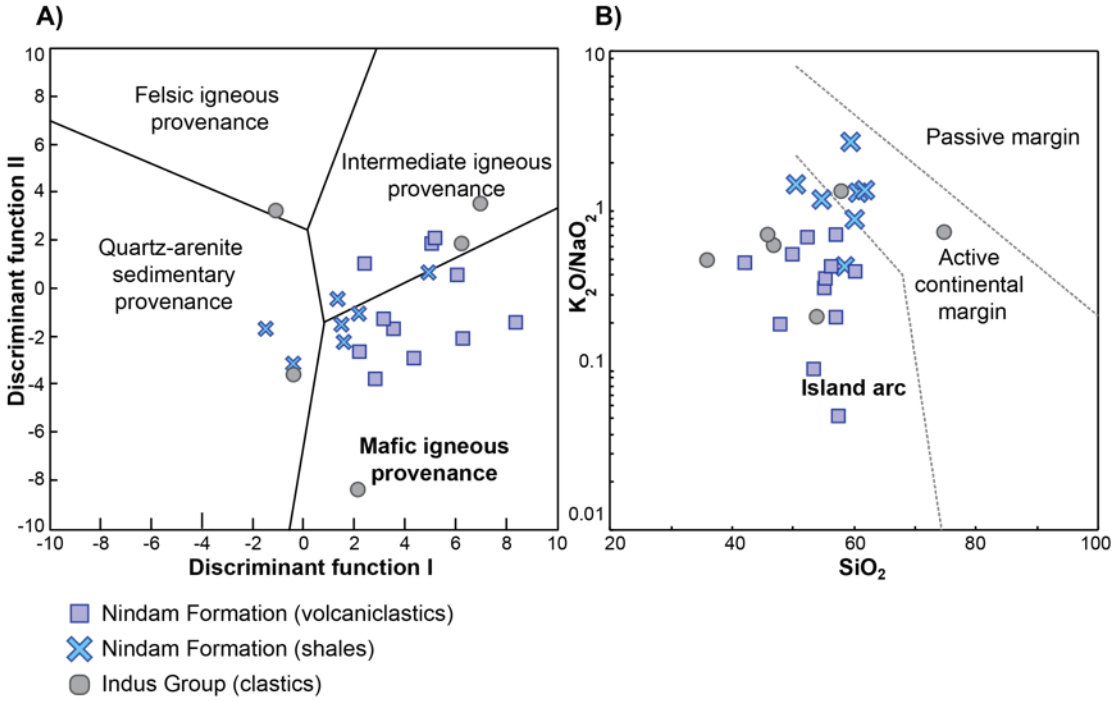

Figure 4.7: Geochemical plots. **A)** Major element sedimentary discriminant function analysis diagram of Roser and Korsch (1988); **B)** Major element tectonic discrimination diagram of Roser and Korsch (1986).

4.5.4 Detrital zircon geochronology

4.5.4.1 Detrital zircon grain description

Ten volcaniclastic samples from the Nindam Formation were selected for detrital zircon U-Pb dating (Supporting Information Table S4.4 and Table S4.5). Samples were collected perpendicular to strike across the formation between the townships of Lamayuru and Khalsi (Figure **4.2**). Detrital zircon grains are subhedral to euhedral, clear to transparent purple in colour and range between 70-250 µm in their longest dimension. Some grains are rounded to subrounded, suggesting that they had extensive residence times in sedimentary systems. Aside from these, the majority of the grains, both fragments and whole crystals show magmatic oscillatory zoning in CL images. Where oscillatory zoning is observed it is commonly truncated by the grain's external surface. Grain exteriors when examined in transmitted light, often demonstrate pitting. These features are common across all populations, not only older, detrital grains. Eight-hundred and forty-one grains in total were analysed using a combination of LA-ICP-MS (n = 791) and SHRIMP (n = 50). Out of these, 695 analysed spots acquired concordant U-Pb ages (Supporting Information Text, Figure S4.1). The youngest population of each sample was determined by examining the youngest analytically indistinguishable group and taking the weighted mean average of those zircons grains with concordant $^{206}Pb/^{238}U$ ages (Ma), where $n \geq 2$ and MSWD ≤ 1 (Supporting Information Text, Figure S4.2).

4.5.4.2 Detrital zircon populations

Cathodoluminescence (CL) images of representative zircon grains are shown in Figure **4.8**. All detrital zircon U-Pb ages are plotted as histograms in stratigraphic order (Figure **4.9**). Most (66%, *n* = 430) of the zircons analysed fall in the Lower to Upper Cretaceous (Aptian to Santonian, 84-125 Ma) age range. Detailed detrital zircon U-Pb geochronology descriptions are provided in Supporting Information Text. Zircon U-Pb data using LA-ICP-MS and SHRIMP are provided in Supporting Table S4.4 and Table S4.5, respectively.

Other older, detrital zircon populations include:

(i) Precambrian (total = 18%, *n* = 115):
   a. Neoarchean (>2500 Ma, <1%, *n* = 2)
   b. Paleoproterozoic (Siderian – Statherian, 3%, *n* = 18, 2444-1627 Ma)
   c. Mesoproterozoic (Calymmian – Stenian, 8%, *n* = 54, 1588-1000 Ma)
   d. Neoproterozoic (Tonian – Edicaran, 6%, *n* = 41, 988-541 Ma)

(ii) Cambrian to Lower Devonian (Fortunian to Lochkovian, 2%, *n* = 10, 540-418 Ma)

(iii) Permian to Upper Triassic (Roadian to Rhaetian, 1%, *n* = 9, 271-205 Ma)

(iv) Lower to Upper Jurassic (Pliensbachian to Tithonian, 12%, *n* = 75, 185-145 Ma)

(v) Lower Cretaceous (Valanginian to Barremian, 1%, *n* = 8, 138-126 Ma)

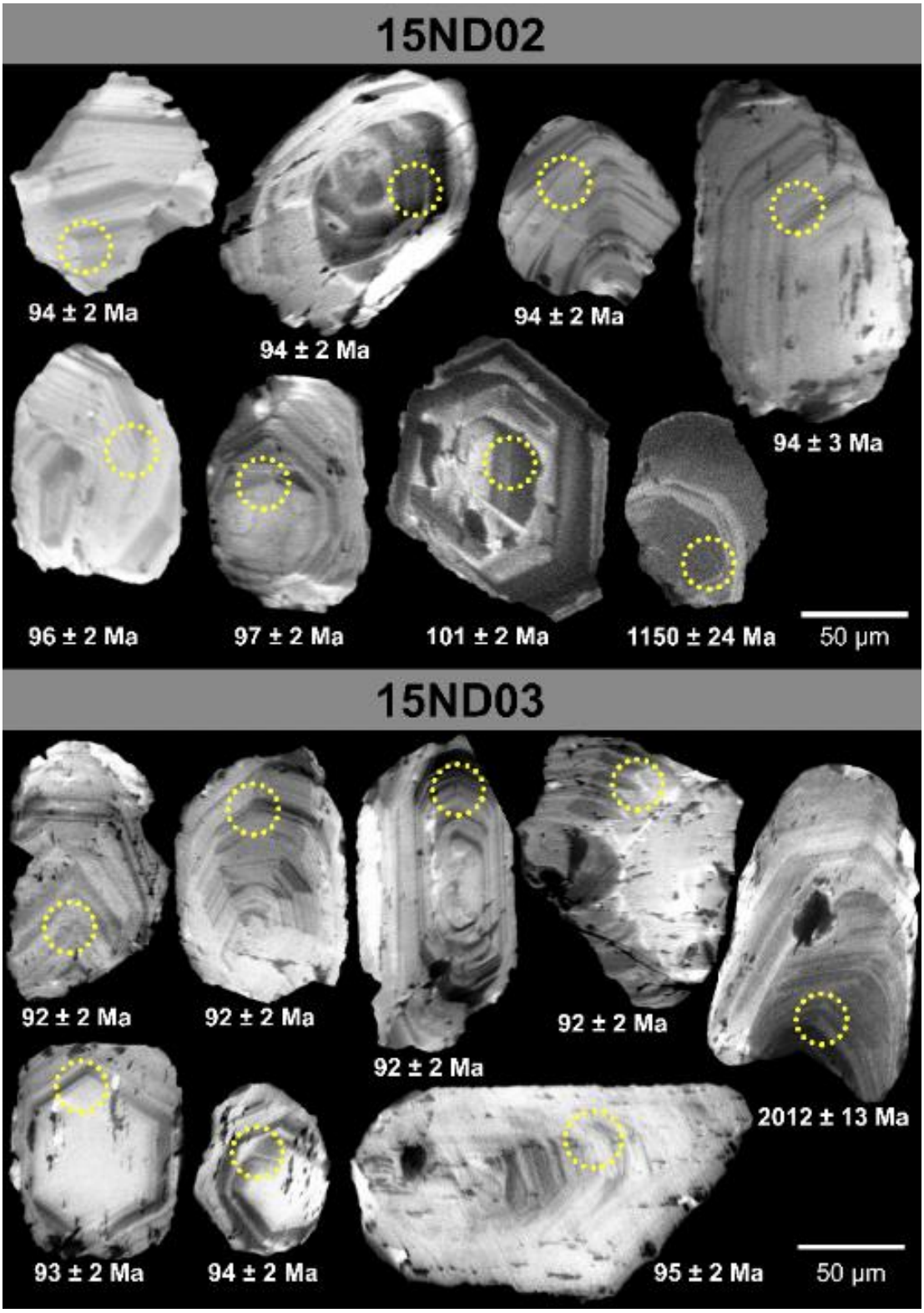

Figure 4.8: Representative zircon grains from samples 15ND02 and 15ND03 of the Nindam Formation. The yellow circles denote SHRIMP analytical sites and corresponding $^{206}Pb/^{238}U$ ages (if <1000 Ma) and $^{207}Pb/^{206}Pb$ ages (if >1000 Ma).

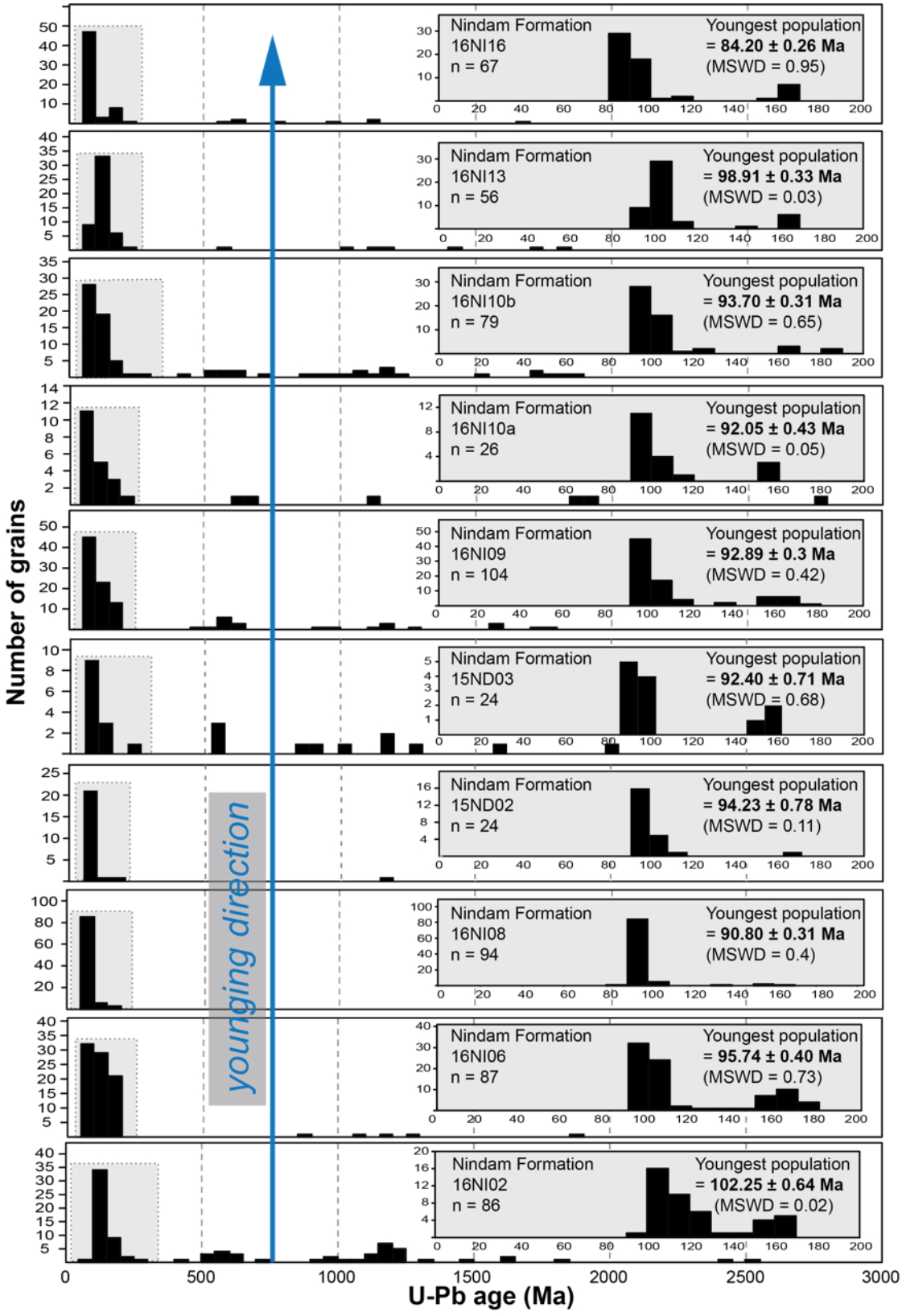

Figure 4.9: Probability density distribution plots from volcaniclastic rocks of the Nindam Formation, displayed in stratigraphic order where the top of the diagram is the northern-most sample.

4.6 Discussion

4.6.1 Maximum depositional age

The youngest analytically indistinguishable zircon population within the Nindam Formation is 84 ± 1 Ma (1σ, MSWD = 0.95, *n* = 3) and came from the stratigraphically uppermost sample (16NI16) at the northern end of the traverse (Figure **4.2**). The youngest zircon population for the lowermost (southernmost) unit sampled (16NI02) is 102 ± 1 Ma (1σ, MSWD = 0.02, *n* = 2). Generally, the youngest zircon population in each sample becomes progressively younger up-sequence (Figure **4.9**) indicating that deposition of the Nindam Formation was contemporaneous with active volcanism of the Dras Arc. This is consistent with the model argued by Amato and Pavlis (2010) that the youngest grains in forearc basins are typically synchronous with sedimentation. The exception is sample 16NI13 (Figure **4.9**), which has a youngest zircon population of 99 Ma but is underlain by samples with a youngest zircon population of 94 Ma and overlain by a sample with 84 Ma and therefore does not fit the overall northward younging trend. There are three explanations for this. A) The sample does not contain zircons sourced from contemporaneous volcanism at the time of deposition but rather sourced slightly older, more deeply eroded arc volcanic rocks. B) The youngest syn-depositional zircons are volumetrically swamped by more abundant, slightly older zircons and sampling did not detect the rarer younger zircons in this sample. In which case, with 56 grains analysed, then it is 95% certain that such a 'missed' age group forms <1.4% of the zircon population (Compston & Pidgeon, 1986; Dodson et al., 1988). C) Minor folding and/or faulting within the sequence has disrupted or reversed the stratigraphy locally, resulting in a sample being slightly out of sequence with those to the north and south. Distinct, asymmetric tight folds were mapped in the mid-part of the section and correspond with sample 16NI08 being younger (~91 Ma) than the overlying samples (Figure **4.2**B).

Sedimentation rates in forearc settings are generally high, albeit variable (Einsele, 2013). Our results show a difference in depositional age between the base (~102 Ma) and the top (~84 Ma) of the Nindam Formation, indicating deposition over at least 18 million years for this portion of the forearc basin sequence. This equates to an average sedimentation rate of 228 m/m.y., which is comparable to sedimentation rates in modern forearc basins such as Izu-Bonin Forearc (100-300 m/m.y.) and New Hebrides/Vanuatu Forearc (44-180 m/m.y.; Underwood et al., 1995).

The youngest zircon population when all samples are combined spans a period from 84-125 Ma, consistent with previously reported fossil ages (Reuber, 1989; Robertson & Degnan, 1994; Sutre, 1990; Thieuloy et al., 1990). This large (66% of total grains analysed) youngest zircon

population dominates, reflecting the flux of material from the active arc at the time of sedimentation. This same situation of arc detritus dominating forearc basins has also been shown for modern (e.g., Mariana and Tonga arcs, Western Pacific) and ancient (e.g., Jurassic Talkeetna Formation of Alaska) settings (Draut & Clift, 2006). This probably corresponds with the lifespan of the Dras Arc, suggesting it initiated around 125 Ma and was active for at least 41 Ma. The Dras Arc may have been active for longer, up until its eventual collision with India, leading to its extinction. However, the upper (younger) part of the Nindam Formation is truncated against the thrust fault marked by the Mongyu Mélange on the northern contact of our section and consequently there is no way of knowing how much of the upper Nindam Formation is missing in the section between Khalsi and Lamayuru. In the Zanskar Gorge section, the Nindam Formation is faulted against the Jurutze Formation which has a youngest detrital zircon age of 53 ± 1 Ma (Henderson et al., 2010). The Jurutze Formation has previously been interpreted as a younger continuation of the Nindam Formation (Clift et al., 2001, 2002b) but also part of the same Tar Group sequence which stratigraphically grades up into the Sumda and Chogdo formations (Henderson et al., 2011). Whilst the Jurutze Formation has a similar age and provenance to the Chogdo Formation and may be part of the same sequence, we think that comparisons between Cretaceous Nindam Formation and the Eocene Tar Group are incompatible and therefore the supposed stratigraphic relationship between Nindam and Jurutze formations is suspect and requires further validation. The upper (younger) sections of accreted ophiolites and arcs are usually the first to be eroded in an active arc-continent collision (Draut & Clift, 2013) given that the sequences are not dramatically tilted (e.g., Oman Ophiolite); it is possible that the youngest portions of the Dras-Nindam terrane are completely missing or only locally preserved, for example, the Paleocene Dras II volcanic rocks south of Kargil (Robertson & Degnan, 1994). The detrital record of syn- to post-collisional conglomerates, such as the Chilling Formation, may provide answers as to the upper extent of arc activity but no such data exists at present for this unit.

4.6.2 Provenance

4.6.2.1 Petrological and geochemical signatures

The dominant lithic clasts within the Nindam Formation conglomerates and volcaniclastic sandstones are basaltic to andesitic volcanic rocks and pelagic limestone with minor amounts of chert and siltstone. There is a distinct lack of quartz clasts, which is consistent with interpretations by Robertson and Degnan (1994) of deposition within a forearc basin of an intraoceanic island arc of a predominantly mafic composition. Interpretations of the Nindam Formation as being the forearc basin of the southern margin of Eurasia (Fuchs, 1982; Henderson et al., 2010; Honegger et al., 1982; Najman et al., 2017) are at odds with the geological evidence

presented here and by Robertson and Degnan (1994) that the Nindam Formation represents the forearc basin of an intraoceanic island arc system. The Ladakh and Karakoram arcs are characterised by continental magmatism dominated by felsic, silica-saturated compositions. Clasts of igneous rocks of this type are not observed anywhere within the Dras-Nindam terrane. The distinct absence of quartz combined with whole rock geochemical data suggests that the source of the Nindam Formation sediment is volcanic island-arc derived. Basalts of the Dras Formation are characterised by low Nb/La ratios, low Nb concentrations and low enrichment of incompatible elements, including negative Nb, Ta, K and Ti anomalies in REE plots which are consistent with intraoceanic island arc signatures (Figure **4.6**F; Supporting Information Table S4.3). In contrast, samples collected from the Tar and Indus groups north of the Mongyu Mélange, which separates them from the Nindam Formation, contain abundant granite clasts (Figure **4.3**F) and are generally more silica rich (Figure **4.7**A and 4.7B; Supporting Information Table S4.3).

4.6.2.2 Pre-Cretaceous detrital zircon populations

The Nindam Formation contains pre-Cretaceous detrital zircon that are significant in terms of provenance. A distinct age peak between 135-185 Ma (11%) occurs in all samples. This coincides with ages (88-170 Ma) reported from the Spongtang Ophiolite and associated Spong Arc (Buckman et al., 2018; Pedersen et al., 2001). Our interpretation of these grains being sourced from the Spongtang Massif, presumably a much larger ophiolitic thrust sheet that was thrust over the northern margin of India than is present now, fits the observation of abundant ultramafic and serpentinite clasts at the base of the Nindam Formation. The interpretation of the Dras and Nindam formations as the forearc basin of the Ladakh Arc (Fuchs, 1982; Henderson et al., 2010; Honegger et al., 1982; Najman et al., 2017) is inconsistent with the ages reported from the Ladakh Batholith which range from between 75 - 45 Ma (White et al., 2011) which is much younger than the youngest (~84 Ma) portions of the Nindam Formation reported here. The only other potential source region for these Jurassic to Lower Cretaceous zircons would be the Jurassic-Cretaceous (162-95 Ma) Karakoram Batholith on the southern margin of Eurasia (Borneman et al., 2015; Heuberger et al., 2007; Le Fort et al., 1983). However, this continental arc is dominated by felsic, silica-saturated magmatism and was situated on the northern margin of the Mesotethyan Ocean (Shyok Ocean), which separated Eurasia from the northward-moving Lhasa terrane (Li et al., 2016; Zhou et al., 2016). The Dras-Nindam terrane developed south of the Karakoram and Ladakh arcs within the Neotethyan Ocean, and therefore it is unlikely that detritus from the Karakoram Arc made its way across the Mesotethyan Ocean, around the Lhasa terrane and across the Neotethyan Ocean before entering the forearc basin of the Dras Arc. It is more likely that the forearc region of the Dras Arc was host to the earlier Spongtang Ophiolite

and Spong Arc, which eroded directly into the adjacent forearc basin of the Nindam Formation contributing 11% of total zircon grains analysed.

A small number of Permian to Triassic (200-271 Ma) zircons occur and make up less than 1% of the total population and may represent material derived from the Permo-Triassic Panjal Traps of India (Rehman et al., 2016; Shellnutt et al., 2011). Anomalously high Th/U is expected from such mafic rocks. The eight grains produced an average of 0.73, with the highest ratio being 1.05. Although these values are not extraordinarily high, they do suggest the grains are derived from mafic rocks. Detrital zircon studies of Eurasian-derived samples with the Himalayas are commonly distinguished by their distinct Mesozoic peaks associated with the magmatism within the Qiangtang Arc (Zhai et al., 2013). The fact that the Nindam Formation appears devoid of Carboniferous to Triassic zircons suggests it was not sourcing detritus from the active, southern Eurasian margin. A small (2%) population of Early Palaeozoic (418-540 Ma) zircons are present within the Nindam Formation. This is consistent with derivation from northern Gondwana which experienced the Kurgiakh Orogeny (Myrow et al., 2016) or equivalent "Bhimphedian Orogeny" of Cawood et al. (2007) during the Cambrian to Ordovician.

A distinct "Gondwanan" Precambrian detrital component can be identified within most samples, with input ranging between 6-42% (average 18%) of total grain ages. Unlike many intraoceanic island arcs that are dominated by a unimodal detrital zircon population (Draut & Clift, 2013; Manton et al., 2017a; Zhang et al., 2019), the Dras-Nindam terrane contains a distinct Gondwanan inheritance reflecting input from a continental source. There are no reports of any Gondwanan basement to the Dras Arc from which these zircons could have been sourced. The Neotethyan Ocean was bound to the south and north by peri-Gondwanan terranes of northern India and the Lhasa terrane respectively (Figure **4.11**) so either, or both, of these peri-Gondwanan terranes could have been a source region. Submarine fans may well have dispersed sediment from either Lhasa or India in a manner similar to the channelling of Himalayan-derived sediment into the Bay of Bengal and along the Sunda Trench as far south as Sunda Straight, with sediment being transported up to ~3000 km (Moore et al., 1982). Similar sediment transport distances have been reported for the Hikurangi Channel off the east coast of New Zealand, which sees gravity flows and deep-water currents moving sediment north into the Kermadec Trench, some ~2000 km distance (Lewis & Barnes, 1999). Therefore, it is entirely possible that the Precambrian zircons in the Nindam Formation were sourced from either the northern margin of India or the Lhasa terrane and migrated along the trench or forearc basin associated with the Dras intraoceanic island arc. It is worth noting that the Lhasa terrane had docked with Eurasia by the Late Cretaceous and was bound by the Trans-Himalayan Batholith to the south. If this active continental margin was a source region to the Nindam Formation, a zircon signature similar to

the Xigaze Group in Tibet (Figure **4.10**) should be recorded, but this is not the case. Thus, we suggest that the Gondwanan inheritance observed in the Nindam Formation is derived entirely from the Indian margin into an originally NNE-SSW trending trench, as proposed by Buckman et al. (2018), that initiated along a major transform fault (Figure **4.11**). If the original orientation of the Dras Arc and subduction complex was perpendicular to the northern margin of India then this would allow the migration of Indian-derived sediment into either the backarc, forearc or trench in manner similar to the Barbados Trench striking perpendicular to the South American continent (Macdonald et al., 2000).

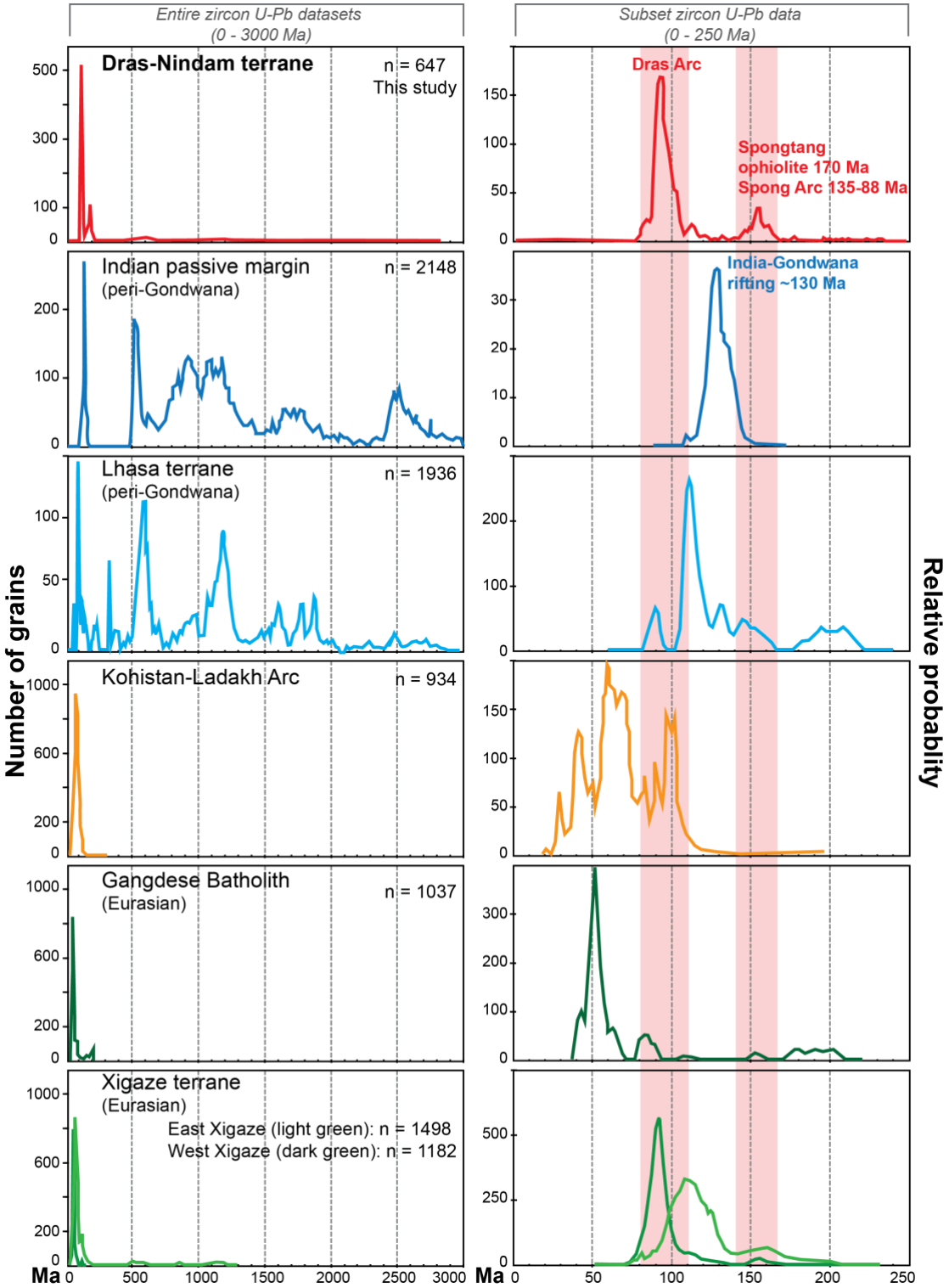

Figure 4.10: Compilation detrital zircon datasets from major Himalayan terranes. Dras-Nindam terrane (this study) detrital zircon ages compared to ages from the Indian passive margin (Najman et al. 2017), Lhasa terrane (Lai et al. 2019), Kohistan-Ladakh Arc (Najman et al. 2017), Gangdese Batholith (Najman et al. 2017) and Xigaze terrane (Hu et al. 2016b). Those datasets on the left have ages ranging from 0-3000 Ma. Those datasets on the right show a subset of the former from 0-250 Ma. For a full list of references used to compile these datasets, refer to Supporting Information Text.

4.6.3 Tectonic implications

4.6.3.1 Where and when did the Dras Arc form?

The youngest zircon population within the Nindam Formation shows that the Dras Arc was active between 125 Ma to at least 84 Ma, although it may have continued being active until its final collision with Gondwanan continental crust during the Eocene. All geological evidence points towards the Dras Arc forming in an intraoceanic island arc setting within the Neotethyan Ocean between the northern margin of India and the southern margin of the Lhasa terrane, which was an active continental margin in Tibet (Gangdese Batholith) but transitional to an island arc in Ladakh and Kohistan. The orientation of the trench and arc is normally interpreted as roughly E-W at 90° to the overall spreading direction, possibly also to reflect the fact that it was eventually accreted onto the E-W trending margin of northern India which now controls the orientation of the Indus-Yarlung-Tsangpo Suture. However, Reuber (1986) and Buckman et al. (2018) suggested the original orientation of the subduction zone responsible for formation of the supra-subduction zone ophiolites and subsequently the Dras Arc may have been more of a N-S orientation that coincided with major transform faults formed during separation of the Lhasa terrane from northern Gondwana (India). Transform faults are important sites of potential subduction initiation due to the juxtaposition of old and new ocean crust with contrasting density (Stern, 2004; Stern & Bloomer, 1992; Zhou et al., 2018). Recent paleomagnetic studies of the Semail Ophiolite in Oman (Morris et al., 2016) reveal that it initiated in a NE-SW orientation before being rotated 90° about a hinge point on the NW Arabian margin. We suggest that the Himalayan Neotethyan ophiolite-arc complexes, including the Dras Arc, were initially formed in a similar manner along roughly N-S orientated transform faults between India and southern Eurasia. A N-S trending trench and arc system between the Lhasa terrane and Indian block would potentially funnel sediment from both continental blocks into submarine fans dispersing sediment along the axis of the trench and subsequently into the developing accretionary complex and forearc basin (Figure **4.11**). It is important to note that a classic accretionary complex associated with the Nindam Formation is not observed. Instead, there is a serpentinite matrix mélange at the faulted contact between the base of the Nindam Formation and the Lamayuru Complex (India), which contains abundant peridotite-gabbro-basalt-chert blocks. Similarly, in the basal units of the Nindam Formation clasts in mass-flow conglomerates show this same clast assemblage. It may be that the accretionary complex was tectonically eroded upon collision with India and incorporated into the mélange. The Nindam Formation may well have been deposited in an extensional forearc basin before the process of arc-continent collision changed the setting to being tectonically erosive.

4.6.3.2 Collisional history of the Dras Arc

The question of whether the Dras Arc first collided with Eurasia or India is controversial. Early researchers (Coward et al., 1987; Honegger et al., 1982; Khan et al., 1993; Searle et al., 1999) interpret these arcs as being part of the same system, which sees northward subduction underneath the southern margin of Eurasia. Fuchs (1982) and Honegger et al. (1982) suggested that this arc evolved throughout the Jurassic to Cretaceous in a forearc region of a convergent margin on the southern margin of Eurasia. In their interpretation, the forearc basin developed on top of ophiolitic basement in front of the Ladakh Batholith as part of a single subduction complex responsible for the consumption of the entire Neotethyan Ocean, before the onset of the India-Eurasia continent-continent collision at ~55 Ma. Although this model is elegant in its simplicity, there are inconsistencies that do not fit the hypothesis, revolving around evidence that some ophiolite and arc terranes along the Indus Suture appear to have completely juvenile, intraoceanic characteristics rather than having developed in marginal continental basins.

Intrusive suites of the Kohistan and Ladakh batholiths are similar in both age and composition to the Gangdese Batholith (Figure **4.10**); therefore, it is likely that these entities are in fact related (Ravikant et al., 2009; Reichardt et al., 2010; Shellnutt et al., 2014; Weinberg & Dunlap, 2000). We emphasise that the southern margin of Eurasia was an active continental margin throughout most of the Carboniferous to Mesozoic and as such should be a major sediment contributor to any proximal basin developing along its margin. The distinct lack of Carboniferous to Jurassic detrital zircon populations in the Nindam Formation but the presence of a distinct Indian (Gondwanan) signature indicates that the Dras Arc developed as an intraoceanic island arc separate to the continental arc (Karakoram and Qiangtang arcs) developing on the southern margin of Eurasia. Corfield et al. (2001) and Clift et al. (2000) have noted the juvenile, intraoceanic nature of the Dras Arc and associated Nindam Formation, along with ophiolites along the Indus Suture all of which have no provenance links to felsic volcanism associated with the Ladakh Batholith. Corfield et al. (2001) suggested that the Dras Arc developed above a separate subduction system to both the southern margin of Eurasia (Ladakh Batholith) and the Spong Arc. They invoked three north-dipping subduction zones to explain the coeval development of these three separate entities and interpret the Dras Arc to have collided with Eurasia following the closure of the Shyok Ocean preceding final continent-continent collision of India and Eurasia. The results presented here align with the interpretation of the Dras Arc being juvenile and intraoceanic in nature. However, the strong 135-185 Ma inheritance in the Nindam Formation (Figure **4.10**; Supporting Information Text, Figure S4.1) reflects uplift and erosion of the supra-subduction zone Spongtang Ophiolite and associated Spong Arc into the forearc basin of the slightly younger Dras Arc as suggesting they may be part of the same

subduction complex (Buckman et al., 2018). Changes in the dip of subduction systems result in alternating periods of extension or compression which can easily uplift and expose forearc ophiolites or accretionary prisms to erosion into adjacent depocenters and this is reflected in the ophiolitic (peridotite, chert, limestone) clast compositions in the basal sections of the Nindam Formation. Thus, we provide an alternate model of accretion which sees the Dras Arc colliding with the passive margin of India before final continent collision (Figure **4.11**).

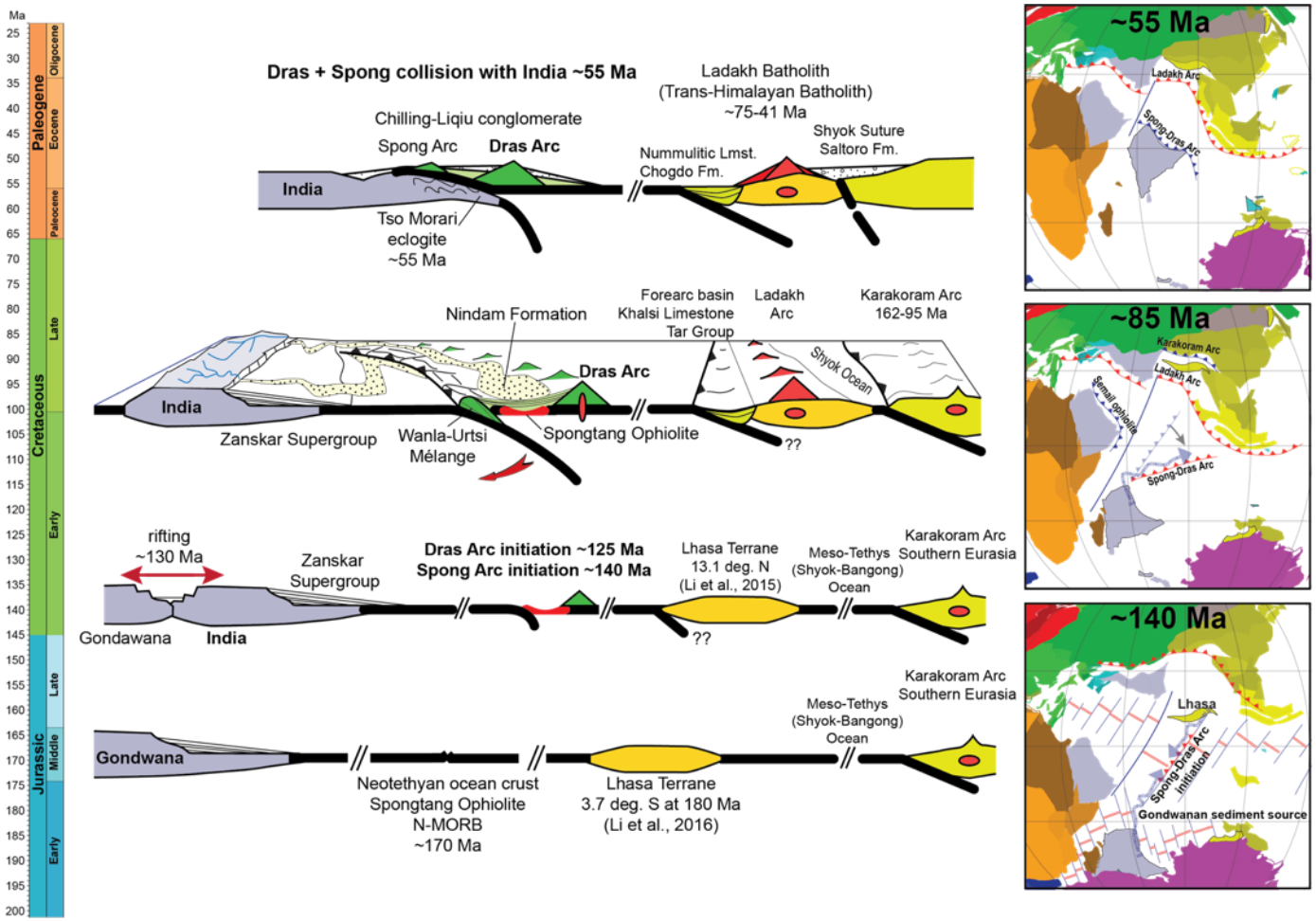

Figure 4.11: Time-space tectonic reconstruction for the intraoceanic Neotethyan Dras Arc. Plate reconstructions are modified from the GPlates model of Seton et al. (2012). Modifications of the model are based on new paleomagnetic data for the Lhasa terrane (LT) by Zhou et al. (2016) and Li et al. (2016) who have the Lhasa terrane much further south from the Triassic to Cretaceous than in the model of Seton et al. (2012). Likewise, paleomagnetic data from Klootwijk et al. (1979) has the Ladakh Batholith positioned further south at 23°N. This reconstruction builds on the model of Buckman et al. (2018) who proposed that the Spongtang ophiolite and Dras Arc evolved as an intraoceanic island arc system that developed as a result of spontaneous subduction at ~136 Ma along a NNE-SSW transform fault in the Neotethyan Ocean. This ophiolite-arc complex collided with India at ~55 Ma at roughly equatorial latitude while the Ladakh Batholith (Trans-Himalayan Batholith) developed closer to the southern margin of Eurasia before final continental collision at ~35 Ma.

4.7 Conclusions

(i) The Nindam Formation volcaniclastic rocks represent distal deep-marine deposits sourced largely from the Dras Arc and record Cretaceous intraoceanic island arc activity spanning a 41-million-year period between ~84-125 Ma. The youngest detrital zircons in each of the samples becomes progressively younger up through the sequence indicating deposition at the base began at ≤102 Ma and continued until ≤84 Ma at the top of the sequence.

(ii) A distinct "Gondwanan" zircon signature comprised of Precambrian peaks at ~514-988 Ma, ~1000-1588 Ma, ~1627-2444 Ma and ~2500 Ma occurs in all samples and derived from the northern Indian margin via far-travelled sediment.

(iii) All geological evidence suggests the Nindam Formation was deposited in an intraoceanic forearc basin setting with little to no influence from continental rocks. Therefore, the Dras-Nindam terrane does not represent the forearc basin to the southern Eurasian margin nor the forearc to the Ladakh Batholith but is more akin to island arc development associated with the Indus supra-subduction zone ophiolites.

(iv) Minor and slightly older detrital zircon populations occur at ~135-185 Ma and these correspond with reported ages of intraoceanic Neotethyan ophiolites, such as Spongtang and Nidar, which probably represent ophiolitic forearc basement to the Dras Arc and establish a link between the Spong and Dras arcs. Given that the Spongtang Ophiolite and Spong Arc were clearly obducted onto the Indian margin during the early Eocene we suggest that the intraoceanic Dras + Spong Arc first collided and accreted onto the passive margin of India rather than Eurasia prior to continent-continent collision of India and Eurasia.

4.8 Acknowledgments

This project was partially supported by the GeoQuEST Research Centre and a Small Project Grant (2017) from the University of Wollongong. The authors would like to thank A.H.F Robertson and two anonymous reviewers for their constructive comments and useful suggestions, which vastly improved the content of this manuscript. Editor J. Geissman and Special Section Organiser J. Ali are thanked for prompt handling of the manuscript. The authors would like to thank J. Punchok for guidance in Ladakh. We would also like to thank W.M. Saktura and S.L. Walsh for assistance in the field. T. McMahon is thanked for CL imaging. This research has been conducted with the support of the Australian Government Research Training Program Scholarship awarded to J.M.J. Walsh. There are no declarations of interest. All data presented is available in Supporting Information.

4.9 Coauthor contributions

Walsh, Jessica, M.J.
GeoQuEST Research Centre, School of Earth, Atmospheric and Life Sciences,
University of Wollongong, Wollongong, NSW 2522, Australia.
Position: PhD candidate
Email: jw063@uowmail.edu.au
Credit author statement: Conceptualisation, Methodology, Investigation, Data Curation, Writing - Original Draft, Writing - Review & Editing, Visualisation.

Buckman, Solomon:
GeoQuEST Research Centre, School of Earth, Atmospheric and Life Sciences,
University of Wollongong, Wollongong, NSW 2522, Australia.
Position: Senior lecturer in economic geology
Email: solomon@uow.edu.au
Credit author statement: Conceptualisation, Methodology, Investigation, Writing - Original Draft, Writing - Review & Editing, Supervision, Funding acquisition.

Nutman, Allen, P.
GeoQuEST Research Centre, School of Earth, Atmospheric and Life Sciences,
University of Wollongong, Wollongong, NSW 2522, Australia.
Position: Professor in igneous and metamorphic petrology
Email: anutman@uow.edu.au
Credit author statement: Methodology, Writing - Review & Editing, Supervision.

Zhou, Renjie

School of Earth and Environmental Sciences,

The University of Queensland, Brisbane, QLD 4072, Australia.

Position: Lecturer in tectonics

Email: renjie.zhou@uq.edu.au

Credit author statement: Investigation, Methodology, Data Curation, Writing - Review & Editing.

4.10 Supporting information

Age and provenance of the Nindam Formation, Ladakh, NW Himalaya: Evolution of the intraoceanic Dras Arc before collision with India

Jessica M.J. Walsh[1], Solomon Buckman[1], Allen P. Nutman[1], and Renjie Zhou[2]

[1]GeoQuEST Research Centre, School of Earth, Atmospheric and Life Sciences, University of Wollongong, Wollongong, NSW 2522, Australia.
[2]School of Earth and Environmental Sciences, The University of Queensland, Brisbane, QLD 4072, Australia.

Overview

The following information includes further support for the results and discussion sections of Chapter 4, referred to in-text as 'Supporting Information Text'. The first section (Supporting Information: Results) of the Supporting Information includes a detailed description of detrital zircon U-Pb geochronology results from the Nindam Formation, Ladakh, NW India, first describing the composite dataset and then each sample including major age groupings. The second section (Supporting Information: Discussion) of the Supporting Information includes a full list of the references used to compile "*Figure* **4.11**: Compilation detrital zircon datasets from major Himalayan terranes".

Following this are tabulated data, and includes:

- Table S4.1: Sample localities and lithological descriptions
- Table S4.2: Point counting data
- Table S4.3: Whole rock geochemistry
- Table S4.4: Detrital zircon U-Pb results using LA-ICP-MS
- Table S4.5: Detrital zircon U-Pb results using SHRIMP

4.10.1 Supporting information: Results

4.10.1.1 Detrital zircon U-Pb geochronology

4.10.1.1.1 Composite dataset

Eight-hundred and forty-one grains in total were analysed using a combination of LA-ICP-MS (n = 791) and SHRIMP (n = 50). Out of these, 695 analysed spots acquired concordant ages. See Figure S4.1. On examining all samples, most of the sites (66%) fall in the 125 ± 1 Ma-84 ± 1 Ma range.

Major age groupings of the composite Nindam Formation volcaniclastic samples are:

(i) Precambrian (total = 18%, n = 115):
   a. Neoarchean (>2500 Ma, <1%, n = 2)
   b. Paleoproterozoic (Siderian – Statherian, 3%, n = 18, ca. 2444-1627 Ma)
   c. Mesoproterozoic (Calymmian – Stenian, 8%, n = 54, ca. 1588-1000 Ma)
   d. Neoproterozoic (Tonian – Edicaran, 6%, n = 41, ca. 988-541 Ma)

(ii) Cambrian to Lower Devonian (Fortunian to Lochkovian, 2%, n = 10, ca. 540-418 Ma)

(iii) Permian to Upper Triassic (Roadian to Rhaetian, 1%, n = 8, ca. 271-205 Ma)

(iv) Lower to Upper Jurassic (Pliensbachian to Tithonian, 12%, n = 75, ca. 185-145 Ma)

(v) Lower Cretaceous (Valanginian to Barremian, 1%, n = 8, ca. 138-126 Ma)

(vi) Lower to Upper Cretaceous (Aptian to Santonian, 66%, n = 430, ca. 125-84 Ma) age range

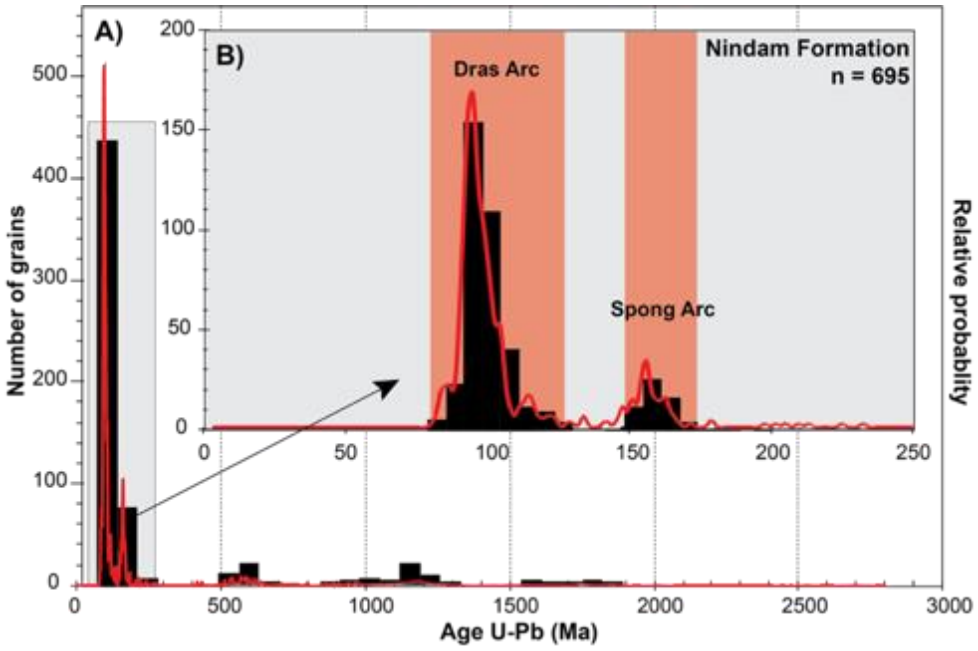

Figure S4.1: Probability density distribution plot for all the Nindam Formation samples, analysed using a combination of LA-ICP-MS (n = 791) and SHRIMP (n = 50). **A)** Entire dataset, between 0-3000 Ma, where 695 grains acquired concordant ages ranging from 2698 ± 17 Ma-81 ± 1 Ma; **B)** Subset data between 0-250 Ma, showing Dras Arc and Spong Arc peaks.

4.10.1.1.2 Sample 16NI02

One-hundred and thirteen grains in Sample 16NI02 were randomly chosen for zircon U-Pb analysis using LA-ICP-MS. Out of these, 86 sites acquired concordant ages. Contents of U and Th are 11-931 ppm and 5-769 ppm respectively, with Th/U ratios varying 0.12-2.76. The $^{206}Pb/^{238}U$ zircon ages range from 2531 ± 11 Ma-100 ± 1 Ma, most of which (40%) fall in the 133 ± 3 Ma-100 ± 1 Ma range.

Major age groupings are:

(i) Neoarchean to Neoproterozoic (41%, ca. 2531-573 Ma)
(ii) Cambrian (Terreneuvian to Series 2, 3%, ca. 534-513 Ma)
(iii) Upper Triassic (Norian, 2%, ca. 209-205 Ma)
(iv) Middle to Upper Jurassic (Bajocian to Tithonian, 12%, ca. 169-145 Ma)
(v) Lower Cretaceous (Valanginian to Albian, 40%, ca. 133-100 Ma)

In addition, there are 435 ± 2 Ma and 257 ± 4 Ma grains. The age of the youngest analytically indistinguishable group from this sample is **102.25 ± 0.64 Ma** (MSWD = 0.02, *n* = 2). See Figure S4.2 for the youngest grain populations from each sample. The youngest grain from this sample is 100 ± 1 Ma based on only one analysis of grain (1σ).

4.10.1.1.3 Sample 16NI06

One-hundred and five grains in Sample 16NI06 were randomly chosen for zircon U-Pb analysis using LA-ICP-MS. Out of these, 87 sites acquired concordant ages. Contents of U and Th are 22-1705 ppm and 10-3510 ppm respectively, with Th/U ratios varying 0.28-1.98. The $^{206}Pb/^{238}U$ zircon ages range from 1881 ± 11 Ma-95 ± 1 Ma, most of which (69%) falls in the 137 ± 1 Ma-95 ± 1 Ma range.

Major age groupings are:

(i) Paleoproterozoic to Neoproterozoic (6%, ca. 1881-865 Ma)
(ii) Lower to Upper Jurassic (Toarcian to Tithonian, 25%, ca. 177-150 Ma)
(iii) Lower Cretaceous (Valanginian to Albian, 37%, ca. 137-100 Ma)
(iv) Upper Cretaceous (Cenomanian, 32%, ca. 99-95 Ma)

The age of the youngest analytically indistinguishable group from this sample is **95.74 ± 0.40 Ma** (MSWD = 0.73, *n* = 3).

4.10.1.1.4 Sample 16NI08

One-hundred and fourteen grains in Sample 16NI08 were randomly chosen for zircon U-Pb analysis using LA-ICP-MS. Out of these, 94 sites acquired concordant ages. Contents of U and Th are 34-467 ppm and 14-513 ppm respectively, with Th/U ratios varying 0.32-1.39. The $^{206}Pb/^{238}U$ zircon ages range from 162 ± 1 Ma-89 ± 1 Ma, most of which range from 138 ± 1 Ma-89 ± 1 Ma (97%).

Major age groupings are:

(i) Upper Jurassic (Oxfordian to Kimmeridgian, 3%, ca. 162-154 Ma)
(ii) Lower Cretaceous (Valanginian to Albian, 9%, ca. 138-100 Ma)
(iii) Upper Cretaceous (Cenomanian to Turonian, 88%, ca. 99-89 Ma)

The age of the youngest analytically indistinguishable group from this sample is **90.80 ± 0.31 Ma** (MSWD = 0.40, *n* = 3). The youngest grain from this sample is 89 ± 1 Ma based on only one analysis of grain (1σ).

4.10.1.1.5 Sample 15ND02

Twenty-five grains in Sample 15ND02 were randomly chosen for zircon U-Pb analysis using SHRIMP. Out of these, 24 analysed sites concordant ages. Contents of U and Th are 25-1266 ppm and 9-1247 ppm respectively, with Th/U ratios varying 0.33-1.73. The $^{206}Pb/^{238}U$ zircon ages range from 1150 ± 24 Ma-94 ± 2 Ma, most of which (92%) fall in the 110 ± 2 Ma-94 ± 2 Ma range.

Major age groupings are:

(i) Lower Cretaceous (Albian, 21%, ca. 110-101 Ma)
(ii) Upper Cretaceous (Cenomanian, 71%, ca. 99-94 Ma)

In addition, there are 1150 ± 24 Ma and 163 ± 3 Ma grains. The age of the youngest analytically indistinguishable group from this sample is **94.23 ± 0.78 Ma** (MSWD = 0.11, *n* = 6).

4.10.1.1.6 Sample 15ND03

Twenty-five grains in Sample 15ND03 were randomly chosen for zircon U-Pb analysis using SHRIMP. Out of these, 24 sites acquired concordant ages. Contents of U and Th are 56-519 ppm and 17-346 ppm respectively, with Th/U ratios varying 0.14-1.71. The $^{206}Pb/^{238}U$ zircon ages

range from 2012 ± 13 Ma-92 ± 2 Ma most of which (42%) fall in the Paleo- to Neoproterozoic (2012 ± 13 Ma-548 ± 8 Ma) range.

Major age groupings are:

(i) Paleoproterozoic to Neoproterozoic (42%, ca. 2012-548 Ma)
(ii) Upper Jurassic (Kimmeridgian 13%, ca. 156-153 Ma)
(iii) Upper Cretaceous (Cenomanian, 38%, ca. 96-92 Ma)

In addition, there are 538 ± 8 Ma and 234 ± 4 Ma grains. The age of the youngest analytically indistinguishable group from this sample is **92.40 ± 0.71 Ma** (MSWD = 0.68, *n* = 6).

4.10.1.1.7 Sample 16NI09

One-hundred and thirty-eight grains in Sample 16NI09 were randomly chosen for zircon U-Pb analysis using LA-ICP-MS. Out of these, 104 sites acquired concordant ages. Contents of U and Th are 27-1341 ppm and 3-1524 ppm respectively, with Th/U ratios varying 0.02-1.95. The $^{206}Pb/^{238}U$ zircon ages range from 1766 ± 13 Ma-92 ± 0 Ma most of which (65%) fall in the 138 ± 1 Ma-92 ± 0 Ma range.

Major age groupings are:

(i) Paleoproterozoic to Neoproterozoic (20%, ca. 1766-557 Ma)
(ii) Middle to Upper Jurassic (Aalenian to Kimmeridgian, 13%, ca. 173-152 Ma)
(iii) Lower Cretaceous (Valanginian to Albian, 24%, ca. 138-100 Ma)
(iv) Upper Cretaceous (Cenomanian, 41%, ca. 99-92 Ma)

In addition, there are 536 ± 2 Ma and 491 ± 5 Ma grains. The age of the youngest analytically indistinguishable group from this sample is **92.89 ± 0.3 Ma** (MSWD = 0.42, *n* = 3). The youngest grain from this sample is 92 ± 0 Ma based on only one analysis of grain (1σ).

4.10.1.1.8 Sample 16NI10a

Fifty-five grains in Sample 16NI10a were randomly chosen for zircon U-Pb analysis using LA-ICP-MS. Out of these, 26 sites acquired concordant ages. Contents of U and Th are 30-518 ppm and 21-612 ppm respectively, with Th/U ratios varying 0.14-1.24. The $^{206}Pb/^{238}U$ zircon ages range from 2698 ± 17 Ma-92 ± 1 Ma most of which (62%) fall in the 117 ± 1 Ma-92 ± 1 Ma range.

Major age groupings are:

(i) Neoarchean to Neoproterozoic (19%, ca. 2698-568 Ma)
(ii) Upper Jurassic (Oxfordian to Kimmeridgian, 12%, ca. 157-151 Ma)
(iii) Lower Cretaceous (Aptian to Albian, 23%, ca. 117-100 Ma)
(iv) Upper Cretaceous (Cenomanian, 39%, ca. 99-92 Ma)

In addition, there are 539 ± 2 Ma and 213 ± 1 Ma grains. The age of the youngest analytically indistinguishable group from this sample is **92.05 ± 0.43 Ma** (MSWD = 0.05, *n* = 2).

4.10.1.1.9 Sample 16NI10b

One-hundred and eleven grains in Sample 16NI10b were randomly chosen for zircon U-Pb analysis using LA-ICP-MS. Out of these, 79 sites acquired concordant ages. Contents of U and Th are 45-982 ppm and 19-1236 ppm respectively, with Th/U ratios varying 0.13-2.01. The $^{206}Pb/^{238}U$ zircon ages range from 1863 ± 11 Ma-93 ± 1 Ma, most of which (59%) fall in the 127 ± 2 Ma-93 ± 1 Ma range.

Major age groupings are:

(i) Paleoproterozoic to Neoproterozoic (29%, ca. 1863-541 Ma)
(ii) Lower to Upper Jurassic (Pilensbachian to Oxfordian, 6%, ca. 185-161 Ma)
(iii) Lower Cretaceous (Barremian to Albian, 25%, ca. 127-100 Ma)
(iv) Upper Cretaceous (Cenomanian, 34%, ca. 99-93 Ma)

In addition, there are 511 ± 2 Ma, 418 ± 2 Ma, 271 ± 2 Ma and 218 ± 1 Ma grains. The age of the youngest analytically indistinguishable group from this sample is **93.70 ± 0.31 Ma** (MSWD = 0.65, *n* = 5).

4.10.1.1.10 Sample 16NI13

Sixty-seven grains in Sample 16NI13 were randomly chosen for zircon U-Pb analysis using LA-ICP-MS. Out of these, 56 sites acquired concordant ages. Contents of U and Th are 42-818 ppm and 35-656 ppm respectively, with Th/U ratios varying 0.22-1.19. The $^{206}Pb/^{238}U$ zircon ages range from 1848 ± 12 Ma-96 ± 1 Ma, most of which (73%) fall in the 116 ± 2 Ma-96 ± 1 Ma range.

Major age groupings are:

(i) Paleoproterozoic to Neoproterozoic (13%, ca. 1848-587 Ma)
(ii) Middle to Upper Jurassic (Callovian to Tithonian, 13%, ca. 164-146 Ma)
(iii) Lower Cretaceous (Aptian to Albian, 63%, ca. 116-100 Ma)
(iv) Upper Cretaceous (Cenomanian, 11%, ca. 99-96 Ma)

In addition, there is a 221 ± 1 Ma grain. The age of the youngest analytically indistinguishable group from this sample is **98.91 ± 0.33 Ma** (MSWD = 0.03, *n* = 3). The youngest grain from this sample is 96 ± 1 Ma based on only one analysis of grain (1σ).

4.10.1.1.11 Sample 16NI16

Eighty-eight grains in Sample 16NI16 were randomly chosen for zircon U-Pb analysis using LA-ICP-MS. Out of these, 67 sites acquired concordant ages. Contents of U and Th are 27-649 ppm and 12-599 ppm respectively, with Th/U ratios varying 0.17-2.47. The $^{206}Pb/^{238}U$ zircon ages range from 1677 ± 15 Ma-81 ± 1 Ma, most of which (75%) fall in the 117 ± 1 Ma-81 ± 1 Ma range.

Major age groupings are:

(i) Paleoproterozoic to Neoproterozoic (12%, ca. 1677-570 Ma)
(ii) Middle Triassic to Upper Jurassic (13%, ca. 242-152 Ma)
(iii) Lower Cretaceous (Aptian to Albian, 5%, ca. 117-101 Ma)
(iv) Upper Cretaceous (Cenomanian to Campanian, 70%, ca. 97-81 Ma)

The age of the youngest analytically indistinguishable group from this sample is **84.20 ± 0.26 Ma** (MSWD = 0.95, *n* = 3). The youngest grain from this sample is 81 ± 1 Ma based on only one analysis of grain (1σ).

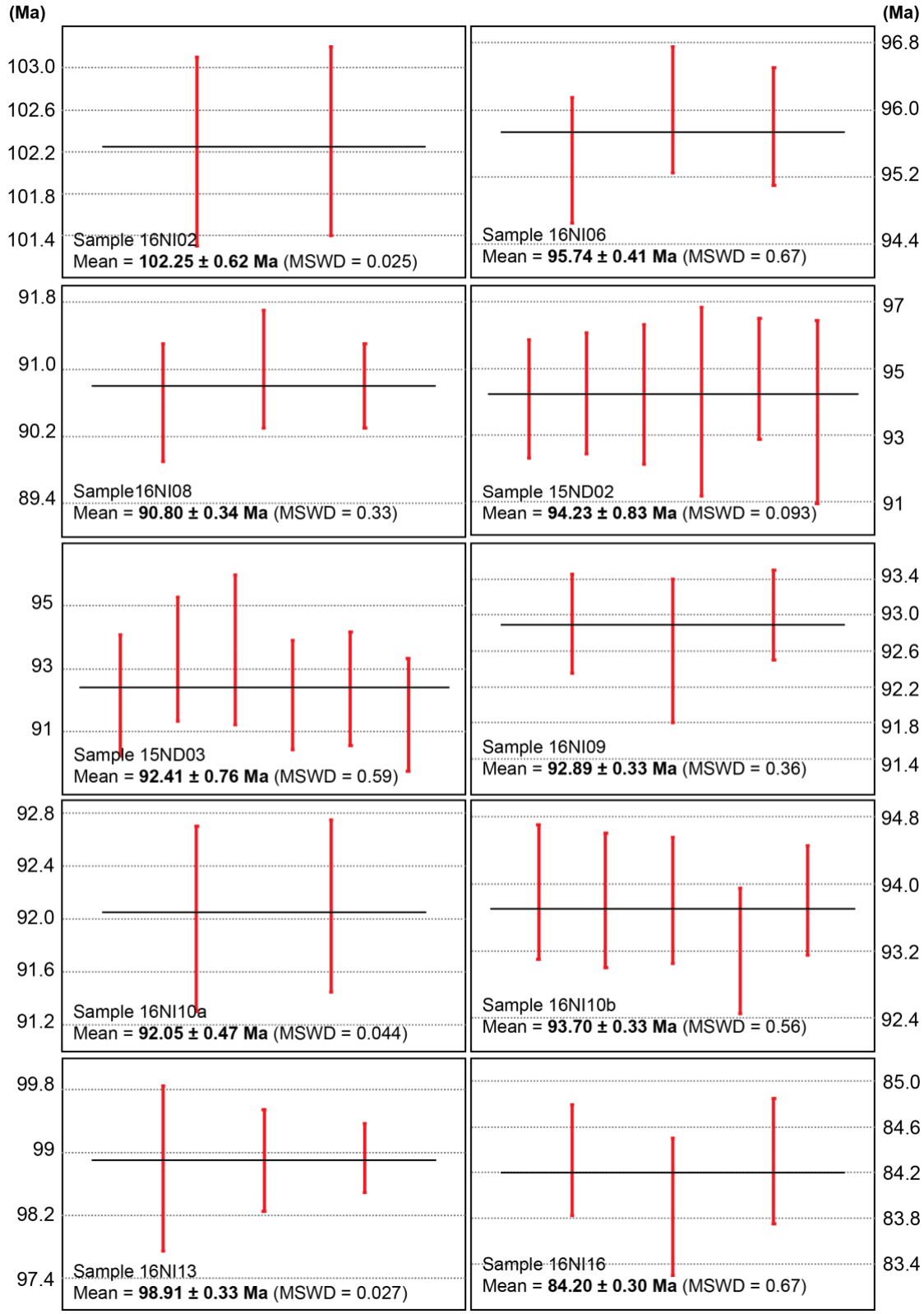

Figure S4.2: Weighted mean averages (WMAs) of the youngest analytically indistinguishable zircon populations within each sample of the Nindam Formation, where n ≥ 2 and MSWD ≤ 1. The data are presented in stratigraphic order (16NI02, 16NI06, 16NI08, 15ND02, 15ND03, 16NI09, 16NI10a, 16NI10b, 16NI13, 16NI16).

4.10.2 Supporting information: Discussion

The following references accompany "*Figure* **4.11**: Compilation detrital zircon datasets from major Himalayan terranes".

Dras-Nindam Formation

All age data sourced from this study.

Indian passive margin (peri-Gondwana)

Sourced from Najman et al. (2017), who compiled from a variety of sources (Clift et al., 2014; Gehrels et al., 2008; Hu et al., 2010).

- Najman, Y., Jenks, D., Godin, L., Boudagher-Fadel, M., Millar, I., Garzanti, E., & Bracciali, L. (2017). The Tethyan Himalayan detrital record shows that India–Asia terminal collision occurred by 54 Ma in the Western Himalaya. *Earth and Planetary Science Letters*, 459, 301-310, Figure 6.

Lhasa terrane (peri-Gondwana)

Sourced from Lai et al. (2019), who compiled from a variety of sources (Chu et al., 2006; Gehrels et al., 2011; Leier et al., 2007a; Leier et al., 2007b; Li et al., 2014; Zhang et al., 2011; Zhu et al., 2009a; Zhu et al., 2011a; Zhu et al., 2011b).

- Lai, W., Hu, X., Garzanti, E., Xu, Y., Ma, A., & Li, W. (2019). Early Cretaceous sedimentary evolution of the northern Lhasa terrane and the timing of initial Lhasa-Qiangtang collision. *Gondwana Research*, Figure 8g.

Kohistan-Ladakh island arc (KLIA)

Sourced from Najman et al. (2017), who compiled from a variety of sources (Bosch et al., 2011; Bouilhol et al., 2013; Bouilhol et al., 2011; Henderson et al., 2011; Heuberger et al., 2007; Honegger et al., 1982; Jagoutz et al., 2009; Khan et al., 2009; Krol et al., 1996; Ravikant et al., 2009; Schaltegger et al., 2002; Schärer et al., 1984a; Schärer et al., 1984b; Singh et al., 2007; Upadhyay et al., 2008; Weinberg and Dunlap, 2000; White et al., 2011).

- Najman, Y., Jenks, D., Godin, L., Boudagher-Fadel, M., Millar, I., Garzanti, E., & Bracciali, L. (2017). The Tethyan Himalayan detrital record shows that India–Asia terminal collision occurred by 54 Ma in the Western Himalaya. *Earth and Planetary Science Letters*, 459, 301-310, Figure 6.

Gangdese Batholith (Eurasian)

Sourced from Najman et al. (2017), who compiled from a variety of sources (Chu et al., 2006; Ji et al., 2009; Lee and Whitehouse, 2007; Mo et al., 2005; Quidelleur et al., 1997; Schärer et al., 1984b; Wen et al., 2008; Zhang et al., 2007; Zhu et al., 2011b; Zhu et al., 2009b).

- Najman, Y., Jenks, D., Godin, L., Boudagher-Fadel, M., Millar, I., Garzanti, E., & Bracciali, L. (2017). The Tethyan Himalayan detrital record shows that India–Asia terminal collision occurred by 54 Ma in the Western Himalaya. *Earth and Planetary Science Letters*, 459, 301-310, Figure 6.

Xigaze terrane (Eurasian)

Sourced from Hu et al. (2016b), who compiled from a variety of sources (Aitchison et al., 2011; An et al., 2014; Orme et al., 2015; Wu et al., 2010).

- Hu, X., Wang, J., BouDagher-Fadel, M., Garzanti, E., & An, W. (2016). New insights into the timing of the India–Asia collision from the Paleogene Quxia and Jialazi formations of the Xigaze forearc basin, South Tibet. *Gondwana Research*, 32, 76-92, Figure 9.

Table S4.1 Sample localities and descriptions (Chapter 4)

Sample	Lithology	Latitude (°N)	Longitude (°E)	Methods					
				Petrography	XRD	Point counting	Whole rock geochemistry	LA-ICP-MS	SHRIMP
Nindam Formation (Dras-Nindam terrane)									
15ND02	Volcaniclastic	34.299306	76.821907	✓	✓	✓	✓		✓
15ND03	Volcaniclastic	34.299306	76.821907	✓	✓	✓	✓		✓
16NI01	Volcaniclastic	34.290241	76.796616	✓	✓	✓	✓		
16NI02	Volcaniclastic	34.291197	76.797656	✓	✓	✓	✓	✓	
16NI03	Volcaniclastic	34.293108	76.798713	✓	✓	✓	✓		
16NI04a	Red shale	34.293442	76.799553	✓	✓		✓		
16NI04b	Green shale	34.293442	76.799553	✓	✓		✓		
16NI05	Volcaniclastic	34.293642	76.800117	✓			✓		
16NI06	Volcaniclastic	34.294031	76.801244	✓	✓	✓	✓	✓	
16NI07a	Red shale	34.297511	76.818375	✓	✓		✓		
16NI07b	Green shale	34.297511	76.818375	✓	✓		✓		
16NI08	Volcaniclastic	34.297907	76.818928	✓	✓	✓	✓	✓	
16NI09	Volcaniclastic	34.299621	76.819450	✓	✓	✓	✓	✓	
16NI10a	Volcaniclastic	34.300028	76.821108	✓				✓	
16NI10b	Volcaniclastic	34.300028	76.821108	✓			✓	✓	
16NI11	Black shale	34.299480	76.823704	✓	✓		✓		
16NI13	Volcaniclastic	34.299321	76.825496	✓	✓	✓	✓	✓	
16NI15a	Red shale	34.299678	76.832744	✓	✓		✓		
16NI15b	Green shale	34.299678	76.832744	✓	✓		✓		
16NI16	Volcaniclastic	34.301581	76.834222	✓	✓	✓	✓	✓	

Dras Volcanics (Dras-Nindam terrane)						
17NI01	Volcaniclastic	34.476810	76.229460	✓		✓
17NI02	Basalt	34.477020	76.230000	✓		✓
17NI03	Basalt	34.474220	76.232480	✓		✓
17NI04	Volcaniclastic	34.468530	76.242530	✓		✓
17NI05	Volcaniclastic	34.461160	76.264360	✓		✓
17NI06	Basalt	34.450410	76.272940	✓		✓
17NI07	Basalt	34.441340	76.283340	✓		✓
17NI09	Basalt	34.436170	76.284260	✓		✓
17NI10	Basalt	34.435550	76.284040	✓		✓
17NI11	Basalt	34.425570	76.283590	✓		✓
Indus Group						
16HN01a	Conglomerate	34.329514	76.836692	✓	✓	✓
16HN02	Conglomerate	34.330070	76.836281	✓		✓
16NM01	Sandstone	34.246964	77.199300	✓	✓	✓
16BT01	Conglomerate	34.180608	77.338903	✓	✓	✓
Khalsi Limestone						
16KH01	Limestone	34.315356	76.874558	✓	✓	✓
16KH02	Limestone	34.234236	77.060503	✓	✓	✓

Notes:
Fieldwork was undertaken during May-June 2015, 2016 and 2017 in the Ladakh region, Jammu and Kashmir, NW India.

Table S4.2 Point counting data (Chapter 4)

Sample	15ND02	15ND03	16NI01	16NI02	16NI03	16NI06	16NI08	16NI09	16NI13	16NI16
Lithology	Volcaniclastic	Volcaniclastic	Volcaniclastic	Volcaniclastic	Volcaniclastic	Volcaniclastic	Volcaniclastic	Volcaniclastic	Volcaniclastic	Volcaniclastic
Formation	Nindam Fm	Nindam Fm	Nindam Fm	Nindam Fm	Nindam Fm	Nindam Fm	Nindam Fm	Nindam Fm	Nindam Fm	Nindam Fm
Quartz-poly (Qp)	1	2	8	1	0	2	0	1	3	0
Quartz-mono (Qm)	7	15	17	12	17	22	9	20	11	5
Quartz-chert (Qc)	76	72	154	186	170	109	100	132	49	35
Total quartz (Q)	**84**	**89**	**179**	**199**	**187**	**133**	**109**	**153**	**63**	**40**
Plagiolclase (P)	54	16	47	16	22	13	59	36	90	118
K-feldspar (K)	46	4	46	13	28	11	88	57	21	19
Total feldspar (F)	**100**	**20**	**93**	**29**	**50**	**24**	**147**	**93**	**111**	**137**
Lithic-volcanic (Lv)	128	199	93	109	111	258	60	142	203	139
Lithic-meta (Lm)	0	0	0	0	0	0	0	0	0	0
Lithic-sedi (Ls)	0	0	0	0	0	0	0	0	0	0
Lithic-plutonic (Lp)	0	0	1	1	0	0	0	0	0	0
Total lithic (L)	**128**	**199**	**94**	**110**	**111**	**258**	**60**	**142**	**203**	**139**
Muscovite (Mm)	0	0	0	0	0	0	0	0	0	0

Biotite (Mb)	0	0	0	3	0	0	0	1	0	0
Total mica (M)	**0**	**0**	**0**	**3**	**0**	**0**	**0**	**1**	**0**	**0**
Cal-cement (Ccal)	0	0	0	0	0	0	0	0	0	0
Ferr-cemment (Cferr)	0	0	0	0	0	0	0	0	0	0
Sil-cement (Csil)	0	0	0	0	0	0	0	0	0	0
Total cement (C)	**0**	**0**	**0**	**0**	**0**	**0**	**0**	**0**	**0**	**0**
Matrix (Mx)	0	0	0	0	0	0	0	0	0	0
Clino-pyr (Cpx)	2	4	0	0	0	0	0	0	3	2
Ortho-pyr (Opx)	0	0	1	1	0	0	0	0	0	0
Total pyroxene (P)	**2**	**4**	**1**	**1**	**0**	**0**	**0**	**0**	**3**	**2**
Opaque	57	22	7	8	8	5	32	42	21	20
Calcite	121	78	89	138	115	60	26	53	43	81
Chlorite	38	58	38	13	29	19	125	16	56	81
Serpentinite	0	0	0	0	0	0	0	0	0	0
Amphibole	0	0	2	0	0	0	1	0	0	0
Misc.	0	0	0	0	0	0	0	0	0	0
Total	**500**	**500**	**503**	**501**	**500**	**499**	**500**	**500**	**500**	**500**

*Sample	15ND02	15ND03	16NI01	16NI02	16NI03	16NI06	16NI08	16NI09	16NI13	16NI16
Quartz-poly (Qp)	1	2	8	1	0	2	0	1	3	0
Quartz-mono (Qm)	7	15	17	12	17	22	9	20	11	5
Total quartz (Q)	**8**	**17**	**25**	**13**	**17**	**24**	**9**	**21**	**14**	**5**
Plagiolclase (P)	54	16	47	16	22	13	59	36	90	118
K-feldspar (K)	46	4	46	13	28	11	88	57	21	19
Total feldspar (F)	**100**	**20**	**93**	**29**	**50**	**24**	**147**	**93**	**111**	**137**
Lithic-volcanic (Lv)	128	199	93	109	111	258	60	142	203	139
Quartz-chert (Qc)	76	72	154	186	170	109	100	132	49	35
Total lithic (L)	**204**	**271**	**247**	**295**	**281**	**367**	**160**	**274**	**252**	**174**
Total points	**312**	**308**	**365**	**337**	**348**	**415**	**316**	**388**	**377**	**316**

†Sample	15ND02	15ND03	16NI01	16NI02	16NI03	16NI06	16NI08	16NI09	16NI13	16NI16
Quartz-poly (Qp)	0.32	0.65	2.19	0.30	0.00	0.48	0.00	0.26	0.80	0.00
Quartz-mono (Qm)	2.24	4.87	4.66	3.56	4.89	5.30	2.85	5.15	2.92	1.58
Total quartz (Q)	2.56	5.52	6.85	3.86	4.89	5.78	2.85	5.41	3.71	1.58
Plagiolclase (P)	17.31	5.19	12.88	4.75	6.32	3.13	18.67	9.28	23.87	37.34
K-feldspar (K)	14.74	1.30	12.60	3.86	8.05	2.65	27.85	14.69	5.57	6.01
Total feldspar (F)	32.05	6.49	25.48	8.61	14.37	5.78	46.52	23.97	29.44	43.35
Lithic-volcanic (Lv)	41.03	64.61	25.48	32.34	31.90	62.17	18.99	36.60	53.85	43.99
Quartz-chert (Qc)	24.36	23.38	42.19	55.19	48.85	26.27	31.65	34.02	13.00	11.08
Total lithic (L)	65.38	87.99	67.67	87.54	80.75	88.43	50.63	70.62	66.84	55.06
Total points (%)	100	100	100	100	100	100	100	100	100	100

Notes:

*Simplified for QFL diagrams (raw point counting values).

†Simplified for QFL diagrams (raw point counting values converted to %).

Table S4.3 Whole rock geochemistry (Chapter 4)

Sample	15ND02	15ND03	16NI01	16NI02	16NI03	16NI05	16NI06	16NI08	16NI09	16NI10b	16NI13	16NI16
Affinity	Nindam Fm.	Nindam Fm.	Nindam Fm.	Nindam Fm.	Nindam Fm.	Nindam Fm.	Nindam Fm.	Nindam Fm.	Nindam Fm.	Nindam Fm.	Nindam Fm.	Nindam Fm.
Rock type	Volcaniclastic	Volcaniclastic	Volcaniclastic	Volcaniclastic	Volcaniclastic	Volcaniclastic	Volcaniclastic	Volcaniclastic	Volcaniclastic	Volcaniclastic	Volcaniclastic	Volcaniclastic
Latitude (°N)	34.29931	34.29931	34.29024	34.29120	34.29311	34.29364	34.29403	34.29791	34.29962	34.30003	34.29932	34.30158
Longitude (°E)	76.82191	76.82191	76.79662	76.79766	76.79871	76.80012	76.80124	76.81893	76.81945	76.82111	76.82550	76.83422
Majors (%)												
SiO_2	55.66	55.69	47.95	50.10	52.65	42.23	59.90	57.70	57.06	57.42	57.10	53.59
TiO_2	0.70	0.63	0.89	0.64	0.54	0.52	0.55	0.60	0.66	0.62	0.72	0.75
Al_2O_3	13.54	14.56	12.23	12.17	12.72	10.84	12.97	16.13	13.65	15.62	16.45	15.12
Fe_2O_3	7.15	5.77	9.85	6.30	4.88	5.85	5.77	6.41	7.03	6.42	7.31	8.42
MnO	0.10	0.10	0.14	0.11	0.15	0.26	0.08	0.11	0.10	0.08	0.09	0.08
MgO	3.49	2.35	2.90	2.49	1.95	2.04	2.57	3.21	3.71	2.71	4.47	4.19
CaO	8.51	8.47	12.70	13.27	12.02	20.73	7.92	8.47	7.35	5.76	5.76	6.54
Na_2O	3.03	4.09	2.48	2.21	2.41	1.73	2.51	3.22	2.75	3.49	3.37	4.01
K_2O	1.09	1.35	0.48	1.16	1.61	0.80	1.06	0.17	1.19	2.43	0.73	0.41
SO_3	0.04	0.01	0.02	0.32	0.01	0.01	0.03	0.01	0.01	0.01	0.22	0.63
P_2O_5	0.33	0.13	0.13	0.11	0.12	0.16	0.12	0.12	0.10	0.15	0.13	0.08
LOI	6.66	6.65	10.09	10.90	11.13	15.61	6.33	4.49	5.99	4.51	4.28	6.34
Total	100.31	99.80	99.85	99.77	100.20	100.78	99.81	100.63	99.59	99.21	100.63	100.17
MFW indices (Ohata & Arai, 2007)												
M	75.72	66.22	88.24	76.93	65.52	83.06	69.08	87.31	72.96	55.54	76.28	83.88
F	15.49	25.69	6.12	15.89	26.59	12.18	20.75	6.77	16.59	31.60	12.94	8.65
W	8.80	8.10	5.64	7.19	7.89	4.76	10.17	5.92	10.45	12.86	10.78	7.47
Total	100	100	100	100	100	100	100	100	100	100	100	100

Trace elements (ppm)												
Ag	0.07	0.09	0.08	0.08	0.08	0.04	0.07	0.05	0.08	0.09	0.09	0.09
Al (%)	7.09	7.44	6.40	6.34	6.84	5.68	6.68	9.28	7.39	8.35	8.50	7.72
As	3.6	3.1	1.8	5.2	6.4	4.7	4.2	3.1	4.4	2.9	6.7	9.2
Ba	160	190	110	160	260	100	120	70	150	380	120	100
Bi	0.08	0.18	0.12	0.12	0.16	0.22	0.17	0.07	0.13	0.15	0.2	0.11
Br	<1	<1	<1	<1	<1	<1	<1	<1	<1	<1	<1	<1
Cd	0.07	0.07	0.11	0.16	0.07	0.13	0.14	0.08	0.06	0.06	0.10	0.11
Ce	17.10	16.90	22.00	20.20	21.10	31.70	28.90	15.75	21.90	18.20	16.25	12.55
Cl	32	34	33	35	28	22	26	69	26	64	67	54
Co	19.4	14.2	19.0	15.1	12.5	14.6	14.5	20.2	20.3	14.4	22.4	30.6
Cr	62	35	26	26	16	19	18	39	61	40	68	93
Cs	2.00	2.01	1.20	2.93	3.96	2.26	1.79	0.50	1.85	3.38	1.60	1.35
Cu	32.7	35.3	24.4	31.9	31.9	19.2	31.8	23.6	32.6	38.0	46.7	28.7
Dy	2.49	2.58	2.76	2.71	2.97	3.06	3.42	2.03	2.32	2.27	2.07	1.62
Er	1.42	1.46	1.60	1.64	1.78	1.76	1.96	1.16	1.43	1.36	1.22	0.95
Eu	0.79	0.75	0.85	0.85	0.88	1.02	0.85	0.84	0.79	0.81	0.77	0.69
Fe (%)	5.01	3.96	6.33	4.17	3.38	3.92	3.85	4.70	4.88	4.52	5.05	5.69
Ga	15.45	13.90	13.80	12.70	12.15	11.95	13.90	20.90	15.75	17.30	18.25	16.00
Gd	2.28	2.37	2.55	2.43	2.71	3.14	3.02	2.18	2.35	2.39	2.08	1.60
Ge	0.24	0.14	0.15	0.13	0.13	0.13	0.14	0.14	0.13	0.13	0.15	0.15
Hf	1.4	1.5	1.3	1.5	1.5	1.4	1.6	1.1	1.4	1.3	1.6	1.1
Hg	3	2	3	1	3	1	3	2	3	2	3	2
Ho	0.48	0.52	0.55	0.55	0.62	0.61	0.69	0.42	0.48	0.47	0.42	0.33
Ir	0	0	0	0	0	0	0	0	0	0	0	0
K (%)	0.85	1.02	0.36	0.89	1.30	0.61	0.81	0.14	0.94	1.98	0.55	0.31
La	9.0	8.2	11.6	10.1	11.5	17.3	14.6	7.2	10.0	8.2	7.2	6.0
Lu	0.21	0.21	0.24	0.24	0.27	0.26	0.29	0.18	0.22	0.20	0.18	0.13
Mg (%)	2.05	1.35	1.64	1.42	1.16	1.18	1.49	2.06	2.27	1.65	2.67	2.43
Mn (%)	811	737	1050	797	1140	1980	615	953	768	648	723	630
Mo	0.39	0.26	0.14	0.26	0.18	0.49	0.24	0.19	0.28	0.19	0.43	0.36

Na (%)	2.21	2.94	1.66	1.50	1.74	1.14	1.84	2.65	2.17	2.67	2.53	2.91
Nb	2.5	2.8	2.8	2.6	2.2	2.4	3.3	2	2.2	2.7	2.4	2.2
Nd	10.0	10.5	10.9	10.7	11.2	15.0	14.2	9.7	10.8	10.3	9.5	7.0
Ni	27.4	19.7	14.3	14.0	10.3	15.4	10.7	26.9	30.0	21.3	32.9	49.7
Os	0	0	0	0	0	0	0	0	0	0	0	0
P (%)	460	560	500	460	530	580	540	500	450	700	530	370
Pb	8.0	7.9	5.7	9.0	7.6	11.9	12.1	8.0	7.6	4.5	15.2	9.2
Pd	0	0	0	0	0	0	0	0	0	0	0	0
Pr	2.25	2.28	2.46	2.42	2.53	3.54	3.37	2.12	2.51	2.30	2.11	1.56
Rb	23.7	26.4	16.6	30.7	51.2	28.3	24.6	2.4	32.2	65.8	12.3	5.7
Re	<0.002	<0.002	<0.002	<0.002	<0.002	<0.002	<0.002	<0.002	<0.002	<0.002	<0.002	0.002
S (%)	<0.01	<0.01	<0.01	0.12	<0.01	<0.01	0.01	<0.01	<0.01	<0.01	0.09	0.24
Sb	0.55	0.44	1.08	0.56	0.57	0.70	0.58	0.48	0.56	0.45	0.72	0.48
Sc	17.6	17.3	18.6	16.4	15.8	13.9	15.1	18.8	19.9	18.8	19.8	18.8
Se	<1	<1	1	1	<1	<1	<1	<1	<1	<1	1	1
Sm	2.32	2.47	2.38	2.48	2.56	3.12	3.04	2.24	2.38	2.29	2.17	1.61
Sn	0.9	0.9	0.9	0.9	0.8	0.9	1.1	0.7	0.8	0.8	0.9	0.8
Sr	401	398	237	285	278	273	219	655	392	374	257	402
Ta	0.16	0.18	0.17	0.17	0.14	0.16	0.24	0.14	0.15	0.18	0.15	0.14
Tb	0.35	0.38	0.40	0.40	0.42	0.46	0.48	0.32	0.37	0.37	0.33	0.25
Th	2.33	2.80	2.78	3.34	2.66	2.70	4.76	1.75	2.48	2.39	2.01	1.40
Ti (%)	0.408	0.353	0.502	0.360	0.316	0.300	0.313	0.356	0.376	0.370	0.412	0.430
Tm	0.22	0.21	0.25	0.25	0.27	0.27	0.30	0.18	0.20	0.20	0.18	0.14
U	0.6	0.7	0.7	0.8	0.6	0.6	1.0	0.4	0.6	0.6	0.5	0.4
V	192	147	231	159	128	105	128	167	178	159	190	203
W	7.1	4.2	3.0	3.3	0.8	3.4	4.1	8.0	4.7	2.9	4.7	3.5
Y	15.6	15.1	17.9	17.3	19.1	20.6	20.5	12.4	15.0	14.1	12.8	9.8
Yb	1.38	1.38	1.61	1.68	1.84	1.79	1.98	1.20	1.46	1.36	1.24	0.94
Zn	85	72	95	77	73	89	75	87	87	77	90	81
Zr	45.8	48.5	49.3	54.1	50.5	48.5	53.4	27.6	43.4	37.6	48.1	36.5

Sample	17NI01	17NI04	17NI02	17NI03	17NI06	17NI09	17NI10	17NI11
Affinity	Dras Vol.	Dras Vol.	Dras Vol.	Dras Vol.	Dras Vol.	Dras Vol.	Dras Vol.	Dras Vol.
Rock type	Volcaniclastic	Volcaniclastic	Basalt	Basalt	Basalt	Basalt	Basalt	Basalt
Latitude (°N)	34.47681	34.46853	34.47702	34.47422	34.45041	34.43617	34.43555	34.42557
Longitude (°E)	76.22946	76.24253	76.23000	76.23248	76.27294	76.28426	76.28404	76.28359
Majors (%)								
SiO_2	53.49	50.87	49.99	48.83	43.99	44.77	47.38	48.89
TiO_2	0.76	0.74	0.92	0.93	0.59	0.78	0.74	0.74
Al_2O_3	16.49	18.90	15.98	17.66	15.47	16.37	18.79	16.51
Fe_2O_3	8.64	8.63	12.56	11.66	7.75	7.92	7.80	9.96
MnO	0.17	0.21	0.21	0.15	0.16	0.13	0.14	0.18
MgO	4.23	4.86	4.89	3.69	6.75	8.41	6.07	7.78
CaO	9.29	5.60	9.19	9.27	14.76	13.61	10.12	7.38
Na_2O	2.28	4.66	2.35	3.98	2.66	2.23	3.39	3.72
K_2O	0.17	0.78	1.03	0.47	0.24	0.14	0.72	0.52
SO_3	0.02	0.02	0.03	0.03	0.02	0.31	0.05	0.14
P_2O_5	0.24	0.21	0.28	0.31	0.13	0.25	0.31	0.21
LOI	4.12	4.37	2.42	2.87	7.30	4.95	4.34	3.81
Total	99.90	99.84	99.84	99.85	99.83	99.87	99.85	99.84
MFW indices (Ohata & Arai, 2007)								
M	93.17	93.91	93.04	95.47	96.43	95.15	95.22	94.61
F	6.64	5.94	6.73	4.39	3.48	4.72	4.66	5.23
W	0.19	0.16	0.23	0.14	0.09	0.13	0.12	0.15
Total	100	100	100	100	100	100	100	100
Trace elements (ppm)								
Ag	0.04	0.03	0.02	0.07	0.03	0.04	0.05	0.04
Al (%)	8.42	7.39	8.05	6.91	7.99	6.59	7.71	8.11
As	0.9	3.1	1	0.7	0.9	0.7	0.9	0.8
Ba	30	170	150	70	60	50	80	100

Bi	0.02	0.05	0.02	0.03	0.03	0.04	0.05	0.04
Br	0	0	0	0	0	0	0	0
Cd	0.09	0.04	0.06	0.07	0.11	0.12	0.11	0.13
Ce	22.30	17.65	22.20	16.90	16.15	25.80	23.60	16.60
Cl	0	0	0	0	0	0	0	0
Co	29.9	30.2	35.9	35.7	31.1	32	26.7	35.8
Cr	29	51	18	10	267	76	94	153
Cs	0.81	0.78	1.26	1.35	0.42	0.69	1.07	0.65
Cu	34.1	72.5	55.3	187.0	44.1	77.5	75.2	83.1
Dy	3.56	3.27	4.23	3.55	2.53	3.16	2.85	2.95
Er	2.24	2.05	2.58	2.23	1.64	1.82	1.65	1.79
Eu	1.01	0.96	1.24	1.09	0.70	1.11	1.01	0.92
Fe (%)	5.76	5.50	8.21	7.05	5.10	4.95	4.98	6.52
Ga	16.80	16.30	17.35	17.80	14.60	17.05	18.55	14.70
Gd	3.28	3.05	3.96	3.36	2.24	3.29	2.90	2.92
Ge	0.17	0.15	0.12	0.13	0.26	0.21	0.16	0.16
Hf	2.3	2.0	2.2	2.1	1.2	2.0	1.8	1.6
Hg	0	0	0	0	0	0	0	0
Ho	0.73	0.68	0.85	0.72	0.53	0.61	0.56	0.59
Ir	0	0	0	0	0	0	0	0
K (%)	0.18	0.56	0.83	0.34	0.26	0.14	0.48	0.40
La	10.2	7.1	9.3	6.6	7.2	10.8	10.4	7.1
Lu	0.36	0.31	0.42	0.35	0.26	0.27	0.26	0.28
Mg (%)	2.39	2.38	2.7	1.85	3.54	4.22	3.1	4.62
Mn (%)	1300	1500	1570	1150	1230	935	1070	1340
Mo	0.68	0.5	0.44	0.3	0.08	0.23	0.23	0.1
Na (%)	1.73	3.38	1.94	2.80	2.00	1.65	2.38	2.74
Nb	1.6	1.5	2.1	1.5	1.0	1.8	2.0	1.1
Nd	13.9	11.5	15.4	12.5	9.2	15.4	14.3	11.5
Ni	22.7	36.8	19.6	13.8	106.0	70.0	92.7	85.9
Os	0	0	0	0	0	0	0	0
P (%)	1000	890	1250	1320	470	1030	1210	920

Pb	3.1	3.7	2.0	3.1	3.8	2.3	2.9	2.2
Pd	0	0	0	0	0	0	0	0
Pr	2.99	2.46	3.14	2.49	2.04	3.36	3.12	2.36
Rb	6.9	7.0	22.1	4.5	6.6	1.8	7.1	4.7
Re	<0.002	<0.002	<0.002	<0.002	0.002	<0.002	<0.002	<0.002
S (%)	<0.01	0.01	<0.01	0.01	<0.01	0.01	0.01	0.07
Sb	9.67	2.51	2.30	7.52	2.10	2.91	0.53	2.31
Sc	29.3	23.4	36.9	24.8	32.7	23.3	23.1	36.9
Se	<1	<1	<1	1	<1	<1	<1	<1
Sm	3.25	2.91	3.80	3.10	2.10	3.48	3.06	2.81
Sn	0.9	0.9	1.3	1.1	0.7	0.9	1.0	0.7
Sr	130	383	362	344	183.5	177	301	220
Ta	0.18	0.14	0.17	0.15	0.10	0.13	0.14	0.09
Tb	0.57	0.54	0.68	0.59	0.41	0.54	0.48	0.50
Th	2.68	2.10	2.52	1.39	2.22	2.61	2.59	1.24
Ti (%)	0.434	0.408	0.546	0.502	0.335	0.407	0.403	0.420
Tm	0.32	0.29	0.37	0.32	0.24	0.26	0.24	0.24
U	0.6	0.5	0.4	0.4	0.9	0.6	0.6	0.3
V	241	228	305	335	223	223	244	279
W	57.2	35.4	17.6	37.3	27.3	15.0	22.6	13.2
Y	22.0	19.2	25.1	20.8	16.0	18.0	16.4	17.7
Yb	2.16	1.98	2.47	2.14	1.62	1.69	1.60	1.72
Zn	74	82	84	84	62	52	59	79
Zr	78.7	52.4	67.6	68.0	35.7	61.4	55.5	47.0

Sample	16NI04a	16NI04b	16NI07a	16NI07b	16NI11	16NI15a	16NI15b
Affinity	Nindam Fm.	Nindam Fm.	Nindam Fm.	Nindam Fm.	Nindam Fm.	Nindam Fm.	Nindam Fm.
Rock type	Shale	Shale	Shale	Shale	Shale	Shale	Shale
Latitude (°N)	34.29344	34.29344	34.29751	34.29751	34.29948	34.29968	34.29968
Longitude (°E)	76.79955	76.79955	76.81838	76.81838	76.82370	76.83274	76.83274
Majors (%)							
SiO_2	59.62	60.74	50.84	55.72	61.81	60.40	58.35
TiO_2	0.62	0.62	0.55	0.56	0.67	0.50	0.38
Al_2O_3	15.80	14.94	12.82	13.59	15.58	14.05	11.30
Fe_2O_3	7.41	5.20	5.67	5.56	5.74	5.23	4.46
MnO	0.14	0.11	0.16	0.11	0.06	0.09	0.09
MgO	2.89	2.10	2.26	2.69	2.94	2.44	3.25
CaO	3.30	4.96	12.91	8.87	2.93	6.95	9.83
Na_2O	1.15	2.45	1.32	1.61	2.19	1.61	1.99
K_2O	2.99	2.10	1.91	1.95	2.85	1.98	0.87
SO_3	< 0.01	< 0.01	0.01	0.00	0.73	0.01	0.00
P_2O_5	0.14	0.11	0.15	0.12	0.12	0.13	0.09
LOI	5.41	5.75	10.95	9.01	4.52	6.69	9.70
Total	99.47	99.07	99.53	99.80	100.14	100.06	100.31
MFW indices (Ohata & Arai, 2007)							
M	44.90	51.51	68.23	63.65	44.90	56.71	72.10
F	22.39	32.06	20.92	23.29	30.21	27.65	19.92
W	32.71	16.43	10.85	13.06	24.90	15.64	7.99
Total	100	100	100	100	100	100	100
Trace elements (ppm)							
Ag	0.07	0.09	0.06	0.07	0.18	0.05	0.11
Al (%)	8.15	7.67	6.82	7.26	8.1	7.56	6.10
As	3.7	2.5	4.7	2.6	7.6	3.7	0.6
Ba	370	240	210	230	460	390	180
Bi	0.20	0.22	0.25	0.24	0.56	0.37	0.13
Br	<1	<1	<1	<1	<1	<1	<1
Cd	0.03	0.05	0.08	0.08	0.10	0.04	0.02

Ce	30.4	27.0	33.7	37.5	31.4	36.8	11.5
Cl	24	33	43	22	12	39	17
Co	16.3	11.0	14.6	14.0	19.4	14.8	15.7
Cr	39	27	28	35	46	33	25
Cs	8.07	5.38	5.19	5.83	6.91	5.08	2.38
Cu	52.3	56.0	46.4	71.2	81.4	35.4	66.9
Dy	3.19	3.14	3.03	3.35	3.20	2.86	1.54
Er	1.80	1.75	1.77	2.00	1.8	1.61	0.81
Eu	0.90	0.90	0.92	0.97	0.94	0.93	0.51
Fe (%)	5.03	3.61	3.91	3.94	4.02	3.76	3.14
Ga	19.85	16.40	15.25	16.55	19.35	17.65	12.45
Gd	3.10	3.00	3.15	3.43	3.25	3.04	1.62
Ge	0.17	0.15	0.13	0.15	0.14	0.15	0.10
Hf	1.7	2.1	2.2	2.3	2.1	1.6	1.4
Hg	3	3	1	2	1	3	2
Ho	0.63	0.62	0.64	0.69	0.64	0.57	0.30
Ir	0	0	0	0	0	0	0
K (%)	2.37	1.66	1.49	1.55	2.33	1.61	0.70
La	14.7	11.8	15.2	16.5	13.0	16.9	5.0
Lu	0.27	0.24	0.27	0.31	0.27	0.23	0.12
Mg (%)	1.69	1.25	1.36	1.64	1.76	1.49	1.98
Mn (%)	1120	849	1260	929	478	734	729
Mo	0.31	0.18	0.40	0.23	0.51	0.30	0.14
Na (%)	0.82	1.86	0.97	1.16	1.44	1.28	1.48
Nb	6.6	6.1	5.5	6.2	6.4	6.2	2.9
Nd	15.5	14.7	15.5	17.0	16.0	16.8	6.6
Ni	25.8	19.7	27.3	26.4	27.8	28.9	23.8
Os	0	0	0	0	0	0	0
P (%)	640	480	570	530	640	580	390
Pb	4.7	5.2	14.1	10.1	19.6	14.8	7.0
Pd	0	0	0	0	0	0	0
Pr	3.74	3.34	3.73	4.13	3.75	4.20	1.47
Rb	100.5	60.9	75.7	74.4	82.3	71.1	34.6
Re	<0.002	<0.002	<0.002	<0.002	0.002	<0.002	<0.002

S (%)	<0.01	<0.01	<0.01	<0.01	0.3	<0.01	<0.01
Sb	0.79	0.57	0.64	0.50	0.81	0.76	0.39
Sc	18.8	15.9	14.6	15.8	17.8	13.8	9.6
Se	<1	<1	<1	<1	1	<1	<1
Sm	3.32	3.27	3.28	3.57	3.54	3.38	1.60
Sn	1.9	2.0	1.5	1.6	1.7	1.5	0.7
Sr	144.0	180.0	216.0	194.5	139.5	194.0	301.0
Ta	0.44	0.44	0.40	0.47	0.46	0.43	0.19
Tb	0.48	0.46	0.48	0.54	0.50	0.46	0.25
Th	6.64	5.97	6.45	7.13	5.85	5.76	2.94
Ti (%)	0.355	0.361	0.318	0.331	0.404	0.303	0.229
Tm	0.28	0.27	0.27	0.30	0.27	0.23	0.12
U	1.2	0.9	1.1	1.3	1.2	0.8	0.7
V	123	110	97	110	146	93	56
W	1.4	1.1	1.0	1.2	2.3	2.6	2.3
Y	18.1	18.6	20.0	22.4	17.8	18.1	8.7
Yb	1.82	1.68	1.81	2.12	1.86	1.60	0.84
Zn	114	86	92	96	115	82	85
Zr	59.5	70.5	77.1	78.0	68.7	55.8	45.6

Sample	16HN01a	16HN02	16NM01	16BT01	16KH01	16KH02
Affinity	Indus Group	Indus Group	Indus Group	Indus Group	Khalsi Limestone	Khalsi Limestone
Rock type	Conglomerate	Conglomerate	Sandstone	Conglomerate	Limestone/Marl	Limestone/Marl
Latitude (°N)	34.32951	34.33007	34.24696	34.18061	34.31536	34.23424
Longitude (°E)	76.83669	76.83628	77.19930	77.33890	76.87456	77.06050
Majors (%)						
SiO_2	54.68	58.05	45.76	75.04	35.80	47.44
TiO_2	0.61	0.73	0.49	0.32	0.34	0.42
Al_2O_3	16.16	16.41	7.27	13.10	8.40	10.26
Fe_2O_3	9.08	7.58	4.06	2.73	3.59	3.38
MnO	0.18	0.10	0.05	0.06	0.26	0.05
MgO	6.12	4.14	2.21	0.46	1.42	1.66
CaO	7.00	4.22	20.11	1.30	27.64	17.75
Na_2O	1.82	2.06	1.11	3.82	1.36	1.92
K_2O	0.40	2.57	0.77	2.82	0.65	1.12
SO_3	0.00	< 0.01	0.02	< 0.01	0.02	0.67
P_2O_5	0.12	0.05	0.13	0.04	0.16	0.09
LOI	3.46	3.73	18.23	1.16	21.12	15.32
Total	99.62	99.62	100.22	100.84	100.76	100.07
MFW indices (Ohata & Arai, 2007)						
M	83.79	56.93	83.51	11.87	81.83	69.91
F	5.93	21.42	11.64	73.45	14.91	24.95
W	10.28	21.65	4.85	14.68	3.26	5.15
Total	100	100	100	100	100	100
Trace elements (ppm)						
Ag	0.04	0.04	0.07	0.05	0.05	0.09
Al (%)	8.83	9.06	4.05	7.04	4.70	6.96
As	5.2	16.3	19.2	12.5	4.4	2.4
Ba	80	400	140	510	170	430
Bi	0.08	0.35	0.12	0.28	0.25	0.21
Br	<1	<1	<1	<1	<1	<1
Cd	0.07	0.09	0.09	0.10	0.08	0.08

Ce	12.05	34.4	43.6	41.0	38.2	38.0
Cl	43	69	39	17	26	64
Co	31.1	28.3	7.6	4.3	8.2	6.4
Cr	67	128	102	3	17	22
Cs	0.59	8.71	2.15	1.36	2.26	3.10
Cu	15.2	19.7	14.6	8.5	30.5	21.9
Dy	2.57	3.51	2.41	2.34	3.44	3.33
Er	1.71	2.15	1.24	1.44	2.17	1.78
Eu	0.75	1.08	0.96	0.74	0.98	1.00
Fe (%)	6.46	5.49	2.91	1.89	2.57	3.00
Ga	16.85	18.85	9.75	14.15	10.40	13.25
Gd	2.36	3.34	2.97	2.42	3.59	3.46
Ge	0.44	0.41	0.10	0.12	0.10	0.08
Hf	0.5	0.8	0.9	0.3	1.7	1.1
Hg	1	2	3	2	3	2
Ho	0.57	0.74	0.44	0.49	0.73	0.65
Ir	0	0	0	0	0	0
K (%)	0.31	2.15	0.65	2.28	0.55	1.17
La	4.9	15.6	20.4	20.6	19.0	18.6
Lu	0.26	0.29	0.16	0.23	0.32	0.23
Mg (%)	3.82	2.56	1.35	0.32	0.86	1.26
Mn (%)	0	0	0	0	0	0
Mo	0.09	0.26	0.20	0.58	0.26	0.17
Na (%)	1.44	1.58	0.75	3.02	0.82	1.64
Nb	1.3	5.1	7.3	6.2	3.5	3.4
Nd	8.1	16.2	19.1	15.9	18.0	16.6
Ni	62.5	90.1	59.0	2.1	15.3	13.1
Os	0	0	0	0	0	0
P (%)	0	0	0	0	0	0
Pb	6.2	19.6	7.9	17.9	5.3	5.6
Pd	0	0	0	0	0	0
Pr	1.68	3.93	4.76	4.34	4.27	4.02
Rb	4.4	95.6	35.6	85.9	27.6	34
Re	<0.002	<0.002	<0.002	<0.002	<0.002	0.005

S (%)	<0.01	<0.01	<0.01	<0.01	<0.01	0.32
Sb	0.37	1.08	0.44	0.45	0.36	0.37
Sc	23.4	26.8	8.7	5.5	8.7	11.8
Se	<1	<1	<1	<1	<1	1
Sm	2.11	3.53	3.65	2.88	3.74	3.61
Sn	0.6	1.4	1.1	1.4	1.0	1.1
Sr	449	211	581	209	406	799
Ta	0.08	0.34	0.48	0.53	0.23	0.22
Tb	0.38	0.54	0.43	0.37	0.54	0.53
Th	1.11	7.94	6.71	9.30	4.13	2.67
Ti (%)	0.313	0.42	0.280	0.184	0.212	0.301
Tm	0.25	0.31	0.17	0.22	0.32	0.25
U	0.2	1.3	1.4	2.5	0.8	0.7
V	228	170	71	41	68	81
W	6.5	7.9	4.6	8.2	1.9	3.7
Y	16.5	22.2	14.2	15.5	26.5	19.4
Yb	1.78	2.08	1.18	1.61	2.28	1.69
Zn	88	86	48	36	55	74
Zr	10.1	20.4	30.8	5.0	61.2	33.4

Notes:

Major and trace element analysis was conducted at the University of Wollongong (UOW). Additional trace and rare-earth element (REE) analyses were undertaken at Australian Laboratory Services (ALS) Minerals Division, Brisbane, Australia using the geochemical procedure code: ME-MS81.

The above listed geochemical data has been combined in text (including figures) with other data available in the below listed literature. This data is compiled online and is available through the relevant paper corresponding to this chapter (Walsh et al., 2019). It is also available from the original papers; these are as follows:

- Bhat, I. M., Ahmad, T., & Rao, D. S. (2019). The tectonic evolution of the Dras arc complex along the Indus Suture Zone, western Himalaya: Implications for the Neo-Tethys Ocean geodynamics. Journal of Geodynamics, 124, 52-66.
- Clift, P. D., Degnan, P. J., Hannigan, R., & Blusztajn, J. (2000). Sedimentary and geochemical evolution of the Dras forearc basin, Indus suture, Ladakh Himalaya, India. Geological Society of America Bulletin, 112(3), 450-466.
- Corfield, R. I., Searle, M. P., & Pedersen, R. B. (2001). Tectonic setting, origin, and obduction history of the Spontang Ophiolite, Ladakh Himalaya, NW India. The Journal of Geology, 109(6), 715-736.

Table S4.4 Detrital zircon U-Pb results using LA-ICP-MS (Chapter 4)

Labels	U (ppm)	Th (ppm	Th/U	$^{238}U/^{206}Pb^*$	$^{207}Pb/^{206}Pb^*$	age $^{206}Pb/^{238}U^*$	age $^{207}Pb/^{206}Pb^*$	% conc	Rejected
16NI02 (W67) - volcaniclastic									
1.1	151	92	0.63	54.11 ± 0.94	0.0489 ± 0.0032	118 ± 1			
~~2.1~~	~~549~~	~~487~~	~~0.89~~	~~4.71 ± 0.03~~	~~0.0791 ± 0.0005~~	~~1174 ± 6~~	~~1174 ± 12~~	~~-5.8%~~	Yes
3.1	931	402	0.45	2.19 ± 0.01	0.1590 ± 0.0006	2444 ± 3	2444 ± 6	0.8%	
~~4.1~~	~~73~~	~~65~~	~~0.88~~	~~48.10 ± 1.10~~	~~0.0702 ± 0.0060~~	~~133 ± 2~~			Yes
5.1	335	389	1.18	43.96 ± 0.47	0.0507 ± 0.0016	145 ± 1			
6.1	178	249	1.35	56.24 ± 0.79	0.0493 ± 0.0020	114 ± 1			
7.1	85	64	0.77	51.15 ± 1.00	0.0504 ± 0.0026	125 ± 1			
8.1	411	49	0.12	9.63 ± 0.11	0.0598 ± 0.0010	638 ± 3			
~~9.1~~	~~203~~	~~118~~	~~0.59~~	~~5.77 ± 0.08~~	~~0.0712 ± 0.0011~~	~~963 ± 16~~			Yes
10.1	241	285	1.18	11.65 ± 0.10	0.0575 ± 0.0010	531 ± 2			
11.1	52	36	0.69	59.10 ± 1.70	0.0507 ± 0.0053	108 ± 2			
12.1	84	162	1.92	10.59 ± 0.39	0.0610 ± 0.0045	581 ± 11			
~~13.1~~	~~1682~~	~~539~~	~~0.33~~	~~27.22 ± 0.25~~	~~0.0525 ± 0.0007~~	~~233 ± 1~~			Yes
14.1	126	110	0.85	58.62 ± 0.91	0.0500 ± 0.0024	109 ± 1			
15.1	169	255	1.52	5.02 ± 0.06	0.0794 ± 0.0010	1186 ± 12	1186 ± 24	1.2%	
16.1	186	122	0.67	53.73 ± 1.40	0.0531 ± 0.0030	119 ± 2			
17.1	138	78	0.58	39.49 ± 0.51	0.0513 ± 0.0016	161 ± 1			
18.1	110	96	0.86	60.86 ± 0.92	0.0512 ± 0.0030	105 ± 1			
19.1	29	14	0.48	60.64 ± 1.40	0.0506 ± 0.0049	105 ± 1			
20.1	112	76	0.70	51.71 ± 0.98	0.0521 ± 0.0035	123 ± 1			
21.1	185	155	0.87	39.75 ± 0.41	0.0509 ± 0.0020	160 ± 1			
22.1	127	78	0.63	59.42 ± 1.30	0.0507 ± 0.0036	108 ± 1			
~~23.1~~	~~162~~	~~108~~	~~0.69~~	~~4.99 ± 0.06~~	~~0.0775 ± 0.0009~~	~~1129 ± 12~~	~~1129 ± 23~~	~~-4.4%~~	Yes
24.1	148	88	0.61	4.61 ± 0.03	0.0821 ± 0.0009	1242 ± 11	1242 ± 22	-2.1%	
25.1	153	132	0.88	4.87 ± 0.04	0.0795 ± 0.0008	1183 ± 11	1183 ± 21	-1.8%	
26.1	253	324	1.32	3.40 ± 0.03	0.1013 ± 0.0008	1649 ± 7	1649 ± 14	-0.7%	
27.1	81	124	1.56	4.94 ± 0.07	0.0825 ± 0.0027	1221 ± 23	1221 ± 45	2.8%	
~~28.1~~	~~71~~	~~24~~	~~0.35~~	~~9.78 ± 0.29~~	~~0.0663 ± 0.0034~~	~~627 ± 9~~			Yes
29.1	283	110	0.39	4.36 ± 0.04	0.0855 ± 0.0007	1324 ± 9	1324 ± 17	-0.5%	
30.1	110	147	1.36	10.18 ± 0.10	0.0608 ± 0.0012	604 ± 3			
31.1	136	126	0.91	59.45 ± 0.99	0.0507 ± 0.0032	108 ± 1			
32.1	161	193	1.08	64.27 ± 1.10	0.0475 ± 0.0026	100 ± 1			
33.1	185	107	0.58	53.79 ± 0.64	0.0500 ± 0.0021	119 ± 1			
34.1	187	126	0.68	58.96 ± 0.61	0.0497 ± 0.0018	108 ± 1			
35.1	252	272	1.07	14.34 ± 0.12	0.0566 ± 0.0009	435 ± 2			

| | | |

71.1	119	124	1.08	5.08	±	0.05	0.0804	±	0.0010	1201	±	12	1201	±	24	3.6%					
~~72.1~~	~~863~~	~~1070~~	~~1.28~~	~~6.01~~	~~±~~	~~0.18~~	~~0.0813~~	~~±~~	~~0.0006~~	~~990~~	~~±~~	~~16~~	~~1227~~	~~±~~	~~15~~	~~19.3%~~					Yes
73.1	65	39	0.61	50.84	±	1.90	0.0540	±	0.0064	126	±	2									
74.1	279	276	1.01	51.52	±	1.20	0.0512	±	0.0028	124	±	2									
~~75.1~~	~~455~~	~~792~~	~~1.76~~	~~45.19~~	~~±~~	~~1.70~~	~~0.0560~~	~~±~~	~~0.0034~~	~~141~~	~~±~~	~~3~~									Yes
76.1	716	769	1.05	30.34	±	0.26	0.0514	±	0.0010	209	±	1									
77.1	614	243	0.41	24.63	±	0.67	0.0530	±	0.0021	257	±	4									
78.1	369	261	0.71	38.70	±	1.10	0.0492	±	0.0019	164	±	2									
79.1	83	52	0.65	53.11	±	1.90	0.0560	±	0.0075	120	±	2									
80.1	66	41	0.62	40.34	±	0.60	0.0500	±	0.0028	158	±	1									
~~81.1~~	~~43~~	~~92~~	~~2.21~~	~~4.99~~	~~±~~	~~0.08~~	~~0.1044~~	~~±~~	~~0.0041~~	~~1696~~	~~±~~	~~37~~	~~1696~~	~~±~~	~~74~~	~~30.6%~~					Yes
82.1	317	186	0.60	6.37	±	0.04	0.0703	±	0.0006	940	±	3									
83.1	132	76	0.60	50.25	±	0.75	0.0510	±	0.0024	127	±	1									
~~84.1~~	~~1881~~	~~165~~	~~0.09~~	~~19.17~~	~~±~~	~~0.21~~	~~0.0514~~	~~±~~	~~0.0004~~	~~328~~	~~±~~	~~1~~									Yes
85.1	97	80	0.83	5.06	±	0.07	0.0791	±	0.0012	1176	±	15	1176	±	30	1.3%					
~~86.1~~	~~143~~	~~69~~	~~0.48~~	~~38.46~~	~~±~~	~~2.80~~	~~0.0589~~	~~±~~	~~0.0056~~	~~165~~	~~±~~	~~7~~									Yes
~~87.1~~	~~113~~	~~68~~	~~0.57~~	~~1.90~~	~~±~~	~~0.09~~	~~0.2108~~	~~±~~	~~0.0025~~	~~2911~~	~~±~~	~~10~~	~~2911~~	~~±~~	~~19~~	~~6.6%~~					Yes
88.1	116	120	1.07	5.01	±	0.16	0.0799	±	0.0017	1193	±	22	1193	±	44	1.8%					
89.1	141	107	0.76	60.31	±	0.86	0.0466	±	0.0026	106	±	1									
90.1	232	466	2.00	11.57	±	0.09	0.0579	±	0.0008	534	±	2									
91.1	88	90	1.02	60.57	±	1.20	0.0504	±	0.0029	106	±	1									
92.1	166	278	1.72	5.14	±	0.05	0.0793	±	0.0010	1181	±	13	1181	±	26	2.9%					
93.1	409	350	0.88	2.08	±	0.02	0.1674	±	0.0010	2531	±	6	2531	±	11	0.1%					
94.1	56	113	2.08	5.07	±	0.04	0.0791	±	0.0013	1175	±	17	1175	±	33	1.2%					
95.1	120	80	0.69	40.83	±	0.86	0.0509	±	0.0040	156	±	2									
96.1	100	102	1.04	62.62	±	1.10	0.0497	±	0.0039	102	±	1									
97.1	129	110	0.89	47.96	±	2.00	0.0545	±	0.0047	133	±	3									
98.1	25	23	0.94	5.19	±	0.06	0.0778	±	0.0024	1114	±	30	1114	±	59	-2.0%					
99.1	107	89	0.86	61.96	±	1.00	0.0513	±	0.0037	103	±	1									
100.1	314	108	0.36	5.83	±	0.07	0.0752	±	0.0011	1070	±	15	1070	±	30	4.7%					
~~101.1~~	~~305~~	~~141~~	~~0.45~~	~~6.75~~	~~±~~	~~0.07~~	~~0.0711~~	~~±~~	~~0.0006~~	~~890~~	~~±~~	~~4~~									Yes
102.1	112	69	0.64	60.28	±	1.90	0.0517	±	0.0063	106	±	2									
103.1	312	204	0.68	40.93	±	0.63	0.0489	±	0.0016	156	±	1									
~~104.1~~	~~178~~	~~156~~	~~0.88~~	~~54.11~~	~~±~~	~~0.86~~	~~0.0803~~	~~±~~	~~0.0042~~	~~118~~	~~±~~	~~1~~	~~1149~~	~~±~~	~~96~~	~~89.7%~~					Yes
105.1	66	47	0.74	62.50	±	1.20	0.0477	±	0.0032	102	±	1									

~~106.1~~	~~196~~	~~184~~	~~0.97~~	~~2.10~~	~~±~~	~~0.02~~	~~0.1718~~	~~±~~	~~0.0010~~	~~2575~~	~~±~~	~~5~~	~~2575~~	~~±~~	~~10~~	~~2.5%~~	Yes
107.1	102	104	1.04	53.91	±	0.77	0.0511	±	0.0031	119	±	1					
~~108.1~~	~~440~~	~~1133~~	~~2.63~~	~~42.63~~	~~±~~	~~0.71~~	~~0.0541~~	~~±~~	~~0.0024~~	~~150~~	~~±~~	~~1~~					Yes
109.1	203	284	1.42	56.95	±	1.20	0.0506	±	0.0029	112	±	1					
110.1	94	251	2.76	5.13	±	0.10	0.0777	±	0.0017	1128	±	22	1128	±	44	-1.8%	
111.1	81	89	1.14	12.08	±	0.18	0.0586	±	0.0016	513	±	3					
112.1	129	74	0.58	37.74	±	2.00	0.0510	±	0.0031	169	±	4					
~~113.1~~	~~251~~	~~225~~	~~0.91~~	~~45.89~~	~~±~~	~~1.50~~	~~0.0755~~	~~±~~	~~0.0039~~	~~139~~	~~±~~	~~3~~	~~1100~~	~~±~~	~~100~~	~~87.4%~~	Yes

Labels	U (ppm)	Th (ppm	Th/U	$^{238}U/^{206}Pb*$	$^{207}Pb/^{206}Pb*$	age $^{206}Pb/^{238}U*$	age $^{207}Pb/^{206}Pb*$	% conc	Rejected
16NI06 (W67) - volcaniclastic									
1.1	43	25	0.56	67.66 ± 1.40	0.0494 ± 0.0037	95 ± 1			
2.1	365	433	1.16	62.42 ± 0.61	0.0476 ± 0.0013	102 ± 0			
~~3.1~~	~~452~~	~~664~~	~~1.38~~	~~62.19 ± 0.59~~	~~0.0616 ± 0.0017~~	~~103 ± 0~~			Yes
4.1	146	119	0.79	39.62 ± 0.39	0.0491 ± 0.0016	161 ± 1			
5.1	266	214	0.77	6.96 ± 0.08	0.0686 ± 0.0006	865 ± 5			
6.1	89	54	0.59	61.77 ± 1.20	0.0491 ± 0.0033	104 ± 1			
~~7.1~~	~~196~~	~~421~~	~~2.05~~	~~62.70 ± 0.88~~	~~0.0578 ± 0.0022~~	~~102 ± 1~~			Yes
8.1	87	52	0.57	52.36 ± 4.10	0.0499 ± 0.0071	122 ± 5			
9.1	234	248	0.96	63.17 ± 0.64	0.0498 ± 0.0018	101 ± 1			
10.1	1705	3510	1.98	42.61 ± 0.39	0.0493 ± 0.0011	150 ± 1			
11.1	367	412	1.06	63.78 ± 0.64	0.0494 ± 0.0011	100 ± 0			
12.1	232	152	0.63	64.18 ± 0.62	0.0489 ± 0.0017	100 ± 0			
13.1	68	41	0.58	56.09 ± 1.30	0.0508 ± 0.0032	114 ± 1			
14.1	91	102	1.07	5.09 ± 0.04	0.0786 ± 0.0010	1163 ± 12	1163 ± 24	0.5%	
15.1	123	182	1.35	64.56 ± 0.88	0.0489 ± 0.0023	99 ± 1			
16.1	419	557	1.24	63.86 ± 0.56	0.0488 ± 0.0012	100 ± 0			
17.1	147	158	1.02	64.35 ± 0.79	0.0496 ± 0.0018	99 ± 1			
18.1	148	236	1.10	37.81 ± 0.54	0.0505 ± 0.0025	168 ± 1			
19.1	147	133	0.86	41.88 ± 0.95	0.0504 ± 0.0017	152 ± 2			
20.1	131	128	0.92	40.98 ± 0.72	0.0509 ± 0.0035	155 ± 1			
21.1	222	108	0.46	35.84 ± 0.96	0.0527 ± 0.0042	177 ± 3			
22.1	326	237	0.68	65.70 ± 0.75	0.0492 ± 0.0013	97 ± 1			
23.1	134	100	0.72	63.41 ± 2.00	0.0505 ± 0.0041	101 ± 2			
24.1	134	159	1.12	61.65 ± 0.74	0.0498 ± 0.0020	104 ± 1			
25.1	91	66	0.70	66.31 ± 0.81	0.0470 ± 0.0023	97 ± 1			
26.1	277	158	0.55	64.85 ± 0.53	0.0500 ± 0.0017	99 ± 0			
~~27.1~~	~~116~~	~~68~~	~~0.56~~	~~41.31 ± 1.00~~	~~0.0538 ± 0.0027~~	~~154 ± 2~~			Yes
~~28.1~~	~~835~~	~~903~~	~~1.01~~	~~58.00 ± 2.30~~	~~0.0504 ± 0.0013~~	~~110 ± 2~~			Yes
~~29.1~~	~~211~~	~~214~~	~~0.98~~	~~65.92 ± 0.74~~	~~0.0526 ± 0.0020~~	~~97 ± 1~~			Yes
30.1	152	124	0.79	37.78 ± 0.53	0.0507 ± 0.0025	168 ± 1			
31.1	45	22	0.48	64.18 ± 1.50	0.0512 ± 0.0043	100 ± 1			
~~32.1~~	~~645~~	~~1041~~	~~1.57~~	~~61.92 ± 0.53~~	~~0.0627 ± 0.0024~~	~~103 ± 0~~			Yes
33.1	83	56	0.66	61.12 ± 2.00	0.0505 ± 0.0029	105 ± 2			
34.1	90	63	0.67	38.21 ± 0.38	0.0493 ± 0.0020	167 ± 1			
35.1	957	1285	1.31	37.44 ± 0.26	0.0494 ± 0.0005	170 ± 1			

36.1	352	468	1.30	64.39 ± 2.90	0.0501 ± 0.0036	99 ± 2					
~~37.1~~	~~440~~	~~327~~	~~0.70~~	~~5.75 ± 0.05~~	~~0.0960 ± 0.0006~~	~~1547 ± 6~~	~~1547 ± 11~~		~~33.2%~~		Yes
~~38.1~~	~~164~~	~~101~~	~~0.60~~	~~63.86 ± 0.66~~	~~0.0761 ± 0.0027~~	~~100 ± 1~~					Yes
39.1	202	107	0.53	65.19 ± 2.40	0.0512 ± 0.0060	98 ± 2					
40.1	89	82	0.91	61.58 ± 2.50	0.0483 ± 0.0041	104 ± 2					
~~41.1~~	~~239~~	~~210~~	~~0.82~~	~~56.31 ± 0.58~~	~~0.0592 ± 0.0021~~	~~114 ± 1~~					Yes
42.1	40	29	0.73	64.14 ± 1.30	0.0506 ± 0.0053	100 ± 1					
43.1	130	124	0.95	62.97 ± 0.76	0.0489 ± 0.0020	102 ± 1					
44.1	55	43	0.79	66.14 ± 1.10	0.0500 ± 0.0028	97 ± 1					
45.1	542	301	0.55	60.86 ± 0.97	0.0498 ± 0.0017	105 ± 1					
46.1	719	601	0.82	39.18 ± 0.32	0.0495 ± 0.0007	163 ± 1					
47.1	338	458	1.36	62.62 ± 0.77	0.0482 ± 0.0014	102 ± 1					
~~48.1~~	~~78~~	~~48~~	~~0.62~~	~~59.74 ± 1.30~~	~~0.0532 ± 0.0030~~	~~107 ± 1~~					Yes
49.1	22	10	0.46	66.14 ± 2.30	0.0468 ± 0.0059	97 ± 2					
50.1	88	60	0.61	39.95 ± 0.50	0.0494 ± 0.0022	159 ± 1					
51.1	98	49	0.50	67.07 ± 1.00	0.0484 ± 0.0020	95 ± 1					
52.1	65	40	0.62	66.31 ± 1.20	0.0495 ± 0.0031	96 ± 1					
53.1	376	304	0.82	65.06 ± 0.58	0.0498 ± 0.0013	98 ± 0					
54.1	117	53	0.46	64.68 ± 1.50	0.0514 ± 0.0026	99 ± 1					
55.1	308	440	1.39	37.16 ± 0.91	0.0487 ± 0.0015	171 ± 2					
56.1	106	68	0.64	39.23 ± 0.70	0.0517 ± 0.0026	162 ± 1					
57.1	102	47	0.47	63.21 ± 0.95	0.0514 ± 0.0025	101 ± 1					
58.1	228	65	0.28	4.88 ± 0.04	0.0831 ± 0.0006	1272 ± 7	1272 ± 13		5.5%		
59.1	172	144	0.83	37.22 ± 0.52	0.0506 ± 0.0018	171 ± 1					
60.1	226	250	1.11	59.49 ± 0.53	0.0502 ± 0.0017	107 ± 0					
61.1	123	130	1.06	37.59 ± 0.49	0.0503 ± 0.0017	169 ± 1					
62.1	57	32	0.58	65.40 ± 1.20	0.0526 ± 0.0034	98 ± 1					
63.1	203	198	0.95	61.65 ± 0.89	0.0488 ± 0.0018	104 ± 1					
64.1	54	35	0.66	64.68 ± 1.20	0.0513 ± 0.0040	99 ± 1					
65.1	90	70	0.80	66.62 ± 1.10	0.0509 ± 0.0027	96 ± 1					
~~66.1~~	~~253~~	~~191~~	~~0.76~~	~~62.00 ± 0.63~~	~~0.0513 ± 0.0016~~	~~103 ± 1~~					Yes
67.1	132	92	0.71	39.34 ± 0.48	0.0497 ± 0.0019	162 ± 1					
~~68.1~~	~~5~~	~~8~~	~~1.79~~	~~9.71 ± 1.40~~	~~0.6800 ± 0.0290~~	~~611 ± 37~~	~~4681 ± 73~~		~~86.9%~~		Yes
69.1	57	39	0.70	63.45 ± 1.00	0.0489 ± 0.0034	101 ± 1					
70.1	164	120	0.75	41.00 ± 0.42	0.0486 ± 0.0014	155 ± 1					

~~71.1~~	~~517~~	~~646~~	~~1.23~~	~~66.58 ± 0.62~~	~~0.0501 ± 0.0011~~	~~96 ± 0~~						Yes
~~72.1~~	~~169~~	~~102~~	~~0.63~~	~~62.31 ± 1.10~~	~~0.0741 ± 0.0039~~	~~103 ± 1~~						Yes
73.1	136	99	0.74	65.49 ± 1.10	0.0495 ± 0.0024	98 ± 1						
~~74.1~~	~~123~~	~~92~~	~~0.76~~	~~39.14 ± 0.58~~	~~0.0631 ± 0.0044~~	~~163 ± 1~~						Yes
75.1	157	169	1.08	39.89 ± 0.43	0.0487 ± 0.0020	160 ± 1						
76.1	69	60	0.87	64.85 ± 1.20	0.0513 ± 0.0035	99 ± 1						
77.1	347	377	1.08	63.90 ± 0.72	0.0491 ± 0.0014	100 ± 1						
78.1	122	104	0.83	63.33 ± 1.60	0.0497 ± 0.0031	101 ± 1						
79.1	160	193	1.21	5.44 ± 0.05	0.0761 ± 0.0007	1095 ± 10	1095 ± 19		0.7%			
80.1	151	71	0.46	63.90 ± 0.78	0.0505 ± 0.0020	100 ± 1						
81.1	102	48	0.47	65.49 ± 1.20	0.0499 ± 0.0029	98 ± 1						
82.1	103	77	0.72	65.83 ± 0.91	0.0503 ± 0.0026	97 ± 1						
83.1	239	257	1.05	62.27 ± 0.63	0.0484 ± 0.0012	103 ± 1						
84.1	109	64	0.57	39.70 ± 0.45	0.0489 ± 0.0020	160 ± 1						
85.1	82	56	0.66	65.10 ± 1.10	0.0523 ± 0.0026	98 ± 1						
86.1	68	56	0.79	65.83 ± 1.40	0.0509 ± 0.0031	97 ± 1						
87.1	166	248	1.45	62.54 ± 0.60	0.0477 ± 0.0017	102 ± 0						
88.1	70	49	0.66	66.45 ± 1.60	0.0525 ± 0.0034	96 ± 1						
89.1	75	45	0.57	40.31 ± 0.52	0.0510 ± 0.0026	158 ± 1						
90.1	63	46	0.71	65.79 ± 1.20	0.0501 ± 0.0039	97 ± 1						
~~91.1~~	~~321~~	~~427~~	~~1.29~~	~~66.23 ± 1.40~~	~~0.0554 ± 0.0039~~	~~97 ± 1~~						Yes
92.1	384	495	1.26	63.82 ± 0.55	0.0468 ± 0.0012	100 ± 0						
93.1	175	308	1.69	39.86 ± 0.85	0.0526 ± 0.0035	160 ± 2						
94.1	193	67	0.31	2.95 ± 0.03	0.1151 ± 0.0007	1881 ± 6	1881 ± 11		0.0%			
~~95.1~~	~~351~~	~~434~~	~~1.20~~	~~44.31 ± 0.87~~	~~0.0559 ± 0.0029~~	~~144 ± 2~~						Yes
96.1	285	215	0.72	65.10 ± 0.59	0.0493 ± 0.0014	98 ± 0						
97.1	228	143	0.61	66.80 ± 0.90	0.0503 ± 0.0025	96 ± 1						
~~98.1~~	~~304~~	~~332~~	~~1.05~~	~~62.38 ± 1.70~~	~~0.0624 ± 0.0025~~	~~103 ± 1~~						Yes
99.1	74	40	0.53	64.14 ± 1.30	0.0513 ± 0.0033	100 ± 1						
100.1	142	92	0.63	38.42 ± 0.69	0.0516 ± 0.0018	166 ± 2						
101.1	217	205	0.92	56.75 ± 0.77	0.0493 ± 0.0016	113 ± 1						
102.1	132	134	1.00	46.55 ± 0.58	0.0505 ± 0.0021	137 ± 1						
103.1	109	98	0.86	62.97 ± 0.83	0.0484 ± 0.0022	102 ± 1						
104.1	277	206	0.72	62.58 ± 0.61	0.0494 ± 0.0016	102 ± 0						
105.1	290	228	0.76	65.32 ± 0.68	0.0493 ± 0.0014	98 ± 1						

Labels	U (ppm)	Th (ppm	Th/U	$^{238}U/^{206}Pb^*$	$^{207}Pb/^{206}Pb^*$	age $^{206}Pb/^{238}U^*$	age $^{207}Pb/^{206}Pb^*$	% conc	Rejected
16NI08 (W67) - volcaniclastic									
1.1	69	39	0.52	65.92 ± 1.00	0.0465 ± 0.0028	97 ± 1			
~~2.1~~	~~98~~	~~55~~	~~0.54~~	~~68.12 ± 0.99~~	~~0.0517 ± 0.0019~~	~~94 ± 1~~			Yes
3.1	81	42	0.49	66.23 ± 0.94	0.0512 ± 0.0025	97 ± 1			
4.1	66	31	0.45	66.84 ± 1.30	0.0525 ± 0.0030	96 ± 1			
5.1	105	49	0.45	65.40 ± 0.86	0.0504 ± 0.0021	98 ± 1			
~~6.1~~	~~34~~	~~13~~	~~0.35~~	~~65.27 ± 1.60~~	~~0.0629 ± 0.0068~~	~~98 ± 1~~			Yes
7.1	81	44	0.52	66.49 ± 0.90	0.0451 ± 0.0022	96 ± 1			
8.1	58	26	0.43	68.26 ± 1.10	0.0499 ± 0.0034	94 ± 1			
9.1	294	331	1.07	62.58 ± 0.58	0.0492 ± 0.0016	102 ± 0			
10.1	113	57	0.48	67.11 ± 0.85	0.0501 ± 0.0022	95 ± 1			
11.1	56	24	0.42	65.75 ± 1.50	0.0464 ± 0.0034	97 ± 1			
~~12.1~~	~~303~~	~~432~~	~~0.98~~	~~41.98 ± 0.39~~	~~0.0642 ± 0.0015~~	~~152 ± 1~~			Yes
13.1	170	89	0.50	58.41 ± 1.50	0.0493 ± 0.0029	109 ± 1			
14.1	114	59	0.51	65.83 ± 1.00	0.0482 ± 0.0023	97 ± 1			
15.1	104	76	0.71	63.41 ± 0.94	0.0486 ± 0.0019	101 ± 1			
16.1	71	24	0.33	66.01 ± 1.20	0.0466 ± 0.0034	97 ± 1			
~~17.1~~	~~110~~	~~56~~	~~0.49~~	~~67.61 ± 1.40~~	~~0.0521 ± 0.0025~~	~~95 ± 1~~			Yes
18.1	84	45	0.53	63.57 ± 2.50	0.0493 ± 0.0061	101 ± 2			
19.1	363	513	1.39	41.32 ± 0.80	0.0484 ± 0.0019	154 ± 2			
20.1	254	110	0.41	64.60 ± 0.78	0.0504 ± 0.0016	99 ± 1			
21.1	127	57	0.46	67.16 ± 1.30	0.0516 ± 0.0027	95 ± 1			
~~22.1~~	~~119~~	~~76~~	~~0.56~~	~~66.01 ± 0.93~~	~~0.0549 ± 0.0032~~	~~97 ± 1~~			Yes
~~23.1~~	~~105~~	~~67~~	~~0.56~~	~~63.05 ± 0.93~~	~~0.0558 ± 0.0030~~	~~101 ± 1~~			Yes
24.1	118	70	0.60	65.96 ± 0.84	0.0498 ± 0.0028	97 ± 1			
~~25.1~~	~~91~~	~~52~~	~~0.57~~	~~65.02 ± 1.40~~	~~0.0630 ± 0.0070~~	~~98 ± 1~~			Yes
26.1	132	113	0.84	39.42 ± 0.45	0.0505 ± 0.0019	162 ± 1			
27.1	200	151	0.72	67.84 ± 1.10	0.0494 ± 0.0022	94 ± 1			
28.1	239	132	0.56	68.03 ± 1.40	0.0501 ± 0.0029	94 ± 1			
29.1	110	46	0.43	66.36 ± 1.30	0.0497 ± 0.0024	96 ± 1			
30.1	164	113	0.70	40.08 ± 0.47	0.0506 ± 0.0016	159 ± 1			
~~31.1~~	~~83~~	~~42~~	~~0.51~~	~~65.45 ± 1.60~~	~~0.0536 ± 0.0035~~	~~98 ± 1~~			Yes
32.1	134	54	0.41	66.62 ± 1.20	0.0483 ± 0.0023	96 ± 1			
33.1	254	238	0.88	64.14 ± 0.69	0.0488 ± 0.0018	100 ± 1			
34.1	341	160	0.46	67.89 ± 0.91	0.0483 ± 0.0015	94 ± 1			
35.1	170	122	0.69	65.10 ± 1.20	0.0510 ± 0.0026	98 ± 1			

| | | |

| | | |

106.1	133	75	0.56	69.20 ± 0.94	0.0485 ± 0.0018	93 ± 1
107.1	189	87	0.45	70.47 ± 0.79	0.0478 ± 0.0019	91 ± 1
108.1	153	70	0.45	66.53 ± 1.40	0.0484 ± 0.0021	96 ± 1
109.1	134	66	0.46	65.88 ± 1.20	0.0496 ± 0.0023	97 ± 1
110.1	88	42	0.48	66.49 ± 2.10	0.0499 ± 0.0037	96 ± 1
111.1	191	117	0.60	70.13 ± 0.78	0.0485 ± 0.0019	91 ± 0
112.1	80	32	0.40	67.66 ± 1.40	0.0508 ± 0.0030	95 ± 1
113.1	212	130	0.60	67.52 ± 1.70	0.0492 ± 0.0025	95 ± 1
114.1	134	71	0.52	68.87 ± 1.20	0.0497 ± 0.0026	93 ± 1

Labels	U (ppm)	Th (ppm	Th/U	$^{238}U/^{206}Pb^*$	$^{207}Pb/^{206}Pb^*$	age $^{206}Pb/^{238}U^*$	age $^{207}Pb/^{206}Pb^*$	% conc	Rejected
16NI09 (W67) - volcaniclastic									
1.1	135	102	0.77	61.61 ± 0.69	0.0507 ± 0.0023	104 ± 1			
2.1	81	40	0.50	68.07 ± 1.70	0.0523 ± 0.0032	94 ± 1			
~~3.1~~	~~452~~	~~283~~	~~0.64~~	~~7.98 ± 0.07~~	~~0.0673 ± 0.0005~~	~~761 ± 3~~			Yes
4.1	99	60	0.63	36.79 ± 0.85	0.0544 ± 0.0041	173 ± 2			
5.1	35	31	0.87	66.31 ± 1.40	0.0483 ± 0.0051	97 ± 1			
6.1	254	85	0.33	10.47 ± 0.08	0.0595 ± 0.0007	588 ± 2			
7.1	200	135	0.68	58.11 ± 2.20	0.0526 ± 0.0031	110 ± 2			
8.1	122	103	0.85	67.48 ± 2.30	0.0505 ± 0.0047	95 ± 2			
9.1	142	118	0.86	68.87 ± 0.83	0.0478 ± 0.0024	93 ± 1			
10.1	89	40	0.48	5.89 ± 0.07	0.0715 ± 0.0014	960 ± 21			
11.1	43	20	0.47	64.14 ± 1.40	0.0547 ± 0.0050	100 ± 1			
12.1	847	177	0.21	3.21 ± 0.02	0.1069 ± 0.0004	1747 ± 3	1747 ± 7	-0.2%	
13.1	152	65	0.44	54.35 ± 2.60	0.0542 ± 0.0054	117 ± 4			
14.1	87	42	0.50	68.17 ± 1.90	0.0485 ± 0.0044	94 ± 1			
15.1	830	1524	1.95	39.20 ± 0.26	0.0492 ± 0.0007	162 ± 1			
16.1	99	67	0.66	55.68 ± 2.40	0.0484 ± 0.0035	114 ± 3			
17.1	97	41	0.41	66.40 ± 0.90	0.0496 ± 0.0031	96 ± 1			
~~18.1~~	~~442~~	~~281~~	~~0.65~~	~~4.16 ± 0.07~~	~~0.0912 ± 0.0009~~	~~1450 ± 10~~	~~1450 ± 19~~	~~4.3%~~	Yes
19.1	62	28	0.46	6.47 ± 0.29	0.0790 ± 0.0064	926 ± 21	1170 ± 170	20.9%	
20.1	131	68	0.53	3.64 ± 0.06	0.0978 ± 0.0017	1588 ± 16	1588 ± 32	1.5%	
21.1	85	36	0.43	59.92 ± 1.80	0.0546 ± 0.0041	107 ± 2			
22.1	122	56	0.47	4.61 ± 0.06	0.0837 ± 0.0011	1281 ± 13	1281 ± 25	1.2%	
23.1	46	23	0.50	63.05 ± 1.50	0.0510 ± 0.0041	101 ± 1			
24.1	159	94	0.59	55.01 ± 0.71	0.0501 ± 0.0017	116 ± 1			
~~25.1~~	~~36~~	~~18~~	~~0.50~~	~~50.74 ± 2.20~~	~~0.2370 ± 0.0200~~	~~126 ± 3~~	~~3060 ± 130~~	~~95.9%~~	Yes
26.1	118	49	0.39	65.88 ± 1.00	0.0502 ± 0.0028	97 ± 1			
27.1	62	36	0.53	68.26 ± 1.70	0.0503 ± 0.0044	94 ± 1			
28.1	75	68	0.91	69.16 ± 1.20	0.0498 ± 0.0042	93 ± 1			
29.1	99	41	0.40	65.66 ± 0.89	0.0494 ± 0.0022	98 ± 1			
~~30.1~~	~~264~~	~~250~~	~~0.94~~	~~2.09 ± 0.01~~	~~0.1622 ± 0.0007~~	~~2478 ± 3~~	~~2478 ± 7~~	~~-1.9%~~	Yes
31.1	138	65	0.48	39.87 ± 1.10	0.0507 ± 0.0035	160 ± 2			
32.1	51	27	0.50	62.58 ± 1.40	0.0517 ± 0.0037	102 ± 1			
33.1	142	103	0.71	61.73 ± 0.90	0.0508 ± 0.0026	104 ± 1			
34.1	127	48	0.36	67.80 ± 1.30	0.0501 ± 0.0025	94 ± 1			
35.1	91	40	0.43	66.67 ± 0.87	0.0525 ± 0.0035	96 ± 1			

36.1	65	27	0.40	68.03 ± 1.00	0.0494 ± 0.0033	94 ± 1					
37.1	115	89	0.75	66.67 ± 0.97	0.0480 ± 0.0022	96 ± 1					
38.1	388	595	1.47	41.07 ± 0.41	0.0496 ± 0.0011	155 ± 1					
~~39.1~~	~~146~~	~~82~~	~~0.55~~	~~62.93 ± 1.90~~	~~0.0557 ± 0.0051~~	~~102 ± 2~~					Yes
~~40.1~~	~~98~~	~~33~~	~~0.33~~	~~2.05 ± 0.02~~	~~0.1589 ± 0.0012~~	~~2444 ± 6~~	~~2444 ± 12~~		~~-4.8%~~		Yes
~~41.1~~	~~140~~	~~76~~	~~0.52~~	~~64.39 ± 1.50~~	~~0.0549 ± 0.0039~~	~~99 ± 1~~					Yes
42.1	96	62	0.63	3.54 ± 0.03	0.0979 ± 0.0009	1581 ± 9	1581 ± 17		-1.3%		
~~43.1~~	~~62~~	~~29~~	~~0.44~~	~~65.79 ± 1.20~~	~~0.0534 ± 0.0034~~	~~97 ± 1~~					Yes
44.1	116	65	0.54	67.57 ± 0.93	0.0478 ± 0.0022	95 ± 1					
45.1	237	175	0.71	69.78 ± 0.71	0.0500 ± 0.0018	92 ± 0					
46.1	272	271	0.97	61.46 ± 0.64	0.0485 ± 0.0016	104 ± 1					
47.1	75	33	0.43	41.96 ± 0.71	0.0516 ± 0.0027	152 ± 1					
~~48.1~~	~~226~~	~~143~~	~~0.62~~	~~63.41 ± 2.00~~	~~0.0586 ± 0.0049~~	~~101 ± 2~~					Yes
49.1	283	295	1.02	64.56 ± 0.68	0.0497 ± 0.0014	99 ± 1					
50.1	111	70	0.62	39.51 ± 0.49	0.0497 ± 0.0018	161 ± 1					
51.1	108	34	0.32	67.61 ± 0.97	0.0494 ± 0.0027	95 ± 1					
52.1	107	51	0.45	68.31 ± 1.00	0.0507 ± 0.0029	94 ± 1					
53.1	168	85	0.50	67.25 ± 0.95	0.0502 ± 0.0023	95 ± 1					
~~54.1~~	~~148~~	~~84~~	~~0.54~~	~~59.21 ± 1.40~~	~~0.0621 ± 0.0047~~	~~108 ± 1~~					Yes
55.1	153	94	0.61	68.31 ± 1.30	0.0487 ± 0.0025	94 ± 1					
56.1	81	50	0.62	65.79 ± 1.10	0.0496 ± 0.0028	97 ± 1					
57.1	331	366	1.10	40.02 ± 0.35	0.0492 ± 0.0012	159 ± 1					
58.1	39	60	1.53	4.98 ± 0.06	0.0799 ± 0.0016	1198 ± 20	1198 ± 39		1.5%		
59.1	34	24	0.69	63.86 ± 3.20	0.0530 ± 0.0140	100 ± 2					
60.1	149	52	0.35	3.72 ± 0.03	0.0962 ± 0.0009	1550 ± 9	1550 ± 17		0.9%		
61.1	82	48	0.60	67.52 ± 1.10	0.0517 ± 0.0046	95 ± 1					
62.1	63	62	1.02	10.58 ± 0.10	0.0585 ± 0.0013	582 ± 3					
63.1	87	84	0.98	67.52 ± 1.20	0.0493 ± 0.0031	95 ± 1					
64.1	194	10	0.05	11.52 ± 0.11	0.0586 ± 0.0012	536 ± 2					
65.1	116	47	0.42	67.66 ± 0.93	0.0505 ± 0.0025	95 ± 1					
66.1	113	57	0.53	62.34 ± 0.85	0.0510 ± 0.0030	103 ± 1					
67.1	134	89	0.70	66.27 ± 1.10	0.0505 ± 0.0032	97 ± 1					
68.1	1245	41	0.03	10.67 ± 0.10	0.0593 ± 0.0005	577 ± 2					
69.1	171	69	0.43	62.42 ± 1.20	0.0470 ± 0.0022	102 ± 1					
70.1	105	55	0.54	64.47 ± 0.96	0.0479 ± 0.0027	99 ± 1					

71.1	116	116	1.05	5.41 ± 0.05	0.0764 ± 0.0013	1104 ± 17	1104 ± 34	0.9%		
72.1	441	528	1.26	63.37 ± 0.62	0.0492 ± 0.0017	101 ± 1				
73.1	205	226	0.90	68.26 ± 0.99	0.0482 ± 0.0022	94 ± 1				
74.1	180	88	0.51	66.98 ± 1.10	0.0508 ± 0.0025	96 ± 1				
75.1	484	378	0.82	10.50 ± 0.07	0.0597 ± 0.0006	586 ± 2				
~~76.1~~	~~136~~	~~129~~	~~0.97~~	~~3.95 ± 0.04~~	~~0.0941 ± 0.0009~~	~~1508 ± 9~~	~~1508 ± 18~~	~~3.6%~~	Yes	
~~77.1~~	~~84~~	~~42~~	~~0.51~~	~~38.17 ± 3.40~~	~~0.0667 ± 0.0088~~	~~166 ± 8~~			Yes	
~~78.1~~	~~71~~	~~37~~	~~0.52~~	~~51.68 ± 2.00~~	~~0.0846 ± 0.0059~~	~~124 ± 3~~	~~1280 ± 140~~	~~90.4%~~	Yes	
79.1	110	3	0.02	9.60 ± 0.09	0.0617 ± 0.0013	639 ± 3				
80.1	195	102	0.52	3.13 ± 0.02	0.1081 ± 0.0008	1766 ± 7	1766 ± 13	-1.2%		
81.1	79	35	0.44	61.24 ± 1.80	0.0506 ± 0.0054	104 ± 2				
~~82.1~~	~~144~~	~~282~~	~~1.91~~	~~4.58 ± 0.05~~	~~0.1315 ± 0.0013~~	~~2114 ± 9~~	~~2114 ± 18~~	~~39.8%~~	Yes	
~~83.1~~	~~198~~	~~123~~	~~0.60~~	~~61.01 ± 1.60~~	~~0.0644 ± 0.0039~~	~~105 ± 1~~			Yes	
84.1	87	49	0.54	66.14 ± 1.50	0.0456 ± 0.0028	97 ± 1				
85.1	112	52	0.44	68.12 ± 1.20	0.0513 ± 0.0025	94 ± 1				
86.1	82	44	0.50	66.49 ± 1.30	0.0542 ± 0.0043	96 ± 1				
87.1	119	95	0.77	65.40 ± 1.10	0.0523 ± 0.0030	98 ± 1				
88.1	73	51	0.66	65.23 ± 1.20	0.0531 ± 0.0033	98 ± 1				
89.1	86	51	0.55	65.32 ± 1.00	0.0507 ± 0.0031	98 ± 1				
90.1	158	102	0.62	65.36 ± 1.10	0.0520 ± 0.0038	98 ± 1				
~~91.1~~	~~229~~	~~169~~	~~0.67~~	~~62.03 ± 1.10~~	~~0.0555 ± 0.0029~~	~~103 ± 1~~			Yes	
~~92.1~~	~~341~~	~~453~~	~~1.22~~	~~62.58 ± 0.65~~	~~0.0508 ± 0.0015~~	~~102 ± 1~~			Yes	
93.1	185	196	0.94	40.18 ± 0.48	0.0509 ± 0.0018	159 ± 1				
94.1	276	235	0.78	62.81 ± 0.73	0.0480 ± 0.0017	102 ± 1				
95.1	237	246	0.93	39.53 ± 0.53	0.0502 ± 0.0015	161 ± 1				
96.1	106	60	0.51	65.49 ± 1.30	0.0515 ± 0.0031	98 ± 1				
~~97.1~~	~~223~~	~~204~~	~~0.71~~	~~31.14 ± 0.65~~	~~0.1906 ± 0.0098~~	~~204 ± 2~~	~~2724 ± 86~~	~~92.5%~~	Yes	
98.1	110	67	0.56	64.39 ± 0.90	0.0510 ± 0.0029	99 ± 1				
99.1	131	63	0.45	46.38 ± 0.65	0.0504 ± 0.0022	138 ± 1				
100.1	27	18	0.63	12.71 ± 0.27	0.0623 ± 0.0048	491 ± 5				
~~101.1~~	~~151~~	~~85~~	~~0.51~~	~~67.98 ± 1.10~~	~~0.0524 ± 0.0026~~	~~94 ± 1~~			Yes	
102.1	150	82	0.49	63.86 ± 0.95	0.0515 ± 0.0030	100 ± 1				
103.1	248	141	0.53	5.23 ± 0.08	0.0788 ± 0.0010	1169 ± 12	1169 ± 23	3.5%		
104.1	30	18	0.58	61.58 ± 1.90	0.0532 ± 0.0054	104 ± 2				
105.1	164	116	0.67	66.31 ± 0.80	0.0473 ± 0.0022	97 ± 1				

106.1	765	208	0.25	10.26 ± 0.08	0.0598 ± 0.0005	599 ± 2						
107.1	1341	625	0.44	40.26 ± 0.24	0.0493 ± 0.0006	158 ± 0						
108.1	169	136	0.76	66.14 ± 0.93	0.0490 ± 0.0021	97 ± 1						
~~109.1~~	~~498~~	~~233~~	~~0.45~~	~~5.84 ± 0.04~~	~~0.0717 ± 0.0005~~	~~977 ± 7~~						Yes
110.1	282	435	1.54	38.17 ± 0.45	0.0511 ± 0.0017	167 ± 1						
111.1	167	110	0.66	38.08 ± 0.66	0.0490 ± 0.0023	167 ± 1						
112.1	54	43	0.76	62.42 ± 1.90	0.0513 ± 0.0042	102 ± 1						
113.1	326	323	0.99	39.78 ± 0.38	0.0491 ± 0.0013	160 ± 1						
~~114.1~~	~~146~~	~~280~~	~~1.93~~	~~4.91 ± 0.06~~	~~0.0779 ± 0.0010~~	~~1141 ± 13~~	~~1141 ± 26~~			~~-4.7%~~		Yes
~~115.1~~	~~216~~	~~148~~	~~0.66~~	~~54.61 ± 0.76~~	~~0.0520 ± 0.0021~~	~~117 ± 1~~						Yes
116.1	61	29	0.49	59.70 ± 2.00	0.0540 ± 0.0056	107 ± 2						
~~117.1~~	~~108~~	~~61~~	~~0.58~~	~~46.51 ± 2.20~~	~~0.0643 ± 0.0052~~	~~138 ± 3~~						Yes
~~118.1~~	~~237~~	~~78~~	~~0.35~~	~~59.03 ± 1.20~~	~~0.0609 ± 0.0032~~	~~108 ± 1~~						Yes
~~119.1~~	~~201~~	~~125~~	~~0.65~~	~~58.69 ± 1.50~~	~~0.0616 ± 0.0035~~	~~109 ± 1~~						Yes
120.1	440	587	1.33	61.05 ± 0.93	0.0497 ± 0.0016	105 ± 1						
~~121.1~~	~~191~~	~~123~~	~~0.67~~	~~44.84 ± 2.00~~	~~0.0860 ± 0.0093~~	~~142 ± 3~~	~~1090 ± 200~~			~~87.0%~~		Yes
~~122.1~~	~~463~~	~~482~~	~~1.06~~	~~60.13 ± 0.74~~	~~0.0514 ± 0.0015~~	~~106 ± 1~~						Yes
~~123.1~~	~~118~~	~~73~~	~~0.65~~	~~52.19 ± 2.60~~	~~0.0544 ± 0.0041~~	~~122 ± 3~~						Yes
~~124.1~~	~~253~~	~~297~~	~~1.22~~	~~34.26 ± 0.79~~	~~0.0587 ± 0.0030~~	~~186 ± 2~~						Yes
~~125.1~~	~~379~~	~~208~~	~~0.56~~	~~29.77 ± 0.34~~	~~0.0523 ± 0.0011~~	~~213 ± 1~~						Yes
~~126.1~~	~~161~~	~~214~~	~~1.37~~	~~9.57 ± 0.35~~	~~0.0640 ± 0.0019~~	~~640 ± 11~~						Yes
~~127.1~~	~~242~~	~~158~~	~~0.67~~	~~53.25 ± 1.40~~	~~0.0532 ± 0.0027~~	~~120 ± 2~~						Yes
128.1	131	109	0.84	65.49 ± 0.94	0.0494 ± 0.0026	98 ± 1						
129.1	397	254	0.67	68.82 ± 0.75	0.0494 ± 0.0016	93 ± 1						
130.1	314	110	0.35	11.09 ± 0.15	0.0596 ± 0.0008	557 ± 3						
131.1	69	32	0.47	64.10 ± 1.90	0.0497 ± 0.0040	100 ± 2						
132.1	384	257	0.66	48.50 ± 1.30	0.0478 ± 0.0017	132 ± 2						
~~133.1~~	~~129~~	~~100~~	~~0.66~~	~~68.45 ± 1.40~~	~~0.0555 ± 0.0034~~	~~94 ± 1~~						Yes
134.1	511	422	0.81	9.47 ± 0.10	0.0615 ± 0.0007	647 ± 3						
~~135.1~~	~~117~~	~~90~~	~~0.77~~	~~61.12 ± 2.20~~	~~0.0661 ± 0.0074~~	~~105 ± 2~~						Yes
136.1	166	128	0.77	64.89 ± 1.30	0.0523 ± 0.0045	99 ± 1						
137.1	182	129	0.73	5.07 ± 0.06	0.0792 ± 0.0008	1174 ± 11	1174 ± 21			1.1%		
138.1	348	362	1.05	9.96 ± 0.08	0.0612 ± 0.0007	617 ± 2						

Labels	U (ppm)	Th (ppm	Th/U	$^{238}U/^{206}Pb*$	$^{207}Pb/^{206}Pb*$	age $^{206}Pb/^{238}U*$	age $^{207}Pb/^{206}Pb*$	% conc	Rejected
16NI10a (W67) - conglomerate									
1.1	30	22	0.73	62.23 ± 2.20	0.0525 ± 0.0068	103 ± 2			
2.1	113	58	0.49	69.54 ± 0.97	0.0499 ± 0.0029	92 ± 1			
~~3.1~~	~~101~~	~~49~~	~~0.49~~	~~66.45 ± 1.30~~	~~0.0681 ± 0.0042~~	~~96 ± 1~~			~~Yes~~
4.1	201	234	1.16	63.73 ± 0.72	0.0475 ± 0.0021	100 ± 1			
5.1	300	328	1.09	42.23 ± 0.41	0.0494 ± 0.0016	151 ± 1			
~~6.1~~	~~449~~	~~600~~	~~1.32~~	~~63.78 ± 0.72~~	~~0.0507 ± 0.0017~~	~~100 ± 1~~			~~Yes~~
7.1	135	100	0.72	66.49 ± 1.90	0.0483 ± 0.0041	96 ± 1			
8.1	172	157	0.90	67.80 ± 0.96	0.0494 ± 0.0023	94 ± 1			
9.1	117	66	0.56	67.20 ± 0.95	0.0495 ± 0.0027	95 ± 1			
10.1	286	316	1.07	64.10 ± 0.67	0.0471 ± 0.0017	100 ± 1			
11.1	518	607	1.14	64.60 ± 0.54	0.0492 ± 0.0012	99 ± 0			
12.1	473	511	1.07	65.92 ± 0.68	0.0477 ± 0.0013	97 ± 0			
13.1	335	310	0.85	61.43 ± 0.65	0.0490 ± 0.0016	104 ± 1			
14.1	489	612	1.24	42.03 ± 0.32	0.0501 ± 0.0010	152 ± 1			
15.1	232	269	1.17	10.85 ± 0.14	0.0596 ± 0.0016	568 ± 4			
~~16.1~~	~~419~~	~~493~~	~~1.16~~	~~67.70 ± 1.10~~	~~0.0521 ± 0.0020~~	~~95 ± 1~~			~~Yes~~
17.1	255	244	0.97	40.55 ± 0.67	0.0493 ± 0.0018	157 ± 1			
18.1	154	87	0.57	67.66 ± 1.50	0.0526 ± 0.0039	95 ± 1			
~~19.1~~	~~117~~	~~58~~	~~0.50~~	~~67.93 ± 1.10~~	~~0.0609 ± 0.0031~~	~~94 ± 1~~			~~Yes~~
~~20.1~~	~~143~~	~~66~~	~~0.45~~	~~66.71 ± 1.40~~	~~0.0530 ± 0.0031~~	~~96 ± 1~~			~~Yes~~
~~21.1~~	~~172~~	~~155~~	~~0.89~~	~~45.27 ± 0.86~~	~~0.0649 ± 0.0029~~	~~141 ± 1~~			~~Yes~~
22.1	74	45	0.61	63.09 ± 1.30	0.0464 ± 0.0029	101 ± 1			
23.1	281	249	0.84	65.92 ± 1.00	0.0496 ± 0.0017	97 ± 1			
24.1	357	110	0.30	3.12 ± 0.06	0.1098 ± 0.0008	1795 ± 7	1795 ± 14	0.1%	
~~25.1~~	~~132~~	~~100~~	~~0.75~~	~~16.51 ± 0.19~~	~~0.0585 ± 0.0020~~	~~379 ± 2~~			~~Yes~~
~~26.1~~	~~75~~	~~43~~	~~0.53~~	~~33.06 ± 0.86~~	~~0.0827 ± 0.0065~~	~~192 ± 2~~	~~1050 ± 150~~	~~81.7%~~	~~Yes~~
~~27.1~~	~~156~~	~~90~~	~~0.58~~	~~46.17 ± 1.60~~	~~0.1046 ± 0.0064~~	~~138 ± 2~~	~~1590 ± 110~~	~~91.3%~~	~~Yes~~
~~28.1~~	~~614~~	~~568~~	~~0.92~~	~~52.08 ± 1.60~~	~~0.0612 ± 0.0022~~	~~123 ± 2~~			~~Yes~~
~~29.1~~	~~241~~	~~112~~	~~0.46~~	~~2.21 ± 0.05~~	~~0.2157 ± 0.0022~~	~~2948 ± 9~~	~~2948 ± 17~~	~~18.6%~~	~~Yes~~
~~30.1~~	~~111~~	~~69~~	~~0.60~~	~~29.33 ± 1.60~~	~~0.1590 ± 0.0150~~	~~216 ± 6~~	~~2280 ± 160~~	~~90.5%~~	~~Yes~~
~~31.1~~	~~79~~	~~37~~	~~0.46~~	~~65.53 ± 1.80~~	~~0.0598 ± 0.0056~~	~~98 ± 1~~			~~Yes~~
~~32.1~~	~~158~~	~~138~~	~~0.87~~	~~23.13 ± 0.25~~	~~0.0635 ± 0.0024~~	~~273 ± 2~~			~~Yes~~
~~33.1~~	~~122~~	~~54~~	~~0.44~~	~~66.67 ± 1.50~~	~~0.0933 ± 0.0073~~	~~96 ± 1~~	~~1310 ± 120~~	~~92.7%~~	~~Yes~~
~~34.1~~	~~58~~	~~36~~	~~0.61~~	~~65.57 ± 2.90~~	~~0.0654 ± 0.0078~~	~~98 ± 2~~			~~Yes~~
~~35.1~~	~~317~~	~~196~~	~~0.62~~	~~61.50 ± 1.20~~	~~0.0549 ± 0.0022~~	~~104 ± 1~~			~~Yes~~

| | | |

Labels	U (ppm)	Th (ppm	Th/U	$^{238}U/^{206}Pb*$	$^{207}Pb/^{206}Pb*$	age $^{206}Pb/^{238}U*$	age $^{207}Pb/^{206}Pb*$	% conc	Rejected
16NI10b (W67) - conglomerate									
1.1	149	85	0.56	66.49 ± 0.82	0.0478 ± 0.0020	96 ± 1			
~~2.1~~	~~126~~	~~107~~	~~0.66~~	~~53.28 ± 0.89~~	~~0.0625 ± 0.0030~~	~~120 ± 1~~			Yes
3.1	46	92	2.01	5.13 ± 0.07	0.0779 ± 0.0014	1130 ± 18	1130 ± 36	-1.7%	
4.1	982	135	0.13	38.64 ± 0.94	0.0498 ± 0.0009	165 ± 2			
5.1	176	83	0.48	52.91 ± 5.30	0.0496 ± 0.0043	121 ± 7			
~~6.1~~	~~327~~	~~79~~	~~0.24~~	~~4.52 ± 0.03~~	~~0.0820 ± 0.0006~~	~~1244 ± 8~~	~~1244 ± 15~~	~~-3.5%~~	Yes
7.1	58	35	0.59	63.13 ± 1.30	0.0487 ± 0.0037	101 ± 2			
8.1	137	59	0.42	10.28 ± 0.08	0.0604 ± 0.0010	598 ± 2			
9.1	179	85	0.47	11.42 ± 0.12	0.0574 ± 0.0010	541 ± 3			
~~10.1~~	~~123~~	~~144~~	~~1.15~~	~~4.82 ± 0.05~~	~~0.0777 ± 0.0016~~	~~1133 ± 20~~	~~1133 ± 40~~	~~-7.2%~~	Yes
~~11.1~~	~~142~~	~~283~~	~~1.97~~	~~10.06 ± 0.11~~	~~0.0591 ± 0.0011~~	~~611 ± 3~~			Yes
12.1	122	49	0.39	3.06 ± 0.04	0.1103 ± 0.0015	1803 ± 13	1803 ± 26	-0.9%	
13.1	272	40	0.15	2.96 ± 0.07	0.1140 ± 0.0007	1863 ± 6	1863 ± 11	-0.5%	
~~14.1~~	~~191~~	~~224~~	~~1.16~~	~~20.06 ± 0.35~~	~~0.0561 ± 0.0025~~	~~314 ± 3~~			Yes
15.1	312	223	0.71	34.36 ± 0.32	0.0512 ± 0.0011	185 ± 1			
~~16.1~~	~~372~~	~~222~~	~~0.58~~	~~6.61 ± 0.14~~	~~0.0724 ± 0.0017~~	~~909 ± 9~~			Yes
17.1	171	84	0.48	65.49 ± 1.10	0.0509 ± 0.0028	98 ± 1			
18.1	179	97	0.54	50.43 ± 1.50	0.0499 ± 0.0019	127 ± 2			
19.1	54	34	0.63	66.27 ± 1.90	0.0536 ± 0.0050	97 ± 1			
~~20.1~~	~~170~~	~~106~~	~~0.62~~	~~5.53 ± 0.08~~	~~0.0791 ± 0.0015~~	~~1169 ± 19~~	~~1169 ± 38~~	~~8.4%~~	Yes
21.1	127	60	0.46	63.73 ± 1.80	0.0517 ± 0.0042	100 ± 1			
22.1	169	142	0.82	68.17 ± 1.20	0.0496 ± 0.0024	94 ± 1			
~~23.1~~	~~119~~	~~93~~	~~0.76~~	~~3.36 ± 0.03~~	~~0.0992 ± 0.0010~~	~~1605 ± 10~~	~~1605 ± 19~~	~~-4.7%~~	Yes
~~24.1~~	~~84~~	~~100~~	~~1.14~~	~~9.87 ± 0.10~~	~~0.0574 ± 0.0015~~	~~622 ± 3~~			Yes
~~25.1~~	~~372~~	~~134~~	~~0.38~~	~~2.28 ± 0.03~~	~~0.1556 ± 0.0009~~	~~2408 ± 5~~	~~2408 ± 10~~	~~2.8%~~	Yes
26.1	45	19	0.43	60.61 ± 1.90	0.0532 ± 0.0066	106 ± 2			
27.1	53	25	0.47	62.15 ± 1.40	0.0483 ± 0.0042	103 ± 1			
28.1	194	139	0.72	61.12 ± 0.92	0.0482 ± 0.0022	105 ± 1			
29.1	655	940	1.30	66.27 ± 0.62	0.0485 ± 0.0012	97 ± 0			
30.1	543	816	1.45	60.42 ± 0.60	0.0487 ± 0.0014	106 ± 1			
31.1	299	307	1.04	62.66 ± 1.40	0.0502 ± 0.0025	102 ± 1			
32.1	67	35	0.52	65.62 ± 1.30	0.0479 ± 0.0035	98 ± 1			
33.1	77	38	0.49	64.85 ± 1.20	0.0490 ± 0.0032	99 ± 1			
~~34.1~~	~~49~~	~~39~~	~~0.76~~	~~62.11 ± 2.40~~	~~0.0555 ± 0.0042~~	~~103 ± 2~~			Yes
35.1	113	58	0.52	65.40 ± 0.91	0.0489 ± 0.0025	98 ± 1			

36.1	113	54	0.48	63.53 ± 2.90	0.0541 ± 0.0062	101 ± 3					
37.1	48	22	0.47	67.16 ± 1.40	0.0476 ± 0.0046	95 ± 1					
38.1	70	38	0.53	64.06 ± 1.20	0.0456 ± 0.0034	100 ± 1					
39.1	120	66	0.53	68.21 ± 1.20	0.0517 ± 0.0028	94 ± 1					
40.1	97	66	0.69	66.62 ± 1.00	0.0530 ± 0.0046	96 ± 1					
41.1	98	149	1.55	10.79 ± 0.10	0.0597 ± 0.0013	571 ± 3					
42.1	53	26	0.51	67.20 ± 1.50	0.0485 ± 0.0036	95 ± 1					
43.1	180	106	0.60	68.26 ± 1.20	0.0505 ± 0.0032	94 ± 1					
44.1	78	41	0.53	67.57 ± 1.60	0.0529 ± 0.0045	95 ± 1					
45.1	55	24	0.45	66.71 ± 1.40	0.0541 ± 0.0043	96 ± 1					
46.1	75	48	0.65	59.95 ± 1.50	0.0499 ± 0.0047	107 ± 1					
47.1	324	198	0.62	5.68 ± 0.08	0.0742 ± 0.0009	1044 ± 12	1044 ± 24	-0.2%			
48.1	59	41	0.69	63.49 ± 1.80	0.0498 ± 0.0036	101 ± 1					
49.1	155	106	0.66	65.57 ± 1.30	0.0490 ± 0.0024	98 ± 1					
50.1	94	67	0.69	59.67 ± 1.80	0.0544 ± 0.0059	107 ± 2					
51.1	100	50	0.49	62.97 ± 1.40	0.0501 ± 0.0036	102 ± 1					
52.1	106	50	0.48	66.27 ± 1.10	0.0511 ± 0.0055	97 ± 1					
53.1	103	57	0.55	68.68 ± 1.10	0.0498 ± 0.0026	93 ± 1					
54.1	162	81	0.49	63.53 ± 0.96	0.0483 ± 0.0022	101 ± 1					
55.1	83	38	0.46	64.77 ± 0.99	0.0482 ± 0.0027	99 ± 1					
56.1	630	210	0.33	10.00 ± 0.07	0.0599 ± 0.0006	615 ± 2					
57.1	111	58	0.52	64.72 ± 0.86	0.0513 ± 0.0029	99 ± 1					
58.1	278	269	0.94	34.31 ± 0.38	0.0506 ± 0.0012	185 ± 1					
59.1	366	191	0.51	68.17 ± 0.92	0.0498 ± 0.0016	94 ± 1					
~~60.1~~	~~129~~	~~140~~	~~1.08~~	~~3.30 ± 0.02~~	~~0.0988 ± 0.0010~~	~~1600 ± 10~~	~~1600 ± 19~~	~~-6.7%~~			Yes
~~61.1~~	~~49~~	~~27~~	~~0.53~~	~~61.54 ± 2.00~~	~~0.0755 ± 0.0076~~	~~104 ± 2~~					Yes
62.1	107	64	0.59	63.69 ± 1.10	0.0502 ± 0.0024	100 ± 1					
~~63.1~~	~~838~~	~~52~~	~~0.06~~	~~4.96 ± 0.04~~	~~0.0786 ± 0.0005~~	~~1161 ± 6~~	~~1161 ± 11~~	~~-2.0%~~			Yes
64.1	146	76	0.51	65.70 ± 0.97	0.0485 ± 0.0033	97 ± 1					
65.1	93	44	0.46	66.49 ± 1.10	0.0508 ± 0.0031	96 ± 1					
~~66.1~~	~~171~~	~~144~~	~~0.83~~	~~3.59 ± 0.03~~	~~0.0964 ± 0.0008~~	~~1553 ± 8~~	~~1553 ± 16~~	~~-2.0%~~			Yes
~~67.1~~	~~194~~	~~113~~	~~0.56~~	~~6.16 ± 0.21~~	~~0.0902 ± 0.0010~~	~~968 ± 14~~	~~1426 ± 20~~	~~32.1%~~			Yes
~~68.1~~	~~542~~	~~410~~	~~0.71~~	~~38.55 ± 0.71~~	~~0.0549 ± 0.0015~~	~~165 ± 2~~					Yes
69.1	156	157	1.01	5.36 ± 0.06	0.0761 ± 0.0010	1093 ± 13	1093 ± 26	-0.8%			
70.1	157	91	0.57	64.56 ± 1.20	0.0497 ± 0.0021	99 ± 1					

71.1	125	80	0.54	54.88 ± 0.88	0.0501 ± 0.0023	116 ± 1					
72.1	411	431	1.00	14.93 ± 0.12	0.0549 ± 0.0008	418 ± 2					
73.1	499	231	0.35	39.67 ± 0.39	0.0497 ± 0.0012	161 ± 1					
74.1	665	510	0.77	29.13 ± 0.18	0.0500 ± 0.0008	218 ± 1					
75.1	832	1236	1.50	4.98 ± 0.07	0.0798 ± 0.0004	1191 ± 6	1191 ± 11		0.9%		
76.1	119	59	0.50	60.46 ± 1.70	0.0506 ± 0.0039	106 ± 1					
77.1	218	174	0.80	3.21 ± 0.06	0.1074 ± 0.0011	1751 ± 10	1751 ± 19		0.2%		
~~78.1~~	~~112~~	~~191~~	~~1.76~~	~~4.92 ± 0.07~~	~~0.0819 ± 0.0013~~	~~1232 ± 16~~	~~1232 ± 32~~		~~3.0%~~		Yes
~~79.1~~	~~250~~	~~118~~	~~0.46~~	~~3.08 ± 0.03~~	~~0.1091 ± 0.0007~~	~~1784 ± 6~~	~~1784 ± 11~~		~~-1.5%~~		Yes
~~80.1~~	~~72~~	~~36~~	~~0.50~~	~~44.25 ± 2.60~~	~~0.1240 ± 0.0082~~	~~144 ± 5~~	~~1900 ± 120~~		~~92.4%~~		Yes
~~81.1~~	~~59~~	~~25~~	~~0.42~~	~~55.25 ± 5.00~~	~~0.0619 ± 0.0085~~	~~116 ± 7~~					Yes
~~82.1~~	~~115~~	~~123~~	~~1.07~~	~~38.26 ± 0.81~~	~~0.0562 ± 0.0023~~	~~166 ± 2~~					Yes
~~83.1~~	~~531~~	~~379~~	~~0.72~~	~~4.98 ± 0.04~~	~~0.0874 ± 0.0024~~	~~1378 ± 27~~	~~1378 ± 54~~		~~14.4%~~		Yes
~~84.1~~	~~315~~	~~150~~	~~0.47~~	~~5.37 ± 0.06~~	~~0.0753 ± 0.0006~~	~~1077 ± 8~~	~~1077 ± 15~~		~~-2.2%~~		Yes
85.1	677	223	0.33	12.11 ± 0.10	0.0576 ± 0.0006	511 ± 2					
86.1	292	222	0.76	8.31 ± 0.09	0.0642 ± 0.0008	733 ± 4					
87.1	246	111	0.47	6.59 ± 0.07	0.0683 ± 0.0008	910 ± 4					
88.1	68	24	0.37	60.17 ± 2.10	0.0549 ± 0.0050	106 ± 2					
89.1	123	112	0.93	3.74 ± 0.04	0.0958 ± 0.0010	1541 ± 10	1541 ± 19		0.9%		
~~90.1~~	~~208~~	~~344~~	~~1.66~~	~~10.57 ± 0.09~~	~~0.0662 ± 0.0010~~	~~583 ± 2~~					Yes
91.1	145	117	0.81	23.33 ± 0.40	0.0533 ± 0.0018	271 ± 2					
92.1	131	83	0.63	6.16 ± 0.08	0.0727 ± 0.0014	970 ± 6					
~~93.1~~	~~117~~	~~48~~	~~0.41~~	~~55.65 ± 1.90~~	~~0.0600 ± 0.0036~~	~~115 ± 2~~					Yes
~~94.1~~	~~60~~	~~34~~	~~0.52~~	~~67.34 ± 1.60~~	~~0.0625 ± 0.0044~~	~~95 ± 1~~					Yes
95.1	71	50	0.71	4.84 ± 0.04	0.0816 ± 0.0013	1230 ± 15	1230 ± 30		1.7%		
96.1	91	58	0.65	6.75 ± 0.06	0.0696 ± 0.0013	890 ± 4					
97.1	274	249	0.92	4.99 ± 0.09	0.0793 ± 0.0013	1175 ± 17	1175 ± 33		-0.2%		
98.1	296	177	0.60	3.20 ± 0.05	0.1070 ± 0.0011	1748 ± 10	1748 ± 20		-0.2%		
99.1	81	53	0.66	5.56 ± 0.05	0.0750 ± 0.0012	1061 ± 17	1061 ± 33		-0.6%		
100.1	181	158	0.88	67.98 ± 1.30	0.0512 ± 0.0031	94 ± 1					
101.1	74	32	0.42	64.72 ± 1.60	0.0526 ± 0.0037	99 ± 1					
102.1	58	39	0.67	38.37 ± 0.93	0.0510 ± 0.0029	166 ± 2					
~~103.1~~	~~189~~	~~194~~	~~1.02~~	~~36.55 ± 0.54~~	~~0.0538 ± 0.0021~~	~~174 ± 1~~					Yes
~~104.1~~	~~616~~	~~890~~	~~1.44~~	~~38.14 ± 0.46~~	~~0.0541 ± 0.0017~~	~~167 ± 1~~					Yes
105.1	64	57	0.94	5.07 ± 0.10	0.0803 ± 0.0016	1186 ± 20	1186 ± 40		2.2%		

| | | |

Labels	U (ppm)	Th (ppm	Th/U	$^{238}U/^{206}Pb*$	$^{207}Pb/^{206}Pb*$	age $^{206}Pb/^{238}U*$	age $^{207}Pb/^{206}Pb*$	% conc	Rejected
16NI13 (W67) - volcaniclastic									
1.1	92	38	0.42	63.17 ± 1.10	0.0485 ± 0.0029	101 ± 1			
2.1	46	52	1.12	5.12 ± 0.06	0.0787 ± 0.0016	1148 ± 20	1148 ± 40	-0.2%	
3.1	205	160	0.78	60.53 ± 0.66	0.0496 ± 0.0018	106 ± 1			
4.1	316	159	0.49	57.90 ± 1.10	0.0520 ± 0.0031	110 ± 1			
5.1	111	65	0.59	39.28 ± 0.52	0.0496 ± 0.0019	162 ± 1			
6.1	630	153	0.22	39.51 ± 0.36	0.0505 ± 0.0009	161 ± 1			
7.1	136	87	0.64	59.88 ± 1.00	0.0483 ± 0.0023	107 ± 1			
8.1	818	643	0.78	3.17 ± 0.09	0.1070 ± 0.0013	1749 ± 11	1749 ± 22	-1.0%	
9.1	139	127	0.92	63.53 ± 0.81	0.0473 ± 0.0023	101 ± 1			
10.1	214	134	0.62	64.14 ± 0.69	0.0487 ± 0.0018	100 ± 1			
11.1	140	65	0.46	39.45 ± 0.59	0.0492 ± 0.0020	161 ± 1			
12.1	195	54	0.28	3.87 ± 0.06	0.0911 ± 0.0014	1447 ± 15	1447 ± 29	-2.5%	
~~13.1~~	~~131~~	~~78~~	~~0.60~~	~~40.82 ± 1.80~~	~~0.1950 ± 0.0120~~	~~156 ± 4~~	~~2740 ± 110~~	~~94.3%~~	Yes
~~14.1~~	~~236~~	~~301~~	~~1.30~~	~~10.60 ± 0.13~~	~~0.0628 ± 0.0017~~	~~581 ± 4~~			Yes
15.1	233	339	1.44	56.05 ± 1.10	0.0514 ± 0.0031	114 ± 1			
16.1	74	41	0.52	64.72 ± 1.40	0.0500 ± 0.0031	99 ± 1			
17.1	100	65	0.66	61.46 ± 1.20	0.0486 ± 0.0026	104 ± 1			
~~18.1~~	~~131~~	~~91~~	~~0.71~~	~~58.75 ± 0.85~~	~~0.0593 ± 0.0025~~	~~109 ± 1~~			Yes
19.1	218	187	0.75	62.11 ± 0.70	0.0484 ± 0.0021	103 ± 1			
20.1	177	96	0.55	10.49 ± 0.10	0.0601 ± 0.0011	587 ± 3			
21.1	338	323	0.96	3.06 ± 0.05	0.1130 ± 0.0008	1848 ± 6	1848 ± 12	1.2%	
22.1	270	187	0.71	62.15 ± 0.59	0.0492 ± 0.0017	103 ± 0			
23.1	278	241	0.89	60.39 ± 0.85	0.0503 ± 0.0017	106 ± 1			
24.1	304	282	0.95	59.95 ± 0.74	0.0489 ± 0.0013	107 ± 1			
25.1	179	149	0.84	59.45 ± 0.76	0.0485 ± 0.0019	108 ± 1			
26.1	149	136	0.93	60.39 ± 0.85	0.0516 ± 0.0025	106 ± 1			
~~27.1~~	~~308~~	~~352~~	~~1.18~~	~~61.35 ± 0.65~~	~~0.0608 ± 0.0020~~	~~104 ± 1~~			Yes
28.1	718	530	0.74	59.52 ± 0.57	0.0486 ± 0.0010	107 ± 0			
29.1	507	656	1.33	61.69 ± 0.56	0.0488 ± 0.0012	104 ± 0			
30.1	284	241	0.85	61.96 ± 0.67	0.0490 ± 0.0016	103 ± 1			
~~31.1~~	~~196~~	~~176~~	~~0.91~~	~~39.46 ± 0.78~~	~~0.0535 ± 0.0021~~	~~161 ± 2~~			Yes
32.1	42	98	2.37	5.12 ± 0.13	0.0800 ± 0.0016	1184 ± 20	1184 ± 40	3.0%	
33.1	158	146	0.95	60.68 ± 0.88	0.0503 ± 0.0020	105 ± 1			
34.1	157	115	0.76	38.74 ± 0.48	0.0487 ± 0.0017	164 ± 1			
35.1	276	157	0.58	38.74 ± 0.35	0.0489 ± 0.0013	164 ± 1			

36.1	168	172	1.05	60.24 ± 0.85	0.0488 ± 0.0021	106 ± 1					
37.1	154	105	0.69	59.92 ± 0.83	0.0506 ± 0.0039	107 ± 1					
38.1	145	81	0.56	66.40 ± 1.10	0.0506 ± 0.0025	96 ± 1					
39.1	106	67	0.64	59.63 ± 0.88	0.0492 ± 0.0028	107 ± 1					
40.1	146	131	0.91	60.06 ± 1.30	0.0487 ± 0.0022	106 ± 1					
41.1	643	343	0.55	28.64 ± 0.25	0.0504 ± 0.0008	221 ± 1					
~~42.1~~	~~220~~	~~387~~	~~1.63~~	~~39.32 ± 0.68~~	~~0.0603 ± 0.0018~~	~~162 ± 1~~					Yes
43.1	115	103	0.91	59.03 ± 0.82	0.0496 ± 0.0021	108 ± 1					
~~44.1~~	~~171~~	~~152~~	~~0.88~~	~~61.43 ± 1.20~~	~~0.0946 ± 0.0058~~	~~104 ± 1~~	~~1410 ± 130~~		~~92.6%~~		Yes
~~45.1~~	~~331~~	~~243~~	~~0.75~~	~~41.75 ± 0.42~~	~~0.0536 ± 0.0016~~	~~153 ± 1~~					Yes
~~46.1~~	~~106~~	~~229~~	~~1.54~~	~~5.14 ± 0.09~~	~~0.0946 ± 0.0015~~	~~1510 ± 16~~	~~1510 ± 31~~		~~24.1%~~		Yes
47.1	155	138	0.91	62.93 ± 0.80	0.0497 ± 0.0026	102 ± 1					
48.1	269	261	0.99	59.92 ± 0.69	0.0479 ± 0.0017	107 ± 1					
49.1	350	387	1.13	62.54 ± 0.60	0.0483 ± 0.0013	102 ± 0					
50.1	179	133	0.75	61.58 ± 0.65	0.0500 ± 0.0021	104 ± 1					
51.1	180	174	0.98	64.72 ± 0.87	0.0492 ± 0.0021	99 ± 1					
52.1	304	305	1.00	63.41 ± 0.64	0.0496 ± 0.0015	101 ± 1					
53.1	167	112	0.68	39.65 ± 0.56	0.0524 ± 0.0024	161 ± 1					
54.1	80	39	0.50	62.74 ± 0.89	0.0479 ± 0.0028	102 ± 1					
55.1	124	59	0.48	55.13 ± 1.40	0.0535 ± 0.0045	116 ± 2					
56.1	125	125	1.01	62.81 ± 0.93	0.0491 ± 0.0026	102 ± 1					
57.1	201	139	0.70	62.03 ± 0.83	0.0515 ± 0.0052	103 ± 1					
58.1	457	614	1.37	64.27 ± 0.73	0.0485 ± 0.0015	100 ± 1					
~~59.1~~	~~74~~	~~69~~	~~0.95~~	~~68.54 ± 1.50~~	~~0.0536 ± 0.0037~~	~~93 ± 1~~					Yes
60.1	166	166	1.01	43.54 ± 0.78	0.0499 ± 0.0023	146 ± 1					
61.1	424	455	1.09	64.64 ± 0.59	0.0489 ± 0.0015	99 ± 0					
62.1	354	381	1.06	65.62 ± 0.68	0.0487 ± 0.0018	98 ± 1					
63.1	88	35	0.40	5.87 ± 0.05	0.0737 ± 0.0012	1023 ± 16	1023 ± 32		0.9%		
64.1	184	156	0.85	61.27 ± 1.30	0.0532 ± 0.0042	104 ± 1					
65.1	158	128	0.81	64.43 ± 1.80	0.0508 ± 0.0044	99 ± 1					
~~66.1~~	~~438~~	~~441~~	~~1.01~~	~~60.24 ± 1.10~~	~~0.0544 ± 0.0022~~	~~106 ± 1~~					Yes
67.1	469	555	1.19	64.27 ± 0.61	0.0490 ± 0.0017	100 ± 0					

Labels	U (ppm)	Th (ppm	Th/U	$^{238}U/^{206}Pb^*$	$^{207}Pb/^{206}Pb^*$	age $^{206}Pb/^{238}U^*$	age $^{207}Pb/^{206}Pb^*$	% conc	Rejected
16NI16 (W67) - volcaniclastic									
1.1	316	274	0.85	38.82 ± 0.45	0.0501 ± 0.0013	164 ± 1			
2.1	36	12	0.33	68.54 ± 1.70	0.0502 ± 0.0045	93 ± 1			
3.1	74	36	0.48	69.30 ± 1.40	0.0497 ± 0.0040	92 ± 1			
4.1	27	13	0.47	5.09 ± 0.08	0.0778 ± 0.0019	1131 ± 24	1131 ± 48	-2.2%	
5.1	102	46	0.46	71.58 ± 1.10	0.0493 ± 0.0028	89 ± 1			
6.1	103	54	0.52	73.37 ± 1.20	0.0479 ± 0.0027	87 ± 1			
7.1	65	60	0.92	69.54 ± 1.50	0.0502 ± 0.0043	92 ± 1			
8.1	60	38	0.60	71.84 ± 1.40	0.0481 ± 0.0035	89 ± 1			
9.1	62	26	0.42	68.68 ± 1.50	0.0522 ± 0.0034	93 ± 1			
10.1	300	53	0.17	6.21 ± 0.09	0.0712 ± 0.0006	963 ± 7			
11.1	263	264	0.97	75.93 ± 0.89	0.0491 ± 0.0020	84 ± 0			
12.1	98	71	0.71	69.59 ± 1.20	0.0493 ± 0.0030	92 ± 1			
13.1	141	83	0.59	37.97 ± 0.60	0.0509 ± 0.0020	168 ± 2			
14.1	150	106	0.71	72.89 ± 0.95	0.0498 ± 0.0025	88 ± 1			
15.1	86	33	0.35	70.92 ± 1.40	0.0504 ± 0.0033	90 ± 1			
16.1	95	41	0.43	68.82 ± 1.30	0.0497 ± 0.0030	93 ± 1			
17.1	67	32	0.47	38.34 ± 0.48	0.0490 ± 0.0025	166 ± 1			
18.1	92	48	0.52	69.69 ± 1.50	0.0475 ± 0.0032	92 ± 1			
19.1	530	252	0.44	66.76 ± 0.48	0.0480 ± 0.0011	96 ± 0			
20.1	42	28	0.65	71.94 ± 1.90	0.0520 ± 0.0046	89 ± 1			
21.1	97	70	0.72	71.33 ± 2.10	0.0507 ± 0.0048	90 ± 1			
22.1	649	599	0.88	74.46 ± 0.89	0.0479 ± 0.0012	86 ± 1			
~~23.1~~	~~56~~	~~38~~	~~0.62~~	~~70.72 ± 1.70~~	~~0.1050 ± 0.0100~~	~~91 ± 1~~	~~1340 ± 200~~	~~93.2%~~	Yes
24.1	194	261	1.01	77.10 ± 2.00	0.0503 ± 0.0038	83 ± 1			
25.1	48	32	0.66	73.42 ± 1.80	0.0544 ± 0.0051	87 ± 1			
26.1	260	172	0.65	75.19 ± 0.85	0.0473 ± 0.0017	85 ± 0			
27.1	162	118	0.72	76.34 ± 1.10	0.0469 ± 0.0023	84 ± 1			
28.1	279	116	0.42	10.06 ± 0.08	0.0603 ± 0.0008	611 ± 2			
29.1	195	120	0.60	38.99 ± 0.44	0.0509 ± 0.0017	163 ± 1			
30.1	121	48	0.39	69.69 ± 1.10	0.0499 ± 0.0028	92 ± 1			
31.1	199	112	0.55	72.99 ± 0.98	0.0481 ± 0.0021	88 ± 1			
32.1	199	181	0.87	37.85 ± 0.42	0.0490 ± 0.0014	168 ± 1			
33.1	56	27	0.47	74.52 ± 2.60	0.0477 ± 0.0069	86 ± 1			
34.1	255	169	0.66	39.65 ± 0.45	0.0504 ± 0.0017	161 ± 1			
~~35.1~~	~~65~~	~~42~~	~~0.64~~	~~71.17 ± 2.40~~	~~0.0627 ± 0.0054~~	~~90 ± 1~~			Yes

36.1	64	27	0.43	63.09 ± 1.30	0.0483 ± 0.0035	101 ± 1						
~~37.1~~	~~86~~	~~33~~	~~0.37~~	~~68.17 ± 1.20~~	~~0.0545 ± 0.0038~~	~~94 ± 1~~						Yes
38.1	107	78	0.69	75.76 ± 1.40	0.0497 ± 0.0026	85 ± 1						
39.1	84	81	0.96	74.85 ± 1.50	0.0454 ± 0.0033	86 ± 1						
40.1	357	295	0.82	73.64 ± 0.72	0.0475 ± 0.0015	87 ± 0						
41.1	59	41	0.69	41.81 ± 1.20	0.0542 ± 0.0052	152 ± 2						
42.1	241	176	0.74	9.81 ± 0.08	0.0605 ± 0.0008	625 ± 2						
43.1	40	27	0.68	73.42 ± 1.90	0.0510 ± 0.0051	87 ± 1						
~~44.1~~	~~60~~	~~49~~	~~0.81~~	~~73.31 ± 1.60~~	~~0.0566 ± 0.0043~~	~~87 ± 1~~						Yes
45.1	184	271	1.47	75.99 ± 1.00	0.0481 ± 0.0021	84 ± 1						
46.1	206	130	0.64	26.18 ± 0.26	0.0510 ± 0.0014	242 ± 1						
47.1	113	98	0.85	73.10 ± 1.20	0.0490 ± 0.0027	88 ± 1						
48.1	73	29	0.40	67.11 ± 1.10	0.0471 ± 0.0034	95 ± 1						
49.1	323	380	1.16	74.24 ± 0.95	0.0472 ± 0.0018	86 ± 1						
50.1	109	46	0.43	68.63 ± 1.20	0.0464 ± 0.0029	93 ± 1						
51.1	203	188	0.91	77.28 ± 1.10	0.0501 ± 0.0024	83 ± 1						
~~52.1~~	~~157~~	~~232~~	~~1.17~~	~~35.61 ± 0.44~~	~~0.0718 ± 0.0030~~	~~179 ± 1~~						Yes
53.1	68	24	0.36	71.53 ± 3.20	0.0488 ± 0.0093	90 ± 2						
54.1	288	169	0.57	74.02 ± 0.88	0.0475 ± 0.0018	87 ± 1						
55.1	56	40	0.72	70.57 ± 2.40	0.0553 ± 0.0077	91 ± 1						
56.1	148	75	0.51	67.43 ± 0.98	0.0481 ± 0.0026	95 ± 1						
~~57.1~~	~~92~~	~~51~~	~~0.55~~	~~69.59 ± 1.20~~	~~0.0536 ± 0.0036~~	~~92 ± 1~~						Yes
58.1	150	110	0.71	75.47 ± 1.10	0.0485 ± 0.0029	85 ± 1						
~~59.1~~	~~65~~	~~58~~	~~0.89~~	~~47.46 ± 1.30~~	~~0.1110 ± 0.0120~~	~~134 ± 2~~	~~1570 ± 190~~		~~91.4%~~			Yes
60.1	169	138	0.82	54.64 ± 0.87	0.0506 ± 0.0032	117 ± 1						
~~61.1~~	~~118~~	~~104~~	~~0.86~~	~~42.59 ± 0.86~~	~~0.2216 ± 0.0095~~	~~150 ± 2~~	~~2937 ± 69~~		~~94.9%~~			Yes
62.1	75	37	0.48	67.02 ± 1.50	0.0490 ± 0.0039	96 ± 1						
63.1	172	71	0.40	10.82 ± 0.08	0.0588 ± 0.0011	570 ± 2						
64.1	218	174	0.78	73.31 ± 1.00	0.0488 ± 0.0022	87 ± 1						
65.1	203	99	0.46	3.38 ± 0.03	0.1030 ± 0.0008	1677 ± 8	1677 ± 15		0.4%			
66.1	157	69	0.43	66.05 ± 1.40	0.0519 ± 0.0042	97 ± 1						
67.1	166	89	0.48	69.69 ± 1.00	0.0497 ± 0.0026	92 ± 1						
~~68.1~~	~~152~~	~~93~~	~~0.55~~	~~67.66 ± 1.70~~	~~0.0562 ± 0.0036~~	~~95 ± 1~~						Yes
69.1	152	62	0.38	68.26 ± 1.20	0.0494 ± 0.0026	94 ± 1						
~~70.1~~	~~292~~	~~189~~	~~0.60~~	~~67.52 ± 0.89~~	~~0.0507 ± 0.0021~~	~~95 ± 1~~						Yes

71.1	85	62	0.70	75.47 ± 1.50	0.0520 ± 0.0039	85 ± 1						
~~72.1~~	~~126~~	~~89~~	~~0.67~~	~~55.10 ± 0.83~~	~~0.0555 ± 0.0028~~	~~116 ± 1~~						Yes
~~73.1~~	~~615~~	~~384~~	~~0.60~~	~~39.23 ± 0.40~~	~~0.0509 ± 0.0011~~	~~162 ± 1~~						Yes
74.1	237	150	0.61	78.74 ± 1.10	0.0478 ± 0.0020	81 ± 1						
~~75.1~~	~~145~~	~~62~~	~~0.41~~	~~54.14 ± 1.80~~	~~0.2460 ± 0.0150~~	~~118 ± 2~~	~~3072 ± 93~~		~~96.2%~~			Yes
~~76.1~~	~~130~~	~~73~~	~~0.54~~	~~11.90 ± 0.17~~	~~0.0610 ± 0.0016~~	~~520 ± 3~~						Yes
77.1	457	552	1.02	54.82 ± 0.81	0.0497 ± 0.0016	117 ± 1						
~~78.1~~	~~442~~	~~459~~	~~0.99~~	~~40.24 ± 0.41~~	~~0.0516 ± 0.0014~~	~~158 ± 1~~						Yes
79.1	61	58	0.90	75.76 ± 2.60	0.0525 ± 0.0066	85 ± 1						
80.1	143	154	1.03	4.99 ± 0.05	0.0777 ± 0.0014	1131 ± 18	1131 ± 35		-4.2%			
~~81.1~~	~~118~~	~~118~~	~~0.94~~	~~47.33 ± 1.10~~	~~0.3640 ± 0.0130~~	~~135 ± 2~~	~~3751 ± 56~~		~~96.4%~~			Yes
~~82.1~~	~~38~~	~~14~~	~~0.34~~	~~69.49 ± 2.10~~	~~0.0703 ± 0.0080~~	~~92 ± 1~~						Yes
~~83.1~~	~~240~~	~~151~~	~~0.60~~	~~74.79 ± 1.00~~	~~0.0521 ± 0.0029~~	~~86 ± 1~~						Yes
~~84.1~~	~~114~~	~~48~~	~~0.41~~	~~64.43 ± 1.40~~	~~0.0810 ± 0.0110~~	~~99 ± 1~~						Yes
~~85.1~~	~~334~~	~~206~~	~~0.58~~	~~63.41 ± 1.10~~	~~0.1310 ± 0.0067~~	~~101 ± 1~~	~~2074 ± 83~~		~~95.1%~~			Yes
86.1	107	57	0.51	39.53 ± 0.64	0.0522 ± 0.0026	161 ± 1						
87.1	195	504	2.47	7.58 ± 0.07	0.0658 ± 0.0010	799 ± 3						
~~88.1~~	~~247~~	~~144~~	~~0.54~~	~~72.94 ± 1.30~~	~~0.0674 ± 0.0034~~	~~88 ± 1~~						Yes

Notes:

All analytical errors are given a 1σ.

Concordance and $^{207}Pb/^{206}Pb$ ages only given for >1000 Ma old sites.

Samples highlighted in red strikethrough have been rejected and therefore excluded from age calculations.

*Corrected for common Pb using measured ^{204}Pb and Cumming and Richards (1975) common Pb composition for likely age of rock.

Table S4.5 Detrital zircon U-Pb results using SHRIMP (Chapter 4)

Labels	Site	U/ppm	Th/ppm	Th/U	f206%	$^{238}U/^{206}Pb*$			$^{207}Pb/^{206}Pb*$			age $^{206}Pb/^{238}U*$			age $^{207}Pb/^{206}Pb*$			%conc	Rejected?
15ND02 (W55) - volcaniclastic																			
1.1	r, m, osc	545	657	1.21	0.48	65.03	±	1.04	0.045	±	0.0044	99	±	2	-	-		-	
2.1	f, e, osc	170	93	0.55	0.97	68.53	±	1.30	0.041	±	0.0107	94	±	2	-	-		-	
3.1	r, m, h	71	43	0.61	4.66	68.75	±	1.60	0.014	±	0.0352	96	±	2	-	-		-	
4.1	r, m, h	173	193	1.12	1.56	64.59	±	1.21	0.034	±	0.0129	101	±	2	-	-		-	
5.1	f, e, osc	148	79	0.53	0.62	65.34	±	1.25	0.049	±	0.0095	98	±	2	-	-		-	
6.1	r, e, osc	195	113	0.58	0.85	68.31	±	1.32	0.042	±	0.0094	94	±	2	-	-		-	
7.1	p, e, osc	234	214	0.92	0	61.76	±	2.70	0.052	±	0.0057	103	±	4	-	-		-	
8.1	r, m, osc	138	66	0.48	0.4	67.02	±	1.31	0.045	±	0.0083	96	±	2	-	-		-	
9.1	r, m, osc	25	9	0.38	10.7	73.56	±	2.36	-0.042	±	0.091	95	±	3	-	-		-	
10.1	f, e, osc	109	57	0.52	0.75	65.47	±	1.37	0.053	±	0.0118	97	±	2	-	-		-	
~~11.1~~	r, e, osc	~~83~~	~~39~~	~~0.46~~	~~1.31~~	~~66.80~~	~~±~~	~~NaN~~	~~0.036~~	~~±~~	~~NaN~~	~~97~~	~~±~~	~~2~~	-	-		-	Yes
12.1	f, m, osc	77	34	0.45	3.81	68.30	±	1.47	0.02	±	0.0299	96	±	2	-	-		-	
13.1	f, e, osc	86	38	0.44	4.7	70.21	±	1.54	0.003	±	0.032	96	±	2	-	-		-	
14.1	r, e, osc	76	25	0.33	0	66.11	±	1.57	0.048	±	0.0053	97	±	2	-	-		-	
15.1	f, m, osc	992	885	0.89	0.14	61.85	±	0.96	0.047	±	0.0021	104	±	2	-	-		-	
16.1	f, m, osc	98	52	0.53	1.03	68.62	±	1.53	0.038	±	0.0147	94	±	2	-	-		-	
17.1	r, m, h	29	16	0.56	25.32	80.98	±	2.65	-0.131	±	0.133	94	±	3	-	-		-	
18.1	f, m, osc	180	206	1.14	1.08	65.00	±	1.20	0.041	±	0.0109	99	±	2	-	-		-	
19.1	f, m, osc	172	102	0.60	0	66.97	±	1.30	0.056	±	0.0037	95	±	2	-	-		-	
20.1	p, m, osc	1266	1247	0.99	0.18	62.99	±	0.97	0.049	±	0.002	101	±	2	-	-		-	
21.1	p, m, osc	145	89	0.61	0	66.21	±	1.28	0.052	±	0.004	96	±	2	-	-		-	
22.1	f, m, osc	104	59	0.57	1.14	68.94	±	2.02	0.039	±	0.018	94	±	3	-	-		-	
23.1	r, m, osc	89	61	0.68	0.38	39.26	±	0.76	0.047	±	0.0079	163	±	3	-	-		-	
24.1	f, e, osc	149	67	0.45	1.39	58.70	±	1.23	0.036	±	0.2174	110	±	2	-	-		-	
25.1	f, e, osc	353	609	1.73	0.03	5.08	±	0.08	0.078	±	0.001	1158	±	16	1150	±	24	-0.69	

Labels	Site	U/ppm	Th/ppm	Th/U	f206%	$^{238}U/^{206}Pb^*$			$^{207}Pb/^{206}Pb^*$			age $^{206}Pb/^{238}U^*$			age $^{207}Pb/^{206}Pb^*$			%conc	Rejected?
15ND03 (W55) - volcaniclastic																			
1.1	r, m, osc	292	132	0.45	0.04	5.22	±	0.08	0.08	±	0.0011	1127	±	16	1186	±	27	4.69	
2.1	f, e, osc	118	17	0.14	0.25	5.62	±	0.09	0.073	±	0.0024	1057	±	15	1024	±	65	-3.13	
3.1	f, m, osc	84	33	0.39	7.27	71.74	±	1.50	0.017	±	0.0405	92	±	2	-		-	-	
4.1	r, m, osc	189	115	0.61	1.88	69.14	±	1.29	0.034	±	0.0362	94	±	2	-		-	-	
5.1	p, e, osc	107	45	0.43	1.48	68.81	±	1.46	0.045	±	0.0168	93	±	2	-		-	-	
6.1	r, m, osc	109	53	0.49	1	67.70	±	1.39	0.047	±	0.0137	95	±	2	-		-	-	
7.1	r, m, osc	142	48	0.34	0	11.50	±	0.18	0.058	±	0.0018	538	±	8	-		-	-	
8.1	r, m, osc	56	27	0.48	4.68	70.95	±	1.78	0.013	±	0.0405	94	±	2	-		-	-	
9.1	f, e, osc	169	77	0.46	0	69.33	±	1.32	0.049	±	0.0036	92	±	2	-		-	-	
10.1	f, e, osc	295	185	0.63	0.09	11.27	±	0.17	0.058	±	0.0015	548	±	8	-		-	-	
11.1	f, e, osc	334	192	0.58	0	2.92	±	0.04	0.124	±	0.0009	1881	±	24	2012	±	13	5.74	
12.1	r, m, osc	166	62	0.37	1.88	70.17	±	1.38	0.036	±	0.0413	92	±	2	-		-	-	
13.1	f, m, h	146	122	0.83	0.03	3.70	±	0.06	0.097	±	0.0014	1538	±	21	1576	±	26	2.22	
~~14.1~~	~~r, m, h~~	~~83~~	~~88~~	~~1.06~~	~~0.29~~	~~7.15~~	~~±~~	~~NaN~~	~~0.067~~	~~±~~	~~NaN~~	~~844~~	~~±~~	~~13~~	-		-	-	Yes
15.1	r, e, h	95	162	1.71	0.2	11.02	±	0.18	0.06	±	0.004	559	±	9	-		-	-	
16.1	r, m, osc	71	29	0.41	0.29	6.51	±	0.11	0.071	±	0.0034	920	±	14	945.5	±	96	2.62	
17.1	r, e, h	163	111	0.68	0.02	4.84	±	0.07	0.082	±	0.0014	1208	±	17	1249		32	3.09	
18.1	f, e, osc	173	89	0.52	0.54	70.02	±	1.38	0.047	±	0.0084	92	±	2	-		-	-	
19.1	f, e, osc	123	32	0.26	0	5.37	±	0.08	0.079	±	0.0015	1098	±	16	1159	±	38	5.02	
20.1	p, m, h	519	253	0.49	0.2	27.10	±	0.42	0.05	±	0.0088	234	±	4	-		-	-	
21.1	r, e, h	352	221	0.63	0.47	41.27	±	0.64	0.046	±	0.004	155	±	2	-		-	-	
22.1	p, e, osc	215	177	0.82	0.43	66.56	±	1.16	0.046	±	0.0066	96	±	2	-		-	-	
23.1	f, e, osc	315	346	1.10	0.43	41.92	±	0.68	0.046	±	0.0043	153	±	2	-		-	-	
24.1	f, e, osc	106	86	0.82	0.47	7.13	±	0.11	0.064	±	0.0061	849	±	13	750.7	±	190	-12.72	
25.1	f, e, osc	189	105	0.56	0	40.75	±	0.72	0.051	±	0.0027	156	±	3	-		-	-	

Notes:

Site grain type and analysis location: p=prism, rou=rounded by abrasion, f=fragment, e=end, m=middle. Site CL imagery: osc=oscillatory zoned, h=homogeneous, hd=homogeneous dark, low luminescence. All analytical errors are given a 1σ. Concordance and $^{207}Pb/^{206}Pb$ ages only given for >1000 Ma old sites.

*corrected for common Pb using measured ^{204}Pb and Cumming and Richards (1975) common Pb composition for likely age of rock.

F206% is the amount of ^{206}Pb modelled as non-radiogenic, based on measured ^{204}Pb.

Samples highlighted in red strikethrough have been rejected and therefore excluded from age calculations.

Comments for the rejected grains can be found online with the associated published paper (Walsh et al., 2019).

Chapter Five: The significance of Upper Jurassic felsic volcanic rocks within the incipient, intraoceanic Dras Arc, Ladakh, NW India

Jessica M.J. Walsh[1], Solomon Buckman[1], Allen P. Nutman[1], and Renjie Zhou[2]

[1]GeoQuEST Research Centre, School of Earth, Atmospheric and Life Sciences, University of Wollongong, Wollongong, NSW 2522, Australia.

[2]School of Earth and Environmental Sciences, The University of Queensland, Brisbane, QLD 4072, Australia.

Research highlights:

- Upper Jurassic U-Pb zircon ages for a felsic tuff (160 ± 3 Ma) and trachydacite (156 ± 1 Ma) within the Dras Volcanics in Ladakh, NW India represent the oldest reported ages from the poorly dated Dras Arc.
- These Upper Jurassic felsic volcanics represent a small volume of adakitic magmatism associated with arc initiation within a volcanic pile dominated by mafic volcanic rocks, typical of intraoceanic island arcs.
- The known lifespan of the Dras Arc is extended to about a 100 m.y. period between initiation around ~160 Ma and final collision with the northern margin of India during the Palaeocene between 60-50 Ma.

Key words:

Felsic volcanism, adakitic, intraoceanic, Dras Arc, Ladakh Himalaya

Citation:

Walsh, J. M., Buckman, S., Nutman, A. P., & Zhou, R. (2020). The significance of Upper Jurassic felsic volcanic rocks within the incipient, intraoceanic Dras Arc, Ladakh, NW Himalaya. *Gondwana Research, 90*, 199-219 [7 citations as of 5th February 2021; Google Scholar]. https://doi.org/10.1016/j.gr.2020.11.007

Foreword:

This chapter addresses the second objective of this project; '*to constrain the timing of initiation and early evolution of the Dras Arc using zircon U-Pb geochronology of extrusive (Dras Volcanics) and intrusive (Kargil Intrusives) magmatic episodes'*.

5.1 Abstract

The Dras Arc is an island arc terrane located along the Indus Suture within the Ladakh Himalaya. To the north it is juxtaposed against the Eurasian Ladakh Batholith and to the south it is thrust over the Lamayuru Complex and Indian passive margin. Establishing the timing of inception and final collision of the Dras Arc is imperative to reconstructions of the Neotethyan Ocean and timing of arc-continent collisions, prior to the terminal India-Eurasia continental collision. We describe and date felsic tuffs and adakitic felsic volcanic rock interbedded within the dominantly basaltic-andesitic Dras volcanic complex. These felsic volcanic units yield Upper Jurassic zircon U-Pb ages of 160 ± 3 and 156 ± 1 Ma respectively, making these the oldest reported units within the Dras Arc. We also report zircon U-Pb geochronologic and whole rock geochemical results for the Kargil Intrusives which intrudes the volcanic complex. Previous ages for the intrusives have been reproduced (102 ± 2 Ma and 101 ± 2 Ma), and a second, much younger phase (80 ± 1 Ma) has been identified as one of the youngest igneous phases within the Dras Arc. The presence of felsic, adakitic volcanism early in the evolution of the Dras Arc is consistent with the adolescent stages of island arc systems, in which dehydration melting of underplated arc or subducted oceanic crust generates small volumes of felsic magmas. Thus, the intraoceanic Dras Arc initiated in the Neotethyan Ocean during the Late Jurassic, much earlier than previously reported, and possibly was active right up to collision during the late Palaeocene between 60-50 Ma. It is likely that the Dras Arc developed together with the Spongtang Ophiolite-Spong Arc complex and the intraoceanic Zedong terrane of Tibet, before first colliding and accreting onto the passive margin of India, prior to the terminal continental collision (see below Graphical Abstract).

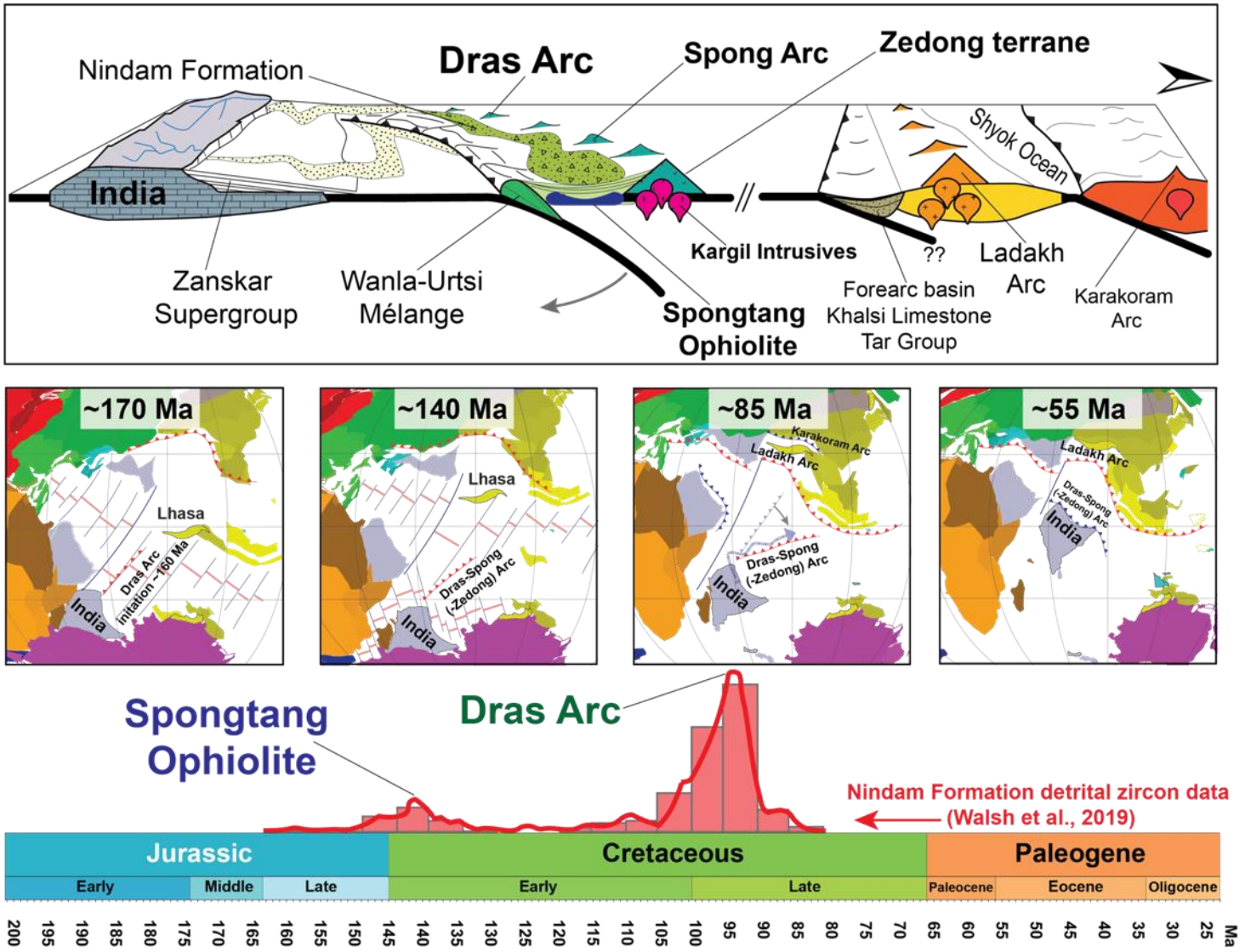

Graphical Abstract

5.2 Introduction

The Dras Arc of the Ladakh Himalaya, NW India, located along the Indus Suture, the western extent of the Indus-Yarlung-Tsangpo Suture (IYTS; Figure **5.1**A), is an island arc terrane sandwiched between the Indian and Eurasian continents. The origins and evolution of this unit have been central to ongoing debates over the nature and timing of closure of the Neotethyan Ocean and final continental collision to form the Himalaya (Bhat et al., 2019; Brookfield and Reynolds, 1981; Clift et al., 2000; Clift et al., 2002a; Clift et al., 2002b; Corfield et al., 2001; Frank, 1977; Honegger et al., 1982; Hu et al., 2016a; Klootwijk et al., 1984; Reuber, 1989; Robertson and Degnan, 1994; Rolland, 2002; Searle, 1983, 1986; Thakur, 1981; Walsh et al., 2019). Debate revolves around whether the Dras Arc developed as part of the southern Eurasian margin, namely the forearc basin to the Kohistan and/or Ladakh arcs, (Bouilhol et al., 2013; Burg, 2011), or as a separate intraoceanic island arc system that initiated in the Neotethyan Ocean (Buckman et al., 2018; Corfield et al., 2001; Coward et al., 1987; Walsh et al., 2019). See Figure **5.2**. It has also been suggested that the Dras Arc may be related to the intraoceanic Spongtang Ophiolite-Spong Arc complex (Buckman et al., 2018; Klootwijk et al., 1984; Walsh et al., 2019). Lack of age constraints has resulted in a poor understanding of the early history of inception and formation of the Dras Arc. Jurassic ages have not been recorded from Dras Arc terrane igneous rocks, although detrital zircon studies of the Nindam Formation, which is interpreted as sourced from the Spongtang Ophiolite and overlying Spong Arc system (Walsh et al., 2019), reveal a distinct Upper Jurassic to Cretaceous (135-185 Ma) zircon population.

We report Upper Jurassic ages of 160 ± 3 Ma and 156 ± 1 Ma for a felsic tuff and trachydacite, respectively, from the Dras Volcanics. The Kargil Intrusives intrudes the surrounding arc volcanic rocks and records magmatic pulses at ~103-101 Ma (Honegger et al., 1982; Schärer et al., 1984a) and ~82-70 Ma (Brookfield and Reynolds, 1981; Honegger et al., 1982). We reproduce ages for the Kargil Intrusives, including the first magmatic pulse (102 ± 2 Ma and 101 ± 2 Ma), but also report a younger pulse at 80 ± 1 Ma. These zircon U-Pb ages are combined with whole rock geochemistry to constrain better the early history of inception and formation of the Dras Arc within the Neotethyan Ocean. Key questions investigated here are: (i) when did the Dras Arc first initiate? (ii) where in the Neotethyan Ocean did it evolve? And (iii) what subduction system is this arc related to? Understanding the initiation of the Dras Arc from the Ladakh Himalaya, NW India provides crucial information for crustal growth of the Indian (Gondwanan) passive margin and dynamics of the Neotethyan Ocean prior to ocean consumption and collision of India with Eurasia.

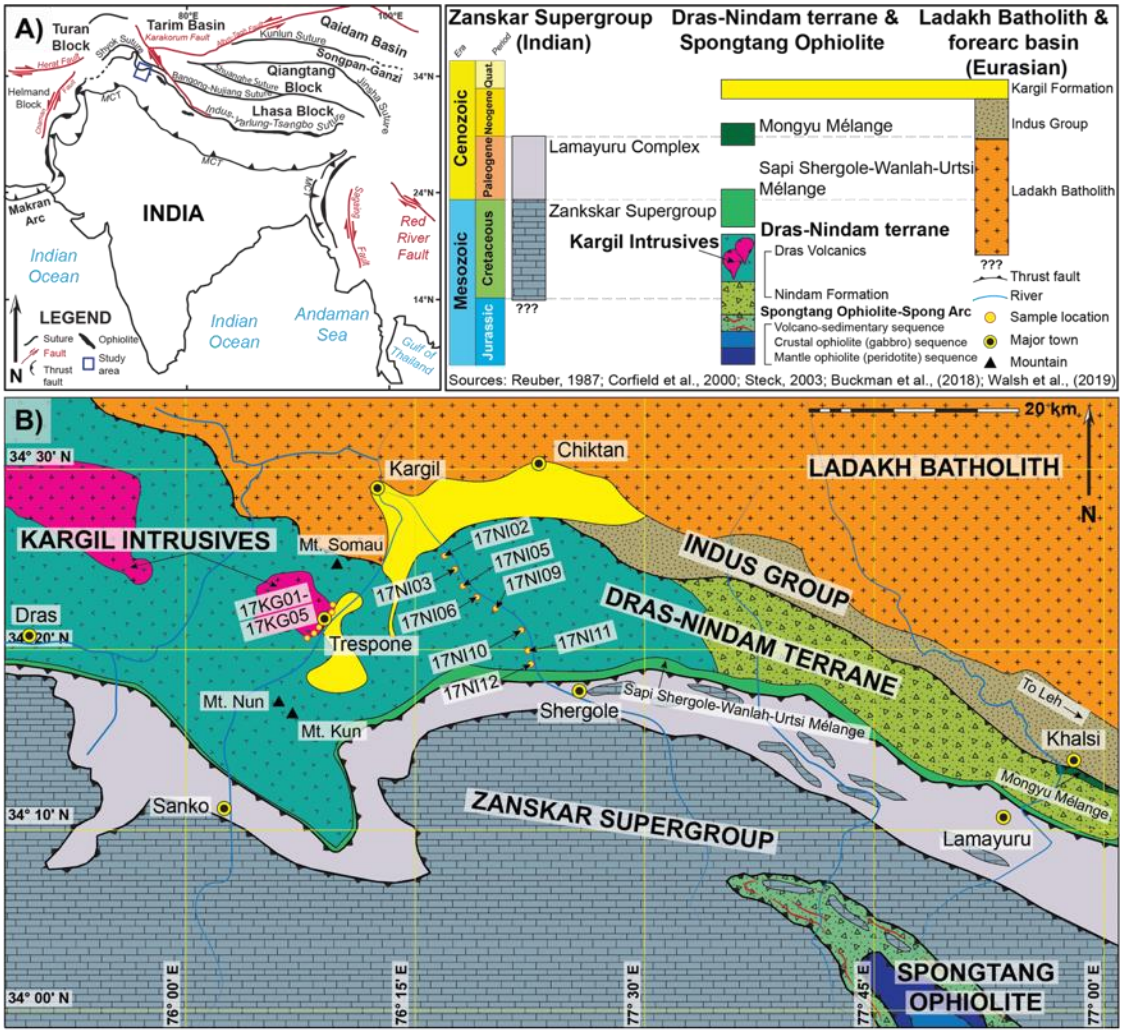

Figure 5.1: Regional tectonic setting of the Himalayan-Tibetan Orogen and regional geology map of the Dras-Nindam terrane, Ladakh, NW India. **A)** Regional tectonic setting of the Himalayan-Tibetan Orogen. The study area is shown with a rectangle. Modified after Buckman et al., (2018) and Walsh et al., (2019); **B)** Regional geology map of the Dras-Nindam terrane, Ladakh, NW India. Sample localities are shown. Modified after Reuber, (1989), Robertson and Degnan, (1994), Steck, (2003), Buckman et al., (2018) and Walsh et al., (2019).

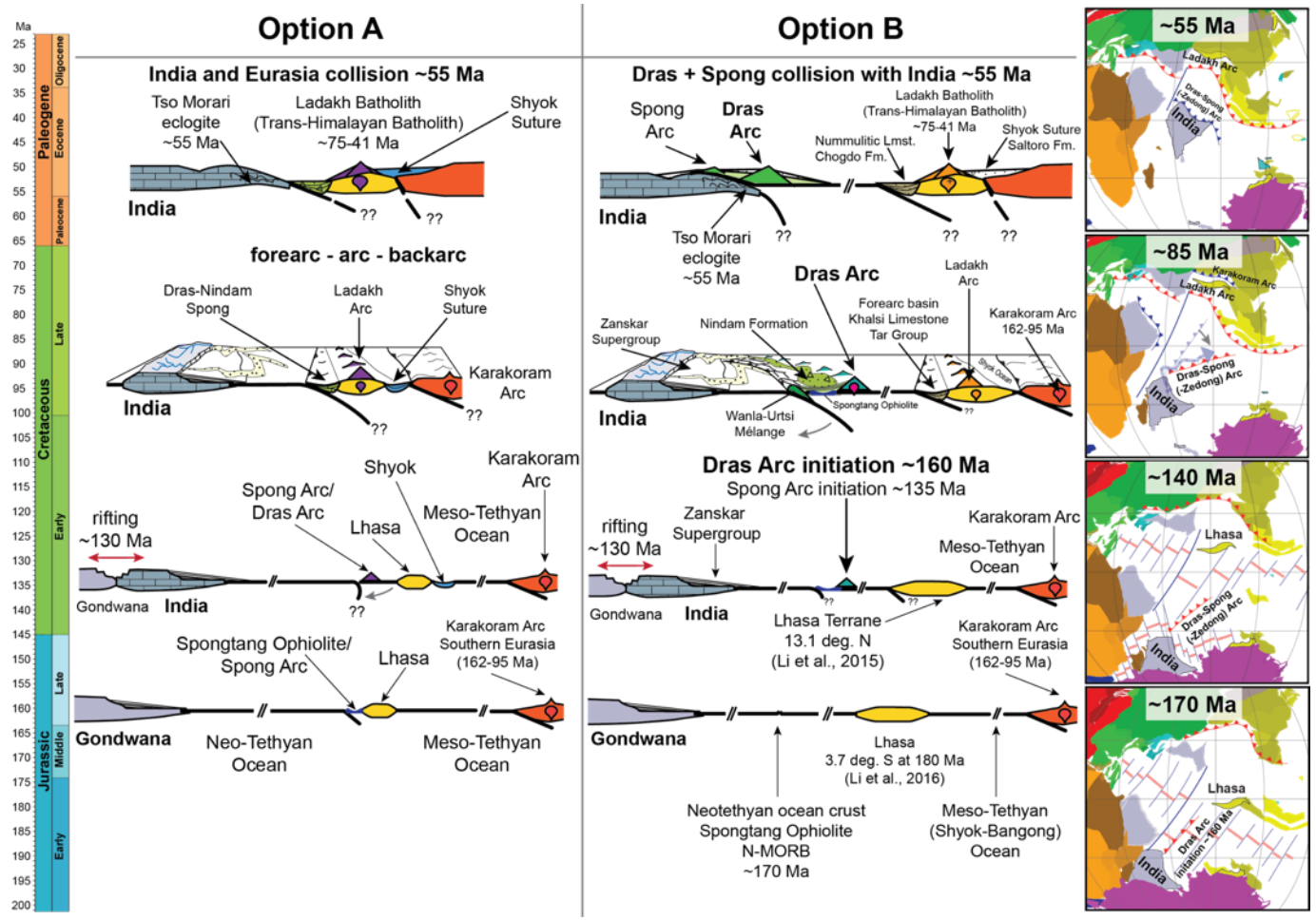

Figure 5.2: Geodynamic model of the Dras Arc. **A)** This interpretation has the Dras-Nindam complex as having evolved throughout the Jurassic to Cretaceous in a forearc region of a convergent margin on the southern margin of Eurasia (Fuchs, 1982; Honegger et al., 1982). This forearc basin developed on top of ophiolitic basement in front of the Ladakh Arc (Trans-Himalayan Batholith) as part of a single subduction complex responsible for the consumption of the entire Neotethyan Ocean, before the onset of the India-Eurasia continent-continent collision at about 55 Ma (Fuchs, 1982); **B)** Our interpretation showing the Dras Arc having evolved as an intraoceanic island arc system that developed as a result of subduction at ~160 Ma along a NNE-SSW transform fault in the Neotethyan Ocean (Buckman et al., 2018). This volcanic arc ophiolite collided with India at ~55 Ma at roughly equatorial latitude, while the Ladakh Batholith (Trans-Himalayan Batholith) developed closer to the southern margin of Eurasia before final continental collision.

5.3 Geological setting

The Dras-Nindam terrane of the Ladakh Himalaya, NW India, is located along the Indus Suture, the western extent of the Indus-Yarlung-Tsangpo Suture (IYTS; Figure **5.1**A). This terrane is dominated by basaltic-andesites of the Dras Volcanics in the west, and in the east the unit transitions into dominantly forearc volcaniclastic rocks of the Nindam Formation (Bhat et al., 2019; Clift et al., 2000; Clift et al., 2002b; Dietrich et al., 1983; Fuchs, 1982; Honegger et al., 1982; Reuber, 1989; Robertson and Degnan, 1994; Schärer et al., 1984a; Sharma et al., 1978; Walsh et al., 2019). To the north, the terrane is faulted against the Eurasian Ladakh Batholith and associated forearc basin material of the Tar Group (Henderson et al., 2010) and the post-collisional Indus Group. This thrust fault contact is marked by the serpentinite-matrix Mongyu Mélange (Robertson, 2000). To the south, the Dras-Nindam terrane is thrust over the Lamayuru Complex and Indian passive margin Zanskar Supergroup. Discontinuous slivers of ophiolitic mélanges occur along this southern contact, for example the Sapi-Shergole, Wanlah and Urtsi mélanges (Corfield and Searle, 2000; Groppo et al., 2016; Honegger et al., 1989; Robertson, 2000; Robertson and Degnan, 1994), for which there have been reports of rare high-pressure metamorphic rocks (e.g., blueschist; Honegger et al., 1982; Groppo et al., 2016). At the type-section near Dras township, the Dras Volcanics have been described as irregular basaltic to basaltic-andesite flows, intercalated with volcaniclastic rocks, pyroclastic material and radiolarite (Bhat et al., 2019; Honegger et al., 1982; Reuber, 1989). Minor dolerite sills and dykes are common, along with tuff layers and rare andesites. Radiometric K-Ar dating of amphiboles from the Dras Volcanics produced an age cluster between 105-95 Ma, with one exception from a fine-grained fraction which produced an age of 79 ± 3 Ma (Reuber et al., 1989). Sharma et al. (1978) also produced a younger K-Ar age of 78 ± 1 Ma for the Dras Volcanics, sampled from Chiktan township (~35 km ENE of Kargil; see Table **5.1** for radiometric dating of the Dras Volcanics). This sample was associated with the northern ophiolitic mélange zone, which may be comparable to the Mongyu Mélange farther to the east. It has been suggested that this younger age used for the Dras Volcanics could represent metamorphic overprint and is considered secondary, relating to deformation (Bhat et al., 2019; Reuber et al., 1989).

Although some radiometric dating has been acquired for the Dras Volcanics, the majority of the age constraints come from either cross-cutting and intrusive relationships of the gabbroic to granodioritic rocks from the Kargil Intrusives or intercalated fossiliferous sedimentary layers. Granodiorite from the Kargil Intrusives sampled near Kargil have zircon U-Pb multi-grain TIMS ages of 103 ± 3 Ma and 101 ± 2 Ma (Honegger et al., 1982; Schärer et al., 1984a). Reuber et al. (1989) dated a diorite pluton from this same suite, producing a biotite K-Ar age of 94 ± 3 Ma. However, this latter result has been interpreted as a cooling age, with the crystallisation age closer

to those ages produced by Honegger et al. (1982) and Schärer et al. (1984a), i.e., ~103 and ~101 Ma. However, Brookfield and Reynolds (1981) produced a younger age for the intrusive complex, with a syenite intruding the Dras Volcanics at Kargil producing a hornblende $^{40}Ar/^{39}Ar$ age of 82 ± 6 Ma. Honegger et al. (1982) also dated granodioritic intrusions near Mount Somau (~10 km SW of Kargil) producing K-Ar (biotite and white mica) ages of 75 ± 3 Ma and 70 ± 3 Ma (see Table **5.1** for radiometric dating of the Kargil Intrusives). Interbedded calcareous layers within the Dras Volcanics yielded Albian to Cenomanian (113-94 Ma) *Orbitolina* (Reuber et al., 1989) and an ammonite (*Oxytropidoceras*) reported from Kargil was proposed to be late Albian (Thieuloy et al., 1990). Sections of the Dras Volcanics are reportedly underlain by plutonic mafic cumulates and Middle-Upper Jurassic (Callovian-Tithonian; 166-145 Ma) radiolarian cherts (Honegger et al., 1982).

Upadhyay and Sinha (1998) were the first to suggest the forearc Nindam Formation received sediment not only from the Dras Arc, but also the leading passive margin of India. Following this work, palynological studies from the Nindam forearc basin produced Permian, Mesozoic and Palaeocene palynomorphs from volcaniclastic sandstones (Upadhyay et al., 2004). The Permian and Mesozoic palynomorphs were found to be of Gondwanan affinity and are suggested to be derived from the Indian passive margin (Upadhyay et al., 2004). Palynomorphs of Palaeocene age (~66-56 Ma) were also reported from the Nindam Formation and were assumed to be derived from nearby newly emerging, vegetated islands, comparable to the modern Andaman and Nicobar Islands of the Bay of Bengal (Upadhyay et al., 2004). This Palaeocene age is the youngest reported age for the Nindam Formation. Recent detrital zircon studies (Walsh et al., 2019) did not produce a population younger than ~84 Ma, however it should be noted that the youngest section of the Nindam Formation is faulted against the Mongyu Mélange thrust fault on the northern contact and thus the youngest portions are probably truncated and missing from this section (Walsh et al., 2019). Indeed, establishing the age of the youngest rocks within the Dras Arc is critical to constraining the timing of collision of this intraoceanic island arc with India but has yet to be established. This paper focusses on the oldest reported volcanic rocks within the Dras volcanic pile, which has implications as to the timing of initiation of intraoceanic subduction and island arc development.

Table 5.1: Published radiometric dating of the Dras Volcanics and Kargil Intrusives, Ladakh Himalaya, NW India.

Dras Volcanics						
Age (Ma)	Error (Ma)	Method	Mineral	Lithology	Comments	Reference
77.50	1.00	K-Ar	amphibole	volcanic rock	Sampled at Chiktan township (~35km ENE of Kargil), associated with the northern ophiolitic mélange zone (possibly comparable to the Mongyu Mélange).	Sharma et al. (1978)
78.50	2.90	K-Ar	green hornblende	porphyritic tuff	Sampled north of Thasgam (~20 km SW of Kargil), considered secondary and related to the deformation affecting the northern part of the Dras Volcanics (possibly comparable to the Mongyu Mélange).	Reuber et al. (1989)
95.80	2.80	K-Ar	green hornblende	porphyritic tuff	Commonly cited in literature as one of the samples that contribute to ages clustering between 105-95 Ma. Sampled north of Thasgam.	Reuber et al. (1989)
96.60	6.50	K-Ar	green hornblende	diabase dyke	Commonly cited in literature as one of the samples that contribute to ages clustering between 105-95 Ma. Sampled at Tringdo.	Reuber et al. (1989)
103.80	2.80	K-Ar	green hornblende	porphyritic tuff	Commonly cited in literature as one of the samples that contribute to ages clustering between 105-95 Ma. Sampled at Sanku.	Reuber et al. (1989)
156.46	1.26	U-Pb (LA-ICP-MS)	zircon	trachydacite	Sampled between Kargil and Shergole. Position: 34.42543°N, 76.28400°E. Sample 17NI12	**This study**
160.10	2.60	U-Pb (LA-ICP-MS and SHRIMP)	zircon	felsic tuff	Sampled between Kargil and Shergole. Position: 34.46116°N, 76.26436°E. Sample 17NI05.	**This study**

Kargil Intrusives

Age (Ma)	Error (Ma)	Method	Mineral	Lithology	Comments	Reference
69.80	3.20	K-Ar	white mica	granodiorite	Sampled near Mount Somau (~10 km SW of Kargil). Originally mapped as Ladakh Intrusives.	Honegger et al. (1982)
74.40	2.50	K-Ar	biotite	granodiorite	Sampled near Mount Somau (~10 km SW of Kargil). Originally mapped as Ladakh Intrusives.	Honegger et al. (1982)
80.25	1.18	U-Pb (LA-ICP-MS)	zircon	granodiorite	Sampled along the National Highway 301, following the Suru River between Kargil and Trespone. Position: 34.50611°N, 76.12524°E. Sample 17KG04.	**This study**
82.00	6.00	$^{40}Ar/^{39}Ar$	hornblende	syenite	Sampled near Kargil, intruding into the Dras Volcanics.	Brookfield and Reynolds, (1981)
94.40	2.70	K-Ar	biotite	diorite	Sampled south of Mount Somau. This age produced is assumed to be a cooling age, meaning crystallisation age is closer to those ages produced by Honegger et al., (1982) and Scharer et al., (1984).	Reuber et al. (1989)
100.65	1.54	U-Pb (LA-ICP-MS)	zircon	diorite	Sampled along the National Highway 301, following the Suru River between Kargil and Trespone. Position: 34.45593°N, 76.0702°E. Sample 17KG02.	**This study**
101.00	2.00	U-Pb (TIMS)	zircon	granodiorite	Sampled near Kargil, intruding into the Dras Volcanics.	Schärer et al. (1984a)
101.87	1.68	U-Pb (LA-ICP-MS)	zircon	granodiorite	Sampled along the National Highway 301, following the Suru River between Kargil and Trespone. Position: 34.45591°N, 76.07023°E. Sample 17KG01.	**This study**
102.80	3.20	U-Pb (TIMS)	zircon	granodiorite	Sampled near Kargil, intruding into the Dras Volcanics.	Honegger et al. (1982)

5.4 Methods

5.4.1 Field geology

Representative samples of the Dras Volcanics were targeted, which were collected across strike following the Srinagar-Leh National Highway 1 and Wakha River, between the city of Kargil and township of Shergole (Figure **5.1**B). Representative samples of the Kargil Intrusives were collected along the National Highway 301 following the Suru River, between the township of Trespone and city of Kargil (Figure **5.1**B), in order to test earlier dates for these intrusives (Brookfield and Reynolds, 1981; Honegger et al., 1982; Reuber et al., 1989; Schärer et al., 1984a).

5.4.2 Whole rock geochemistry

Five representative samples from the Kargil Intrusives and eight representative samples from the Dras Volcanics were crushed using a tungsten carbide TEMA ring mill. Major elements were determined by X-ray fluorescence (XRF), using a Spectro-analytical XEPOS XRF spectrometer at the University of Wollongong (UOW), Australia. Depending on elemental concentrations estimated in trace element analysis, different types of flux were used for the fused buttons (Norrish and Chappell, 1977). Pure metaborate was used for high silica samples, 35.3% tetraborate to 64.7% metaborate was used for mafic samples, and 57% tetraborate to 43% metaborate was used for ultramafic samples.

Trace and the rare-earth element (REE) analyses were undertaken at the Australian Laboratory Services (ALS) Minerals Division, Brisbane, Australia using ICP-MS. All samples from this study were analysed using the geochemical procedure code ME-MS81 (30-element package). Lithium metaborate and tetraborate were used as fluxes with and after fusing in a furnace with the resultant glass being dissolved in nitric, hydrochloric and hydrofluoric acid mixes. This solution was then analysed by ICP-MS. Standards OREAS 120 and STSD-1, as well as five sample duplicates and three blanks, were analysed in order to determine the error tolerance (analytical error ± 10%). Refer to Supporting Information Table S5.1 for description and locality of samples and Supporting Information Table S5.2 for whole rock major and trace element compositions of samples from the Dras Volcanics and Kargil Intrusives.

5.4.3 Zircon U-Pb geochronology

Refer to Supporting Information Text for details on zircon preparation and further method description for LA-ICP-MS and SHRIMP. Refer to Supporting Information Table S5.3 for zircon U-Pb results for the Dras Volcanics and Kargil Intrusives.

5.4.3.1 LA-ICP-MS

A total of 82 zircon grains were chosen from two samples from the Dras Volcanics (sample 17NI05: felsic tuff, *n* = 28; sample 17NI12: trachydacite, *n* = 54) and a total of 120 zircon grains were chosen from three samples from the Kargil Intrusives (sample 17KG01: granodiorite, *n* = 30; sample 17KG02: diorite, *n* = 30; sample 17KG04: granodiorite, *n* = 60) for U-Pb dating by Laser Ablation Inductively Coupled Plasma Mass Spectrometry (LA-ICP-MS) at Centre for Geoanalytical Mass Spectrometry (CGMS), The University of Queensland (UQ), Australia, following methods similar to those in Zhou et al., (2020). The zircon 91500, which has a $^{206}Pb/^{238}U$ age of 1062.4 ± 0.4 Ma and $^{206}Pb/^{207}Pb$ age of 1065.4 ± 0.3 Ma (Wiedenbeck et al., 1995), was used as the primary reference material. No common Pb correction on zircon 91500 was undertaken. TEMORA II was also employed as a secondary reference material, which has a $^{206}Pb/^{238}U$ age of 416.78 ± 0.33 Ma (Black et al., 2004). Reduction of raw data was accomplished using the program *IOLITE* (Paton et al., 2011). Calculated mean ages and mixture modelling results are presented at 2 σ. $^{206}Pb/^{238}U$ ages are reported for <1000 Ma grains. No grains produced ages >1000 Ma, however $^{207}Pb/^{206}Pb$ ages and ratios are reported to evaluate the level of common Pb, concordance and detect inheritance.

5.4.3.2 SHRIMP

A further six grains from the Dras Volcanics felsic tuff (sample 17NI05) were reanalysed along their margins using the Sensitive High-Resolution Ion Microprobe (Reverse Geometry; SHRIMP-RG) instrument at the Australian National University (ANU), Australia to double check the interpretations of Jurassic ages acquired by LA-ICP-MS. U-Th abundance was calibrated based on the reference zircon SL13 (U = 238 ppm). $^{206}Pb/^{238}U$ were corrected using the TEMORA II standard with a concordant age of 416.78 ± 0.33 Ma (Black et al., 2004). The raw data were reduced using the new ANU in-house program *POXI-SC*. Calculated mean ages and mixture modelling results are presented at 2 σ. $^{206}Pb/^{238}U$ ages are reported for <1000 Ma grains. No grains produced ages >1000 Ma.

5.5 Results

5.5.1 Dras Volcanics

5.5.1.1 Field geology

Representative samples of the Dras Volcanics were collected across strike following the Srinagar-Leh National Highway 1 and Wakha River, between the city of Kargil and township of

Shergole (Figure **5.1**B). Sample lithologies and localities are provided in Supporting Information Table S5.1. The Dras Volcanics along this section are predominantly composed of massive basaltic to basaltic-andesite flows, intercalated with minor volcaniclastic rocks, rare felsic volcanics and associated tuffs (Figure **5.3**). Individual lava flows were previously approximated to be 15-20 m thick, measured south of the township of Pashkum (Honegger et al., 1982). At the base of the Dras Volcanics pillow basalts (Honegger et al., 1982; Reibel and Juteau, 1981) and radiolarian cherts, occurring as interbedded layers within the volcanic rocks have been reported (Dietrich et al., 1983). In the vicinity of Kargil underlying the Dras Volcanics, subordinate gabbros have been described as representing relic magma chambers or the core to the Dras Arc (Honegger et al., 1982; Reuber, 1989). However, gabbroic blocks were only ever observed within the serpentinite mélange along the southern contact with the Lamayuru Complex which is also host to rare blueschist blocks (Groppo et al., 2016; Honegger et al., 1989). A suite of granodiorite-diorite-gabbro intrudes the Dras Volcanics at Kargil and are collectively referred to as the Kargil Intrusives or Kargil Intrusive Suite (Bhat et al., 2019; Dietrich et al., 1983; Honegger et al., 1982; Schärer et al., 1984a). The Dras Volcanics have undergone sub-greenschist alteration with chlorite and epidote. Farther east, where volcanic rocks transition into coeval volcaniclastic rocks of the Nindam Formation, the type-section for this unit is located between the townships of Lamayuru and Khalsi (Robertson and Degnan, 1994; Walsh et al., 2019).

5.5.1.2 Petrography

5.5.1.2.1 Basaltic andesites

The Dras Volcanics are dominated by vesicular basaltic andesites which are generally plagioclase- and augite-phyric and only affected by sub-greenschist facies metamorphism (Figure **5.4**A-C). Small plagioclase laths within a glassy groundmass often define trachytic flow textures around phenocrysts and vesicles (Figure **5.4**B, C). Phenocrysts of augite and plagioclase are abundant with some samples displaying glomerophyric textures (Figure **5.4**C). Fractures are commonly infilled by quartz and calcite, whereas vesicles are generally infilled with chlorite (Figure **5.4**A-C). Accessory minerals include ilmenite, magnetite, apatite, zircon, chromite and pyrite (see Supporting Information Table S5.2: CIPW normalisation).

5.5.1.2.2 Trachydacite

A porphyritic trachydacite (sample 17NI12) collected from the lowest observed stratigraphic level at the southern margin of the Dras Volcanics, contains rounded and partially altered plagioclase phenocrysts and glomerocrysts. These coarse but rounded glomerocrysts show signs

of resorption with the surrounding aphanitic, felsic groundmass suggesting they may have been in a state of disequilibrium during cooling and crystallisation (Figure **5.4**D-F). Euhedral hornblende phenocrysts show less rounding and less resorbtion with the surrounding matrix suggesting they crystallised in equilibrium with the surrounding felsic melt. (Figure **5.4**E, F). Anhedral blobs of quartz containing small zircon inclusions occur within the felsic groundmass along with minor biotite and albite. These were the last minerals to crystallise from this dacitic melt (Figure **5.4**E, F). Fractures are commonly green from alteration minerals (chlorite and epidote). Accessory minerals include diopside, ilmenite, magnetite and apatite.

5.5.1.2.3 Felsic tuff

The fine-grained, felsic tuff (sample 17NI05) displays well-defined, laminated and graded bedding between 0.1-2 cm thick, suggesting it settled through a deep-water environment (Figure **5.4**G, H). Small vitric fragments and plagioclase phenocrysts occur within a fine-grained, devitrified ash matrix (Figure **5.4**I). Cubes of diagenetic pyrite occur within the matrix and veinlets are filled with secondary calcite and quartz (Figure **5.4**H, I).

5.5.1.3 Whole rock geochemistry

Whole rock major and trace element compositions of the representative samples are given in Supporting Information Table S5.2. The geochemical analyses presented here are combined with previous analyses of the Dras Volcanics, Kargil Intrusives, Spongtang Ophiolite-Spong Arc complex, Zedong terrane and Luobusha Ophiolite (Aitchison et al., 2007b; Bhat et al., 2019; Buckman et al., 2018; Corfield et al., 2001; Liu et al., 2020; Malpas et al., 2003; Zhang et al., 2014; Zhong, 2006). Alteration effects are addressed in Supporting Information Text. Refer also to Supporting Information Figure S5.1.

Basaltic andesite samples for the Dras Volcanics have a SiO_2 range between 44-53 wt.% (LOI ranges 2.4-7.3 wt.%). One trachydacite (sample 17NI12) contains 65 wt.% SiO_2, and a felsic tuff (sample 17NI05) has 76 wt.% SiO_2. The Dras Volcanics generally contain high Fe_2O_3 + MgO (4-25%). Ratios of K_2O/Na_2O range between 0.03-1.01 and TiO_2 contents range from 0.29-1.13 wt.% (with the felsic tuff and trachydacite samples both at the lowest end of this range). Some basaltic samples demonstrate boninitic characteristics (MgO > 8 wt.% and TiO_2 < 0.5 wt.%; Crawford et al., 1989; see also Walsh et al., 2019).

The total alkali versus silica (TAS; Le Maitre et al., 1986) diagram shows that the Dras Volcanics form a tight cluster between the fields of picro-basalt and basalt (Figure **5.6**A). The immobile element rock classification diagram (Winchester and Floyd, 1977) plots the Dras

Volcanics as largely basaltic-andesites (this study), with some samples (Bhat et al., 2019) plotting as more evolved (Figure **5.6**B). The tectonic discrimination diagram (V/Ti/1000) of Shervais (1982) shows the Dras Volcanics data spread from island-arc tholeiite (IAT; this study) transitioning to MORB (Bhat et al., 2019; Figure **5.6**C). Similarly, the tectonic discrimination diagram (Ti/Zr) of Pearce and Cann (1973) plots Dras Volcanics as a near linear pattern, transitional between IAT, MORB and calc-alkaline basalts (Figure **5.6**D). The Th/Yb-Nb/Yb diagram (Pearce, 2008) plots the majority of samples from the Dras Volcanics in the island-arc field, rather than within the N- to E-MORB array (**Figure 5.6**E). In the MORB-normalised trace element plot (Figure **5.6**F; Sun and McDonough., 1989), high field strength element (HFSE) concentrations are generally low to moderate, with negative anomalies reflected in Nb, Ta, Zr and Ti. Large ion lithophile element (LILE) concentrations are variable with Rb and Ba both exhibiting negative anomalies, while K and Sr demonstrate positive anomalies. Chondrite-normalised REE plots and discussion are in Supporting Information Text and Figure S5.2.

The trachydacite (sample 17NI12) meets the requirements for a low-magnesium adakitic lava (Defant and Drummond, 1990; Defant and Kepezhinskas, 2001) in that it displays concentrations of $SiO_2 \geq 56$ wt.% (65 wt.%), $Al_2O_3 \geq 15$ wt.% (17 wt.%), MgO < 3 wt.%, rarely > 6 wt.% (2 wt.%), $Na_2O > 3.5$ wt.% (7 wt.%), Sr ≥ 400 ppm (614 ppm), Y ≤ 18 ppm (15 ppm), Yb ≤ 1.9 ppm (1.5 ppm) and Sr/Y ≥ 40 (40.13). A MORB-normalised trace element plot (Figure **5.6**F) shows a strongly positive Sr anomaly and an absent to slightly positive Eu anomaly, typical of slab-derived adakitic melts (Defant and Kepezhinskas, 2001). The only adakite criteria this sample falls short of is its La/Yb of 12.74, which should ideally be ≥ 20 (see Supporting Information Table S5.2 for adakite investigation). Adakitic rocks contain typical arc signatures including negative Nb and Ta anomalies; the trachydacite is consistent with this, as are the Dras Volcanics. All of the Dras Volcanics have $Al_2O_3 \geq 15$ wt.% (16-19 wt. %), with some samples demonstrating Y ≤ 18 ppm (16-18 ppm), Yb ≤ 1.9 ppm (1.6-1.7 ppm), consistent with a garnet-rich eclogitic melt source. Adakite classification plots, including Figure **5.7**A La_N/ Yb_N vs. Yb_N (Martin, 1999); Figure **5.7**B Mg# vs. SiO_2 (Stern and Kilian, 1996); Figure **5.7**C Sr/Y vs. Y diagram (Defant and Drummond, 1990) show the trachydacite (sample 17NI12) plotting as adakite or in adjacent fields.

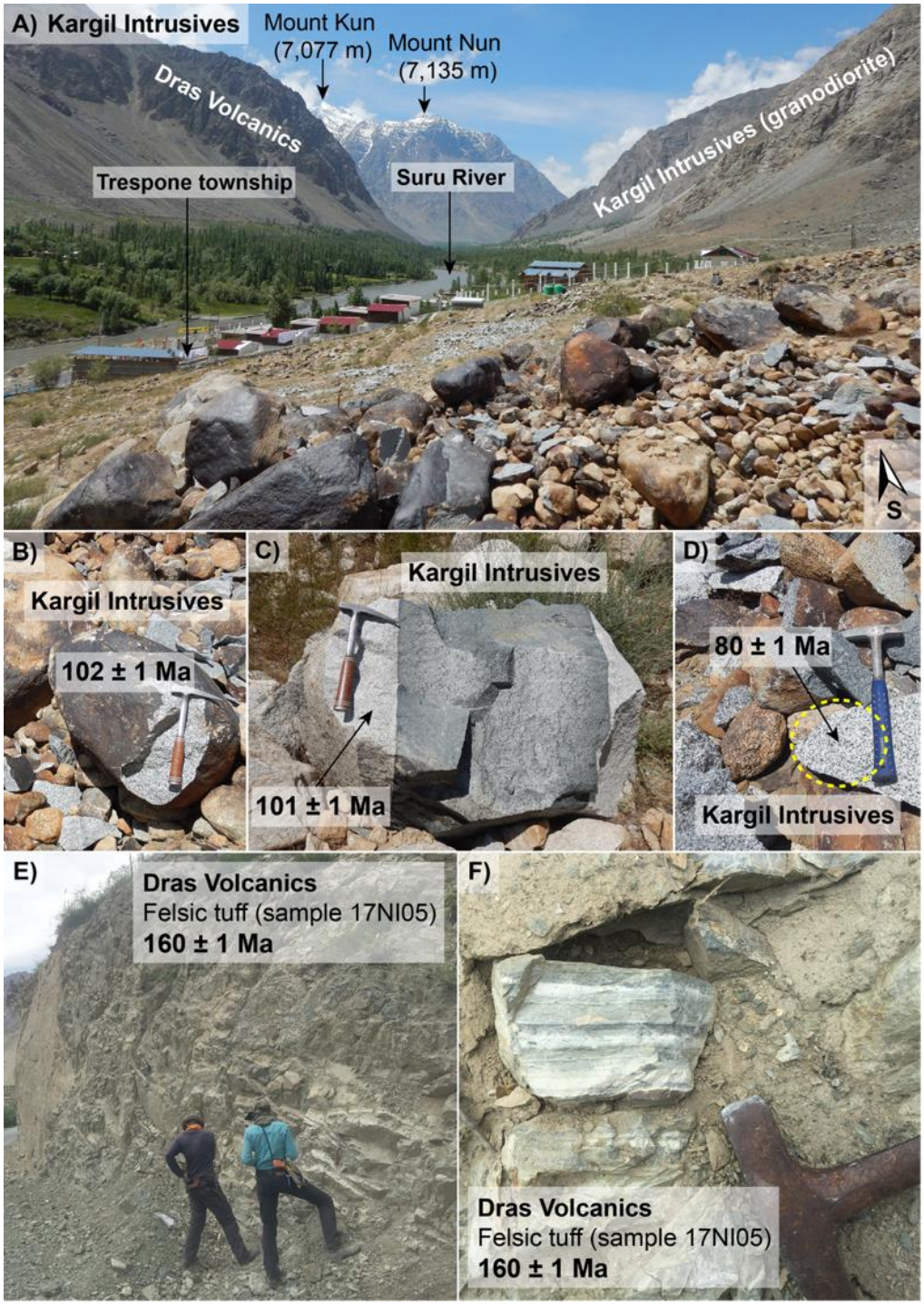

Figure 5.3: Field relations of the Dras Volcanics and Kargil Intrusives. **A)** Regional overview of the Kargil Intrusive mountains, orientated S-SE along the Suru River at the township of Trespone (south-west of the city of Kargil). Position: 34.45591°N, 76.07023°E; **B)** Representative samples from the Kargil Intrusives. Two granodiorite-diorite samples produced zircon U-Pb ages of 102 ± 2 Ma and 101 ± 2 Ma (samples 17KG01 and 17KG02, respectively), while another granodiorite sample produced an age of 80 ± 1 Ma (sample 17KG04). Position: 34.45593°N, 76.0702°E; **C)** Dolerite sills and dykes with sharp contacts are commonly observed cross cutting the Kargil Intrusives. Position: 34.50608°N, 76.12528°E; **D)** The Kargil Intrusives include medium to coarse grained granodiorites and diorites, with minor gabbro. Position: 34.50611°N, 76.12524°E; **E)** Representative samples from the Dras Volcanics collected along strike following the Srinagar-Leh Highway and Wakha River, between the city of Kargil and township of Shergole. Position: 34.46116°N, 76.26436°E; **F)** Felsic tuff within the dominantly andesitic volcanic rocks of the Dras Volcanics (sample 17NI05), which yielded a zircon U-Pb age of 160 ± 3 Ma. Position: 34.46116°N, 76.26436°E.

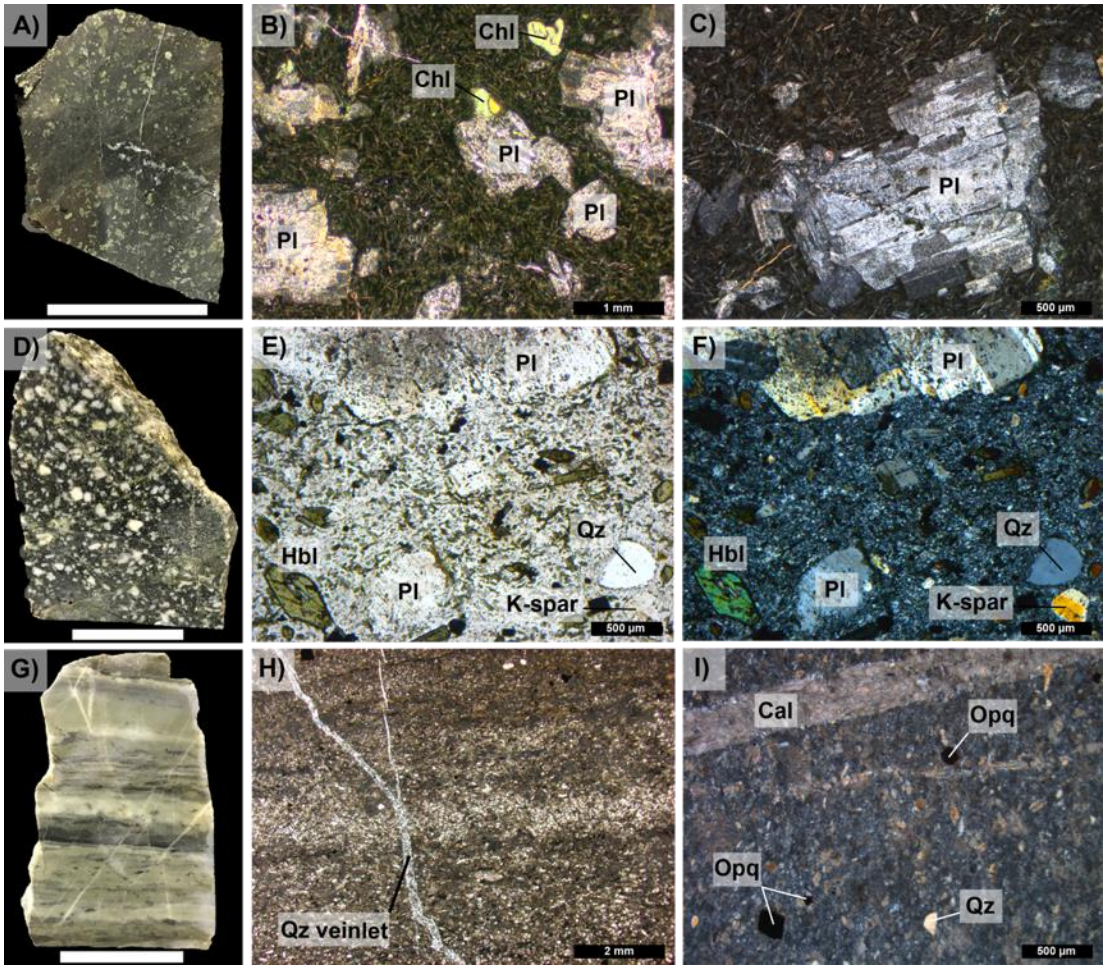

Figure 5.4: Representative hand specimen and thin section photomicrographs of the Dras Volcanics. Scale bars = 2.5 cm, unless otherwise indicated. **A)** Basalt hand specimen (sample 17NI03); **B)** Small plagioclase laths within a glassy ground mass often define trachytic flow textures around phenocrysts and vesicles (PPL; sample 17NI03); **C)** Phenocrysts of augite and plagioclase are abundant with some samples displaying glomerophyric textures (XPL; sample 17NI03)**; D)** Trachydacite 'adakite' hand specimen (sample 17NI12); **E)** Rounded glomerocrysts of largely plagioclase show signs resorption with the surrounding aphanitic, felsic groundmass, suggesting they may have in a state of disequilibrium during cooling and crystallisation (PPL; sample 17NI12); **F)** Euhedral phenocrysts of hornblende show less rounding and less resorbtion with the surrounding matrix suggesting they crystallised in equilibrium with the surrounding felsic melt (XPL; sample 17NI12); **G)** Felsic tuff hand specimen (sample 17NI05); **H)** The fine-grained, felsic tuff displays well-defined, laminated and graded bedding between 0.1-2 cm thick, suggesting it settled through a deep-water environment (PPL; sample 17NI05); **I)** Small vitric fragments and albite phenocrysts occur within a fine-grained, devitrified ash matrix (XPL; sample 17NI05); Where, Cal = calcite; Chl = chlorite; Hbl = hornblende; K-feldspar = potassium feldspar; Pl = plagioclase; Opq = opaque mineral; Qz = quartz.

5.5.2 Kargil Intrusives

5.5.2.1 Field geology

Representative samples of the Kargil Intrusives were collected along the National Highway 301 following the Suru River, between the township of Trespone and city of Kargil (Figure **5.1**B). Sample lithologies and localities are provided in Supporting Information Table S5.1. The sampled intrusives are predominantly medium- to coarse-grained granodiorites and diorites, with minor gabbro (Figure **5.3**). Dolerite sills and dykes are also commonly observed (Figure **5.3**C). Unlike the surrounding Dras Volcanics, these intrusives show no signs of pervasive metamorphism. Our samples are from the same pluton previously dated as 103 ± 3 Ma and 101 ± 2 Ma by Honegger et al. (1982) and Schärer et al. (1984a), respectively.

5.5.2.2 Petrography

5.5.2.2.1 Granodiorite-diorite

The granodiorite (samples 17KG01 and 17KG04) to diorite (sample 17KG02) are medium- to coarse-grained and equigranular (Figure **5.5**A-F). Mineralogy consists predominantly of plagioclase, hornblende, quartz and biotite with accessory opaques.

5.5.2.2.2 Gabbro

The gabbros (samples 17KG03 and 17KG05; Supporting Information Table S5.2: CIPW normalisation) are medium-grained and equigranular, dominated by clinopyroxene and plagioclase, with no observable layering or planar fabric (Figure **5.5**G-I). Late igneous biotite has grown along the edges of some pyroxene grains, occurring as a reaction between early igneous pyroxenes and residual K-rich magma (Figure **5.5**H, I). Opaque minerals are common throughout and occur predominantly within or along the edges of pyroxenes.

5.5.2.3 Whole rock geochemistry

Granodiorite-diorite samples from the Kargil Intrusives have a broad SiO_2 range between 56-75 wt.%. The more felsic sample (17KG04) has low MgO (0.3 wt.%), Mg# (18), CaO (2 wt.%), Cr (5 ppm) and Ni (3 ppm). The other samples have higher MgO (2-4 wt.%), Mg# (27-31), CaO (6-8 wt.%), Cr (10-78 ppm) and Ni (7-24 ppm). The majority of the granodiorite-diorite samples have moderate K_2O (0.96-2.03 wt.%), and low TiO_2 (0.16-0.7 wt.%), Fe_2O_3 (1-9 wt.%), P_2O_5 (0.06-0.11 wt.%), Zr (8-17 ppm), Nb (1.9-4.1 ppm) and Y (5-20 ppm). Gabbros from the Kargil Intrusives have a narrow SiO_2 range between 46-51 wt.%. The most mafic gabbro (sample KG5; Bhat et al., 2019) has high MgO (12 wt.%), Mg# (55), CaO (16 wt.%), Cr (154 ppm) and Ni (56

ppm), compared to other samples which are in the range of MgO (5-8 wt.%), Mg# (40-47), CaO (9-12 wt.%), Cr (32-150 ppm) and Ni (27-76 ppm). The majority of the gabbros have low K_2O (0.06-0.52 wt.%), and moderate TiO_2 (0.75-1.28 wt.%), Fe_2O_3 (8-13 wt.%), P_2O_5 (0.04-0.26 wt.%), Zr (11-55 ppm), Nb (0.3-2.5 ppm) and Y (7-19 ppm). The most mafic samples are generally at the lowest end of these ranges. Whole rock major and trace element compositions of representative samples are given in Supporting Information Table S5.2.

The total alkali versus silica (TAS; Le Maitre et al., 1986) diagram shows that the Kargil Intrusives are in the fields of low alkali mafic to felsic rocks (Figure **5.6**A). The immobile element rock classification diagram (Winchester and Floyd, 1977) plots the Kargil Intrusives as a tight cluster in the equivalent gabbroic field, with one outlier (sample 17KG04) plotting as alkaline (Figure **5.6**B). Similarly, the tectonic discrimination diagram (Ti/Zr) of Pearce and Cann (1973) plot the Kargil Intrusives closest to the IAT field (Figure **5.6**D). The Th/Yb-Nb/Yb diagram (Pearce, 2008) plots the majority of samples from the Kargil Intrusives in the island-arc field, rather than within the N- to E-MORB array (Figure **5.6**E). In the MORB-normalised trace element plot (Figure **5.6**F; Sun and McDonough., 1989), high field strength element (HFSE) concentrations are generally low to moderate, with negative anomalies reflected in Nb, Ta, Zr and Ti for the Kargil Intrusives. The majority of the Kargil Intrusives have typical calc-alkaline affinities, however one granodioritic sample (17KG04) does meet the majority of adakitic characteristics (Figure **5.7**; see Supporting Information Table S5.2 for adakite investigation).

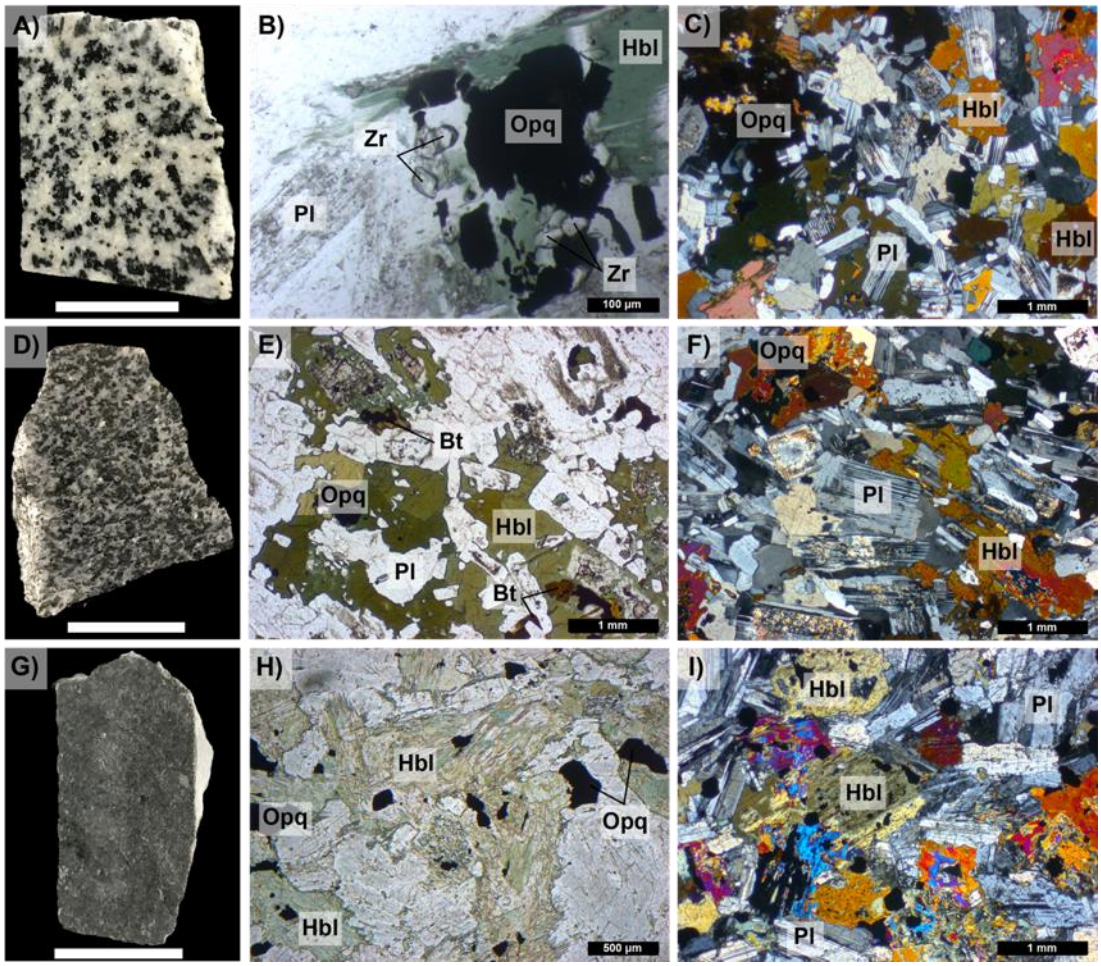

Figure 5.5: Representative hand specimen and thin section photomicrographs of the Kargil Intrusives. Scale bars = 2.5 cm, unless otherwise indicated. **A)** Granodiorite hand specimen (sample 17KG01); **B)** Medium- to coarse-grained and equigranular granodiorite dominated by plagioclase and quartz. Large, accessory zircons are present (PPL; sample 17KG01); **C)** Granodiorite consisting of plagioclase, hornblende, quartz and biotite (XPL; sample 17KG01); **D)** Diorite hand specimen (sample 17KG02); **E)** Biotite-rich diorite (PPL; sample 17KG02); **F)** Dioritic sample consisting predominantly of plagioclase, hornblende, quartz and biotite, but with less quartz (XPL; sample 17KG02); **G)** Gabbro hand specimen (sample 17KG05); **H)** Medium-grained, equigranular, massive gabbro dominated by clinopyroxene and plagioclase, (PPL; sample 17KG05); **I)** Gabbro contains late igneous biotite grown along the edges of some pyroxene grains indicative of a reaction between early crystallised pyroxenes and residual K-rich magma (XPL; sample 17KG05). Where, Bt = biotite; Hbl = hornblende; Pl = plagioclase; Opq = opaque mineral; Qz = quartz; Zr = zircon.

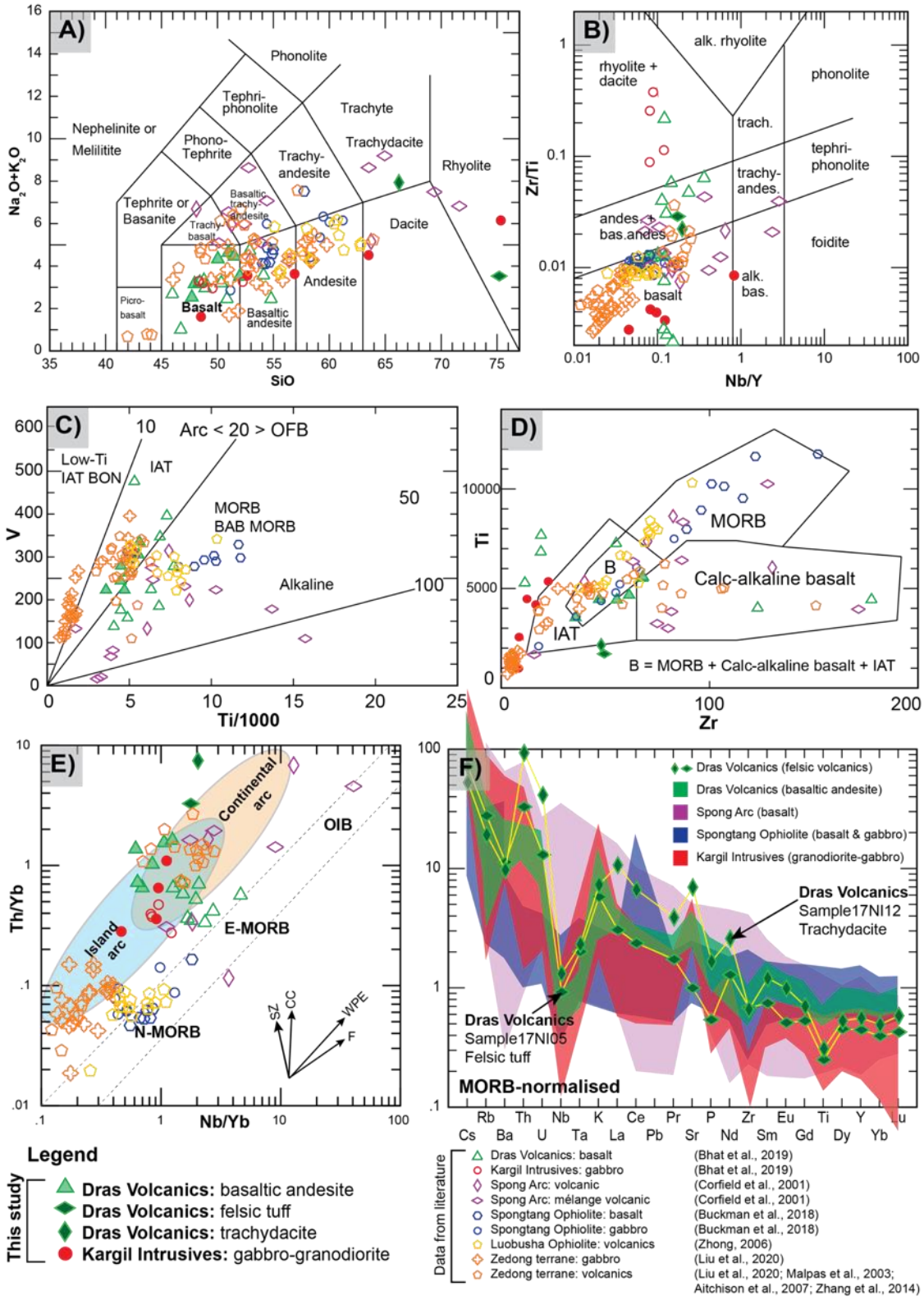

Figure 5.6: Geochemical plots of the Dras Volcanics, Kargil Intrusives and Spongtang Ophiolite-Spong Arc complex. Analyses presented here are combined with previous data (Aitchison et al., 2007b; Bhat et al., 2019; Buckman et al., 2018; Corfield et al., 2001; Liu et al., 2020; Malpas et al., 2003; Zhang et al., 2014; Zhong, 2006). **A)** Total alkali vs. silica diagram (TAS; Le Maitre et al., 1986); **B)** Immobile element rock classification diagram (Winchester and Floyd, 1977); **C)** Tectonic discrimination diagram (V/Ti/1000; Shervais, 1982); **D)** Tectonic discrimination diagram (Ti/Zr; Pearce, 1973); **E)** Mid-ocean ridge basalt (MORB) array diagram (Pearce, 2008); **F)** Extended MORB-normalised REE diagram (Sun and McDonough, 1989).

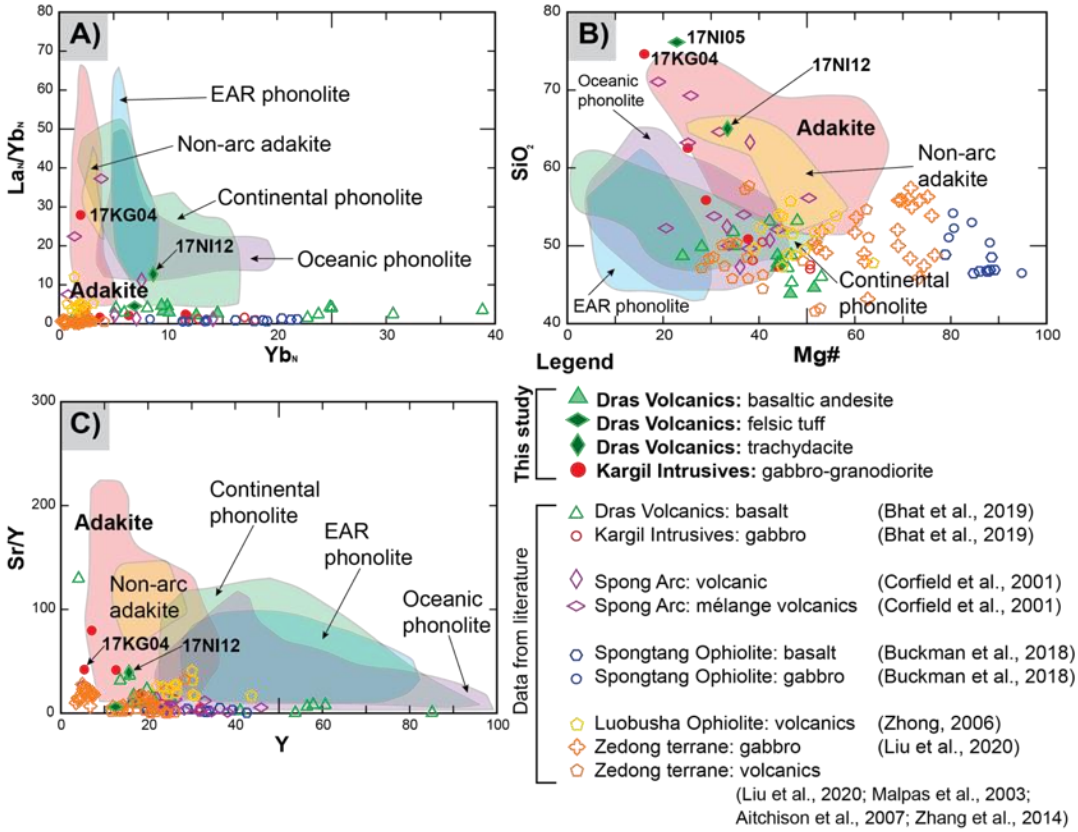

Figure 5.7: Adakite classification and discrimination plots. Analyses presented here are combined with previous data (Aitchison et al., 2007b; Bhat et al., 2019; Buckman et al., 2018;Iet al., 2001; Liu et al., 2020; Malpas et al., 2003; Zhang et al., 2014; Zhong, 2006). **A)** Chondrite-normalised La/Yb vs. Yb (Martin, 1999); **B)** Mg# vs. SiO_2 (Stern and Kilian, 1996); **C)** Sr/Y vs. Y diagram (Defant and Drummond, 1990). Fields include global trends for adakites, non-arc adakites, continental phonolites, East African Rift (EAR) phonolites and oceanic phonolites (GEOROC Database, after Mazza et al., 2017).

5.5.3 Zircon U-Pb geochronology

Zircon U-Pb geochronologic results for the Dras Volcanics and Kargil Intrusives are presented in Table **5.2**, whereby the weighted mean $^{206}Pb/^{238}U$ age for each sample includes only the youngest crystallisation population. Figure **5.8** displays cathodoluminescence (CL) images of representative zircon grains for each of the samples. Figure **5.9** displays probability density plots for the Dras Volcanics and Kargil Intrusives. Figure **5.10** and Figure **5.11** display concordia and weighted mean plots for Dras Volcanics and Kargil Intrusives, respectively. Refer to Supporting Information Text for zircon grain descriptions. Refer also to Supporting Information Table S5.3 for reduced zircon U-Pb data with details provided for rejected grains and Table S5.4 for mixture modelling results. See Supporting Information Figure S5.3-S5.6 for CL images of analysed zircon grains.

As a first stage of investigation, standard techniques were used where relative probability plots and weighted mean averages were plotted for each sample from the Dras Volcanics and Kargil Intrusives to; (i) visually assess the spread of the data and, (ii) determine whether multiple age populations were present in the samples. The zircon U-Pb data from the two Dras Volcanics samples (felsic tuff sample 17NI05 and trachydacite sample 17NI12) and one sample from the Kargil Intrusives (granodiorite sample 17KG04) demonstrated significant scatter of $^{206}Pb/^{238}U$ age outside analytical uncertainty. Reasons for this could be, but not limited to, multiple zircon age populations and complex Pb-loss. In order to provide an independent estimate of the number and possible ages of components present in the geochronological datasets from the Dras Volcanics and the Kargil Intrusives, where appropriate the 'mixture modelling' algorithm of Sambridge and Compston (1995) using *Isoplot 4.15* (Ludwig et al., 2003) was used to unmix statistical age populations or groups. From such groupings for each of the samples, weighted mean $^{238}U/^{206}Pb$ ages were calculated and uncertainties are reported at 2 σ. The 'unmix' function in *Isoplot* relies on finding the best fit (maximum likelihood) set of ages and proportions for a given number of assumed components. In order to limit bias, the estimate of the component age and proportion was assigned to *Isoplot* to calculate. The number of components was increased to an optimal number, whereby there is little improvement in either the relative misfit of the data or when the additional age component is very similar to the previous. Individual errors will often overlap by this methodology, but the accumulation of many analyses will reveal deviations from a single gaussian distribution, which in combination with duplicate analyses on some grains and the CL imagery will establish for example Pb-loss from a single population or a multi-component population. Refer to Supporting Information Table S5.4 for mixture modelling results.

Table 5.2: Zircon U-Pb results for samples from the Dras Volcanics and Kargil Intrusives.

Unit	Lithology	Sample ID	Age range (Ma)	[1] Weighted mean $^{206}Pb/^{238}U$ age	[2] MSWD and sample number (*n*)
Dras Volcanics	felsic tuff	17NI05	175 ± 5 to 158 ± 4	160 ± 3 Ma	MSWD = 0.47 *n* = 11
Dras Volcanics	trachydacite	17NI12	173 ± 5 to 148 ± 4	156 ± 1 Ma	MSWD = 0.93 *n* = 28
Kargil Intrusives	granodiorite	17KG01	107 ± 5 to 98 ± 5	102 ± 2 Ma	MSWD = 0.86 *n* = 29
Kargil Intrusives	diorite	17KG02	104 ± 6 to 98 ± 4	101 ± 2 Ma	MSWD = 0.52 *n* = 29
Kargil Intrusives	granodiorite	17KG04	102 ± 4 to 77 ± 4	80 ± 1 Ma	MSWD = 1.8 *n* = 40

Notes:

All analytical errors are given at 2 σ.

[1] Weighted mean $^{206}Pb/^{238}U$ age includes only the youngest crystallisation population (Ma). Details are given in Supporting Information Text for those samples with older, inherited populations with more complex components.

[2] MSWD = mean square weighted deviation.

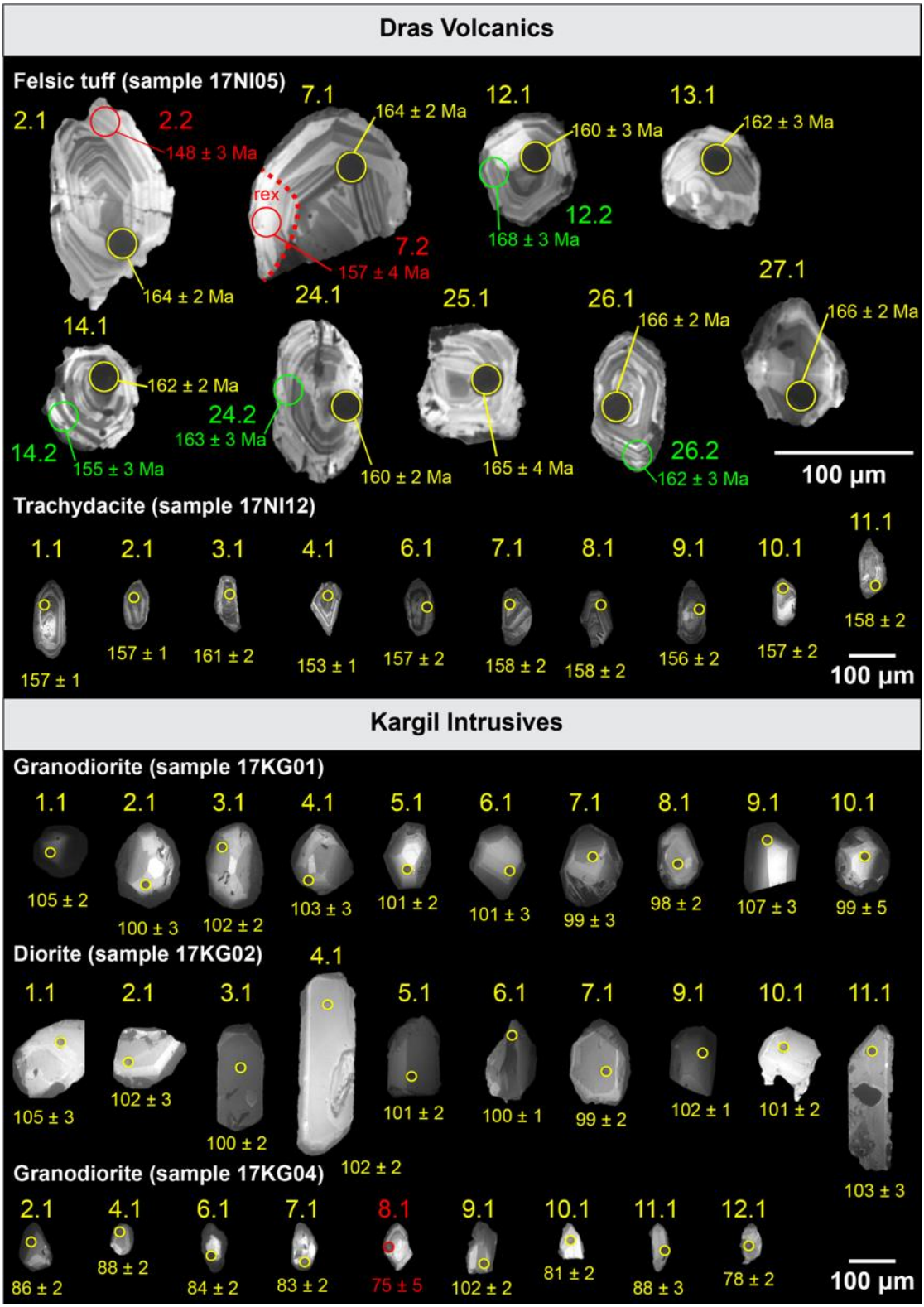

Figure 5.8: Cathodoluminescence (CL) images of representative zircon grains from the Dras Volcanics (felsic tuff sample 17NI05 and trachydacite sample 17NI12) and the Kargil Intrusives (granodiorite sample 17KG01, diorite sample 17KG02 and granodiorite sample 17KG04). The yellow and green spots denote LA-ICP-MS and SHRIMP analytical sites, respectively, with corresponding $^{206}Pb/^{238}U$ ages (Ma). Red spots denote rejected grains (excluded from final age calculations). Where 'rex' denotes recrystallised zone. All analytical errors are given at 2σ.

5.5.3.1 Dras Volcanics

5.5.3.1.1 Felsic tuff (sample 17NI05)

A total of 28 zircon grains with 34 analytical sites from a Dras Volcanics felsic tuff (sample 17NI05) were dated (LA-ICP-MS, n = 28; SHRIMP n = 6). Three analyses (grains 10.1, 18.1 and 19.1) were rejected from final age assessments on the basis of being discordant (refer to Supporting Information Table S5.3 for details on rejected grains). An additional two analyses (sites 2.2. and 7.2) were rejected due to Pb loss (site 2.2) and the analytical site being on a recrystallised (rex) zone (7.2). The remaining 25 analyses yielded concordant U-Pb ages, with $^{206}Pb/^{238}U$ ages from 175 ± 5 Ma to 158 ± 4 Ma. The weighted mean age was taken for those grains with duplicate analyses. Following this, mixture modelling revealed three components in the $^{206}Pb/^{238}U$ age distribution (refer to Supporting Information Table S5.4 for the results of mixture modelling experiments using *Isoplot*):

(i) 175 ± 5 Ma (n = 1)
(ii) 165 ± 2 Ma (MSWD = 0.65, n = 13)
(iii) 160 ± 3 Ma (MSWD = 0.47, n = 11)

The youngest age population of **160 ± 3 Ma** is inferred to represent the crystallisation age of the felsic tuff from the Dras Arc, while the other two components are inherited zircon grains from older events. Refer to Supporting Information Table S5.3 for reduced zircon U-Pb data.

5.5.3.1.2 Trachydacite (sample 17NI12)

A total of 54 zircon grains from a Dras Volcanics trachydacite (sample 17NI12) were dated. Seven analyses were rejected on the basis of being discordant. The remaining 47 analyses yielded concordant U-Pb ages, with $^{206}Pb/^{238}U$ ages from 173 ± 5 Ma to 148 ± 4 Ma. Four components were identified producing the following $^{206}Pb/^{238}U$ ages:

(i) 172 ± 5 Ma (MSWD = 1.6, n = 2)
(ii) 162 ± 3 Ma (MSWD = 0.45 , n = 8)
(iii) 156 ± 1 Ma (MSWD = 0.93, n = 28)
(iv) 151 ± 3 Ma (MSWD = 2.0, n = 9)

The second youngest population of **156 ± 1 Ma** is inferred to represent the crystallisation age of the trachydacite from the Dras Arc (refer to Supporting Information Text for discussion and Figure S5.7). Inspection of the CL images demonstrates the apparently youngest ages, including the mixture modelling component of 151 ± 3 Ma, contain a higher proportion of sites where CL imagery show variable recrystallisation (‘rex’) with the destruction of sharp-margined oscillatory

zoning compared with sites falling in the 156 ± 1 Ma population. This means that there was probably later disturbance following the magmatic zircon crystallisation, and therefore the 156 ± 1 Ma is a better estimate of the magmatic age for the trachydacite (sample 17NI12).

5.5.3.2 Kargil Intrusives

5.5.3.2.1 Granodiorite (sample 17KG01)

A total of 30 zircon grains from a Kargil Intrusives granodiorite (sample 17KG01) were dated. One analysis (grain 21.1) was rejected on the basis of being discordant. The remaining 29 analyses yielded concordant U-Pb ages, with $^{206}Pb/^{238}U$ ages from 107 ± 5 Ma to 98 ± 5 Ma, which had a tight cluster with a weighted mean $^{206}Pb/^{238}U$ age of **102 ± 2 Ma** (MSWD = 0.86; *n* = 29). This age is inferred to represent the crystallisation age of this granodiorite from the Kargil Intrusives.

5.5.3.2.2 Diorite (sample 17KG02)

A total of 30 zircon grains from a Kargil Intrusives diorite (sample 17KG02) were dated. One analysis (grain 8.1) was rejected on the basis of being discordant. The remaining 29 analyses yielded I ages, with $^{206}Pb/^{238}U$ ages from 104 ± 6 Ma to 98 ± 4 Ma, which had a tight cluster with a weighted mean $^{206}Pb/^{238}U$ age of **101 ± 2 Ma** (MSWD = 0.52; *n* = 29). This age is inferred to represent the crystallisation age of this diorite from the Kargil Intrusives.

5.5.3.2.3 Granodiorite (17NI04)

A total of 60 zircon grains from a Kargil Intrusives granodiorite (sample 17KG04) were dated. Thirteen analyses were rejected on the basis of being discordant and one grain was rejected due to Pb loss (grain 8.1). The remaining 46 analyses yielded concordant U-Pb ages, with $^{206}Pb/^{238}U$ ages from 102 ± 4 Ma to 77 ± 4 Ma. Three components were identified, producing the following $^{206}Pb/^{238}U$ ages:

(i) 100 ± 3 Ma (MSWD = 3.1, *n* = 2)
(ii) 87 ± 3 Ma (MSWD = 0.61, *n* = 4)
(iii) 80 ± 1 Ma (MSWD = 1.8, *n* = 40)

The youngest age population of **80 ± 1 Ma** is inferred to represent the crystallisation age of this granodiorite from the Kargil Intrusives, while the other two components are inherited zircon grains from older events.

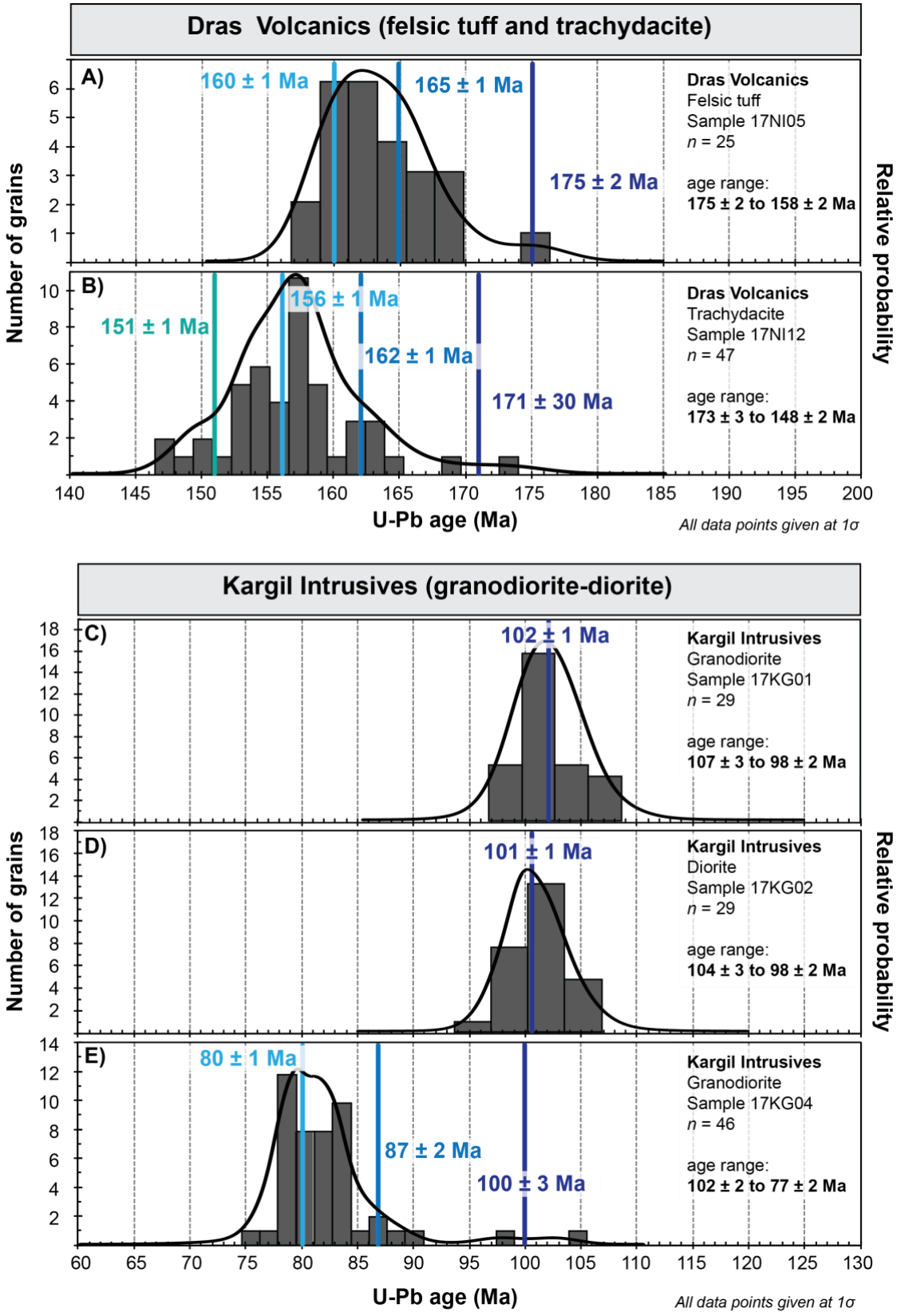

Figure 5.9: Probability density plots for the Dras Volcanics and Kargil Intrusives. **A)** Sample 17NI05 – felsic tuff (age range: 175 ± 5 Ma to 158 ± 4 Ma); **B)** Sample 17NI12 – trachydacite (age range: 173 ± 5 Ma to 148 ± 4 Ma); **C)** Sample 17KG01 – granodiorite (age range: 107 ± 5 Ma to 98 ± 5 Ma); **D)** Sample 17KG02 – diorite (age range: 104 ± 6 Ma to 98 ± 4 Ma); **E)** Sample 17KG04 – granodiorite (age range: 102 ± 4 Ma to 77 ± 4 Ma).

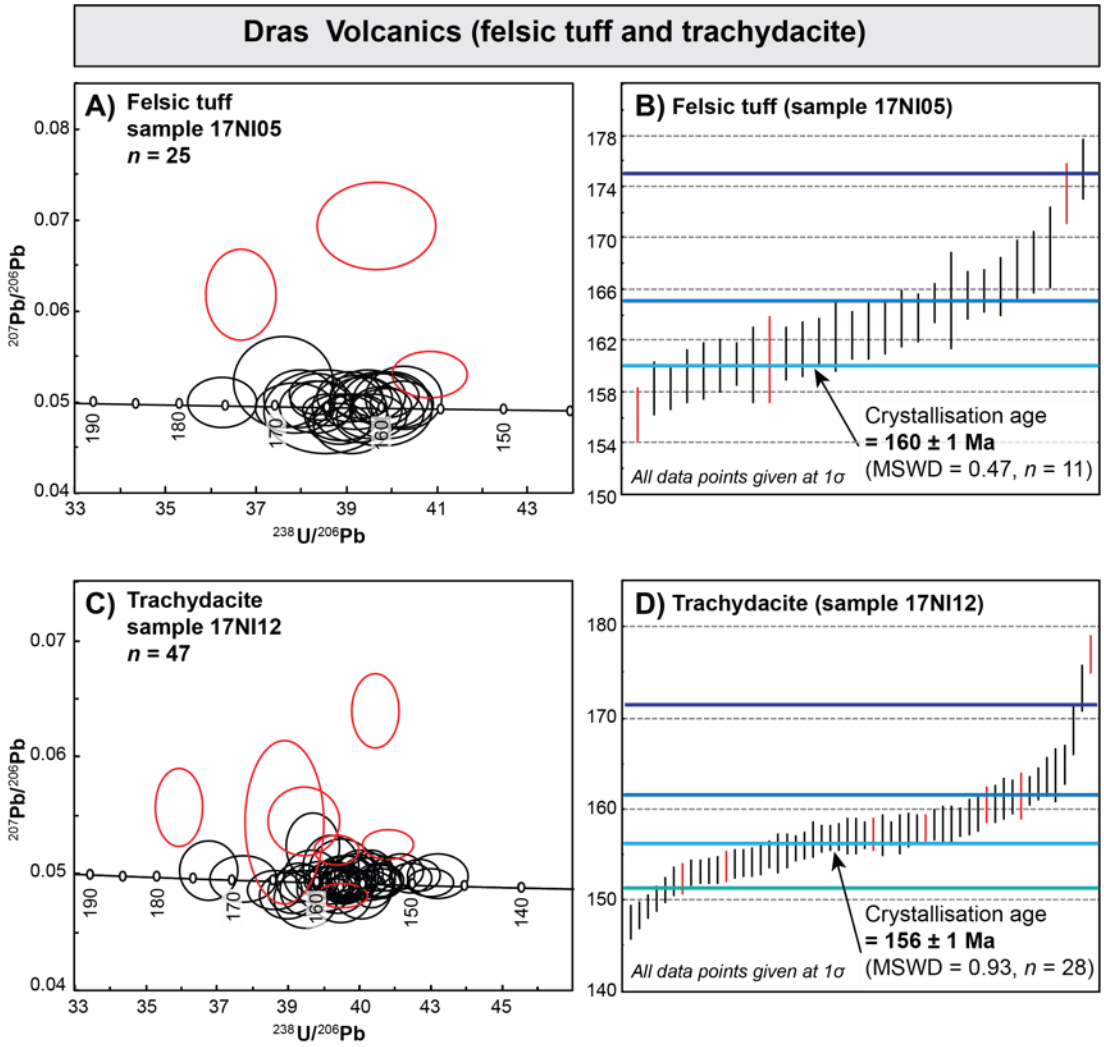

Figure 5.10: Dras Volcanics zircon U-Pb geochronology using LA-ICP-MS and SHRIMP. **A)** Felsic tuff (sample 17NI05) concordia plot demonstrating $^{206}Pb/^{238}U$ ages from 175 ± 5 Ma to 158 ± 4 Ma; **B)** Felsic tuff (sample 17NI05) weighted mean average plot demonstrating three magmatic components producing $^{206}Pb/^{238}U$ ages of 175 ± 5 Ma (*n* = 1), 165 ± 2 Ma (mean square weighted deviation = 0.65, *n* = 13) and 160 ± 3 Ma (MSWD = 0.47, *n* = 11). The youngest age of 160 ± 3 Ma is inferred to represent the crystallisation age of the felsic tuff from the Dras Arc, while the other two components are inherited zircon grains from older events; **C)** Trachydacite (sample 17NI12) concordia plot demonstrating $^{206}Pb/^{238}U$ ages from 173 ± 5 Ma to 148 ± 4 Ma; **D)** Trachydacite (sample 17NI12) weighted mean average plot demonstrating four magmatic components producing $^{206}Pb/^{238}U$ ages of 172 ± 5 Ma (MSWD = 1.6, *n* = 2), 162 ± 3 Ma (MSWD = 0.45, *n* = 8), 156 ± 1 Ma (MSWD = 0.93, *n* = 28) and 151 ± 3 Ma (MSWD = 2.0, *n* = 9). The second youngest age of 156 ± 1 Ma is inferred to represent the crystallisation age of the trachydacite from the Dras Arc. Those analyses in red have been rejected and not used for final age calculations. See Supporting Information Table S5.3 for comments on rejected grains.

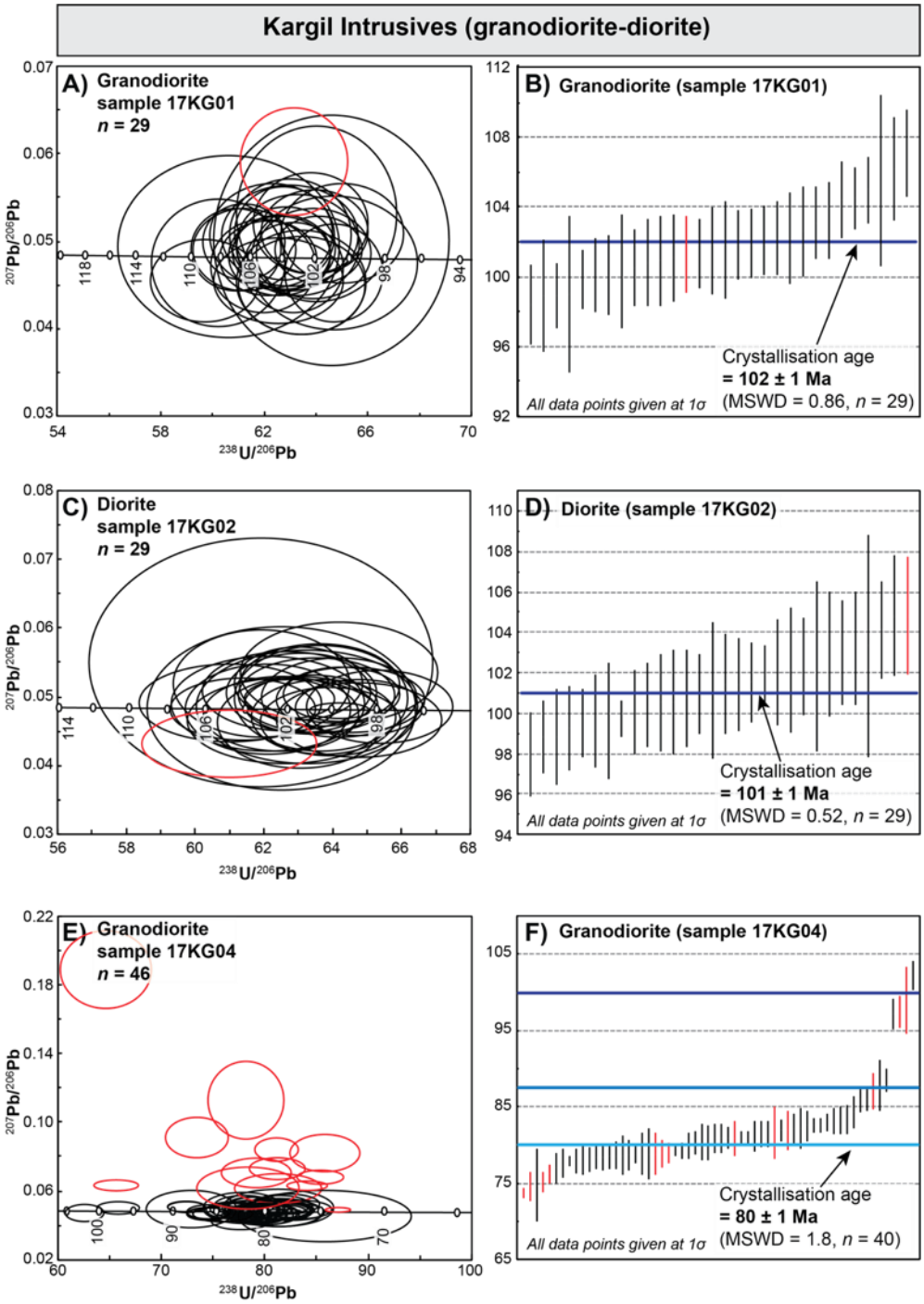

Figure 5.11: Kargil Intrusives zircon U-Pb geochronology using LA-ICP-MS. **A)** Granodiorite (sample 17KG01) concordia plot demonstrating $^{206}Pb/^{238}U$ ages from 107 ± 5 Ma to 98 ± 5 Ma; **B)** Granodiorite (sample 17KG01) weighted mean average plot demonstrating a $^{206}Pb/^{238}U$ age of 102 ± 2 Ma (MSWD = 0.86; *n* = 29). This age is inferred to represent the crystallisation age of this granodiorite from the Kargil Intrusives; **C)** Diorite (sample 17KG02) concordia plot demonstrating $^{206}Pb/^{238}U$ ages from 104 ± 6 Ma to 98 ± 4 Ma; **D)** Diorite (sample 17KG02) weighted mean average plot demonstrating a $^{206}Pb/^{238}U$ age of 101 ± 2 Ma (MSWD = 0.52; *n* = 29). This age is inferred to represent the crystallisation age of this diorite from the Kargil Intrusives; **E)** Granodiorite (sample 17KG04) concordia plot demonstrating $^{206}Pb/^{238}U$ ages from 102 ± 4 Ma I) Granodiorite (sample 17KG04) weighted mean average plot demonstrating three magmatic components producing $^{206}Pb/^{238}U$ ages of 100 ± 3 Ma (MSWD = 3.1, *n* = 2), 87 ± 4 Ma (MSWD = 0.61, *n* = 4) and 80 ± 1 Ma (MSWD = 1.8, *n* = 40). The youngest age of 80 ± 1 Ma is inferred to represent the crystallisation age of this granodiorite from the Kargil Intrusives, while the other three components are inherited zircon grains from older events. Those analyses in red have been rejected and not used for final age calculations. See Supporting Information Table S5.3 for comment on rejected grains.

5.6 Discussion

5.6.1 Previous work and interpretations of the Dras Arc

The Dras Arc is central to tectonic models and reconstructions focused on the opening and closure of the Neotethyan Ocean, through to the terminal continental collision of India with Eurasia. Until recently there have been only a limited number of age constraints for this island arc terrane. Some researchers suggest the Dras Arc is simply the forearc portion of the larger Ladakh-Kohistan Arc that developed on the southern margin of Eurasia, similar to the modern-day Aleutian Arc (Rolland et al., 2000; Sutre, 1990). However, geological evidence has also suggested that the Dras Arc developed in the Neotethyan Ocean as an intraoceanic arc throughout the Cretaceous (Bhat et al., 2019; Brookfield and Reynolds, 1981; Clift et al., 2000; Clift et al., 2002a; Clift et al., 2002b; Corfield et al., 2001; Frank, 1977; Honegger et al., 1982; Klootwijk et al., 1984; Reuber, 1989; Robertson and Degnan, 1994; Searle, 1983, 1986; Thakur, 1981). Finally, most voluminous granitic magmatism in the Ladakh Arc occurred between ~66-46 Ma and is predominantly composed of highly evolved, felsic granites (White et al., 2011; Figure **5.12**). All of the felsic Ladakh Batholith plutons occur north of a major thrust fault marked by the Mongyu Mélange between the Ladakh Batholith and associated Tar Group to the north and the basaltic volcanic rocks and volcaniclastics of the Dras Volcanics and Nindam Formation, respectively. None of the granitic Ladakh Batholith plutons or dykes extend south past the Mongyu Mélange and no granitic clasts or quartz-rich detritus eroding off the Ladakh Arc are found within volcaniclastic units of the Nindam Formation, underlining a unique spatial and temporal tectonic history that favours the interpretation that the Ladakh and Dras arcs evolved as unique entities above separate subduction zones, before being amalgamated together during collision. Until now, the oldest units within the Dras Arc were thought to be Cretaceous (Brookfield and Reynolds, 1981; Honegger et al., 1982; Reuber, 1989; Reuber et al., 1989; Schärer et al., 1984a; Sharma et al., 1978); however, our results extend arc inception to at least the Late Jurassic.

5.6.2 Tectonic evolution of the Dras Arc

The Dras Arc was thought to have initiated sometime between the Upper Jurassic to Upper Cretaceous (Honegger et al., 1982; Reuber, 1989; Robertson and Degnan, 1994; Clift et al., 2000; Clift et al., 2002b). However, to date, there have been no age constraints on the early onset of arc magmatism from dating igneous rocks, to support the detrital zircon studies of Walsh et al. (2019) showing that Upper Jurassic zircons were being shed into the Nindam Formation from local sources. The first zircon U-Pb data reported here from the Dras Volcanics are an Upper Jurassic felsic tuff 160 ± 3 Ma (Oxfordian) and trachydacite 156 ± 1 Ma (Kimmeridgian). These

Upper Jurassic volcanic rocks are distinctly felsic in composition, in stark contrast to the dominantly mafic (basaltic to andesitic) composition of the majority of the Dras Arc volcanism. Rare felsic volcanism in island arc systems is sometimes associated with the adolescent stages of arc development in which dehydration melting of underplated arc or oceanic crust generates small volumes of felsic magmas, for example, the Raoul Volcano within the Tonga-Kermadec Arc, south-west Pacific Ocean (Smith et al., 2003). Other "adakitic" felsic melts are produced by partial melting of young, oceanic crust of basaltic (eclogitic) composition (Defant and Drummond, 1990). Extraction of lower crustal melts through underplating and dehydration melting creates an infertile source which inhibits any further felsic melt generation after which more voluminous basaltic-andesitic arc melts are then generated within the hydrated, mantle wedge (Smith et al., 2003). However, Defant and Drummond (1990) point out that partial melting of the lower crust by underplating should yield magmas with negative Eu anomalies and Al_2O_3 <15 wt.% because basalt will not reach the amphibolite-eclogite transition under most arcs and thus, will display signatures of plagioclase fractionation. True slab-derived adakitic melts produce high-Al (>15 wt.%), corundum CIPW normative, silica-rich (≥ 56 wt.%) melts characterised by high Sr/Y ratios and absent to slightly positive Eu anomalies, which reflect the incompatible nature of Sr and Eu in the absence of plagioclase crystallisation and the retention of Y in the garnet-rich eclogite source rock during partial melting. Sample 17NI12 (trachydacite) collected from lowest-known stratigraphic level and southern margin of the Dras Volcanic pile near the township of Shergole appears to fit most of the characteristics of a low-Mg adakite produced by partial melting of subducted ocean crust. The adakitic geochemistry of the felsic samples, combined with the Late Jurassic age, reveals a previously undocumented phase of felsic magmatism early in the development of the Dras Arc, which we propose is related to subduction of young, hot oceanic crust soon after subduction initiation. Some of the granodiorites (eIG04) display similar adakitic characteristics but these are much younger (~80 Ma) and developed within a more mature island arc during the peak of arc magmatism rather than during arc initiation.

Another possible explanation for a transition to more felsic volcanism in island arc settings is prolonged fractional crystallisation, from an original parent basaltic-andesitic magma composition (e.g., Rioux et al., 2010; Garrido et al., 2006). However, this would more likely occur in the final stages of arc evolution where the presence of thickened arc crust favours more extensive fractionation of magma batches in their ascent. The Kargil Intrusives is mafic magma emplaced in the core of the Dras Arc magmatic section that then underwent extended fractionation to evolve granodioritic compositions, which rose into the overlying volcanic pile at ~103 Ma. According to our geochronology, a second pulse of magmatism occurred at ~80 Ma. Felsic volcanism can also occur during the final stages of island arc development and particularly

just prior to collision and accretion onto continental margins due to the potential influx of continental-derived sediment being channelled into the trench and being partially subducted and added to the mantle wedge and arc volcanics (e.g., Ordovician Macquarie Arc of eastern Australia; Zhang et al., 2019). We suspect that the upper portions of the Dras-Nindam terrane have been truncated and lost against the northern suture (Walsh et al., 2019). However, Upadhyay et al., (2004) report equatorial, Palaeocene palynomorphs from the Nindam Formation close to the southern mélange zone (Sapi-Shergole Mélange; Figure **5.1**) at Shergole. These fossils also reveal a strong Gondwanan provenance, and they interpret that the forearc region of the Dras Arc was located just outboard of the northern margin of India and receiving India-derived sediment right up until collision and accretion between 50-60 Ma. These findings are corroborated by detrital zircon studies of the Nindam Formation (Walsh et al., 2019), which also reveal a small but distinct Gondwanan inheritance in addition to the Late Jurassic to Cretaceous arc-derived zircons. This led Walsh et al., (2019) to suggest that the Dras Arc probably initiated with the Spong Arc along a transform fault at 90° to the Indian margin before rotating clockwise and eventually colliding with the northern margin of India during the Palaeocene. The strongly juvenile and intraoceanic nature of the Dras Arc along with the distinct Gondwanan (Indian) inheritance strongly suggests this arc developed outboard of India on the southern margin of the Neotethyan Ocean, rather than as the forearc basement of the Ladakh Arc on the southern margin of Eurasia.

5.6.3 Collision and accretion of the Dras Arc

Initially, many researchers favoured that the Dras Arc first accreted onto the Eurasian margin (Clift et al., 2000; Clift et al., 2002a; Clift et al., 2002b; Corfield et al., 2001; Henderson et al., 2010; Henderson et al., 2011; Reuber, 1989; Robertson and Degnan, 1994). This interpretation was founded upon the Dras Volcanics being intruded by the Kargil Intrusives (~103-70 Ma; Brookfield and Reynolds, 1981; Honegger et al., 1982; Schärer et al., 1984a; Reuber et al., 1989; this study), which were proposed to be equivalent to the plutonic rocks in the Ladakh Arc. This was used as evidence for the Dras Arc colliding with the southern margin of Eurasia during the Late Cretaceous, prior to the intrusion of the granodioritic rocks and final continent-continent collision, with India. However, previous zircon geochronology provides no evidence of Ladakh Arc magmatism exceeding 85 Ma, with a distinct magmatic peak between 66-46 Ma, with only minor inheritance between 85-75 Ma (e.g., Singh et al., 2007; Ravikant et al., 2009; White et al., 2011). On this basis, it has instead been suggested that the Kargil Intrusives are not related to, or associated with, the Ladakh Arc, and as such is not evidence for the collision and accretion of the Dras Arc onto the Eurasian margin (Buckman et al., 2018; Walsh et al., 2019). Other workers favour a reconstruction which sees accretion first of the Dras Arc onto the Indian margin

(Klootwijk et al., 1979; Brookfield and Reynolds, 1981; Searle, 1983; Buckman et al., 2018). The first detailed detrital zircon study of the Nindam Formation (Walsh et al., 2019) revealed a predominantly Cretaceous (~125-84 Ma) source of zircons but a distinct older Upper Jurassic population between ~185-135 Ma along with a subdued but consistent influx of Precambrian Gondwanan (Indian-derived) zircons. This led Walsh et al., (2019) to conclude that the Dras Arc collided first with India rather than Eurasia at ~55 Ma, based on partial subduction of the northern Indian continental margin to form the 55 Ma Tso Morari eclogite (de Sigoyer et al., 2000). Upadhyay and Sinha (1998, 2004) have also argued that the forearc Nindam Formation is host to Gondwanan-derived sediment and pollen although, they do not necessarily relate this to collision with the Indian margin. Buckman et al., (2018) also suggested that the Dras and Spong arcs are part of the same island arc complex that, instead of developing separately (e.g., Corfield et al., 2011), developed as part of the same subduction system which first collided with India during the lower Eocene. It is also possible that this system is related to the Upper Jurassic intraoceanic Zedong terrane of Tibet (McDermid et al., 2002).

5.6.4 Regional correlations

Many researchers follow the model of Rolland et al. (2002) who interpret the Indus ophiolites, island arc (Dras Arc), continental arc (Ladakh Arc) and Shyok Ophiolite as part of a single forearc, arc, backarc system that evolved above a single subduction zone that alternated between periods of rollback and outboard island arc development, to periods of slab flattening and more continental arc magmatism (Figure **5.2**A). Recent work has also suggested that a large-scale subduction zone existed in the northern Neotethyan domain between Anatolia and Eurasia (Rolland et al., 2020). However, other models (Figure **5.2**B) treat each of these entities as separate terranes, with potentially unique tectonic histories involving two or more north-dipping subduction zones (Aitchison et al., 2000; Buckman et al., 2018; Pedersen et al., 2001). The Upper Jurassic ages acquired for felsic rocks from the Dras Volcanics have important implications for potential regional correlations and distinctions between the Dras, Ladakh, Shyok and Kohistan arcs in the NW Himalaya. In terms of making correlations between the Dras Arc and Ladakh Arc, there are very few geochemical or geochronological similarities and therefore very little evidence to suggest the two terranes are related, apart from their proximity either side of the Mongyu Mélange. The Ladakh Arc granites clearly intrude the Shyok Volcanics and the equivalent felsic Khardung Volcanics are a distinct group of volcaniclastics which unconformably overlie both Ladakh Arc granites and Shyok volcanic basement rocks. More similarities exist between the Dras and Shyok volcanic rocks, but these units are separated by considerable distance across strike of several units and structures, notably the Mongyu Mélange. Upper Jurassic (gabbronorite 159 ± 1 Ma; plagiogranite 152 ± 2 Ma) zircon ages obtained for

the gabbroic intrusive equivalent (Changma Complex) of the Shyok Volcanics along the Shyok Suture to the north of the Ladakh Range indicate a similar age between the Dras and Shyok arc rocks (Saktura et al., 2020). However, the Shyok volcanic arc ophiolite is not necessarily equivalent to the Dras Arc volcanic rocks found across strike and much further south. Saktura et al. (2020) point out that the Shyok Ophiolite contains typical arc basalts and boninites (Thanh et al., 2012) more typical of an island arc and forearc setting, which suggest that interpretations of the Shyok volcanic arc ophiolite as a backarc to the Ladakh Arc and the Dras Arc as the forearc material of a single, north-dipping subduction zone are problematic and possibly oversimplistic. The Shyok volcanic arc ophiolite is intruded by crosscutting felsic intrusives of the younger (~66-46 Ma) Ladakh Batholith, which has been well dated (Ravikant et al., 2009; Singh et al., 2007; White et al., 2011), whilst the Dras Arc contains no true Ladakh Arc intrusive rocks or detritus (Walsh et al., 2019). Interbedded foraminifera-bearing limestones of the 'Sedimentary Unit' within the Shyok Volcanics yield Albian-Cenomanian aged fossils (e.g., Chang La; Rolland et al., 2000). Similar aged interbedded fossiliferous units are also reported for the Dras Volcanics (Dras I unit; Reuber, 1989; Fuchs, 1982). Whilst the Dras Arc was active at the same time as the Shyok volcanic arc ophiolite (Saktura et al., 2020) they are separated by considerable distance across the strike of several units and major structures, notably the Mongyu Mélange, and thus correlations are difficult at best.

The serpentinite-matrix Mongyu Mélange separates the Ladakh Arc to the north from the Dras-Nindam terrane to the south. Although this northern mélange zone has previously been described (e.g., Robertson, 2000), some workers do not recognise the occurrence of a suture between these two terranes possibly because it would be inconsistent with a model involving a single arc and collision. The Mongyu Mélange is a disrupted serpentinite-matrix mélange, and not at all similar to the serpentinised ultramafic-mafic intrusive bodies sometimes found within the Ladakh Batholith, for example, those occurring in the Ladakh Range (Rolland et al., 2000).

The contrasting forearc basins, these being the Nindam Formation of the Dras Arc and the Chogdo Formation of the Ladakh Arc, are vastly different in their depositional environments and composition. For example, the ~100-80 Ma Nindam Formation is deep marine derived interbedded volcaniclastics and pelagic shales with minor ultramafic-, basalt- and chert-rich conglomerates (Walsh et al., 2019), whereas the ~51 Ma Chogdo Formation is shallow marine derived quartz-rich siliciclastics and carbonates with abundant granite clasts (Henderson et al., 2011). The post-collisional Chilling Formation is an important marker unit and is dated as ~55 Ma (Henderson et al., 2011). This formation is dominated by a combination of ultramafic clasts derived from the Dras volcanic arc ophiolite and quartzite from India, however no granitic clasts from the Ladakh Arc have been reported (Henderson et al., 2011).

Lastly, there is no reported continuity between the Dras and Ladakh arcs. There is no observed Ladakh Batholith derived crosscutting dyke or stitching pluton to relate these two terranes. We recognise that the presence of either of these features within the Dras Volcanics would disprove the allochthonous terrane model. However, all available evidence suggests that the Dras Arc and Shyok volcanic arc ophiolite were likely developing as separate island arc terranes at about the same time in the Neotethyan and Mesotethyan oceans respectively, but the Ladakh Arc is distinctly continental (Bhutani et al., 2009; Clift et al., 2002b) and developed after closure of the Mesotethyan Ocean along the Shyok Suture beginning at ~85 Ma (Borneman et al., 2015).

We acknowledge that there are similarities between the Dras Arc and some elements of the "Kohistan Arc" of Pakistan such as the Chilas Complex (~86 Ma) in the south (Schaltegger et al., 2002) and the Late Jurassic Matum Das arc intrusives in the north (Jagoutz et al., 2018; Schaltegger et al., 2003). However, we also caution that the single arc above a single north-dipping subduction zone model dominates interpretations of what is broadly grouped as the "Kohistan Arc" and thus the distinctions between ophiolite, island arc and continental arc terranes that are being recognised in Tibet (Aitchison et al., 2007b) and Ladakh (Buckman et al., 2018) may not have been adequately considered for the Pakistan section of the Neotethyan suture zone.

It has been tentatively proposed that the Kohistan Arc developed on oceanic lithosphere as old as 175 Ma (Bosch et al., 2011), with the volcanic arc having started to form at least by 118 Ma (Dhuime et al., 2007), but possibly earlier at 135 Ma (Bosch et al., 2011). The Kohistan Arc has a distinctly similar Cretaceous (135-81 Ma) magmatic episode of intraoceanic activity (Bosch et al., 2011; Dhuime et al., 2007; Schaltegger et al., 2002; Yamamoto et al., 2005) to the Dras Arc (125-84 Ma; Walsh et al., 2019). These two arc systems also share commonalities regarding intraoceanic geochemical signatures of different lithological units (Burg et al., 1998; Dhuime et al., 2007; Dhuime et al., 2009).

However, although there are distinct similarities between the two, there are some complicating factors which inhibit an unequivocal genetic link between both the Dras and Kohistan arcs. The Nanga Parbat syntaxis is a structural constraint and due to this feature, there are no continuous units from the Ladakh to Kohistan regions. Therefore, although the lower crustal Chilas Complex of the Kohistan Arc in the west is generally regarded as being equivalent to the Dras Volcanics of the Dras Arc in the east (Bilqees et al., 2016; Khan et al., 1989; Schaltegger et al., 2002), there is no continuation of these outcrops due to the syntaxis. Another complicating factor comes from the word 'Kohistan' being used to describe both the volcanic arc system and the batholith. Some

workers prefer to envisage a continuation or relatedness between the two or exchange one for the other, leading to misinterpretations throughout the literature. The last complicating factor is that the Kohistan Arc has been interpreted as having collided with Eurasia before final continent-continent collision (Bosch et al., 2011; Schaltegger et al., 2002; Yamamoto et al., 2005). This is at odds with the evidence for the Dras Arc, which is interpreted as having collided with the passive Indian margin (Buckman et al., 2018; Walsh et al., 2019) prior to the continental collision of India with Eurasia. We are reluctant to make correlations through the syntaxis and acknowledge other compounding factors which do not allow for an undeniable link between the Dras and 'Kohistan' arcs. We appreciate the similarities and believe more work is required in this area to determine the relatedness of these two arc terranes.

We agree that it is likely that the largely granitic intrusive suites of both the Ladakh and Kohistan batholiths are equivalent, with previous studies finding similarity in their age and composition (Ravikant et al., 2009; Reichardt et al., 2010; Rolland et al., 2000; Rolland et al., 2002; Shellnutt et al., 2014; Weinberg and Dunlap, 2000). Together with the Gangdese Batholith these form the Trans-Himalayan Batholith that extended along the entire southern margin of Eurasia. We tentatively suggest that the Chilas Complex to the south of the Kohistan Batholith may not actually belong to the Kohistan Arc system, and as with the Dras and Ladakh arcs, may indeed be two separate terranes. Whereas the Chilas Complex and Dras Volcanics are representative of Neotethyan intraoceanic arc systems, the Kohistan and Ladakh batholiths are representative of continental arc volcanism on the active Eurasian margin.

The Dras Arc has some distinct similarities with the Jurassic island arc Zedong terrane found along the equivalent Neotethyan Yarlung-Zangpo Suture in Tibet (Aitchison et al., 2007b; Aitchison et al., 2000; Liu et al., 2020; McDermid et al., 2002). McDermid et al. (2002) propose that the Zedong terrane is an island arc complex that was active from at least the Late Jurassic to Early-mid Cretaceous and was emplaced onto the Indian margin. It has since been suggested that emplacement of this intraoceanic arc occurred at ~55 Ma, before terminal collision between India and Eurasia at about ~34 Ma (Aitchison et al., 2007a; Aitchison et al., 2000). There are striking similarities between the Zedong terrane and the Dras Arc. Using a combination of U-Pb and $^{40}Ar/^{39}Ar$ dating techniques, the Zedong terrane has proto-arc crust transitioning from MORB- to IAT-like ranging in age of ~163-154 Ma (Liu et al., 2020; Zhong, 2006), with the main arc edifice active ~162-152 Ma (McDermid et al., 2002; Zhang et al., 2014). Late boninite-like dykes have also been identified and dated at ~149 Ma (Liu et al., 2020). This study on the inception of the intraoceanic Dras Arc has produced similar Upper Jurassic dates for a felsic tuff (160 ± 3 Ma) and trachydacite (156 ± 1 Ma). Boninite-like lavas have also been identified within the Dras Volcanics (Walsh et al., 2019). Volcanics of the Zedong terrane plot very similarly to that of the

Dras Volcanics and are consistent with intraoceanic island arc signatures (Figure **5.6**). Associated MORB-like ophiolitic volcanic rocks (Luobusha Ophiolite; ~163 Ma) and early dykes of the Zedong terrane are analogous to typical island arc tholeiites, whereas late dykes are similar to boninite-like lavas (~149 Ma). Based on this, Liu et al. (2020) proposed that the Zedong terrane experienced multi-stage partial melting of a mantle source, with gradually enhanced subduction influences to the mantle source through time. There are no reports of felsic volcanic rocks within the Zedong terrane, however Malpas et al. (2003) collected andesitic lavas, which although not felsic, does meet the majority of the characteristics of an adakitic lava (Figure **5.7**), and may provide more insight into the multi-stage partial melting suggested by Liu et al. (2020). It is likely that the Dras Arc is the western extension of this laterally extensive but narrow tectonically bounded island arc complex and includes both the Spongtang Ophiolite-Spong Arc complex and intraoceanic Zedong terrane. We propose that this allochthonous island arc complex developed within the Neotethyan Ocean as a result of north-directed subduction, with obduction of this terrane onto the northern margin of India occurring at about the Palaeocene-Eocene boundary, prior to terminal continental collision of India and Eurasia.

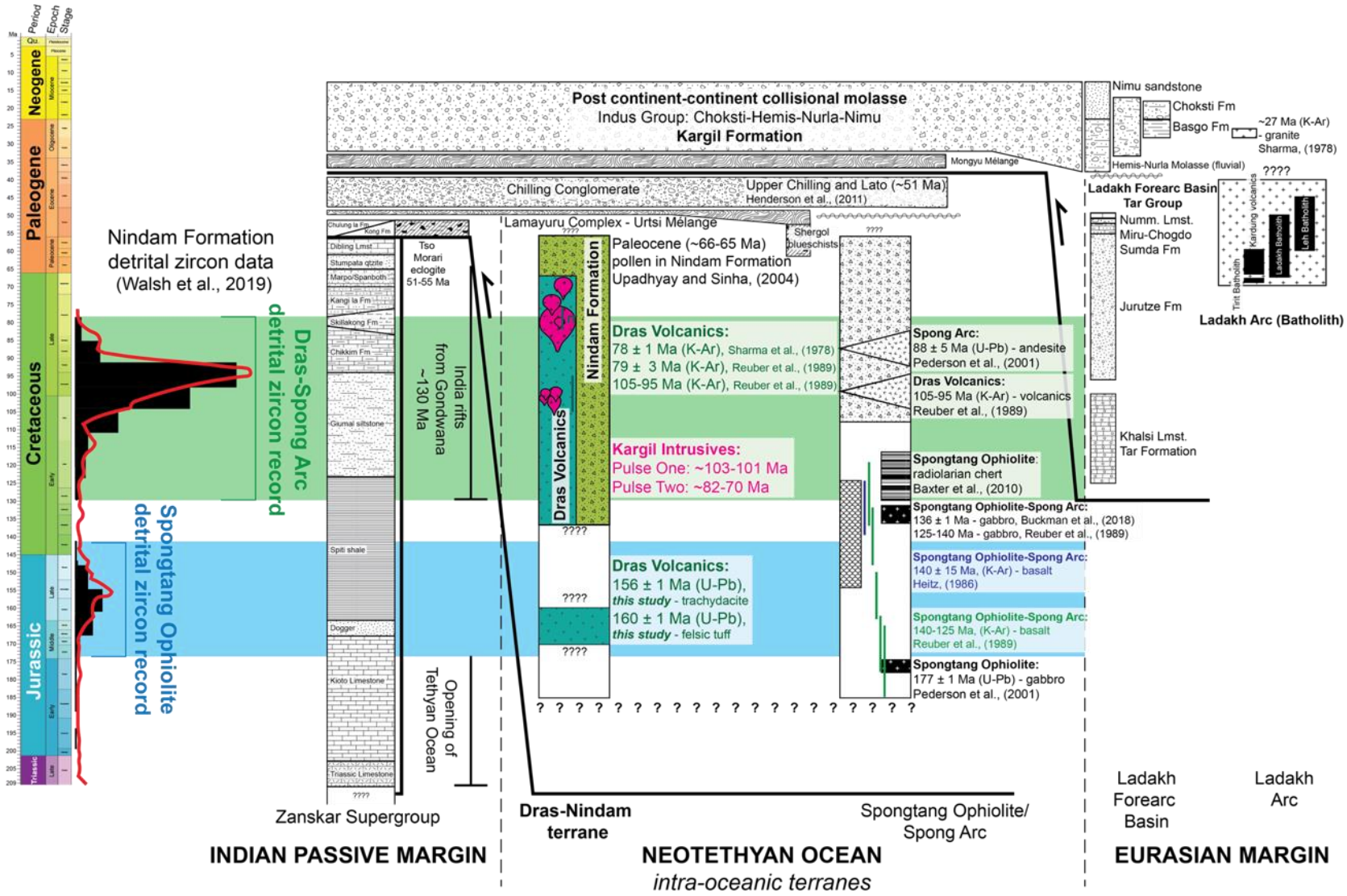

Figure 5.12: Time-space diagram for the evolution of the Neotethyan Dras Arc in relation to the northern, passive margin of India and the active continental margin of southern Eurasia. For a full list of references, refer to Supporting Information Text.

5.7 Conclusions

(i) Upper Jurassic felsic volcanic ages relating to the inception of the intraoceanic Dras Arc have been acquired for a felsic tuff (160 ± 3 Ma) and trachydacite (156 ± 1 Ma) making these the oldest recorded ages within the Dras Arc.

(ii) These Upper Jurassic felsic volcanic rocks have distinctly low-Mg adakitic characteristics typically associated with melts derived from partial melting of basaltic ocean crust, possibly during incipient stages of arc development.

(iii) Previous ages for the Kargil Intrusives have been reproduced (102 ± 2 Ma and 101 ± 2 Ma), including a much younger magmatic pulse (80 ± 1 Ma).

(iv) Whole rock geochemistry indicates that volcanic rocks from the Dras Arc are consistent with intraoceanic island arc signatures and are similar to those of the nearby Spongtang Ophiolite-Spong Arc complex and the intraoceanic Zedong terrane of Tibet.

(v) The Dras-Spong intraoceanic arc initiated in the Neotethyan Ocean just outboard of the northern margin of India during the Upper Jurassic. This is much earlier than previously reported, with arc activity spanning at least 100 m.y. between initiation around ~160 Ma and final collision with northern margin of India sometime in the Palaeocene between 60-50 Ma.

5.8 Acknowledgements

This project was partially supported by the GeoQuEST Research Centre and a Small Project Grant (2017) from the University of Wollongong. This research has also been conducted with the support of the Australian Government Research Training Program Scholarship awarded to J.M.J Walsh. Thank you to W.M. Saktura for fieldwork assistance, geochemical analyses and discussions. J. Punchok is thanked for guidance in Ladakh. We would also like to thank S.L. Walsh for assistance in the field. Careful reviews from two anonymous reviewers are gratefully acknowledged. Editor S. Kwon is thanked for prompt handling of the manuscript. Data used are listed in the references, figures and supporting information. There are no declarations of interest.

5.9 Coauthor contributions

Walsh, Jessica, M.J.

GeoQuEST Research Centre, School of Earth, Atmospheric and Life Sciences,

University of Wollongong, Wollongong, NSW 2522, Australia.

Position: PhD candidate

Email: jw063@uowmail.edu.au

Credit author statement: Conceptualisation, Methodology, Investigation, Data Curation, Writing - Original Draft, Writing - Review & Editing, Visualisation.

Buckman, Solomon

GeoQuEST Research Centre, School of Earth, Atmospheric and Life Sciences,

University of Wollongong, Wollongong, NSW 2522, Australia.

Position: Senior lecturer in economic geology

Email: solomon@uow.edu.au

Credit author statement: Conceptualisation, Methodology, Investigation, Writing - Original Draft, Writing - Review & Editing, Supervision, Funding Acquisition.

Nutman, Allen, P.

GeoQuEST Research Centre, School of Earth, Atmospheric and Life Sciences,

University of Wollongong, Wollongong, NSW 2522, Australia.

Position: Professor in igneous and metamorphic petrology

Email: anutman@uow.edu.au

Credit author statement: Methodology, Writing - Review & Editing, Supervision.

Zhou, Renjie

School of Earth and Environmental Sciences,

The University of Queensland, Brisbane, QLD 4072, Australia.

Position: Lecturer in tectonics

Email: renjie.zhou@uq.edu.au

Credit author statement: Investigation, Methodology, Data Curation, Writing - Review & Editing

5.10 Supporting information

The significance of Upper Jurassic felsic volcanic rocks within the incipient, intraoceanic Dras Arc, Ladakh, NW Himalaya

Jessica M.J. Walsh[1], Solomon Buckman[1], Allen P. Nutman[1], and Renjie Zhou[2]

[1]GeoQuEST Research Centre, School of Earth, Atmospheric and Life Sciences, University of Wollongong, Wollongong, NSW 2522, Australia.
[2]School of Earth and Environmental Sciences, The University of Queensland, Brisbane, QLD 4072, Australia.

Overview

The following information includes further support for the methods, results and discussion sections of Chapter 5, referred to in-text as 'Supporting Information Text'. The first section (Supporting Information: Methods) of the Supporting Information includes a detailed description of zircon U-Pb geochronologic methods used for samples from the Dras Volcanics and Kargil Intrusives, Ladakh Himalaya, NW India, which describes zircon preparation, LA-ICP-MS and SHRIMP methodologies. The second section (Supporting Information: Results) of the Supporting Information includes detailed results related to whole rock geochemistry and geochronology. The third section (Supporting Information: Discussion) of the Supporting Information includes a full list of the references used to compile "*Figure* **5.12**: Time-space diagram for the evolution of the Neotethyan Dras Arc in relation to the northern, passive margin of India and the active continental margin of southern Eurasia".

Following this are tabulated data, and includes:

- Table S5.1: Sample localities and lithological descriptions
- Table S5.2: Whole rock geochemistry
- Table S5.3: Zircon U-Pb results using LA-ICP-MS and SHRIMP
- Table S5.4: Results of mixture modelling experiments

5.10.1 Supporting information: Methods

5.10.1.1 Zircon U-Pb geochronology

5.10.1.1.1 Zircon preparation

Zircons were separated at the Institute of Hebei Regional Geology Survey, China. The samples were chipped in a pre-contaminated jaw crusher, using a subsample first. Chips were thoroughly washed with water prior to being ground into a coarse powder using a jaw crusher. The coarse powder was separated into heavy and light fractions using heavy liquids to obtain the >3.31 zircon-bearing fraction. The heavy fraction was washed and dried prior to being passed through a Franz Isodynamic Magnetic Separator to obtain zircons (normally the non-magnetic fraction at 2A). Zircon grains were examined using a binocular microscope, handpicked and mounted with standard TEMORA II grains on double-sided tape on a glass plate, which were then cast with epoxy resin in a mould. TEMORA II was distributed as several clusters of grains in different parts of the zircon mount to increase confidence in the accuracy of calibration of U-Pb across the entire mount when analysed. The mounts were ground on 1200 grade wet and dry paper to reveal approximately half sections through the grains and then polished with 1 µm diamond paste. Transmitted and reflected light photomicrographs were taken, along with cathodoluminescence (CL) images. The CL images were obtained using a Scanning Electron Microscope (SEM) JEOL JSM-6490LV with a 15-kV conventional tungsten filament thermionic source coupled with a Gatan MonoCL4 used in polychromatic mode at the Electron Microscope Centre (EMC), Innovation Campus, University of Wollongong (UOW).

5.10.1.1.2 LA-ICP-MS

A total of 82 zircon grains were chosen from two samples from the Dras Volcanics (sample 17NI05: felsic tuff, $n = 28$; sample 17NI12: trachydacite, $n = 54$) and a total of 120 zircon grains were chosen from three samples from the Kargil Intrusives (sample 17KG01: granodiorite, $n = 30$; sample 17KG02: diorite, $n = 30$; sample 17KG04: granodiorite, $n = 60$) for U-Pb dating by Laser Ablation Inductively Coupled Plasma Mass Spectrometry (LA-ICP-MS) at Centre for Geoanalytical Mass Spectrometry (CGMS), The University of Queensland (UQ), Australia, following methods similar to those in Zhou et al. (2020). Laser ablation was undertaken using an ASI RESOlution 193 ArF nm excimer laser system. Following evacuation of air, He carrier gas was introduced into the laser cell at a flow rate of 0.35 l/min. 0.05 l/min of N_2 gas was also introduce to the laser cell to enhance the measurement sensitivity. The gas mixture was then introduced into the plasma torch of a Thermo iCAP RQ quadruple ICP-MS with 0.85 l/min Ar nebuliser gas. No reaction gas was employed. The laser was run with a 30 µm diameter round spot at 10 Hz, with a measured instrument laser-fluence (laser pulse energy per unit area) of 2.9

J/cm^2. For each spot, 5 s of blank was collected, followed by 25 s of ablation and 10 s of wash out. Prior to data acquisition, ICP-MS signals were optimised during tuning. Parameters particular to the analytical session include, ~400 K cps of ^{238}U counts, ~1 of ^{238}U/^{232}Th, ~0.21 of ^{206}Pb/^{238}U were achieved for measuring NIST612 glass using line scans of 3 µm/s, 10 Hz, 50 µm round laser pit, and 3 J/cm^2. The following isotopes were collected using a single collector: ^{88}Sr (dwell time=0.005 s), ^{91}Zr (dwell time=0.001 s), ^{200}Hg (dwell time=0.01 s), ^{204}Pb + ^{204}Hg (dwell time=0.01 s), ^{206}Pb (dwell time=0.045 s), ^{207}Pb (dwell time=0.055 s), ^{208}Pb (dwell time=0.01 s), ^{232}Th (dwell time=0.01 s), ^{238}U (dwell time=0.01 s). A single cycle took ~0.155 s. Therefore, during a 25 s ablation, ~160 measurements were made on each mass. From the session, a ^{206}Pb/^{238}U age of 419.0 ± 1.1 Ma, uncorrected for common Pb (95% confidence, n = 93, MSWD = 7.7) for the TEMORA II secondary reference material was obtained, which has a TIMS ^{206}Pb/^{238}U age of 416.78 ± 0.33 Ma determined by ID TIMS (Black et al., 2004). Calculated mean ages and mixture modelling results are presented at 2 σ. ^{206}Pb/^{238}U ages are reported for <1000 Ma grains. No grains produced ages >1000 Ma, however ^{207}Pb/^{206}Pb ages and ratios are reported to evaluate the level of common Pb, concordance and detect inheritance.

5.10.1.1.3 SHRIMP

A total of six grains (analytical sites 2.2, 7.2, 12.2, 14.2, 24.2 and 26.2) from the Dras Volcanics felsic tuff (sample 17NI05) were chosen for zircon U-Pb dating using the Sensitive High-Resolution Ion Microprobe (Reverse Geometry; SHRIMP-RG) instrument at the Australian National University (ANU), Australia. The purpose behind this investigation was to test the validity of the Jurassic age of for the Dras Volcanics by producing absolute U-Pb analyses on the margins of grains that had already been analysed (using LA-ICP-MS). Analytical sites on the grain margins were focused on those with continuous oscillatory zonation throughout. Zircon mounts were cleaned and coated with ~10 nm of high purity Au (>99.999%) before analysis. The analytical procedure followed Williams (1998). U-Th abundance was calibrated based on the reference zircon SL13 (U = 238 ppm). A total of six cycles were made at each of the nominal mass stations: ^{196}Zr, ^{204}Pb, background $^{204.1}$Pb, Pb (^{206}Pb, ^{207}Pb, ^{208}Pb), ^{238}U, ^{248}ThO (^{232}Th + ^{16}O) and ^{254}UO (^{238}U + ^{16}O). Parameters particular to the analytical session include a spot size of ~15-20 µm, with the primary O_2^- ion beam of 5 nA. TEMORA II was analysed for U-Pb calibration after every two analytical sites (four times in total). The raw data were reduced using the program *POXI-SC*. ^{206}Pb/^{238}U were corrected using the TEMORA II standard with a concordant age of 416.78 ± 0.33 Ma (Black et al., 2004). The reduced and calibrated data were then assessed and plotted using *Isoplot 4.15* (Ludwig et al., 2003). Calculated mean ages and mixture modelling results are presented at 2 σ. ^{206}Pb/^{238}U ages are reported for <1000 Ma grains. No grains produced ages >1000 Ma.

5.10.2 Supporting information: Results

5.10.2.1 Whole rock geochemistry

5.10.2.1.1 Alteration

Fresh and homogenous samples were collected for geochemical analysis, whereby surficial exterior layers were removed to ensure only fresh rock was used. To account for ancient weathering, the mafic-felsic-weathering (MFW) ternary diagram (Ohta and Arai, 2007) was used to demonstrate that the samples collected were indeed unweathered. Samples from the Dras Volcanics (this study: n = 8; Bhat et al., 2019: n = 10), Kargil Intrusives (this study: n = 5; Bhat et al., 2019: n = 4), Spongtang Ophiolite (Buckman et al., 2018: n = 14), Spong Arc (Corfield et al., 2001: n = 15), Zedong terrane (Aitchison et al., 2007b: n = 5; Liu et al., 2020: n = 29; Malpas et al., 2003: n = 2; Zhang et al., 2014: n = 8), and Luobusha Ophiolite (Zhong, 2006: n = 15) indicate minimal weathering, with the majority of samples falling into the field of fresh calc-alkaline/mafic igneous rocks on the MFW ternary diagram (Ohta and Arai, 2007; Figure S5.1). With regard to lithological classification and tectonic discrimination diagrams (Figure **5.6**), those elements which are the least susceptible to both weathering and hydrothermal alteration have been utilised (MacLean, 1990). The majority of these are immobile elements, including high field strength elements (HFSE) and rare-earth elements (REE).

5.10.2.1.2 Chondrite-normalised REE

Chondrite-normalised REE patterns for the basalts of the Dras Volcanics (Figure S5.2a) show slight light to heavy REE enrichment (LREE/ HREE, e.g., La_N/Yb_N = 1.6 – 5.3), similar to the Kargil Intrusives (Figure S5.2b; LREE/HREE, e.g., La_N/Yb_N = 1.7 – 4.0). Two exceptions to this are a Dras Volcanics trachydacite (sample 17NI12) and Kargil Intrusives granodiorite (sample 17KG04), both which demonstrate a pronounced enrichment of LREE compared to HREE (LREE/HREE, e.g., La_N/Yb_N = 11.2 and 27.8 and, respectively). Figure S5.2c compares chondrite normalised REE patterns of samples from the Dras Volcanics and Kargil Intrusives.

With regard to the Dras Volcanics, there is a diversity between samples, with varying negative Eu anomalies ranging between 0.78 – 0.99 and positive Eu anomalies demonstrating a range between 1.00 – 1.14. With regard to the Kargil Intrusives, negative Eu anomalies occur in those samples which are relatively more felsic in composition, i.e., granodioritic-dioritic (notably, samples 17KG01, 17KG02 and 17KG04; where Eu/Eu^* = 0.86 – 0.97), while those which are gabbroic in composition demonstrate positive Eu anomalies (1.14 – 2.49). Refer to Supporting Information Table S5.2 for calculated values.

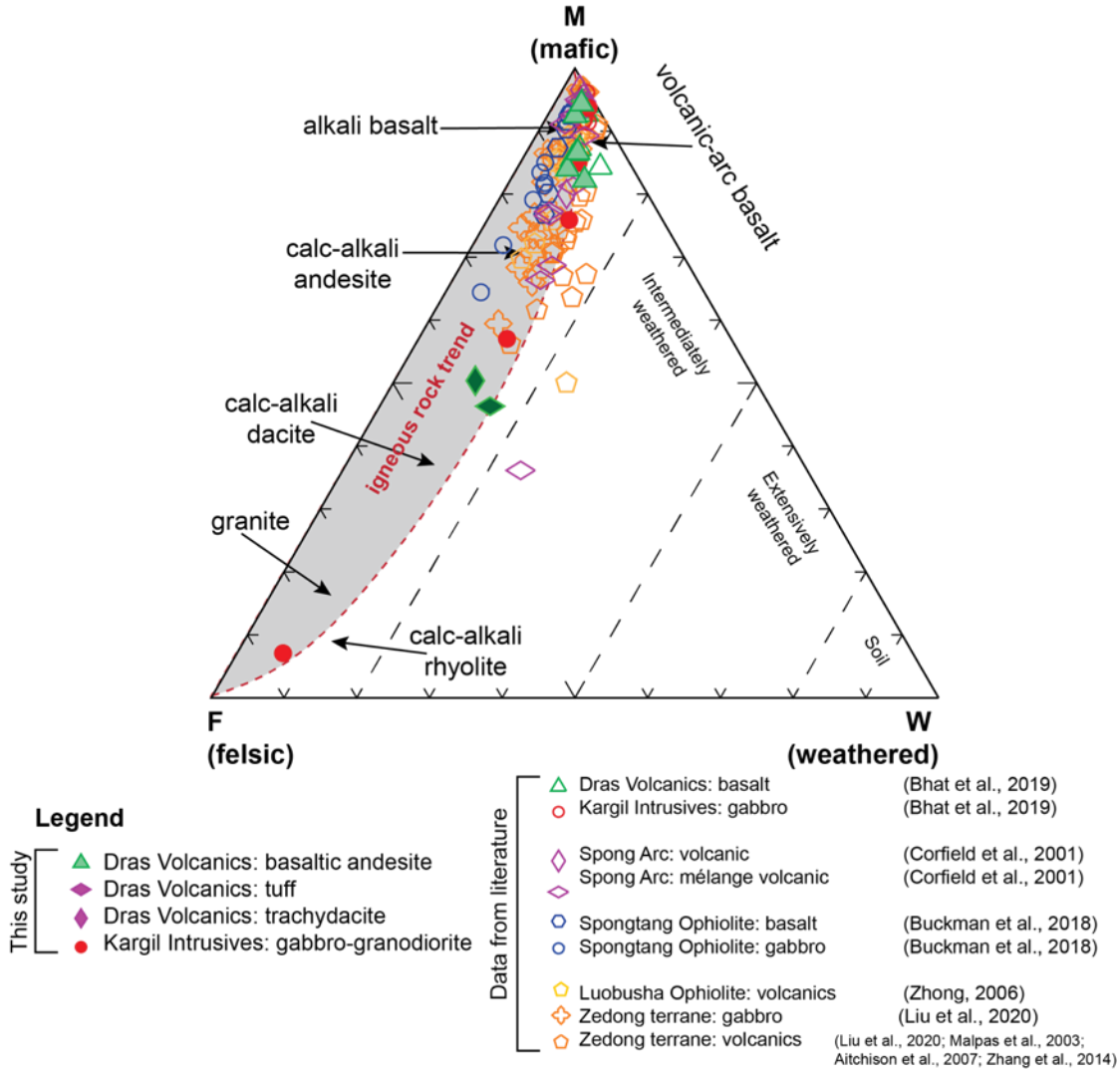

Figure S5.1: Mafic-felsic-weathering (MFW) ternary diagram of Ohta and I). Samples from this study are combined with previous analyses of the Dras Volcanics, Kargil Intrusives, Spongtang Ophiolite- Spong Arc complex, Zedong terrane and Luobusha Ophiolite (Aitchison et al., 2007b; Bhat et al., 2019; Buckman et al., 2018; Corfield et al., 2001; Liu et al., 2020; Malpas et al., 2003; Zhang et al., 2014; Zhong, 2006).

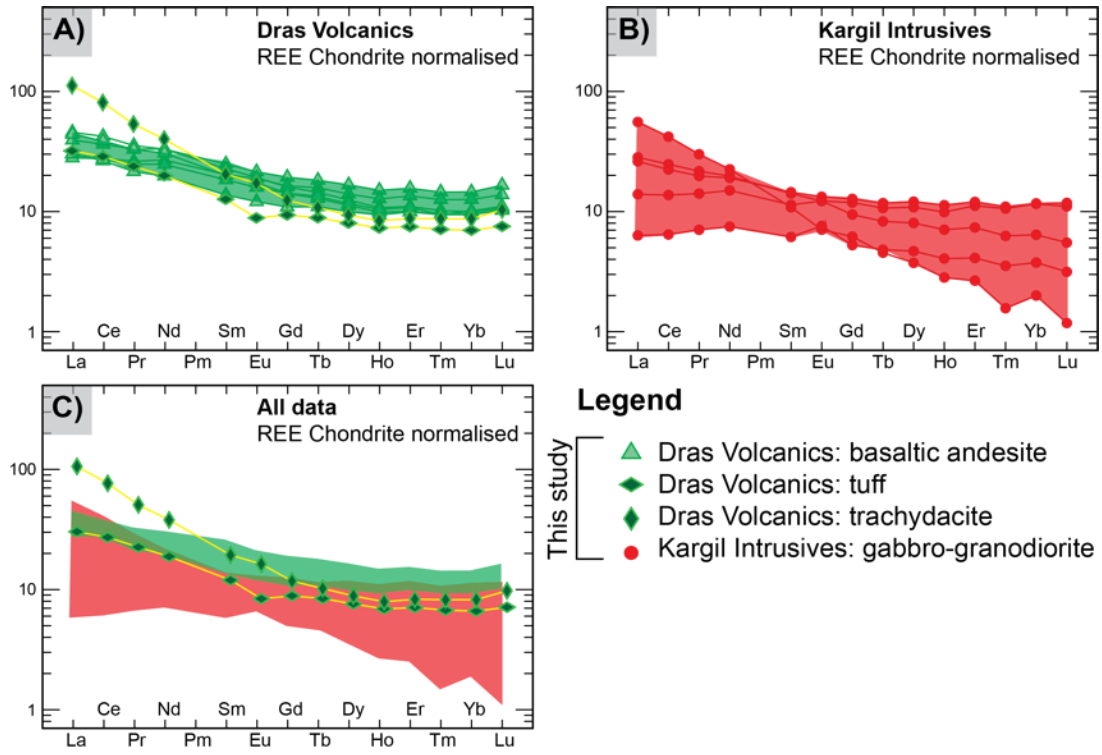

Figure S5.2: Chondrite-normalised REE patterns for the Dras Volcanics and Kargil Intrusives (Sun and McDonough, 1989). **A)** Dras Volcanics chondrite-normalised plot; **B)** Kargil Intrusives chondrite-normalised plot; **C)** Combined chondrite-normalised plot, including the Dras Volcanics and Kargil Intrusives and Spongtang Ophiolite-Arc complex.

5.10.2.2 Zircon U-Pb geochronology

5.10.2.2.1 Zircon grain descriptions

5.10.2.2.1.1 Dras Volcanics

Felsic tuff (sample 17NI05)

The zircon yield for a felsic tuff (sample 17NI05) from the Dras Volcanics was high, with approximately 500 grains separated. Grains are typically stubby or equant, with a lesser proportion maintaining prismatic euhedral habit. The longest dimension of grains from the felsic tuff ranges between 50-150 μm, with the average approximately 70 μm. Cathodoluminescence (CL) imaging typically shows grains with thin, complex magmatic oscillatory zoning, which is often truncated. Refer to Figure S5.3 for CL images of representative zircon grains, showing LA-ICP-MS analytical sites and ages (Ma).

Trachydacite (sample 17NI12)

The zircon yield for a trachydacite (sample 17NI12) from the Dras Volcanics was high, with >1000 grains separated. Grains are typically long, aside from those grains which appear to be fragments. The majority of grains have maintained a prismatic euhedral habit. The longest

dimension of grains from the trachydacite ranges between 70-250 μm, with the average approximately 100 μm. Cathodoluminescence imaging typically shows grains with magmatic oscillatory fine-scale zoning. In most grains the zonation is truncated. Refer to Figure S5.4 for CL images of representative zircon grains, showing LA-ICP-MS analytical sites and ages (Ma).

5.10.2.2.1.2 Kargil Intrusives

Granodiorite (sample 17KG01)

The zircon yield for a granodiorite (sample 17KG01) from the Kargil Intrusives was high, with >1000 grains separated. Grains show a diversity of shapes, ranging between stubby and prismatic with most being euhedral. Common among the grains are sharp, well-maintained edges. The longest dimensions of grains from the granodiorite ranges between 50-200 μm, with the average approximately 120 μm. Cathodoluminescence images show broad zonation, interpreted as magmatic. Refer to Figure S5.5 for CL images of representative zircon grains, showing LA-ICP-MS analytical sites and ages (Ma).

Diorite (sample 17KG02)

The zircon yield for a diorite (sample 17KG02) from the Kargil Intrusives was high, with >1000 grains separated. Grains are euhedral and show a diversity of shapes, ranging between stubby and prismatic. The longest dimensions of grains range between 70-300 μm, with the average approximately 150 μm. Some grains feature cracking, fracturing and regions of apparent recrystallisation. Refer to Figure S5.5 for CL images of representative zircon grains, showing LA-ICP-MS analytical sites and ages (Ma).

Granodiorite (sample 17KG04)

The zircon yield for a granodiorite (sample 17KG04) from the Kargil Intrusives was high, with >1000 grains separated. Grains are typically long, aside from those grains which appear to be fragments. The majority of grains have maintained prismatic or euhedral habit with sharp edges. The longest dimension of grains from the granodiorite ranges between 50-150 μm, with the average approximately 70 μm. Cathodoluminescence imaging shows a variety of different patterns. Some grains demonstrate typical magmatic oscillatory zonation, while other show recrystallisation with random regions of high and low luminescence. There are also grains which are completely homogenous, however these are rare. Some grains also feature cracking and fracturing. Refer to Figure S5.6 for CL images of representative zircon grains, showing LA-ICP-MS analytical sites and ages (Ma).

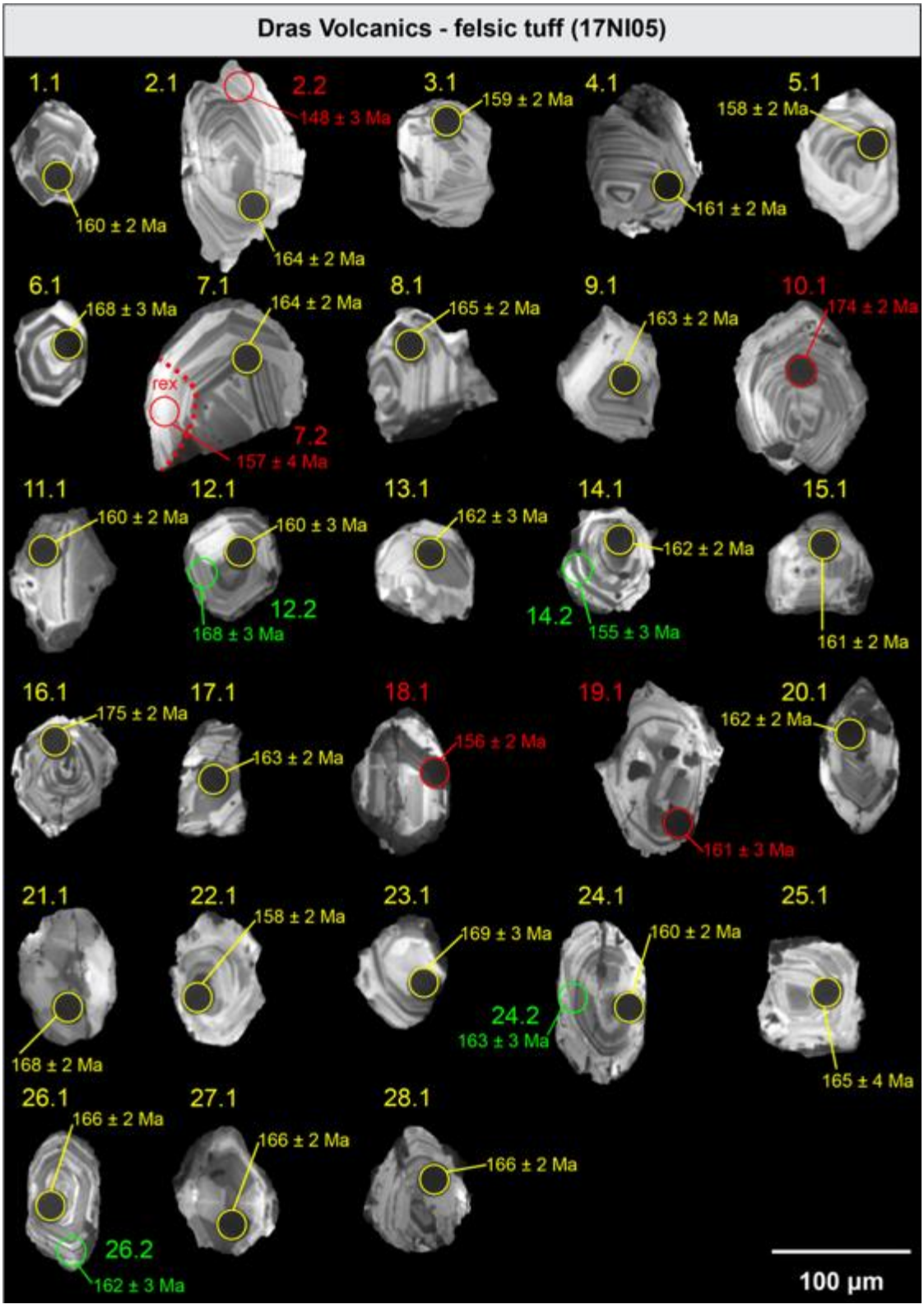

Figure S5.3: Cathodoluminescence (CL) images of representative zircons from a felsic tuff (sample 17NI05) of the Dras Volcanics. Spots represent LA-ICP-MS (yellow) and SHRIMP (green) analytical sites with $^{206}Pb/^{238}U$ ages. All analytical errors are given at 2σ. Rejected grains (red) have been omitted from final age calculations. Where 'rex' denotes recrystallised zone. Refer to Supporting Information Table S5.3 for reduced data and comments on rejected grains.

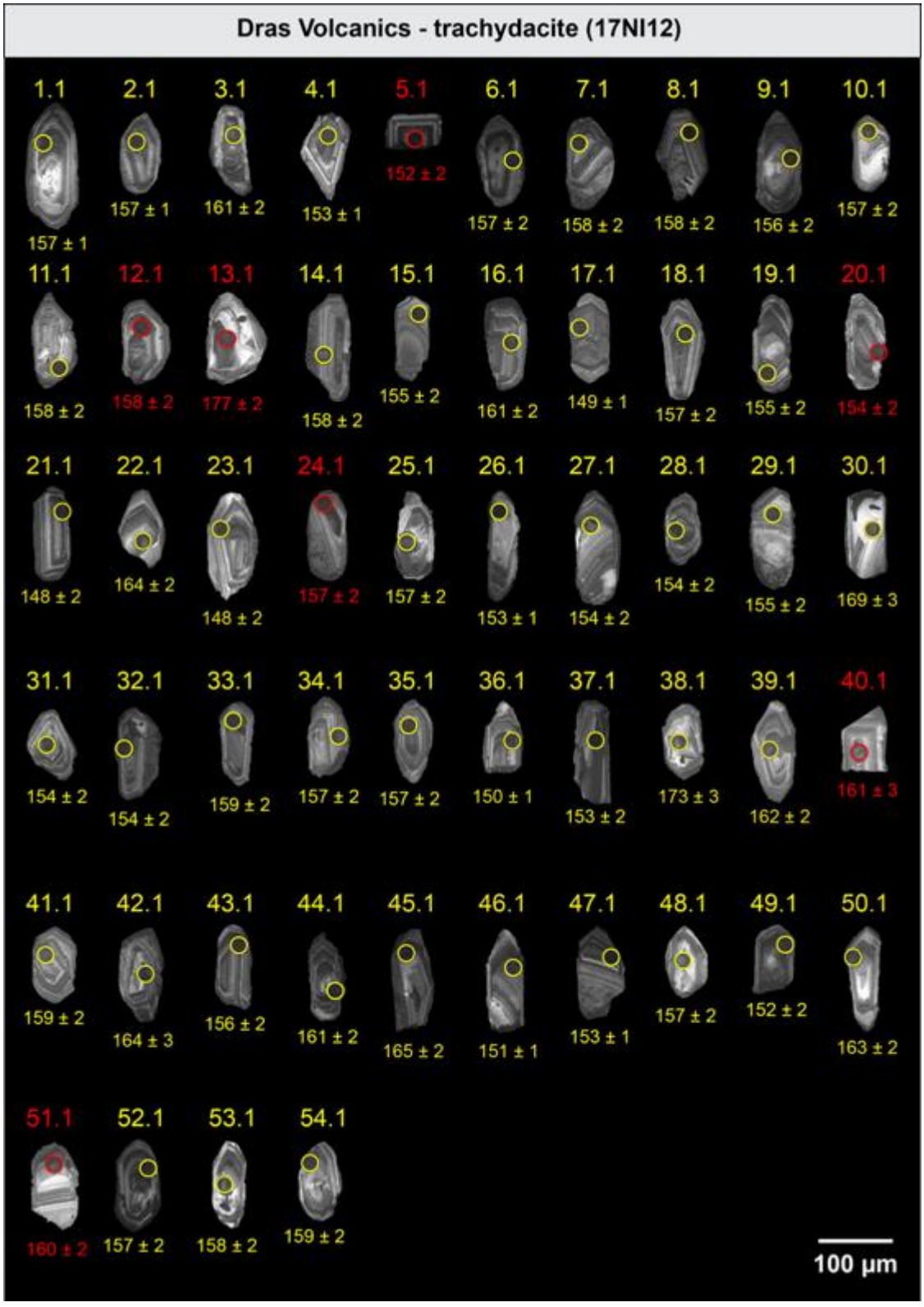

Figure S5.4: Cathodoluminescence (CL) images of representative zircons from a trachydacite (sample 17NI12) of the Dras Volcanics. Spots represent LA-ICP-MS analytical sites with $^{206}Pb/^{238}U$ ages. All analytical errors are given at 2σ. Rejected grains (red) have been omitted from final age calculations. Refer to Supporting Information Table S5.3 for reduced data and comments on rejected grains.

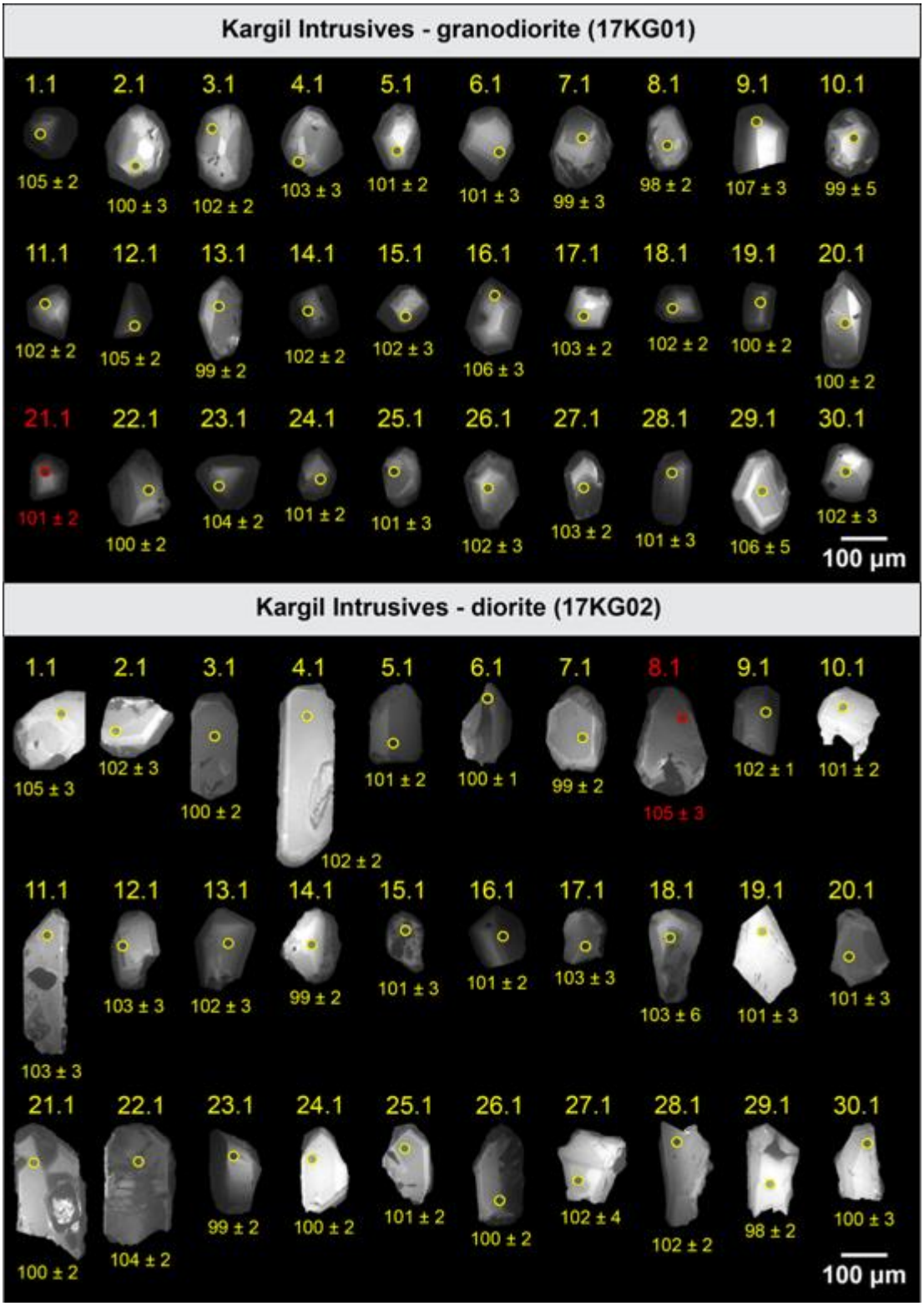

Figure S5.5: Cathodoluminescence (CL) images of representative zircons from a granodiorite and diorite (sample 17KG01 and 17KG02) of the Kargil Intrusives. Spots represent LA-ICP-MS analytical sites with $^{206}Pb/^{238}U$ ages. All analytical errors are given at 2σ. Rejected grains (red) have been omitted from final age calculations. Refer to Supporting Information Table S5.3 for reduced data and comments on rejected grains.

Figure S5.6: Cathodoluminescence (CL) images of representative zircons from a granodiorite (sample 17KG04) of the Kargil Intrusives. Spots represent LA-ICP-MS analytical sites with $^{206}Pb/^{238}U$ ages. All analytical errors are given at 1σ. Rejected grains (red) have been omitted from final age calculations. Refer to Supporting Information Table S5.3 for reduced data and comments on rejected grains.

5.10.2.2.2 Trachydacite (sample 17NI12) age determination

Mixture modelling was 'blind' to the CL imagery – after rejection of analyses with definitely discordant U-Pb ages. However, closer inspection of the CL images does show that the apparently youngest ages, including the mixture modelling component of 151 ± 3 Ma, contain a higher proportion of sites where CL imagery show variable recrystallisation ('rex') with the destruction of sharp-margined oscillatory zoning (Figure S5.7a) compared with sites falling in the 156 ± 1 Ma population (Figure S5.7b). This means that there was probably later disturbance following the magmatic zircon crystallisation, and that the 156 ± 1 Ma is a better estimate of the magmatic age for the trachydacite (sample 17NI12). Furthering this, referring to the mixture modelling data (Supporting Information Table S5.4) for the trachydacite (sample 17NI12) it is noted that the second component, i.e., 156 ± 1 Ma makes up 60% of the total age data, whereas for comparison the first component, i.e., 151 ± 3 Ma only makes up 20% (with the last two components making up the remaining 20%). Note, all ages are reported at 2 σ.

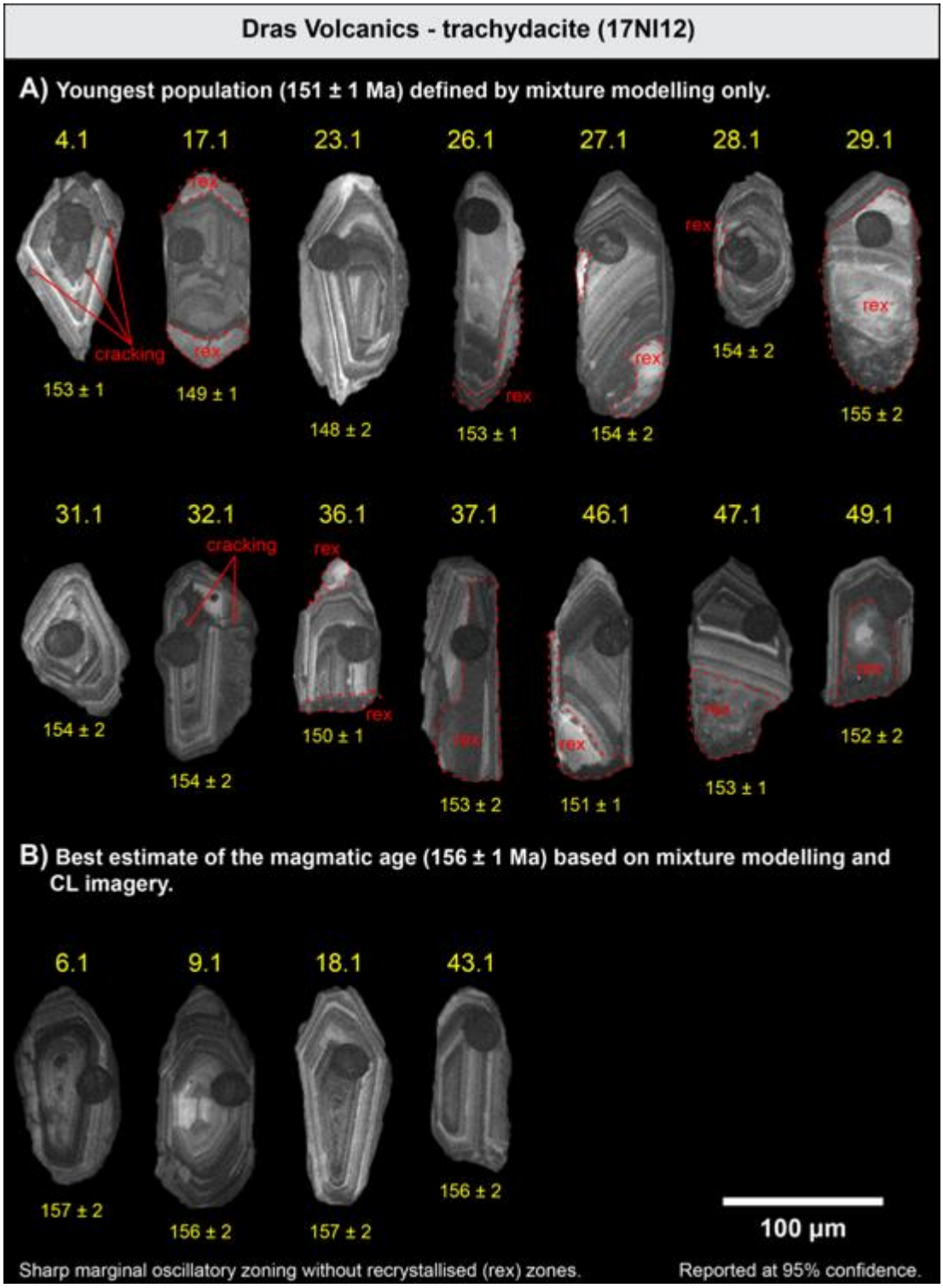

Figure S5.7: Investigation of the youngest population of zircon grains of the trachydacite (sample 17NI12) from the Upper Jurassic Dras Volcanics. **A)** Youngest population defined by mixture modelling only. Many of the grains display zones of recrystallisation ('rex'), cracking/fracturing and truncation leading to the destruction of sharp-margined oscillatory zoning; **B)** Best estimate of the magmatic age (156 ± 1 Ma) based on both mixture modelling and CL imagery, where grains of this population maintain sharp-margined oscillatory zonation. Note, only representative grains have been chosen.

5.10.3 Supporting information: Discussion

The following references accompany "*Figure* **5.12**: Time-space diagram for the evolution of the Neotethyan Dras Arc in relation to the northern, passive margin of India and the active continental margin of southern Eurasia".

Indian passive margin

Brookfield and Andrews-Speed (1984); Najman et al. (2017); Reuber et al. (1987); Robertson and Degnan (1993).

Dras-Nindam terrane

Reuber et al. (1989); Sharma et al. (1978); Upadhyay et al. (2004); Walsh et al. (2019).

Kargil Intrusives

Brookfield and Reynolds (1981); Honegger et al. (1982); Reuber et al. (1989); Schärer et al. (1984a).

Spongtang Ophiolite-Spong Arc

Baxter et al. (2010); Buckman et al. (2018); Heitz (1986); Pedersen et al. (2001); Reuber et al. (1989).

Ladakh forearc basin

Henderson et al. (2010); Henderson et al. (2011); Zhou et al. (2020).

Transhimalaya

Ravikant et al. (2009); Sharma et al. (1978); Singh et al. (2007); St-Onge et al. (2010); Upadhyay et al. (2008); Weinberg and Dunlap (2000).

Table S5.1: Sample localities and descriptions (Chapter 5)

Sample	Lithology	Latitude (°N)	Longitude (°E)	Methods			
				Petrography (thin section)	Whole rock geochemistry	Zircon U-Pb LA-ICP-MS	Zircon U-Pb SHRIMP
Dras Volcanics							
17NI05	felsic tuff	34.46116	76.26436	✓	✓	✓	✓
17NI12	trachydacite	34.42543	76.28400	✓	✓	✓	
17NI02	basalt	34.47702	76.23000	✓	✓		
17NI03	basalt	34.47422	76.23248	✓	✓		
17NI06	basalt	34.45041	76.27294	✓	✓		
17NI09	basalt	34.43617	76.28426	✓	✓		
17NI10	basalt	34.43555	76.28404	✓	✓		
17NI11	basalt	34.42557	76.28359	✓	✓		
Kargil Intrusives							
17KG01	granodiorite	34.45591	76.07023	✓	✓	✓	
17KG02	diorite	34.45593	76.07020	✓	✓	✓	
17KG03	gabbro	34.50608	76.12528	✓	✓		
17KG04	granodiorite	34.50611	76.12524	✓	✓	✓	
17KG05	gabbro	34.55085	76.13792	✓	✓		

Notes:
Fieldwork was undertaken during May-June 2017 in the Ladakh region, Jammu and Kashmir, NW India.

Table S5.2: Whole rock geochemistry (Chapter 5)

Sample	17NI05	17NI12	17NI02	17NI03	17NI06	17NI09	17NI10	17NI11
Affinity	Dras Volcanics	Dras Volcanics	Dras Volcanics	Dras Volcanics	Dras Volcanics	Dras Volcanics	Dras Volcanics	Dras Volcanics
Rock type	felsic tuff	trachydacite	basalt	basalt	basalt	basalt	basalt	basalt
Latitude (N°)	34.46116	34.42543	34.47702	34.47422	34.45041	34.43617	34.43555	34.42557
Longitude (E°)	76.26436	76.28400	76.23000	76.23248	76.27294	76.28426	76.28404	76.28359
Majors (%)								
SiO_2	76.14	65.10	49.99	48.83	43.99	44.77	47.38	48.89
TiO_2	0.29	0.36	0.92	0.93	0.59	0.78	0.74	0.74
Al_2O_3	11.36	16.48	15.98	17.66	15.47	16.37	18.79	16.51
Fe_2O_3	3.43	4.06	12.56	11.66	7.75	7.92	7.80	9.96
MnO	0.05	0.11	0.21	0.15	0.16	0.13	0.14	0.18
MgO	1.02	2.04	4.89	3.69	6.75	8.41	6.07	7.78
CaO	2.47	2.57	9.19	9.27	14.76	13.61	10.12	7.38
Na_2O	3.18	7.25	2.35	3.98	2.66	2.23	3.39	3.72
K_2O	0.43	0.58	1.03	0.47	0.24	0.14	0.72	0.52
SO_3	0.00	0.03	0.03	0.03	0.02	0.31	0.05	0.14
P_2O_5	0.03	0.17	0.28	0.31	0.13	0.25	0.31	0.21
LOI	1.54	1.12	2.42	2.87	7.30	4.95	4.34	3.81
Total	**100**	**100**	**100**	**100**	**100**	**100**	**100**	**100**
MFW indices (Ohata & Arai, 2007)								
M	46	50	82	87	93	94	84	87
F	39	39	8	7	4	2	9	6
W	15	11	10	7	3	3	7	7
Total (%)	100	100	100	100	100	100	100	100
Trace elements (ppm)								
Ag	0.04	0.03	0.02	0.07	0.03	0.04	0.05	0.04
Al (%)	5.96	7.26	8.05	6.91	7.99	6.59	7.71	8.11
As	1.7	2.3	1.0	0.7	0.9	0.7	0.9	0.8
Ba	70	60	150	70	60	50	80	100
Be	0.69	0.77	0.00	0.00	0.00	0.00	0	0
Bi	0.13	0.13	0.02	0.03	0.03	0.04	0.05	0.04
Ca (%)	2.04	2.23	0.00	0.00	0.00	0.00	0.00	0.00
Cd	0.02	0.04	0.06	0.07	0.11	0.12	0.11	0.13
Ce	17.40	48.80	22.20	16.90	16.15	25.80	23.60	16.60
Co	15.3	17.3	35.9	35.7	31.1	32.0	26.7	35.8
Cr	21	20	18	10	267	76	94	153
Cs	0.49	0.36	1.26	1.35	0.42	0.69	1.07	0.65
Cu	46.2	20.5	55.3	187	44.1	77.5	75.2	83.1
Fe (%)	2.77	3.1	8.21	7.05	5.1	4.95	4.98	6.52
Ga	9.01	15.45	17.35	17.80	14.60	17.05	18.55	14.70
Ge	0.13	0.17	0.12	0.13	0.26	0.21	0.16	0.16
Hf	1.6	1.6	2.2	2.1	1.2	2.0	1.8	1.6
In	0.039	0.027	0.000	0.000	0.000	0.000	0.000	0.000
K (%)	0.34	0.43	0.83	0.34	0.26	0.14	0.48	0.40
La	7.5	26.1	9.3	6.6	7.2	10.8	10.4	7.1
Li	11.9	2.9	0.0	0.0	0.0	0.0	0.0	0.0

Mg (%)	0.74	1.33	2.70	1.85	3.54	4.22	3.10	4.62
Mn	473	874	1570	1150	1230	935	1070	1340
Mo	0.07	0.25	0.44	0.30	0.08	0.23	0.23	0.10
Na (%)	2.60	5.00	1.94	2.80	2.00	1.65	2.38	2.74
Nb	2.1	3.0	2.1	1.5	1.0	1.8	2.0	1.1
Ni	15.4	21.3	19.6	13.8	106.0	70.0	92.7	85.9
P	270	830	1250	1320	470	1030	1210	920
Pb	8.8	7.7	2.0	3.1	3.8	2.3	2.9	2.2
Rb	15.2	10.5	22.1	4.5	6.6	1.8	7.1	4.7
Re	0.002	0.002	<0.002	<0.002	0.002	<0.002	<0.002	<0.002
S (%)	0.01	0.01	<0.01	0.01	<0.01	0.1	0.01	0.07
Sb	7.55	0.60	2.30	7.52	2.10	2.91	0.53	2.31
Sc	13.4	10.7	36.9	24.8	32.7	23.3	23.1	36.9
Se	1	1	<1	1	<1	<1	<1	<1
Sn	1.0	0.8	1.3	1.1	0.7	0.9	1.0	0.7
Sr	87.8	614.0	362.0	344.0	183.5	177.0	301.0	220.0
Ta	0.26	0.30	0.17	0.15	0.10	0.13	0.14	0.09
Te	0.05	0.05	0.00	0.00	0.00	0.00	0.00	0.00
Th	3.86	10.95	2.52	1.39	2.22	2.61	2.59	1.24
Ti (%)	0.186	0.230	0.546	0.502	0.335	0.407	0.403	0.420
Tl	0.08	0.07	0.00	0.00	0.00	0.00	0.00	0.00
U	0.6	1.9	0.4	0.4	0.9	0.6	0.6	0.3
V	71	86	305	335	223	223	244	279
W	71.8	73.4	17.6	37.3	27.3	15.0	22.6	13.2
Y	12.2	15.3	25.1	20.8	16	18	16.4	17.7
Zn	45	51	84	84	62	52	59	79
Zr	49.5	48.0	67.6	68.0	35.7	61.4	55.5	47.0
Dy	2.02	2.36	4.23	3.55	2.53	3.16	2.85	2.95
Er	1.23	1.44	2.58	2.23	1.64	1.82	1.65	1.79
Eu	0.51	0.99	1.24	1.09	0.70	1.11	1.01	0.92
Gd	1.91	2.53	3.96	3.36	2.24	3.29	2.90	2.92
Ho	0.41	0.47	0.85	0.72	0.53	0.61	0.56	0.59
Lu	0.19	0.26	0.42	0.35	0.26	0.27	0.26	0.28
Nd	9.2	18.5	15.4	12.5	9.2	15.4	14.3	11.5
Pr	2.24	5.02	3.14	2.49	2.04	3.36	3.12	2.36
Sm	1.92	3.10	3.80	3.10	2.10	3.48	3.06	2.81
Tb	0.33	0.40	0.68	0.59	0.41	0.54	0.48	0.50
Tm	0.18	0.22	0.37	0.32	0.24	0.26	0.24	0.24
Yb	1.18	1.47	2.47	2.14	1.62	1.69	1.60	1.72

Calculated values

Mg#	23	33	28	24	47	51	44	44
ΣREE (La-Lu)	186.93	396.47	318.05	258.71	204.01	293.39	270.41	231.76
ΣLREE (La-Eu)	124.70	319.65	187.76	147.49	123.74	197.95	183.32	140.78
ΣHREE (Gd-Lu)	62.23	76.81	130.29	111.21	80.27	95.43	87.09	90.99
LREE/HREE	2.00	4.16	1.44	1.33	1.54	2.07	2.10	1.55
$(La/Yb)_N$	4.56	12.74	2.70	2.21	3.19	4.58	4.66	2.96
$(La/Lu)_N$	4.23	10.76	2.37	2.02	2.97	4.29	4.29	2.72

$(Gd/Yb)_N$	1.34	1.42	1.33	1.30	1.14	1.61	1.50	1.40
La_N	31.65	110.13	39.24	27.85	30.38	45.57	43.88	29.96
Yb_N	6.94	8.65	14.53	12.59	9.53	9.94	9.41	10.12
Sr/Y	7.20	40.13	14.42	16.54	11.47	9.83	18.35	12.43
δEu^*	0.81	1.08	0.98	1.03	0.99	1.00	1.04	0.98

Sample	17KG01	17KG02	17KG03	17KG04	17KG05
Affinity	Kargil Intrusives	Kargil Intrusives	Kargil Intrusives	Kargil Intrusives	Kargil Intrusives
Rock type	granodiorite	diorite	gabbro	granodiorite	gabbro
Latitude (N°)	34.45591	34.45593	34.50608	34.50611	34.55085
Longitude (E°)	76.07023	76.07020	76.12528	76.12524	76.13792
Majors (%)					
SiO_2	62.62	55.96	50.99	74.62	47.41
TiO_2	0.43	0.70	0.89	0.16	0.75
Al_2O_3	16.93	17.68	19.23	14.41	18.33
Fe_2O_3	6.08	9.02	8.29	1.44	10.38
MnO	0.18	0.19	0.13	0.06	0.15
MgO	2.04	3.67	5.02	0.28	8.16
CaO	6.35	8.37	9.49	2.06	11.94
Na_2O	3.25	2.62	2.93	4.08	1.48
K_2O	1.22	0.96	0.52	2.03	0.10
SO_3	0.02	0.11	0.07	0.01	0.04
P_2O_5	0.11	0.10	0.12	0.06	0.04
LOI	0.64	0.49	2.17	0.68	1.06
Total	**100**	**100**	**100**	**100**	**100**
MFW indices (Ohata & Arai, 2007)					
M	57	76	85	7	94
F	31	13	7	87	1
W	12	11	8	6	5
Total (%)	100	100	100	100	100
Trace elements (ppm)					
Ag	0.02	0.05	0.22	0.03	0.02
Al (%)	8.19	8.17	7.80	6.69	8.25
As	2.4	2.0	6.6	0.6	2.6
Ba	380	240	140	390	50
Be	0.55	0.41	0.38	0.93	0.18
Bi	0.02	0.03	0.02	0.02	0.02
Ca (%)	4.73	5.43	6.09	1.55	7.78
Cd	0.04	0.10	0.07	0.02	0.07
Ce	15.15	13.70	8.40	25.70	3.94
Co	22.3	27.5	37.3	14.7	48.6
Cr	78	10	32	5	108
Cs	2.13	1.44	1.51	2.34	0.33
Cu	14.7	50.9	64.8	5.4	12.2
Fe (%)	4.16	5.77	5.09	1.46	6.47
Ga	15.95	16.30	20.10	14.35	19.30
Ge	0.07	0.09	0.14	0.12	0.15

Hf	0.5	0.8	0.9	0.4	0.5
In	0.044	0.048	0.051	0.013	0.048
K (%)	0.93	0.70	0.40	1.48	0.11
La	6.7	6.2	3.3	13.2	1.5
Li	18.6	10.2	40.8	28.3	7.3
Mg (%)	1.46	1.97	2.39	0.33	4.21
Mn	1280	1310	932	528	1080
Mo	0.62	0.83	0.16	0.19	0.20
Na (%)	2.32	1.83	2.07	2.95	1.18
Nb	2.2	1.9	1.0	4.1	0.3
Ni	23.7	7.0	27.3	2.6	70.5
P	460	380	480	300	150
Pb	5.5	6.1	4.3	10.5	2.1
Rb	27.6	19.0	5.6	53.1	1.0
Re	0.011	0.002	0.002	0.002	0.002
S (%)	0.01	0.01	0.02	0.01	0.01
Sb	0.85	6.22	0.74	10.3	0.49
Sc	13.2	27.0	23.1	3.0	29.9
Se	1	1	1	1	1
Sn	0.7	0.8	0.6	0.7	0.4
Sr	363	240	524	215	539
Ta	0.31	0.25	0.24	0.56	0.22
Te	0.05	0.05	0.05	0.05	0.05
Th	2.15	1.29	0.39	6.18	0.18
Ti (%)	0.233	0.364	0.463	0.109	0.409
Tl	0.19	0.14	0.10	0.30	0.02
U	0.5	0.3	0.1	0.6	0.1
V	82	197	215	18	280
W	112.5	87.7	125.0	148.5	110.0
Y	18.1	19.8	12.3	5.0	6.7
Zn	79	87	78	40	88
Zr	8.6	16.6	22.6	8.4	12.4
Dy	2.76	3.07	2.04	0.95	1.19
Er	1.85	1.99	1.22	0.44	0.68
Eu	0.71	0.77	0.71	0.41	0.44
Gd	2.44	2.62	1.94	1.27	1.08
Ho	0.56	0.64	0.40	0.16	0.23
Lu	0.28	0.30	0.14	0.03	0.08
Nd	9.2	8.9	7.0	10.5	3.5
Pr	2.06	1.88	1.34	2.85	0.67
Sm	2.16	2.22	1.74	1.66	0.94
Tb	0.40	0.44	0.31	0.17	0.18
Tm	0.27	0.28	0.16	0.04	0.09
Yb	1.97	1.99	1.09	0.34	0.64

Calculated values

Mg#	25	29	38	16	44
ΣREE (La-Lu)	208.48	209.61	138.76	192.79	74.41
ΣLREE (La-Eu)	120.77	115.18	80.36	168.09	41.04
ΣHREE (Gd-Lu)	87.71	94.43	58.40	24.70	33.37
LREE/HREE	1.38	1.22	1.38	6.81	1.23
$(La/Yb)_N$	2.44	2.23	2.17	27.85	1.68
$(La/Lu)_N$	2.56	2.21	2.53	47.16	2.01
$(Gd/Yb)_N$	1.02	1.09	1.47	3.09	1.40
La_N	28.27	26.16	13.92	55.70	6.33
Yb_N	11.59	11.71	6.41	2.00	3.76
Sr/Y	20.06	12.12	42.60	43.00	80.45
δEu^*	0.95	0.98	1.18	0.86	1.34

Notes:

Major element analysis was conducted at the University of Wollongong (UOW). Additional trace and rare-earth element (REE) analyses were undertaken at Australian Laboratory Services (ALS) Minerals Division, Brisbane, Australia using the geochemical procedure code: ME-MS81.

$^*\delta Eu = EuN/(\sqrt{(SmN \times GdN)})$

The above listed geochemical data has been combined in text (including figures) with other data available in the below listed literature. This data is compiled online and is available through the relevant paper corresponding to this chapter (Walsh et al., 2020). It is also available from the original papers; these are as follows:

- Aitchison, J. C., McDermid, I. R. C., Ali, J. R., Davis, A. M., & Zyabrev, S. V. (2007). Shoshonites in southern Tibet record Late Jurassic rifting of a Tethyan intraoceanic island arc. The Journal of geology, 115(2), 197-213.
- Bhat, I. M., Ahmad, T., & Rao, D. S. (2019). The tectonic evolution of the Dras arc complex along the Indus Suture Zone, western Himalaya: Implications for the Neo-Tethys Ocean geodynamics. Journal of Geodynamics, 124, 52-66.
- Buckman, S., Aitchison, J. C., Nutman, A. P., Bennett, V. C., Saktura, W. M., Walsh, J. M., & Hidaka, H. (2018). The Spongtang Massif in Ladakh, NW Himalaya: an Early Cretaceous record of spontaneous, intraoceanic subduction initiation in the Neotethys. Gondwana Research, 63, 226-249.
- Corfield, R. I., Searle, M. P., & Pedersen, R. B. (2001). Tectonic setting, origin, and obduction history of the Spontang Ophiolite, Ladakh Himalaya, NW India. The Journal of Geology, 109(6), 715-736.
- Liu, W., Zhong, Y., Sun, Z., Yakymchuk, C., Gu, M., Tang, G., & Xia, B. (2020). The Late Jurassic Zedong ophiolite: A remnant of subduction initiation within the Yarlung Zangbo Suture Zone (southern Tibet) and its tectonic implications. Gondwana Research, 78, 172-188.
- Malpas, J., Zhou, M. F., Robinson, P. T., & Reynolds, P. H. (2003). Geochemical and geochronological constraints on the origin and emplacement of the Yarlung Zangbo ophiolites, Southern Tibet. Geological Society, London, Special Publications, 218(1), 191-206.
- Zhang, L. L., Liu, C. Z., Wu, F. Y., Ji, W. Q., & Wang, J. G. (2014). Zedong terrane revisited: An intraoceanic arc within Neo-Tethys or a part of the Asian active continental margin? Journal of Asian Earth Sciences, 80, 34-55.

Table S5.3: Zircon U-Pb results using LA-ICP-MS and SHRIMP (Chapter 5)

Sample ID	Analysis ID	U (ppm)	Th (ppm)	Th/U	$^{238}U/^{206}Pb$	$^{207}Pb/^{206}Pb$	age $^{206}Pb/^{238}U$	age $^{207}Pb/^{206}Pb$	Sr (cps)	Rejected
17NI05 (W102) - felsic tuff										
1.1	m, eq, osc	163.2	105.6	0.647	39.8883 ± 0.5410	0.0488 ± 0.0018	159.6 ± 2.2	162.0 ± 82.0	364	
2.1	e, p, osc	183.4	121.8	0.664	38.8803 ± 0.5291	0.0483 ± 0.0017	163.7 ± 2.2	121.0 ± 73.0	274	
2.2	e, p, osc	185.0	-	-	42.8828 ± 0.9153	0.0554 ± 0.0065	147.6 ± 3.1	429.9 ± 240.6	-	yes
3.1	e, fr, osc	141.7	103.4	0.730	39.9840 ± 0.5436	0.0502 ± 0.0020	159.2 ± 2.1	190.0 ± 83.0	237	
4.1	e, p, osc	215.3	162.9	0.757	39.5570 ± 0.5164	0.0484 ± 0.0016	160.9 ± 2.1	126.0 ± 71.0	218	
5.1	e, p, osc	197.0	125.7	0.638	40.2577 ± 0.5510	0.0504 ± 0.0023	158.2 ± 2.1	195.0 ± 96.0	230	
6.1	e, p, osc	453.0	314.0	0.693	37.8501 ± 0.5731	0.0494 ± 0.0018	168.1 ± 2.5	155.0 ± 80.0	1540	
7.1	m, fr, osc	227.0	188.0	0.828	38.8500 ± 0.4528	0.0476 ± 0.0015	163.8 ± 1.9	81.0 ± 67.0	254	
7.2	e, fr, osc	105.0	-	-	41.0039 ± 0.9251	0.0417 ± 0.0191	156.6 ± 3.5	6.35E-09 ± 632.9	-	yes
8.1	e, fr, osc	399.0	358.0	0.897	38.5951 ± 0.3724	0.0491 ± 0.0011	164.9 ± 1.6	148.0 ± 50.0	234	
9.1	m, fr, osc	173.5	109.3	0.630	39.0778 ± 0.4734	0.0505 ± 0.0018	162.9 ± 2.0	202.0 ± 80.0	289	
10.1	e, p, osc	270.7	215.3	0.795	36.6703 ± 0.5110	0.0618 ± 0.0033	173.5 ± 2.4	610.0 ± 110.0	1590	yes
11.1	e, p, hl	280.6	234.1	0.834	39.7773 ± 0.4272	0.0495 ± 0.0014	160.1 ± 1.7	169.0 ± 64.0	291	
12.1	m, eq, osc	297.8	258.5	0.868	39.7614 ± 0.7431	0.0493 ± 0.0027	160.1 ± 3.0	140.0 ± 120.0	530	
12.2	e, eq, osc	308.0	-	-	37.8402 ± 0.6083	0.0488 ± 0.0086	168.3 ± 2.7	136.6 ± 369.1	-	
13.1	e, fr, osc	114.3	74.3	0.650	39.2311 ± 0.6464	0.0493 ± 0.0024	162.2 ± 2.7	135.0 ± 100.0	286	
14.1	e, eq, osc	275.0	253.0	0.920	39.3236 ± 0.4484	0.0504 ± 0.0015	161.9 ± 1.8	197.0 ± 63.0	430	
14.2	e, eq, osc	270.0	-	-	41.5727 ± 0.7044	0.0393 ± 0.0141	154.8 ± 2.6	0 ± 0	-	
15.1	e, fr, osc	139.8	120.9	0.865	39.4633 ± 0.5451	0.0506 ± 0.0019	161.3 ± 2.2	220.0 ± 84.0	223	
16.1	e, eq, osc	341.0	266.0	0.780	36.2582 ± 0.4996	0.0499 ± 0.0018	175.4 ± 2.4	166.0 ± 73.0	258	
17.1	m, p, osc	154.6	129.7	0.839	39.1083 ± 0.5506	0.0476 ± 0.0021	162.7 ± 2.2	83.0 ± 86.0	315	
18.1	e, p, osc	305.0	340.0	1.115	40.8330 ± 0.5502	0.0530 ± 0.0017	156.2 ± 2.1	328.0 ± 70.0	640	yes
19.1	e, p, osc	200.1	124.8	0.624	39.6668 ± 0.8654	0.0693 ± 0.0032	160.5 ± 3.4	881.0 ± 98.0	2060	yes
20.1	e, p, osc	210.0	199.0	0.948	39.2003 ± 0.4610	0.0489 ± 0.0013	162.4 ± 1.9	137.0 ± 58.0	480	
21.1	e, p, hl	118.9	83.5	0.702	37.9651 ± 0.5189	0.0504 ± 0.0021	167.6 ± 2.3	212.0 ± 88.0	227	
22.1	e, fr, osc	189.0	152.0	0.804	40.2253 ± 0.4531	0.0497 ± 0.0017	158.3 ± 1.8	187.0 ± 74.0	278	
23.1	e, fr, osc	132.6	84.5	0.637	37.6081 ± 0.7213	0.0521 ± 0.0033	169.2 ± 3.2	250.0 ± 140.0	470	
24.1	e, p, osc	177.5	173.7	0.979	39.7931 ± 0.5384	0.0506 ± 0.0016	160.0 ± 2.1	219.0 ± 67.0	420	
24.2	e, p, osc	275.0	-	-	39.2264 ± 0.6526	0.0452 ± 0.0106	163 ± 2.7	0.001836 ± 443.4	-	
25.1	m, fr, osc	153.6	94.5	0.615	38.5357 ± 0.9058	0.0489 ± 0.0030	165.1 ± 3.8	190.0 ± 120.0	470	
26.1	e, p, osc	292.7	180.9	0.618	38.3730 ± 0.4123	0.0509 ± 0.0015	165.9 ± 1.7	222.0 ± 62.0	460	
26.2	e, p, osc	467.0	-	-	39.3953 ± 0.6304	0.047 ± 0.0053	162 ± 2.6	49.21 ± 250.1	-	
27.1	e, fr, osc	249.0	198.0	0.795	38.4468 ± 0.4434	0.0502 ± 0.0014	165.5 ± 1.9	195.0 ± 61.0	304	
28.1	e, fr, osc	106.9	65.8	0.615	38.3289 ± 0.5289	0.0494 ± 0.0019	166.2 ± 2.3	184.0 ± 79.0	292	

Sample ID	Analysis ID	U (ppm)	Th (ppm)	Th/U	$^{238}U/^{206}Pb$	$^{207}Pb/^{206}Pb$	age $^{206}Pb/^{238}U$	age $^{207}Pb/^{206}Pb$	Sr (cps)	Rejected
17NI12 (W101) - trachydacite										
1.1	e, p, osc	705.0	693.0	0.983	40.5680 ± 0.3621	0.0487 ± 0.0008	156.9 ± 1.4	128.0 ± 36.0	880	
2.1	e, p, osc	750.0	710.0	0.947	40.5186 ± 0.3776	0.0492 ± 0.0008	157.3 ± 1.4	159.0 ± 39.0	850	
3.1	m, p, osc	280.0	294.0	1.050	39.4789 ± 0.5767	0.0478 ± 0.0016	161.2 ± 2.3	78.0 ± 70.0	670	
4.1	m, p, osc	1111.0	1559.0	1.403	41.6493 ± 0.3816	0.0495 ± 0.0006	153.0 ± 1.4	173.0 ± 30.0	1190	
5.1	e, fr, osc	614.0	898.0	1.463	41.7886 ± 0.4715	0.0526 ± 0.0008	152.4 ± 1.7	299.0 ± 36.0	1030	yes
6.1	e, p, osc	526.0	515.0	0.979	40.5515 ± 0.3947	0.0492 ± 0.0011	157.0 ± 1.5	161.0 ± 49.0	640	
7.1	e, p, osc	463.0	420.0	0.907	40.3389 ± 0.4394	0.0492 ± 0.0010	157.8 ± 1.7	151.0 ± 47.0	650	
8.1	e, p, osc	667.0	617.0	0.925	40.2091 ± 0.5012	0.0493 ± 0.0009	158.4 ± 2.0	159.0 ± 39.0	480	
9.1	e, p, osc	410.0	385.0	0.939	40.8998 ± 0.4015	0.0498 ± 0.0013	155.7 ± 1.5	186.0 ± 54.0	590	
10.1	e, p, osc	350.0	346.0	0.989	40.6504 ± 0.5288	0.0496 ± 0.0013	156.6 ± 2.0	174.0 ± 56.0	385	
11.1	e, p, osc	667.0	665.0	0.997	40.2577 ± 0.4376	0.0498 ± 0.0009	158.2 ± 1.7	173.0 ± 40.0	1010	
12.1	m, p, osc	678.0	617.0	0.910	40.3551 ± 0.4234	0.0520 ± 0.0008	157.8 ± 1.6	284.0 ± 37.0	740	yes
13.1	m, p, osc	495.0	569.0	1.149	35.9195 ± 0.4387	0.0557 ± 0.0022	177.0 ± 2.1	419.0 ± 90.0	1100	yes
14.1	e, p, osc	377.0	307.0	0.814	40.3877 ± 0.5057	0.0484 ± 0.0012	157.7 ± 1.9	109.0 ± 53.0	570	
15.1	e, p, hl	1053.0	1029.0	0.977	40.9668 ± 0.5035	0.0492 ± 0.0008	155.4 ± 1.9	148.0 ± 36.0	1090	
16.1	m, p, osc	284.0	216.0	0.761	39.6511 ± 0.5188	0.0498 ± 0.0015	160.5 ± 2.1	190.0 ± 64.0	820	
17.1	e, p, osc	992.0	1368.0	1.379	42.6803 ± 0.3825	0.0499 ± 0.0009	149.3 ± 1.3	187.0 ± 40.0	870	
18.1	m, p, osc	747.0	588.0	0.787	40.5351 ± 0.3943	0.0495 ± 0.0010	157.1 ± 1.5	163.0 ± 44.0	640	
19.1	e, p, osc	838.0	939.0	1.121	41.0846 ± 0.3882	0.0501 ± 0.0009	155.0 ± 1.5	188.0 ± 38.0	890	
20.1	e, p, osc	502.0	493.0	0.982	41.4422 ± 0.4465	0.0639 ± 0.0021	153.7 ± 1.7	720.0 ± 71.0	1010	yes
21.1	e, p, osc	750.0	753.0	1.004	43.1779 ± 0.5593	0.0498 ± 0.0013	147.6 ± 1.9	185.0 ± 57.0	890	
22.1	m, p, osc	353.0	305.0	0.864	38.9712 ± 0.5164	0.0482 ± 0.0013	163.5 ± 2.2	117.0 ± 59.0	500	
23.1	e, p, osc	1007.0	1048.0	1.041	42.9738 ± 0.4248	0.0493 ± 0.0008	148.3 ± 1.5	162.0 ± 36.0	980	
24.1	e, p, osc	1270.0	1323.0	1.042	40.5022 ± 0.4757	0.0482 ± 0.0007	157.2 ± 1.8	106.0 ± 33.0	1170	yes
25.1	e, p, osc	308.2	300.0	0.973	40.5022 ± 0.6070	0.0503 ± 0.0018	157.2 ± 2.3	215.0 ± 80.0	810	
26.1	e, p, hl	669.0	1157.0	1.729	41.5800 ± 0.3976	0.0494 ± 0.0009	153.2 ± 1.4	159.0 ± 39.0	700	
27.1	e, p, osc	810.0	727.0	0.898	41.2541 ± 0.4765	0.0490 ± 0.0009	154.4 ± 1.7	141.0 ± 40.0	2200	
28.1	e, p, osc	640.0	640.0	1.000	41.3223 ± 0.3927	0.0504 ± 0.0009	154.1 ± 1.5	205.0 ± 41.0	1090	
29.1	e, p, osc	263.0	184.0	0.700	41.0509 ± 0.5898	0.0491 ± 0.0019	155.2 ± 2.2	162.0 ± 85.0	820	
30.1	m, p, osc	356.0	320.0	0.899	37.7359 ± 0.6123	0.0496 ± 0.0013	168.6 ± 2.7	169.0 ± 55.0	540	
31.1	m, fr, osc	301.8	322.0	1.067	41.3394 ± 0.4443	0.0496 ± 0.0016	154.1 ± 1.6	174.0 ± 69.0	270	
32.1	e, p, osc	517.0	459.0	0.888	41.3565 ± 0.4276	0.0500 ± 0.0010	154.0 ± 1.6	191.0 ± 43.0	660	
33.1	e, p, osc	999.0	1250.0	1.251	40.1606 ± 0.4193	0.0486 ± 0.0007	158.5 ± 1.6	121.0 ± 34.0	780	
34.1	e, p, osc	411.0	404.0	0.983	40.5515 ± 0.5262	0.0497 ± 0.0012	157.0 ± 2.0	175.0 ± 52.0	690	
35.1	e, p, osc	542.6	559.0	1.030	40.6504 ± 0.3801	0.0492 ± 0.0009	156.7 ± 1.5	157.0 ± 40.0	710	

36.1	e, fr, osc	772.0	757.0	0.981	42.4268	±	0.3960	0.0497	±	0.0008	150.1	±	1.4	175.0	±	37.0	860								
37.1	m, p, osc	622.0	1249.0	2.008	41.5455	±	0.4488	0.0495	±	0.0010	153.3	±	1.6	159.0	±	45.0	1480								
38.1	m, p, osc	313.0	421.0	1.345	36.7512	±	0.5403	0.0503	±	0.0017	173.3	±	2.6	232.0	±	78.0	1250								
39.1	m, p, osc	412.0	390.9	0.949	39.2927	±	0.4169	0.0492	±	0.0011	162.0	±	1.7	156.0	±	50.0	530								
40.1	m, fr, osc	193.0	213.0	1.104	39.4322	±	0.6531	0.0545	±	0.0019	161.4	±	2.6	383.0	±	79.0	12600	yes							
41.1	e, p, osc	206.1	185.2	0.899	40.0320	±	0.5128	0.0487	±	0.0013	159.1	±	2.0	130.0	±	59.0	980								
42.1	m, p, osc	372.0	296.0	0.796	38.8803	±	0.7256	0.0544	±	0.0046	163.7	±	3.0	360.0	±	190.0	1790								
43.1	e, p, osc	694.2	550.0	0.792	40.8163	±	0.4165	0.0490	±	0.0009	156.0	±	1.6	148.0	±	39.0	680								
44.1	e, p, osc	262.0	229.0	0.874	39.4633	±	0.4672	0.0486	±	0.0014	161.3	±	1.9	123.0	±	63.0	2540								
45.1	e, p, osc	457.0	395.0	0.864	38.6100	±	0.5068	0.0486	±	0.0011	164.8	±	2.2	121.0	±	50.0	800								
46.1	e, p, osc	667.0	688.0	1.031	42.1585	±	0.4088	0.0502	±	0.0010	151.1	±	1.4	202.0	±	46.0	910								
47.1	e, p, osc	884.0	697.0	0.788	41.6147	±	0.3637	0.0492	±	0.0008	153.1	±	1.3	151.0	±	38.0	1050								
48.1	m, p, osc	208.0	240.0	1.154	40.4695	±	0.5732	0.0484	±	0.0017	157.3	±	2.2	125.0	±	75.0	460								
49.1	e, p, osc	786.0	1162.0	1.478	41.8761	±	0.4384	0.0500	±	0.0009	152.1	±	1.6	184.0	±	42.0	930								
50.1	e, p, osc	405.0	344.0	0.849	39.1083	±	0.4435	0.0485	±	0.0012	162.8	±	1.8	120.0	±	53.0	720								
51.1	m, p, osc	286.0	247.0	0.864	39.6825	±	0.4882	0.0523	±	0.0019	160.4	±	2.0	270.0	±	81.0	2770	yes							
52.1	e, p, osc	1398.0	2250.0	1.609	40.5680	±	0.5266	0.0493	±	0.0007	157.0	±	2.0	163.0	±	32.0	1070								
53.1	e, p, osc	283.1	243.6	0.860	40.2091	±	0.5174	0.0506	±	0.0018	158.4	±	2.0	215.0	±	79.0	500								
54.1	e, p, osc	618.0	694.0	1.123	39.9361	±	0.4785	0.0496	±	0.0010	159.4	±	1.9	177.0	±	45.0	800								

Sample ID	Analysis ID	U (ppm)	Th (ppm)	Th/U	$^{238}U/^{206}Pb$	$^{207}Pb/^{206}Pb$	age $^{206}Pb/^{238}U$	age $^{207}Pb/^{206}Pb$	Sr (cps)	Rejected
17KG01 (W101) - granodiorite										
1.1	m, eq, hl	77.9	31.9	0.409	60.9013 ± 1.1498	0.0491 ± 0.0031	105.0 ± 1.9	130.0 ± 130.0	311	
2.1	e, p, sec	38.0	18.7	0.493	64.0205 ± 2.0493	0.0531 ± 0.0066	100.3 ± 3.3	300.0 ± 240.0	360	
3.1	e, p, sec	77.9	52.4	0.673	62.8141 ± 1.2626	0.0492 ± 0.0031	101.8 ± 2.0	140.0 ± 130.0	420	
4.1	e, eq, sec	65.2	29.4	0.451	62.3053 ± 1.5916	0.0506 ± 0.0039	102.6 ± 2.6	160.0 ± 150.0	218	
5.1	m, p, sec	47.4	21.7	0.458	63.7755 ± 1.4642	0.0520 ± 0.0038	100.5 ± 2.2	210.0 ± 140.0	264	
6.1	e, p, sec	43.7	20.6	0.472	63.4115 ± 1.6486	0.0453 ± 0.0039	100.9 ± 2.6	-30.0 ± 150.0	268	
7.1	m, p, sec	79.6	50.9	0.639	64.6831 ± 2.1338	0.0475 ± 0.0050	98.9 ± 3.2	70.0 ± 210.0	310	
8.1	m, p, sec	76.9	66.4	0.863	65.0195 ± 1.5642	0.0509 ± 0.0038	98.4 ± 2.3	230.0 ± 160.0	540	
9.1	e, fr, sec	75.8	31.2	0.412	59.7015 ± 1.3901	0.0455 ± 0.0031	107.1 ± 2.5	-30.0 ± 130.0	283	
10.1	m, eq, sec	84.0	32.2	0.383	64.5995 ± 3.0046	0.0501 ± 0.0094	99.0 ± 4.5	120.0 ± 380.0	760	
11.1	m, eq, sec	67.9	26.7	0.394	62.5782 ± 1.2923	0.0483 ± 0.0030	102.2 ± 2.1	110.0 ± 120.0	325	
12.1	e, fr, hl	85.0	34.2	0.402	61.1995 ± 1.0487	0.0499 ± 0.0029	104.5 ± 1.8	180.0 ± 120.0	347	
13.1	m, p, sec	52.4	39.4	0.752	64.6831 ± 1.2552	0.0464 ± 0.0037	98.9 ± 1.9	0.0 ± 150.0	440	
14.1	m, fr, hl	87.5	58.8	0.672	62.6566 ± 1.2563	0.0487 ± 0.0029	102.1 ± 2.0	110.0 ± 120.0	286	
15.1	m, eq, sec	48.4	31.3	0.647	63.0120 ± 1.5485	0.0507 ± 0.0042	101.5 ± 2.5	150.0 ± 170.0	306	
16.1	e, p, sec	126.0	52.6	0.417	60.2047 ± 1.7036	0.0476 ± 0.0048	106.2 ± 3.0	100.0 ± 210.0	850	
17.1	m, eq, sec	81.2	33.9	0.417	61.9579 ± 1.3436	0.0472 ± 0.0035	103.2 ± 2.2	80.0 ± 140.0	380	
18.1	m, eq, hl	60.0	30.0	0.500	62.7353 ± 1.2594	0.0509 ± 0.0035	101.9 ± 2.0	160.0 ± 140.0	410	
19.1	m, p, hl	69.1	33.5	0.485	63.9386 ± 1.3491	0.0511 ± 0.0032	100.1 ± 2.1	210.0 ± 130.0	344	
20.1	m, p, sec	135.0	85.4	0.633	64.1026 ± 1.1095	0.0490 ± 0.0025	99.8 ± 1.7	130.0 ± 110.0	331	
21.1	m, eq, hl	77.4	56.8	0.734	63.1313 ± 1.3949	0.0591 ± 0.0040	101.3 ± 2.2	500.0 ± 140.0	358	yes
22.1	m, fr, osc	57.0	24.2	0.424	63.8978 ± 1.4699	0.0486 ± 0.0034	100.1 ± 2.3	130.0 ± 130.0	227	
23.1	m, eq, hl	82.3	33.9	0.412	61.2370 ± 1.3125	0.0491 ± 0.0031	104.4 ± 2.2	170.0 ± 120.0	276	
24.1	m, p, hl	67.5	38.0	0.563	63.1313 ± 1.2754	0.0470 ± 0.0034	101.3 ± 2.0	20.0 ± 140.0	248	
25.1	e, p, sec	46.3	21.2	0.458	63.2911 ± 1.5623	0.0496 ± 0.0038	101.1 ± 2.5	160.0 ± 150.0	265	
26.1	m, p, sec	49.4	18.6	0.376	62.9723 ± 1.7448	0.0507 ± 0.0038	101.5 ± 2.8	190.0 ± 140.0	168	
27.1	m, p, osc	84.6	53.8	0.636	62.1504 ± 1.2361	0.0481 ± 0.0028	103.1 ± 2.1	110.0 ± 120.0	333	
28.1	e, p, hl	84.9	50.5	0.595	63.4518 ± 1.6105	0.0449 ± 0.0037	100.8 ± 2.5	-70.0 ± 150.0	310	
29.1	m, p, osc	88.2	57.6	0.653	60.6061 ± 2.8283	0.0494 ± 0.0069	105.5 ± 4.9	80.0 ± 270.0	470	
30.1	m, eq, osc	55.8	22.4	0.401	62.5391 ± 1.6427	0.0455 ± 0.0032	102.2 ± 2.6	-20.0 ± 130.0	213	

Sample ID	Analysis ID	U (ppm)	Th (ppm)	Th/U	$^{238}U/^{206}Pb$	$^{207}Pb/^{206}Pb$	age $^{206}Pb/^{238}U$	age $^{207}Pb/^{206}Pb$	Sr (cps)	Rejected
17KG02 (W101) - diorite										
1.1	m, fr, hh	37.5	20.5	0.546	61.0128 ± 1.7496	0.0491 ± 0.0037	104.8 ± 3.0	100.0 ± 150.0	192	
2.1	e, fr, sec	100.2	67.7	0.676	62.6174 ± 1.8821	0.0465 ± 0.0041	102.1 ± 3.1	20.0 ± 170.0	480	
3.1	m, p, hl	117.7	93.6	0.795	64.2674 ± 1.1152	0.0503 ± 0.0026	99.5 ± 1.7	200.0 ± 100.0	470	
4.1	m, p, hh	59.9	53.6	0.895	62.5000 ± 1.4844	0.0475 ± 0.0036	102.3 ± 2.4	50.0 ± 150.0	317	
5.1	m, fr, hl	56.6	37.8	0.668	63.6132 ± 1.5377	0.0517 ± 0.0040	100.5 ± 2.4	240.0 ± 150.0	246	
6.1	e, fr, sec	1388.0	1002.0	0.722	64.1849 ± 0.5768	0.0479 ± 0.0008	99.7 ± 0.9	94.0 ± 35.0	272	
7.1	m, p, sec	104.9	84.8	0.808	64.7668 ± 1.2165	0.0484 ± 0.0027	98.8 ± 1.8	130.0 ± 110.0	358	
8.1	e, fr, hl	71.9	45.4	0.631	61.0128 ± 1.6752	0.0430 ± 0.0032	104.8 ± 2.9	-120.0 ± 130.0	430	yes
9.1	e, fr, hl	212.0	107.9	0.509	62.7353 ± 0.8659	0.0496 ± 0.0019	101.9 ± 1.4	153.0 ± 82.0	185	
10.1	m, fr, hh	76.7	60.4	0.787	63.5324 ± 1.4935	0.0503 ± 0.0036	100.7 ± 2.4	140.0 ± 140.0	430	
11.1	e, p, hh	65.8	53.0	0.805	61.9195 ± 1.6870	0.0519 ± 0.0052	103.2 ± 2.8	180.0 ± 190.0	260	
12.1	e, fr, sec	35.1	25.9	0.738	62.1118 ± 1.8518	0.0490 ± 0.0046	102.9 ± 3.1	110.0 ± 180.0	279	
13.1	m, p, hl	52.0	46.7	0.898	62.6566 ± 1.6096	0.0508 ± 0.0038	102.0 ± 2.6	180.0 ± 150.0	333	
14.1	m, fr, sec	55.7	26.7	0.479	64.7668 ± 1.5940	0.0466 ± 0.0036	98.8 ± 2.4	50.0 ± 150.0	244	
15.1	m, fr, sec	66.4	31.7	0.477	63.2511 ± 2.1204	0.0485 ± 0.0055	101.1 ± 3.4	90.0 ± 220.0	450	
16.1	m, eq, hl	106.0	85.5	0.807	63.3714 ± 1.2851	0.0489 ± 0.0028	100.9 ± 2.0	150.0 ± 120.0	520	
17.1	m, fr, hl	39.0	30.0	0.769	62.1118 ± 1.5817	0.0482 ± 0.0044	103.0 ± 2.6	50.0 ± 170.0	262	
18.1	m, p, sec	27.5	13.6	0.494	61.9195 ± 3.2973	0.0550 ± 0.0120	103.3 ± 5.5	330.0 ± 420.0	0	
19.1	m, fr, hh	34.8	25.5	0.733	63.6537 ± 1.6612	0.0498 ± 0.0051	100.5 ± 2.6	80.0 ± 200.0	460	
20.1	m, fr, sec	41.6	27.9	0.670	63.0517 ± 1.5902	0.0462 ± 0.0044	101.4 ± 2.5	-40.0 ± 180.0	252	
21.1	m, p, sec	69.5	51.0	0.734	63.9386 ± 1.3491	0.0464 ± 0.0033	100.0 ± 2.1	0.0 ± 130.0	310	
22.1	m, p, sec	63.2	55.5	0.878	61.3874 ± 1.3943	0.0481 ± 0.0030	104.1 ± 2.4	90.0 ± 130.0	333	
23.1	m, p, sec	73.2	65.7	0.898	64.5161 ± 1.4152	0.0495 ± 0.0031	99.2 ± 2.1	200.0 ± 130.0	540	
24.1	e, p, hh	55.7	45.5	0.817	64.1849 ± 1.4831	0.0499 ± 0.0038	99.6 ± 2.3	110.0 ± 150.0	440	
25.1	e, p, sec	58.8	47.2	0.803	63.0915 ± 1.4330	0.0506 ± 0.0038	101.4 ± 2.3	150.0 ± 150.0	246	
26.1	m, p, sec	70.0	63.2	0.903	63.7349 ± 1.3811	0.0470 ± 0.0036	100.4 ± 2.1	90.0 ± 150.0	460	
27.1	e, fr, sec	28.3	21.4	0.757	62.5000 ± 2.5781	0.0483 ± 0.0079	102.3 ± 4.2	60.0 ± 310.0	270	
28.1	e, f, sec	77.5	67.1	0.866	63.0120 ± 1.2309	0.0520 ± 0.0035	101.5 ± 2.0	200.0 ± 140.0	410	
29.1	m, p, sec	58.5	40.9	0.699	65.3595 ± 1.4097	0.0486 ± 0.0035	97.9 ± 2.1	170.0 ± 140.0	336	
30.1	e, fr, sec	39.4	23.1	0.586	64.1849 ± 1.8951	0.0535 ± 0.0048	99.6 ± 2.9	280.0 ± 180.0	309	

Sample ID	Analysis ID	U (ppm)	Th (ppm)	Th/U	$^{238}U/^{206}Pb$			$^{207}Pb/^{206}Pb$			age $^{206}Pb/^{238}U$			age $^{207}Pb/^{206}Pb$			Sr (cps)	Rejected
17KG04 (W101) - granodiorite																		
1.1	e, p, sec	2860.0	1252.0	0.438	87.1004	±	0.8345	0.0486	±	0.0007	73.6	±	0.7	124.0	±	34.0	3640	yes
2.1	m, fr, sec	173.0	91.9	0.531	74.5157	±	1.3326	0.0466	±	0.0023	86.0	±	1.5	44.0	±	97.0	880	
3.1	e, eq, sec	352.0	61.4	0.174	85.3971	±	1.4585	0.0680	±	0.0028	75.1	±	1.3	842.0	±	80.0	650	yes
4.1	e, eq, osc	236.5	126.8	0.536	72.4113	±	1.2060	0.0504	±	0.0023	88.4	±	1.5	182.0	±	94.0	1060	
5.1	e, p, osc	68.7	58.8	0.856	73.4754	±	1.9975	0.0907	±	0.0077	87.1	±	2.4	1320.0	±	170.0	600	yes
6.1	e, p, sec	109.4	99.4	0.909	75.9878	±	1.9055	0.0461	±	0.0030	84.3	±	2.1	20.0	±	120.0	820	
7.1	e, p, osc	93.6	67.9	0.725	76.8640	±	1.7724	0.0483	±	0.0032	83.3	±	1.9	90.0	±	130.0	700	
8.1	e, p, osc	65.9	47.5	0.721	85.8369	±	5.5260	0.0450	±	0.0100	74.7	±	4.8	10.0	±	430.0	500	yes
9.1	e, p, sec	72.5	44.7	0.617	62.5782	±	1.2140	0.0466	±	0.0034	102.2	±	2.0	80.0	±	140.0	530	
10.1	e, p, sec	81.5	62.2	0.763	78.6782	±	1.7333	0.0488	±	0.0040	81.4	±	1.8	130.0	±	160.0	580	
11.1	e, p, sec	48.9	36.3	0.742	72.9395	±	2.8729	0.0495	±	0.0072	87.8	±	3.4	80.0	±	270.0	710	
12.1	m, fr, sec	118.4	100.5	0.849	81.7662	±	1.6046	0.0503	±	0.0028	78.3	±	1.5	160.0	±	120.0	810	
13.1	m, fr, osc	81.6	63.3	0.776	82.6446	±	2.0490	0.0480	±	0.0034	77.5	±	1.9	60.0	±	140.0	620	
14.1	e, p, sec	53.5	42.7	0.798	79.7448	±	2.3529	0.0464	±	0.0042	80.3	±	2.4	30.0	±	170.0	570	
15.1	m, fr, hl	77.7	58.1	0.748	78.7402	±	1.7360	0.0499	±	0.0043	81.4	±	1.8	130.0	±	170.0	560	
16.1	e, fr, sec	135.7	133.2	0.982	82.3045	±	1.6258	0.0483	±	0.0027	77.9	±	1.6	90.0	±	110.0	550	
17.1	m, p, osc	30.9	26.8	0.867	78.4314	±	3.2603	0.0617	±	0.0080	81.6	±	3.4	360.0	±	250.0	263	yes
18.1	e, p, osc	93.5	97.0	1.037	81.3008	±	2.7761	0.0471	±	0.0053	78.8	±	2.7	40.0	±	220.0	2840	
19.1	e, p, osc	102.0	87.8	0.861	81.3008	±	3.5693	0.0501	±	0.0072	78.8	±	3.4	160.0	±	280.0	2200	
20.1	e, p, sec	159.9	82.9	0.518	81.2348	±	1.7818	0.0730	±	0.0041	78.9	±	1.8	1000.0	±	110.0	1180	yes
21.1	m, fr, osc	139.1	105.5	0.758	78.2473	±	1.4082	0.0460	±	0.0027	81.9	±	1.4	40.0	±	110.0	580	
22.1	m, p, sec	92.9	73.3	0.789	81.4996	±	1.9262	0.0483	±	0.0036	78.6	±	1.8	100.0	±	140.0	600	
23.1	e, p, sec	93.2	72.8	0.781	79.1766	±	1.8180	0.0502	±	0.0039	80.9	±	1.9	140.0	±	140.0	580	
24.1	e, fr, osc	92.0	64.4	0.700	64.6412	±	2.8832	0.1890	±	0.0150	98.9	±	4.4	2750.0	±	140.0	610	yes
25.1	e, fr, sec	1377.0	1043.0	0.757	80.9454	±	0.7207	0.0479	±	0.0008	79.2	±	0.7	97.0	±	38.0	1390	
26.1	m, p, sec	96.2	83.8	0.871	78.0031	±	1.8862	0.0513	±	0.0040	82.1	±	2.0	160.0	±	150.0	2460	
27.1	m, p, hl	293.8	249.4	0.849	77.2201	±	1.1330	0.0497	±	0.0019	82.9	±	1.2	185.0	±	81.0	660	
28.1	m, fr, osc	92.6	90.8	0.981	77.6398	±	1.8687	0.0425	±	0.0034	82.5	±	2.0	-160.0	±	140.0	870	
29.1	m, p, osc	81.5	67.3	0.826	81.6327	±	1.6660	0.0470	±	0.0030	78.5	±	1.6	40.0	±	120.0	790	
30.1	m, fr, sec	122.8	106.6	0.868	81.6994	±	1.8022	0.0477	±	0.0032	78.4	±	1.7	70.0	±	130.0	610	
31.1	m, fr, hl	538.0	459.0	0.853	79.1139	±	0.8763	0.0489	±	0.0014	81.0	±	0.9	141.0	±	61.0	1020	
32.1	e, p, osc	73.6	59.3	0.806	80.1282	±	1.7335	0.0465	±	0.0041	79.9	±	1.7	10.0	±	160.0	610	
33.1	m, p, hl	1898.0	1840.0	0.969	82.2774	±	0.8123	0.0477	±	0.0009	77.9	±	0.7	80.0	±	41.0	1370	
34.1	e, p, sec	92.2	73.5	0.797	81.9672	±	1.7468	0.0484	±	0.0037	78.1	±	1.6	150.0	±	150.0	640	
35.1	m, p, sec	78.9	59.3	0.752	78.1861	±	2.4452	0.1130	±	0.0150	81.9	±	2.6	1690.0	±	260.0	7300	yes

36.1	m, p, sec	64.0	64.0	1.000	81.4332	±	2.1220	0.0503	±	0.0044	78.7	±	2.0	210.0	±	170.0	590						
37.1	e, p, osc	912.0	182.8	0.200	84.1043	±	1.2732	0.0626	±	0.0020	76.2	±	1.2	682.0	±	69.0	1980	yes					
38.1	e, fr, sec	94.7	95.5	1.008	79.3021	±	1.8238	0.0466	±	0.0035	80.8	±	1.9	60.0	±	140.0	580						
39.1	e, fr, sec	171.4	69.0	0.403	85.8369	±	2.2104	0.0816	±	0.0073	74.6	±	1.9	1260.0	±	190.0	720	yes					
40.1	e, p, sec	110.8	92.8	0.838	79.8722	±	1.5311	0.0463	±	0.0033	80.2	±	1.5	30.0	±	140.0	550						
41.1	m, p, sec	637.0	559.0	0.878	77.5795	±	0.8426	0.0473	±	0.0013	82.6	±	0.9	64.0	±	57.0	1010						
42.1	e, p, sec	708.0	542.0	0.766	77.5795	±	0.8426	0.0476	±	0.0010	82.6	±	0.9	75.0	±	47.0	1040						
43.1	m, fr, hl	436.0	402.0	0.922	79.1139	±	0.8763	0.0462	±	0.0015	81.0	±	0.9	28.0	±	67.0	980						
44.1	e, p, osc	210.5	117.7	0.559	81.1688	±	1.3836	0.0841	±	0.0045	78.9	±	1.3	1250.0	±	110.0	1010	yes					
45.1	e, p, osc	144.9	123.7	0.854	65.8328	±	1.3435	0.0497	±	0.0024	97.2	±	2.0	178.0	±	99.0	319						
46.1	e, fr, hl	78.8	55.6	0.705	79.2393	±	2.0092	0.0496	±	0.0033	81.1	±	2.0	140.0	±	130.0	620						
47.1	e, p, osc	174.7	248.4	1.422	81.3670	±	1.1917	0.0469	±	0.0026	78.7	±	1.1	40.0	±	110.0	680						
48.1	e, eq, sec	111.9	94.5	0.845	77.1010	±	1.5456	0.0491	±	0.0030	83.1	±	1.7	170.0	±	130.0	670						
49.1	e, p, sec	328.0	66.1	0.202	65.6168	±	1.4208	0.0635	±	0.0020	97.5	±	2.1	717.0	±	67.0	1170	yes					
50.1	e, p, osc	115.0	88.6	0.770	76.9823	±	1.7779	0.0487	±	0.0035	83.2	±	1.9	120.0	±	140.0	760						
51.1	e, p, hl	94.8	80.6	0.850	81.3008	±	2.7761	0.0616	±	0.0056	78.8	±	2.7	620.0	±	190.0	1690	yes					
52.1	e, p, osc	88.5	83.6	0.945	79.1766	±	1.5045	0.0469	±	0.0036	80.9	±	1.5	30.0	±	150.0	610						
53.1	m, fr, sec	36.2	26.0	0.718	77.9423	±	2.5515	0.0502	±	0.0058	82.2	±	2.7	40.0	±	210.0	313						
54.1	m, p, osc	89.8	142.0	1.581	79.7448	±	2.2893	0.0470	±	0.0036	80.3	±	2.3	100.0	±	160.0	640						
55.1	e, p, sec	126.0	70.6	0.560	74.5712	±	1.3902	0.0478	±	0.0027	85.9	±	1.6	140.0	±	110.0	800						
56.1	e, fr, sec	74.2	59.1	0.797	82.1693	±	2.0931	0.0521	±	0.0038	78.0	±	2.0	250.0	±	140.0	540						
57.1	e, fr, sec	38.6	29.5	0.764	81.4996	±	2.7233	0.0474	±	0.0052	78.6	±	2.6	0.0	±	210.0	314						
58.1	e, p, osc	74.1	54.7	0.738	83.2640	±	2.1492	0.0495	±	0.0036	77.0	±	2.0	160.0	±	140.0	680						
59.1	e, p, osc	312.7	452.9	1.448	80.9717	±	1.0490	0.0488	±	0.0019	79.2	±	1.0	130.0	±	80.0	740						
60.1	e, fr, sec	91.0	52.7	0.579	79.1766	±	2.2568	0.0703	±	0.0058	80.9	±	2.3	920.0	±	160.0	550	yes					

Notes:

Analysis location and grain description: m = middle, e = end, p = prismatic grain, eq = equant grain, fr = fragment, osc = oscillatory zoned, sec = sector zoned, hl = homogeneous (low luminescence), hh = homogeneous (high luminescence).

LA-ICP-MS analysis conducted on 22nd June 2019 at the University of Queensland (UQ), Brisbane, Australia.

SHRIMP-RG analysis conducted on 30th June 2020 at the Australian National University (ANU), Canberra, Australia.

All analytical errors are given a 1σ.

Samples highlighted in red have been rejected and therefore excluded from age calculations.

Comments for the rejected grains can be found online with the associated published paper (Walsh et al., 2020).

Table S5.4: Results of mixture modelling experiments (Chapter 5)

*Sample ID	Lithology	Formation	Optimal	Components	Age	Error (2 σ)	Fraction	Error (2 σ)	Misfit
17NI05	felsic tuff	Dras Volcanics	Non-optimal	2	162.64	0.91	0.96	0.39	0.879
					175.1	5.3	0.04	-	
			Optimal	3	160.5	2.2	0.43	0.46	0.839
					164.6	2	0.53	0.48	
					175.2	5	0.04	-	
17NI12	trachydacite	Dras Volcanics	Non-optimal	2	154.58	0.77	0.74	0.28	0.778
					162.3	2.8	0.26	-	
			Non-optimal	3	151.37	1.6	0.22	0.19	0.658
					156.73	1.2	0.61	0.26	
					163.96	1.9	0.17	-	
			Optimal	4	151.1	2.6	0.2	0.25	0.636
					156.48	1.8	0.6	0.29	
					162.3	2.2	0.17	0.15	
					171.5	4.7	0.04	-	
17KG01	granodiorite	Kargil Intrusives	Optimal	2	101.87	1.8	0.76	0.37	1
					101.9	5.1	0.24	-	
17KG02	diorite	Kargil Intrusives	Optimal	2	100.58	1.3	0.57	0.38	1
					100.58	1.6	0.43	-	
17KG04	granodiorite	Kargil Intrusives	Non-optimal	2	80.67	0.43	0.96	0.29	0.633
					99.7	2.8	0.04	-	
			Optimal	3	80.25	0.45	0.87	0.28	0.561
					86.5	2	0.09	0.1	
					99.7	2.8	0.04	-	

†Sample ID	Lithology	Formation	Components	Age Primary	Error (2 σ)	Proportion	Age Secondary	Error (2 σ)	Proportion
17NI05	felsic tuff	Dras Volcanics	3	164.6	2	0.53	160.5	2.2	0.43
17NI12	trachydacite	Dras Volcanics	4	156.48	1.8	0.6	151.1	2.6	0.2
17KG01	granodiorite	Kargil Intrusives	2	101.87	1.8	0.76	101.9	5.1	0.24
17KG02	diorite	Kargil Intrusives	2	100.58	1.3	0.57	100.58	1.6	0.43
17KG04	granodiorite	Kargil Intrusives	3	80.25	0.45	0.87	86.5	2	0.09

Notes:

Summary of the results of mixture modelling giving the optimal number of components in each sample population examined together with their modelled ages. Optimal values (green) for peak position are based on the point at which increasing the number of components no longer improves the misfit or introduces new 'ages', that are similar to existing ones.

* Results of mixture modelling experiments using *Isoplot* showing ages identified, proportion and misfit of the best solution as a fraction of the one component case.
†Summary of the results of mixture modelling giving the preferred number of components in each sample population examined together with their modelled ages.

Chapter Six: Youngest magmatic age (Early Eocene) from the Neotethyan intraoceanic Dras Arc, Ladakh Himalaya, NW India

Jessica M.J. Walsh[1], Solomon Buckman[1] and Allen P. Nutman[1]

[1]GeoQuEST Research Centre, School of Earth, Atmospheric and Life Sciences, University of Wollongong, Wollongong, NSW 2522, Australia.

Research highlights:

- Early Eocene (~53 Ma) U-Pb zircon ages for gabbroic blocks from the Sapi-Shergol mélange along the thrust contact between the intraoceanic Dras Arc and Indian continent represent the youngest recorded ages for this Neotethyan intraoceanic arc complex.
- Importantly, these ages constrain the timing of collision between the Neotethyan, intraoceanic Dras Arc with India to early Eocene, after which final continent-continent (India-Eurasia) collision commenced.

Key words:

Himalaya, Ladakh, gabbroic blocks, arc, collision, mélange, intraoceanic

Citation:

Walsh, J. M., Buckman, S., & Nutman, A. P. (*in prep*). Youngest magmatic age (Early Eocene) from the Neotethyan intraoceanic Dras Arc, Ladakh Himalaya, NW India. (*in prep.)*

Foreword:

This chapter addresses the third objective of this project, this being '*to establish the latest stages of development of the Dras Arc in order to constrain the timing of arc-continent collision*'. Note, this chapter is *in preparation* for submission to the journal Gondwana Research.

6.1 Abstract

The youngest magmatic age in any ophiolite or island arc complex is a critical constraint on the timing of arc-continent collisions because arc magmatism is extinguished when subduction ceases due to collision with buoyant continental crust. The timing and nature of the India-Eurasia collision has been the focus of considerable debate between those in favour of a single continental collision between India and Eurasia at ~55 Ma versus a multi-stage collision involving ophiolite obduction with India, followed by final continental collision sometime later. The Sapi-Shergol mélange developed along the thrust contact between the intraoceanic Dras Arc and Indian Zanskar Supergroup to the south. Ophiolitic blocks within the mélange have been interpreted as the oceanic basement of the Jurassic-Eocene Dras Arc. Early Eocene (53 Ma) zircon ages obtained for gabbroic blocks within the Dras ophiolitic mélange represent the youngest magmatic phase of the Dras Arc before collision with India. Significantly these gabbroic blocks provide a new minimum age constraint for the initial 'soft' collision of an extensive Neotethyan intraoceanic ophiolite and island arc terrane with the northern Indian continental margin in the Ladakh Himalaya, before final 'hard' continental collision of India with Eurasia.

6.2 Introduction

The timing and nature of the India-Eurasia collision to form the Himalaya has been a topic of much discussion revolving around whether there was a single subduction zone and single collision between the passive continental margin of northern India and the active continental Trans-Himalayan Arc along southern Eurasia (Hu et al., 2016; Yin and Harrison, 2000), or multiple subduction zones and multiple collisions, first involving the collision and obduction of intraoceanic arc and ophiolite complexes followed by terminal continent-continent collision sometime later (Aitchison et al., 2007a; Buckman et al., 2018; Corfield et al., 2001). Considerable emphasis has been placed on the recognition of accreted (intraoceanic) arc complexes in orogenic belts, as these can potentially be used for the along-strike correlation of tectono-stratigraphic terranes, and form a key element of geodynamic and paleogeographic reconstructions. The identification of distinctly, intraoceanic, ophiolitic and island arc complexes along the Indus-Yarlung-Tsangpo Suture (IYTS; Aitchison et al., 2007b; Martin et al., 2020; Walsh et al., 2019, 2020) between Indian and Eurasian continental rocks has suggested that at least one Neotethyan island arc complex was first obducted onto the Indian margin prior to final continental collision between India and the Trans-Himalayan Arc (Ladakh Arc) along the active margin of southern Eurasia (Aitchison et al., 2007b). The collision of supra-subduction zone ophiolites or arc complexes with thick, buoyant, continental margins tend to choke and inhibit subduction and, thus terminate arc magmatic processes (Bloomer et al., 1995). Therefore, the youngest age for typical subduction-related magmatic compositions in any ancient arc complex is an important age constraint for the timing of arc collisions and accretion onto continental margins. Previous estimates for the initial obduction of ophiolites onto India include Late Cretaceous based on the presence of ~88 Ma andesites within the Spongtang Massif (Pedersen et al., 2001) to early Eocene based on fossils present in the Indian Zanskar Supergroup (Buckman et al., 2018). Estimates of the age of final continental collision range from ~70 Ma (Yin and Harrison, 2000) to 54 Ma (Najman et al., 2017) based on detrital zircon records for the Kong Slate and Chulung La Formation, to 34 Ma based on the youngest detrital zircon age relating to the final phase of magmatism within the Gangdese Batholith (Aitchison et al., 2007a). We suggest here the maximum age of initial collision of the Dras Arc with India by obtaining the youngest reported ages for this intraoceanic complex, which provides important context for other ophiolitic or island arc rocks along this section Indus-Yarlung-Tsangpo Suture (IYTS). Gabbroic blocks collected from the Sapi-Shergol mélange zone along the basal thrust contact between the intraoceanic Dras Arc and Indian passive margin rocks (Zanskar Supergroup; Figure **6.1**), yield zircon U-Pb ages of ~53 Ma (weighted mean ages ranging 53.4 ± 0.6 Ma to 52.9 ± 0.4 Ma). These early Eocene gabbroic blocks represent the youngest known age for the Neotethyan intraoceanic Dras Arc, and thereby constrain the minimum age of arc magmatism and the

maximum timing of arc-continent (India) collision to after 53 Ma for this segment of the IYTS in the Ladakh Himalaya, NW India.

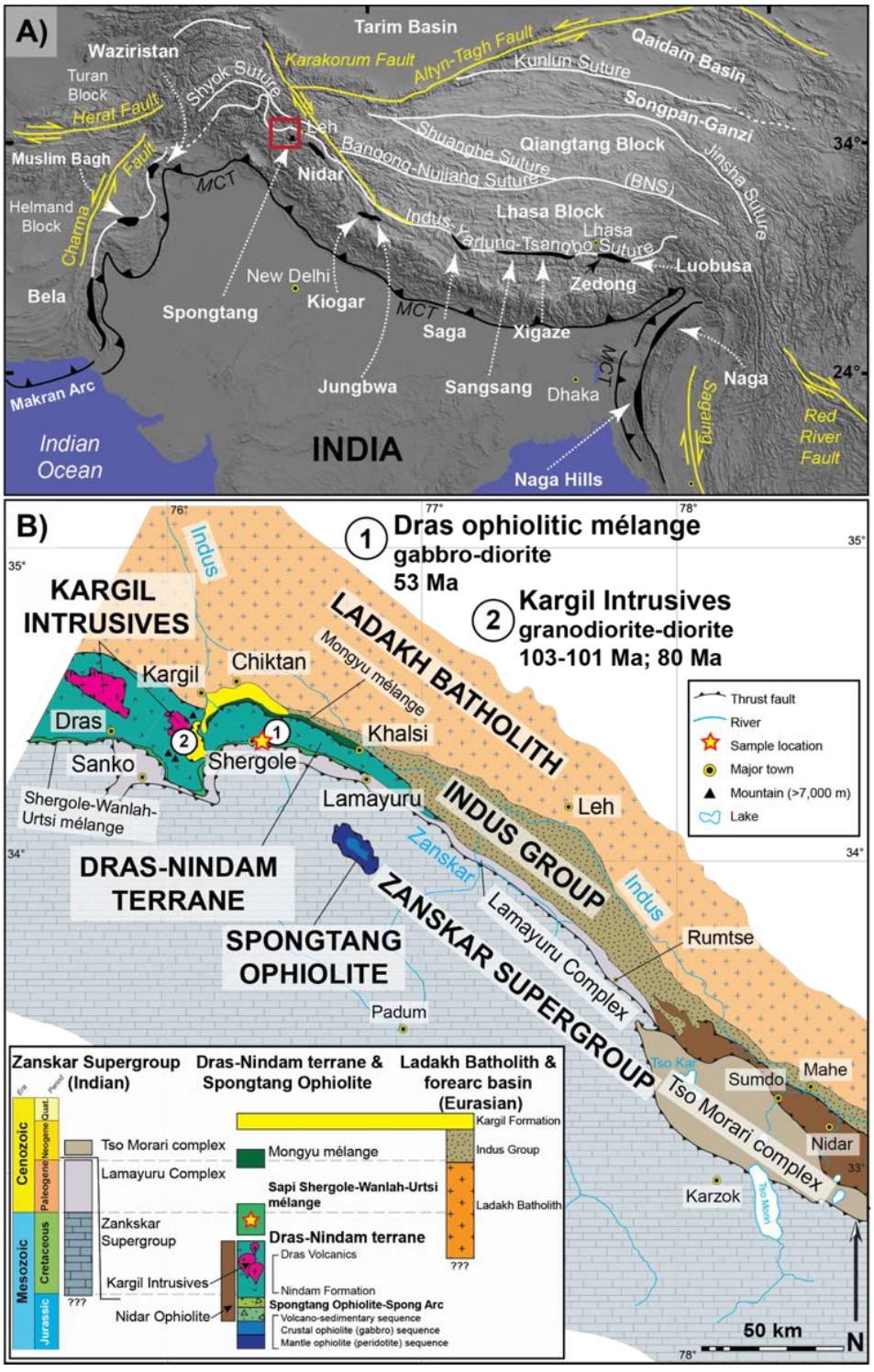

Figure 6.1: Main geological units of the Indus Suture Zone, Ladakh Himalaya, NW India. **A)** Geographic map indicating the location of the study site (red rectangle; after Buckman et al., 2018); **B)** Geological units of the Indus Suture Zone (after Bhattacharya et al., 2020; Corfield et al., 2000; Walsh et al., 2019; 2020).

6.3 Geological setting

The Jurassic-Eocene Dras Arc is a juvenile island arc complex located in Ladakh, NW India along the IYTS between India and Eurasia (Figure **6.1**; Clift et al., 2000; Robertson and Degnan, 1994). This complex consists of the Dras Volcanics in the west (Brookfield et al., 1981; Clift et al., 2002; Dietrich et al., 1983; Radhakrishna et al., 1984; Reuber, 1989) which consist of basaltic-andesites with minor felsic volcanic rocks, some of which have adakitic characteristics (Walsh et al., 2020). Further east, the preserved volcanic pile transitions into a forearc volcaniclastic sequence (Nindam Formation; Garzanti and Haver, 1988; Upadhyay et al., 2004; Sinha and Upadhyay, 1994). Collectively, these units are grouped as the Dras-Nindam terrane (Walsh et al., 2019). At Kargil, the volcanic pile is intruded by mafic to intermediate plutons with ages of ~103-101 Ma and ~80 Ma (Honegger et al., 1982; Schärer et al., 1984; Walsh et al., 2020). The Dras-Nindam terrane rocks are in fault contact with the Ladakh Batholith and associated Indus Group on the Eurasian margin to the north (Bhattacharya et al., 2020; Zhou et al., 2020), with the boundary being marked by extensive development of the serpentinite-matrix Mongyu mélange (Figure **6.1**). The southern margin of the Dras-Nindam terrane is thrust over the Lamayuru Complex and the Zanskar Supergroup (Robertson and Degnan, 1993; Robertson and Sharp, 1998), whose youngest strata were deposited during the early Eocene (Najman et al., 2017). The Sapi-Shergol serpentinite-matrix mélange developed along this thrust contact, and contains sheared blocks of ophiolitic peridotite, gabbro, basalt, blueschist and chert interpreted as oceanic basement to the intraoceanic Dras Arc (Honegger et al., 1989; Robertson, 2000; Mahéo et al., 2006; Groppo et al., 2016; Bhat et al., 2019) and equivalent to the Spongtang Ophiolite and Spong Arc klippe 30 km to the south (Garzanti et al., 1987; Pedersen et al., 2001; Buckman et al., 2018; Catlos et al., 2019). There is the possibility that other intraoceanic terranes along-strike may be correlative tectono-stratigraphic units, for example the Zedong terrane in Tibet (Aitchison et al., 2007b; Aitchison et al., 2000; Liu et al., 2020; McDermid et al., 2002).

The youngest magmatic age of the Dras Arc is currently inferred from the youngest detrital zircon population (84 Ma) in the uppermost sections of the forearc Nindam Formation (Walsh et al., 2019) and the youngest (80 Ma) granodioritic to dioritic intrusive bodies (Honegger et al., 1982; Walsh et al., 2020). Palynological investigations of the Nindam Formation have demonstrated Gondwanan-derived Permian and Mesozoic specimens. Palynomorphs of Palaeocene age represent the youngest reported age for the Dras-Nindam terrane (Upadhyay et al., 2004). The youngest upper sections of this terrane have been truncated against the Mongyu mélange (Robertson, 2000) and thus, the youngest ages of in situ arc magmatism are currently unknown. Therefore, the timing of arc-continent collision remains ambiguous. This is further complicated by competing hypothesis which propose that (i) the Kohistan-Ladakh-Dras arc

formed at one convergent margin with associated sub-basins (Nindam Formation and Indus Group; e.g., Henderson et al., 2010), or (ii) the Kohistan-Ladakh and Dras arcs formed separately, with distinctly different forearc basins (Nindam Formation vs. Indus Group) at separate convergent margins associated either Eurasia or India. It is suggested here that the Kohistan-Ladakh and Dras arc systems are separated by a significant thrust fault marked by the Mongyu mélange, and further that Dras Arc developed as a separate island arc complex to the continental Ladakh Arc which developed further north above a second subduction zone on top of the Jurassic Shyok ophiolite-arc to the north (Saktura et al., 2020).

6.4 Methods

Samples were collected from the ophiolitic Sapi-Shergol mélange which occurs between the southern boundary of the Dras-Nindam terrane and the northern extent of the northern Indian passive margin (Zanskar Supergroup; Figure **6.1**). The closest township to the sampling site is Shergol, with coordinates for samples available in Supporting Information Table S6.1. The mélange is dismembered and is likely represented eastward along strike as the Wanlah and Urtsi ophiolitic mélanges. The Sapi-Shergol mélange exhibits sheared blocks of ophiolitic peridotite, gabbro, basalt, blueschist and chert encased in a serpentinite matrix. It is unknown whether the gabbroic blocks (compositions ranging from gabbro to diorite and K-poor monzonite) were originally dykes or sills, as the intrusives are completely disrupted and occur only as isolated blocks within the mélange.

Four representative gabbroic blocks (samples 17NI17, 17NI18, 17NI19, and 17NI20) were selected for major, trace and rare earth element analysis by X-ray fluorescence (XRF) and laser ablation-inductively coupled plasma-mass spectrometry (LA-ICP-MS; Supporting Information Table S6.2). Zircons from three samples (17NI18, 17NI19, and 17NI20a) were separated at the Institute of Hebei Regional Geology Survey, China. One duplicate sample (17NI20b) was processed for zircon separation at the Australian National University (ANU), Australia. Zircons were dated using LA-ICP-MS at the Centre for Geoanalytical Mass Spectrometry, The University of Queensland, Australia (Supporting Information Table S6.3).

6.5 Results

The representative gabbroic samples (*sensu lato*; compositions ranging from gabbro to diorite and K-poor monzonite) display typical island arc basalt (IAB) and intraoceanic signatures (Figure **6.2**; Supporting Information Figure S6.1-S6.6). In thin sections the samples are medium to coarse-grained and equigranular with plagioclase + clinopyroxene ± kaersutite ± alkali

feldspar ± quartz. There is textural evidence of pockets of residual melt, where incompatible elements partitioned late in crystallisation (Figure **6.2**; Supporting Information Figure S6.1-S6.4).

Zircon grains range from prismatic to stubby to jagged anhedral, the latter habit being typical of those formed in pockets of residual crystallising melt (Figure **6.2**; Supporting Information Figure S6.7-S6.10). The samples demonstrate high Th/U ratios ranging 0.44-1.83, average 0.83 (Supporting Information Table S6.3), typical for magmatic zircons in gabbros and diorites. One hundred and seventeen analyses of 117 zircon grains from four gabbroic samples yield $^{206}Pb/^{238}U$ ages between 71.2 ± 5.8 to 50.5 ± 2.6 Ma (2σ). With weighted mean $^{206}Pb/^{238}U$ ages for all samples being early Eocene (Ypresian), ranging 53.4 ± 0.6 Ma to 52.9 ± 0.4 Ma, expressed at 95% confidence (Table **6.1**; Figure **6.2**; Supporting Information Figures S6.11 and S6.12). Methods, detailed results and tabulated data are presented in the Supporting Information.

Table 6.1: Zircon U-Pb geochronologic ages of gabbroic blocks from the ophiolitic Sapi-Shergol mélange.

Sample number	Weighted mean age (Ma)*	Age range (Ma)			MSWD†	Grains analysed	Lithology
Sapi-Shergol ophiolitic mélange							
17NI18	53.1 ± 0.6	61.4 ± 10.2	to	50.7 ± 2.1	2.1	27	gabbroic diorite
17NI19	52.9 ± 0.4	61.4 ± 8.0	to	51.1 ± 3.2	1.3	29	diorite
17NI20a	53.3 ± 0.9	71.2 ± 5.8	to	50.9 ± 3.0	2.6	29	gabbroic diorite
17NI20b	53.4 ± 0.6	59.7 ± 3.2	to	50.5 ± 2.6	2.3	29	gabbroic diorite

Note:
All analytical errors are given at 2σ.
Uncorrected for common Pb.
See also Supporting Information Table S6.3 for zircon U-Pb geochronologic data.
*Weighted mean $^{206}Pb/^{238}U$ age (Ma) given for analysed zircon grains using LA-ICP-MS expressed at 95% confidence.
†Where, MSWD = mean square weighted deviation.

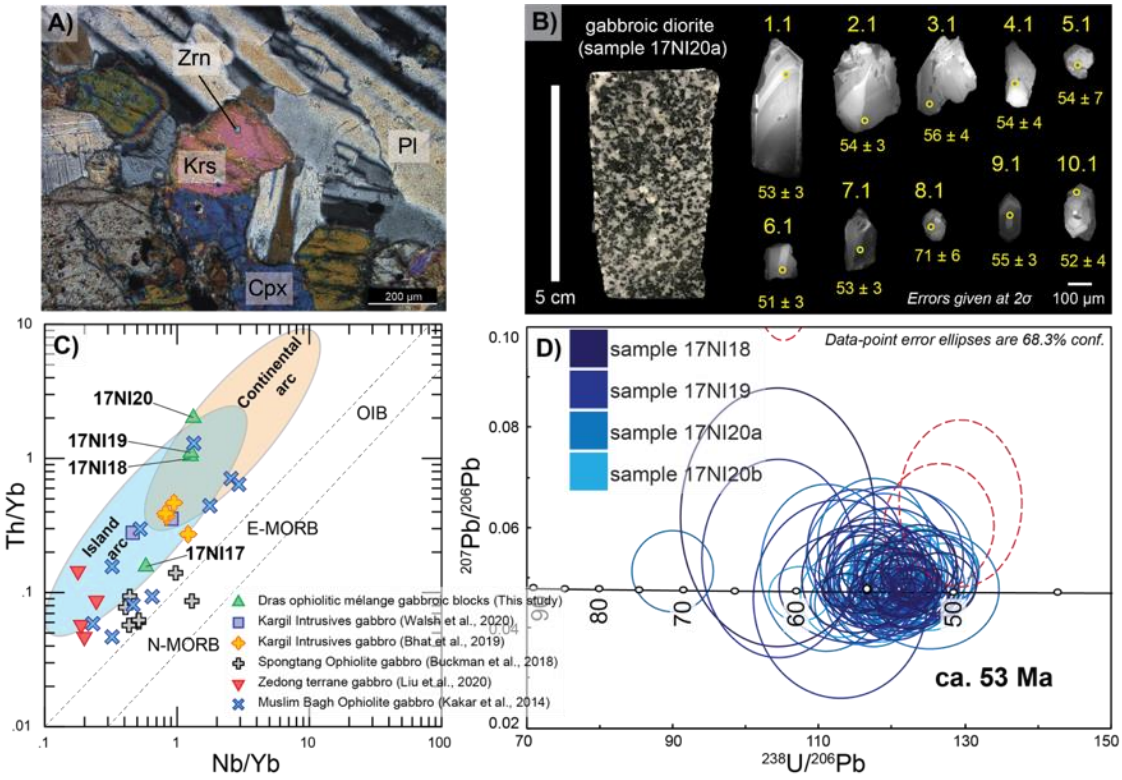

Figure 6.2: Whole rock geochemical and zircon U-Pb geochronologic data of gabbroic blocks from the Sapi-Shergol mélange. **A)** Representative photomicrograph of a gabbroic block (sample 17NI17) demonstrating the presence of kaersutite (Krs) within the mineral assemblage. Where, Cpx = clinopyroxene; Pl = plagioclase; Zrn = zircon; **B)** Representative hand sample (sample 17NI20) of a gabbroic diorite block and zircon grains with analytical sites and ages (Ma). Analytical errors are given at 2σ; **C)** Mid-ocean ridge basalt (MORB) array diagram (Pearce, 2008); **D)** Tera-Wasserburg concordia plot of gabbroic blocks from samples (17NI18, 17NI19, 17NI20a, 17NI20b). Data are plotted uncorrected for common Pb at 95% confidence.

6.6 Discussion

6.6.1 Initiation, maturation, and accretion of the Dras Arc

The oldest reported *in situ* magmatic ages for the Dras Arc are Upper Jurassic (160 ± 3 Ma; Walsh et al., 2020) felsic (adakitic) volcanic rocks that occur as minor trachydacite and tuffaceous layers within the otherwise dominantly basaltic to andesitic Dras volcanic pile. These older ages correlate with that of a diorite (177 ± 1 Ma) from the Spongtang Ophiolite (Pedersen et al., 2001), as well as a distinct Lower Jurassic to Cretaceous (~185-135 Ma) detrital zircon population from the Nindam Formation (Walsh et al., 2019). The Spongtang Massif is preserved as an isolated klippe just to the south of the Dras-Nindam terrane (Garzanti et al., 1987; Pedersen et al., 2001; Buckman et al., 2018; Catlos et al., 2019) and is probably the equivalent forearc portion of the Dras Arc (Buckman et al., 2018). These units were thrust farther south over the Indian continental margin before back-thrusting uplifted the underlying Lower Eocene Indian Zanskar Supergroup (Najman et al., 2017) units during the final stages of continental collision,

to isolate the Spongtang Ophiolite thrust sheet from the equivalent Dras Arc (Buckman et al., 2018; Walsh et al., 2020). The Dras Arc likely initiated and developed throughout the Late Jurassic to Eocene on Neotethyan MORB-like oceanic crust (Buckman et al., 2018; Corfield et al., 2001), with extensive magmatism occurring between ~125-84 Ma evidenced by detrital zircon geochronology, which also revealed Gondwanan provenance as determined from forearc basin material of the Nindam Formation (Walsh et al., 2019). Palynomorphs of Palaeocene age from the forearc Nindam Formation have also been identified, which represent the youngest reported fossil age for the Dras-Nindam terrane (Upadhyay et al., 2004). These Palaeocene palynomorphs ages correlate well with early Eocene ages presented here for arc-related gabbroic blocks from the Sapi-Shergol mélange, proposed to be the youngest magmatic age for the intraoceanic Dras Arc; therefore, constraining the minimum age of arc magmatism and the maximum age of arc-continent (India) collision to after 53 Ma for this segment of the Indus Suture.

There are other Neotethyan ophiolite and arc complexes which have similar Jurassic inception ages to the Dras Arc, including the Masirah Ophiolite of Oman (Smewing et al., 1991), Spongtang Ophiolite of Ladakh (Pedersen et al., 2001), Kiogar Ophiolite (Chan et al., 2015), Jungbwa Ophiolite (Miller et al., 2003), intraoceanic Zedong terrane (McDermid et al., 2002) and Luobusa Ophiolite (Zhou et al., 2002) of Tibet. Whereas the youngest ages for other Indus-Yarlung-Tsangpo ophiolite and arc complexes include Muslim Bagh (~80 Ma; Kakar et al., 2012) and Bela ophiolites (~66-65 Ma; Ahmed, 1993) of Pakistan, and the Spong Arc in Ladakh (~88 Ma; Pedersen et al., 2001). In contrast, the youngest ophiolite ages farther east in Tibet are ~120 Ma (Chan et al., 2015).

6.6.2 Mechanisms for incorporation of Eocene gabbroic blocks in the Sapi-Shergol mélange

The young Eocene arc-related gabbroic blocks within the Sapi-Shergol mélange lack any known equivalent-aged outcrops within the Dras-Nindam terrane. It may be that the youngest portions of the Dras Arc were tectonically eroded and truncated during collision and uplift, and thus only the older portions of the arc remain. It is also possible that the frontal (near trench) forearc portions of the arc were tectonically eroded during subduction and collision, and only minor fragments of the youngest arc magmatic phases were captured in the return flow of a choked subduction channel (Cloos, 1993) and preserved as isolated blocks in the Sapi-Shergol mélange.

It may be that the younger sections of the Dras-Nindam terrane are yet to be identified and dated. However, the presence of Palaeocene fossils in the forearc Nindam Formation (Upadhyay et al., 2004) and now early Eocene gabbroic blocks within the Sapi-Shergol mélange provide compelling evidence for the evolution of the Dras Arc up until at least 53 Ma. The Dras Arc likely collided with India soon after crystallisation of these 53 Ma gabbroic rocks, which slightly precedes the 50-47 Ma eclogite metamorphism at Tso Morari (de Sigoyer et al., 2000; Donaldson et a., 2013). We suggest that early Eocene eclogites relate to the first phase of ophiolite-arc collision with India, rather than final continental collision that occurs sometime later after termination of the continental Ladakh Arc nearer the Eocene-Oligocene boundary (Figure **6.3**).

6.6.3 Collision of the Dras Arc with India and closure of the Neotethyan Ocean

The presence of early Eocene gabbroic blocks in the Sapi-Shergol mélange resolves a long-standing debate about the timing of collision of intraoceanic arc and ophiolitic complexes with northern India. Corfield et al. (2001) argued for a Cretaceous (~70 Ma) collision based on three subducting systems between India and Eurasia, where the Spongtang Ophiolite-Spong Arc complex first collides with India whilst the Dras-Kohistan Arc collides and accretes onto the Eurasian margin, before final continental collision at ~55 Ma. However, Buckman et al. (2018) discuss that the Spongtang Massif is thrust over early Eocene units of the Indian Zanskar Supergroup; thus, collision must be post-early Eocene. Our early Eocene ages from gabbroic blocks of the Sapi-Shergol mélange fit with the latter interpretation, as they represent the youngest magmatic ages for the Dras Arc, before collision and accretion onto the Indian continental margin.

There is increasing evidence for a two-stage collision model eastward in Tibet along the IYTS involving two north-dipping subduction zones and an initial arc-continent (Dras-India) collision during the early Eocene, followed by terminal continent-continent collision between India and Eurasia later, possibly as late as 34 Ma in Tibet (Aitchison et al., 2007a) but as yet this is currently unresolved in the Ladakh Himalaya, westward in NW India. Whilst most eclogite ages coincide with the first phase of arc-continent collision between 50-47 Ma, reports of 34-28 Ma eclogites at Stak in Pakistan (Kouketsu et al., 2016) may relate to final continent-continent collision. In Ladakh, the youngest reported detrital zircon population relating to Ladakh Arc activity is ~41 Ma (Henderson et al., 2010), suggesting that arc magmatism along the southern margin of Eurasia (Ladakh Arc) continued unabated for at least 10 million years. There is a sudden drop in convergence rates between India and Eurasia from 15 cm/yr at 50 Ma to about 7.5 cm/yr at 40 Ma (Copley et al., 2010). This drop in the rate of convergence possibly coincides with collision of the Dras Arc with India after 53 Ma, which further suggests that at least 1000 km of ocean

crust separated the India-Dras margin from the active continental Ladakh Arc along southern Eurasia at during the early Eocene at 53 Ma (Figure **6.3**).

6.7 Conclusions

Early Eocene (~53 Ma) U-Pb zircon ages of gabbroic blocks from the Sapi-Shergol mélange along the thrust contact between the intraoceanic Dras Arc and Indian continent represent the youngest magmatic ages for this Neotethyan intraoceanic complex. Eocene ages for other intraoceanic arc or ophiolite terranes are yet to be discovered within the Indus-Yarlung-Tsangpo Suture zone, which will provide important additional information on the complex histories of these continental margins (i.e., India and Eurasia) before orogenesis has even taken place. Importantly, these ages constrain the timing of collision between the Neotethyan, intraoceanic Dras Arc with India to early Eocene, after which final continent-continent (India-Eurasia) collision commenced.

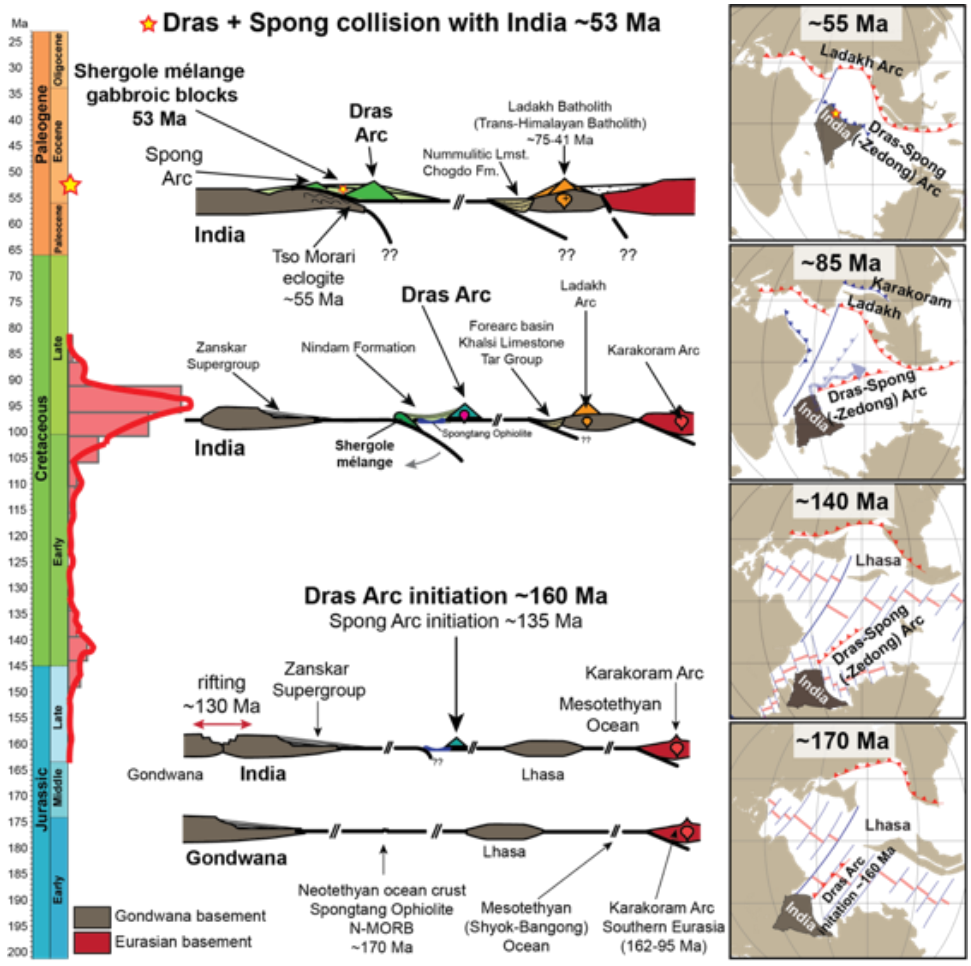

Figure 6.3: Tectonic evolution of the Dras Arc from inception during the Upper Jurassic to final stages of magmatism in the Eocene and final accretion and collision with the passive margin of India (~55 Ma). Adapted from Walsh et al. (2019; 2020). Shyok Suture evolution from Saktura et al. (2020).

6.8 Acknowledgements

This study was partially supported by the GeoQuEST Research Centre and a Small Project Grant (2017) from the University of Wollongong. This research has also been conducted with the support of the Australian Government Research Training Program Scholarship awarded to J.M.J. Walsh. Thank you to W.M. Saktura for fieldwork assistance, geochemical analyses, and discussions. J. Punchok is thanked for guidance and logistical support in Ladakh. R. Zhou is thanked for LA-ICP-MS analyses and data reduction of zircon U-Pb geochronologic data. A.P. Nutman is thanked for discussions.

6.9 Coauthor contributions

Walsh, Jessica, M.J.

GeoQuEST Research Centre, School of Earth, Atmospheric and Life Sciences,

University of Wollongong, Wollongong, NSW 2522, Australia.

Position: PhD candidate

Email: jw063@uowmail.edu.au

Credit author statement: Conceptualisation, Methodology, Investigation, Data Curation, Writing - Original Draft, Writing - Review & Editing, Visualisation.

Buckman, Solomon

GeoQuEST Research Centre, School of Earth, Atmospheric and Life Sciences,

University of Wollongong, Wollongong, NSW 2522, Australia.

Position: Senior lecturer in economic geology

Email: solomon@uow.edu.au

Credit author statement: Conceptualisation, Methodology, Investigation, Writing - Original Draft, Writing - Review & Editing, Supervision, Funding Acquisition.

Nutman, Allen, P.

GeoQuEST Research Centre, School of Earth, Atmospheric and Life Sciences,

University of Wollongong, Wollongong, NSW 2522, Australia.

Position: Professor in igneous and metamorphic petrology

Email: anutman@uow.edu.au

Credit author statement: Methodology, Writing - Review & Editing, Supervision.

6.10 Supporting information

Youngest magmatic age (Early Eocene) from the Neotethyan intraoceanic Dras Arc, Ladakh Himalaya, NW India

Jessica M.J. Walsh[1], Solomon Buckman[1] and Allen P. Nutman[1]

[1]GeoQuEST Research Centre, School of Earth, Atmospheric and Life Sciences, University of Wollongong, Wollongong, NSW 2522, Australia.

Overview

The following information includes further support for the methods and results sections of Chapter 6, referred to in-text as 'Supporting Information Text'. The first section (Supporting Information: Methods) includes detailed descriptions of whole rock geochemical and zircon U-Pb geochronologic methods used for gabbroic samples from the ophiolitic Sapi-Shergol mélange, Ladakh Himalaya, NW India. The second section (Supporting Information: Results) includes detailed results related to petrography, whole rock geochemistry and geochronology.

Following this are tabulated data, and includes:

- Table S6.1: Sample localities and lithological descriptions
- Table S6.2: Whole rock geochemistry
- Table S6.3: Zircon U-Pb results using LA-ICP-MS

6.10.1 Supporting information: Methods

6.10.1.1 Whole rock geochemistry

Four representative gabbroic samples (17NI17, 17NI18, 17NI19 and 17NI20) from the Sapi-Shergol mélange were crushed using a tungsten carbide (WC) TEMA ring mill. Major elements were determined by X-ray fluorescence (XRF), using a Spectro-analytical XEPOS XRF spectrometer at the University of Wollongong (UOW), Australia. Based on elemental concentrations estimated in trace element analysis, the flux used for the fused buttons was 35.3% tetraborate to 64.7% metaborate (Norrish and Chappell, 1977).

Trace and the rare-earth element (REE) analyses were undertaken at the Australian Laboratory Services (ALS) Minerals Division, Brisbane, Australia using ICP-MS. All samples from this study were analysed using the geochemical procedure code ME-MS81 (30-element package). Lithium metaborate and tetraborate were used as fluxes with and after fusing in a furnace with the resultant melt being dissolved in nitric, hydrochloric, and hydrofluoric acid mixes. This solution was then analysed by ICP-MS. Standards OREAS 120 and STSD-1, as well as five sample duplicates and three blanks, were analysed in order to determine the error tolerance (analytical error ± 10%). Refer to Supporting Information Table S6.1 for description and locality of samples and Supporting Information Table S6.2 for whole rock major and trace element compositions of gabbroic samples from the Sapi-Shergol mélange.

6.10.1.2 Zircon U-Pb geochronology

6.10.1.2.1 Zircon preparation

Zircons were separated at the Institute of Hebei Regional Geology Survey, China. The samples (17NI18, 17NI19, 17NI20) were chipped in a pre-contaminated jaw crusher, using a subsample first. Chips were thoroughly washed with water prior to being ground into a coarse powder using a jaw crusher. The coarse powder was separated into heavy and light fractions using heavy liquids to obtain the >3.31 zircon-bearing fraction. The heavy fraction was washed and dried prior to being passed through a Franz Isodynamic Magnetic Separator to obtain zircons (normally the non-magnetic fraction at 2A).

One sample was duplicated (17NI20) with zircons being separated at the Australian National University (ANU), Australia. The samples were chipped in a pre-contaminated jaw crusher. Chips were thoroughly water washed then dried, prior to coarse powdering in a WC mill. The coarse powder was then ‘de-slimed’ by placing in a large beaker of water, with gentle overflow, so that micro-scale dust was removed. Following drying, samples were treated with bromoform

(specific gravity = 2.84) and diiodomethane (specific gravity = 3.31) in tapped glass funnels, in order to obtain the >3.31 zircon-bearing fraction. The >3.31 fraction was passed through a Franz Isodynamic Magnetic Separator, to obtain zircons (normally the fraction non-magnetic at 1.25A).

Zircon grains were examined using a binocular microscope, handpicked, and mounted with standard TEMORA II grains on double-sided tape on a glass plate, which were then cast with epoxy resin in a mould. TEMORA II was distributed as several clusters of grains in different parts of the mount to increase confidence in the accuracy of calibration of U-Pb across the entire mount when analysed. The mount was ground on 1200 grade wet and dry paper to reveal approximately half sections through the grains and then polished with 1 µm diamond paste. Transmitted and reflected light photomicrographs were taken, along with cathodoluminescence (CL) images. The CL images were obtained using a Scanning Electron Microscope (SEM) JEOL JSM-6490LV with a 15-kV conventional tungsten filament thermionic source coupled with a Gatan MonoCL4 used in polychromatic mode at the Electron Microscope Centre (EMC), Innovation Campus, University of Wollongong (UOW).

6.10.1.2.2 LA-ICP-MS

A total of 117 zircon grains were chosen from four samples from the Sapi-Shergol mélange (sample 17NI18: gabbroic diorite, *n* = 29; sample 17NI19: diorite, *n* = 30; sample 17NI20a: gabbroic diorite, *n* = 29; sample 17NI20b: gabbroic diorite, *n* = 29) for U-Pb dating by Laser Ablation Inductively Coupled Plasma Mass Spectrometry (LA-ICP-MS) at the Centre for Geoanalytical Mass Spectrometry (CGMS), The University of Queensland (UQ), Australia, following methods similar to those in Walsh et al. (2020). Refer to Supporting Information Table S6.3 for zircon U-Pb results using LA-ICP-MS for gabbroic samples from the Sapi-Shergol mélange.

The zircon 91500, which has a $^{206}Pb/^{238}U$ age of 1062.4 ± 0.4 Ma and $^{206}Pb/^{207}Pb$ age of 1065.4 ± 0.3 Ma (Wiedenbeck et al., 1995), was used as the primary reference material. TEMORA II was also employed as a secondary reference material, which has a $^{206}Pb/^{238}U$ age of 416.78 ± 0.33 Ma (Black et al., 2004). Laser ablation was undertaken using an ASI RESOlution 193 ArF nm excimer laser system. Following evacuation of air, He carrier gas was introduced into the laser cell at a flow rate of 0.35 l/min. 0.05 l/min of N_2 gas was also introduce to the laser cell to enhance the measurement sensitivity. The gas mixture was then introduced into the plasma torch of a Thermo iCAP RQ quadruple ICP-MS with 0.85 l/min Ar nebuliser gas. No reaction gas was employed. The laser was run with a 30 µm diameter round spot at 10 Hz, with a measured instrument laser-fluence (laser pulse energy per unit area) of 2.9 J/cm^2. For each spot, 5 s of

blank was collected, followed by 25 s of ablation and 10 s of wash out. Prior to data acquisition, ICP-MS signals were optimized during tuning. Parameters particular to the analytical session include, ~400 K cps of ^{238}U counts, ~1 of $^{238}U/^{232}Th$, ~0.21 of $^{206}Pb/^{238}U$ were achieved for measuring NIST612 glass using line scans of 3 µm/s, 10 Hz, 50 µm round laser pit, and 3 J/cm^2. The following isotopes were collected using a single collector: ^{88}Sr (dwell time=0.005 s), ^{91}Zr (dwell time=0.001 s), ^{200}Hg (dwell time=0.01 s), $^{204}Pb + ^{204}Hg$ (dwell time=0.01 s), ^{206}Pb (dwell time=0.045 s), ^{207}Pb (dwell time=0.055 s), ^{208}Pb (dwell time=0.01 s), ^{232}Th (dwell time=0.01 s), ^{238}U (dwell time=0.01 s). A single cycle took ~0.155 s. Therefore, during a 25 s ablation, ~160 measurements were made on each mass. Reduction of raw data was accomplished using the program *IOLITE* (Paton et al., 2011). No common Pb correction on zircon 91500 or the unknowns was undertaken. From the session, a $^{206}Pb/^{238}U$ age of 419.0 ± 1.1 Ma, uncorrected for common Pb (95% confidence, n = 93, MSWD = 7.7) for the TEMORA II secondary reference material was obtained, which has a TIMS $^{206}Pb/^{238}U$ age of 416.78 ± 0.33 Ma determined by ID TIMS (Black et al., 2004). Calculated mean $^{206}Pb/^{238}U$ ages are presented at 95% confidence.

6.10.2 Supporting information: Results

6.10.2.1 Petrography

6.10.2.1.1 Gabbro (sample 17NI17)

The gabbro (sample 17NI17) is medium-grained and equigranular, dominated by plagioclase, clinopyroxene and kaersutitic amphibole with no observable layering or planar fabric (Figure S6.1A-F). Plagioclase grains are dusty due to alteration, with some displaying internal zonation patterns (Figure S6.1B). Primary magmatic kaersutitic amphibole commonly exhibits actinolite alteration around grain edges (Figure S6.1C-F). Opaque minerals are common throughout and occur predominantly within or along the edges of pyroxenes and amphiboles.

6.10.2.1.2 Gabbroic diorite (sample 17NI18)

The alkalic gabbroic diorite (sample 17NI18) is medium-grained and equigranular (Figure S6.2A-F). It is dominated by plagioclase, pyroxene and potassium feldspar (K-feldspar), with minor quartz. There is evidence of pockets of residual melt, where silica-saturated K-feldspar-rich melt has crystallised late and occurs as unaltered K-feldspar (microcline) and quartz. This is particularly evident in plane-polarised light (PPL; Figure S6.2B-C). Zircon occurs in the residual melt domains, where incompatible elements (i.e., zirconium) partitioned before crystallisation. There is no evidence in the $^{206}Pb/^{238}U$ age spectra to suggest bimodality, therefore the explanation of a residual melt is preferred over partial melt segregations forming in a separate event after

magmatic crystallisation. Plagioclase often exhibits perthitic growth around grain edges, with some displaying altered cores (Figure S6.2F).

6.10.2.1.3 Diorite (sample 17NI19))

The diorite (sample 17NI19) is coarse-grained and equigranular, dominated by plagioclase, quartz, pyroxene and K-feldspar (Figure S6.3A-F). Early formed plagioclase is dusty due to alteration, while later stage quartz and K-feldspar occurs as unaltered grains with sharp edges (Figure S6.3C, D). Quartz occurs as interstitial grains with no cross cutting or embayment on older plagioclase grains. Zircons are observed occurring in the residual stage along with quartz and K-feldspar.

6.10.2.1.4 Gabbroic diorite (17NI20)

The gabbroic diorite (sample 17NI20) is medium-grained and equigranular, dominated by plagioclase, pyroxene, K-feldspar with minor quartz (Figure S6.4A-F). Plagioclase (likely anorthite) are severely altered to zoisite, having been saussuritised (Figure S6.4B-F). Characteristic plagioclase multiple twinning is rarely observed. K-feldspar and quartz are typically unaltered and occur as globular clusters (Figure S6.4C, D). Original amphiboles are converted to chlorite (Figure S6.4C-F).

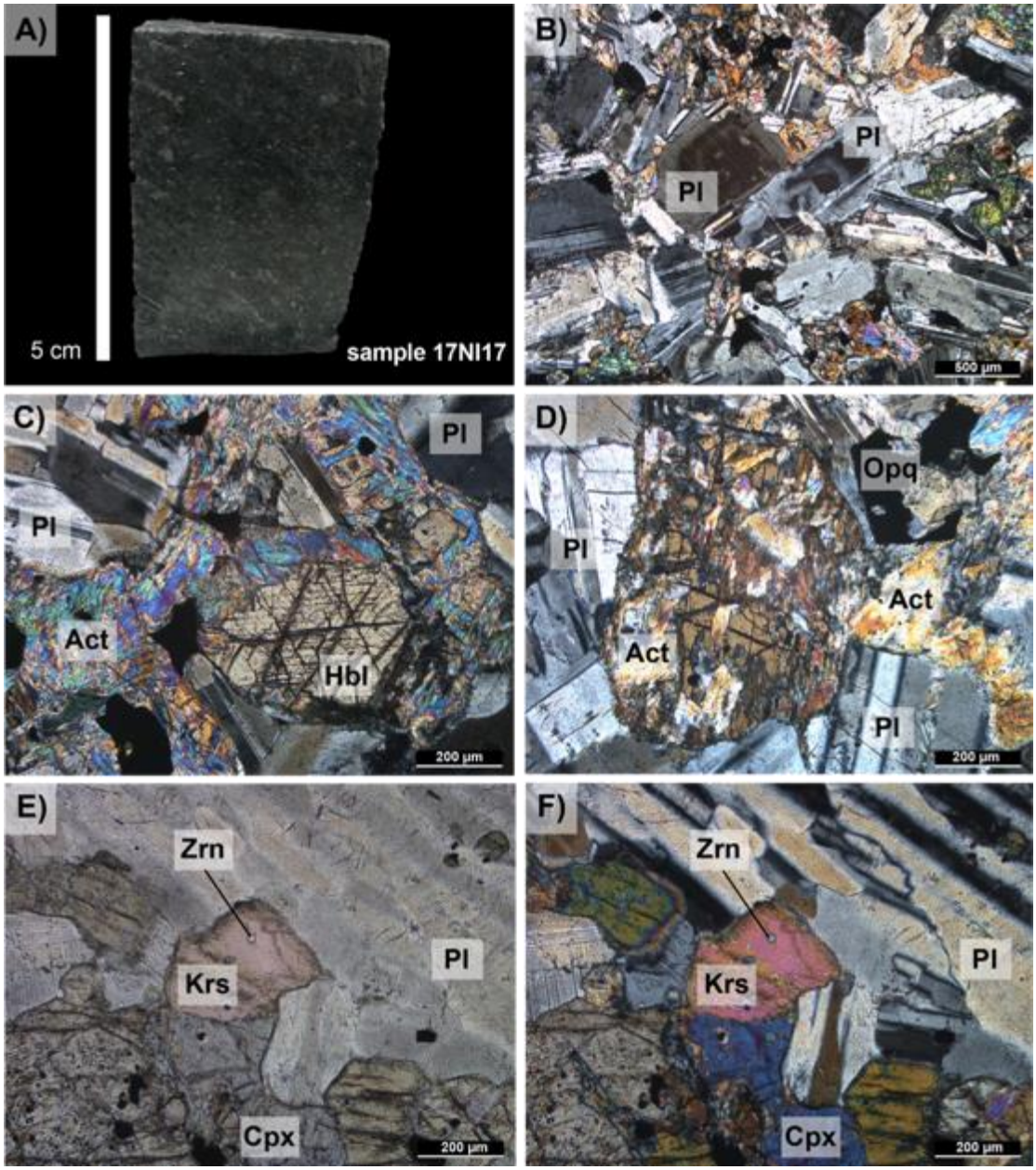

Figure S6.1: Representative hand specimen and photomicrographs of gabbro (sample 17NI17) from the Dras ophiolitic mélange (Sapi-Shergol mélange). **A)** Gabbro hand specimen (scale bar = 5 cm); **B)** Internal zonation patterns in plagioclase grains (XPL); **C) & D**) Amphibole often exhibits actinolite alteration around grain edges (XPL); **E)** Pink high Ti bearing amphibole kaersutite observed (PPL); and **F)** Kaersutite (XPL). Where, Act = actinolite; Cpx = clinopyroxene; Hbl = hornblende; Krs = kaersutite; Pl = plagioclase; Opq = opaque mineral; Zrn = zircon.

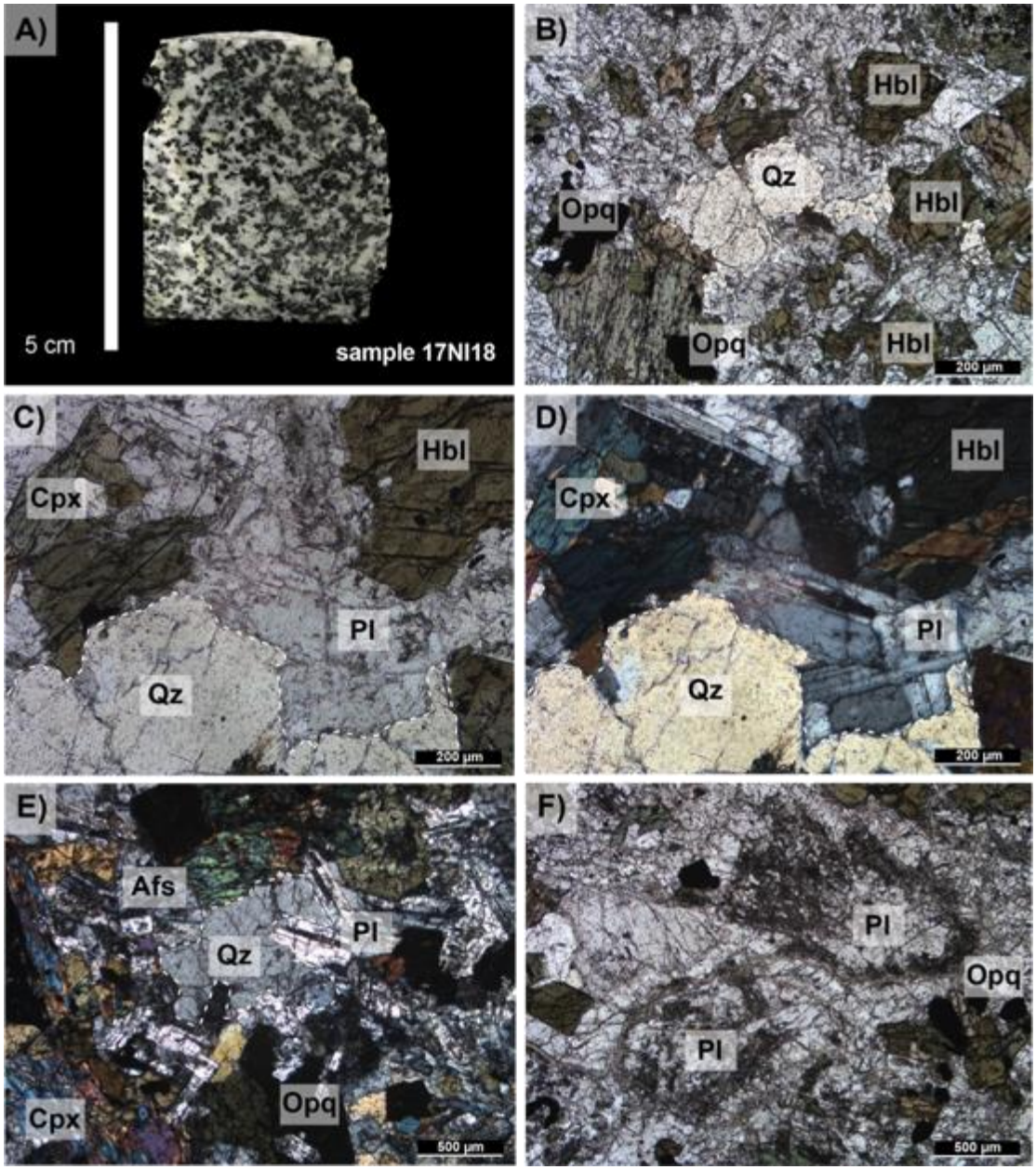

Figure S6.2: Representative hand specimen and photomicrographs of gabbroic diorite (sample 17NI18) from the Dras ophiolitic mélange (Sapi-Shergol mélange). **A)** Gabbroic diorite hand specimen (scale bar = 5 cm); **B) – E)** Pockets of residual melt, where silica-saturated K-feldspar-rich melt has crystallised late and occurs as unaltered K-feldspar (microcline) and quartz; **F)** Plagioclase exhibiting perthitic growth around grain edges and altered cores (PPL). Where, Afs = alkali feldspar; Cpx = clinopyroxene; Hbl = hornblende; Pl = plagioclase; Opq = opaque mineral; Qz = quartz.

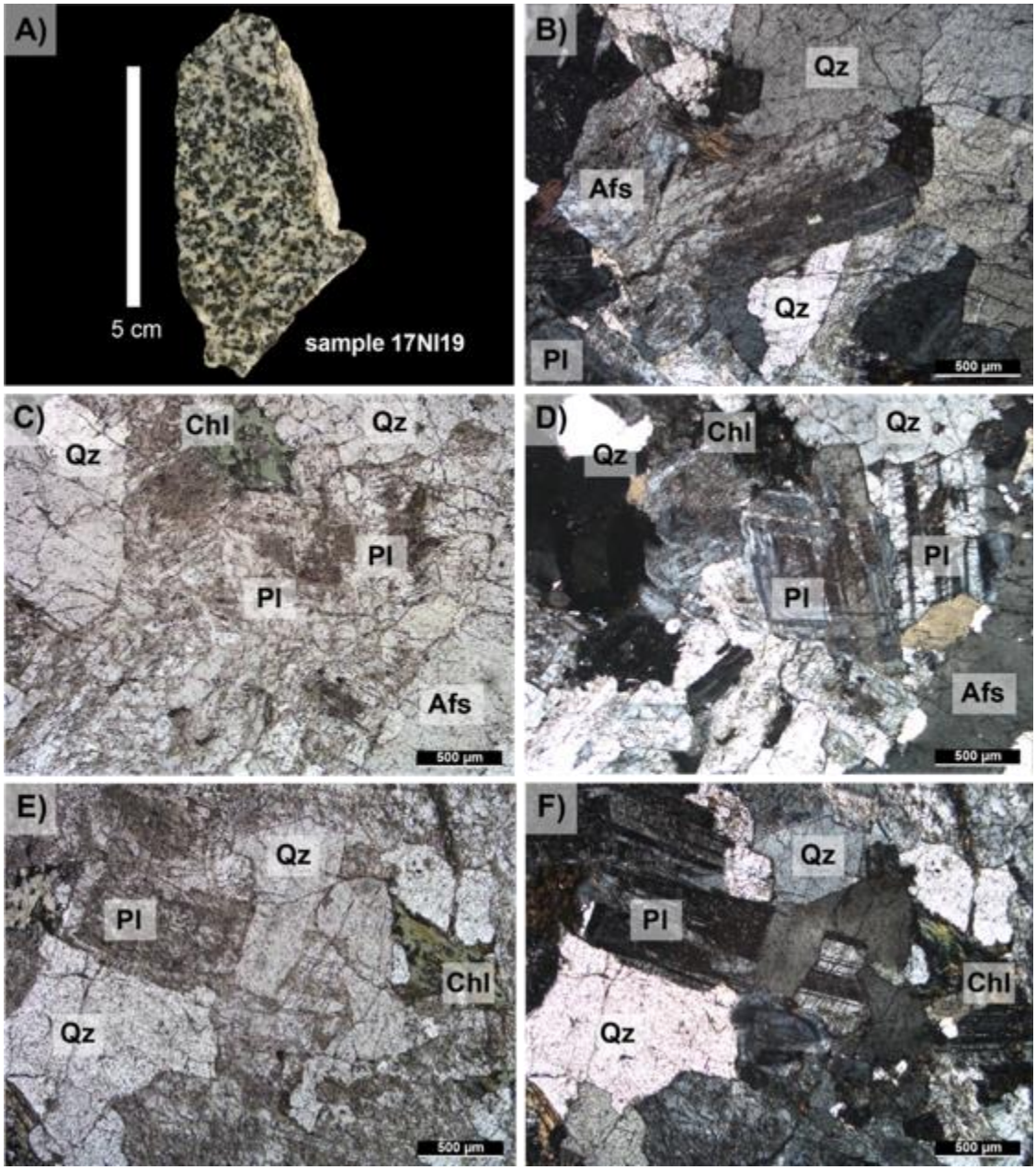

Figure S6.3: Representative hand specimen and photomicrographs of diorite (sample 17NI19) from the Dras ophiolitic mélange (Sapi-Shergol mélange). **A)** Diorite hand specimen (scale bar = 5 cm); **B) – F)** Plagioclase is dusty due to alteration, while later stage quartz and K-feldspar occurs as unaltered grains with sharp edges. Where, Chl = chlorite; Afs = alkali feldspar; Pl = plagioclase; Opq = opaque mineral; Qz = quartz.

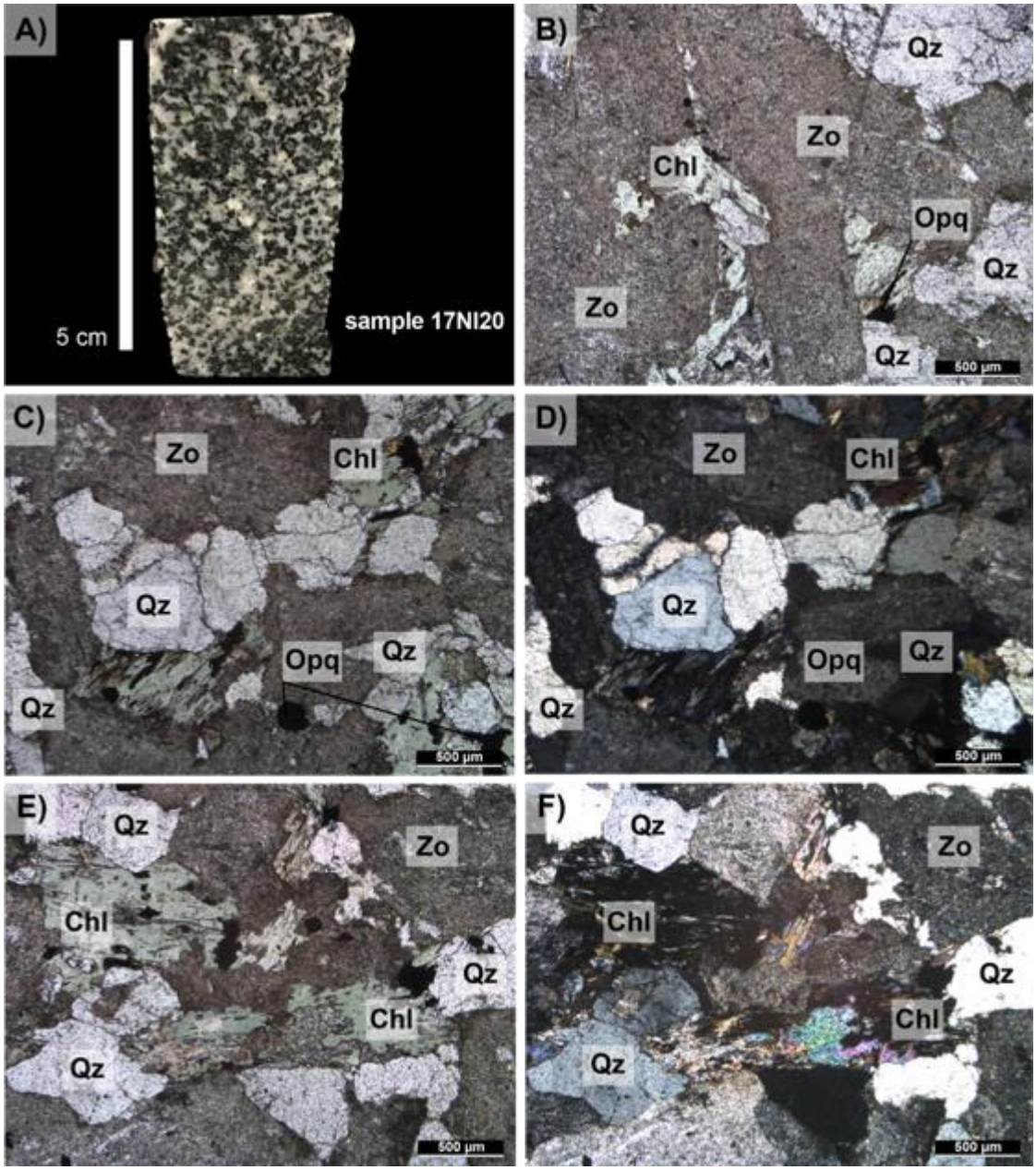

Figure S6.4: Representative hand specimen and photomicrographs of gabbroic diorite (sample 17NI20) from the Dras ophiolitic mélange (Sapi-Shergol mélange). **A)** Gabbroic diorite hand specimen (scale bar = 5 cm); **B)** Plagioclase are severely altered to zoisite, having been saussuritised (PPL); **C) & D)** K-feldspar and quartz are typically unaltered and occur as globular clusters; **E) & F)** Original amphiboles are converted to chlorite. Where, Chl = chlorite; Opq = opaque mineral; Qz = quartz; Zo = zoisite.

6.10.2.2 Whole rock geochemistry

6.10.2.2.1 Alteration

Fresh and homogenous samples were collected for geochemical analysis, whereby surficial exterior layers were removed to ensure only fresh rock was used. To account for ancient weathering, the mafic-felsic-weathering (MFW) ternary diagram (Ohta and Arai, 2007) was used to demonstrate that the samples collected were indeed unweathered. Gabbroic samples from the ophiolitic Sapi-Shergol mélange (this study: n = 4), Kargil Intrusives (Bhat et al., 2019: n = 4; Walsh et al., 2020: n = 2), Spongtang Ophiolite (Buckman et al., 2018: n = 7), Zedong terrane (Liu et al., 2020: n = 4) and Muslim Bagh Ophiolite (Kakar et al., 2014: n = 10) indicate minimal weathering, with the majority of samples falling into the field of fresh calc-alkaline/mafic igneous rocks on the MFW ternary diagram (Ohta and Arai, 2007; Figure S6.5).

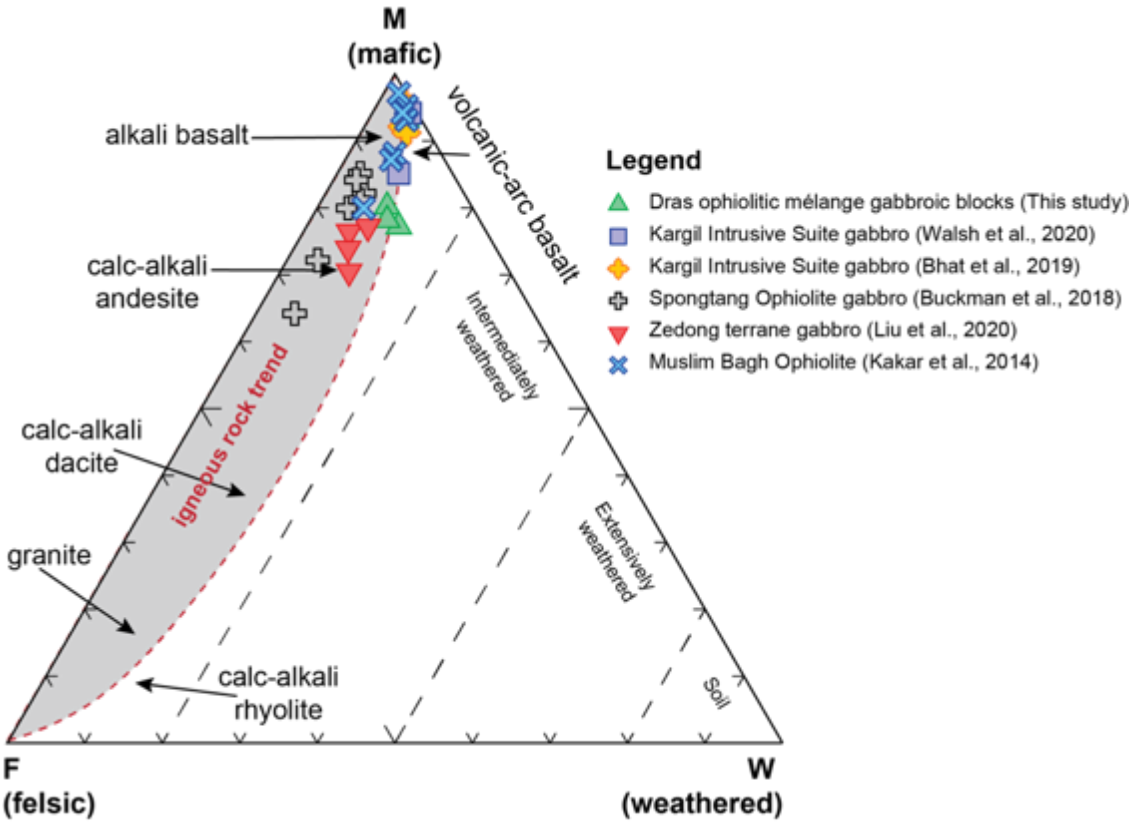

Figure S6.5: Mafic-felsic-weathering (MFW) ternary diagram of Ohta and Arai (2007). Samples from this study (Sapi-Shergol mélange gabbroic blocks) are combined with previous analyses of gabbroic samples from the Kargil Intrusives, Spongtang Ophiolite, Zedong terrane and Muslim Bagh Ophiolite (Bhat et al., 2019; Buckman et al., 2018; Kakar et al., 2014; Liu et al., 2020; Walsh et al., 2020).

6.10.2.2.2 Detailed results

Refer to Supporting Information Table S6.1 for description and locality of samples and Supporting Information Table S6.2 for whole rock major and trace element compositions of samples from the Dras ophiolitic mélange (Sapi-Shergol mélange). Samples range from gabbroic (e.g., sample 17NI17) to dioritic (e.g., sample 17NI19; Fig. DR6A). The gabbroic blocks demonstrate typical island arc and MORB-normalised patterns consistent with intraoceanic signatures (Fig. DR6B and DR6C). The samples have a SiO_2 range between 46-60%. The more mafic sample (17NI17) has relatively high amounts of MgO (6%), Mg# (34), CaO (12%), and low Cr (22 ppm) and Ni (19 ppm), reflecting the presence of normative olivine and anorthite. Whereas comparatively the other samples have relatively low amounts of MgO (4-5%), Mg# (32-36), CaO (6-9%), and relatively high Cr (40-146 ppm) and Ni (23-159 ppm). The majority of the gabbroic blocks have low K_2O (0.10-1.31%), and moderate TiO_2 (0.84-1.07%), Fe_2O_3 (8-11%), P_2O_5 (0.03-0.22), Zr (10-23 ppm), Nb (0.3-3.2 ppm) and Y (6-28 ppm). The more mafic sample (17NI17) is consistently at the lowest end of these ranges, aside from Fe_2O_3 (11%).

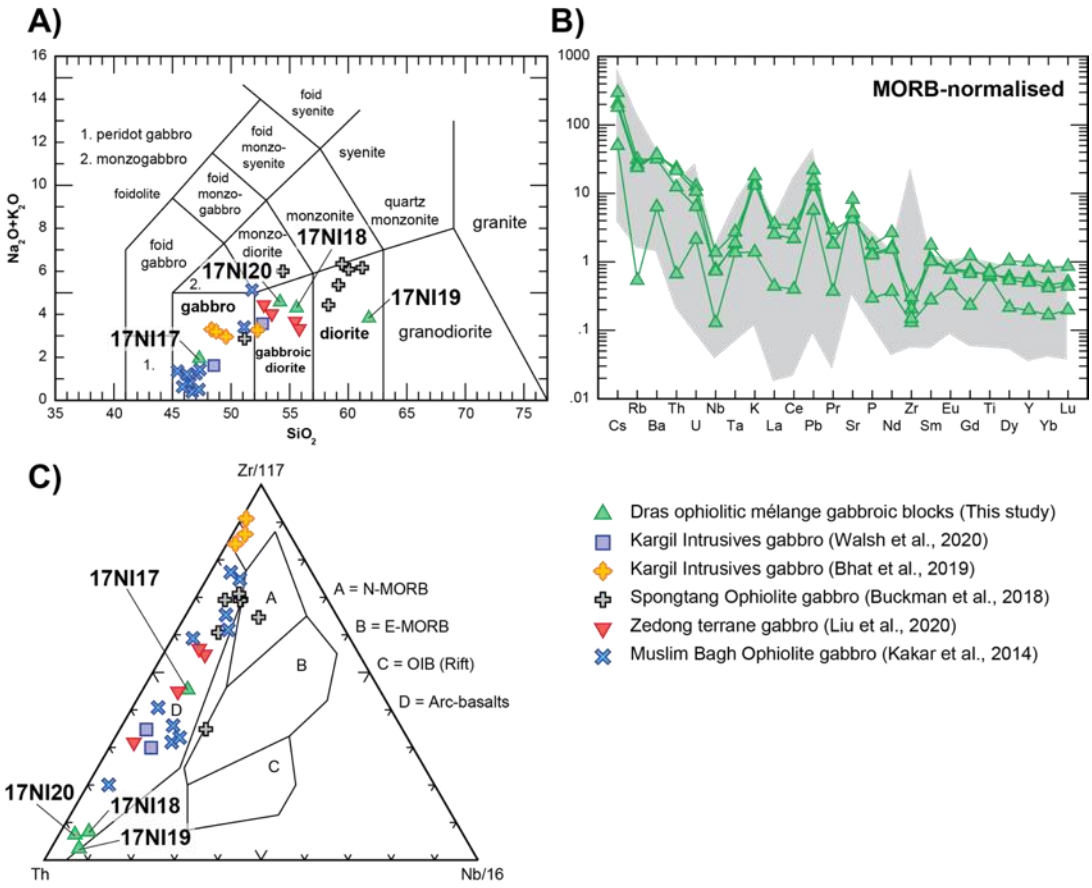

Figure S6.6: Whole rock geochemistry for the Dras ophiolitic mélange gabbroic blocks. Analyses presented here are combined with previous data (Bhat et al., 2019; Buckman et al., 2018; Kakar et al., 2014; Liu et al., 2020; Walsh et al., 2020). **A)** Total alkali vs. silica (TAS) diagram of Le Maitre et al. (1986); **B)** Extended MORB-normalised REE diagram, where data from the literature is combined in the grey field (Sun and McDonough, 1989); **C)** Volcanic rock tectonic discrimination ternary diagram of Wood (1980).

6.10.2.3 Zircon U-Pb geochronology

6.10.2.3.1 Overview

Zircon U-Pb geochronologic data using LA-ICP-MS for gabbroic blocks from the Dras ophiolitic mélange (Sapi-Shergol mélange) are presented in Table **6.1** (main manuscript; Chapter 6). All analytical errors are given a 2σ, while weighted mean averages are given at 95% confidence. See also Supporting Information Table S6.3 for zircon U-Pb geochronologic data.

Zircon grains range from prismatic to stubby to jagged anhedral, typical of those formed in pockets of residual crystallising melt (main manuscript Figure **6.2**; Supporting Information Figure S6.7-S6.10). Also, the predominance of tabular zoning is typical of zircons crystallising from a mafic to intermediate melt, rather than the fine-scale oscillatory zonation, typical of crystallisation from a granitic melt (Hoskin and Schaltegger, 2003). The samples also demonstrate high Th/U ratios ranging 0.44-1.83, average 0.83 (Supporting Information Table S6.3), typical for magmatic zircons in gabbros to diorites. The longest dimension of grains range between 50-500 μm.

One hundred and seventeen analyses of 117 zircon grains from four gabbroic samples yield $^{206}Pb/^{238}U$ ages between 71.2 ± 5.8 to 50.5 ± 2.6 Ma (Fig. DR11 and DR12). Where, sample 17NI18 yielded a weighted mean $^{206}Pb/^{238}U$ age of 53.1 ± 0.6 Ma (MSWD = 2.1, *n* = 27), sample 17NI19 yielded a weighted mean $^{206}Pb/^{238}U$ age of 52.9 ± 0.4 Ma (MSWD = 1.3, *n* = 29), sample 17NI20a yielded a weighted mean $^{206}Pb/^{238}U$ age of 53.3 ± 0.9 Ma (MSWD = 2.6, *n* = 29) and sample 17NI20b yielded a weighted mean $^{206}Pb/^{238}U$ age of 53.4 ± 0.6 Ma (MSWD = 2.3, *n* = 29). The $^{206}Pb/^{238}U$ ages (Ma) are presented without correct for common Pb. The samples (17NI18, 17NI19, 17NI20a, 17NI20b) all demonstrate very tight clustered age data (Figure S6.11 and S6.12), with very few grains (three out of 117) rejected from final age assessments on the basis of being discordant, therefore the age estimates can still be regarded as accurate.

6.10.2.3.2 Detailed results

6.10.2.3.2.1 Gabbroic diorite (sample 17NI18)

A total of 29 zircon grains from a gabbroic diorite (sample 17NI18) of the Dras ophiolitic mélange (Sapi-Shergol mélange) were dated (Figure S6.7). Two analyses (grains 1.1 and 10.1) were rejected from final age assessments on the basis of being discordant, possibly due to low U (ppm) and Th (ppm). The remaining 27 analyses yielded concordant U-Pb ages, with $^{206}Pb/^{238}U$ ages from 61.4 ± 10.2 Ma to 50.7 ± 2.6 Ma (2σ), with a weighted mean $^{206}Pb/^{238}U$ age of **53.1 ± 0.6 Ma** (MSWD = 2.1, *n* = 27, 95% confidence). This age is inferred to represent the

crystallisation age of this sample. Refer to Supporting Information Table S6.3 for reduced zircon U-Pb data. Refer to Figure S6.11 for concordia and weighted mean plots, and Figure S6.12 for histogram plots.

6.10.2.3.2.2 Diorite (sample 17NI19)

A total of 30 zircon grains from diorite (sample 17NI19) were dated (Figure S6.8). One analysis (grains 10.1) was rejected from final age assessments on the basis of being discordant, possibly due to low U (ppm) and Th (ppm). The remaining 29 analyses yielded U-Pb ages indistinguishable from concordant, with $^{206}Pb/^{238}U$ ages from 61.4 ± 8.0 Ma to 51.1 ± 3.2 Ma (2σ), with a weighted mean $^{206}Pb/^{238}U$ age of **52.9 ± 0.4 Ma** (MSWD = 1.3, *n* = 29, 95% confidence), This age is inferred to represent the crystallisation age of this sample. Refer to Supporting Information Table S6.3 for reduced zircon U-Pb data. Refer to Figure S6.11 for concordia and weighted mean plots, and Figure S6.12 for histogram plots.

6.10.2.3.2.3 Gabbroic diorite (17NI20a)

A total of 29 zircon grains from gabbroic diorite (sample 17NI20a) were dated (Figure S6.9). The analyses yielded U-Pb ages indistinguishable from concordant, with $^{206}Pb/^{238}U$ ages from 71.2 ± 5.8 Ma to 50.9 ± 3.0 Ma (2σ), with a weighted mean $^{206}Pb/^{238}U$ age of **53.3 ± 0.9 Ma** (MSWD = 2.6, *n* = 29, 95% confidence). This age is inferred to represent the crystallisation age of this sample. Refer to Supporting Information Table S6.3 for reduced zircon U-Pb data and comments on rejected grains. Refer to Figure S6.11 for concordia and weighted mean plots, and Figure S6.12 for histogram plots.

6.10.2.3.2.4 Gabbroic diorite (17NI20b)

A total of 29 zircon grains from gabbroic diorite (sample 17NI20b) were dated (Figure S6.10). The analyses yielded U-Pb ages indistinguishable from concordant, with $^{206}Pb/^{238}U$ ages from 59.7 ± 3.2 Ma to 50.5 ± 2.6 Ma (2σ), with a weighted mean $^{206}Pb/^{238}U$ age of **53.4 ± 0.6 Ma** (MSWD = 2.3, *n* = 29, 95% confidence). This age is inferred to represent the crystallisation age of this sample. Refer to Supporting Information Table S6.3 for reduced zircon U-Pb data and comments on rejected grains. Refer to Figure S6.11 for concordia and weighted mean plots, and Figure S6.12 for histogram plots.

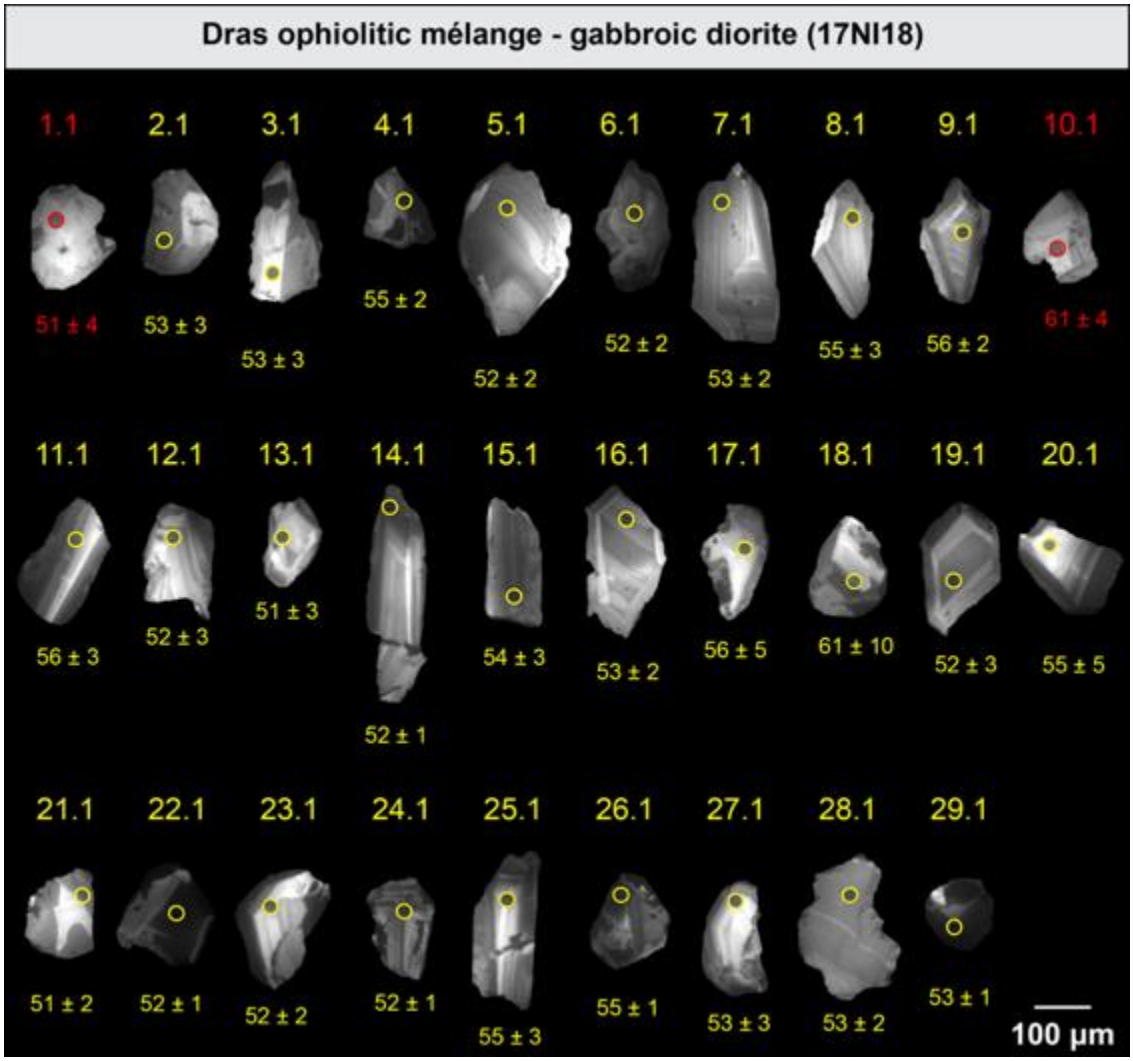

Figure S6.7: Cathodoluminescence (CL) images of representative zircon grains from gabbroic diorite (sample 17NI18) of the Dras ophiolitic mélange (Sapi-Shergol mélange). Spots represent LA-ICP-MS analytical sites with $^{206}Pb/^{238}U$ ages (Ma). All analytical errors are given at 2σ. Rejected grains (red) have been omitted from final age calculations. Refer to Supporting Information Table S6.3 for reduced data and Supporting Text for comments on rejected grains (grains 1.1 and 10.1).

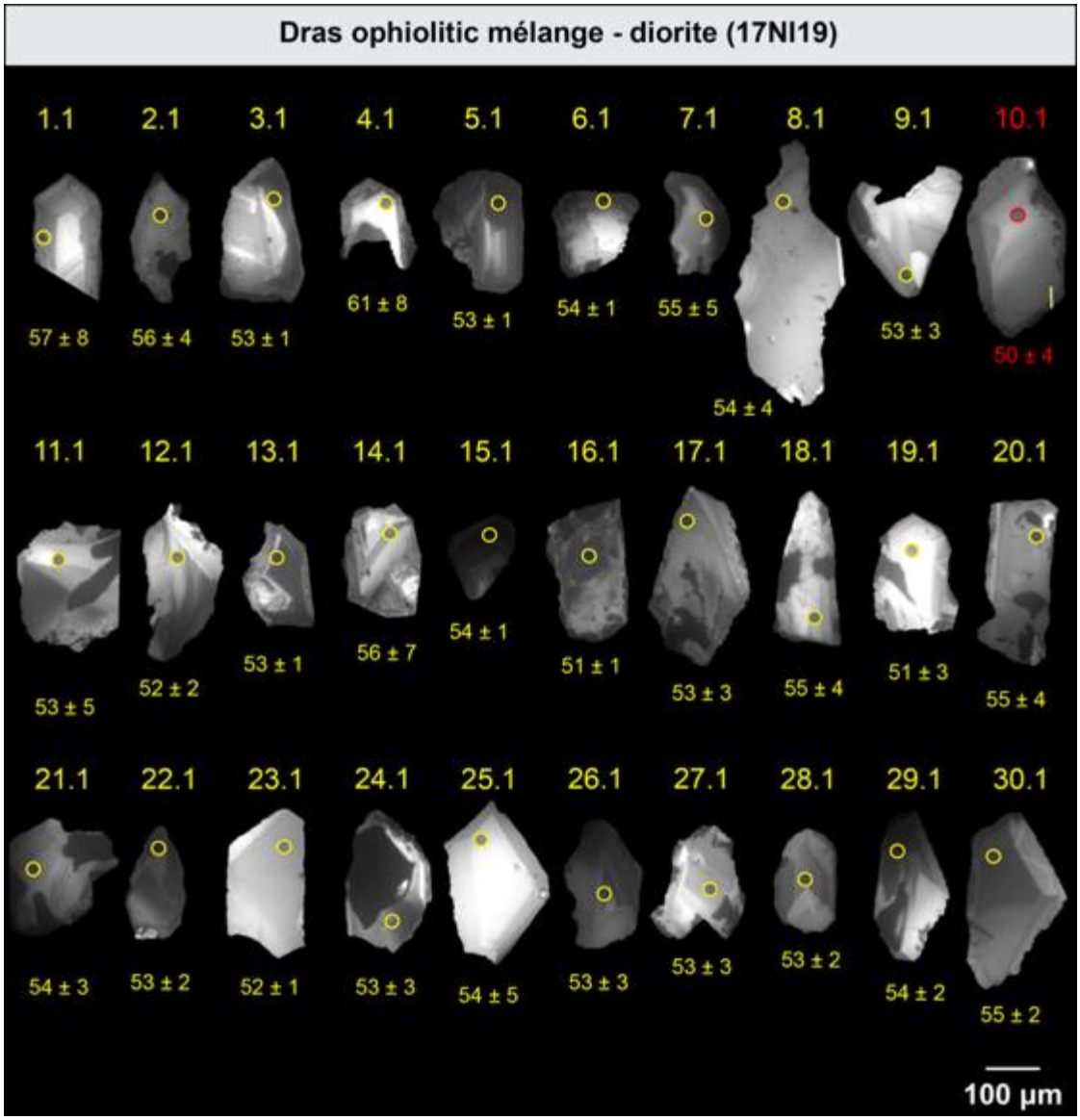

Figure S6.8: Cathodoluminescence images of representative zircon grains from diorite (sample 17NI19) of the Dras ophiolitic mélange (Sapi-Shergol mélange). Spots represent LA-ICP-MS analytical sites with $^{206}Pb/^{238}U$ ages (Ma). All analytical errors are given at 2σ. Rejected grain (red) has been omitted from final age calculations. Refer to Supporting Information Table S6.3 for reduced data and Supporting Text for comments on the rejected grain (grain 10.1).

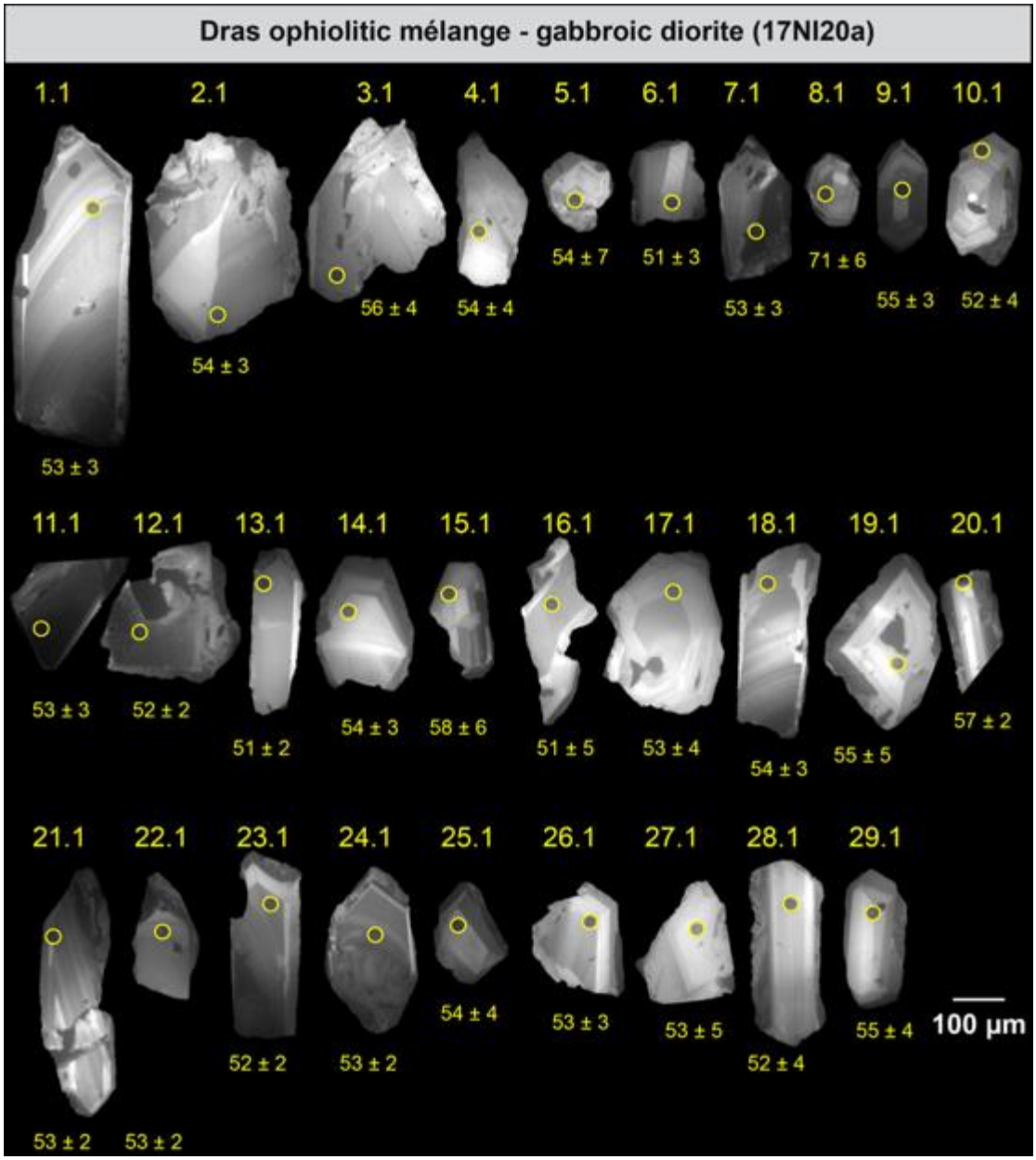

Figure S6.9: Cathodoluminescence images of representative zircon grains from gabbroic diorite (sample 17NI20a) of the Dras ophiolitic mélange (Sapi-Shergol mélange). Spots represent LA-ICP-MS analytical sites with $^{206}Pb/^{238}U$ ages (Ma). All analytical errors are given at 2σ. Refer to Supporting Information Table S6.3 for reduced data.

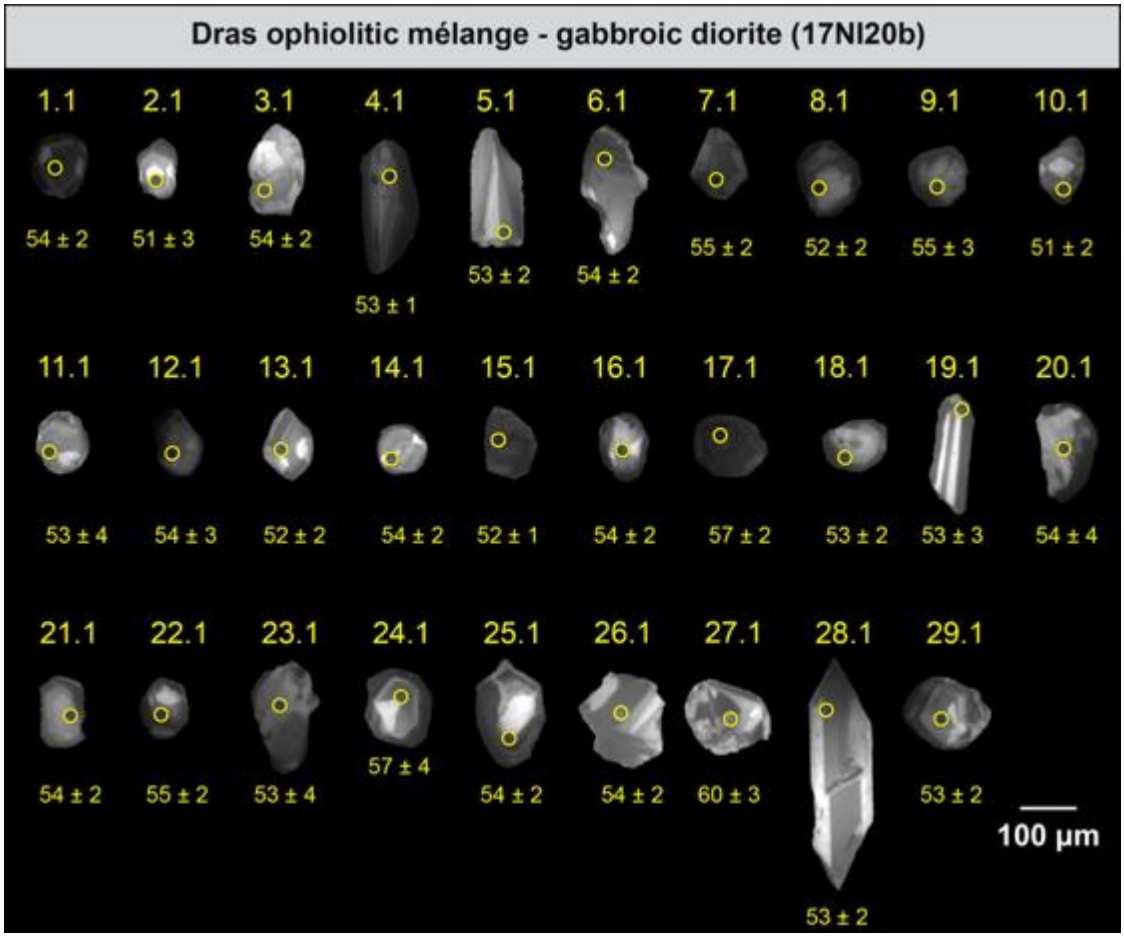

Figure S6.10: Cathodoluminescence images of representative zircon grains from gabbroic diorite (sample 17NI20b) of the Dras ophiolitic mélange (Sapi-Shergol mélange). Spots represent LA-ICP-MS analytical sites with $^{206}Pb/^{238}U$ ages (Ma). All analytical errors are given at 2σ. Refer to Supporting Information Table S6.3 for reduced data.

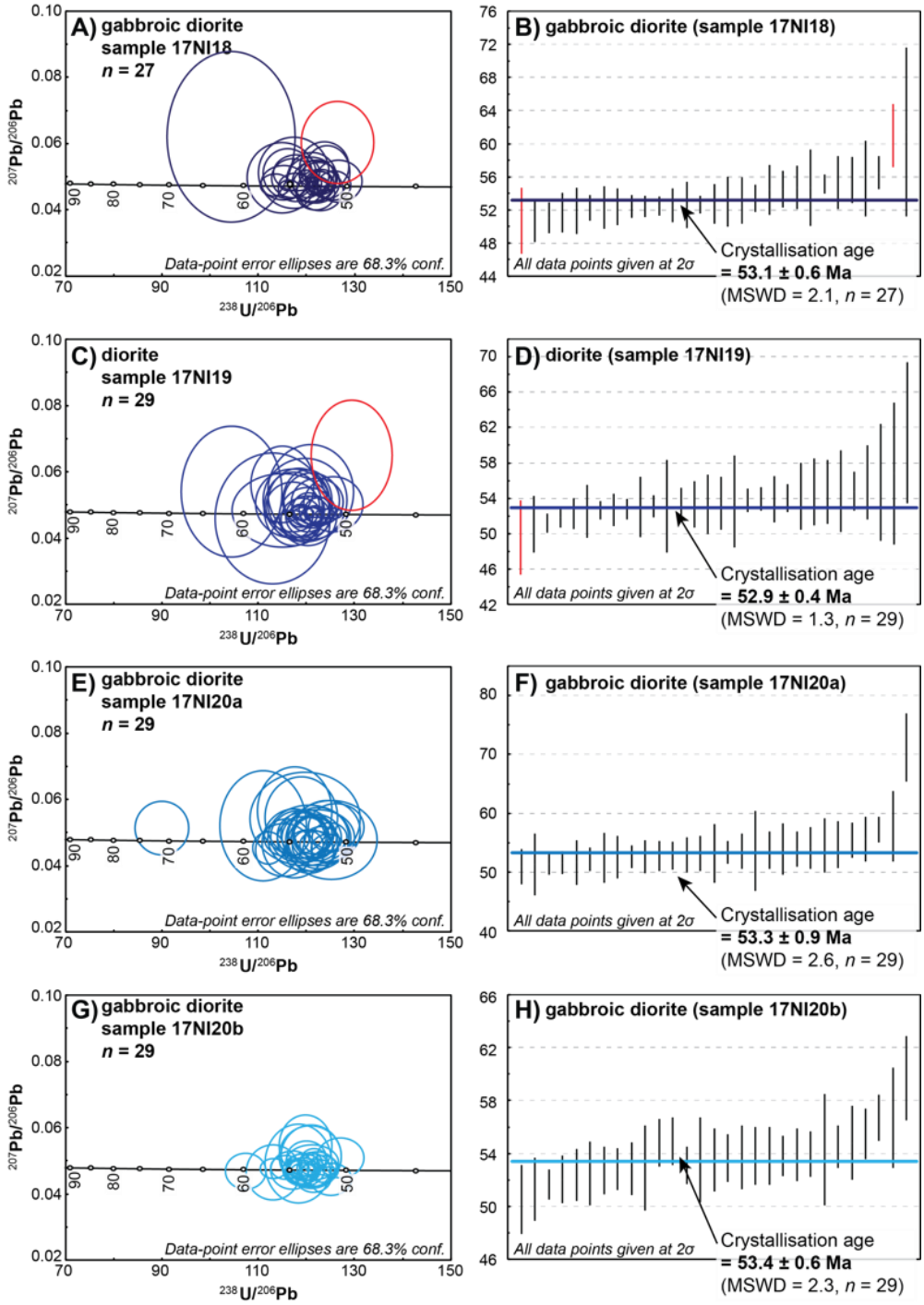

Figure S6.11: Dras ophiolitic mélange (Sapi-Shergol mélange) zircon U-Pb geochronology using LA-ICP-MS. **(A)** Gabbroic diorite (sample 17NI18) concordia plot demonstrating $^{206}Pb/^{238}U$ ages from 61.4 ± 10.2 Ma to 50.7 ± 2.6 Ma; **(B)** Gabbroic diorite (sample 17NI18) with a weighted mean $^{206}Pb/^{238}U$ age of 53.1 ± 0.6 Ma (MSWD = 2.1, *n* = 27, 95% confidence); **(C)** Diorite (sample 17NI19) concordia plot demonstrating $^{206}Pb/^{238}U$ ages from 61.4 ± 8.0 Ma to 51.1 ± 3.2 Ma; **(D)** Diorite (sample 17NI19) with a weighted mean $^{206}Pb/^{238}U$ age of 52.9 ± 0.4 Ma (MSWD = 1.3, *n* = 29, 95% confidence); **E)** Gabbroic diorite (sample 17NI20a) concordia plot demonstrating $^{206}Pb/^{238}U$ ages from 71.2 ± 5.8 Ma to 50.9 ± 3.0 Ma; **(F)** Gabbroic diorite (sample 17NI20a) with a weighted mean $^{206}Pb/^{238}U$ age of 53.3 ± 0.9 Ma (MSWD = 2.6, *n* = 29, 95% confidence); **(G)** Gabbroic diorite (sample 17NI20b) concordia plot demonstrating $^{206}Pb/^{238}U$ ages from 59.7 ± 3.2 Ma to 50.5 ± 2.6 Ma; and **(H)** Gabbroic diorite (sample 17NI20b) with a weighted mean $^{206}Pb/^{238}U$ age of 53.4 ± 0.6 Ma (MSWD = 2.3, *n* = 29, 95% confidence). Those analyses in red have been rejected and not used for final age calculations. Refer to Supporting Information Table S6.3 for reduced data.

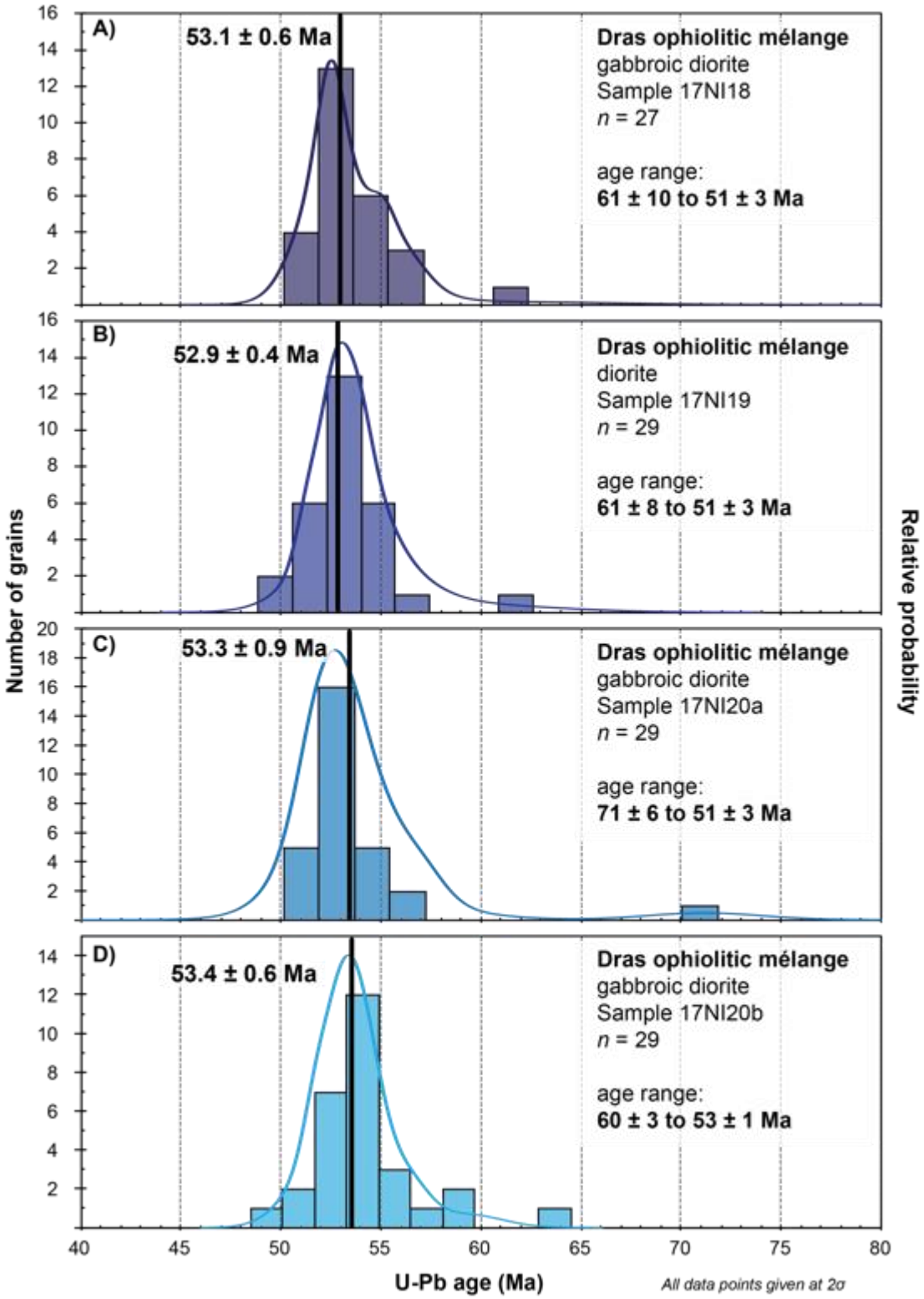

Figure S6.12: Probability density plots for the Dras ophiolitic mélange (Sapi-Shergol mélange) using LA-ICP-MS. **(A)** Gabbroic diorite (sample 17NI18) with $^{206}Pb/^{238}U$ ages from 61.4 ± 10.2 Ma to 50.7 ± 2.6 Ma (2σ); **(B)** Diorite (sample 17NI19) with $^{206}Pb/^{238}U$ ages from 61.4 ± 8.0 Ma to 51.1 ± 3.2 Ma (2σ); **(C)** Gabbroic diorite (sample 17NI20a) with $^{206}Pb/^{238}U$ ages from 71.2 ± 5.8 Ma to 50.9 ± 3.0 Ma (2σ); and **(D)** Gabbroic diorite (sample 17NI20b) with $^{206}Pb/^{238}U$ ages from 59.7 ± 3.2 Ma to 50.5 ± 2.6 Ma (2σ). Refer to Supporting Information Table S6.3 for reduced data.

Table S6.1: Sample localities and descriptions (Chapter 6)

Sample	Lithology	Latitude (°N)	Longitude (°E)	Methods			
				Petrography	Whole rock geochemistry	LA-ICP-MS	Mineral separation location
Ophiolitic Sapi-Shergol mélange							
17NI17	gabbro	34.40266	76.29816	✓	✓	[*]N.D.	[†]China
17NI18	gabbroic diorite	34.40264	76.29819	✓	✓	✓	China
17NI19	diorite	34.40259	76.29822	✓	✓	✓	China
17NI20a	gabbroic diorite	34.40256	76.29830	✓	✓	✓	[§]Australia
17NI20b	gabbroic diorite	34.40256	76.29830	N.D.	N.D.	✓	China

Notes:

Fieldwork was undertaken during May-June 2017 in the Ladakh region, Jammu and Kashmir, NW India.

[*]N.D. = not determined.

[†]China = Institute of Hebei Regional Geology Survey, China.

[§]Australia = Australian National University (ANU).

Table S6.2: Whole rock geochemistry (Chapter 6)

Sample	17NI17	17NI18	17NI19	17NI20
Affinity	Dras Ophiolitic mélange	Dras Ophiolitic mélange	Dras Ophiolitic mélange	Dras Ophiolitic mélange
Rock type	Gabbro	Gabbroic diorite	Diorite	Gabbroic diorite
Latitude (N°)	34.40266	34.40266	34.40266	34.40266
Longitude (E°)	76.29816	76.29816	76.29816	76.29816
Majors (*wt.%)				
SiO_2	46.38	53.99	59.97	52.79
TiO_2	0.84	0.96	1.07	1.02
Al_2O_3	21.52	17.03	14.23	17.50
Fe_2O_3	10.62	8.36	8.56	8.60
MnO	0.14	0.13	0.12	0.14
MgO	5.55	4.72	4.01	4.94
CaO	12.15	8.42	6.07	8.71
Na_2O	1.81	3.14	2.76	3.14
K_2O	0.10	1.03	0.95	1.31
SO_3	0.06	0.01	0.00	0.12
P_2O_5	0.03	0.17	0.22	0.15
LOI	0.60	1.87	1.88	1.38
Total (wt.%)	**100**	**100**	**100**	**100**
MFW indices (Ohata & Arai, 2007)				
M	93	80	77	78
F	2	11	11	12
W	5	9	12	10
Total (%)	**100**	**100**	**100**	**100**
Trace elements (†ppm)				
Ag	0.05	0.08	0.07	0.15
Al	92400	82200	68300	80400
As	1.2	3.8	2.4	2.9
Ba	40	200	230	230
Be	0.17	0.58	0.64	0.54
Bi	0.01	0.04	0.02	0.04
Ca	79800	53500	42900	57200
Cd	0.07	0.06	0.03	0.07
Ce	2.98	16.3	25.9	16.4
Co	45.0	37.5	34.5	36.8
Cr	22	146	40	62
Cs	0.35	2.07	1.44	1.26
Cu	102.5	90.3	23.6	241.0
Fe	67500	55600	58100	56600

Ga	22.50	19.00	18.75	19.85
Ge	0.13	0.13	0.17	0.15
Hf	0.4	1.0	0.7	1.2
In	0.040	0.055	0.056	0.071
K	600	7600	6700	9600
La	1.1	6.3	8.9	6.3
Li	7.2	14.3	17.6	11.5
Mg	72000	143000	176000	115000
Mn	1010	948	946	1050
Mo	0.05	0.11	0.16	0.41
Na	14300	22800	21300	22700
Nb	0.3	1.8	3.2	1.7
Ni	19.2	159.0	23.4	53.4
P	150	680	900	640
Pb	1.7	6.6	3.8	4.7
Rb	0.3	17.5	14.7	13.3
Re	0.002	0.002	0.002	0.002
S	200	100	100	400
Sb	3.10	1.01	6.48	0.92
Sc	24.8	21.7	24.8	24.5
Se	1	1	1	1
Sn	0.4	1.0	1.4	1.3
Sr	736	449	380	477
Ta	0.18	0.24	0.36	0.25
Te	0.05	0.05	0.05	0.05
Th	0.08	1.48	2.79	2.57
Ti	4590	4870	5610	5300
Tl	0.02	0.11	0.09	0.07
U	0.1	0.3	0.6	0.5
V	335	192	200	227
W	94.1	79.8	109.5	75.2
Y	5.5	15.8	27.8	14.1
Zn	81	93	90	87
Zr	9.6	15.1	11.0	22.6
Dy	0.98	2.74	4.72	2.43
Er	0.60	1.58	2.71	1.40
Eu	0.46	0.81	0.81	0.79
Gd	0.85	2.72	4.47	2.49
Ho	0.19	0.53	0.93	0.48
Lu	0.09	0.23	0.39	0.20
Nd	2.7	11.8	19.4	11.1
Pr	0.49	2.44	3.86	2.39
Sm	0.73	2.85	4.60	2.67

Tb	0.16	0.47	0.79	0.43
Tm	0.08	0.22	0.38	0.19
Yb	0.51	1.41	2.50	1.27
Calculated values				
Mg#	34	36	32	36
ΣREE (La-Lu)	62.1	218.2	345.3	206.3
ΣLREE (La-Eu)	33.2	136.8	206.1	133.4
ΣHREE (Gd-Lu)	28.9	81.5	139.2	72.9
LREE/HREE	1.1	1.7	1.5	1.8
$(La/Yb)_N$	1.5	3.2	2.6	3.6
$(La/Lu)_N$	1.3	2.9	2.4	3.4
$(Gd/Yb)_N$	1.4	1.6	1.5	1.6
δEu^*	1.8	0.9	0.5	0.9

Notes:

Major element analysis was conducted at the University of Wollongong (UOW). Additional trace and rare-earth element (REE) analyses were undertaken at Australian Laboratory Services (ALS) Minerals Division, Brisbane, Australia using the geochemical procedure code: ME-MS81.

*wt.% = weight percent.

† ppm = parts per million.

The above listed geochemical data has been combined in text (including figures) with other data available in the below listed literature. This data is compiled online and is available through the relevant paper corresponding to this chapter. It is also available from the original papers; these are as follows:

- Bhat, I. M., Ahmad, T., & Rao, D. S. (2019). The tectonic evolution of the Dras arc complex along the Indus Suture Zone, western Himalaya: Implications for the Neo-Tethys Ocean geodynamics. *Journal of Geodynamics*, 124, 52-66.
- Buckman, S., Aitchison, J. C., Nutman, A. P., Bennett, V. C., Saktura, W. M., Walsh, J. M., Kachovich, S., & Hidaka, H. (2018). The Spongtang Massif in Ladakh, NW Himalaya: an Early Cretaceous record of spontaneous, intraoceanic subduction initiation in the Neotethys. *Gondwana Research*, 63, 226-249.
- Kakar, M. I., Collins, A. S., Mahmood, K., Foden, J. D., & Khan, M. (2012). U-Pb zircon crystallization age of the Muslim Bagh ophiolite: Enigmatic remains of an extensive pre-Himalayan arc. *Geology*, *40*(12), 1099-1102.
- Liu, W., Zhong, Y., Sun, Z., Yakymchuk, C., Gu, M., Tang, G., & Xia, B. (2020). The Late Jurassic Zedong ophiolite: A remnant of subduction initiation within the Yarlung Zangbo Suture Zone (southern Tibet) and its tectonic implications. *Gondwana Research*, 78, 172-188.
- Walsh, J. M., Buckman, S., Nutman, A. P., & Zhou, R. (2020). The significance of Upper Jurassic felsic volcanic rocks within the incipient, intraoceanic Dras Arc, Ladakh, NW Himalaya. *Gondwana Research*.

Table S6.3: Zircon U-Pb results using LA-ICP-MS (Chapter 6)

Sample ID	Analysis ID	U (ppm)	Th (ppm)	Th/U	$^{238}U/^{206}Pb$	$^{207}Pb/^{206}Pb$	age $^{206}Pb/^{238}U$	Sr (cps)	Rejected
17NI18 (W101) - gabbroic block									
1.1	m, fr, hl	36.3	20.5	0.5634	126.5823 ± 4.9672	0.0591 ± 0.0080	50.7 ± 2.0	219	Yes
2.1	m, f, sec	84.9	86.2	1.0153	121.9512 ± 3.2719	0.0484 ± 0.0042	52.6 ± 1.4	260	
3.1	m, fr, sec	58.8	36.3	0.6168	121.2121 ± 3.3792	0.0496 ± 0.0050	53.0 ± 1.5	323	
4.1	e, fr, sec	207.0	134.0	0.6473	117.7856 ± 2.3585	0.0468 ± 0.0028	54.5 ± 1.1	410	
5.1	m, fr, osc	301.0	268.0	0.8904	122.8501 ± 1.8111	0.0480 ± 0.0023	52.2 ± 0.8	590	
6.1	m, fr, sec	151.1	73.6	0.4871	122.5490 ± 2.5531	0.0498 ± 0.0030	52.4 ± 1.1	520	
7.1	m, fr, osc	522.0	484.0	0.9272	122.1001 ± 2.3854	0.0508 ± 0.0027	52.6 ± 1.0	770	
8.1	m, fr, osc	91.4	50.1	0.5481	117.2333 ± 2.8862	0.0496 ± 0.0039	54.7 ± 1.3	336	
9.1	m, fr, osc	234.0	126.0	0.5385	113.6364 ± 2.0661	0.0475 ± 0.0022	56.5 ± 1.0	480	
10.1	e, fr, osc	50.8	24.0	0.4724	105.2632 ± 3.2133	0.1220 ± 0.0120	61.0 ± 1.9	297	Yes
11.1	m, p, osc	132.0	69.0	0.5227	115.3403 ± 3.0598	0.0482 ± 0.0034	55.6 ± 1.4	210	
12.1	m, fr, osc	179.0	114.9	0.6419	122.8501 ± 3.1694	0.0460 ± 0.0041	52.3 ± 1.3	500	
13.1	e, fr, sec	91.2	77.2	0.8465	126.5823 ± 3.2046	0.0487 ± 0.0042	50.7 ± 1.3	220	
14.1	e, p, osc	892.0	693.0	0.7769	122.3840 ± 1.3929	0.0471 ± 0.0013	52.5 ± 0.6	810	
15.1	m, fr, osc	107.0	96.4	0.9009	117.9245 ± 3.1984	0.0512 ± 0.0036	54.4 ± 1.5	226	
16.1	m, o, osc	213.0	271.0	1.2723	120.1923 ± 1.8780	0.0478 ± 0.0027	53.4 ± 0.8	480	
17.1	m, fr, sec	27.5	17.9	0.6509	114.9425 ± 4.7562	0.0497 ± 0.0070	55.8 ± 2.3	173	
18.1	m, fr, sec	17.0	7.6	0.4478	104.3841 ± 8.7168	0.0620 ± 0.0170	61.4 ± 5.1	0	
19.1	m, p, osc	69.4	66.1	0.9524	123.7624 ± 3.3698	0.0531 ± 0.0049	51.9 ± 1.4	420	
20.1	m, fr, osc	34.3	16.5	0.4810	117.3709 ± 4.8216	0.0512 ± 0.0071	54.7 ± 2.3	218	
21.1	e, fr, sec	171.5	130.3	0.7598	125.7862 ± 2.2151	0.0473 ± 0.0029	51.1 ± 0.9	295	
22.1	m, fr, sec	504.0	762.0	1.5119	122.4890 ± 1.6504	0.0488 ± 0.0019	52.4 ± 0.7	610	
23.1	m, fr, osc	55.8	33.7	0.6047	124.2236 ± 3.0863	0.0514 ± 0.0053	51.7 ± 1.2	138	
24.1	m, fr, osc	479.0	442.0	0.9228	122.4590 ± 1.4996	0.0472 ± 0.0018	52.4 ± 0.7	530	
25.1	m, p, osc	104.3	76.0	0.7287	116.1440 ± 3.3724	0.0509 ± 0.0050	55.3 ± 1.6	230	
26.1	e, fr, sec	1610.0	2450.0	1.5217	116.4280 ± 1.2200	0.0474 ± 0.0011	55.1 ± 0.6	980	
27.1	e, fr, osc	144.5	66.0	0.4564	120.9190 ± 3.3629	0.0492 ± 0.0044	53.1 ± 1.4	410	
29.1	m, fr, osc	100.7	117.5	1.1668	121.8027 ± 2.6705	0.0449 ± 0.0033	52.7 ± 1.2	298	
30.1	m, fr, sec	1179.0	949.0	0.8049	121.9661 ± 1.2644	0.0460 ± 0.0011	52.6 ± 0.6	1010	

Sample ID	Analysis ID	U (ppm)	Th (ppm)	Th/U	$^{238}U/^{206}Pb$	$^{207}Pb/^{206}Pb$	age $^{206}Pb/^{238}U$	Sr (cps)	Rejected
17NI19 (W101) - gabbroic block									
1.1	e, p, osc	22.0	10.2	0.464	112.9944 ± 7.9160	0.0460 ± 0.0130	56.8 ± 4.0	210	
2.1	m, fr, hl	37.2	18.1	0.487	115.0748 ± 4.3699	0.0563 ± 0.0076	55.8 ± 2.1	227	
3.1	m, fr, osc	466.0	453.0	0.972	120.9482 ± 1.4190	0.0467 ± 0.0017	53.1 ± 0.6	610	
4.1	e, fr, sec	28.9	21.3	0.737	104.4932 ± 6.8789	0.0540 ± 0.0130	61.4 ± 4.0	360	
5.1	m, fr, osc	872.0	1057.0	1.212	121.9512 ± 1.2046	0.0480 ± 0.0012	52.7 ± 0.5	620	
6.1	e, fr, osc	730.0	868.0	1.189	119.1043 ± 1.5604	0.0476 ± 0.0014	53.9 ± 0.7	660	
7.1	m, fr, sec	37.7	23.2	0.615	117.2333 ± 5.0851	0.0504 ± 0.0069	54.8 ± 2.3	113	
8.1	e, fr, hh	38.8	31.3	0.807	118.4834 ± 4.2115	0.0507 ± 0.0068	54.2 ± 1.9	208	
9.1	e, fr, sec	75.4	69.9	0.927	120.3369 ± 3.0410	0.0465 ± 0.0041	53.3 ± 1.3	333	
10.1	m, p, sec	33.7	18.7	0.554	129.3661 ± 5.5227	0.0650 ± 0.0110	49.6 ± 2.1	198	Yes
11.1	m, fr, sec	20.6	11.1	0.537	120.9190 ± 5.8486	0.0539 ± 0.0094	53.1 ± 2.6	244	
12.1	m, fr, osc	283.0	190.0	0.671	122.8501 ± 2.1129	0.0484 ± 0.0026	52.3 ± 0.9	296	
13.1	m, fr, sec	926.0	1444.0	1.559	121.6693 ± 1.3619	0.0471 ± 0.0015	52.8 ± 0.6	830	
14.1	m, fr, osc	61.5	34.9	0.567	115.0748 ± 6.8859	0.0483 ± 0.0073	55.8 ± 3.3	340	
15.1	m, fr, osc	727.0	950.0	1.307	119.4030 ± 1.4257	0.0474 ± 0.0012	53.8 ± 0.7	520	
16.1	m, p, sec	1476.0	2705.0	1.833	125.3761 ± 1.3361	0.0475 ± 0.0011	51.2 ± 0.5	660	
17.1	e, fr, sec	101.2	85.9	0.849	121.0654 ± 3.8108	0.0514 ± 0.0055	53.0 ± 1.7	210	
18.1	m, fe, sec	40.5	19.7	0.486	117.3709 ± 3.9950	0.0489 ± 0.0073	54.7 ± 1.9	245	
19.1	m, p, sec	54.9	41.1	0.749	125.6281 ± 4.1034	0.0503 ± 0.0055	51.1 ± 1.6	277	
20.1	e, p, sec	54.3	38.4	0.707	117.2333 ± 3.7108	0.0494 ± 0.0049	54.7 ± 1.8	231	
21.1	m, fr, osc	78.4	38.5	0.491	119.0476 ± 2.8345	0.0458 ± 0.0042	53.9 ± 1.3	182	
22.1	e, fr, sec	156.1	137.1	0.878	120.4819 ± 2.1774	0.0486 ± 0.0034	53.3 ± 1.0	165	
23.1	m, p, hh	1438.0	1951.0	1.357	123.9004 ± 1.3202	0.0474 ± 0.0010	51.8 ± 0.6	1000	
24.1	m, fr, sec	55.3	40.6	0.734	120.3369 ± 3.9099	0.0466 ± 0.0058	53.3 ± 1.7	242	
25.1	m, p, hh	52.0	26.8	0.516	119.7605 ± 5.7370	0.0515 ± 0.0083	53.6 ± 2.6	220	
26.1	m, fr, osc	73.1	43.1	0.590	122.2494 ± 3.5868	0.0509 ± 0.0047	52.5 ± 1.5	208	
27.1	m, fr, sec	51.3	46.0	0.897	120.1923 ± 3.3226	0.0513 ± 0.0062	53.4 ± 1.5	290	
28.1	m, p, osc	183.1	132.1	0.721	121.8027 ± 2.2254	0.0484 ± 0.0029	52.7 ± 0.9	277	
29.1	m, fr, sec	409.0	496.0	1.213	118.9061 ± 1.6966	0.0468 ± 0.0023	54.0 ± 0.8	980	
30.1	m, p, sec	239.0	243.0	1.017	117.2333 ± 2.4739	0.0442 ± 0.0028	54.8 ± 1.1	405	

Sample ID	Analysis ID	U (ppm)	Th (ppm)	Th/U	$^{238}U/^{206}Pb$	$^{207}Pb/^{206}Pb$	age $^{206}Pb/^{238}U$	Sr (cps)	Rejected
17NI20a (W101) - gabbroic block									
1.1	m, p, osc	128.3	118.1	0.920	121.8027 ± 2.9672	0.0487 ± 0.0040	52.7 ± 1.3	310	
2.1	m, fr, sec	58.8	57.6	0.980	120.0480 ± 3.4588	0.0496 ± 0.0049	53.5 ± 1.5	248	
3.1	m, fr, sec	45.2	31.4	0.695	115.3403 ± 3.8580	0.0448 ± 0.0052	55.6 ± 1.9	296	
4.1	m, fr, sec	29.1	16.9	0.581	119.0476 ± 4.9603	0.0546 ± 0.0081	53.9 ± 2.2	219	
5.1	m, fr, osc	36.1	19.7	0.547	119.7605 ± 7.6016	0.0542 ± 0.0093	53.6 ± 3.4	270	
6.1	m, fr, sec	83.2	63.2	0.760	126.2626 ± 3.8261	0.0516 ± 0.0047	50.9 ± 1.5	265	
7.1	m, p, sec	65.3	54.8	0.839	120.6273 ± 3.3467	0.0443 ± 0.0044	53.2 ± 1.5	282	
8.1	m, p, osc	72.0	31.8	0.442	90.0090 ± 3.6457	0.0514 ± 0.0053	71.2 ± 2.9	277	
9.1	m, p, osc	126.0	103.0	0.817	115.8749 ± 3.0882	0.0485 ± 0.0037	55.4 ± 1.5	420	
10.1	e, p, osc	121.8	106.6	0.875	122.5490 ± 4.9560	0.0485 ± 0.0056	52.4 ± 2.1	540	
11.1	e, fr, sec	54.2	35.7	0.659	121.3592 ± 3.3875	0.0467 ± 0.0054	52.9 ± 1.5	238	
12.1	m, fr, sec	194.0	172.8	0.891	123.1527 ± 2.4267	0.0476 ± 0.0028	52.2 ± 1.0	250	
13.1	e, p, hl	165.8	162.1	0.978	124.8439 ± 2.3379	0.0487 ± 0.0029	51.4 ± 0.9	390	
14.1	m, p, osc	50.2	29.5	0.587	119.4743 ± 3.5685	0.0479 ± 0.0046	53.7 ± 1.6	258	
15.1	e, fr, sec	80.7	75.5	0.936	110.9878 ± 5.9128	0.0520 ± 0.0110	57.8 ± 3.0	620	
16.1	m, fr, sec	40.1	40.6	1.011	125.1564 ± 6.2657	0.0478 ± 0.0079	51.3 ± 2.6	310	
17.1	m, p, sosc	46.1	25.0	0.542	122.3990 ± 4.1948	0.0483 ± 0.0061	52.5 ± 1.8	244	
18.1	m, fr, osc	75.1	78.8	1.049	119.0476 ± 3.4014	0.0491 ± 0.0045	53.9 ± 1.5	236	
19.1	m, p, osc	20.1	11.4	0.565	117.6471 ± 5.1211	0.0566 ± 0.0088	54.5 ± 2.3	0	
20.1	e, p, osc	142.0	127.0	0.894	112.1076 ± 2.1366	0.0454 ± 0.0032	57.2 ± 1.1	303	
21.1	e, p, osc	101.3	105.5	1.041	121.5067 ± 2.8051	0.0495 ± 0.0040	52.8 ± 1.2	540	
22.1	m, p, osc	152.0	87.2	0.574	120.3369 ± 2.1721	0.0460 ± 0.0031	53.4 ± 1.0	530	
23.1	m, p, osc	171.0	177.2	1.036	124.5330 ± 2.3263	0.0451 ± 0.0029	51.6 ± 1.0	440	
24.1	m, p, osc	194.6	182.3	0.937	122.1001 ± 2.2363	0.0463 ± 0.0028	52.6 ± 1.0	390	
25.1	m, p, osc	54.4	33.8	0.622	118.6240 ± 3.9401	0.0488 ± 0.0052	54.1 ± 1.8	213	
26.1	m, fr, osc	72.6	42.0	0.578	122.1001 ± 3.4289	0.0485 ± 0.0047	52.6 ± 1.4	344	
27.1	m, fr, osc	36.3	19.6	0.540	120.6273 ± 5.6749	0.0484 ± 0.0066	53.2 ± 2.5	220	
28.1	m, p, osc	121.5	169.3	1.393	124.3781 ± 4.4863	0.0504 ± 0.0061	51.6 ± 1.9	220	
29.1	m, p, osc	37.3	20.8	0.559	117.5088 ± 4.4187	0.0467 ± 0.0069	54.6 ± 2.0	252	

Sample ID	Analysis ID	U (ppm)	Th (ppm)	Th/U	$^{238}U/^{206}Pb$	$^{207}Pb/^{206}Pb$	age $^{206}Pb/^{238}U$	Sr (cps)	Rejected
17NI20b (W101) - gabbroic block									
1.1	m, p, osc	195.0	172.0	0.882	119.1895 ± 2.2730	0.0470 ± 0.0026	53.8 ± 1.1	580	
2.1	m, fr, osc	169.9	166.9	0.982	127.0648 ± 3.2291	0.0509 ± 0.0040	50.5 ± 1.3	250	
3.1	m, fr, osc	246.0	181.9	0.739	119.6172 ± 2.0032	0.0475 ± 0.0023	53.7 ± 0.9	290	
4.1	m, p, osc	339.3	397.0	1.170	120.8751 ± 1.6072	0.0492 ± 0.0022	53.1 ± 0.7	500	
5.1	e, p, osc	302.0	373.0	1.235	121.5067 ± 2.3622	0.0448 ± 0.0028	52.9 ± 1.0	500	
6.1	m, fr, osc	408.0	492.0	1.206	119.3317 ± 1.7088	0.0466 ± 0.0017	53.8 ± 0.8	460	
7.1	m, fr, hl	405.0	187.5	0.463	117.9245 ± 1.8078	0.0475 ± 0.0019	54.5 ± 0.8	540	
8.1	m, fr, osc	181.3	194.6	1.073	122.5490 ± 2.2527	0.0464 ± 0.0027	52.4 ± 1.0	319	
9.1	m, fr, hl	88.7	46.1	0.520	117.0960 ± 3.0165	0.0473 ± 0.0038	54.8 ± 1.4	262	
10.1	e, fr, osc	254.2	265.3	1.044	125.1564 ± 2.8195	0.0444 ± 0.0032	51.3 ± 1.2	520	
11.1	e, fr, sec	273.3	247.4	0.905	120.7729 ± 4.2300	0.0513 ± 0.0061	53.1 ± 1.8	700	
12.1	e, fr, sec	67.4	38.1	0.565	119.9041 ± 3.5942	0.0546 ± 0.0061	53.5 ± 1.6	170	
13.1	m, fr, osc	235.0	200.0	0.851	123.4568 ± 2.1338	0.0475 ± 0.0027	52.0 ± 0.9	333	
14.1	e, fr, osc	167.5	118.3	0.706	119.4743 ± 2.8548	0.0472 ± 0.0032	53.7 ± 1.2	420	
15.1	m, fr, osc	2190.0	3980.0	1.817	124.3472 ± 1.3916	0.0469 ± 0.0009	51.6 ± 0.6	670	
16.1	m, fr, sec	156.7	136.2	0.869	119.4743 ± 2.2839	0.0477 ± 0.0031	53.8 ± 1.1	540	
17.1	m, fr, hl	417.0	375.0	0.899	113.2503 ± 1.7956	0.0477 ± 0.0020	56.7 ± 0.9	350	
18.1	e, fr, sec	393.0	363.5	0.925	121.6545 ± 1.7760	0.0503 ± 0.0023	52.8 ± 0.8	440	
19.1	e, p, osc	228.5	162.4	0.711	121.2121 ± 3.6731	0.0495 ± 0.0035	52.9 ± 1.6	730	
20.1	m, fr, sec	73.6	46.9	0.637	118.3432 ± 4.6217	0.0492 ± 0.0078	54.3 ± 2.1	280	
21.1	e, p, osc	122.4	77.1	0.629	120.0480 ± 2.7382	0.0508 ± 0.0034	53.5 ± 1.2	202	
22.1	m, fr, sec	294.0	302.0	1.027	115.7407 ± 2.0094	0.0480 ± 0.0023	55.5 ± 1.0	530	
23.1	m, fr, sec	41.5	37.6	0.906	121.0654 ± 4.1039	0.0512 ± 0.0063	53.0 ± 1.8	224	
24.1	m, p, sec	95.0	90.0	0.947	113.1222 ± 3.7110	0.0466 ± 0.0055	56.7 ± 1.9	300	
25.1	m, fr, sec	209.0	193.2	0.924	119.0476 ± 2.2676	0.0465 ± 0.0024	53.9 ± 1.0	540	
26.1	m, fr, osc	408.0	354.0	0.868	119.0476 ± 1.9841	0.0475 ± 0.0018	54.0 ± 0.9	450	
27.1	m, fr, sec	177.0	91.2	0.515	107.5269 ± 2.7749	0.0468 ± 0.0036	59.7 ± 1.6	420	
28.1	m, p, osc	144.2	184.2	1.277	122.2494 ± 2.6901	0.0476 ± 0.0034	52.5 ± 1.2	470	
29.1	m, p, osc	170.4	141.8	0.832	121.8027 ± 2.0770	0.0472 ± 0.0032	52.7 ± 0.9	480	

Notes:

Analysis location and grain description: m = middle, e = end, p = prismatic grain, eq = equant grain, fr = fragment, osc = oscillatory zoned, sec = sector zoned, hl = homogeneous (low luminescence), hh = homogeneous (high luminescence).

Analysis conducted on 22nd June 2019 using LA-ICP-MS (University of Queensland).

All analytical errors are given a 1σ.

Samples highlighted in red have been rejected and therefore excluded from age calculations. See Supporting Information Text (Chapter 6) for details explaining rejected grains.

Chapter Seven: Discussion

7.1 Overview

The Dras-Nindam terrane is a distinct belt of basaltic-andesites of the Dras Volcanics, intercalated with forearc volcaniclastic rocks of the Nindam Formation, situated along the Indus Suture Zone of the India-Eurasia collision in the Ladakh Himalaya, NW India (Figure **3.1**). Given the unambiguous stratigraphic relationship between the Dras Volcanics and Nindam Formation compared to the clearly faulted contacts marked by extensive mélange with both the Eurasian post-collisional Indus Group and Ladakh Batholith to the north, and the Indian Lamayuru Complex and Zanskar Supergroup to the south, the term 'Dras-Nindam terrane' is used, and has been used throughout this thesis, to collectively refer to this dominantly mafic island arc complex.

The overarching aim of this investigation was to test competing hypotheses regarding the tectonic evolution of the Dras-Nindam terrane of the Ladakh Himalaya. Broadly, the tectonic evolution of the Dras-Nindam terrane has been based on two competing hypotheses: (i) the Dras Arc evolved throughout the Jurassic to Cretaceous in a forearc region of a convergent margin on the southern margin of Eurasia, where the forearc basin developed on top of ophiolitic basement in front of the Ladakh Arc (Trans-Himalayan Batholith) as part of a single subduction complex responsible for the consumption of the entire Neotethyan Ocean, before the onset of the India-Eurasia continent-continent collision at about 55 Ma (Fuchs, 1982; Honegger et al., 1982) or, (ii) the complex developed in a juvenile, intraoceanic setting with Neotethyan ophiolites along the Indus Suture Zone (Clift et al., 2000; Corfield et al., 2001), baring no provenance links to felsic volcanism associated with the Ladakh Arc, before collision and accretion (onto either India or Eurasia). These competing concepts are visualised in Figure **1.3** and Figure **1.4**.

The results of this investigation provide unequivocal evidence that the Dras Arc and associated forearc volcaniclastic Nindam Formation developed in an intraoceanic realm, as opposed to the forearc region of a convergent setting on the southern margin of Eurasia. Detrital zircon age data has constrained the maximum age of deposition of the Nindam Formation as being ~84 Ma revealed by the youngest zircon population (Figure **4.9**; Figure S4.2). Provenance studies of these volcaniclastic turbidites within the Nindam Formation (Table **4.1**; Figure **4.5**) have assisted in determining that this terrane is truly an intraoceanic island arc system separate to the Ladakh Arc (Eurasian margin). Minor Gondwana-derived detritus in the forearc Nindam Formation provides

new evidence for the Dras-Nindam terrane developing proximally to this passive margin, before first colliding with India and subsequent continent-continent collision (Chapter 4; Walsh et al., 2019). This corroborates with previously published data by Upadhyay et al. (2004), who reported equatorial Palaeocene palynomorphs from the Nindam Formation close to the southern mélange zone near the township of Shergol. These fossils reveal a strong Gondwanan provenance, which provided reasoning for the earlier interpretation that the forearc region of the Dras Arc was located just outboard of the northern margin of India and received India-derived sediment right up until collision and accretion between 50-60 Ma (Figure **4.11**). Accretion of intraoceanic arcs onto first a southern Gondwanan margin is not unique in the Alpine-Himalayan system. For example, in Iraq (Kurdistan) the late Cretaceous Hasanbag and the early Cenozoic Walash-Naopurdan arcs were accreted onto the Arabian sub-continent before the final closure of the Neotethyan Ocean (Ali et al., 2019).

Magmatic phases related to the Dras Arc including extrusive (Dras Volcanics; Figure **5.10**) and intrusive (Kargil Intrusives; Figure **5.11**) episodes were investigated using zircon U-Pb geochronology and determined the oldest Upper Jurassic ages for felsic volcanic rocks, interbedded with the dominantly basaltic to andesitic volcanic pile of the Dras Volcanics (Table **5.1**; Table **5.2**). This is the oldest known age for the Dras Arc and relates to arc inception and early development (Figure **5.12**). These ages combined with detrital studies of the Nindam Formation (Chapter 4; Walsh et al., 2019) suggest that the Dras Arc is related to, and likely developed with, the Spongtang Ophiolite-Spong Arc complex of Ladakh and the intraoceanic Zedong terrane of Tibet (Chapter 5; Walsh et al., 2020). Gabbroic blocks within the southern mélange zone at the thrust contact with passive margin Indian rocks were targeted for zircon U-Pb dating which established the latest stages of development of the Dras-Nindam terrane as ~53 Ma (Figure **6.2**). This is the youngest age acquired for typical subduction-related magmatic components of the Dras Arc and is a critical age constraint for the timing of arc-continent collision. This youngest Eocene age fits well other data and interpretations, including: (i) that of Buckman et al. (2018) where they proposed that the collision age of 48-45 Ma for the Tso Morari eclogite suggested by de Sigoyer et al. (2000) marks the onset of collision and obduction of the Dras Arc (Nidar Ophiolite at this locality) with India, rather than representing the timing of final continental collision and; (ii) Palaeocene aged palynomorphs of Gondwanan provenance from the Nindam Formation (Upadhyay et al., 2004). Therefore, the Dras Arc initiated at ~160 Ma, before final collision with the northern margin of India at or before ~53 Ma, with arc activity spanning at least ~107 m.y., with final continent-continent collision of India into Eurasia occurring sometime after this. As first proposed by Aitchison et al. (2007a) this could have possibly occurred as late as ~34 Ma. See Figure **6.3** (Chapter 6; Walsh et al., *in prep.*).

More broadly, this investigation has contributed to existing models on the development of intraoceanic arcs and their collision and accretion onto continents, shedding further light on the mechanisms behind the growth of continental crust (Charvet, 2013; Lee et al., 2007; Rioux et al., 2007). Continental collision is often preceded by the accretion of numerous intraoceanic terranes (ophiolites, island arcs, accretionary complexes, or seamounts), such as the case with the Dras-Nindam terrane colliding and accreting onto the passive margin of India, prior to terminal continent-continent collision between India and Eurasia. The recognition of oceanic, island arc terranes onto continental margins is often complicated by the intense deformation and fragmentation associated with collision, uplift, dissection by major strike-slip faults, and subsequent erosion.

This work has also contributed to knowledge on the life cycle of the Neotethyan Ocean. The Himalaya Orogen, along with its western continuation through Iran and Iraq into the European Alps and eastward into southeast Asia, contains a wealth of information detailing the interaction of a *fixed* Eurasian plate with southern Gondwanan-derived continental blocks, and numerous Tethyan intraoceanic terranes which occurred between these two dominant features. As a point of clarification, the Tethyan Ocean is used here as an all-encompassing term to describe the vast ocean that existed between Eurasia and Gondwana during the Palaeozoic to Cenozoic (Fergusson et al., 2016). The break-up of the supercontinent Gondwana into discrete continental terranes (e.g., Lhasa terrane) and the northward migration of these blocks at different time intervals, are responsible for the division of the Tethyan Ocean into the Paleotethyan, Mesotethyan and Neotethyan oceans (Fergusson et al., 2016; Furnes et al., 2020; Smith et al., 1981; Şengör, 1979; 1984). The work here has focussed on the Neotethyan domain, for which previous work (contributions from many workers, but compiled by Furnes et al., 2020; see references therein) has established three main age ranges for intraoceanic arc and ophiolitic complexes of the Alpine-Himalaya Orogen, which extends from the Iberian Peninsula to the Indochina Peninsula in the east. These are, (i) Permo-Triassic (252-201 Ma), Jurassic (201-145 Ma), and (iii) Cretaceous (145-66 Ma). In addition to this, other workers have documented active intraoceanic complexes into the Cenozoic (e.g., Bela Ophiolite of Pakistan; 70-65 Ma; Ahmed, 1993; Gnos et al., 1998). The work of this thesis has extended the last age range of intraoceanic arc and ophiolitic complexes from Cretaceous to Eocene (145-53 Ma; Chapter 6; Walsh et al., *in prep.*), further contributing to knowledge on the formation and development of different seaways in the Neotethyan Ocean.

This investigation has also contributed to previous work proposing that Neotethyan arc initiation and ophiolite development occurred at overlapping time intervals, starting in the Late Jurassic, and ended with accretion onto the Indian passive margin (Aitchison et al., 2000;

Aitchison et al., 2007a; 2007b; Aitchison and Davis, 2004; Allègre et al., 1984; Buckman et al., 2018; Chan et al., 2015; Davis et al., 2002; Ding et al., 2005; Guilmette et al., 2009, 2012; Hébert et al., 2012; Malpas et al., 2003; Searle, 1983; 1986; Searle et al., 1997; Walsh et al., 2019, 2020). It is important to note that some researchers have suggested that a large-scale subduction zone existed in the northern Neotethyan Ocean, between Anatolia and Eurasia (Rolland et al., 2020). However, this is cautioned, as making large regional correlations over significant structural constraints, such as the Nanga Parbat syntaxis (see Chapter 5 for further discussion) separating the Ladakh and Kohistan regions, or major fault zones (e.g., Owen Fracture Zone), could result in drawing relationships between units which may have been developing at the same time, but existed in separate oceanic domains (i.e., Mesotethyan vs. Neotethyan oceans) and therefore, may not be geodynamically related or consanguineous. For the purposes of this work, it is preferred to compare those data which exist for Neotethyan intraoceanic arc and ophiolite complexes occurring across the Indus-Yarlung-Tsangpo Suture from Tibet in the east to further west in Ladakh. In the eastern extent of the suture zone (Yarlung-Tsangpo Suture) there exists discontinuous oceanic remnants, ranging in age from 163-119 Ma (Figure **7.1**), where the oldest complex is the Zedong terrane (163-152 Ma; Liu et al., 2020; McDermid et al., 2002; Zhang et al., 2014; Zhong, 2006) and the youngest is the Jungbwa (also referred to as Yungbwa; 119-121 Ma; Lee et al., 2009; Xia et al., 2011). While in the western extent of the suture zone (Indus Suture), the Ladakh Himalaya contains the Kiogar Ophiolite (159 Ma; Chan et al., 2015), Nidar Ophiolite (120 Ma; Zyabrev et al., 2008), Spongtang Ophiolite (177 Ma; Pedersen et al., 2001) and Spong Arc complex (135-88 Ma; Buckman et al., 2018; Pedersen et al., 2001), and the Dras-Nindam terrane (160 Ma; Walsh et al., 2020). Refer to Figure **7.1**.

Most intraoceanic arc and ophiolitic complexes occurring in the Indus-Yarlung-Tsangpo Suture from the Ladakh Himalaya to Tibet are assumed to have been emplaced or obducted onto the northern passive margin of India during the Late Cretaceous to Eocene (Hébert et al., 2012 Searle, 2019; Searle et al., 1987; 1997; Walsh et al., *in prep.*; Chapter 6). However, it remains unresolved whether Gondwanan accretion and obduction of these Neotethyan intraoceanic arc and ophiolite complexes was diachronous. Indeed, identifying *obduction* itself is a difficult enough task without being hindered by continental collision with its subsequent overprinting deformation and back-thrusting. In saying this, there are some metamorphic rocks occurring along the Indus-Yarlung-Tsangpo Suture which may provide the rationale for the timing of emplacement and obduction (Figure **7.1**). For example, from the ophiolitic mélange associated with the Xigaze and Luobusha ophiolites occurring in Tibet, high-grade metamorphic soles have ages of 127-123 Ma (Guilmette et al., 2009) and 88-81 Ma (Malpas et al., 2003), respectively. It is worth noting that similar metamorphic sole ages have been reported for ophiolitic remnants occurring in Oman (Semail; 95-93 Ma; Searle and Cox, 2002; Warren et al., 2003) and Pakistan

(Muslim Bagh; 71-65 Ma; Mahmood et al., 1995). Refer to Figure **7.1**. While work in Ladakh has suggested that ophiolite obduction occurred much later in the Eocene, with Buckman et al. (2018) proposing that the Spongtang Ophiolite was emplaced on the Indian margin post-early Eocene, based on the lower Eocene Kong Slates and Chulung La Formation being below the massif thrust sheet. Work from this thesis has provided further evidence for Eocene emplacement, with 53 Ma gabbroic blocks from the Dras Arc ophiolitic mélange. These are the youngest magmatic ages for the complex and provide a critical constraint on arc-continent collision occurring after this time. Chan et al. (2015) proposed that all the ophiolites and intraoceanic arc complexes along the Himalaya may have been emplaced during an event that spanned ~20 million years. This work extends that range to ~74 million years (127-53 Ma). Currently unknown is whether emplacement occurred as a continuous, prolonged event, or whether there were distinct episodes of emplacement occurring during the (i) early Cretaceous, (ii) late Cretaceous and (iii) early Eocene. Although likely, there is not currently enough evidence to unequivocally determine diachronous accretion of Neotethyan intraoceanic arc and ophiolitic complexes onto the northern passive margin of India. What is undeniable though, is that these Neotethyan-derived oceanic complexes must have been emplaced prior to the terminal continent-continent collision between Indian and Eurasia and subsequent uplift of the Himalaya Orogen.

The following sections provide contributions from Chapters 4-6, where the chapters are papers which have been accepted or in preparation for publication. The last section of this chapter provides recommendations for future research related to the Dras-Nindam terrane and units associated with the Indus Suture Zone, Ladakh Himalaya, NW India.

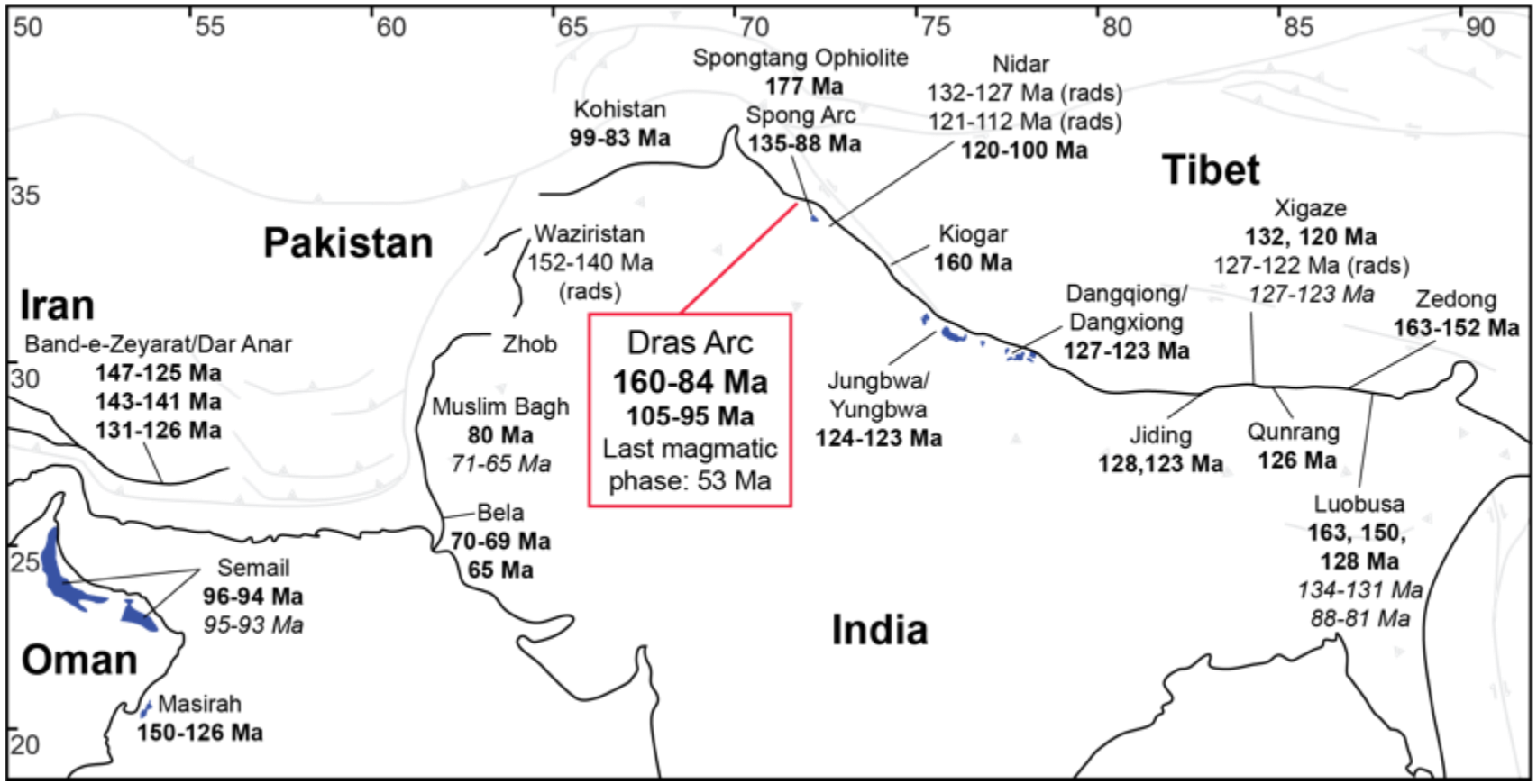

Figure 7.1: Intraoceanic arc and ophiolitic complexes occurring along the Indus-Yarlung-Tsangpo Suture. Adapted from Chan et al. 2015. Igneous crystallisation ages are shown in **bold**. Radiolarian biostratigraphic ages are displayed with 'rads'. Metamorphic ages are shown in *italics*. Sources for the age data (zircon U-Pb geochronology, radiolarian biostratigraphy or ^{40}Ar-^{39}Ar geochronology) are as follows: Masirah: (Smewing et al., 1991); Semail: (Searle and Cox, 1999; 2002; Warren et al., 2003);Band-e-Zeyarat/Dar Anar: (Ghazi et al., 2004; Hassanipak et al., 1996; McCall, 1985); Bela: (Ahmed, 1993; Gnos et al., 1998); Muslim Bagh: (Kakar et al., 2012; Mahmood et al., 1995); Zhob: (no age data found – however, petrology and geochemistry for the Zhob ophiolite is detailed in Ahmed et al., 2020); Waziristan: (Khan et al., 2004); Kohistan: (Schaltegger et al., 2002); Spongtang Ophiolite: (Pedersen et al., 2001); Spong Arc: (Buckman et al., 2018; Pedersen et al., 2001); Dras Arc: (Reuber et al., 1989; Walsh et al., 2019; 2020: Walsh et al., *in prep*); Nidar: (Kojima et al., 2001; Mahéo et al., 2004; Zyabrev et al., 2008); Kiogar: (Chan et al., 2015); Jungbwa/Yungbwa: (Chan et al., 2015); Dangqiong/ Dangxiong: (Chan et al., 2015); Jiding: (Li et al., 2009; Wang et al., 2006); Xigaze: (Chan et al., 2015; Göpel et al., 1984; Guilmette et al., 2009; Zyabrev et al., 2003); Qunrang: (Li et al., 2009); Zedong: (Liu et al., 2020; McDermid et al., 2002; Zhang et al., 2014; Zhong, 2006); Luobusa: (Chan et al., 2015; Malpas et al., 2003; Zhang et al., 2016 Zhong et al., 2006).

7.2 Discussions from Chapter Four

Age and provenance of the Nindam Formation, Ladakh, NW Himalaya: Evolution of the intraoceanic Dras Arc before collision with India

Objective I

To determine the maximum age of deposition and provenance of the Nindam Formation using detrital zircon U-Pb geochronology to ascertain whether the Dras Arc was intraoceanic or continental-related.

The forearc basin volcaniclastic rocks of the Nindam Formation provide an important archive of information related to the Dras Arc and the Himalayan Orogen more broadly. Detrital zircon geochronology (Chapter 4; Walsh et al., 2019) has revealed a youngest population of ~84 Ma, representing the maximum age of deposition of the sequence. Consistent with previous studies (Clift et al., 2000; Robertson and Degnan, 1994), the Nindam Formation demonstrates younging towards the north, where generally the youngest zircon population in each sample becomes progressively younger up-sequence (Figure **4.9**). This is indicative of contemporaneous deposition of the Nindam with active volcanism of the Dras Arc. When all the samples are combined, the composite detrital zircon population spans 125-84 Ma, which based on this dataset alone, allowed for the proposition that the Dras Arc was active continuously for at least 41 Ma. However, the Dras Arc is actually much older than ~125 Ma, with arc initiation occurring during the Upper Jurassic (Chapter 5; Walsh et al., 2020).

There has been long-standing debate as to whether the Nindam Formation represents the forearc basin of the southern Eurasian margin (Fuchs, 1982; Henderson et al., 2010; Honegger et al., 1982; Najman et al., 2017), or the forearc basin of an intraoceanic arc system (Robertson and Degnan, 1994). See Figure **1.3** and Figure **1.4** for these competing concepts. This study has demonstrated that, based on petrographic point counting, the dominant lithic clasts in sandstones and conglomerates of the Nindam Formation are basaltic to andesitic and pelagic limestone, with minor chert and siltstone (Figure **4.5**). This directly contrasts the composition of the Ladakh and Karakorum Batholiths (Trans-Himalayan Batholith), which are characterised by felsic and silica-saturated components (Figure **4.3**). Whole rock geochemical data combined with point counting dominated by mafic clasts and distinct absence of quartz suggests that the main source of the Nindam Formation detritus is volcanic arc derived (Figure **4.6** and Figure **4.7**).

Unlike many intraoceanic arcs that are dominated by a unimodal detrital zircon population, the forearc volcaniclastic Nindam Formation to the Dras Arc contains pre-Cretaceous detrital zircon populations. Fitting the observation of abundant ultramafic and serpentinite clasts in the stratigraphic lowermost sections of the Nindam Formation, detrital zircon geochronology (Figure S4.1) also demonstrated a significant age population (185-135 Ma), which coincides with those ages (177-88 Ma) reported for the Spongtang Ophiolite and Spong Arc (Buckman et al., 2018; Pedersen et al., 2001). This link between the Dras-Nindam terrane and Spongtang Ophiolite-Spong Arc complex is vitally important, given that the latter obducted onto the Indian margin during the early Eocene. This, combined with rare Gondwanan zircon provenance (Figure **5.9**; Figure S4.1) and evidence for Indian-derived palynomorphs from the forearc Nindam Formation (Upadhyay et al., 2004), provides the rationale that the Dras Arc also collided and accreted onto India rather than Eurasia, prior to terminal continent-continent collision of India and Eurasia.

Notably, a minor 'Gondwanan' zircon signature comprised of Precambrian peaks occurs in all samples, with input contributing on average 18% of total grain ages. There are no reports of the basement rock to the Dras Arc being Gondwanan. However, at this time the Neotethyan Ocean was bound to the north and south by Gondwanan-derived components, these being the Lhasa terrane and India, respectively. It is also important to note that during this time (Late Cretaceous) the Lhasa terrane had docked with the southern Eurasian margin; thus, it could be expected that this now active continental margin was a source region for the Nindam Formation. This, however, is not the case and there is no convincing evidence for the continental forearc basin to the Lhasa + southern margin of Eurasia (i.e., Xigaze Group) contributing continental detritus into the Nindam Formation (Figure **4.10**). There are parallels here with that observed in western Iran, where the Sanandaj-Sirjan Zone of Gondwana provenance has docked first onto Eurasia, by closure of the Paleotethyan Ocean (Fergusson et al., 2016).

It is therefore proposed that the Gondwanan inheritance recorded in the Nindam Formation is attributed entirely from the passive margin of northern India. Moreover, it is suggested that this Indian-derived detritus entered the Nindam Formation along an originally NNE-SSW trending trench (Buckman et al., 2018) that initiated along a major transform fault occurring in the Neotethyan Ocean (Figure **4.11**).

7.3 Discussions from Chapter Five

The significance of Upper Jurassic felsic volcanic rocks within the incipient, intraoceanic Dras Arc, Ladakh, NW Himalaya

Objective II

To constrain the timing of initiation and early evolution of the Dras Arc using zircon U-Pb geochronology of extrusive (Dras Volcanics) and intrusive (Kargil Intrusives) magmatic episodes.

Important to characterising the tectonic evolution of any intraoceanic arc complex is to determine arc initiation and early development. The Dras Arc has been reported as having initiated during the Jurassic to Cretaceous (Clift et al., 2000; Clift et al., 2002b; Honegger et al., 1982; Reuber, 1989; Robertson and Degnan, 1994), however this study confirms the earliest age through the dating of rare, felsic volcanic rocks interbedded with the predominantly basaltic to andesitic Dras Volcanics (Chapter 5; Walsh et al., 2020). These findings have produced the first zircon U-Pb data from the Dras Volcanics, which are an Upper Jurassic felsic tuff 160 ± 3 Ma (Oxfordian) and trachydacite 156 ± 1 Ma (Kimmeridgian), relating to the inception of the intraoceanic Dras Arc (Figure **5.9** and Figure **5.10**).

Although rare, felsic volcanism in island arc systems is sometimes associated with the adolescent stages of arc development due to the dehydration melting of underplated arc or oceanic crust, other adakitic felsic melts are produced by partial melting of young, oceanic crust of basaltic (eclogitic) composition (Defant and Drummond, 1990; Castillo, 2012). These Upper Jurassic felsic rocks from the Dras Volcanics have distinctly low-Mg adakitic geochemical characteristics, typically associated with melts derived from the partial melting of subducted basaltic ocean crust (Figure **5.7**). This investigation has revealed a previously undocumented phase of felsic magmatism early in the development of the Dras Arc, which is proposed to be related to the subduction of young, hot oceanic crust soon after subduction initiation during incipient stages of arc development.

Previous work has based age constraints for the Dras Volcanics on cross-cutting and intrusive relationships of the gabbroic to granodioritic rocks from the Kargil Intrusives. This investigation reproduced (102 ± 2 Ma and 101 ± 2 Ma) those original ages (Honegger et al., 1982; Schärer et al., 1984a), while also producing a much younger pulse (80 ± 1 Ma; Figure **5.9** and Figure **5.11**). Initially, it was favoured that the Dras Arc first accreted onto the Eurasian margin using the

Kargil Intrusives as evidence, which were proposed to be equivalent to the Ladakh Arc (Figure **1.3**). However, with no such Middle Cretaceous (~103-101 Ma) age data existing for the Ladakh Arc, it has instead been suggested that the Kargil Intrusives are not related to, or associated with, the Ladakh Arc and as such is not evidence for the collision and accretion of the Dras Arc onto the Eurasian margin (Buckman et al., 2018; Walsh et al., 2019). Rather, this study combined with the detrital zircon study of the Nindam Formation (Chapter 4; Walsh et al., 2019) provides further evidence for the Dras Arc colliding and accreting first with India rather than Eurasia at ~55 Ma (see Chapter 5 Graphical Abstract). The basis for the Eocene arc-continent collision age is based on (i) partial subduction of the northern Indian continental margin to form the 55 Ma Tso Morari eclogite (de Sigoyer et al., 2000), and (ii) Gondwanan-derived (Permian and Mesozoic) palynomorphs from volcaniclastic sandstones of the Nindam Formation, with Palaeocene aged palynomorphs also identified, represent the youngest reported age for the Nindam Formation (Upadhyay et al., 2004).

With regard to regional correlations, similar whole rock geochemical and geochronologic age data indicates that volcanic rocks from the Dras Arc are consistent with intraoceanic island arc signatures and are similar to those of the nearby the Spongtang Ophiolite-Spong Arc complex (Buckman et al., 2018) and the intraoceanic Zedong terrane of Tibet (Aitchison et al., 2000; McDermid et al., 2002). It is therefore proposed that the Dras-Spong-Zedong intraoceanic arc initiated in the Neotethyan Ocean just outboard of the northern margin of India during the Upper Jurassic. This is much earlier than previously reported, with arc activity spanning at least 100 m.y. between initiation around ~160 Ma and final collision with northern margin of India sometime in the Palaeocene between 60-50 Ma.

7.4 Discussions from Chapter Six

Youngest magmatic age (Early Eocene) from the Neotethyan intraoceanic Dras Arc, Ladakh Himalaya, NW India

Objective III

To establish the latest stages of development of the Dras Arc in order to constrain the timing of arc-continent collision.

Determining the latest stages of development in any intraoceanic arc or ophiolitic complex is vital to understanding and constraining the timing of accretion and obduction, respectively. Therefore, the youngest age for typical subduction-related magmatic rocks provides a critical constraint for the timing of arc collision, which must precede terminal continent-continent collision. Providing robust radiometric dating for these youngest magmatic components is important for understanding collision zones as complex geological regions which are not necessarily restricted to the collision of two continents but may include the accretion of numerous intraoceanic terranes prior to final continental collision.

Considerable emphasis has been placed on the recognition of accreted (intraoceanic) arc complexes in orogenic belts, as these can potentially be used for the along-strike correlation of tectono-stratigraphic terranes, and form a key element of geodynamic and paleogeographic reconstructions. This investigation provides a limit for the maximum possible age for arc-continent collision and accretion by obtaining the youngest ages for ophiolitic rocks in an Indus-Yarlung-Tsangpo Suture mélange (Chapter 6; Walsh et al., *in prep.*). Arc-related gabbroic blocks from the Sapi-Shergol mélange (Figure **6.1**), which developed along the thrust contact between the intraoceanic Dras Arc and Indian passive margin rocks (Zanskar Supergroup), yield zircon U-Pb ages of ~53 Ma (weighted average ages ranging 53.4 ± 0.6 Ma to 52.9 ± 0.4 Ma, expressed at 95% confidence). These early Eocene gabbroic blocks represent the youngest Neotethyan ophiolite or island arc rocks along the entire Indus-Yarlung-Tsangpo Suture, and thereby constrain the minimum age of arc magmatism and the maximum age of arc-continent (India) collision to after 53 Ma for this segment of the suture zone in the Ladakh Himalaya, NW India (Figure **6.2**).

The accretion of the Dras Arc complex during the Palaeocene has been based on (i) the 48-45 Ma collision age of the Tso Morari eclogite representing the partially subducted Indian continental margin (de Sigoyer et al., 2000), and (ii) Palaeocene aged palynomorphs from the

Nindam Formation (Upadhyay et al., 2004). The youngest ages for other Indus-Yarlung-Tsangpo ophiolite and arc complexes include the ~80 Ma Muslim Bagh (Kakar et al., 2012) and ~66-65 Ma Bela ophiolites (Ahmed, 1993) of Pakistan, and the ~88 Ma Spong Arc of Ladakh (Pedersen et al., 2001). In contrast, the youngest ophiolite ages farther east in Tibet are ~120 Ma (Chan et al., 2015; Hébert et al., 2012). From this study, these new ages provide a new minimum age constraint for the collision of Neotethyan intraoceanic ophiolite and island arc terranes with the Indian continental margin in the Ladakh Himalaya. A complete history for the Dras Arc can now be ascertained from the results derived from this (Chapter 6), and the previous two studies (Chapter 4 and 5); the Dras Arc likely collided with India soon after the crystallisation of these ~53 Ma gabbroic blocks which corresponds with the onset of eclogite metamorphism between 50-47 Ma (de Sigoyer et al., 2000), but this precedes final continental collision between India (+Dras Arc) and Eurasia (+Ladakh Arc). It is also important to note that eclogites in such settings will have two sources, (i) fragments within the extinguished subduction channels, exhumed to crustal levels; and (ii) double thickening of the crust during collision, where mafic rocks in the base of the tectonically-thickened crust can develop eclogite assemblages (such as in mafic dykes cutting continental basement).

Therefore, the Dras Arc was a long-lived intraoceanic island arc complex that spanned at least ~108 m.y., between initiation around ~160 Ma, peak arc magmatism between 125-84 Ma and a final arc magmatic phase at ~53 Ma, before the onset of 'phase 1' arc-continent collision which extinguished any further arc magmatism and led to partial continental subduction and eclogite metamorphism between 50-47 Ma (Figure **6.3**). Final 'phase 2' involves the Ladakh Arc along the southern margin of Eurasia being extinguished by continent-continent collision leading to the uplift of the Himalaya.

7.5 Future recommendations

Geological exposure in the remote mountains of Ladakh provides the ideal natural laboratory for investigations of the Himalayan Orogen and an opportunity to provide new, accurate and much needed geological data to ongoing debates. However, there are many geo-political complexities surrounding field site access in the Ladakh Himalaya, NW India. The following recommendations are presented assuming that field campaigns are undertaken with respect for culture, political sensitivities, and environmental concern.

Recommendations for future research are as follows:

- Radiolarian microfauna have been extracted from cherts associated with the Spongtang massif (Spong Arc) and Nidar Ophiolite producing Early to Middle Cretaceous biostratigraphic ages (Baxter et al., 2010; Kojima et al., 2001; Zyabrev et al., 2008). Sections of the Dras Volcanics are reportedly underlain by Middle-Upper Jurassic (Callovian-Tithonian; 166-145 Ma) radiolarian cherts (Honegger et al., 1982). Radiolarite also exists in both the Urtsi and Wanlah mélanges (southern mélange zone bordering the Dras-Nindam terrane). Radiolarian biostratigraphy of these, combined with established radiometric ages would further constrain the evolution of the Neotethyan Ocean and associated intraoceanic terranes.
- The Mongyu Mélange (or northern mélange zone), separating the Ladakh Arc to the north from the Dras-Nindam terrane to the south, is a disrupted serpentinite-matrix mélange (Robertson, 2000). This mélange requires detailed mapping and sampling to constrain the nature and timing of emplacement in order to make comparisons with the mélange zones developed along the southern margin of the Dras Arc.
- The occurrence of young Eocene gabbroic portions of the Dras Arc exclusively within the Sapi-Shergol mélange (Chapter 6: Walsh et al., *in prep.*) but the lack of any known equivalent aged outcrops elsewhere within the Dras-Nindam terrane is worthy of further investigation. It would be interesting to attempt to identify other younger portions of the Dras Arc. More work is required in terms of dating gabbroic blocks within mélange zones along the entire Indus-Yarlung-Zangpo Suture to potentially discover more young Eocene phases of the ophiolite-arc rocks and establish any diachroneity to the closure of the Neotethyan Ocean.
- It has been proposed that the Dras Arc is regionally correlated with the Zedong terrane of Tibet and possibly the Kohistan Arc (not Kohistan Batholith) of Pakistan (Chapter 5; Walsh et al., 2020). The genetic relatedness of other Neotethyan intraoceanic terranes, such as the Bela Ophiolite (Ahmed, 1993) and Muslim Bagh Ophiolite (Kakar et al., 2012) complexes of Pakistan should also be examined. It is also interesting to

note that there are other Neotethyan arc fragments which are Cretaceous and Eocene age located in Kurdistan (Ali et al., 2019). Therefore, there are complexities eastward in Iran and Iraq, where similar ages have been identified. The collision of these Cretaceous arc complexes occurred first with Arabia, not Eurasia, so in that sense there are some similarities.

- There is still much work to be done on the Dras Volcanics, of the Dras-Nindam terrane. For example, some samples from this unit displayed high MgO (>8 wt.%) and low TiO_2 (<0.5 wt.%) possibly indicating the presence of boninitic lavas (Crawford et al., 1989). See Chapter 4 (Walsh et al., 2019). Boninites have considerable tectonic significance as they are commonly linked to earliest arc volcanism following intraoceanic subduction initiation (Pearce and Reagan, 2019). Identifying and dating these boninitic lavas within the Dras Volcanics has the potential to even further constrain and identify the timing of initiation and early evolution of the Dras Arc.
- Another important rock type that is commonly linked to a particular tectonic setting is adakite. The presence of adakitic rocks generally demonstrates the partial melting of metamorphosed (eclogitic) basalt or the fractional crystallisation of island arc magmas (Arth and Hanson, 1972; Martin, 1986). One Upper Jurassic sample from the Dras Volcanics (trachydacite, sample 17NI12) fits most of the characteristics of a low-Mg adakite produced by partial melting of subducted ocean crust (Chapter 5; Walsh et al., 2020). It would be important to locate and confirm the presence of more adakitic rocks in the volcanic pile, to further document this phase of felsic magmatism early in the development of the Dras Arc, which is likely related to the subduction of young, hot oceanic crust soon after subduction initiation.
- A felsic tuffaceous layer in the Dras Volcanics has produced the oldest known radiometric age (160 ± 3 Ma) for this formation (Chapter 5; Walsh et al., 2020). Only one sample yielded zircon large enough to acquire a zircon U-Pb age (using LA-ICP-MS). This oldest age could be further examined by targeting coarse 'sandy' tuff layers within the Dras Volcanics and using a higher-precision instrument (e.g., SHRIMP) with a smaller volume analytical site more appropriate for small, difficult to date zircon grains.
- Although some Lu-Hf isotopic data exists for zircon from the Indus Group (Molasse), which demonstrates exclusively Ladakh Batholith-related detritus in the lowest-most stratigraphic levels (Wu et al., 2007; Zhou et al., 2020), there is a distinct lack of isotopic and trace element data for zircon grains from the forearc volcaniclastic Nindam Formation. The limitation of the dataset presented here for the Nindam Formation (Chapter 4) is recognised, as the trace element and isotopic composition of

the zircon grains, combined with paleomagnetic studies would provide further important information on the tectonic origin and position of this unit and others (i.e., Dras Volcanics) of the Dras-Nindam terrane. Regarding the Nindam Formation, this unit contains pre-Cretaceous detrital zircon that are significant in terms of provenance (Chapter 4; Walsh et al., 2019). It would be of interest to confirm whether these detrital zircon populations are dominantly juvenile or may include continental influence. For example:

  - There is a distinct age peak between 185-135 Ma, that coincides with ages reported for the Spongtang Ophiolite-Spong Arc complex (Buckman et al., 2018; Pedersen et al., 2001). Preliminary work was undertaken on this population; however, more is required to create a significant dataset to detail the setting and history of these rocks in which the zircon grains crystallised.
  - A small number of Permian to Triassic (200-271 Ma) zircons occur which make up less than 1% of the total population of the Nindam Formation and may represent material derived from the Permo-Triassic Panjal Traps of India (Rehman et al., 2016; Shellnutt et al., 2011).
  - A small (2%) population of Early Palaeozoic (418-540 Ma) zircons are present within the Nindam Formation. This is consistent with derivation from northern Gondwana which experienced the Kurgiakh Orogeny (Myrow et al., 2016) or equivalent "Bhimphedian Orogeny" of Cawood et al. (2007) during the Cambrian to Ordovician.
  - The Dras-Nindam terrane contains a distinct Gondwanan inheritance reflecting input from a continental source (Walsh et al., 2019). This detrital component can be identified within most samples, with input ranging between 6-42% (average 18%) of total grain ages. Although there have been no reports of any Gondwanan basement to the Dras Arc from which these zircons could have been sourced, it would be of interest to investigate and confirm this.

- There is a distinct absence of paleomagnetic studies of the Dras-Nindam terrane. Some early work exists for other units, such as the Ladakh Batholith (e.g., Klootwijk et al., 1979), however no recent data exists for the Nindam Formation or Dras Volcanics. A preliminary investigation was undertaken, with magnetic measurements made at the Palaeomagnetism Laboratory, Australian National University (ANU), under the guidance of Dr Derya Gürer (The University of Queensland). Specifically, testing the paleolatitude of the Dras Arc at discrete time intervals would determine whether this system evolved as an intraoceanic island arc system that developed as a result of spontaneous subduction at ~160 Ma along a NNE-SSW transform fault in the Neotethyan Ocean.

- The Chilling Formation occurs sporadically along the southern contact of the Dras-Nindam terrane and the northern Indian passive margin rocks (Lamayuru Complex and Zanskar Supergroup). This unit is dominated by green-purple-red siltstones, shales and mass-flow conglomerates, with clasts similar to those from the southern mélange zone (ophiolitic-derived peridotite, gabbro, basalt, chert and volcaniclastic material). Other clasts are similar to the Zanskar Supergroup and Lamayuru Complex (nummulitic limestone and quartzite, respectively). Very little data currently exists for this unit, however the detrital record of syn- to post-collisional conglomerates from the Chilling Formation, may provide further answers as to the youngest events of the Dras Arc (combined with work from Chapter 6; Walsh et al., *in prep.*).
- The shallow-water platform carbonates of the Khalsi Limestone (Khalsi Formation or Khalsi Flysch) are stratigraphically included as part of the Tar Group (Ladakh forearc basin) and occur to the north of the volcaniclastic sandstones and turbidites of the Nindam Formation. The Jurutze Formation and the Khalsi Limestone are considered the oldest sections of the Tar Group (Henderson et al., 2010), with the latter biostratigraphically dated as Lower Cretaceous (Mathur and Vogel, 1988). There is, however, some disagreement about the stratigraphic arrangement of the Khalsi Limestone, within or separate to the Tar Group (Clift et al., 2002a). Detrital zircon and provenance studies may assist is determining the relatedness exclusively to the Eurasian margin, or to the Dras-Nindam terrane pre- or syn-collision with India.

Chapter Eight: Conclusion

The Himalaya represent the ongoing collision between the Indian and Eurasian continents and the deformed sedimentary sequences along the suture zone record the closure of the vast Neotethyan Ocean. The tectonic evolution of the Himalaya Orogen is far more complicated than some portray, with numerous intraoceanic terranes getting caught between the two continents before terminal collision. The Dras-Nindam terrane, of the Indus Suture Zone, Ladakh Himalaya, NW India, represents one such intraoceanic terrane which makes up a component of a vast subduction system that extended from the westward Spongtang Ophiolite-Spong Arc in Ladakh to the Zedong terrane in Tibet farther east. The work presented here provides important answers to questions related to the initiation, early development, and accretion of the Dras-Nindam terrane onto the passive Indian margin.

The results of this investigation have demonstrated that the Dras-Spong intraoceanic arc initiated in the Neotethyan Ocean just outboard of the northern margin of India during the Upper Jurassic, and that some of these earliest low-Mg adakitic felsic volcanic rocks are derived from partial melting of basaltic ocean crust, likely during incipient stages of arc development. The deep-marine volcaniclastic rocks of the Nindam Formation indicate deposition in an intraoceanic forearc basin setting with little to no influence from continental rocks, but more akin to island arc development associated with the Indus supra-subduction zone ophiolites. Early Eocene ages relating to the latest stages of the intraoceanic Dras arc-ophiolite complex acquired for gabbroic blocks from the Sapi-Shergol mélange at the southern thrust contact with the Indian Zanskar Supergroup (~53 Ma), indicate that the intraoceanic island arc complex was long-lived. In conclusion, the Dras Arc was a long-lived intraoceanic island arc complex that spanned at least ~108 m.y., between initiation around ~160 Ma, peak arc magmatism between 125-84 Ma and a final arc magmatic phase at ~53 Ma, before the onset of ‘phase 1’ arc-continent collision which extinguished any further arc magmatism and led to partial continental subduction and eclogite metamorphism between 50-47 Ma. Final ‘phase 2’ involves the Ladakh Arc along the southern margin of Eurasia being extinguished by continent-continent collision leading to the uplift of the Himalaya (Figure **8.1**).

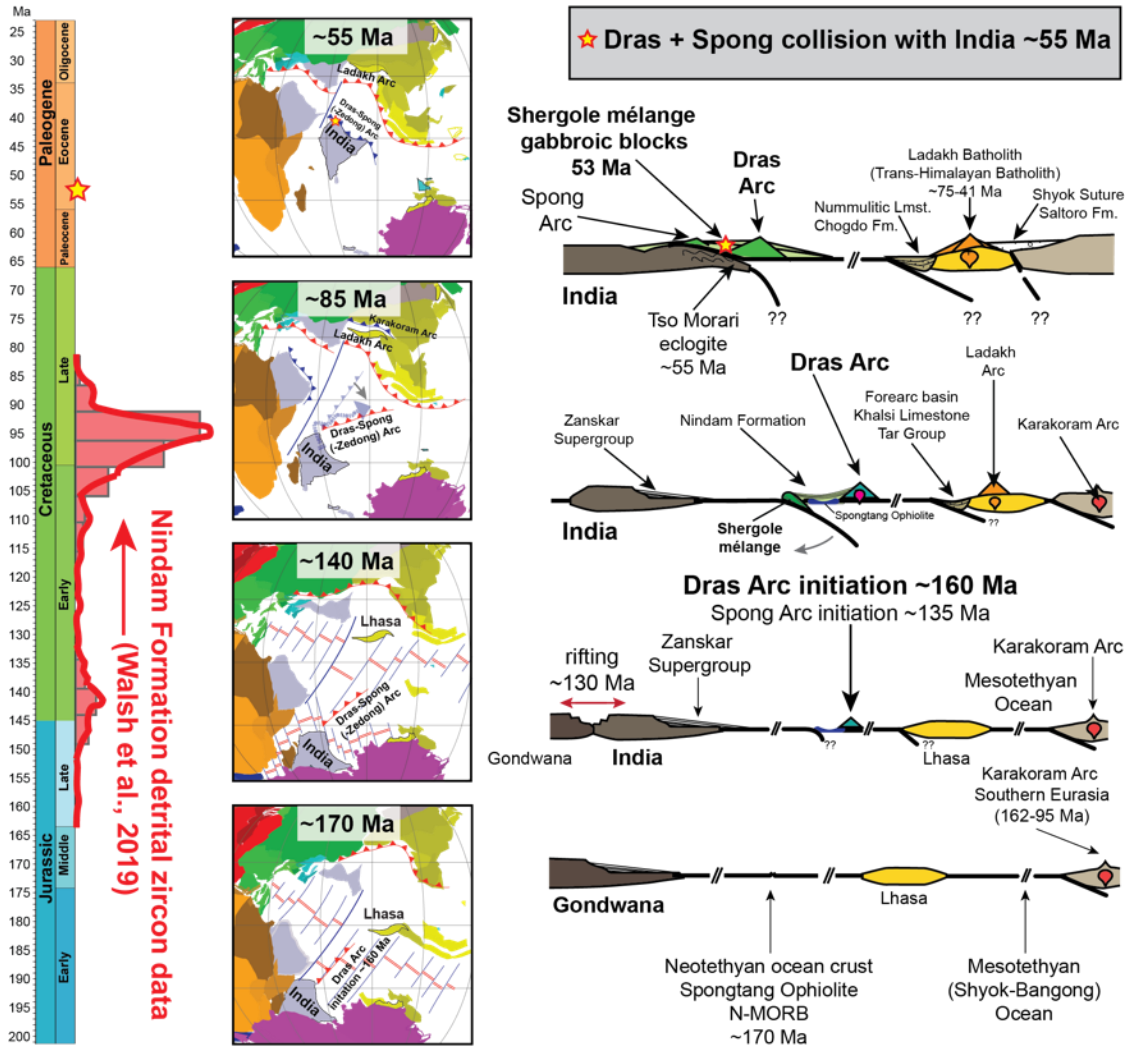

Figure 8.1: Tectonic evolution of the Dras Arc from inception during the Upper Jurassic to final stages of magmatism in the Eocene and final accretion and collision with the passive margin of India (~55 Ma). Adapted from Walsh et al. (2019; 2020); Walsh et al. (*in prep.*).

Appendices

Appendix A: Conference abstracts and proceedings

Overview

The following information (Appendix A) includes further details for conference abstracts and proceedings undertaken during candidature. Links are provided for those conferences which maintain online records, otherwise all information is presented here. The oral and poster presentations conducted alongside research for this thesis are as follows:

A1: Australian Earth Sciences Convention (AESC; 2021)
A2: American Geophysical Union (AGU), Fall Meeting (2020)
A3: Dorothy Hill Women in Earth Sciences Symposium (DHS; 2019)
A4: European Geosciences Union (EGU) General Assembly (2019)
A5: American Geophysical Union (AGU), Fall Meeting (2017)
A6: Dorothy Hill Women in Earth Sciences Symposium (DHS; 2017)

Appendix B: Coauthor contribution framework following 'Contributor Roles Taxonomy' (CRediT)

Overview

The following information (Appendix B) includes tabulated information relating to the 'Contributor Roles Taxonomy' (CRedIT) as outlined by Allen et al. (2019). Here, terms and definitions are included, which have been used throughout the thesis (Chapters 4-6) to acknowledge coauthor contributions. The table is as follows:

B1: Contributor Roles Taxonomy (CRedIT)

Appendix A: Conference abstracts and proceedings

A1 Australian Earth Sciences Convention (AESC), Core to Cosmos. Virtual Conference. February 2021. Oral presentation.

"Unravelling the Himalaya: One intraoceanic arc at a time"

Jessica M.J. Walsh[1], Solomon Buckman[1], Allen Nutman[1], and Renjie Zhou[2]

[1]GeoQuEST Research Centre, School of Earth, Atmospheric and Life Sciences, University of Wollongong, NSW 2522, Australia. [2]School of Earth and Environmental Sciences, University of Queensland, Brisbane, QLD 4067, Australia.

Theme: Rapid *Fire Session – Early Career Earth Scientists*

There's no geological artist quite like Earth's inferno, responsible for dynamic plate tectonics. When continents collide, mountain ranges like the Himalaya rise. This process is not simple and often other features are caught in the collision zone.

We all know the old joke about how the only things that could survive a nuclear apocalypse would be Big Macs and cockroaches. Now, if we turn to the inorganic world of minerals and apply a similar logic – what is abundant, near-indestructible and persistent? My answer would be 'zircon'. Zircon is a type of mineral found in many rocks, where if you compare a rock to a cake, minerals are the ingredients. They first form in molten rock or magma with high proportions of the elements: zirconium, silica and uranium, which we analyse to establish an isotopic age. Zircons are incredibly durable and resistant to chemical attack; these robust little grains no larger than sand can withstand the tests of geological time, surviving erosion, transport and even extreme pressure-temperature conditions, known as high-grade metamorphism. Amazingly, these minerals have growth bands similar to tree rings, which record the different conditions under which they formed. Zircons are used to date igneous and metamorphic rocks across the globe including the oldest minerals on Earth at 4.4 Ga from Jack Hills in WA, which are only just younger than the meteorites that coalesced to form Earth some 4.5 Ga.

Like a tiny time-capsule, zircon can record momentous geological events which occurred millions if not billions of years ago. Here's where my research comes in. I study rocks from the highest mountain range on earth, the Himalaya. I collect rocks and bring them back to the lab. Like reverse engineering a cake, the ingredients are divided out – in other words, the minerals

are separated. What I specifically look at are what's called detrital zircons in sedimentary rocks. These are derived from the weathering and erosion of surrounding rocks and tell us about the age and nature of the source rocks at the time of deposition. In some cases, they are the only remaining evidence of once vast ocean basins like the Tethys Ocean that separated Gondwana from Eurasia. The tricky part is that like cockroaches, zircons are incredibly abundant. On the mountain range scale two or more infestations of detrital zircons from different origins may deposit within the same topographic low. Therefore, determining the original source of the zircon grains can be complicated. The Himalaya indisputably formed due to the collision of India into Eurasia. What isn't well understood and what my research aims to provide clarity on, is what happened before this continent-continent collision.

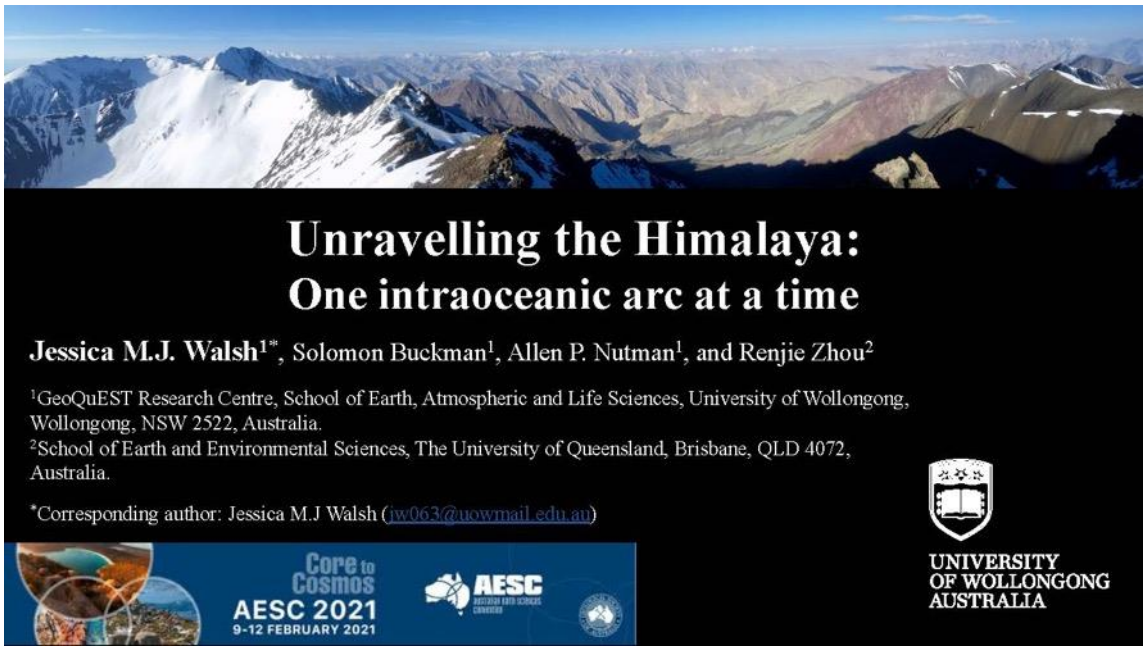

A2 American Geophysical Union (AGU) Fall Meeting. Virtual Conference. December 2020. Abstract number: T029-06. Oral presentation.

"Upper Jurassic adakitic felsic volcanism within the incipient, intraoceanic Dras Arc, Ladakh, NW Himalaya"

Jessica M.J. Walsh[1], Solomon Buckman[1], Allen Nutman[1], and Renjie Zhou[2]

[1]GeoQuEST Research Centre, School of Earth, Atmospheric and Life Sciences, University of Wollongong, NSW 2522, Australia.[2]School of Earth and Environmental Sciences, University of Queensland, Brisbane, QLD 4067, Australia.

The Dras Arc is an island arc terrane located along the Indus Suture within the Ladakh Himalaya. To the north it is juxtaposed against the Eurasian Ladakh Batholith and to the south it is thrust over the Lamayuru Complex and Indian passive margin. Establishing the timing of inception and final collision of the Dras Arc is imperative to reconstructions of the Neotethyan Ocean and timing of arc-continent collisions, prior to the terminal India-Asia continental collision. We describe and date felsic tuffs and adakitic felsic volcanic rock interbedded within the dominantly basaltic-andesitic Dras volcanic complex. These felsic volcanic units yield Upper Jurassic zircon U-Pb ages of 160 ± 3 and 156 ± 1 Ma respectively, making these the oldest reported units within the Dras Arc. We also report zircon U-Pb geochronologic and whole rock geochemical results for the Kargil Intrusives which intrudes the volcanic complex. Previous ages for the intrusives have been reproduced (102 ± 2 Ma and 101 ± 2 Ma), and a second, much younger phase (80 ± 1 Ma) has been identified as one of the youngest igneous phases within the Dras Arc.

The presence of felsic, adakitic volcanism early in the evolution of the Dras Arc is consistent with the adolescent stages of island arc systems, in which dehydration melting of underplated arc or subducted oceanic crust generates small volumes of felsic magmas. Thus, the intraoceanic Dras Arc initiated in the Neotethyan Ocean during the Upper Jurassic, much earlier than previously reported, and possibly was active right up to collision during the late Palaeocene between 60-50 Ma. It is likely that the Dras Arc developed together with the Spongtang Ophiolite-Spong Arc complex and the intraoceanic Zedong terrane of Tibet, before first colliding and accreting onto the passive margin of India, prior to the terminal continental collision.

A3 Dorothy Hill Women in Earth Sciences Symposium, Brisbane, Australia. November 2019. Abstract number: DHS19-27. Poster presentation.

"Age and provenance of the Nindam Formation, Ladakh, NW Himalaya: Evolution of the intraoceanic Dras Arc before collision with India"

Jessica M.J. Walsh[1], Solomon Buckman[1], Allen Nutman[1], and Renjie Zhou[2]

[1]GeoQuEST Research Centre, School of Earth, Atmospheric and Life Sciences, University of Wollongong, NSW 2522, Australia. [2]School of Earth and Environmental Sciences, University of Queensland, Brisbane, QLD 4067, Australia.

The Dras Arc in NW India Himalaya is a belt of basaltic-andesites intercalated with volcaniclastic rocks of the Nindam Formation situated along the Indus Suture between India and Eurasia. Debates exist as to whether these rocks developed in a forearc basin to the Eurasian margin or as part of an intraoceanic island arc system that collided with either India or Eurasia before final continental collision. Detrital zircons from the Nindam Formation yield age spectra with dominant youngest age populations of ~84-125 Ma, corresponding with arc magmatism. Slightly older, smaller populations occur at ~135-185 Ma, corresponding with reported ages of Neotethyan ophiolites (e.g., Spongtang). A distinct "Gondwanan" signature also occurs in all samples. The basal section of the Nindam Formation reveals the presence to the andesite and tonalite clasts, plus ophiolitic components. There is a distinct absence of quartz or felsic granitic clasts, suggesting that the Nindam Formation did not develop as a forearc basin to the Ladakh Batholith, but rather as a separate intraoceanic island arc. We suggest that the Dras and Spong arcs are the same intraoceanic island arc system that developed as a result of subduction initiation along NNE-SSW transform faults perpendicular to the Indian and Eurasia continents.

AGE AND PROVENANCE OF THE NINDAM FORMATION, LADAKH, NW HIMALAYA: EVOLUTION OF THE INTRAOCEANIC DRAS ARC BEFORE COLLISION WITH INDIA

Walsh, Jessica M.J.,[1] Buckman, Solomon.,[1] Nutman, Allen P., and[2] Zhou, Renjie.

[1] GeoQuEST Research Centre, School of Earth, Atmosphere and Life Sciences, University of Wollongong, NSW
[2] School of Earth and Environmental Sciences, The University of Queensland, Brisbane, QLD

1. Abstract

TOPIC:
The Dras Arc in the Ladakh Himalaya, NW India, is a belt of basaltic-andesites intercalated with forearc volcaniclastic rocks of the Nindam Formation. Collectively, these form the Dras-Nindam terrane and are situated along the Indus Suture between India and Eurasia.

PROBLEM:
The provenance and age range of the Dras-Nindam terrane is not well constrained. THUS its development as either a forearc basin to the Eurasian margin or as an intraoceanic island arc remains ambiguous.

AIMS:
(i) To determine the age of the Dras-Nindam terrane
(ii) To determine the provenance of the forearc Nindam Formation.
(iii) To 'test' competing hypotheses regarding the tectonic setting, evolution and collisional history of the Dras Arc.

2. Methods

To address the debate surrounding the Dras-Nindam terrane, integrated methods were used:

3. Field Relations

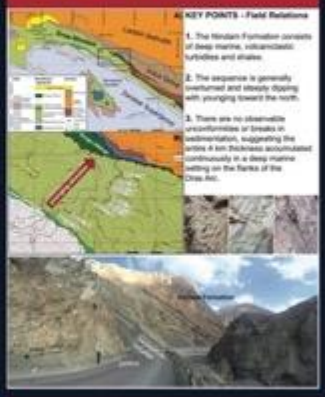

4. Petrology

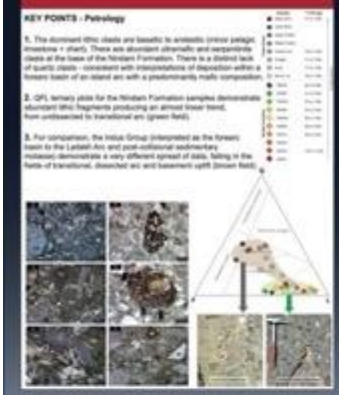

5. Geochemistry

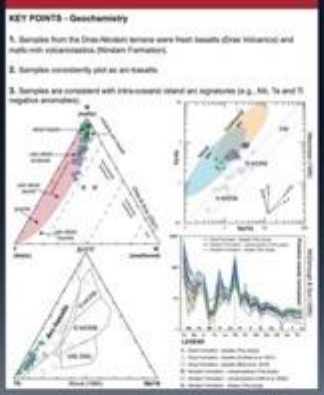

6. Geochronology

7. Tectonic Implications

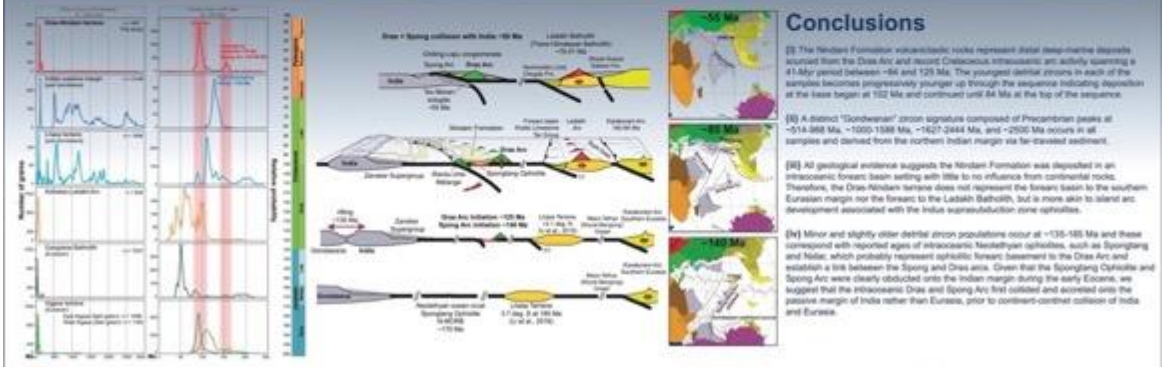

Conclusions

(i) The Nindam Formation volcaniclastic rocks represent distal deep-marine deposits sourced from the Dras Arc and record Cretaceous intraoceanic arc activity spanning a 41-Myr period between ~84 and 125 Ma. The youngest detrital zircons in each of the samples becomes progressively younger up through the sequence indicating deposition at the base began at 152 Ma and continued until 84 Ma at the top of the sequence.

(ii) A distinct "Gondwanan" zircon signature composed of Precambrian peaks at ~514-968 Ma, ~1000-1588 Ma, ~1627-2444 Ma, and ~2500 Ma occurs in all samples and derived from the northern Indian margin via far-traveled sediment.

(iii) All geological evidence suggests the Nindam Formation was deposited in an intraoceanic forearc basin setting with little to no influence from continental rocks. Therefore, the Dras-Nindam terrane does not represent the forearc basin to the southern Eurasian margin nor the forearc to the Ladakh Batholith, but is more akin to island arc development associated with the Indus supraubduction zone ophiolites.

(iv) Minor and slightly older detrital zircon populations occur at ~135-185 Ma and these correspond with reported ages of intraoceanic Neotethyan ophiolites, such as Spongtang and Nidar, which probably represent ophiolitic forearc basement to the Dras Arc and establish a link between the Spong and Dras arcs. Given that the Spongtang Ophiolite and Spong Arc were clearly obducted onto the Indian margin during the early Eocene, we suggest that the intraoceanic Dras and Spong Arc first collided and accreted onto the passive margin of India rather than Eurasia, prior to continent-continet collision of India and Eurasia.

Correspondence: **Jessica Walsh**
Email: jw063@uowmail.edu.au
Twitter: @__JessicaWalsh

Citation: Walsh, J.M.J., Buckman, S., Nutman, A.P., & Zhou, R. (2019). Age and provenance of the Nindam Formation, Ladakh, NW Himalaya: Evolution of the intraoceanic Dras Arc before collision with India. *Tectonics, 38.*

GeoQuEST Research Centre

UNIVERSITY OF WOLLONGONG AUSTRALIA

A4 European Geosciences Union (EGU) General Assembly, Vienna, Austria. April 2019. Abstract number: EGU2019-413. Oral presentation.

"Age and provenance of the Dras Arc, Ladakh, NW Himalaya:
A detrital zircon record of the Nindam Formation"

Jessica M.J. Walsh[1], Solomon Buckman[1], Allen Nutman[1], and Renjie Zhou[2]

[1]GeoQuEST Research Centre, School of Earth, Atmospheric and Life Sciences, University of Wollongong, NSW 2522, Australia. [2]School of Earth and Environmental Sciences, University of Queensland, Brisbane, QLD 4067, Australia.

Many aspects of the Himalaya Orogen remain unresolved, including the timing of final "hard" continent-continent collision and the nature of earlier "soft" collisions involving intraoceanic arcs with either India or Eurasia. The Dras Arc in NW India is a distinct belt of basaltic-andesites and calci-volcaniclastic rocks (Nindam Formation) situated along the Indus Suture. Debates exist as to whether it developed as the forearc basin to the Eurasian margin or as a purely intraoceanic island arc that may have collided with either India or Eurasia before final continental collision. Detrital zircons from the Nindam Formation volcaniclastic rocks yield U-Pb age spectra with a dominant youngest age population of ~120-84 Ma corresponding with arc magmatism. The youngest detrital zircons in each of the samples becomes progressively younger up through the sequence indicating deposition at the base began at about 100 Ma and continued until ~84 Ma at the top of the sequence. Smaller and slightly older peaks occur at ~135 Ma and ~150-185 Ma and these correspond with reported ages of Neotethyan ophiolites such as Spongtang and Nidar. An ophiolitic source is reflected by the presence of abundant ophiolitic serpentinite and tonalitic clasts near the base and throughout the Nindam Formation, while granitic clasts sourced from the Ladakh/Karakoram batholiths are completely absent, which suggests that the Nindam Formation did not develop as a forearc basin to the Ladakh Arc of southern Eurasia but rather a separate intraoceanic island arc. A distinct "Gondwanan" signature comprised of Precambrian peaks at ~500 Ma, 800-1300 Ma, 1700-2000 and ~2500 Ma occurs in all samples. Gondwanan source rocks occur either side of the Neotethyan Ocean during the Cretaceous as the Lhasa terrane to the north and India to the south so either of these peri-Gondwanan blocks could've shed sediment that was transported as submarine fans into the trench associated with the Dras Arc. Sandstone provenance analysis indicates that the Nindam Formation evolved from an undissected arc to dissected arc over a period of ~15 Ma. The Nindam Formation is distinctly different to the more quartz-rich sediments of the coeval Tar Group and post-collisional Indus

Group which have a distinct Eurasian (Ladakh and Karakoram arc) source. We interpret the Nindam Formation to represent the fore arc basin to the Dras Arc which first collided and accreted onto the passive margin of India prior to “hard” continent- continent collision of India and Eurasia. Link available here.

A5 American Geophysical Union (AGU) Fall Meeting. New Orleans, Louisiana, USA. December 2017. Abstract number: T43E-02. Oral presentation.

"The Age, Origin and Collision of the Spongtang Ophiolite, Ladakh Himalaya"

Solomon Buckman[1], Jonathan C Aitchison[2], Allen P. Nutman[1], Vickie C Bennett[3], **Jessica M.J. Walsh[1]**, Wanchese M Saktura[1], Sarah Kachovich[1] and Lauren Langlois[1]

[1]GeoQuEST Research Centre, School of Earth, Atmospheric and Life Sciences, University of Wollongong, NSW 2522, Australia. [2]School of Earth and Environmental Sciences, University of Queensland, Brisbane, QLD 4067, Australia.[3]Research School of Earth Sciences, Australian National University, Canberra, ACT 2600, Australia

The Spongtang Ophiolite in Ladakh Himalaya was the first fragment of the Neotethyan Ocean to collide with India before the final India-Asia continental collision. However, its age, origin and timing of obduction are yet to be fully established which restricts our understanding of the evolution of the Indus Suture and India-Asia collision. The Spongtang Ophiolite consists of a flat lying klippe of oceanic crust that sits structurally above the Cretaceous to Eocene Indian passive margin Zanskar Group. Previously, only one isotopic U-Pb (SIMS) date (177±1 Ma) has been obtained from the gabbro. Radiolarians from red cherts are Early Cretaceous (mid-Valanginian–mid-Aptian range). Andesites in the overlying Spong Arc volcanic rocks yield younger Cretaceous age (88±5 Ma), which is interpreted by some to constrain the age of obduction onto India as late Cretaceous. However, early reports of possible Eocene radiolarian assemblages within black cherty shales of the underlying Chulung La Formation (Kong slate), constrains the obduction age to Eocene rather than Cretaceous. Recent detrital zircon studies of the Kong and Chulung La formations found that the youngest detrital zircon age is ~53 Ma establishing this as the maximum depositional age. The Indian margin must have received detrital zircons from the intraoceanic Spong Arc up until ~53 Ma suggesting collision of these two elements didn't occur until Eocene, or that these units are post-collisional. This study involved zircon U- Pb SHRIMP dating of gabbro which reveal an Early Cretaceous age (~135 Ma) in contrast to previously established Middle Jurassic age, and strongly positive εHf values of +14 to +16 indicating intraoceanic origins. We also report newly discovered garnet bearing, amphibolitised metasediments (metamorphic sole) of the Indian Zanskar Supergroup structurally underlying the ophiolite which may provide the key to establishing timing of ophiolite obduction and refine models regarding the timing and nature of collision between India and Asia. Link available here.

Plain-Language Summary:

A fundamental observation of Earth's crust is that it is composed of either continental or oceanic crust. While continental crust is readily observed, oceanic crust is denser and lies beneath deep oceans or is recycled back into the mantle via subduction processes. Fragments of oceanic crust, called "ophiolites" are sometimes preserved in mountain zones marking the collision of continents. These ophiolites are important because they are the only record of once, vast ocean basins, such as the Neotethyan Ocean, that separated India from Asia. Establishing the age of these ophiolites and the timing of emplacement on continental margins is critical to making accurate plate tectonic reconstructions which help us understand the processes involved in continental growth. The Himalaya is an ongoing, slow motion, collision between two continents but the timing of initiation of this collision is a topic of much debate. Our work concentrates on establishing the age of the Spongtang Ophiolite in Ladakh and metamorphosed Indian crustal rocks involved in the initial collision of the ophiolite with India.

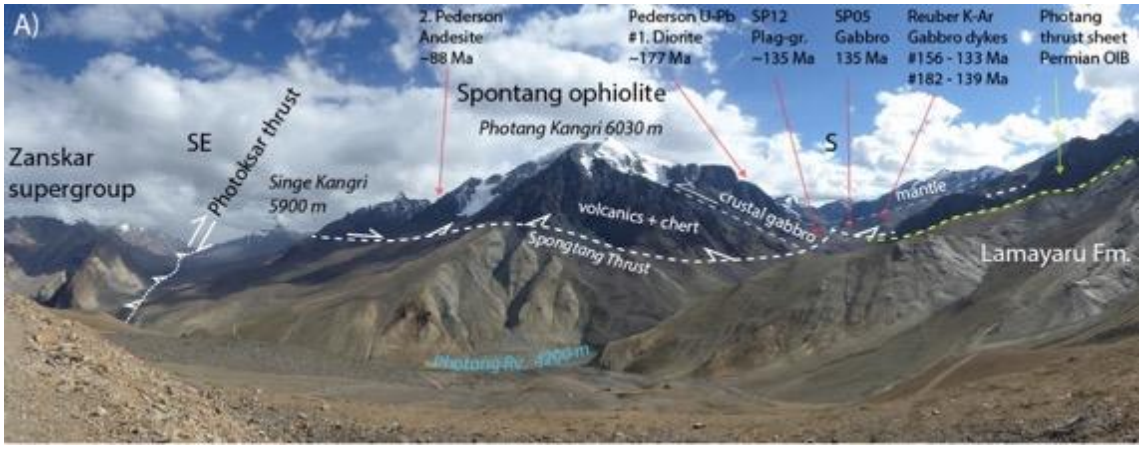

A6 Dorothy Hill Women in Earth Sciences Symposium, Brisbane, Australia. November 2017. Abstract number: DHS17-12. Poster presentation.

"Tectonic evolution of the Dras-Nindam terrane along the Indus Suture Zone, Ladakh Himalaya, NW India"

Jessica M.J. Walsh[1], Solomon Buckman[1] and Allen Nutman[1]

[1]GeoQuEST Research Centre, School of Earth, Atmospheric and Life Sciences, University of Wollongong, NSW 2522, Australia.

The Himalaya is the largest active orogen on the face of the Earth; as such it provides an ideal natural laboratory for the study of global tectonics and mountain building processes. It represents ongoing continent-continent collision between India and Eurasia, resulting from the closure of the vast Tethyan Ocean. This dramatic geological feature is used as the textbook example for continental-collision and resultant orogenesis, elevating mountain belts and by and large being the main contributor to continental growth. The overarching aim of this project is to test competing hypotheses regarding the tectonic evolution of the Dras-Nindam terrane that occurs along the Indus suture zone of the India-Eurasia collision in Ladakh Himalaya, NW India. There is general consensus that the basaltic-andesitic volcanic rocks of the Dras Arc are of island arc affinity and these volcanic rocks are overlain by deep marine volcaniclastic conglomerates, turbidites, cherts, siltstones and tuffs of the Nindam Formation. Island arc terranes are important features to recognise in orogens as they host many of the world's largest porphyry Cu-Au-Mo deposits, for example, the porphyry Cu-Au systems of the Macquarie Arc in the Lachlan Orogen.

Early interpretations of the Dras-Nindam units suggested this island arc evolved throughout the Jurassic to Cretaceous in a forearc region of a convergent margin on the southern margin of Eurasia in front of the Ladakh Arc as part of a single subduction complex responsible for the consumption of the entire Neotethyan Ocean before the onset of the India-Eurasia continent-continent collision. However, other researchers noted the juvenile, intraoceanic nature of the Dras-Nindam terrane and invoked multiple north-dipping subduction zones to explain the coeval development of the intraoceanic Dras-Nindam with the more continental Trans-Himalayan Arc, also known as the Ladakh Arc. Radiolarians extracted from cherts collected from two related ophiolitic mélange zones near the townships of Wanlah and Urtsi, Ladakh, NW India have well-preserved tests and can be assigned broadly as Cretaceous in age. These are the first well-preserved and clearly imaged radiolarians from these mélange zones. They are significantly older

than fossils previously reported for this mélange which has greatly assisted in refining the timing of deep-water sedimentation in the Neotethyan Ocean and therefore better constrains the timing of oceanic crust, intraoceanic island arc and subduction complex generation.

[1] GeoQuEST Research Center, School of Earth and Environmental Sciences, University of Wollongong
[2] Research School of Earth Sciences, Australian National University

TECTONIC EVOLUTION OF THE DRAS-NINDAM TERRANE ALONG THE INDUS SUTURE ZONE, LADAKH HIMALAYA, NW INDIA

Jessica Walsh[1], Solomon Buckman[1], Allen Nutman[1], Vicki Bennett[2]

UNIVERSITY OF WOLLONGONG AUSTRALIA

Aim

The overarching aim of this investigation is to test competing hypotheses regarding the tectonic evolution of the Dras-Nindam terrane that occurs along the Indus Suture Zone of the India-Asia collision in the Ladakh Himalaya, NW India.

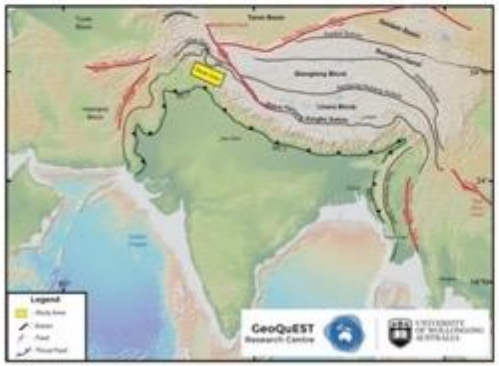

Background

The provenance and age range of the Dras-Nindam terrane is not well constrained and thus its development as either a juvenile, intra-oceanic island arc or a marginal fore-arc basin to southern Eurasia remains ambiguous. Its collision with either Eurasia or India before final continent-continent collision also is not clear leading to multiple, conflicting tectonic reconstructions that require further testing. Constraining the age of accreted Neo-Tethys ocean crust via radiolarian and conodont biostratigraphy of chert blocks within the Wanla-Urtsi mélange between the Dras-Nindam terrane and the India Lamayuru Complex is a crucial aspect of this investigation.

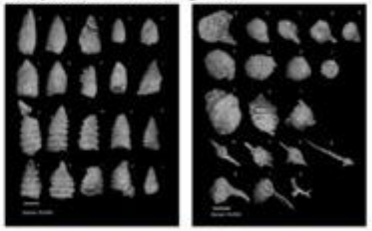

Field Context

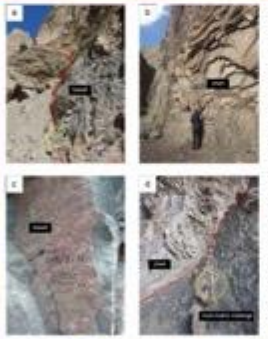

Featured here is the Wanlah-Urtsti mélange of Ladakh, NW India. Mélange zones are integral to tectonic reconstructions because they are a mixture of all crustal elements involved in subduction and subsequent collision and often include ophiolitic fragments of gabbro-basalt-chert scraped off the subducting plate (Neo-Tethys Ocean) as well as blocks of the overriding island arc (Dras-Nindam terrane) and the continental crust onto which the intra-oceanic terrane was emplaced (India or Asia).

U O W

Appendix B: Coauthor contribution framework following 'Contributor Roles Taxonomy' (CRediT)

Table B1: Contributor Roles Taxonomy (CRediT)

Term	Definition
Conceptualisation	Ideas, formulation, or evolution of overarching research goals and aims.
Methodology	Development or design of methodology; creation of models.
Software	Programming, software development; designing computer programs; implementation of the computer code and supporting algorithms; testing of existing code components.
Validation	Verification, whether as a part of the activity or separate, of the overall replication/reproducibility of results/experiments and other research outputs.
Formal analysis	Application of statistical, mathematical, computational, or other formal techniques to analyse or synthesize study data.
Investigation	Conducting a research and investigation process, specifically performing the experiments, or data/evidence collection.
Resources	Provision of study materials, reagents, materials, patients, laboratory samples, animals, instrumentation, computing resources, or other analysis tools.
Data curation	Management activities to annotate (produce metadata), scrub data and maintain research data (including software code, where it is necessary for interpreting the data itself) for initial use and later re-use.
Writing – original draft	Preparation, creation and/or presentation of the published work, specifically writing the initial draft (including substantive translation).
Writing – review and editing	Preparation, creation and/or presentation of the published work by those from the original research group, specifically critical review, commentary, or revision – including pre- or post-publication stages.
Visualisation	Preparation, creation and/or presentation of the published work, specifically visualisation/data presentation.
Supervision	Oversight and leadership responsibility for the research activity planning and execution, including mentorship external to the core team.
Project administration	Management and coordination responsibility for the research activity planning and execution.
Funding acquisition	Acquisition of the financial support for the project leading to this publication.

Note: Reproduced from Allen et al. (2019).

References

Acton, G. D., 1999, Apparent polar wander of India since the Cretaceous with implications for regional tectonics and true polar wander: Mem. Geol. Soc. India, v. 44, p. 129-175.

Ahmad, T., Tanaka, T., Sachan, H., Asahara, Y., Islam, R., and Khanna, P., 2008, Geochemical and isotopic constraints on the age and origin of the Nidar Ophiolitic Complex, Ladakh, India: implications for the Neo-Tethyan subduction along the Indus suture zone: Tectonophysics, v. 451, no. 1-4, p. 206-224.

Ahmed, A., Kakar, M. I., Naeem, A., Ahmed, N., Khan, M., and Panezai, M., 2020, Geology and Petrology of Omzha Block, Zhob Ophiolite, northern Balochistan, Pakistan: Pakistan Journal of Geology, v. 1, no. ahead-of-print.

Ahmed, Z., 1993, Leucocratic rocks from the Bela ophiolite, Khuzdar district, Pakistan: Geological Society, London, Special Publications, v. 74, no. 1, p. 89-100.

Aitchison, J. C., Ali, J. R., and Davis, A. M., 2007a, When and where did India and Asia collide?: Journal of Geophysical Research: Solid Earth, v. 112, no. B5.

Aitchison, J., McDermid, I., Ali, J., Davis, A., and Zyabrev, S., 2007b, Shoshonites in southern Tibet record Late Jurassic rifting of a Tethyan intraoceanic island arc: The Journal of geology, v. 115, no. 2, p. 197-213.

Aitchison, J. C., and Buckman, S., 2012, Accordion vs. quantum tectonics: Insights into continental growth processes from the Paleozoic of eastern Gondwana: Gondwana Research, v. 22, no. 2, p. 674-680.

Aitchison, J. C., and Davis, A. M., 2004, Evidence for the multiphase nature of the India-Asia collision from the Yarlung Tsangpo suture zone, Tibet: Geological Society, London, Special Publications, v. 226, no. 1, p. 217-233.

Aitchison, J. C., Davis, A. M., Abrajevitch, A. V., Ali, J. R., Liu, J., Luo, H., McDermid, I. R., and Ziabrev, S. V., 2003, Stratigraphic and sedimentological constraints on the age and tectonic evolution of the Neotethyan ophiolites along the Yarlung Tsangpo suture zone, Tibet: Geological Society, London, Special Publications, v. 218, no. 1, p. 147-164.

Aitchison, J. C., Davis, A. M., Liu, J., Luo, H., Malpas, J. G., McDermid, I. R., Wu, H., Ziabrev, S. V., and Zhou, M.-f., 2000, Remnants of a Cretaceous intra-oceanic subduction system

within the Yarlung–Zangbo suture (southern Tibet): Earth and Planetary Science Letters, v. 183, no. 1, p. 231-244.

Aitchison, J. C., Davis, A. M., and Luo, H., 2002, New constraints on the India–Asia collision: the lower Miocene Gangrinboche conglomerates, Yarlung Tsangpo suture zone, SE Tibet: Journal of Asian Earth Sciences, v. 21, no. 3, p. 251-263.

Aitchison, J. C., Xia, X., Baxter, A. T., and Ali, J. R., 2011, Detrital zircon U–Pb ages along the Yarlung-Tsangpo suture zone, Tibet: implications for oblique convergence and collision between India and Asia: Gondwana Research, v. 20, no. 4, p. 691-709.

Ali, S. A., Nutman, A. P., Aswad, K. J., and Jones, B. G., 2019, Overview of the tectonic evolution of the Iraqi Zagros thrust zone: Sixty million years of Neotethyan ocean subduction: Journal of Geodynamics.

Allègre, C., Courtillot, V., Tapponnier, P., Hirn, A., Mattauer, M., Coulon, C., Jaeger, J., Achache, J., Schaerer, U., and Marcoux, J., 1984, Structure and evolution of the Himalaya–Tibet orogenic belt: Nature, v. 307, no. 5946, p. 17.

Allen, L., O'Connell, A., and Kiermer, V., 2019, How can we ensure visibility and diversity in research contributions? How the Contributor Role Taxonomy (CRediT) is helping the shift from authorship to contributorship: Learned Publishing, v. 32, no. 1, p. 71-74.

Amato, J. M., and Pavlis, T. L., 2010, Detrital zircon ages from the Chugach terrane, southern Alaska, reveal multiple episodes of accretion and erosion in a subduction complex: Geology, v. 38, no. 5, p. 459-462.

An, W., Hu, X., Garzanti, E., BouDagher-Fadel, M. K., Wang, J., and Sun, G., 2014, Xigaze forearc basin revisited (South Tibet): Provenance changes and origin of the Xigaze Ophiolite: Bulletin, v. 126, no. 11-12, p. 1595-1613.

Arth, J. G., and Hanson, G. N., 1972, Quartz diorites derived by partial melting of eclogite or amphibolite at mantle depths: Contributions to Mineralogy and Petrology, v. 37, no. 2, p. 161-174.

Bas, M. L., Maitre, R. L., Streckeisen, A., and Zanettin, B., 1986, A chemical classification of volcanic rocks based on the total alkali-silica diagram: Journal of petrology, v. 27, no. 3, p. 745-750.

Bassoullet, J., Colchen, M., Marcoux, J., and Mascle, G., 1981, Les masses calcaires du flysch Triasico-Jurassique de Lamayuru (zone de la suture de L'Indus, Himalaya du Ladakh): klippes sédimentaires et élements de plate-forme rémanies: Rivista Italiana di Paleontologia e Stratigrafia, v. 86, no. 4, p. 825-844.

Baxter, A. T., Aitchison, J. C., Ali, J. R., Chan, J. S.-L., and Chan, G. H. N., 2016, Detrital chrome spinel evidence for a Neotethyan intra-oceanic island arc collision with India in the Paleocene: Journal of Asian Earth Sciences, v. 128, p. 90-104.

Baxter, A. T., Aitchison, J. C., Ali, J. R., and Zyabrev, S. V., 2010, Early Cretaceous radiolarians from the Spongtang massif, Ladakh, NW India: implications for Neo-Tethyan evolution: Journal of the Geological Society, v. 167, no. 3, p. 511-517.

Bhat, I. M., Ahmad, T., and Rao, D. S., 2019, The tectonic evolution of the Dras arc complex along the Indus Suture Zone, western Himalaya: Implications for the Neo-Tethys Ocean geodynamics: Journal of Geodynamics, v. 124, p. 52-66.

Bhattacharya, G., Robinson, D. M., and Wielicki, M. M., 2020, Detrital zircon provenance of the Indus Group, Ladakh, NW India: Implications for the timing of the India-Asia collision and other syn-orogenic processes: GSA Bulletin.

Bhutani, R., Pande, K., and Venkatesan, T., 2009, ^{40}Ar–^{39}Ar dating of volcanic rocks of the Shyok suture zone in north–west trans-Himalaya: Implications for the post-collision evolution of the Shyok suture zone: Journal of Asian Earth Sciences, v. 34, no. 2, p. 168-177.

Bilqees, R., Qasim Jan, M., Asif Khan, M., and Windley, B. F., 2016, Silicate-oxide mineral chemistry of mafic–ultramafic rocks as an indicator of the roots of an island arc: The Chilas Complex, Kohistan (Pakistan): Island Arc, v. 25, no. 1, p. 4-27.

Black, L. P., Kamo, S. L., Allen, C. M., Davis, D. W., Aleinikoff, J. N., Valley, J. W., Mundil, R., Campbell, I. H., Korsch, R. J., and Williams, I. S., 2004, Improved $^{206}Pb/^{238}U$ microprobe geochronology by the monitoring of a trace-element-related matrix effect; SHRIMP, ID–TIMS, ELA–ICP–MS and oxygen isotope documentation for a series of zircon standards: Chemical Geology, v. 205, no. 1-2, p. 115-140.

Bloomer, S. H., Taylor, B., Macleod, C. J., Stern, R. J., Fryer, P., Hawkins, J. W., and Johnson, L., 1995, Early arc volcanism and the ophiolite problem: a perspective from drilling in the western Pacific: Active margins and marginal basins of the western Pacific, v. 88, p. 1-30.

Borneman, N. L., Hodges, K. V., Van Soest, M. C., Bohon, W., Wartho, J. A., Cronk, S. S., and Ahmad, T., 2015, Age and structure of the Shyok suture in the Ladakh region of northwestern India: implications for slip on the Karakoram fault system: Tectonics, v. 34, no. 10, p. 2011-2033.

Bosch, D., Garrido, C. J., Bruguier, O., Dhuime, B., Bodinier, J.-L., Padròn-Navarta, J. A., and Galland, B., 2011, Building an island-arc crustal section: time constraints from a LA-ICP-MS zircon study: Earth and Planetary Science Letters, v. 309, no. 3-4, p. 268-279.

Bouilhol, P., Jagoutz, O., Hanchar, J. M., and Dudas, F. O., 2013, Dating the India–Eurasia collision through arc magmatic records: Earth and Planetary Science Letters, v. 366, p. 163-175.

Bouilhol, P., Schaltegger, U., Chiaradia, M., Ovtcharova, M., Stracke, A., Burg, J.-P., and Dawood, H., 2011, Timing of juvenile arc crust formation and evolution in the Sapat Complex (Kohistan–Pakistan): Chemical Geology, v. 280, no. 3-4, p. 243-256.

Brookfield, M., and Reynolds, P., 1981, Late Cretaceous emplacement of the Indus suture zone ophiolitic mélanges and an Eocene-Oligocene magmatic arc on the northern edge of the Indian plate: Earth and Planetary Science Letters, v. 55, no. 1, p. 157-162.

Brookfield, M. E., and Andrews-Speed, C. P., 1984, Sedimentology, petrography and tectonic significance of the shelf, flysch and molasse clastic deposits across the Indus Suture Zone, Ladakh, NW India: Sedimentary Geology, v. 40, no. 4, p. 249-286.

Buckman, S., Aitchison, J. C., Nutman, A. P., Bennett, V. C., Saktura, W. M., Walsh, J. M., Kachovich, S., and Hidaka, H., 2018, The Spongtang Massif in Ladakh, NW Himalaya: an Early Cretaceous record of spontaneous, intra-oceanic subduction initiation in the Neotethys: Gondwana Research, v. 63, p. 226-249.

Burg, J., Bodinier, J., Chaudhry, S., Hussain, S., and Dawood, H., 1998, Infra-arc mantle-crust transition and intra-arc mantle diapirs in the Kohistan Complex (Pakistani Himalaya): petro-structural evidence: Terra Nova-Oxford, v. 10, no. 2, p. 74-80.

Burg, J.-P., 2011, The Asia–Kohistan–India collision: review and discussion, Arc-continent collision, Springer, p. 279-309.

Carr, M. J., and Gazel, E., 2017, Igpet software for modeling igneous processes: examples of application using the open educational version: Mineralogy and Petrology, v. 111, no. 2, p. 283-289.

Castillo, P. R., 2012, Adakite petrogenesis: Lithos, v. 134, p. 304-316.

Cawood, P. A., and Buchan, C., 2007, Linking accretionary orogenesis with supercontinent assembly: Earth-Science Reviews, v. 82, no. 3-4, p. 217-256.

Cawood, P. A., Johnson, M. R., and Nemchin, A. A., 2007, Early Palaeozoic orogenesis along the Indian margin of Gondwana: Tectonic response to Gondwana assembly: Earth and Planetary Science Letters, v. 255, no. 1-2, p. 70-84.

Chan, G. H. N., Aitchison, J. C., Crowley, Q. G., Horstwood, M. S., Searle, M. P., Parrish, R. R., and Chan, J. S.-L., 2015, U–Pb zircon ages for Yarlung Tsangpo suture zone ophiolites, southwestern Tibet and their tectonic implications: Gondwana Research, v. 27, no. 2, p. 719-732.

Chang, C., and Zheng, X., 1973, Tectonic features of the mount Jolmo Lungma region in southern Tibet, China: Chinese Journal of Geology, v. 1, p. 1-12.

Charvet, J., 2013, Late Paleozoic–Mesozoic tectonic evolution of SW Japan: A review–Reappraisal of the accretionary orogeny and revalidation of the collisional model: Journal of Asian Earth Sciences, v. 72, p. 88-101.

Cherchi, A., Gupta, V. J., & Schroeder, R., 1984, Late Aptian calcareous algae and larger foraminifera from Khalsi, Ladakh, India. *Bull Ind Geol Assoc*, *17*, 145-157.

Condie, K.C., 2015. *Earth as an evolving planetary system*. Academic Press

Chu, M.-F., Chung, S.-L., Song, B., Liu, D., O'Reilly, S. Y., Pearson, N. J., Ji, J., and Wen, D.-J., 2006, Zircon U-Pb and Hf isotope constraints on the Mesozoic tectonics and crustal evolution of southern Tibet: Geology, v. 34, no. 9, p. 745-748.

Clift, P., Degnan, P., Hannigan, R., and Blusztajn, J., 2000, Sedimentary and geochemical evolution of the Dras forearc basin, Indus suture, Ladakh Himalaya, India: Geological Society of America Bulletin, v. 112, no. 3, p. 450-466.

Clift, P. D., Carter, A., and Jonell, T. N., 2014, U–Pb dating of detrital zircon grains in the Paleocene Stumpata Formation, Tethyan Himalaya, Zanskar, India: Journal of Asian Earth Sciences, v. 82, p. 80-89.

Clift, P. D., Carter, A., Krol, M., and Kirby, E., 2002a, Constraints on India-Eurasia collision in the Arabian sea region taken from the Indus Group, Ladakh Himalaya, India: Geological Society, London, Special Publications, v. 195, no. 1, p. 97-116.

Clift, P. D., Hannigan, R., Blusztajn, J., and Draut, A. E., 2002b, Geochemical evolution of the Dras–Kohistan Arc during collision with Eurasia: evidence from the Ladakh Himalaya, India: Island Arc, v. 11, no. 4, p. 255-273.

Clift, P. D., Shimizu, N., Layne, G. D., and Blusztajn, J., 2001, Tracing patterns of erosion and drainage in the Paleogene Himalaya through ion probe Pb isotope analysis of detrital K-feldspars in the Indus Molasse, India: Earth and Planetary Science Letters, v. 188, no. 3, p. 475-491.

Cloos, M., 1993, Lithospheric buoyancy and collisional orogenesis: Subduction of oceanic plateaus, continental margins, island arcs, spreading ridges, and seamounts: Geological Society of America Bulletin, v. 105, no. 6, p. 715-737.

Compston, W., and Pidgeon, R., 1986, Jack Hills, evidence of more very old detrital zircons in Western Australia: Nature, v. 321, no. 6072, p. 766.

Coney, P. J., 1989, Structural aspects of suspect terranes and accretionary tectonics in western North America: Journal of Structural Geology, v. 11, no. 1-2, p. 107-125.

Copley, A., Avouac, J. P., and Royer, J. Y., 2010, India-Asia collision and the Cenozoic slowdown of the Indian plate: Implications for the forces driving plate motions: Journal of Geophysical Research: Solid Earth, v. 115, no. B3.

Corfield, R., and Searle, M., 2000, Crustal shortening estimates across the north Indian continental margin, Ladakh, NW India: Geological Society, London, Special Publications, v. 170, no. 1, p. 395-410.

Corfield, R. I., Searle, M. P., and Pedersen, R. B., 2001, Tectonic setting, origin, and obduction history of the Spontang Ophiolite, Ladakh Himalaya, NW India: The Journal of Geology, v. 109, no. 6, p. 715-736.

Coward, M., Butler, R., Khan, M. A., and Knipe, R., 1987, The tectonic history of Kohistan and its implications for Himalayan structure: Journal of the Geological Society, v. 144, no. 3, p. 377-391.

Crawford, A. J., Falloon, T., and Green, D., 1989, Classification, petrogenesis and tectonic setting of boninites.

Cumming, G., and Richards, J., 1975, Ore lead isotope ratios in a continuously changing Earth: Earth and Planetary Science Letters, v. 28, no. 2, p. 155-171.

Danelian, T., and Robertson, A. H., 1997, Radiolarian evidence for the stratigraphy and palaeo-oceanography of the deep-water passive margin of the Indian Plate (Karamba Formation, Indus suture zone, Ladakh Himalaya): Marine Micropaleontology, v. 30, no. 1-3, p. 171-195.

Davis, A. M., Aitchison, J. C., Luo, H., and Zyabrev, S., 2002, Paleogene island arc collision-related conglomerates, Yarlung–Tsangpo suture zone, Tibet: Sedimentary Geology, v. 150, no. 3, p. 247-273.

de Sigoyer, J., Chavagnac, V., Blichert-Toft, J., Villa, I. M., Luais, B., Guillot, S., Cosca, M., and Mascle, G., 2000, Dating the Indian continental subduction and collisional thickening in the northwest Himalaya: Multichronology of the Tso Morari eclogites: Geology, v. 28, no. 6, p. 487-490.

Debon, F., Le Fort, P., Dautel, D., Sonet, J., and Zimmermann, J. L., 1987, Granites of western Karakorum and northern Kohistan (Pakistan): a composite Mid-Cretaceous to upper Cenozoic magmatism: Lithos, v. 20, no. 1, p. 19-40.

Defant, M. J., and Drummond, M. S., 1990, Derivation of some modern arc magmas by melting of young subducted lithosphere: nature, v. 347, no. 6294, p. 662-665.

Defant, M. J., and Kepezhinskas, P., 2001, Evidence suggests slab melting in arc magmas: Eos, Transactions American Geophysical Union, v. 82, no. 6, p. 65-69.

Dewey, J. F., and Bird, J. M., 1970, Mountain belts and the new global tectonics: Journal of Geophysical Research, v. 75, no. 14, p. 2625-2647.

Dewey, J. F., & Şengör, A. C. (1979). Aegean and surrounding regions: complex multiplate and continuum tectonics in a convergent zone. *Geological Society of America Bulletin*, *90*(1), 84-92.

Dhuime, B., Bosch, D., Bodinier, J.-L., Garrido, C., Bruguier, O., Hussain, S. S., and Dawood, H., 2007, Multistage evolution of the Jijal ultramafic–mafic complex (Kohistan, N Pakistan): implications for building the roots of island arcs: Earth and Planetary Science Letters, v. 261, no. 1-2, p. 179-200.

Dhuime, B., Bosch, D., Garrido, C. J., Bodinier, J.-L., Bruguier, O., Hussain, S. S., and Dawood, H., 2009, Geochemical architecture of the lower-to middle-crustal section of a paleo-island arc (Kohistan Complex, Jijal–Kamila area, northern Pakistan): implications for

the evolution of an oceanic subduction zone: Journal of Petrology, v. 50, no. 3, p. 531-569.

Dickinson, W. R., and Suczek, C. A., 1979, Plate tectonics and sandstone compositions: Aapg Bulletin, v. 63, no. 12, p. 2164-2182.

Dietrich, V. J., Frank, W., and Honegger, K., 1983, A Jurassic-Cretaceous island arc in the Ladakh-Himalayas: Journal of Volcanology and Geothermal Research, v. 18, no. 1-4, p. 405-433.

Ding, L., Kapp, P., and Wan, X., 2005, Paleocene–Eocene record of ophiolite obduction and initial India-Asia collision, south central Tibet: Tectonics, v. 24, no. 3.

Dodson, M., Compston, W., Williams, I., and Wilson, J., 1988, A search for ancient detrital zircons in Zimbabwean sediments: Journal of the Geological Society, v. 145, no. 6, p. 977-983.

Donaldson, D. G., Webb, A. A. G., Menold, C. A., Kylander-Clark, A. R., & Hacker, B. R., 2013, Petrochronology of Himalayan ultrahigh-pressure eclogite. *Geology*, *41*(8), 835-838.

Draut, A. E., and Clift, P. D., 2006, Sedimentary processes in modern and ancient oceanic arc settings: Evidence from the Jurassic Talkeetna Formation of Alaska and the Mariana and Tonga arcs, western Pacific: Journal of Sedimentary Research, v. 76, no. 3, p. 493-514.

-, 2013, Differential preservation in the geologic record of intraoceanic arc sedimentary and tectonic processes: Earth-Science Reviews, v. 116, p. 57-84.

Dunlap, W. J., and Wysoczanski, R., 2002, Thermal evidence for early Cretaceous metamorphism in the Shyok suture zone and age of the Khardung volcanic rocks, Ladakh, India: Journal of Asian Earth Sciences, v. 20, no. 5, p. 481-490.

Ewing, T. A., and Müntener, O., 2018, The mantle source of island arc magmatism during early subduction: Evidence from Hf isotopes in rutile from the Jijal Complex (Kohistan arc, Pakistan): Lithos, v. 308, p. 262-277.

Fergusson, C. L., Nutman, A. P., Mohajjel, M., and Bennett, V. C., 2016, The Sanandaj–Sirjan Zone in the Neo-Tethyan suture, western Iran: Zircon U–Pb evidence of late Palaeozoic rifting of northern Gondwana and mid-Jurassic orogenesis: Gondwana Research, v. 40, p. 43-57.

Frank, W., 1977, Geological observations in the Ladakh area (Himalayas): A preliminary report: Schweizerische Mineralogische und Petrographische Mitteilungen Bulletin Suisse de Mineralogie et Petrographie, v. 57, no. 1, p. 89-113.

Fuchs, G., 1982, The geology of western Zanskar: Jahrbuch der Geologischen Bundesanstalt, v. 125, p. 1-50.

Fuchs, G., 1986, The geology of the Markha-Khurnak region in Ladakh (India): Jahrbuch der Geologischen Bundesanstalt, v. 128, p. 403-437.

Fuchs, G., and Willems, H., 1990, The final stages of sedimentation in the Tethyan Zone of Zanskar and their geodynamic significance (Ladakh-Himalaya): Jahrbuch der Geologischen Bundesanstalt Wien, v. 133, no. 2, p. 259-273.

Furnes, H., Dilek, Y., Zhao, G., Safonova, I., and Santosh, M., 2020, Geochemical characterization of ophiolites in the Alpine-Himalayan Orogenic Belt: Magmatically and tectonically diverse evolution of the Mesozoic Neotethyan oceanic crust: Earth-Science Reviews, p. 103258.

Gaetani, M., and Garzanti, E., 1991, Multicyclic history of the Northern India continental margin (Northwestern Himalaya)(1): AAPG Bulletin, v. 75, no. 9, p. 1427-1446.

Gansser, A., 1964, Geology of the Himalayas, 289 pp, Wiley-Interscience, New York.

Gansser, A., 1974, The ophiolite mélange; a worldwide problem on tethyan examples: Eclogae Geology of Helveticae, v. 67, p. 479-507.

Gansser, A., 1980, The significance of the Himalayan suture zone: Tectonophysics, v. 62, no. 1-2, p. 37-52.

Gansser, A., 1991, Facts and theories on the Himalayas: Eclogae Geologicae Helvetiae, v. 84, no. 1, p. 33-59.

Garrido, C. J., Bodinier, J.-L., Burg, J.-P., Zeilinger, G., Hussain, S. S., Dawood, H., Chaudhry, M. N., and Gervilla, F., 2006, Petrogenesis of mafic garnet granulite in the lower crust of the Kohistan paleo-arc complex (Northern Pakistan): implications for intra-crustal differentiation of island arcs and generation of continental crust: Journal of Petrology, v. 47, no. 10, p. 1873-1914.

Garzanti, E., 2019, The Himalayan Foreland Basin from collision onset to the present: a sedimentary–petrology perspective. *Geological Society, London, Special Publications*, *483*(1), 65-122.

Garzanti, E., Baud, A., and Mascle, G., 1987, Sedimentary record of the northward flight of India and its collision with Eurasia (Ladakh Himalaya, India): Geodinamica Acta, v. 1, no. 4-5, p. 297-312.

Garzanti, E., Critelli, S., & Ingersoll, R. V., 1996, Paleogeographic and paleotectonic evolution of the Himalayan Range as reflected by detrital modes of Tertiary sandstones and modern sands (Indus transect, India and Pakistan). *Geological Society of America bulletin*, *108*(6), 631-642

Garzanti, E., Sciunnach, D., Gaetani, M., Corfield, R., Watts, A., and Searle, M., 2005, Discussion on subsidence history of the north Indian continental margin, Zanskar–Ladakh Himalaya, NW India Journal, Vol. 162, 2005, pp. 135–146: Journal of the Geological Society, v. 162, no. 5, p. 889-892.

Garzanti, E., and Van Haver, T., 1988, The Indus clastics: forearc basin sedimentation in the Ladakh Himalaya (India): Sedimentary Geology, v. 59, no. 3-4, p. 237-249.

Gehrels, G., Kapp, P., DeCelles, P., Pullen, A., Blakey, R., Weislogel, A., Ding, L., Guynn, J., Martin, A., and McQuarrie, N., 2011, Detrital zircon geochronology of pre-Tertiary strata in the Tibetan-Himalayan orogen: Tectonics, v. 30, no. 5.

Gehrels, G. E., Valencia, V. A., and Ruiz, J., 2008, Enhanced precision, accuracy, efficiency, and spatial resolution of U-Pb ages by laser ablation–multicollector–inductively coupled plasma–mass spectrometry: Geochemistry, Geophysics, Geosystems, v. 9, no. 3.

Ghazi, A., Hassanipak, A., Mahoney, J., and Duncan, R., 2004, Geochemical characteristics, 40Ar–39Ar ages and original tectonic setting of the Band-e-Zeyarat/Dar Anar ophiolite, Makran accretionary prism, SE Iran: Tectonophysics, v. 393, no. 1-4, p. 175-196.

Global Mapper, L., 2009, Global Mapper Software LLC: Parker, CO.

Göpel, C., Allègre, C. J., and Xu, R.-H., 1984, Lead isotopic study of the Xigaze ophiolite (Tibet): the problem of the relationship between magmatites (gabbros, dolerites, lavas) and tectonites (harzburgites): Earth and Planetary Science Letters, v. 69, no. 2, p. 301-310.

Green, O. R., Searle, M. P., Corfield, R. I., and Corfield, R. M., 2008, Cretaceous-Tertiary carbonate platform evolution and the age of the India-Asia collision along the Ladakh Himalaya (northwest India): The Journal of Geology, v. 116, no. 4, p. 331-353.

Groppo, C., Rolfo, F., Sachan, H. K., and Rai, S. K., 2016, Petrology of blueschist from the Western Himalaya (Ladakh, NW India): Exploring the complex behavior of a lawsonite-bearing system in a paleo-accretionary setting: Lithos, v. 252, p. 41-56.

Guillot, S., Garzanti, E., Baratoux, D., Marquer, D., Mahéo, G., & de Sigoyer, J., 2003, Reconstructing the total shortening history of the NW Himalaya. *Geochemistry, Geophysics, Geosystems*, *4*(7).

Guilmette, C., Hébert, R., Dostal, J., Indares, A., Ullrich, T., Bédard, É., and Wang, C., 2012, Discovery of a dismembered metamorphic sole in the Saga ophiolitic mélange, South Tibet: assessing an Early Cretaceous disruption of the Neo-Tethyan supra-subduction zone and consequences on basin closing: Gondwana Research, v. 22, no. 2, p. 398-414.

Guilmette, C., Hébert, R., Wang, C., and Villeneuve, M., 2009, Geochemistry and geochronology of the metamorphic sole underlying the Xigaze ophiolite, Yarlung Zangbo Suture Zone, south Tibet: Lithos, v. 112, no. 1-2, p. 149-162.

Harris, N. B. W., Ronghua, X., Lewis, C. L., and Chenwei, J., 1988, The geological evolution of Tibet - Plutonic rocks of the 1985 Tibet Geotraverse, Lhasa to Golmud: Philosophical Transactions of the Royal Society of London. Series A, v. 327, no. 1594, p. 145-168.

Hassanipak, A. A., Ghazi, A. M., and Wampler, J. M., 1996, Rare earth element characteristics and K–Ar ages of the Band Ziarat ophiolite complex, southeastern Iran: Canadian Journal of Earth Sciences, v. 33, no. 11, p. 1534-1542.

Hébert, R., Bezard, R., Guilmette, C., Dostal, J., Wang, C., and Liu, Z., 2012, The Indus–Yarlung Zangbo ophiolites from Nanga Parbat to Namche Barwa syntaxes, southern Tibet: First synthesis of petrology, geochemistry, and geochronology with incidences on geodynamic reconstructions of Neo-Tethys: Gondwana Research, v. 22, no. 2, p. 377-397.

Heitz, A., 1986, Datations par méthode K/Ar sur filons du massif ophiolitique de Spongtang, rapport Strasbourg, p. 28.

Henderson, A. L., Najman, Y., Parrish, R., BouDagher-Fadel, M., Barford, D., Garzanti, E., and Andò, S., 2010, Geology of the Cenozoic Indus Basin sedimentary rocks:

Paleoenvironmental interpretation of sedimentation from the western Himalaya during the early phases of India-Eurasia collision: Tectonics, v. 29, no. 6.

Henderson, A. L., Najman, Y., Parrish, R., Mark, D. F., and Foster, G. L., 2011, Constraints to the timing of India–Eurasia collision; a re-evaluation of evidence from the Indus Basin sedimentary rocks of the Indus–Tsangpo Suture Zone, Ladakh, India: Earth-Science Reviews, v. 106, no. 3, p. 265-292.

Heri, A., Aitchison, J., King, J., and Villa, I. M., 2015, Geochronology and isotope geochemistry of Eocene dykes intruding the Ladakh Batholith: Lithos, v. 212, p. 111-121.

Heuberger, S., Schaltegger, U., Burg, J.-P., Villa, I. M., Frank, M., Dawood, H., Hussain, S., and Zanchi, A., 2007, Age and isotopic constraints on magmatism along the Karakoram-Kohistan Suture Zone, NW Pakistan: Evidence for subduction and continued convergence after India-Asia collision: Swiss Journal of Geosciences, v. 100, no. 1, p. 85-107.

Honegger, K., Dietrich, V., Frank, W., Gansser, A., Thöni, M., and Trommsdorff, V., 1982, Magmatism and metamorphism in the Ladakh Himalayas (the Indus-Tsangpo suture zone): Earth and Planetary Science Letters, v. 60, no. 2, p. 253-292.

Honegger, K., Le Fort, P., Mascle, G., and Zimmermann, J. L., 1989, The blueschists along the Indus suture zone in Ladakh, NW Himalaya: Journal of Metamorphic Geology, v. 7, no. 1, p. 57-72.

Honegger, K. H., 1983, Strukturen und Metamorphose im Zanskar Kristallin (Ladakh-Kashmir, Indien): ETH Zurich.

Hoskin, P. W., and Schaltegger, U., 2003, The composition of zircon and igneous and metamorphic petrogenesis: Reviews in mineralogy and geochemistry, v. 53, no. 1, p. 27-62.

Hu, X., Garzanti, E., Wang, J., Huang, W., An, W., and Webb, A., 2016a, The timing of India-Asia collision onset–Facts, theories, controversies: Earth-Science Reviews, v. 160, p. 264-299.

Hu, X., Jansa, L., Chen, L., Griffin, W. L., O'Reilly, S. Y., and Wang, J., 2010, Provenance of Lower Cretaceous Wölong volcaniclastics in the Tibetan Tethyan Himalaya: Implications for the final breakup of eastern Gondwana: Sedimentary Geology, v. 223, no. 3-4, p. 193-205.

Hu, X., Wang, J., BouDagher-Fadel, M., Garzanti, E., and An, W., 2016b, New insights into the timing of the India–Asia collision from the Paleogene Quxia and Jialazi formations of the Xigaze forearc basin, South Tibet: Gondwana Research, v. 32, p. 76-92.

Huang, C., Chien, C., Yao, B., and Chang, C., 2008, The Lichi Mélange: A collision mélange formation along early arcward backthrusts during forearc basin closure, Taiwan arc-continent collision: Special Papers-Geological Society Of America, v. 436, p. 127.

Huang, C.-Y., Chen, W.-H., Wang, M.-H., Lin, C.-T., Yang, S., Li, X., Yu, M., Zhao, X., Yang, K.-M., and Liu, C.-S., 2018, Juxtaposed sequence stratigraphy, temporal-spatial variations of sedimentation and development of modern-forming forearc Lichi Mélange in North Luzon Trough forearc basin onshore and offshore eastern Taiwan: An overview: Earth-Science Reviews, v. 182, p. 102-140.

Huang, C.-Y., Yuan, P. B., Lin, C.-W., Wang, T. K., and Chang, C.-P., 2000, Geodynamic processes of Taiwan arc–continent collision and comparison with analogs in Timor, Papua New Guinea, Urals and Corsica: Tectonophysics, v. 325, no. 1-2, p. 1-21.

Ingersoll, R. V., Bullard, T. F., Ford, R. L., Grimm, J. P., Pickle, J. D., and Sares, S. W., 1984, The effect of grain size on detrital modes: a test of the Gazzi-Dickinson point-counting method: Journal of Sedimentary Research, v. 54, no. 1, p. 103-116.

Jagoutz, O., Bouilhol, P., Schaltegger, U., and Müntener, O., 2018, The isotopic evolution of the Kohistan Ladakh arc from subduction initiation to continent arc collision: Geological Society, London, Special Publications, v. 483, no. 1, p. 165-182.

Jagoutz, O. E., Burg, J.-P., Hussain, S., Dawood, H., Pettke, T., Iizuka, T., and Maruyama, S., 2009, Construction of the granitoid crust of an island arc part I: geochronological and geochemical constraints from the plutonic Kohistan (NW Pakistan): Contributions to Mineralogy and Petrology, v. 158, no. 6, p. 739.

Janoušek, V., Farrow, C. M., and Erban, V., 2006, Interpretation of whole-rock geochemical data in igneous geochemistry: introducing Geochemical Data Toolkit (GCDkit): Journal of Petrology, v. 47, no. 6, p. 1255-1259.

Ji, W.-Q., Wu, F.-Y., Chung, S.-L., Li, J.-X., and Liu, C.-Z., 2009, Zircon U–Pb geochronology and Hf isotopic constraints on petrogenesis of the Gangdese batholith, southern Tibet: Chemical Geology, v. 262, no. 3-4, p. 229-245.

Jianbing, L., and Aitchison, J. C., 2002, Upper paleocene radiolarians from the Yamdrok mélange, south Xizang (Tibet), China: Micropaleontology, p. 145-154.

Kakar, M. I., Collins, A. S., Mahmood, K., Foden, J. D., and Khan, M., 2012, U-Pb zircon crystallization age of the Muslim Bagh ophiolite: Enigmatic remains of an extensive pre-Himalayan arc: Geology, v. 40, no. 12, p. 1099-1102.

Kakar, M. I., Kerr, A. C., Mahmood, K., Collins, A. S., Khan, M., and McDonald, I., 2014, Supra-subduction zone tectonic setting of the Muslim Bagh Ophiolite, northwestern Pakistan: insights from geochemistry and petrology: Lithos, v. 202, p. 190-206.

Kelsey, C., 1965, Calculation of the CIPW norm: Mineralogical Magazine, v. 34, no. 268, p. 276-282.

Khan, M. A., Jan, M. Q., and Weaver, B., 1993, Evolution of the lower arc crust in Kohistan, N. Pakistan: temporal arc magmatism through early, mature and intra-arc rift stages: Geological Society, London, Special Publications, v. 74, no. 1, p. 123-138.

Khan, M. A., Jan, M. Q., Windley, B. F., Tarney, J., and Thirlwall, M. F., 1989, The Chilas mafic-ultramafic igneous complex; the root of the Kohistan island arc in the Himalaya of northern Pakistan: Geological Society of America Special Papers, v. 232, p. 75-94.

Khan, S. D., Walker, D. J., Hall, S. A., Burke, K. C., Shah, M. T., and Stockli, L., 2009, Did the Kohistan-Ladakh island arc collide first with India?: Geological Society of America Bulletin, v. 121, no. 3-4, p. 366-384.

Khan, S. R., Jan, M. Q., Khan, T., and Khan, M. A., 2004, Waziristan Ophiolite: A back-arc basin caught in continental collision, Waziristan, NW Pakistan: Himalayan Journal of Sciences, v. 2, no. 4, p. 176-177.

Klootwijk, C., Sharma, M. L., Gergan, J., Shah, S., and Tirkey, B., 1984, The Indus-Tsangpo suture zone in Ladakh, Northwest Himalaya: Further palaeomagnetic data and implications: Tectonophysics, v. 106, no. 3-4, p. 215-238.

Klootwijk, C., Sharma, M. L., Gergan, J., Tirkey, B., Shah, S., and Agarwal, V., 1979, The extent of Greater India, II. Palaeomagnetic data from the Ladakh intrusives at Kargil, northwestern Himalayas: Earth and Planetary Science Letters, v. 44, no. 1, p. 47-64.

Kojima, S., Tanaka, T., Bagati, T. N., Mishra, M., Kumar, R., Islam, R., Khanna, P., and Ahmad, T., 2001, Early Cretaceous radiolarians from the Indus suture zone, Ladakh, northern India: News of Osaka Micropaleontologists (NOM), v. 12, p. 257-270.

Kouketsu, Y., Hattori, K., Guillot, S., and Rayner, N., 2016, Eocene to Oligocene retrogression and recrystallization of the Stak eclogite in northwest Himalaya: Lithos, v. 240, p. 155-166.

Krol, M. A., Zeitler, P. K., and Copeland, P., 1996, Episodic unroofing of the Kohistan Batholith, Pakistan: Implications from K-feldspar thermochronology: Journal of Geophysical Research: Solid Earth, v. 101, no. B12, p. 28149-28164.

Lai, W., Hu, X., Garzanti, E., Xu, Y., Ma, A., and Li, W., 2019, Early Cretaceous sedimentary evolution of the northern Lhasa terrane and the timing of initial Lhasa-Qiangtang collision: Gondwana Research, v. 73, p. 136-152.

Le Bas, M., 2000, IUGS reclassification of the high-Mg and picritic volcanic rocks: Journal of Petrology, v. 41, no. 10, p. 1467-1470.

Le Fort, P., Michard, A., Sonet, J., and Zimmermann, J., 1983, Petrography, geochemistry and geochronology of some samples from the Karakorum Axial Batholith (northern Pakistan): Granites of Himalayas, Karakorum and Hindu Kush. Institute of Geology, Punjab University, Lahore, p. 377-387.

Le Maitre, R., Streckeisen, A., and Zanettin, B., 1986, A chemical classification of volcanic rocks based on the total alkali-silica diagram: Journal of petrology, v. 27, no. 3, p. 745-750.

Leary, R. J., DeCelles, P. G., Quade, J., Gehrels, G. E., and Waanders, G., 2016, The Liuqu Conglomerate, southern Tibet: Early Miocene basin development related to deformation within the Great Counter Thrust system: Lithosphere, v. 8, no. 5, p. 427-450.

Lee, C.-T. A., Morton, D. M., Kistler, R. W., and Baird, A. K., 2007, Petrology and tectonics of Phanerozoic continent formation: From island arcs to accretion and continental arc magmatism: Earth and Planetary Science Letters, v. 263, no. 3-4, p. 370-387.

Lee, H.-Y., Chung, S.-L., Lo, C.-H., Ji, J., Lee, T.-Y., Qian, Q., and Zhang, Q., 2009, Eocene Neotethyan slab breakoff in southern Tibet inferred from the Linzizong volcanic record: Tectonophysics, v. 477, no. 1-2, p. 20-35.

Lee, J., and Whitehouse, M. J., 2007, Onset of mid-crustal extensional flow in southern Tibet: Evidence from U/Pb zircon ages: Geology, v. 35, no. 1, p. 45-48.

Leier, A. L., DeCelles, P. G., Kapp, P., and Gehrels, G. E., 2007a, Lower Cretaceous strata in the Lhasa Terrane, Tibet, with implications for understanding the early tectonic history of the Tibetan Plateau: Journal of Sedimentary Research, v. 77, no. 10, p. 809-825.

Leier, A. L., Kapp, P., Gehrels, G. E., and DeCelles, P. G., 2007b, Detrital zircon geochronology of Carboniferous–Cretaceous strata in the Lhasa terrane, Southern Tibet: Basin Research, v. 19, no. 3, p. 361-378.

Lewis, K. B., and Barnes, P. M., 1999, Kaikoura Canyon, New Zealand: active conduit from near-shore sediment zones to trench-axis channel: Marine Geology, v. 162, no. 1, p. 39-69.

Li, G., Kohn, B., Sandiford, M., Xu, Z., and Wei, L., 2015, Constraining the age of Liuqu Conglomerate, southern Tibet: Implications for evolution of the India–Asia collision zone: Earth and Planetary Science Letters, v. 426, p. 259-266.

Li, G., Sandiford, M., Liu, X., Xu, Z., Wei, L., and Li, H., 2014, Provenance of Late Triassic sediments in central Lhasa terrane, Tibet and its implication: Gondwana Research, v. 25, no. 4, p. 1680-1689.

Li, J., Xia, B., Liu, L., Xu, L., He, G., Wang, H., Zhang, Y., and Yang, Z., 2009, SHRIMP U–Pb dating for the gabbro in Qunrang ophiolite, Tibet: The geochronology constraint for the development of eastern Tethys basin: Geotectonica et Metallogenia, v. 33, no. 2, p. 294-298.

Li, Z., Ding, L., Lippert, P. C., Song, P., Yue, Y., and van Hinsbergen, D. J., 2016, Paleomagnetic constraints on the Mesozoic drift of the Lhasa terrane (Tibet) from Gondwana to Eurasia: Geology, v. 44, no. 9, p. 727-730.

Li, Z., Ding, L., Song, P., Fu, J., & Yue, Y., 2017, Paleomagnetic constraints on the paleolatitude of the Lhasa block during the Early Cretaceous: implications for the onset of India–Asia collision and latitudinal shortening estimates across Tibet and stable Asia. *Gondwana Research*, *41*, 352-372.

Liu, W., Zhong, Y., Sun, Z., Yakymchuk, C., Gu, M., Tang, G., Zhong, L., Cao, H., Liu, H., and Xia, B., 2020, The Late Jurassic Zedong ophiolite: A remnant of subduction initiation

within the Yarlung Zangbo Suture Zone (southern Tibet) and its tectonic implications: Gondwana Research, v. 78, p. 172-188.

Ludwig, K., Vital, F., Sprudel, F., Pils, W., and Sprudel, R., 2003, User's manual for Isoplot 3.00. A geochronological Toolkit for Microsoft Excel.: Berkeley Geochronology Center, Special Publication No. 4a, Berkeley, California., p. 478-490.

Ma, Y., Yang, T., Bian, W., Jin, J., Zhang, S., Wu, H., & Li, H., 2016, Early Cretaceous paleomagnetic and geochronologic results from the Tethyan Himalaya: Insights into the Neotethyan paleogeography and the India–Asia collision. *Scientific Reports*, *6*(1), 1-11.

Macdonald, R., Hawkesworth, C., and Heath, E., 2000, The Lesser Antilles volcanic chain: a study in arc magmatism: Earth-Science Reviews, v. 49, no. 1-4, p. 1-76.

MacLean, W. H., 1990, Mass change calculations in altered rock series: Mineralium Deposita, v. 25, no. 1, p. 44-49.

Mahéo, G., Bertrand, H., Guillot, S., Mascle, G., Pêcher, A., Picard, C., and De Sigoyer, J., 2000, Témoins d'un arc immature téthysien dans les ophiolites du Sud Ladakh (NW Himalaya, Inde): Comptes Rendus de l'Académie des Sciences-Series IIA-Earth and Planetary Science, v. 330, no. 4, p. 289-295.

Mahéo, G., Bertrand, H., Guillot, S., Villa, I. M., Keller, F., and Capiez, P., 2004, The South Ladakh ophiolites (NW Himalaya, India): an intra-oceanic tholeiitic arc origin with implication for the closure of the Neo-Tethys: Chemical Geology, v. 203, no. 3-4, p. 273-303.

Mahéo, G., Fayoux, C., Guillot, S., Garzanti, E., Capiez, P., and Mascle, G., 2006, Geochemistry of ophiolitic rocks and blueschists from the Sapi-Shergol mélange (Ladakh, NW Himalaya, India): implication for the timing of the closure of the Neo-Tethys ocean: Journal of Asian Earth Sciences, v. 26, p. 695-707.

Mahmood, K., Boudier, F., Gnos, E., Monié, P., and Nicolas, A., 1995, $^{40}Ar/^{39}Ar$ dating of the emplacement of the Muslim Bagh ophiolite, Pakistan: Tectonophysics, v. 250, no. 1-3, p. 169-181.

Malpas, J., Zhou, M.-F., Robinson, P. T., and Reynolds, P. H., 2003, Geochemical and geochronological constraints on the origin and emplacement of the Yarlung Zangbo ophiolites, Southern Tibet: Geological Society, London, Special Publications, v. 218, no. 1, p. 191-206.

Manton, R. J., Buckman, S., Nutman, A. P., and Bennett, V. C., 2017a, Exotic island arc Paleozoic terranes on the eastern margin of Gondwana: Geochemical whole rock and zircon U–Pb–Hf isotope evidence from Barry Station, New South Wales, Australia: Lithos, v. 286, p. 125-150.

Manton, R. J., Buckman, S., Nutman, A. P., Bennett, V. C., and Belousova, E. A., 2017b, U-Pb-Hf-REE-Ti zircon and REE garnet geochemistry of the Cambrian Attunga eclogite, New England Orogen, Australia: Implications for continental growth along eastern Gondwana: Tectonics, v. 36, no. 8, p. 1580-1613.

Martin, C. R., Jagoutz, O., Upadhyay, R., Royden, L. H., Eddy, M. P., Bailey, E., Nichols, C. I., and Weiss, B. P., 2020, Paleocene latitude of the Kohistan–Ladakh arc indicates multistage India–Eurasia collision: Proceedings of the National Academy of Sciences, v. 117, no. 47, p. 29487-29494.

Martin, H., 1986, Effect of steeper Archean geothermal gradient on geochemistry of subduction-zone magmas: Geology, v. 14, no. 9, p. 753-756.

Martin, H., 1999, Adakitic magmas: modern analogues of Archaean granitoids: Lithos, v. 46, no. 3, p. 411-429.

Masse, J. P., & Maresca, M. G., 1997, Late Aptian Radiolitidae (rudist bivalves) from the Mediterranean and Southwest Asiatic regions: taxonomic, biostratigraphic and palaeobiogeographic aspects. Palaeogeography, Palaeoclimatology, Palaeoecology, 128(1-4), 101-110.

Mathur, N., and Vogel, K., 1988, Some rudists from Khalsi Limestone of Indus formation, Ladakh Himalaya: Geobios, v. 21, no. 6, p. 693-707.

Mazza, S. E., Gazel, E., Johnson, E. A., Bizimis, M., McAleer, R., and Biryol, C. B., 2017, Post-rift magmatic evolution of the eastern N orth American “passive-aggressive” margin: Geochemistry, Geophysics, Geosystems, v. 18, no. 1, p. 3-22.

McCall, G. J. H., 1985, Explanatory Text of the Minab Quadrangle Map, 1: 250,000, Geological Survey of Iran.

McDermid, I. R., Aitchison, J. C., Davis, A. M., Harrison, T. M., and Grove, M., 2002, The Zedong terrane: a Late Jurassic intra-oceanic magmatic arc within the Yarlung–Tsangpo suture zone, southeastern Tibet: Chemical Geology, v. 187, no. 3, p. 267-277.

McDonough, W. F., and Sun, S.-S., 1995, The composition of the Earth: Chemical geology, v. 120, no. 3-4, p. 223-253.

Meschede, M., 1986, A method of discriminating between different types of mid-ocean ridge basalts and continental tholeiites: Chemical geology, v. 56, no. 3-4, p. 207-218.

Miller, C., Thöni, M., Frank, W., Schuster, R., Melcher, F., Meisel, T., and Zanetti, A., 2003, Geochemistry and tectonomagmatic affinity of the Yungbwa ophiolite, SW Tibet: Lithos, v. 66, no. 3-4, p. 155-172.

Mo, X., Dong, G., Zhao, Z., Zhou, S., Wang, L., Qiu, R., and Zhang, F., 2005, Spatial and temporal distribution and characteristics of granitoids in the Gangdese, Tibet and implication for crustal growth and evolution: Geological Journal of China Universities, v. 11, no. 3, p. 281-290.

Molnar, P., and Tapponnier, P., 1975, Cenozoic tectonics of Asia: effects of a continental collision: Science, v. 189, no. 4201, p. 419-426.

Montes, C., Rodriguez-Corcho, A.F., Bayona, G., Hoyos, N., Zapata, S. and Cardona, A., 2019. Continental margin response to multiple arc-continent collisions: The northern Andes-Caribbean margin. *Earth-Science Reviews*, *198*, p.102903.

Moore, G. F., Boston, B. B., Strasser, M., Underwood, M. B., and Ratliff, R. A., 2015, Evolution of tectono-sedimentary systems in the Kumano Basin, Nankai Trough forearc: Marine and Petroleum Geology, v. 67, p. 604-616.

Moore, G. F., Curray, J. R., and Emmel, F. J., 1982, Sedimentation in the Sunda Trench and forearc region: Geological Society, London, Special Publications, v. 10, no. 1, p. 245-258.

Morris, A., Meyer, M., Anderson, M. W., and MacLeod, C. J., 2016, Clockwise rotation of the entire Oman ophiolite occurred in a suprasubduction zone setting: Geology, v. 44, no. 12, p. 1055-1058.

Myrow, P. M., Hughes, N. C., McKenzie, N. R., Pelgay, P., Thomson, T. J., Haddad, E. E., and Fanning, C. M., 2016, Cambrian–Ordovician orogenesis in Himalayan equatorial Gondwana: Bulletin, v. 128, no. 11-12, p. 1679-1695.

Najman, Y., Jenks, D., Godin, L., Boudagher-Fadel, M., Millar, I., Garzanti, E., Horstwood, M., and Bracciali, L., 2017, The Tethyan Himalayan detrital record shows that India–Asia

terminal collision occurred by 54 Ma in the Western Himalaya: Earth and Planetary Science Letters, v. 459, p. 301-310.

Norrish, K., and Chappell, B. W., 1977, X-ray fluorescence spectrometry.

O'Brien, P. J., 2019, Eclogites and other high-pressure rocks in the Himalaya: a review: Geological Society, London, Special Publications, v. 483, no. 1, p. 183-213.

Ohta, T., and Arai, H., 2007, Statistical empirical index of chemical weathering in igneous rocks: A new tool for evaluating the degree of weathering: Chemical Geology, v. 240, no. 3-4, p. 280-297.

Orme, D. A., Carrapa, B., and Kapp, P., 2015, Sedimentology, provenance and geochronology of the upper Cretaceous–lower Eocene western Xigaze forearc basin, southernTibet: Basin Research, v. 27, no. 4, p. 387-411.

Parsons, A.J., Hosseini, K., Palin, R. and Sigloch, K., 2020, Geological, geophysical and plate kinematic constraints for models of the India-Asia collision and the post-Triassic central Tethys oceans. Earth-Science Reviews, p.103084.

Paton, C., Hellstrom, J., Paul, B., Woodhead, J., and Hergt, J., 2011, Iolite: Freeware for the visualisation and processing of mass spectrometric data: Journal of Analytical Atomic Spectrometry, v. 26, no. 12, p. 2508-2518.

Patriat, P., and Achache, J., 1984, India–Eurasia collision chronology has implications for crustal shortening and driving mechanism of plates: Nature, v. 311, no. 5987, p. 615-621.

Pearce, J. A., 2008, Geochemical fingerprinting of oceanic basalts with applications to ophiolite classification and the search for Archean oceanic crust: Lithos, v. 100, no. 1-4, p. 14-48.

Pearce, J. A., and Cann, J. R., 1973, Tectonic setting of basic volcanic rocks determined using trace element analyses: Earth and planetary science letters, v. 19, no. 2, p. 290-300.

Pearce, J. A., and Peate, D. W., 1995, Tectonic implications of the composition of volcanic arc magmas: Annual review of Earth and planetary sciences, v. 23, no. 1, p. 251-285.

Pearce, J. A., and Reagan, M. K., 2019, Identification, classification, and interpretation of boninites from Anthropocene to Eoarchean using Si-Mg-Ti systematics: Geosphere, v. 15, no. 4, p. 1008-1037.

Pedersen, R., Searle, M., and Corfield, R., 2001, U–Pb zircon ages from the Spontang ophiolite, Ladakh Himalaya: Journal of the Geological Society, v. 158, no. 3, p. 513-520.

Peterman, E. M., Reddy, S. M., Saxey, D. W., Snoeyenbos, D. R., Rickard, W. D., Fougerouse, D., and Kylander-Clark, A. R., 2016, Nanogeochronology of discordant zircon measured by atom probe microscopy of Pb-enriched dislocation loops: Science advances, v. 2, no. 9, p. e1601318.

Powell, C. M., and Conaghan, P., 1973, Plate tectonics and the Himalayas: Earth and Planetary Science Letters, v. 20, no. 1, p. 1-12.

Quidelleur, X., Grove, M., Lovera, O. M., Harrison, T. M., Yin, A., and Ryerson, F., 1997, Thermal evolution and slip history of the Renbu Zedong Thrust, southeastern Tibet: Journal of Geophysical Research: Solid Earth, v. 102, no. B2, p. 2659-2679.

Radhakrishna, T., Rao, V. D., and Murali, A., 1987, Geochemistry and petrogenesis of ultramafic and mafic plutonic rocks of the Dras ophiolitic mélange, Indus suture (northwest Himalaya): Earth and planetary science letters, v. 82, no. 1-2, p. 136-144.

Ravikant, V., Wu, F.-Y., and Ji, W.-Q., 2009, Zircon U–Pb and Hf isotopic constraints on petrogenesis of the Cretaceous–Tertiary granites in eastern Karakoram and Ladakh, India: Lithos, v. 110, no. 1-4, p. 153-166.

Rehman, H. U., Lee, H.-Y., Chung, S.-L., Khan, T., O'Brien, P. J., and Yamamoto, H., 2016, Source and mode of the Permian Panjal Trap magmatism: evidence from zircon U–Pb and Hf isotopes and trace element data from the Himalayan ultrahigh-pressure rocks: Lithos, v. 260, p. 286-299.

Reibel, G., and Juteau, T., 1981, Dras Volcanics, Indau Suture (Ladakh): Ocean-Floor Tholeites versus Island-arc: Comptes Rendus De Academie Des Sciences Serie II, v. 293, no. 1, p. 57-60.

Reichardt, H., Weinberg, R., Andersson, U., and Fanning, C., 2010, Hybridization of granitic magmas in the source: the origin of the Karakoram Batholith, Ladakh, NW India: Lithos, v. 116, no. 3, p. 249-272.

Reuber, I., 1986, Geometry of accretion and oceanic thrusting of the Spongtang Ophiolite, Ladakh-Himalaya: Nature, v. 321, no. 6070, p. 592.

-, 1989, The Dras arc: two successive volcanic events on eroded oceanic crust: Tectonophysics, v. 161, no. 1-2, p. 93-106.

Reuber, I., 1990, The Shyok ophiolite in Ladakh-Himalaya: relics of the Tethyan oceanic crust overlain by volcanosedimentary arc series of mid-Cretaceous age: Comptes Rendus, Academie des Sciences, Serie II, v. 310, no. 9, p. 1255-1262.

Reuber, I., Colchen, M., and Mevel, C., 1987, The geodynamic evolution of the South-Tethyan, margin in Zanskar, NW-Himalaya, as revealed by the Spongtang ophiolitic mélanges: Geodinamica Acta, v. 1, no. 4-5, p. 283-296.

Reuber, I., Colchen, M., and Mevel, C., 1992, The Spongtang ophiolite and ophiolitic mélanges of the Zanskar, NW Himalaya, tracing the evolution of the closing Tethys in the Upper Cretaceous to the early Tertiary: Himalayan orogen and global tectonics, p. 235-266.

Reuber, I., Montigny, R., Thuizai, R., and Heitz, A., 1989, K-Ar ages of ophiolites and arc volcanics of the Indus suture zone: clues on the early evolution of the Neo-Tethys: Eclogae Geologicae Helvetiae, v. 82, no. 2, p. 699-715.

Rioux, M., Hacker, B., Mattinson, J., Kelemen, P., Blusztajn, J., and Gehrels, G., 2007, Magmatic development of an intra-oceanic arc: High-precision U-Pb zircon and whole-rock isotopic analyses from the accreted Talkeetna arc, south-central Alaska: Geological Society of America Bulletin, v. 119, no. 9-10, p. 1168-1184.

Rioux, M., Mattinson, J., Hacker, B., Kelemen, P., Blusztajn, J., Hanghøj, K., and Gehrels, G., 2010, Intermediate to felsic middle crust in the accreted Talkeetna arc, the Alaska Peninsula and Kodiak Island, Alaska: An analogue for low-velocity middle crust in modern arcs: Tectonics, v. 29, no. 3.

Robertson, A., 2000, Formation of mélanges in the Indus suture zone, Ladakh Himalaya by successive subduction-related, collisional and post-collisional processes during late Mesozoic-late Tertiary time: Geological Society, London, Special Publications, v. 170, no. 1, p. 333-374.

Robertson, A., and Degnan, P., 1994, The Dras arc complex: lithofacies and reconstruction of a Late Cretaceous oceanic volcanic arc in the Indus suture zone, Ladakh Himalaya: Sedimentary Geology, v. 92, no. 1, p. 117-145.

Robertson, A., and Sharp, I., 1998, Mesozoic deep-water slope/rise sedimentation and volcanism along the North-Indian passive margin: evidence from the Karamba Complex, Indus

suture zone (Western Ladakh Himalaya): Journal of Asian Earth Sciences, v. 16, no. 2-3, p. 195-215.

Robertson, A. H., and Collins, A. S., 2002, Shyok Suture Zone, N Pakistan: late Mesozoic–Tertiary evolution of a critical suture separating the oceanic Ladakh Arc from the Asian continental margin: Journal of Asian Earth Sciences, v. 20, no. 3, p. 309-351.

Robertson, A. H., and Degnan, P. J., 1993, Sedimentology and tectonic implications of the Lamayuru Complex: deep-water facies of the Indian passive margin, Indus Suture Zone, Ladakh Himalaya: Geological Society, London, Special Publications, v. 74, no. 1, p. 299-321.

Rolland, Y., 2002, From intra-oceanic convergence to post-collisional evolution: example of the India-Asia convergence in NW Himalaya, from Cretaceous to present: Journal of the Virtual Explorer, v. 8, p. 193-216.

Rolland, Y., Hässig, M., Bosch, D., Bruguier, O., Melis, R., Galoyan, G., Topuz, G., Sahakyan, L., Avagyan, A., and Sosson, M., 2020, The East Anatolia–Lesser Caucasus ophiolite: An exceptional case of large-scale obduction, synthesis of data and numerical modelling: Geoscience Frontiers, v. 11, no. 1, p. 83-108.

Rolland, Y., Pecher, A., and Picard, C., 2000, Middle Cretaceous back-arc formation and arc evolution along the Asian margin: the Shyok Suture Zone in northern Ladakh (NW Himalaya): Tectonophysics, v. 325, no. 1-2, p. 145-173.

Rolland, Y., Picard, C., Pecher, A., Lapierre, H., Bosch, D., and Keller, F., 2002, The cretaceous Ladakh arc of NW himalaya—slab melting and melt–mantle interaction during fast northward drift of Indian Plate: Chemical Geology, v. 182, no. 2-4, p. 139-178.

Roser, B., and Korsch, R., 1986, Determination of tectonic setting of sandstone-mudstone suites using content and ratio: The Journal of Geology, v. 94, no. 5, p. 635-650.

-, 1988, Provenance signatures of sandstone-mudstone suites determined using discriminant function analysis of major-element data: Chemical geology, v. 67, no. 1-2, p. 119-139.

Rowley, D. B., 1996, Age of initiation of collision between India and Asia: A review of stratigraphic data: Earth and Planetary Science Letters, v. 145, no. 1-4, p. 1-13.

-, 1998, Minimum age of initiation of collision between India and Asia north of Everest based on the subsidence history of the Zhepure Mountain section: The Journal of Geology, v. 106, no. 2, p. 220-235.

Sachan, H. K., 2001, Supra-subduction origin of the Nidar ophiolitic sequence, Indus Suture Zone, Ladakh, India: Evidence from mineral chemistry of upper mantle rocks: Ofioliti, v. 26, no. 1, p. 23-32.

Saktura, W. M., Buckman, S., Nutman, A., and Bennett, V., 2019, Age and origin of the Shyok ophiolite-arc complex in Ladakh, NW Himalaya, European Geosciences Union General Assembly 2019, Volume Vol. 21: Vienna, Austria.

Saktura, W. M., Buckman, S., Nutman, A. P., and Bennett, V. C., 2020, Late Jurassic Changmar Complex from the Shyok ophiolite, NW Himalaya: a prelude to the Ladakh Arc: Geological Magazine, p. 1-22.

Sambridge, M., and Compston, W., 1995, Mixture modeling of multi-component data sets with application to ion-probe zircon ages: Earth and Planetary Science Letters, v. 128, no. 3, p. 373-390.

Schaltegger, U., Frank, M., and Burg, J.-P., 2003, A 120 million years record of magmatism and crustal melting in the Kohistan Batholith: EAEJA, p. 6816.

Schaltegger, U., Zeilinger, G., Frank, M., and Burg, J. P., 2002, Multiple mantle sources during island arc magmatism: U–Pb and Hf isotopic evidence from the Kohistan arc complex, Pakistan: Terra Nova, v. 14, no. 6, p. 461-468.

Schärer, U., Hamet, J., and Allègre, C. J., 1984a, The Transhimalaya (Gangdese) plutonism in the Ladakh region: a U-Pb and Rb-Sr study.: Earth and Planetary Science Letters, v. 67, no. 3, p. 327-339.

Schärer, U., Xu, R.-H., and Allègre, C. J., 1984b, UPb geochronology of Gangdese (Transhimalaya) plutonism in the Lhasa-Xigaze region, Tibet: Earth and Planetary Science Letters, v. 69, no. 2, p. 311-320.

Searle, M., 1983, Stratigraphy, structure and evolution of the Tibetan–Tethys zone in Zanskar and the Indus suture zone in the Ladakh Himalaya: Earth and Environmental Science Transactions of The Royal Society of Edinburgh, v. 73, no. 4, p. 205-219.

-, 1986, Structural evolution and sequence of thrusting in the High Himalayan, Tibetan—Tethys and Indus suture zones of Zanskar and Ladakh, Western Himalaya: Journal of Structural Geology, v. 8, no. 8, p. 923-936.

-, 2019, Timing of subduction initiation, arc formation, ophiolite obduction and India–Asia collision in the Himalaya. *Geological Society, London, Special Publications*, *483*(1), 19-37.

Searle, M., Cooper, D., Rex, A., Herren, E., and Colchen, M., 1988, Collision Tectonics of the Ladakh-Zanskar Himalaya: Philosophical Transactions of the Royal Society of London A: Mathematical, Physical and Engineering Sciences, v. 326, no. 1589, p. 117-150.

Searle, M., Corfield, R. I., Stephenson, B., and McCarron, J., 1997, Structure of the North Indian continental margin in the Ladakh–Zanskar Himalayas: implications for the timing of obduction of the Spontang ophiolite, India–Asia collision and deformation events in the Himalaya: Geological Magazine, v. 134, no. 3, p. 297-316.

Searle, M., and Cox, J., 1999, Tectonic setting, origin, and obduction of the Oman ophiolite: Geological Society of America Bulletin, v. 111, no. 1, p. 104-122.

Searle, M., Khan, M. A., Fraser, J., Gough, S., and Jan, M. Q., 1999, The tectonic evolution of the Kohistan-Karakoram collision belt along the Karakoram Highway transect, north Pakistan: Tectonics, v. 18, no. 6, p. 929-949.

Searle, M., Pickering, K., and Cooper, D., 1990, Restoration and evolution of the intermontane Indus molasse basin, Ladakh Himalaya, India: Tectonophysics, v. 174, no. 3-4, p. 301-314.

Searle, M., Warren, C., Waters, D., and Parrish, R., 2004, Structural evolution, metamorphism and restoration of the Arabian continental margin, Saih Hatat region, Oman Mountains: Journal of Structural Geology, v. 26, no. 3, p. 451-473.

Searle, M., Windley, B., Coward, M., Cooper, D., Rex, A., Rex, D., Tingdong, L., Xuchang, X., Jan, M., and Thakur, V., 1987, The closing of Tethys and the tectonics of the Himalaya: Geological Society of America Bulletin, v. 98, no. 6, p. 678-701.

Searle, M. P., and Cox, J., 2002, Subduction zone metamorphism during formation and emplacement of the Semail ophiolite in the Oman Mountains: Geological Magazine, v. 139, no. 3, p. 241-255.

Seton, M., Müller, R., Zahirovic, S., Gaina, C., Torsvik, T., Shephard, G., Talsma, A., Gurnis, M., Turner, M., and Maus, S., 2012, Global continental and ocean basin reconstructions since 200 Ma: Earth-Science Reviews, v. 113, no. 3-4, p. 212-270.

Sharma, K. K., 1987, Crustal growth and two-stage India-Eurasia collision in Ladakh: Tectonophysics, v. 134, no. 1-3, p. 17-28.

Sharma, K. K., Sinha, A. K., Bagdasarian, G., and Gukasian, R. C., 1978, Potassium-argon dating of Dras volcanics, Shyok volcanics and Ladakh granite, Ladakh, northwest Himalaya: Himalayan Geol, v. 8, no. 1, p. 288-295.

Shellnutt, J., Bhat, G., Brookfield, M., and Jahn, B. M., 2011, No link between the Panjal Traps (Kashmir) and the Late Permian mass extinctions: Geophysical Research Letters, v. 38, no. 19.

Shellnutt, J. G., Lee, T.-Y., Brookfield, M. E., and Chung, S.-L., 2014, Correlation between magmatism of the Ladakh Batholith and plate convergence rates during the India–Eurasia collision: Gondwana Research, v. 26, no. 3-4, p. 1051-1059.

Shervais, J. W., 1982, Ti-V plots and the petrogenesis of modern and ophiolitic lavas: Earth and planetary science letters, v. 59, no. 1, p. 101-118.

-, 2001, Birth, death, and resurrection: The life cycle of suprasubduction zone ophiolites: Geochemistry, Geophysics, Geosystems, v. 2, no. 1.

Sinclair, H., and Jaffey, N., 2001, Sedimentology of the Indus Group, Ladakh, northern India: implications for the timing of initiation of the palaeo-Indus River: Journal of the Geological Society, v. 158, no. 1, p. 151-162.

Singh, S., Kumar, R., Barley, M. E., and Jain, A., 2007, SHRIMP U–Pb ages and depth of emplacement of Ladakh Batholith, Eastern Ladakh, India: Journal of Asian Earth Sciences, v. 30, no. 3-4, p. 490-503.

Sinha, A., 1990, Subduction accretion and subduction kneading: A possible mechanism for the incorporation of sedimentary sequences within the ophiolitic mélange belt in the western Ladakh Himalaya, India: J. Him. Geol., v. 1, p. 259-264.

Smewing, J., Abbotts, I., Dunne, L., and Rex, D., 1991, Formation and emplacement ages of the Masirah ophiolite, Sultanate of Oman: Geology, v. 19, no. 5, p. 453-456.

Smith, A. G., Hurley, A. M., & Briden, J. C., 1981, *Phanerozoic paleocontinental world maps*. CUP Archive.

Smith, I. E., Worthington, T. J., Stewart, R. B., Price, R. C., and Gamble, J. A., 2003, Felsic volcanism in the Kermadec arc, SW Pacific: crustal recycling in an oceanic setting: Geological Society, London, Special Publications, v. 219, no. 1, p. 99-118.

Song, S., Zhang, L., Niu, Y., Su, L., Jian, P. and Liu, D., 2005. Geochronology of diamond-bearing zircons from garnet peridotite in the North Qaidam UHPM belt, Northern Tibetan Plateau: a record of complex histories from oceanic lithosphere subduction to continental collision. *Earth and Planetary Science Letters*, *234*(1-2), pp.99-118.

St-Onge, M. R., Rayner, N., and Searle, M. P., 2010, Zircon age determinations for the Ladakh batholith at Chumathang (Northwest India): implications for the age of the India–Asia collision in the Ladakh Himalaya: Tectonophysics, v. 495, no. 3, p. 171-183.

Steck, A., 2003, Geology of the NW Indian Himalaya: Eclogae Geol Helv, v. 96, p. 147-196.

Steck, A., Spring, L., Vannay, J.-C., Masson, H., Bucher, H., Stutz, E., Marchant, R., and Tieche, J.-C., 1993, The tectonic evolution of the Northwestern Himalaya in eastern Ladakh and Lahul, India: Geological Society, London, Special Publications, v. 74, no. 1, p. 265-276.

Stern, C. R., and Kilian, R., 1996, Role of the subducted slab, mantle wedge and continental crust in the generation of adakites from the Andean Austral Volcanic Zone: Contributions to mineralogy and petrology, v. 123, no. 3, p. 263-281.

Stern, R. J., 2004, Subduction initiation: spontaneous and induced: Earth and Planetary Science Letters, v. 226, no. 3-4, p. 275-292.

Stern, R. J., and Bloomer, S. H., 1992, Subduction zone infancy: examples from the Eocene Izu-Bonin-Mariana and Jurassic California arcs: Geological Society of America Bulletin, v. 104, no. 12, p. 1621-1636.

Sterne, E. J., 1979, Report on geological traverses across the Indus-Tsangpo suture zone in Ladakh, northern India: Harvard University.

Sun, S.-S., and McDonough, W.-S., 1989, Chemical and isotopic systematics of oceanic basalts: implications for mantle composition and processes: Geological Society, London, Special Publications, v. 42, no. 1, p. 313-345.

Sutre, E., 1990, Les formations de la marge nord-néotethysienne et les mélanges ophiolitiques de la zone de suture de l'indus en Himalaya du Ladakh, Inde: stratigraphie, tectonique.

Şengör, A. C., 1979, Tethys and its implications. *Nature*, *279*(14), 14

Şengör, A. C., 1984, The Cimmeride orogenic system and the tectonics of Eurasia. *Geological Society of America Special Paper*, *195*, 82.

Thakur, V., 1981, Regional framework and geodynamic evolution of the Indus-Tsangpo suture zone in the Ladakh Himalayas: Earth and Environmental Science Transactions of The Royal Society of Edinburgh, v. 72, no. 2, p. 89-97.

-, 1990, Indus Tsangpo suture zone in Ladakh – its tectonostratigraphy and tectonics: Proceedings of the Indian Academy of Sciences-Earth and Planetary Sciences, v. 99, no. 2, p. 169-185.

Thakur, V., and Misra, D., 1984, Tectonic framework of the Indus and Shyok suture zones in eastern Ladakh, northwest Himalaya: Tectonophysics, v. 101, no. 3-4, p. 207-220.

Thakur, V., and Virdi, N., 1979, Lithostratigraphy, structural framework, deformation and metamorphism of the southeastern region of Ladakh, Kashmir Himalaya, India: Himalayan Geology, v. 9, p. 63-78.

Thanh, N. X., Rajesh, V., Itaya, T., Windley, B., Kwon, S., and Park, C.-S., 2012, A Cretaceous forearc ophiolite in the Shyok suture zone, Ladakh, NW India: Implications for the tectonic evolution of the Northwest Himalaya: Lithos, v. 155, p. 81-93.

Thieuloy, J. P., Reuber, I., Mascle, G., Loan, M. F., Franck, P., and Colchen, M., 1990, Decouverte d'Oxytropidoceras dans la serie volcano-sedimentaire de Dras (Ladakh); consequences geodynamiques: Bulletin de la Société Géologique de France, v. 6, no. 4, p. 583-587.

Thomas, W. A., 2011, Detrital-zircon geochronology and sedimentary provenance: Lithosphere, v. 3, no. 4, p. 304-308.

Underwood, M., Ballance, P. F., Clift, P. D., Hiscott, R. N., Marsaglia, K. M., Pickering, K., and Reid, R. P., 1995, Sedimentation in forearc basins, trenches, and collision zones of the western Pacific: a summary of results from the Ocean Drilling Program: Active Margins and Marginal Basins of the Western Pacific: American Geophysical Union, Geophysical Monograph, v. 88, p. 315-354.

Upadhyay, R., Frisch, W., and Siebel, W., 2008, Tectonic implications of new U–Pb zircon ages of the Ladakh batholith, Indus suture zone, northwest Himalaya, India: Terra Nova, v. 20, no. 4, p. 309-317.

Upadhyay, R., Kar, R., and Sinha, A. K., 2004, Palynological evidence for the Palaeocene evolution of the forearc basin, Indus Suture Zone, Ladakh, India: Terra Nova, v. 16, no. 4, p. 216-225.

Upadhyay, R., and Sinha, A. K., 1998, Tectonic evolution of Himalayan Tethys and subsequent Indian plate subduction along Indus Suture Zone: Proceedings: Indian National Science Academy Part A, v. 64, p. 659-683.

van Haver, T., 1984, Etude stratigraphique, sédimentologique et structurale d'un bassin d'avant arc: exemple du bassin de l'Indus, Ladakh, Himalaya.

van Hinsbergen, D. J., Lippert, P. C., Li, S., Huang, W., Advokaat, E. L., & Spakman, W., 2019, Reconstructing Greater India: Paleogeographic, kinematic, and geodynamic perspectives. *Tectonophysics*, *760*, 69-94.

Walsh, J. M., Buckman, S., Nutman, A. P., and Zhou, R., 2019, Age and provenance of the Nindam Formation, Ladakh, NW Himalaya: evolution of the intraoceanic dras arc before collision with India: Tectonics, v. 38, no. 8, p. 3070-3096.

-, 2020, The significance of Upper Jurassic felsic volcanic rocks within the incipient, intraoceanic Dras Arc, Ladakh, NW Himalaya: Gondwana Research.

Wang, R., Xia, B., Zhou, G., Zhang, Y., Yang, Z., Li, W., Wei, D., Zhong, L., and Xu, L., 2006, SHRIMP zircon U-Pb dating for gabbro from the Tiding ophiolite in Tibet: Chinese Science Bulletin, v. 51, no. 14, p. 1776-1779.

Warren, C. J., Parrish, R. R., Searle, M. P., and Waters, D. J., 2003, Dating the subduction of the Arabian continental margin beneath the Semail ophiolite, Oman: Geology, v. 31, no. 10, p. 889-892.

Weinberg, R. F., and Dunlap, W. J., 2000, Growth and deformation of the Ladakh Batholith, Northwest Himalayas: implications for timing of continental collision and origin of calc-alkaline batholiths: The Journal of Geology, v. 108, no. 3, p. 303-320.

Wen, D.-R., Liu, D., Chung, S.-L., Chu, M.-F., Ji, J., Zhang, Q., Song, B., Lee, T.-Y., Yeh, M.-W., and Lo, C.-H., 2008, Zircon SHRIMP U–Pb ages of the Gangdese Batholith and

implications for Neotethyan subduction in southern Tibet: Chemical Geology, v. 252, no. 3-4, p. 191-201.

White, L. T., Ahmad, T., Ireland, T. R., Lister, G. S., and Forster, M. A., 2011, Deconvolving episodic age spectra from zircons of the Ladakh Batholith, northwest Indian Himalaya: Chemical Geology, v. 289, no. 3, p. 179-196.

White, N. M., Parrish, R. R., Bickle, M. J., Najman, Y. M. R., Burbank, D., & Maithani, A., 2001, Metamorphism and exhumation of the NW Himalaya constrained by U–Th–Pb analyses of detrital monazite grains from early foreland basin sediments. *Journal of the Geological Society*, *158*(4), 625-635

Wiedenbeck, M., Alle, P., Corfu, F., Griffin, W., Meier, M., Oberli, F. v., Quadt, A. v., Roddick, J., and Spiegel, W., 1995, Three natural zircon standards for U-Th-Pb, Lu-Hf, trace element and REE analyses: Geostandards newsletter, v. 19, no. 1, p. 1-23.

Williams, I. S., 1998, U-Th-Pb geochronology by ion microprobe: Applications of microanalytical techniques to understanding mineralizing processes, p. 1-35.

Winchester, J. A., and Floyd, P. A., 1977, Geochemical discrimination of different magma series and their differentiation products using immobile elements: Chemical Geology, v. 20, p. 325-343.

Wood, D. A., 1980, The application of a Th-Hf-Ta diagram to problems of tectonomagmatic classification and to establishing the nature of crustal contamination of basaltic lavas of the British Tertiary Volcanic Province: Earth and Planetary Science Letters, v. 50, no. 1, p. 11-30.

Wu, F.-Y., Ji, W.-Q., Liu, C.-Z., and Chung, S.-L., 2010, Detrital zircon U–Pb and Hf isotopic data from the Xigaze fore-arc basin: constraints on Transhimalayan magmatic evolution in southern Tibet: Chemical Geology, v. 271, no. 1-2, p. 13-25.

Wu, F. Y., Clift, P. D., and Yang, J. H., 2007, Zircon Hf isotopic constraints on the sources of the Indus Molasse, Ladakh Himalaya, India: Tectonics, v. 26, no. 2.

Xia, B., Li, J., Xu, L., Wang, R., and Yang, Z., 2011, Sensitive high resolution ion micro-probe U-Pb zircon geochronology and geochemistry of mafic rocks from the Pulan-Xiangquanhe ophiolite, Tibet: constraints on the evolution of the Neo-tethys: Acta Geologica Sinica-English Edition, v. 85, no. 4, p. 840-853.

Xiao, W., Windley, B., Badarch, G., Sun, S., Li, J., Qin, K., and Wang, Z., 2004, Palaeozoic accretionary and convergent tectonics of the southern Altaids: implications for the growth of Central Asia: Journal of the Geological Society, v. 161, no. 3, p. 339-342.

Yamamoto, H., Kobayashi, K., Nakamura, E., Kaneko, Y., and Kausar, A. B., 2005, U-Pb zircon dating of regional deformation in the lower crust of the Kohistan Arc: International Geology Review, v. 47, no. 10, p. 1035-1047.

Yin, A., and Harrison, T. M., 2000, Geologic evolution of the Himalayan-Tibetan orogen: Annual Review of Earth and Planetary Sciences, v. 28, no. 1, p. 211-280.

Zhai, Q.-g., Jahn, B.-m., Su, L., Wang, J., Mo, X.-X., Lee, H.-y., Wang, K.-l., and Tang, S., 2013, Triassic arc magmatism in the Qiangtang area, northern Tibet: Zircon U–Pb ages, geochemical and Sr–Nd–Hf isotopic characteristics, and tectonic implications: Journal of Asian Earth Sciences, v. 63, p. 162-178.

Zhang, C., Liu, C.-Z., Wu, F.-Y., Zhang, L.-L., and Ji, W.-Q., 2016, Geochemistry and geochronology of mafic rocks from the Luobusa ophiolite, South Tibet: Lithos, v. 245, p. 93-108.

Zhang, L.-L., Liu, C.-Z., Wu, F.-Y., Ji, W.-Q., and Wang, J.-G., 2014, Zedong terrane revisited: An intra-oceanic arc within Neo-Tethys or a part of the Asian active continental margin?: Journal of Asian Earth Sciences, v. 80, p. 34-55.

Zhang, Q., Buckman, S., Bennett, V. C., and Nutman, A., 2019, Inception and early evolution of the Ordovician Macquarie Arc of Eastern Gondwana margin: Zircon U-Pb-Hf evidence from the Molong Volcanic Belt, Lachlan Orogen: Lithos, v. 326, p. 513-528.

Zhang, Q., Nutman, A., Buckman, S., and Bennett, V. C., 2020, What is underneath the juvenile Ordovician Macquarie Arc (eastern Australia)? A question resolved using Silurian intrusions to sample the lower crust: Gondwana Research, v. 81, p. 362-377.

Zhang, Q.-H., Ding, L., Cai, F.-L., Xu, X.-X., Zhang, L.-Y., Xu, Q., and Willems, H., 2011, Early Cretaceous Gangdese retroarc foreland basin evolution in the Selin Co basin, central Tibet: evidence from sedimentology and detrital zircon geochronology: Geological Society, London, Special Publications, v. 353, no. 1, p. 27-44.

Zhang, R., Xu, W., Guo, J., Zong, K., Cai, H., and Yuan, H., 2007, Zircon U-Pb and Hf isotopic composition of deformed granite in the southern margin of the Gangdese belt, Tibet:

Evidence for Early Jurassic subduction of Neo-Tethyan oceanic slab: Acta Petrologica Sinica, v. 23, no. 6, p. 1347-1353.

Zhang, Q., Willems, H., Ding, L., Gräfe, K. U., & Appel, E., 2012, Initial India-Asia continental collision and foreland basin evolution in the Tethyan Himalaya of Tibet: Evidence from stratigraphy and paleontology. *The Journal of Geology*, *120*(2), 175-189.

Zhong, L., 2006, Petrology, Geochemistry and Tectonic Setting of the Luobusa Ophiolite, Southern Xizang (Tibet): Guangzhou Inst. Geochem. Chin. Acad. Sci. Dr. Thesis, p. 1-100.

Zhong, L., Xia, B., Zhang, Y., Wang, R., Wei, D., and Yang, Z., 2006, SHRIMP age determination of the diabase in Luobusa ophiolite, southern Xizang (Tibet): Geological Review, v. 52, no. 2, p. 224-229.

Zhou, R., Aitchison, J. C., Lokho, K., Sobel, E. R., Feng, Y., and Zhao, J.-x., 2020, Unroofing the Ladakh Batholith: constraints from autochthonous molasse of the Indus Basin, NW Himalaya: Journal of the Geological Society.

Zhou, S., Mo, X., Mahoney, J., Zhang, S., Guo, T., and Zhao, Z., 2002, Geochronology and Nd and Pb isotope characteristics of gabbro dikes in the Luobusha ophiolite, Tibet: Chinese Science Bulletin, v. 47, no. 2, p. 144-147.

Zhou, X., Li, Z.-H., Gerya, T. V., Stern, R. J., Xu, Z., and Zhang, J., 2018, Subduction initiation dynamics along a transform fault control trench curvature and ophiolite ages: Geology, v. 46, no. 7, p. 607-610.

Zhou, Y., Cheng, X., Yu, L., Yang, X., Su, H., Peng, X., Xue, Y., Li, Y., Ye, Y., and Zhang, J., 2016, Paleomagnetic study on the Triassic rocks from the Lhasa Terrane, Tibet, and its paleogeographic implications: Journal of Asian Earth Sciences, v. 121, p. 108-119.

Zhu, D.-C., Mo, X.-X., Niu, Y., Zhao, Z.-D., Wang, L.-Q., Liu, Y.-S., and Wu, F.-Y., 2009a, Geochemical investigation of Early Cretaceous igneous rocks along an east–west traverse throughout the central Lhasa Terrane, Tibet: Chemical Geology, v. 268, no. 3-4, p. 298-312.

Zhu, D.-C., Zhao, Z.-D., Niu, Y., Dilek, Y., and Mo, X.-X., 2011a, Lhasa terrane in southern Tibet came from Australia: Geology, v. 39, no. 8, p. 727-730.

Zhu, D.-C., Zhao, Z.-D., Niu, Y., Mo, X.-X., Chung, S.-L., Hou, Z.-Q., Wang, L.-Q., and Wu, F.-Y., 2011b, The Lhasa Terrane: record of a microcontinent and its histories of drift and growth: Earth and Planetary Science Letters, v. 301, no. 1-2, p. 241-255.

Zhu, D.-C., Zhao, Z.-D., Pan, G.-T., Lee, H.-Y., Kang, Z.-Q., Liao, Z.-L., Wang, L.-Q., Li, G.-M., Dong, G.-C., and Liu, B., 2009b, Early cretaceous subduction-related adakite-like rocks of the Gangdese Belt, southern Tibet: products of slab melting and subsequent melt–peridotite interaction?: Journal of Asian Earth Sciences, v. 34, no. 3, p. 298-309.

Zyabrev, S., Aitchison, J., Abrajevitch, A., Davis, A., and Luo, H., 2003, Precise radiolarian age constraints on the timing of ophiolite generation and sedimentation in the Dazhuqu terrane, Yarlung–Tsangpo suture zone, Tibet: Journal of the Geological Society, v. 160, no. 4, p. 591-599.

Zyabrev, S. V., Kojima, S., and Ahmad, T., 2008, Radiolarian biostratigraphic constraints on the generation of the Nidar ophiolite and the onset of Dras arc volcanism: Tracing the evolution of the closing Tethys along the Indus–Yarlung–Tsangpo suture: Stratigraphy, v. 5, no. 1, p. 99-112.